



ÉCOLE
POLYTECHNIQUE
DE BRUXELLES

UNIVERSITÉ LIBRE DE BRUXELLES

Numerical Investigation of Hypersonic
Boundary-Layer Stability and Transition
in the presence of Ablation Phenomena

Thesis presented by Fernando MIRÓ MIRÓ

with a view to obtaining the PhD Degree in Engineering Sciences and
Technology ("Docteur en Sciences de l'Ingénieur et Technologie")
Academic year 2019-2020

Supervisor: Prof. Gérard DEGREZ
Co-supervisor: Dr. Fabio PINNA

Thesis jury:

Herman DECONINCK (Université libre de Bruxelles, President)
Alessandro PARENTE (Université libre de Bruxelles, Secretary)
Helen L. REED (Texas A&M University)
Thierry MAGIN (von Karman Institute for Fluid Dynamics)
Rolf RADESPIEL (Technische Universität Braunschweig)



von KARMAN INSTITUTE
FOR FLUID DYNAMICS



Numerical Investigation of Hypersonic Boundary-Layer Stability and Transition in the presence of Ablation Phenomena

Fernando Miró Miró



Thesis presented in order to obtain the degree of
Doctor of Philosophy in Engineering Sciences
Université libre de Bruxelles
April 2020



Université Libre de Bruxelles
École Polytechnique de Bruxelles
Département d'Aéro-thermo-mécanique



von KARMAN INSTITUTE
FOR FLUID DYNAMICS

von Karman Institute for Fluid Dynamics
Aeronautics and Aerospace Department

Supervisors:

Dr. Fabio Pinna (von Karman Institute for Fluid Dynamics, Belgium)
Prof. Gérard Degrez (Université Libre de Bruxelles, Belgium)

Doctoral Committee:

Prof. Herman Deconinck (Université Libre de Bruxelles, President)
Prof. Alessandro Parente (Université Libre de Bruxelles, Secretary)
Prof. Helen L. Reed (Texas A&M University, USA)
Prof. Thierry E. Magin (von Karman Institute for Fluid Dynamics, Belgium)
Prof. Rolf Radespiel (Technische Universität Braunschweig, Germany)

von Karman Institute for Fluid Dynamics
Aeronautics and Aerospace Department

Waterloosesteenweg 72, 1640 Sint-Genesius-Rode
Phone: +32 359 96 11, <https://www.vki.ac.be>

©2020 by Fernando Miró Miró, PhD candidate
D/yyyy/yyyy/xx, T. Magin, Editor-in-Chief
Published by the von Karman Institute for Fluid Dynamics with permission.

All rights reserved. Permission to use a maximum of two figures or tables and brief excerpts in scientific and educational works is hereby granted provided the source is acknowledged. This consent does not extend to other kinds of copying and reproduction, for which permission requests should be addressed to the Director of the von Karman Institute.

ISBN xxx-x-xxxxx-xxx-x

“All models are wrong, but some are useful.”

George E. P. Box, 1976.

Foreword

Acknowledgment

The importance of the contributions to this dissertation made by people other than myself is so big that it almost feels wrong to sign it off with only my name. First of all, a good starting point is paramount to allow for a good final result, or borrowing Newton's words: "*if I have seen further it is by standing on the shoulders of giants*". I must therefore start by acknowledging the outstanding work done by F. Pinna, K. Groot and many others, and that brought the VESTA toolkit to the perfect point from which to launch this work.

On the personal side, most of the responsibility of the starting point belongs to my family, whom I must thank for teaching me the most important lessons in life.

Regarding the actual work carried out during these past years, I must wholeheartedly thank my adviser Fabio Pinna for his excellent guidance through these turbulent waters. Aside from the uncountable technical lessons I learned from him, his serious and professional working philosophy is probably the most valuable take-away from these years. I must also thank the rest of the VESTA team, who created an excellent inspiring, challenging and fun working environment that allowed us to reach the goals that we targeted. Specially to Ivan Padilla and Ludovico Zanus, with whom I have had the honor of working very closely.

I also have to give a very special thanks to Helen Reed's team at Texas A&M: Ethan Beyak, Koen Groot, Alex Moyes, Travis Kocian, Andrew Riha and Daniel Mullen. Those six months really marked a before and an after in my work. Who would have thought, that long night that we coded the very first version of DEKAF, that it would grow to be the 27 000-line-plus monster that it now is? Without it, this dissertation would be a shadow of what it is. Aside from the development of DEKAF, and the many technical lessons I learned from y'all, you were crucial in keeping me motivated to do this work. In the darkest days of these four years, you made me recover the passion and enthusiasm on research and in knowledge for the sake of knowledge, which is probably one of the most useful assets one can have.

I want to thank also the mutation⁺⁺ team (Thierry Magin, JB Scoggins, Georgios Bellas, Bruno Dias, and many others) and Alessandro Turchi for their invaluable expert advice in themophysical modeling and for their patience.

I also learned a lot from the other collaborations I have had the pleasure of tak-

ing part in. I therefore want to thank the VKI experimental transition group (Tamas Regert, Davide Masutti, Guillaume Grossir, Pieter Dehairs, Nicholas Martin and Maria Gkolia), who helped to make us keep a grasp of reality and not wander too far into our theoretical fantasy world. I want to also thank researchers from other institutions for their input during these collaborations: Viola Wartemann and Alexander Wagner from DLR, Paolo Barbante from Politecnico di Milano, Olaf Marxen from the University of Surrey, Heather Kline from NASA Langley, Miguel Hermanns from Politécnica de Madrid, and Carleton Knisely from LLNL.

The rest of the VKI also deserves mention here, since its unique multidisciplinary work environment constitutes an invaluable source of inspiration.

However, there is more to life than work, which is why I must absolutely thank Milo, Lovi, and the rest of the Brussels crew, who made sure that I was never bored and that I did not lose my mind during these four years. As someone once told me “the way to solve problems is to think about them very very hard, and then clear your mind from them”. The times they pulled me out of the office to go partying or to go on a trip to some corner of the world were absolutely crucial to the second part of this process. Aside from that, I must also thank the rue-de-Pologne family, for not letting me starve, and to yerba mate Rosamonte for keeping me awake, during the last month and a half of thesis-writing madness.

Finally, I must thank the Belgian FNRS for making this work possible, with the financing provided within the framework of the FRIA fellowship.

Reader's note

This dissertation is written in the form that I would have liked to encounter when I started working in the field – constantly thinking of what “*Fernando 2.0*” will need. This is done with the hopes that whoever continues working on these problems can build upon it with the minimal possible effort.

The whole dissertation shares a unified nomenclature, with dimensional quantities having the units specified therein. The only parts of it featuring non-dimensional quantities are Eqs. 8.1-8.5 and app. I.

The author kindly asks the reader to report any eventual typos and/or errors to fernando.miro.miro@vki.ac.be. The most up-to-date version of this dissertation can be found in the researchgate page:

https://www.researchgate.net/profile/Fernando_Miro_Miro/research.

*Brussels, April 2020
Fernando Miró Miró*

Table of Contents

I Framework

1 Context and motivation	1-1
1.1 Space exploration	1-1
1.2 Atmospheric entry	1-2
1.3 TPS ablation	1-4
1.4 Boundary-layer transition	1-5
1.5 Thesis scope	1-7
References	1-10
2 Thermophysical framework	2-1
2.1 Thermodynamic flow assumptions	2-1
2.2 Gas mixtures and reactions	2-3
2.3 Flow equations	2-5
2.3.1 Thermo-chemical non-equilibrium (TCNE)	2-7
2.3.2 Chemical non-equilibrium (CNE) yet in thermal equilibrium	2-10
2.3.3 Local thermo-chemical equilibrium with elemental demixing (LTEED)	2-10
2.3.4 Local thermo-chemical equilibrium with constant elemental composition (LTE)	2-13
2.3.5 Thermal non-equilibrium yet chemically frozen (TNE) . .	2-14
2.3.6 Thermo-chemically frozen gas (TCFG)	2-15
2.3.7 Thermally perfect and chemically frozen gas (TPG) . . .	2-15
2.3.8 Calorically perfect gas (CPG)	2-16
References	2-17
3 Stability and transition	3-1
3.1 Linear theories	3-4
3.1.1 LDNS	3-4
3.1.2 Tri-global stability	3-5
3.1.3 Bi-global stability or 2D-LST	3-5
3.1.4 Linear stability theory	3-7
3.1.5 Linear parabolized stability	3-8
3.2 e^N method	3-9

3.3 Non-linear theories	3-10
3.4 Adjoint theories	3-11
3.5 Physical implications of the choice of the wave parameters	3-11
3.6 Instability mechanisms	3-12
References	3-14
4 Gas properties	4-1
4.1 Thermal properties	4-5
4.2 Transport properties	4-8
4.2.1 Viscosity and thermal conductivity	4-8
4.2.1.1 Blottner-Eucken-Wilke model	4-9
4.2.1.2 Gupta-Wilke model	4-9
4.2.1.3 Sutherland-Eucken-Wilke and Sutherland-Wilke models	4-10
4.2.1.4 Chapman-Enskog model	4-10
4.2.1.5 Brokaw and Yos models	4-11
4.2.2 Diffusion models	4-12
4.2.3 Collisional models	4-16
4.3 Chemical properties	4-21
4.4 Gas-surface interaction model	4-25
4.5 Energy exchange terms	4-28
4.5.1 Vibrational source term	4-29
4.5.2 Electronic source term	4-30
4.5.3 Electron source term	4-30
4.6 Thermodynamic derivatives	4-32
4.6.1 Thermodynamic derivatives of the Chapman-Enskog matrix system	4-34
4.6.2 Thermodynamic derivatives of the Stefan-Maxwell matrix system	4-35
References	4-36
5 Laminar base flow	5-1
5.1 Boundary-layer equations and their self-similar solutions	5-1
5.1.1 CNE boundary-layer equations	5-5
5.1.2 LTEED boundary-layer equations	5-6
5.1.3 LTE boundary-layer equations	5-8
5.1.4 TNE boundary-layer equations	5-8
5.1.5 TCFG boundary-layer equations	5-9
5.1.6 TPG and CPG boundary-layer equations	5-9
5.1.7 Axi-symmetric boundary layers – the Probstein-Elliott transformation	5-10
5.2 Base-flow and stability hypotheses	5-12
5.3 Base-flow inaccuracy propagation to stability predictions	5-13
5.3.1 Base-flow grid convergence	5-14
5.3.2 Interpolation errors	5-15

5.3.3	Stability grid convergence	5-15
5.3.4	Base-flow-induced errors	5-17
5.3.5	The importance of performing joint base-flow-stability grid convergence studies	5-20
5.3.6	Conclusions	5-20
	References	5-23
6	Boundary conditions	6-1
6.1	Wall boundary	6-1
6.1.1	Blowing boundary condition	6-2
6.1.1.1	Porous stability boundary condition (PSBC) . .	6-3
6.1.1.2	Ablation-mimicking continuously-blowing sta- bility boundary condition (AMSCB)	6-5
6.1.2	Thermal boundary conditions	6-6
6.1.3	Concentration boundary conditions	6-7
6.1.4	Perturbation compatibility boundary conditions	6-8
6.2	Freestream boundary	6-9
6.2.1	Shock boundary condition	6-11
	References	6-13

II Tools

7	DEKAF flow solver	7-1
7.1	Shock-jump relations	7-2
7.2	Inviscid non-equilibrium 1-D solver	7-5
7.3	Numerical method	7-6
7.3.1	Mappings	7-9
7.3.2	Initial guess	7-11
7.4	Exploiting spectral accuracy through the GICM interpolation . .	7-13
7.5	Implementation	7-15
7.6	Verification	7-17
7.6.1	CPG non-bleeding flat-plates	7-17
7.6.2	CPG bleeding flat-plates	7-17
7.6.3	Incompressible Falkner-Skan-Cooke equation	7-19
7.6.4	CPG cone	7-21
7.6.5	CNE Mach 10 flat plate	7-22
7.6.6	CNE Oxygen mixture	7-22
7.6.7	6-degree CPG, CNE, and LTE wedge	7-23
7.6.8	20-degree CPG, TPG, and CNE wedge at Mach 18	7-26
7.6.9	15-degree CNE wedge at Mach 35	7-26
7.6.10	TNE flat plate	7-28
7.6.11	10-degree CPG, CNE and LTE cone at Mach 25	7-29
7.6.12	State-of-the-art properties	7-32
7.7	Summary	7-32

References	7-34
8 VESTA's Automatic Derivation and Implementation Tool	8-1
8.1 Stability equations	8-2
8.1.1 Non-dimensionalization convention	8-3
8.1.2 Treatment of the spatial derivatives of the dependent perturbation quantities Q'	8-6
8.1.3 Implementation	8-7
8.1.3.1 Derivation options	8-9
8.1.3.2 Provisional variables	8-11
8.1.3.3 In-line derivatives	8-13
8.1.4 Verification	8-13
8.1.4.1 CPG flow assumption	8-14
8.1.4.2 Porous boundary condition	8-14
8.1.4.3 LTE flow assumption	8-15
8.1.4.4 Shock boundary condition	8-16
8.1.4.5 CNE flow assumption for 2 species	8-18
8.1.4.6 TCNE and CNE flow assumption for 5 species	8-18
8.1.4.7 TCNE flow assumption for 5 species	8-19
8.1.4.8 Orthocurvilinear coordinate system	8-19
8.2 Gas properties	8-21
8.3 Summary	8-24
References	8-25

III Results

9 Surface outgassing and transition	9-1
9.1 Experimental-numerical investigation of an outgassing cone at Mach 6	9-2
9.1.1 Experimental setup	9-2
9.1.2 Numerical setup	9-4
9.1.3 Validation of the porous boundary condition	9-5
9.1.4 Interpretation of the experimental results based on the LST analysis	9-7
9.1.5 Evaluation of non-parallel effects	9-10
9.1.6 Conclusions	9-11
9.2 Sensitivity of instabilities to the composition of the injection gas	9-12
9.2.1 Test conditions and gas modeling	9-13
9.2.2 Case 1: self-similar multi-species blowing	9-15
9.2.2.1 Span-wise wavenumber sweep	9-23
9.2.2.2 Transport model comparison	9-23
9.2.2.3 PSBC-HSBC comparison	9-26
9.2.3 Cases 2-5: non-self-similar He blowing	9-26
9.2.4 Case 5p with Ar blowing	9-34

9.2.5 Conclusions	9-34
9.3 Sensitivity of instabilities to the wall boundary condition	9-36
9.3.1 Baseline case – homogeneous condition	9-37
9.3.2 Porous condition for case O	9-38
9.3.3 Cases M ⁻ , M ⁺ , O, T ⁻ , and T ⁺ for all boundary conditions .	9-41
9.3.4 Porous stabilizing/destabilizing maps and experimental re- sult analysis	9-45
9.3.5 Conclusions	9-47
References	9-49
10 High-enthalpy effects and transition	10-1
10.1 Gas modeling influence on stability predictions	10-1
10.1.1 Case 1 – influence of the transport model	10-2
10.1.2 Case 2 – influence of the diffusion model	10-5
10.1.3 Cases 1 and 2 – influence of the collision model	10-7
10.1.4 Case 3 – influence of the chemical equilibrium model . .	10-11
10.1.5 Case 4 – influence of the chemical kinetic model	10-11
10.1.6 Case 1 – effects of transport modeling on perturbation terms	10-15
10.1.7 Mode shapes	10-15
10.1.8 Conclusions	10-15
10.2 Enhanced and weakened diffusion fluxes	10-19
10.3 Flow-assumption adequacy for different earth entry flow regimes .	10-22
10.3.1 Laminar base-flow field	10-23
10.3.2 LST N-factor curves	10-27
10.3.3 LPSE N-factor curves	10-28
10.3.4 Conclusions	10-28
10.4 Ionization and dissociation	10-30
10.4.1 Laminar base flow	10-32
10.4.2 LST analyses	10-37
10.4.2.1 Consistent base-flow and perturbation hypotheses	10-37
10.4.2.2 Base-flow cooling, diffusion and chemical source term	10-41
10.4.2.3 Equilibrium-perturbation hypothesis	10-44
10.4.2.4 Supersonic modes	10-47
10.4.2.5 Transport model in CPG	10-50
10.4.3 Free-stream boundary condition	10-51
10.4.4 Conclusions	10-51
References	10-55
11 Decoupling ablation-transition problems	11-1
11.1 Flow assumptions	11-2
11.2 Boundary conditions	11-3
11.3 Results	11-5
11.3.1 Wall profiles from the CNE11-Abl case	11-7
11.3.2 Mass injection effects	11-8

11.3.3	Vibrational excitation and air chemistry effects	11-14
11.3.4	Surface chemistry effects	11-18
11.3.5	CPG assumption with different transport models	11-21
11.3.6	Influence of the transport models on the fully-ablating case	11-22
11.3.7	N -factor budgets of the physical phenomena	11-23
11.3.8	Linearized Rankine-Hugoniot relations	11-26
11.4	Conclusions	11-26
	References	11-30

12	Conclusions	12-1
	References	12-9

IV Appendices

A	General relations between species and mixture quantities	A-1
	References	A-4
B	Equilibrium system of equations	B-1
B.1	Equilibrium-composition derivatives with respect to temperature, pressure or elemental fractions	B-2
B.2	The air-5 equilibrium system	B-6
B.3	The air-11 equilibrium system	B-7
B.4	Verification	B-8
	References	B-8
C	Coefficients for the transport properties	C-1
C.1	Coefficients for the polynomial approximation of Chapman- Enskog's theory for transport properties	C-1
C.2	Coefficients for Brokaw and Yos' simplification of Chapman & Enskog's theory for transport properties	C-3
	References	C-4
D	Requirements for the existence of self-similar solutions to the boundary-layer equations	D-1
D.1	CPG with a viscosity power law and with $q_e = q_e(\xi)$	D-2
D.2	CPG with other viscosity laws and $q_e = q_e(\xi)$	D-5
D.3	TPG with $q_e = q_e(\xi)$	D-6
D.4	LTE and LTEED with $q_e = q_e(\xi)$	D-6
D.5	TCFG with $q_e = q_e(\xi)$	D-7
D.6	Surface thermal boundary condition	D-7
D.7	Surface mass injection	D-8
D.8	y -vector rebuilding for $\beta_H \neq 0$	D-8
D.9	Summary	D-9
	References	D-10

E Rebuilding of the wall-normal velocity from a boundary-layer solution	E-1
F Base-flow wall-normal velocity treatment in LST when using the AMSBC	F-1
References	F-2
G Integration matrices of arbitrary-order accuracy	G-1
References	G-2
H Neutral curve Newton-Raphson solver	H-1
References	H-3
I Non-dimensional form of the boundary conditions	I-1
J Gas mixtures and reaction rate constants	J-1
J.1 Air-2	J-1
J.2 Air-2-He	J-1
J.3 Air-2-Ne	J-1
J.4 Air-2-Ar	J-1
J.5 Air-2-CO ₂	J-2
J.6 O-2-Bortner	J-2
J.7 Air-5-Park85	J-2
J.8 Air-5-Park90	J-3
J.9 Air-5-Park01	J-4
J.10 Air-5-Stuckert	J-5
J.11 Air-5-Bortner	J-6
J.12 Air-11-Park93	J-8
J.13 AirC-6-Mortensen	J-11
J.14 AirC-11-Mortensen	J-12
References	J-16
K Species-parameters tables	K-1
K.1 Thermal parameters	K-1
K.2 Transport parameters	K-12
K.3 Collision parameters	K-14
K.3.1 Stuckert's [16] curve fits (Eq. 4.56)	K-14
K.3.2 Gupta <i>et al.</i> 's [15] curve fits (Eq. 4.55)	K-16
K.3.3 Novel curve fits (Eq. 4.57) to recent data	K-18
K.3.3.1 Air neutral species (N, O, NO, N ₂ , O ₂)	K-18
K.3.3.2 Air neutral (N, O, NO, N ₂ , O ₂) and charged species (N ⁺ , O ⁺ , NO ⁺ , N ₂ ⁺ , O ₂ ⁺)	K-20
K.3.3.3 Air neutral species (N, O, NO, N ₂ , O ₂) and argon (Ar)	K-26
K.3.3.4 Air neutral species (N, O, NO, N ₂ , O ₂) and carbon species (CO, CO ₂ , CN, C, C ₂ , C ₃)	K-27
References	K-31

L Collision-integral fits	L-1
L.1 Air collisions of neutral-to-neutral species (N, O, NO, N ₂ , O ₂)	L-1
L.2 Air collisions of charged-to-charged species (N ⁺ , O ⁺ , NO ⁺ , N ₂ ⁺ , O ₂ ⁺ , e ⁻)	L-4
L.3 Air collisions of ion-to-neutral species (N ⁺ , O ⁺ , NO ⁺ , N ₂ ⁺ , O ₂ ⁺ to N, O, NO, N ₂ , O ₂)	L-7
L.4 Air collisions of electron-to-neutral species (e ⁻ to N, O, NO, N ₂ , O ₂)	L-12
L.5 Air collisions of argon-to-neutral species (Ar to N, O, NO, N ₂ , O ₂)	L-14
L.6 Collisions of neutral air and carbon species (N, O, NO, N ₂ , O ₂ and CO, CO ₂ , CN, C, C ₂ , C ₃)	L-15
References	L-20
M Publications	M-1
M.1 Journal papers	M-1
M.2 Conference papers	M-6
References	M-13

Nomenclature

Acronyms

2D-LST	Two-dimensional linear stability theory
3D-LPSE	Three-dimensional parabolized stability equations
3D-NPSE	Three-dimensional non-linear parabolized stability equations
Abl	Full ablating surface-chemistry model
AblBwCstT	Ablation blowing (same mass flow as in the Abl case but without the surface chemistry) and constant temperature
AblT	Ablation with fixed temperature (same as in the Abl case but without the surface energy balance)
AblTBw	Ablation temperature and blowing (same as in the Abl case but without the surface chemistry)
ADIT	Automatic derivation and implementation tool
ADNS	Adjoint direct numerical simulations
AMSBC	Ablation-mimicking stability boundary condition
ASBC	Ablating stability boundary condition (full surface chemistry model)
ATSBC	Ablating isothermal stability boundary condition (without the linearized surface energy balance)
BC	Boundary condition
BEW	Blottner-Eucken-Wilke transport model
BiG	Bi-global stability theory
BL	Boundary layer
CAS	Computer algebra system

CBL	Compressible boundary layer
CE	Chapman & Enskog's transport model
CF	Crossflow waves
CGL	Chebyshev-Gauss-Lobatto
CNE	Chemical non-equilibrium, yet in thermal equilibrium ($\tau_{vib} \ll \tau_{chem} \sim \tau_{flow}$)
CPG	Calorically perfect gas
DEKAF	Digits by Ethan, Koen, Alex and Fernando
DNS	Direct numerical simulations
DPLR	Data-parallel line relaxation
EBAD	Effective binary ambipolar diffusion
EBD	Effective binary diffusion
FD	Finite difference (on an equispaced grid)
FDq	Finite differences of order q (based on non-uniform grid-point distributions)
FP	Flat plate
GICM	Groot-Illingworth-Chebyshev-Malik
GV	Görtler vortices
GW	Gupta-Wilke transport model
HSBC	Homogeneous stability boundary condition (Eq. 6.5)
ISA	International Standard Atmosphere
IXV	Intermediate experimental vehicle
LDNS	Linearized direct numerical simulations
LPSE	Linear parabolized stability equations
LST	Linear stability theory
LTEED	Local thermo-chemical equilibrium with elemental demixing ($\tau_{chem} \sim \tau_{vib} \ll \tau_{flow}$ and $\mathcal{X}_E \neq cst$)
LTE	Local thermo-chemical equilibrium with constant elemental composition ($\tau_{chem} \sim \tau_{vib} \ll \tau_{flow}$ and $\mathcal{X}_E = cst$)

M1	First-mode waves
M2	Second-mode waves
McB	McBride's NASA-7 and NASA-9 thermal model
noBw	No blowing
NPSE	Non-linear parabolized stability equations
ODE	Ordinary differential equation
PLIF	Planar-laser-induced fluorescence
PNS	Parabolized Navier-Stokes
PSBC	Porous stability boundary condition
PSD	Power spectral density
RESBC	Radiative-equilibrium stability boundary condition
RK4	Runge-Kutta method of 4 th order
RRHO	Rigid rotor and harmonic oscillator thermal model
SCEBAD	Self-consistent effective binary ambipolar diffusion
SCEBD	Self-consistent effective binary diffusion
SEW	Sutherland-Eucken-Wilke transport model
SM	Stefan-Maxwell diffusion theory
SSBw	Self-similar blowing (constant \bar{f}_w)
SSM	Supersonic-mode waves
SW	Sutherland-Wilke transport model
TCFG	Thermo-chemically frozen gas ($\tau_{chem} \sim \tau_{vib} \gg \tau_{flow}$)
TCNE	Thermo-chemical non-equilibrium ($\tau_{chem} \sim \tau_{vib} \sim \tau_{flow}$)
TNE	Thermal non-equilibrium, yet chemically frozen gas ($\tau_{chem} \gg \tau_{vib} \sim \tau_{flow}$)
TPG	Thermally perfect gas - chemically frozen but in vibrational equilibrium ($\tau_{flow} \ll \tau_{chem} \& \tau_{flow} \gg \tau_{vib}$)
TPS	Thermal protection system
TriG	Tri-global stability theory

TS	Tollmien-Schlichting waves
TPP	Thermodynamic and transport properties
VESTA	VKI extensible stability and transition analysis

Roman Symbols

\mathcal{A}_E	Elemental thermodiffusion coefficient (Eq. 2.29a) [kg/m-s-K]
$\underline{\mathcal{A}}, \underline{\mathcal{B}}$	Matrices in the generalized eigenvalue problem [various]
a_0	Non-dimensional boundary-layer grouping variable (Eq. 5.5) [-]
a_1	Non-dimensional boundary-layer grouping variable (Eq. 5.5, 5.10 or 5.14) [-]
a_{1s}	Non-dimensional boundary-layer species-specific grouping variable (Eq. 5.5) [-]
a_2	Non-dimensional boundary-layer grouping variable (Eq. 5.5) [-]
$A_{B_{s\ell}^*}, \dots, F_{B_{s\ell}^*}$	Polynomial curve-fit coefficients for the ratio of collision integrals $B_{s\ell}^*$ [-]
a_D	Lagrange multiplier for the diffusion matrix subsystem [s ² /m]
a_{2E}^D	Non-dimensional boundary-layer elemental-diffusion grouping variable (Eq. 5.19 or 5.20) [-]
a_E^g	Non-dimensional boundary-layer elemental-diffusion grouping variable (Eq. 5.14) [-]
a_E^u	Non-dimensional boundary-layer elemental-diffusion grouping variable (Eq. 5.14) [-]
a_{EF}^y	Non-dimensional boundary-layer elemental-diffusion grouping variable (Eq. 5.14) [-]
a^k	Scaling parameter in Eq. 4.48, defined as the maximum value of k_s^E [C-s ² /kg-m ²]
$A_s^\kappa, \dots, E_s^\kappa$	Coefficients in Gupta <i>et al.</i> 's frozen thermal conductivity curve fits [-]
a^{Mk}	Coefficient in Malik's mapping (Eq. 7.16b) [[η]]

$a_{b rs}^{Mod}$	Weighing exponential coefficient in the backward reaction temperature [-]
$a_{f rs}^{Mod}$	Weighing exponential coefficient in the forward reaction temperature [-]
$A_s^\mu, B_s^\mu, C_s^\mu$	Coefficients in Blottner's viscosity curve fits [-]
A_n^P	Polynomial coefficients in Park's 1985 curve fits for the chemical equilibrium constant [K^{n-1}]
A_s^Q	Coefficient for property Q in Yos' transport model [1/[Q]]
A_{av}^Q	Averaged coefficient for property Q in Yos' transport model [1/[Q]]
A_r	Arrhenius pre-exponential constant (for property Q) [[Q]] $\text{K}^{-n_{Tr}}$]
a^{Rot}	Rotational energy integer: $\mathcal{L}/2$ for molecules, 0 for atoms [-]
$A_{s\ell}^*$	Ratio of collision integrals (Eq. 4.58a) [-]
$a_{e s}^\sigma$	Coefficient in the polynomial fitting for the effective electron-neutral energy exchange cross section of species s (Eq. 4.91) [m^2]
a_{sm}^{McB}	Coefficients in the polynomial approximation of the McB thermal model (Eq. 4.9) [K^{M-m+1}]
a_{v1}	Non-dimensional boundary-layer vibrational-electronic-electron grouping variable (Eq. 5.5) [-]
a_{v2}	Non-dimensional boundary-layer vibrational-electronic-electron grouping variable (Eq. 5.5) [-]
$a_{s\ell}^{Vib}$	Vibrational relaxation coefficients in Millikan & White's formula (Eq. 4.83) [$\text{K}^{1/3}$]
a_{1E}^y	Non-dimensional boundary-layer elemental-diffusion grouping variable (Eq. 5.18) [-]
$A_{\Omega_{s\ell}^{(i,j)}, \dots, F_{\Omega_{s\ell}^{(i,j)}}}$	Polynomial curve-fit coefficients for collision integral $\Omega_{s\ell}^{(i,j)}$ [-]
\mathcal{B}_E	Elemental barodiffusion coefficient (Eq. 2.29b) [kg/m-s-Pa]

B	Non-dimensional blowing mass-flow rate (Eqs. 9.1, 9.5, or 9.8) [-]
b^{Mk}	Coefficient in Malik's mapping (Eq. 7.16c) [-]
$B_{s\ell}^Q$	Coefficient for property Q in Yos' transport model [1/[Q]]
$B_{s\ell}^*$	Ratio of collision integrals (Eq. 4.58b) [-]
b_{e-s}^σ	Coefficient in the polynomial fitting for the effective electron-neutral energy exchange cross section of species s (Eq. 4.91) [m ² /K]
b_{sm}^{McB}	Coefficients in the polynomial approximation of the McB thermal model (Eq. 4.9) [K ^{1-m}]
$b_{s\ell}^{Vib}$	Vibrational relaxation coefficients in Millikan & White's formula (Eq. 4.83) [K ^{-1/3}]
c	Chapman-Rubesin parameter (Eq. 5.5) [-]
C_{EF}	Elemental molar diffusion coefficient (Eq. 2.29c) [kg/m-s]
$\underline{\mathcal{C}}_0, \underline{\mathcal{C}}_1, \underline{\mathcal{C}}_2$	Matrices in the non-linear spatial problem [various]
c	Wave speed $\left(= \omega_{\Re}/\sqrt{\alpha_{\Re}^2 + \beta_{\Re}^2}\right)$ [m/s]
c_{EF}^y	Non-dimensional boundary-layer elemental-diffusion grouping variable (Eq. 5.14) [-]
C_p	Heat capacity at constant p [J/mol-K]
c_p	Heat capacity at constant p [J/kg-K]
c_p^{eq}	Equilibrium heat capacity (Eq. 5.15) [J/kg-K]
c_{ptr}	Translational-rotational specific heat capacity (Eq. 4.23a) [J/kg-K]
c_{pv}	Non-dimensional boundary-layer heat-capacity variable (Eq. 5.5) [-]
c_{pv}	Vibrational-electronic-electron specific heat capacity (Eq. 4.23b) [J/kg-K]
c_{pvs}	Non-dimensional boundary-layer species heat-capacity variable (Eq. 5.5) [-]
$C_{s\ell}^*$	Ratio of collision integrals (Eq. 4.58c) [-]

$c_{e \cdot s}^\sigma$	Coefficient in the polynomial fitting for the effective electron-neutral energy exchange cross section of species s (Eq. 4.91) [m^2/K^2]
c_v	Heat capacity at constant volume [J/kg-K]
\mathcal{D}_E	Elemental electric diffusion coefficient (Eq. 2.31) [C-s/m^3]
d_s^j	Species diffusion driving force [$1/\text{m}$]
Da	Damköhler number (Eq. 8.6d) [-]
Da _v	Vibrational Damköhler number (Eq. 8.6e) [-]
D_j^{FDn}	j th coefficient in the n th -order finite-difference stencil to obtain the first derivative with respect to an arbitrary variable q [$1/[q]$]
$\mathcal{D}_{\text{eff } s}$	Effective diffusion coefficient of species s in the mixture [m^2/s]
$\mathcal{D}_{s\ell}$	Multicomponent diffusion coefficient of species s in species ℓ [m^2/s]
$\mathcal{D}_{s\ell}$	Binary diffusion coefficient of the species pair $s - \ell$ [m^2/s]
$\hat{\mathcal{E}}$	Set of all-but-one elements [-]
\mathcal{E}	Set of all elements [-]
e	Internal energy [J/kg]
E_i	Electric field [$\text{kg-m/s}^2\text{-C}$]
Ec	Eckert number (Eq. 5.5) [-]
Ec_p	Pressure Eckert number (Eq. 5.5) [-]
Ec_w	Spanwise Eckert number (Eq. 5.5) [-]
$E_{s\ell}^*$	Ratio of collision integrals (Eq. 4.58d) [-]
\mathcal{E}_{Es}^*	Elemental stoichiometric coefficient of element E in species s [-]
\mathcal{E}_{Es}	Corrected elemental stoichiometric coefficient $\left(\mathcal{E}_{Es} = \mathcal{E}_{Es}^* \frac{\mathcal{M}_E}{\mathcal{M}_s} \right) [-]$
e^{uvw}	Total internal energy (see Eq. 6.30a) [J/kg]
f	Non-dimensional boundary-layer streamwise-velocity variable (Eq. 5.5) [-]

\mathcal{F}	Forcing term in the PSE marching problem [various]
f_w	Self-similar blowing parameter (see Eq. 6.3) [-]
\mathcal{G}	Non-dimensional boundary-layer semi-total-enthalpy variable (Eq. 5.5) [-]
g^{ij}	Metric tensor (see Eq. 2.2) [-]
$G_{s\ell}^{\mathcal{D}}$	Singular diffusion matrix subsystem [s^2/m]
$\check{G}_{s\ell}^{\mathcal{D}}$	Regularized diffusion matrix subsystem [s^2/m]
$G_{s\ell}^{\kappa_H}$	Heavy-particle translational thermal conductivity matrix subsystem [$K \text{ m/W}$]
$G_{s\ell}^{\mu}$	Viscosity matrix subsystem [$m \text{ s/kg}$]
g_s	Non-dimensional boundary-layer species-enthalpy variable (Eq. 5.5) [-]
g_s	Gibbs free energy of a species s (Eq. 4.68) [J/kg]
g_{sm}^{Elec}	Degeneracy of the m -th electronic energy level of species s [-]
g_{sm}^{Vib}	Degeneracy of the m -th vibrational mode of species s [-]
\hbar	Planck's constant ($= 6.626070040 \cdot 10^{-34}$) [$J \text{ s}$]
\mathcal{H}	Set of heavy species (molecules and atoms, but not electrons) [-]
\mathcal{H}	Heavyside step function (Eq. 9.4) [-]
H	Enthalpy per mol [J/mol]
h	Static enthalpy per unit mass [J/kg]
h_1, h_2, h_3	Stretching parameters in an orthocurvilinear coordinate system [-]
h_s^{diss}	Species dissociation energy (see Eq. 4.88 and footnote w) [J/kg]
h_{fs}°	Species formation enthalpy at 0K [J/kg]
$H_{fs}^{298 \text{ K}}$	Species formation enthalpy at 298K [J/mol]
h_s^{ion}	Species ionization energy [J/kg]
h_{por}	Porous-layer height (see Fig. 6.1) [m]

h_{tr}	Translational-rotational enthalpy (Eq. 4.22a) [J/kg]
h_v	Vibrational-electronic-electron enthalpy (Eq. 4.22b) [J/kg]
h^u	Semitotal enthalpy ($= h + u^2/2$) [J/kg]
h^{uvw}	Total enthalpy (see Eq. 6.30b) [J/kg]
θ_{wd}	Wedge inclination angle [deg]
i, j, k, l	Sub- and super-indices corresponding to the spatial directions in co- or contravariant variables the tensorial notation. Other indices do not correspond to tensorial directions . [-]
j	Non-dimensional boundary-layer density variable (Eq. 5.5) [-]
\mathcal{J}^j	Energy diffusion flux [J/m ² -s]
\mathcal{J}_v^j	Vibrational energy diffusion flux [J/m ² -s]
\mathcal{I}_E	Non-dimensional boundary-layer elemental-diffusion-flux variable (Eq. 5.13) [-]
J_E	Elemental diffusion flux (Eq. 2.28 or 2.30) [kg/m ² -s]
\mathcal{I}_s	Non-dimensional boundary-layer species-diffusion-flux variable (Eq. 5.5) [-]
J_s^j	Mass diffusion flux of species s [kg/m ² -s]
κ	Non-dimensional boundary-layer spanwise-velocity variable (Eq. 5.5) [-]
κ_s^E	Grouping parameter (see Eq. 2.13) [C-s ² /kg-m ²]
k_B	Boltzmann's constant ($= 1.38064852 \cdot 10^{-23}$) [m ² -kg/K-s ²]
k_{br}	Backward reaction rate [$(\text{m}^3/\text{mol})^{\sum_s \nu''_{sr}-1} \text{ s}^{-1}$]
$K_{eq\,r}$	Chemical equilibrium constant [$(\text{m}^3/\text{mol})^{\sum_s \nu'_{sr}-\nu''_{sr}}$]
k_{fr}	Forward reaction rate [$(\text{m}^3/\text{mol})^{\sum_s \nu'_{sr}-1} \text{ s}^{-1}$]
k_{fr}^{Oxid}	Reaction rate of the surface oxidation reactions [$(\text{m}^3/\text{mol})^{\sum_\ell \nu'_{\ell r}-1} \text{ m/s}$]
Kn	Knudsen number $\left(= \frac{\text{mean free path}}{\text{geometrical length scale}}\right)$

k_ν^{por}	Grouping parameter (see Eq. 6.11) [-]
ℓ_e	Blasius length based on the boundary-layer edge quantities $\left(= \sqrt{\frac{\mu_e x}{\rho_e u_e}} \right)$ [m]
\mathcal{L}_s	Molecule's linearity factor (3 for non-linear and 2 for linear) [-]
$\underline{\mathcal{L}}, \underline{\mathcal{M}}, \underline{\mathcal{N}}$	Matrices in the PSE marching problem [various]
L	Arbitrary reference length [m]
Le	Lewis number ($= \rho \mathcal{D}_s c_p / \kappa^{Fr}$) [-]
\mathcal{M}	Atomic mass [kg/mol]
\mathcal{M}	Molar mass [kg/mol]
\mathcal{M}^*	Corrected mixture molar mass (see Eq. A.9) [kg/mol]
m	Integer defining the β harmonics in non-linear stability theories [-]
\mathbb{M}_β	Set of integers defining the β harmonics to be considered in non-linear theories [-]
m_μ	Exponential in viscosity power law (Eq. D.4) [-]
\mathbb{M}_ω	Set of integers defining the ω harmonics to be considered in non-linear theories [-]
$\dot{m}_{sw}^{\text{Oxid}}$	Species mass production rate per unit mass due to oxidation reactions [kg/s-m ²]
$\mathcal{M}_r^{\text{Oxid}}$	Molar mass of the oxidizer in an oxidation reaction [kg/mol]
$\dot{m}_{sw}^{\text{Subl}}$	Species mass production rate per unit mass due to sublimation reactions [kg/s-m ²]
\dot{m}_w	Surface blowing mass flow [kg/s-m ²]
m_w^{CL}	Injected mass flow along the centerline of the visible area of the cone ($\theta = 0$) [kg/m ² -s]
\dot{m}_w^{tot}	Total mass flow (Eq. 9.7) [kg/s]
\bar{N}	Base-flow grid size [-]
\tilde{N}	Stability grid size [-]

N	N-factor: natural logarithm of the perturbation amplification factor (see Eq. 3.20) [-]
n	Molecular number density [molecules/m ³]
n^*	Atomic number density [atoms/m ³]
N_A	Avogadro's number ($= 6.022140857 \cdot 10^{23}$) [particles/mol]
N_{dim}	Number of spatial directions [-]
n	Integer defining the ω harmonics in non-linear stability theories [-]
n_{por}	Surface porosity (see Eq. 6.12) [-]
n_{Tr}	Arrhenius temperature exponential constant [-]
p	Pressure [Pa]
p_{Atm}	Atmospheric pressure in standard conditions ($= 101325$) [Pa]
Pr	Prandtl number (Eq. 4.5) [-]
Pr_{tr}	Translational-rotational Prandtl number (Eq. 8.6g) [-]
Pr_v	Vibrational-electronic-electron Prandtl number (Eq. 8.6h) [-]
P_s^{Vap}	Coefficient in the expression for the species vapor pressure (Eq. 4.78) [K]
p_s^{Vap}	Vapor pressure of each species (Eq. 4.78) [Pa]
\mathcal{Q}	Partition function [-]
q_e^-	Elementary charge ($= 1.6021766208981 \cdot 10^{-19}$) [C]
Q^{Elec}	Source of electronic energy [J/m ³ -s]
$Q^{e^- \text{ im}}$	Transfer of translational-to-electronic energy due to electron-impact collisions [J/m ³ -s]
Q^{Hcoll}	Transfer of translational-to-electronic energy due to heavy-particle collisions [J/m ³ -s]
Q_{TV}	Vibrational-electronic-electron energy relaxation source term [J/m ³ -s]
Q_s^{Vap}	Coefficient in the expression for the species vapor pressure (Eq. 4.78) [-]

Q^{V-E}	Transfer of energy due to vibrational-electronic exchanges [J/m ³ -s]
Q^{Vib}	Source of vibrational energy [J/m ³ -s]
\mathcal{R}	Universal gas constant (= 8.31447) [J/K-mol]
R	Mixture-specific gas constant (= \mathcal{R}/\mathcal{M}) [J/kg-K]
r	Radial distance with respect to the body's axis (see Fig. 5.1) [m]
r_0	Radial distance of the body's surface with respect to its axis (see Fig. 5.1) [m]
\mathcal{R}	Set of all reactions occurring in the bulk of the gas (not gas-surface reactions) [-]
\mathcal{R}_{ai}	Set of associative-ionization reactions (see Table 4.3) [-]
\mathcal{R}_{eid}	Set of electron-impact-dissociation reactions (see Table 4.3) [-]
\mathcal{R}_{eii}	Set of electron-impact-ionization reactions (see Table 4.3) [-]
\mathcal{R}^{eq}	Set of equilibrium reactions [-]
\mathcal{R}_{hpii}	Set of heavy-particle-impact-ionization reactions (see Table 4.3) [-]
\mathcal{R}^{Oxid}	Set of all oxidation reactions (Eq. 4.71) [-]
r_k	Local radius of curvature in the direction normal to the marching path [m]
r_{por}	Pore radius (see Fig. 6.1) [m]
R_s	Species-specific gas constant (= $\mathcal{R}/\mathcal{M}_s$) [J/kg-K]
S	Entropy per mol [J/mol-K]
s	Entropy per unit mass [J/kg-K]
S_{base0}	Cone cross-sectional area at the beginning of the porous section ($x = x_{p0}$) [m ²]
Sc	Schmidt number (= $\mu / (\rho \mathcal{D}_s)$) [-]
\mathcal{S}	Set of all species [-]
\mathcal{S}_{atom}	Set of all atomic species [-]

S_{ion}	Set of ion (positively charged) species [-]
S_{mol}	Set of molecular species [-]
S_{neut}	Set of neutral species [-]
S_{Subl}	Set of all sublimating species (Eq. 4.76) [-]
s_{por}	Spacing between pores (see Fig. 6.1) [m]
S_{κ}	Coefficient in Sutherland's law on thermal conductivity (Eq. 4.4) [K]
S_{μ}	Coefficient in Sutherland's law on viscosity (Eq. 4.2) [K]
\mathbb{T}^{ij}	Viscous stress tensor [Pa]
T	Thermal-equilibrium (Eq. 4.7) or translational-rotational (Eq. 4.8) temperature [K]
t	Time [s]
$T_{s\ell}^*$	Reduced temperature of species pair $s-\ell$ (Eq. 4.53) [K]
$T_{s\ell}^{\text{col}}$	Collision temperature of species pair $s-\ell$ (Eq. 4.52) [K]
T^{e^-}	Electron temperature (translational energy of electron species – Eq. 4.6a) [K]
T^{Elec}	Electronic temperature (Eq. 4.6d) [K]
$T_{\kappa_{\text{ref}}}$	Reference temperature for Sutherland's law on thermal conductivity (Eq. 4.4) [K]
$T_{\mu_{\text{ref}}}$	Reference temperature for Sutherland's law on viscosity (Eq. 4.2) or power law (Eq. D.4) [K]
T^{Rot}	Rotational temperature (Eq. 4.6b) [K]
T^{Trans}	Translational temperature (translational energy of heavy species – Eq. 4.6a) [K]
T_s^{Trans}	Translational temperature of each species (Eq. 4.6a) [K]
\mathcal{T}_v	Non-dimensional boundary-layer vibrational-electronic-electron-temperature variable (Eq. 5.5) [-]
T_v	Vibrational-electronic-electron temperature [K]
T^{Vib}	Vibrational temperature (Eq. 4.6c) [K]

\mathcal{U}^j	Velocity components in the Cartesian SR [m/s]
U	Velocity normal to the shock [m/s]
u^j	Velocity components in tensorial notation [m/s]
u_θ	Velocity in the azimuthal direction θ (see Fig. 7.1) [m/s]
u_r	Velocity in the radial direction r (see Fig. 7.1) [m/s]
u_*	Non-dimensional radial velocity (Eq. 7.5) [-]
u, v, w	Velocity components in x, y, z [m/s]
$u_s^{\mathcal{D}}, v_s^{\mathcal{D}}, w^{\mathcal{D}}$	Components of the inverse Stefan-Maxwell matrix (Eq. 4.49) [m^2/s]
v	Transformed wall-normal velocity after the Probstein-Elliott transformation (see Eq. 5.28) [m/s]
\mathcal{V}	Molar volume (Eq. 8.15) [m^3/mol]
\mathcal{V}_Q	Set of independent quantities q that a given dependent quantity Q depends on [-]
X_E	Elemental mole fraction (see Eq. A.11b) [-]
X_s	Species mole fraction (see Eq. A.1b) [-]
X_{CGL}	Set of Chebyshev-Gauss-Lobatto points [-]
\mathcal{X}^j	Spatial coordinates in Cartesian SR [m]
x^j	Spatial coordinates in tensorial notation [m]
x_{p0}, x_{p1}	Location along the surface of the beginning and end of the porous section [m]
x_{tr}	Transition-onset location in the streamwise direction [m]
χ, y	Streamwise and wall-normal coordinates after the Probstein-Elliott transformation (see Eq. 5.27) [m]
x, y, z	Spatial coordinates in a Cartesian reference frame [m]
Y_1^{por}	Shunt admittance (see Eq. 6.9b) [s-m/kg]
\mathcal{Y}_E	Elemental mass fraction (see Eq. A.11a) [-]
Y_s	Species mass fraction (see Eq. A.1a) [-]
y_{sh}	Wall-normal position of the shock [m]

\mathcal{Z}_s	Unit charge of species s [-]
Z_0^{por}	Characteristic impedance of the porous wall (see Eq. 6.8) [kg/m ² -s]
Z_1^{por}	Impedance of the transmission line (see Eq. 6.9a) [kg/m ³ -s]

Greek and Hebrew Symbols

α	Perturbation complex streamwise wave number [1/m]
α_0	Streamwise inclination angle of a body of revolution (see Fig. 5.1) [deg]
α_s^{diff}	Thermal diffusivity of species s (see Eq. 9.6) [m ² /s]
α_r^{Oxid}	Reaction probability of an oxidation reaction (Eq. 4.73) [(m ³ /mol) $^{\sum_{\ell} \nu'_{\ell r} - 1}$]
α_s^{Subl}	Coefficient in the Knudsen-Langmuir equation (Eq. 4.77) [-]
β	Perturbation complex spanwise wave number [1/m]
β_H	Hartree velocity parameter (Eq. 5.5) [-]
$\Delta_{s\ell}^{(i)}$	Coefficients in Yos' and Brokaw's transport models [m ² kg ^{1/2} /J ^{1/2}]
δ_{ab}	Kronecker delta function (1 for $a = b$, 0 otherwise) [-]
δ_H	Boundary-layer height based on the total enthalpy [m]
ϵ	Error defined with Eq. 4.36 [-]
ϵ_0	Permittivity of vacuum ($= 8.854187817620 \cdot 10^{-12}$) [C ² /N·m ²]
ε	Error defined with Eq. 4.51 [-]
ϵ_C	Emisivity of graphite (≈ 0.9) [-]
ϕ	Wave angle ($= \Re(\beta) / \Re(\alpha)$) [deg]
ϕ^μ	Mixing coefficient in Wilke's rule [-]
ζ_s	Species thermal diffusion ratio [-]
$\varphi_{s\ell}$	Coefficient in Brokaw's transport model [-]
ζ_{vs}	Species vibrational-electronic-electron thermal diffusion ratio [-]

Γ_{ik}^j	Christoffel symbol of the second kind (Eq. 2.3) [1/m]
η_s^μ	Mono-species shear viscosity coefficients [kg/m-s]
η	Self-similar boundary-layer variable (Eq. 5.6) [-]
θ	Azimuthal position (see Fig. 7.1) [deg]
θ_c	Cone half angle (see Fig. 7.1) [deg]
θ_{sm}^{Elec}	Activation temperature of the m -th electronic energy level of species s [K]
Θ_H	Hartree semi-total-enthalpy parameter (Eq. 5.5) [-]
θ_{Hv}	Hartree vibrational-electronic-electron-temperature parameter (Eq. 5.5) [-]
θ_r	Arrhenius activation temperature of reaction r [K]
θ_s^{Rot}	Rotational activation temperature [K]
θ_{sm}^{Vib}	Activation temperature of the m -th vibrational mode of species s [K]
θ_{wd}	Wedge inclination angle [deg]
κ^{Fr}	Frozen thermal conductivity [W/K-m]
κ^{eq}	Equilibrium thermal conductivity (Eq. 2.35 or 2.36) [W/K-m]
κ_{ref}	Reference thermal conductivity in Sutherland's law (Eq. 4.4) [W/K-m]
κ_{tr}	Translational-rotational thermal conductivity [W/K-m]
κ_v	Vibrational-electronic-electron thermal conductivity [W/K-m]
λ	Second viscosity coefficient [kg/m-s]
λ_D	Debye shielding length [m]
$\Lambda_{s\ell}^{(i,j)}$	Laguerre-Sonine polynomials in the expressions of κ_e^{Trans} [K-m/W]
Λ_{prop}	Propagation constant (see Eq. 6.10) [1/m]
μ	Dynamic viscosity [kg/m-s]
μ_{ref}	Reference viscosity in Sutherland's law (Eq. 4.2) or power law (Eq. D.4) [kg/m-s]

ν'_{sr}, ν''_{sr}	Stoichiometric coefficient for reactants & products s in reaction r [-]
ξ^i	Spatial integration variable [m]
$\nu_{e\cdot s}$	Effective collision frequency between electrons and species s [1/s]
ξ	Marching boundary-layer variable (Eq. 5.6) [-]
ρ	Mass density [kg/m ³]
$\sigma_s^{e\cdot}$	Effective electron-neutral energy exchange cross section of species s [m ²]
σ_s	Molecule's steric factor (2 for symmetric, 1 for non-symmetric)[-]
σ^{SB}	Stefan-Boltzmann constant ($= 5.67036713 \cdot 10^{-8}$) [W/m ² ·K ⁴]
σ_s^{Vib}	Limiting cross section for vibrational excitation at 50 000 K [m ²]
τ_{chem}	Reference chemical time scale (Eq. 8.8) [s]
$\tau_s^{e\cdot-V}$	Electron-to-vibrational relaxation time (Eq. 4.82) [s]
$\tau_{s\ell}^{\text{MW}}$	Millikan & White's vibrational relaxation times (Eq. 4.83) [s]
τ_s^P	Park's correction to the vibrational relaxation times (Eq. 4.85) [s]
$\tau^{T-e\cdot}$	Heavy-to-electron translational energy relaxation time (Eq. 4.92) [s]
τ_s^{TR-V}	Translational-rotational-to-vibrational relaxation time (Eq. 4.82) [s]
τ_{vib}	Reference energy-relaxation time scale (Eq. 8.9) [s]
$\psi_{s\ell}^Q$	Coefficient for property Q in Yos' transport model [1/[Q]]
ψ_s	Species pressure fraction (see Eq. A.1c) [-]
ω	Perturbation complex frequency [1/s]
$\Omega_{s\ell}^{(i,j)}$	Collision integral of order (i, j) between species s and ℓ [m ²]
$\dot{\omega}_{\text{rad}}$	Surface radiative heat flux (Eq. 6.18) [W/m ²]

$\dot{\Omega}_s$	Non-dimensional boundary-layer species-source-term variable (Eq. 5.5) [-]
$\dot{\omega}_s$	Species production rate [kg/m ³ -s]
$\dot{\omega}_{sr}$	Species production rate of species s due to reaction r [kg/m ³ -s]
$\dot{\Omega}_v$	Non-dimensional boundary-layer vibrational-electronic-electron-source-term variable (Eq. 5.5) [-]
$\bar{\cdot}$	Molar average of the number of atoms per molecule (Eq. A.14) [-]

Sub- and superscripts

q^i	Contravariant vector quantity
q^{ij}	Contravariant tensor quantity
q_i	Covariant vector quantity
q_{ij}	Covariant tensor quantity
$q_{,i}$	Covariant derivative of a quantity
q_{adiab}	Adiabatic conditions
q_e	Electron-species-specific quantity
q_e	Boundary-layer-edge quantity
q_E, q_F	Element-specific quantity
q_{EF}	Element-pair-specific quantity
\underline{q}^H	Hermitian of a vector – complex conjugate and transpose
q_H	Heavy-particle quantity
q_{\max}	Maximum of a variable
q_{\min}	Minimum of a variable
$q_{(m,n)}$	Variable relative to the (m, n) mode in NPSE
$q_{(n)}$	Variable relative to the (n) mode in NPSE
q^{Mod}	Referred to the different energy modes
$O(q)$	Order of magnitude of q is smaller than or equal to

$o(q)$	Order of magnitude of q is smaller than
$\Im(q)$ or q_{\Im}	Imaginary part of a complex variable
$\Re(q)$ or q_{\Re}	Real part of a complex variable
\bar{q}	Base-flow quantity
q'	Perturbation quantity
\tilde{q}	Perturbation-amplitude quantity
q_r	Reaction quantity
q^{Ref}	Reference value of a variable
q_s, q_ℓ	Species-specific quantity
$q_{s\ell}$	Species-pair-specific quantity
q_∞	Pre-shock quantity
q_{sh}	Post-shock quantity
\underline{q}	Discretized 1-D vector
$\underline{\underline{q}}$	Discretized 2-D matrix
\underline{q}^T	Transpose of a vector
$\bar{\bar{q}}$	Pseudo-basic-state quantity (see Eq. 7.11)
\hat{q}	Fluctuation quantity (see Eq. 7.11)
q_{tr}	Relative to the translational-rotational energy grouping
q_v	Relative to the vibrational-electronic-electron energy grouping
q^b	Quantity referred to $k_b r$
q^{eq}	Quantity referred to $K_{\text{eq}} r$
q^f	Quantity referred to $k_f r$
q^\dagger	Complex-conjugate of a variable

Part I

Framework

1

Context and motivation

1.1 Space exploration

The global social, geo-political and environmental scenario of the beginning of the twenty-first century makes the advancement of space exploration a stronger necessity than ever. The expansion of protectionist economic policies and far-right racist and intolerant nationalism [1, 2], the escalation of nuclear armament and the abandonment of post-cold-war non-proliferation treaties [3, 4], or the dangerous levels of atmospheric CO₂ due to human activity [5, 6], all pose major existential threats for humankind and its progress. If one agrees that the survival of human, and eventually post-human, consciousness and intelligence should be one's primary goal [7], it is necessary to search for alternatives allowing to surpass the aforementioned threats. Based on the history of humanity, it seems unlikely that the many parties involved will reach a common agreement allowing to avoid such perils. Space exploration, and the subsequent colonization of extraterrestrial bodies therefore presents itself as probably the only way of ensuring survival in the more-than-likely scenario in which life on Earth, for one reason or another, cannot be continued [8, 9].

Besides the mentioned purely survival motivation behind space exploration, there is also the inherent human inspiration that comes from breaking into the frontiers of the unknown. Places that remain unexplored for long periods of time, normally do so because of the technological challenges that stand on the way. Overcoming these challenges normally leads to the development of multiple tech-

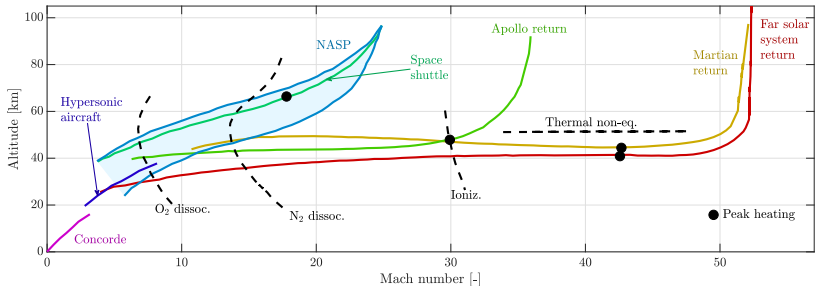


Figure 1.1: Earth entry paths for several missions. Adapted from Howe [11] and Rivell [12].

nologies that can be subsequently used in various ambits of society. An example of this are the more than 2000 inventions that can be found in NASA's spin-off database [10].

1.2 Atmospheric entry

A critical stage present in many planetary missions is the atmospheric entry. Vehicles must reduce their orbital velocities in order to be able to safely land into the planet being approached. A sample of the flight paths for some iconic Earth entry past and future missions is presented in Fig. 1.1, where the data collected by Howe [11] and Rivell [12] is summarized. Atmospheric entry is not exclusive to Earth entries, since it is necessary when approaching the surface of any astronomical body with a gaseous external layer.^a

Atmospheric entry missions are characterized by the large amount of kinetic orbital energy that must be dissipated into the atmosphere. This translates into large heat fluxes that must be withstood by the vehicle's thermal protection system (TPS). The coexistence of multiple physical phenomena around vehicles during atmospheric entries poses a major challenge when modeling and ultimately designing vehicles for them. When a vehicle enters an atmosphere at hypervelocity, a detached bow shock is formed upstream of it. This shock radiates energy into both the preshock and postshock flow, and compacts the undisturbed gas molecules, strongly increasing their translational energy. This translational energy is then transferred into the internal energy modes (rotational, vibrational, and electronic) through a relaxation process. Popular strategies to model these thermally relaxing regions include the use of several temperatures to model various groups of energy modes [13]. Eventually, the high temperatures make molecules dissociate into monoatomic species, and for very fast entries, gases heat up enough to make them

^aMars, Venus or Titan are just some examples.

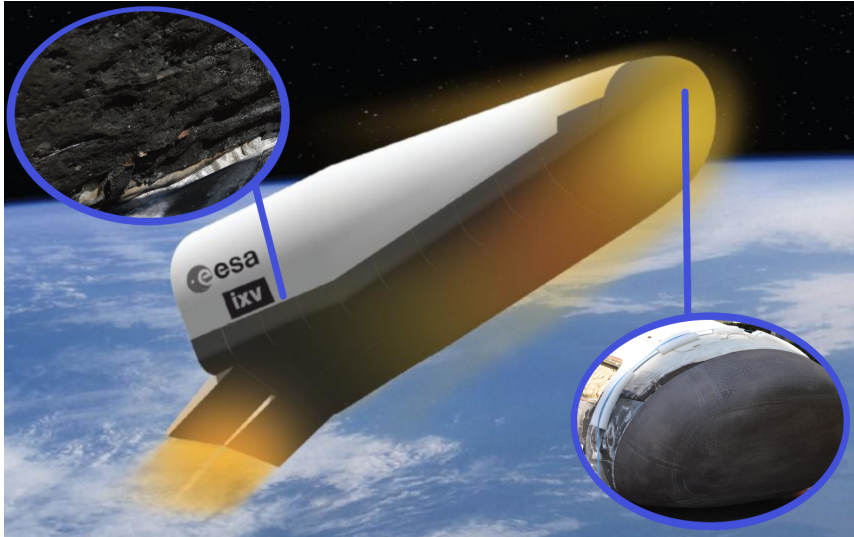


Figure 1.2: IXV sketch by ESA/J. Huart. Copyright 2011. <http://www.esa.int/>. Post-flight close-up pictures taken at the von Karman Institute by T. Regert.

partially ionize due to free electrons detaching from the out-most layer. Close to the surface, there is a recombination of these atomic species into molecules, and depending on the TPS material, an ablation and a recession of it. Also close to the surface, but farther downstream there is a transition of the boundary layer from a laminar to a turbulent regime. Depending on the vehicle geometry, in the event of very strong backward-facing steps, there may also be regions of flow separation and even continuum breakdown and recompression [14]. These phenomena often feature very different and varying characteristic time and length scales, largely complicating any level of coupled computational analysis. For this reason, research efforts have been focused on investigating them individually, with only a few attempts to couple two or more of them [14–16].

Despite the aforementioned lack of knowledge on the aerothermodynamics, TPS designs must ensure the success of the various missions. This is usually accomplished thanks to overly conservative safety coefficients which, due to their empirical non-physics-based nature, may occasionally fail at ensuring the mission's success. Well-known are the tragedies of the Columbia and the Challenger Space-Shuttle missions, that killed fourteen astronauts. Recently, other missions have also notoriously failed during the atmospheric entry phase, yet without a death toll, such as ESA's ExoMars [17]. Even in successful missions, such as ESA's IXV (Intermediate eXperimental Vehicle) flight, preliminary post-flight analysis (Fig. 1.2) suggests that whilst the front TPS withstood the thermal loads without reaching dangerous levels of recession, farther downstream the surface

was strongly charred.

It is therefore clear that there is a strong need to extend the understanding of atmospheric entry physics. In particular, and due to the strongly coupled nature of the various phenomena, one should work towards developing models simultaneously considering the maximum possible amount of these phenomena. The present doctoral research contributes towards this goal by investigating the interaction of shock waves, molecular dissociation and recombination, ionization, TPS ablation, and boundary-layer transition. Only through simplified, yet sufficiently accurate modeling of these couplings and interactions can one shed light on the dominating physical mechanisms. It is the understanding of these mechanisms that will allow humankind to subsequently develop engineering solutions to mitigate the risks of the harsh environment represented by an atmospheric entry. Such solutions constitute the only path towards producing the reliable and efficient vehicles required for a critical stage within space exploration.

1.3 TPS ablation

Depending on the design, speed and heat loads of the mission, the TPS will be ablative or non-ablative [18]. Ablative materials can only be used once, since, when subject to increasing heat load, first their polymeric matrix pyrolyses, and then the fibres ablate and fail [19]. On the other hand non-ablative materials are reusable, but they are not suited for high-enthalpy entries. Fast entry missions, such as those entering Mars, can currently be done exclusively with ablative materials [20, 21]. Such reentry trajectories are characterized by a great amount of kinetic energy to be dissipated to the atmosphere; this is done through TPS burning and erosion. On the other hand, "slow" entry missions such as those in which vehicles return from Low Earth Orbit (LEO), or hypersonic cruise vehicles, can afford to use non-ablative materials [22]. The lower amount of energy to be dissipated allows the TPS to be exposed to the flow without burning.

During the decomposition of an ablative TPS due to the high-enthalpy environment featuring in atmospheric entry missions, the initial pyrolysis stage is characterized by a strong outgassing. The polymeric resin decomposes, injecting into the boundary layer a large amount of hydrocarbons such as C_2H_4 , C_6H_6 , CH_4 , CH_5OH , C_7H_8 , H_2 and H_2O , among others [15]. These products are expelled through the remaining porous fibers of the carbon preform. After the resin has completely pyrolyzed, and as the surface temperature continues to increase, it eventually reaches levels sufficient to activate ablative mechanisms. There is an oxidization and/or a nitridation of the carbon material, which expels products such as CO , CO_2 or CN into the boundary layer. There is also a sublimation of the carbon preform, which results in species such as C , C_2 or C_3 . Other physical phenomena, also occurring during the thermal decomposition of a TPS, are the

spallation or, for certain materials, the melting of the fibers [19].

The modeling of pyrolyzing and ablating surfaces is a very active field of research in itself [14, 15, 23, 24]. There have been outstanding efforts such as those coupling the ablation phenomena with flow radiation [14], with boundary-layer stability [16] or those coupling the material with the flow response in a unified framework [15]. There have also been extensive experimental investigations on the material and flow response in high-enthalpy environments, such as the efforts carried out at the von Karman Institute [25].

Despite it being oftentimes neglected, shock-layer radiation has been seen to play a non-negligible role in reentry scenarios with TPS ablation [14]. Ablation products are excited by the energy radiated from the shock wave, and thus shield the vehicle from the higher radiative heat flux it would otherwise have to withstand.

1.4 Boundary-layer transition

A potential *mission killer* in atmospheric entry is boundary-layer laminar-to-turbulent transition. The highly fluctuating nature of turbulent flows leads to stronger energy mixing than laminar flows, and therefore stronger gradients. These large energy gradients ultimately cause higher surface heat fluxes [26], up to 8 times higher than in a fully laminar regime [27]. TPS sizing is therefore paramount to predict the transition onset and turbulent breakdown locations on the vehicle surface for the various flow regimes encountered during the mission. Consequently, the use of inaccurate transition-modeling tools leads to designs based on the *worst-case scenario*, with an excessive TPS weight allocation. Moreover, having a laminar or a turbulent regime in the boundary layer also affects the vehicle's aerodynamic drag [28], and its maneuverability and control [29]. Understanding the underlying physical mechanisms in the appearance and growth of the instabilities ultimately leading to transition, allows for the development of transition-advancement [30] or transition-delay [31–33] techniques and materials.

Transition is affected by a variety of flow features, such as Reynolds number, Mach number, surface geometry, inflow turbulence and noise, pressure gradients, wall roughness and porosity, boundary layer cooling or heating, or mass injection or suction through the surface [34]. Among those, the effect of TPS thermal decomposition on boundary-layer flows is particularly important, because it directly modifies three of the aforementioned key features:

1. **Roughness and porosity:** the irregular pyrolysis and ablation of the TPS modifies the surface roughness and increases the porosity of the material.
2. **Mass injection or suction:** a series of pyrolysis and ablation subproducts are blown into the boundary layer.

3. **Boundary-layer cooling or heating:** the injected TPS subproducts, as well as the reactions causing them, contribute to modifying the storage of thermal energy within the boundary layer.

High levels of surface roughness have been experimentally observed to enhance natural transition mechanisms and even bypass them, and therefore lead to an earlier transition [35, 36]. Computational investigations also looked into how roughness-induced perturbations enter the boundary-layer [37, 38], and how they develop both for isolated [39, 40] and distributed [41, 42] roughness elements, explaining the experimental observations. Strategically designed distributed roughness has also been reported to damp instabilities in certain conditions [43, 44]. The aforementioned studies were focused on roughness elements with regular shapes, whilst the influence of the irregular roughness introduced by ablation on transition remains largely unknown. The major hurdle encountered in such studies are the logistic challenges of acquiring reliable and meaningful experimental data [45].

Contrarily to the case-dependent observations reported on the effect of roughness on stability, surface mass injection has been consistently observed to destabilize the boundary layer and consequently to advance transition upstream. Wall suction was seen to have the opposite effect. Qualitatively-equivalent results were obtained in both experimental [46] and computational [47–49] investigations. On the contrary, Li *et al.* [49] reported that large blowing rates were predicted to cause a stabilization of the second mode. The companion experimental investigation [50] did not observe the corresponding transition delay, leading the authors to suggest there to be a bypass of the instability development mechanisms for the strongly-blown cases. This bypass could not be modeled with the considered theory. Whilst the aforementioned qualitative effect of non-zero normal velocities at the wall is well-known, its modeling and associated quantitative estimation present room for improvement. In particular, the modeling of the wall-normal velocity perturbation boundary condition was seen to have a large effect on the predicted amplification rate of the instabilities [51]. This is largely due to the influence that the surface porosity parameters have on the development of acoustic instabilities [52, 53]. A rather innovative wall-blowing transition-delay technique was experimentally and computationally investigated by Leyva, Jewell *et al.* [54, 55]. It consists in injecting CO₂ into the boundary layer, such that the excitation of its three vibrational energy modes stabilizes the flow. In the same research framework, Leyva *et al.* [56] numerically investigated the influence of various injection schemes on the transition onset location, concluding that not only one must size appropriately the amount of mass that is injected, but also the shape with which it is injected.

Regarding the effect of air chemistry and gas-surface interaction on boundary-layer instability development, a major constraint is the lack of experimental results to be used in the validation of the various models. Existing high-enthalpy hy-

personics ground-test facilities [57–59] are unable to sustain sufficiently long test times in order to reach the chemical activity encountered in real flights. Flight tests [60–63] remain thus the only source of experimental data. These experiments however feature a major uncertainty in the free-stream conditions, offer very limited data due to the engineering challenge that is taking measurements in such conditions, and are scarce due to their cost. The modeling of the thermodynamic and transport properties of gas mixtures in high-enthalpy environments has been, in itself, a major area of research for the past century [13, 14, 64–69]. Whilst for gases in perfect-gas conditions it is widely accepted to model the transport properties using Sutherland’s law [70] and a constant Prandtl number, there is not an equally accepted and extended set of models for high-enthalpy gases. Consequently, the various attempts of authors to perform boundary-layer stability and transition predictions feature multiple models, leading oftentimes to very different estimations [71, 72]. Despite the modeling-induced quantitative disagreements, the common trend observable is that the boundary-layer cooling induced by molecular dissociation or the excitation of species’ internal energy modes destabilizes the second mode, whilst it stabilizes the first.

1.5 Thesis scope

Within this frame, the present doctoral research addresses the effect of ablation-induced phenomena on hypersonic boundary-layer stability and transition. Numerical investigations are carried out, focusing on the isolated effect of blowing and chemistry, as well as their combined effect during the ablation of a graphite wall. Roughness effects are left out of this analysis. The main research questions to be answered by this dissertation are:

- How do base-flow inaccuracies propagate to the ultimate stability predictions?
- Can the e^N method be applied to wall-blowing scenarios?
- Does the porous-wall boundary condition, developed by Gaponov [73] and Fedorov *et al.* [52] for passive porous walls, present a modeling improvement in scenarios with mass injection?
- What is the underlying reason for the advancement/delay of transition that was experimentally observed when injecting gases lighter/heavier than air [50, 74]?
- How do the boundary-layer-stability characteristics vary as a function of the surface porous arrangement?

- How sensitive are the predictions to the use of inaccurate transport, diffusion, collisional, or chemical models?
- What is the isolated effect of molar diffusion on the perturbation growth rates and frequencies?
- Which flow assumptions are valid at different trajectory points in an atmospheric entry?
- How do high-enthalpy phenomena such as internal-energy-mode-excitation, dissociation, ionization, shock-perturbation coupling, or ablation-product injection contribute to stabilizing or destabilizing the boundary layer?
- Are these effects mostly due to the modification of the base-flow field, or of the perturbations themselves?
- Which phenomenon is the one promoting supersonic modes in high-enthalpy scenarios?

The work focuses on flows in thermal equilibrium, even though the developed tools and the presented framework is valid also for thermal non-equilibrium, based on a two-temperature model separating the translational-rotational from the vibrational-electronic-electron energy modes. Radiation is neglected from all analyses, except for the radiation emitted by the graphite wall going to infinity. Similarly, surface catalysis effects are also neglected. Transition is studied mostly through linear stability theory, in combination with the semiempirical e^N method, used to investigate the behavior of second-mode instabilities. However, the tools developed can be employed with other stability theories relatively easily.

The dissertation is structured as follows. The thermophysical framework (§ 2) and the fundamentals of stability and transition modeling (§ 3) are presented first. An extensive review is then carried out of the various high-temperature models used by authors in the past conducting stability analyses (§ 4). The techniques employed to obtain laminar base flow fields are introduced in § 5, subsequently presenting the particularities of boundary conditions required for both the laminar base flow and the perturbations in § 6. The two main numerical tools developed are introduced in § 7 and 8. The isolated effect of surface mass blowing is explored in § 9, by first validating the use of the porous boundary condition to such situations, then applying it to situations with various injection-gas compositions, and finally performing a parametric study of the influence of the characteristics of the porous wall. In § 10 the accuracy of the high-temperature gas models is evaluated against the state of the art, quantifying the inaccuracies to be expected in the final transition-onset predictions. State-of-the-art models are then employed to perform parametric studies on diffusion effects, on the adequacy of the various flow assumptions for different earth entry flow regimes, and on ionization effects.

The coupled ablation-transition problem is approached in § 11 by looking at the steady ablation of a graphite sample, and decoupling many of the coexisting physical phenomena. Finally, conclusions and recommendations for future research are presented in § 12.

References

- [1] S. Valdez and M. A. Eger. *Neo-nationalism in Western Europe*. European Sociological Review, [31\(1\):115–130](#), 12 2014.
- [2] S. Bangstad. *The New Nationalism and its Relationship to Islam*. In J. E. Fossum, R. Kastoryano, and B. Siim, editors, *Diversity and Contestations over Nationalism in Europe and Canada*, chapter 11, pages 285–311. Palgrave Macmillan, London, 2018.
- [3] J. K. Warden. *Limited Nuclear War : The 21st Century Challenge for the United States*. Lawrence Livermore National Laboratory, and Center for Global Security Research, 2018.
- [4] J. Gower. *The Dangerous Illogic of Twenty-First-Century Deterrence Through Planning for Nuclear Warfighting*. <https://carnegieendowment.org/>. [Published online on March 6th, 2018].
- [5] J. R. Petit, J. Jouzel, D. Raynaud, N. I. Barkov, J.-M. Barnola, I. Basile, M. Bender, J. Chappellaz, M. Davis, G. Delaygue, M. Delmotte, V. M. Kotlyakov, M. Legrand, V. Y. Lipenkov, C. Lorius, L. Pépin, C. Ritz, E. Saltzman, and M. Stievenard. *Climate and atmospheric history of the past 420,000 years from the Vostok ice core, Antarctica*. Nature, [399:429–436](#), 1999.
- [6] S. Solomon, G. K. Plattner, R. Knutti, and P. Friedlingstein. *Irreversible climate change due to carbon dioxide emissions*. Proceedings of the National Academy of Sciences of the United States of America, [106\(6\):1704–1709](#), 2009.
- [7] N. Bostrom. *In defense of posthuman dignity*. Bioethics, [19\(3\):202–214](#), 2005.
- [8] J. Tierny. *A Survival Imperative for Space Colonization*. www.nytimes.com. [Published online on July 17th, 2007].
- [9] R. Highfield. *Colonies in space may be only hope, says Hawking*. www.telegraph.co.uk. [Published online on October 16th, 2001].
- [10] NASA Spin-off Database. <https://spinoff.nasa.gov>. [Online on January 29th, 2019].
- [11] J. T. Howe. *Hypervelocity Atmospheric Flight: Real Gas Flow Fields*. Technical Report TM-101055, NASA, 1989.
- [12] T. Rivell. *Notes on Earth Atmospheric Entry for Mars Sample Return Missions*. Technical Report TP-2006-213486, NASA, 2006.

- [13] M. P. Clarey and R. B. Greendyke. *Thermochemical nonequilibrium processes in weakly ionized air using three-temperature models*. Journal of Thermophysics and Heat Transfer, [33\(2\):425–440](#), 2019.
- [14] J. B. Scoggins. *Development of numerical methods and study of coupled flow, radiation, and ablation phenomena for atmospheric entry*. PhD thesis, Université Paris-Saclay and VKI, 2017.
- [15] P. Schrooten. *Numerical simulation of aerothermal flows through ablative thermal protection systems*. PhD thesis, UCL, 2015.
- [16] C. Mortensen. *Effects of Thermochemical Nonequilibrium on Hypersonic Boundary-Layer Instability in the Presence of Surface Ablation or Isolated Two-Dimensional Roughness*. PhD thesis, UCLA, 2013.
- [17] T. Tolker-Nielsen. *EXOMARS 2016 - Schiaparelli Anomaly Inquiry*. Technical Report DG-I/2017/546/TTN, ESA, 2017.
- [18] B. Laub, M. J. Wright, and E. Venkatapathy. *the Thermal Protection System (TPS) Design and the Relationship to Atmospheric Entry Environments*. In 6th International Planetary Probe Workshop, 2008.
- [19] F. S. Milos and Y. K. Chen. *Ablation, Thermal Response, and Chemistry Program for Analysis of Thermal Protection Systems*. Journal of Spacecraft and Rockets, [50\(1\):137–149](#), 2013.
- [20] J. M. Bouilly, F. Bonnefond, L. Dariol, P. Jullien, and F. Leleu. *Ablative thermal protection systems for entry in Mars atmosphere. A presentation of materials solutions and testing capabilities*. 4th International Planetary Probe Workshop, Pasadena California, 2006.
- [21] E. Venkatapathy, C. E. Szalai, B. Laub, H. H. Hwang, J. L. Conley, J. Arnold, and . Co-authors. *Thermal Protection System Technologies for Enabling Future Sample Return Missions*. NASA, White Paper to the NRC Decadal Primitive Bodies Sub-Panel, Washington DC.
- [22] Y. Liu and Z. Jiang. *Concept of non-ablative thermal protection system for hypersonic vehicles*. AIAA Journal, [51\(3\):584–590](#), 2013.
- [23] A. Turchi. *A Gas-Surface Interaction Model for the Numerical Study of High Temperature Flows Over Pyrolyzing Ablative Materials*. PhD thesis, 2011.
- [24] G. Bellas-Chatzigeorgis. *Development of Advanced Gas-Surface Interaction Models for Chemically Reacting Flows for Re-Entry Conditions*. PhD thesis, von Karman Institute and Politecnico di Milano, 2018.

- [25] B. Helber, A. Turchi, J. B. Scoggins, A. Hubin, and T. E. Magin. *Experimental investigation of ablation and pyrolysis processes of carbon-phenolic ablators in atmospheric entry plasmas*. International Journal of Heat and Mass Transfer, [100:810–824](#), 2016.
- [26] F. P. Incropera, D. P. DeWitt, T. L. Bergman, and A. S. Lavine. *Fundamentals of Heat and Mass Transfer*. John Wiley & sons, 2006.
- [27] E. R. Van Driest. *Investigation of laminar boundary layer in compressible fluids using the Crocco method*. Technical Report TN 2597, NACA/North American Aviation Inc., Washington, January 1952.
- [28] A. H. Whitehead Jr. *NASP Aerodynamics*. AIAA paper, [89-5013](#), 1989.
- [29] C. B. McGinley, S. A. Berry, G. R. Kinder, M. Barnwell, K. C. Wang, and B. S. Kirk. *Review of Orbiter Flight Boundary Layer Transition Data*. In [9th AIAA/ASME Joint Thermophysics and Heat Transfer Conference Proceedings](#), 2006.
- [30] G. Tu, Z. Hu, and N. D. Sandham. *Enhanced instability of supersonic boundary layer using passive acoustic feedback*. Physics of Fluids, [28\(024103\)](#), 2016.
- [31] J. Ren, S. Fu, and A. Hanifi. *Stabilization of the hypersonic boundary layer by finite-amplitude streaks*. Physics of Fluids, [28\(024110\)](#), 2016.
- [32] F. Li, M. M. Choudhari, M. Carpenter, M. R. Malik, C.-L. Chang, and C. Streett. *Control of Crossflow Transition at High Reynolds Numbers Using Discrete Roughness Elements*. AIAA Journal, [54\(1\):39–52](#), 2016.
- [33] A. Wagner. *Passive Hypersonic Boundary Layer Transition Control Using Ultrasonically Absorptive Carbon-Carbon Ceramic with Random Microstructure*. PhD thesis, KU Leuven, 2014.
- [34] T. Cebeci and J. Cousteix. *Modeling and Computation of Boundary-Layer Flows: Laminar, Turbulent and Transitional Boundary Layers in Incompressible Flows : Solutions Manual and Computer Programs*. Horizons Pub., 2001.
- [35] S. P. Schneider. *Effects of Roughness on Hypersonic Boundary-Layer Transition*. Journal of Spacecraft and Rockets, [45\(2\):193–209](#), 2008.
- [36] S. P. Schneider. *Hypersonic Boundary-Layer Transition Experiments on Blunt Bodies with Roughness*. AIAA paper, [2008-501](#), 2008.

- [37] A. Tumin. *Nonparallel Flow Effects on Roughness-Induced Perturbations in Boundary Layers*. Journal of Spacecraft and Rockets, [45\(6\):1176–1184](#), 2008.
- [38] P. Balakumar. *Receptivity of Hypersonic Boundary Layers to Acoustic and Vortical Disturbances*. AIAA paper, [2011-371](#), 2013.
- [39] M. M. Choudhari, F. Li, C.-L. Chang, J. Edwards, M. Kegerise, and R. A. King. *Laminar-Turbulent Transition behind Discrete Roughness Elements in a High-Speed Boundary Layer*. AIAA paper, [2010-1575](#), 2010.
- [40] M. M. Choudhari, F. Li, M. Bynum, M. Kegerise, and R. A. King. *Computations of disturbance amplification behind isolated roughness elements and comparison with measurements*. AIAA paper, [2015-2625](#), 2015.
- [41] S. J. Hein, A. Theiss, A. Di Giovanni, C. Stemmer, T. Schilden, W. Schröder, P. Paredes, M. M. Choudhari, F. Li, and E. Reshotko. *Numerical investigation of roughness effects on transition on spherical capsules*. Journal of Spacecraft and Rockets, [56\(2\):388–404](#), 2019.
- [42] P. Iyer, S. Muppidi, and K. Mahesh. *Roughness-Induced Transition in High Speed Flows*. AIAA paper, [2011-566](#), 2011.
- [43] J. H. Fransson, A. Talamelli, L. Brandt, and C. Cossu. *Delaying transition to turbulence by a passive mechanism*. Physical Review Letters, [96\(6\):1–4](#), 2006.
- [44] K. D. Fong, X. Wang, Y. Huang, X. Zhong, G. R. McKiernan, R. A. Fisher, and S. P. Schneider. *Second mode suppression in hypersonic boundary layer by roughness: Design and experiments*. AIAA Journal, [53\(10\):3138–3143](#), 2015.
- [45] N. Martin, G. Grossir, F. Miró Miró, D. Le Quang, and O. Chazot. *Implementation of a laser-based schlieren system for boundary layer instability investigation in the vki h3 hypersonic wind tunnel*. AIAA paper, [2019-0624](#), 2019.
- [46] S. P. Schneider. *Hypersonic Boundary-Layer Transition with Ablation and Blowing*. Journal of Spacecraft and Rockets, [47\(2\):225–237](#), 2010.
- [47] M. R. Malik. *Prediction and control of transition in supersonic and hypersonic boundary layers*. AIAA Journal, [27\(11\):1487–1493](#), 1989.
- [48] H. B. Johnson, J. E. Gronvall, and G. V. Candler. *Reacting hypersonic boundary layer stability with blowing and suction*. AIAA paper, [2009-938](#), 2009.

- [49] F. Li, M. M. Choudhari, C.-L. Chang, and J. White. *Effects of injection on the instability of boundary layers over hypersonic configurations*. Physics of Fluids, **25**(10), 2013.
- [50] J. G. Marvin and C. M. Akin. *Combined effects of mass addition and nose bluntness on boundary-layer transition*. AIAA Journal, **8**(5):857–863, 1970.
- [51] F. Miró Miró. *Numerical Study of the Stability of a Hypersonic Boundary Layer in the presence of Blowing*. Technical Report TR 2015-28, von Karman Institute for Fluid Dynamics, Brussels, Belgium, 2015.
- [52] A. V. Fedorov, N. D. Malmuth, A. Rasheed, and H. G. Hornung. *Stabilization of hypersonic boundary layers by porous coatings*. AIAA Journal, **39**(4):605–610, 2001.
- [53] S. V. Lukashevich, A. A. Maslov, A. N. Shiplyuk, A. V. Fedorov, and V. G. Soudakov. *Stabilization of High-Speed Boundary Layer Using Porous Coatings of Various Thicknesses*. AIAA Journal, **50**(9):1897–1904, 2012.
- [54] I. A. Leyva, S. J. Laurence, A. W.-K. Beierholm, H. G. Hornung, R. M. Wagnild, and G. V. Candler. *Transition delay in hypervelocity boundary layers by means of CO₂/acoustic instability interactions*. AIAA paper, **2009-1287**, 2009.
- [55] J. S. Jewell, R. M. Wagnild, I. A. Leyva, G. V. Candler, and J. E. Shepherd. *Transition Within a Hypervelocity Boundary Layer on a 5-Degree Half-Angle Cone in Air/CO₂ Mixtures*. AIAA paper, **2013-0523**, 2013.
- [56] I. A. Leyva, J. S. Jewell, S. J. Laurence, H. G. Hornung, and J. E. Shepherd. *On the Impact of Injection Schemes on Transition in Hypersonic Boundary Layers*. AIAA paper, **2009-7204**, 2009.
- [57] H. G. Hornung. *Performance data of the new free-piston shock tunnel at GALCIT*. AIAA/ASME/SAE/ASEE 28th Joint Propulsion Conference and Exhibit, 1992, **92-3943**, 1992.
- [58] K. Itoh, S. Ueda, T. Komuro, K. Sato, H. Tanno, and M. Takahashi. *Hypervelocity aerothermodynamic and propulsion research using a high enthalpy shock tunnel heist*. 9th International Space Planes and Hypersonic Systems and Technologies Conference, **99-499:1-8**, 1999.
- [59] K. Hannemann, J. M. Schramm, and S. Karl. *Recent Extensions to the High Enthalpy Shock Tunnel Göttingen (HEG)*. In 2nd International ARA Days “Ten Years after ARD”, Arcachon, France, 2008.

- [60] C. B. Johnson, P. C. Stainback, K. C. Wicker, and L. R. Boney. *Boundary-Layer Edge Conditions and Transition Reynolds Number Data for a Flight Test at Mach 20 (Reentry F)*. Technical Report TM X-2584, NASA, Washington D.C., 1972.
- [61] S. H. Walker, J. Sherk, D. Shell, R. Schena, J. F. Bergmann, and J. Gladbach. *The DARPA/AF Falcon program: The hypersonic technology vehicle #2 (HTV-2) flight demonstration Phase*. 15th AIAA International Space Planes and Hypersonic Systems and Technologies Conference, [2008-2539](#), 2008.
- [62] R. L. Kimmel, D. Adamczak, A. Paull, R. Paull, J. Shannon, R. Pietsch, M. Frost, and H. Alesi. *HIFiRE-1 Ascent-Phase Boundary-Layer Transition*. Journal of Spacecraft and Rockets, [52\(1\):217–230](#), 2015.
- [63] B. M. Wheaton, D. C. Berridge, T. D. Wolf, R. T. Stevens, and B. E. McGrath. *Boundary Layer Transition (BOLT) Flight Experiment Overview*. AIAA paper, [2018-2892](#), 2018.
- [64] S. Chapman and T. Cowling. *The Mathematical Theory of Non-uniform Gases: An Account of the Kinetic Theory of Viscosity, Thermal Conduction, and Diffusion in Gases*. The University Press, 1939.
- [65] F. G. Blottner, M. Johnson, and M. Ellis. *Chemically Reacting Viscous Flow Program For Multi-Component Gas Mixtures*. Technical Report SC-RR-70-754, Sandia Laboratories, 1971.
- [66] R. N. Gupta, J. M. Yos, R. A. Thompson, and K.-P. Lee. *A review of Reaction Rates and Thermodynamic and Transport Properties for an 11-Species Air Model for Chemical and Thermal Nonequilibrium Calculations to 30000K*. Technical Report RP-1232, NASA, 1990.
- [67] M. Fertig, A. Dohr, and H.-H. Fröhlauf. *Transport Coefficients for High Temperature Nonequilibrium Air Flows*. Journal of Thermophysics and Heat Transfer, [15\(2\):148–156](#), 2001.
- [68] B. J. McBride, M. J. Zehe, and S. Gordon. *NASA Glenn Coefficients for Calculating Thermodynamic Properties of Individual Species*. Technical Report 2002-21155, NASA, 2002.
- [69] T. E. Magin and G. Degrez. *Transport algorithms for partially ionized and unmagnetized plasmas*. Journal of Computational Physics, [198\(2\):424–449](#), 2004.
- [70] W. Sutherland. *The viscosity of gases and molecular force*. Philosophical Magazine Series 5, [36\(223\):507–531](#), 1893.

- [71] G. Stuckert and H. L. Reed. *Linear Disturbances in Hypersonic, Chemically Reacting Shock Layers*. AIAA Journal, **32**(7):1384–1393, 1994.
- [72] M. L. Hudson, N. Chokani, and G. V. Candler. *Linear stability of hypersonic flow in thermochemical nonequilibrium*. AIAA Journal, **35**(6):958–964, 1997.
- [73] S. A. Gaponov. *Effect of the Properties of a Porous Coating on Boundary Layer Stability*. Technical Report TM 75235, NASA, Santa Barbara, CA, 1978.
- [74] C. J. J. Stalmach, J. J. Bertin, T. C. Pope, and M. H. McCloskey. *A Study of Boundary Layer Transition on Outgassing Cones in Hypersonic Flow*. Technical Report CR-1908, NASA, 1971.

2

Thermophysical framework

The accurate prediction of the behavior of fluids requires the use of an appropriate thermophysical framework. Hypersonic flows around vehicles flying at altitudes where the air density allows to assume continuum conditions ($\text{Kn} \ll 1$) can be modeled assuming gas mixtures to behave as a mixture of dilute gases, and using the Navier-Stokes equations to describe them [1].

2.1 Thermodynamic flow assumptions

One may describe a dilute mixture of gases with one of several thermodynamic flow assumptions. In order to understand their modeling implications, one must first be aware of the physical phenomena occurring to gas species at increasing temperatures, which are sketched in Fig. 2.1. Particles can store energy in the form of translation, rotation, vibration or excitation of their electronic levels [3]. At low temperatures, the energy of a particle comes from its translation and rotation. As temperature increases, the molecules start vibrating, and eventually dissociate, thus separating their atoms. As the temperature continues to increase, the particles' bond electrons reach excited energy levels and eventually escape, leading to a partially ionized plasma. Depending on the rate of energy transfer between the different modes, it may be appropriate to model the thermal state of a species with multiple temperatures, describing certain groups of energy modes. There have been research efforts to develop reliable three-temperature models [4, 5], however, the uncertainty in the energy-exchange source terms necessary for the

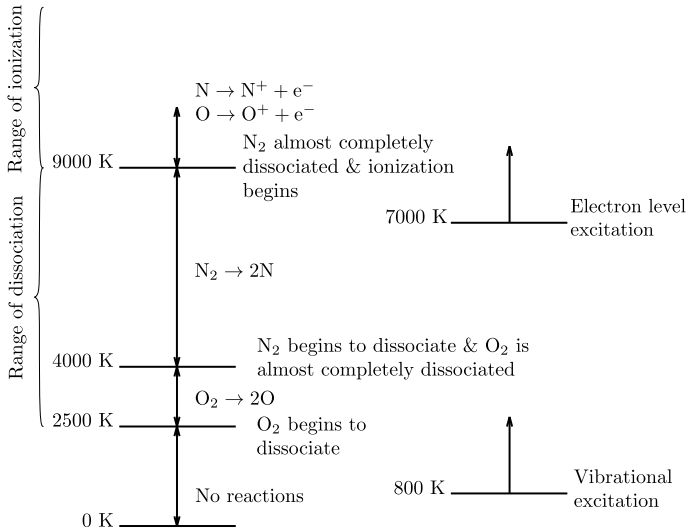


Figure 2.1: Temperature ranges for vibrational excitation, dissociation and ionization for air at 1-atm. Adapted from Anderson [1, Ch. 9.3] and Scoggins & Magin [2]. In general, larger pressures tend to increase the dissociation/ionization activation temperatures, whereas lower pressures decrease them.

correct coupling of the various mode-specific energy equations have established two-temperature models as the most extensively used [3, 6–11].. Two-temperature models typically feature a temperature T describing the heavy-particle translational and the rotational energy modes, and a second temperature T_v describing the vibrational, the electronic and the electron-particle translational energy modes.

The most physically general among the thermodynamic assumptions considered in the present work is (two-temperature) thermo-chemical non-equilibrium (TCNE). TCNE makes no assumption as to the relationship between the vibrational relaxation, chemical and flow time scales ($\tau_{chem} \sim \tau_{vib} \sim \tau_{flow}$). If vibrational relaxation occurs significantly faster than the chemical activity and the flow motion ($\tau_{vib} \ll \tau_{chem} \sim \tau_{flow}$), it is legitimate to assume thermal equilibrium and describe all energy modes with a single temperature T . This is hereinafter referred to as (one temperature) chemical non-equilibrium (CNE). If, on the other hand, the chemical activity is significantly slower than vibrational relaxation and the flow motion ($\tau_{chem} \gg \tau_{vib} \sim \tau_{flow}$), one may model the flow with two temperatures T and T_v , yet neglecting (freezing) the chemical activity. This is referred to as thermal non-equilibrium (TNE). If both the chemical activity and vibrational relaxation are overly faster than the flow motion ($\tau_{chem} \sim \tau_{vib} \ll \tau_{flow}$), one may assume local thermo-chemical equilibrium (LTE). Contrarily, if they are overly slower than the flow motion ($\tau_{chem} \sim \tau_{vib} \gg \tau_{flow}$), one may assume

the mixture to behave like a thermo-chemically frozen gas (TCFG). Finally, if vibrational relaxation occurs substantially faster and the chemical activity is considerably slower than the flow motion ($\tau_{vib} \ll \tau_{flow} \ll \tau_{chem}$), the mixture can be described as a chemically frozen gas, yet in vibrational equilibrium. Authors oftentimes refer to this as a thermally perfect gas (TPG).

The difference between the LTE and LTEED flow assumptions is whether the elemental composition is assumed constant or not. This assumption is acceptable for nitrogen-oxygen mixtures at low temperatures, however it is not for higher temperatures [12] or in situations with foreign-gas injection through the surface, like in ablation scenarios. The differences between the two mathematical treatments are developed in § 2.3.3 and 2.3.4.

A summary of all the aforementioned assumptions can be found in table 2.1. The combinations that are omitted correspond to unrealistic physical assumptions in the environment of hypersonic flights. The relationships between the vibrational-relaxation, chemical and flow time scales can be also visualized through the values of the vibrational and chemical Damköhler numbers (Da_v and Da). The former represents the ratio of flow and the vibrational-relaxation time scales, and the latter the ratio of the flow and the chemical time scales. The orders of magnitude of these non-dimensional parameters for all situations are also included in table 2.1.

An important flow assumption that is excluded from table 2.1 is that of a calorically perfect gas (CPG). Assuming a gas to be calorically perfect implies that its vibrational and electronic energies are neglected, and only the translational and rotational energy modes are taken into consideration. For this reason, it is restricted to thermal ranges below the vibrational activation temperature (see Fig. 2.1). A particle's translational and rotational energy is linear with temperature if atoms are assumed spherical and molecules are assumed to behave like a rigid rotor (see § 4.1). A CPG may be seen as a particular case of a TCFG with the vibrational-electronic-electron temperature (T_v) being much lower than the minimum vibrational activation temperature of any of the molecular species' vibrational modes (θ_{sm}^{Vib}).

The aforementioned two-temperature classification assumes a decoupling between the rotational and vibrational energy modes. However, this is sometimes not an acceptable hypothesis for aggressive lunar or martian atmospheric reentries – see Refs. 3, 13.

2.2 Gas mixtures and reactions

Aside from the flow assumption adopted to describe the thermodynamic behavior of the gas of interest, the other modeling choice determining the range of physical phenomena that can be correctly considered is the gas mixture. The list of species

	Chemical time scale		
	chem. froz.	chem. non-eq.	chem. eq.
	$\tau_{flow} \ll \tau_{chem}$ $Da \ll 1$	$\tau_{flow} \sim \tau_{chem}$ $Da \sim 1$	$\tau_{flow} \gg \tau_{chem}$ $Da \gg 1$
Vibrational time scale	vib. froz. $\tau_{flow} \ll \tau_{vib}$ $Da_v \ll 1$	TCFG	—
	vib. non-eq. $\tau_{flow} \sim \tau_{vib}$ $Da_v \sim 1$	TNE	TCNE
	vib. eq. $\tau_{flow} \gg \tau_{vib}$ $Da_v \gg 1$	TPG	CNE
			LTE or LTEED

Table 2.1: Summary of the various thermodynamic assumptions based on the relation between their chemical, vibrational relaxation, and flow time scales. CPG is a particular case of TCFG with $T_v \ll \min(\theta_{sm}^{Vib})$.

into which the gas mixture is decomposed conditions whether certain chemical reactions may be accounted for by the thermo-chemical model or not.

For instance, taking air as an example, non-reacting air may be approximated with acceptable accuracy as a mixture of two species: diatomic nitrogen and oxygen – [N₂, O₂]. In order to account also for the dissociation of such molecules, one requires the gas mixture to include also atomic nitrogen and oxygen – [N, O, N₂, O₂]. This 4-species mixture however, would implicitly neglect the exchange reactions between these four species, that give rise to the transient appearance of nitric oxide NO during the dissociation of N₂ and O₂. Eventually NO also dissociates into N and O, but nonetheless, an accurate modeling of dissociating air requires a 5-species mixture commonly referred to as air-5 – [N, O, NO, N₂, O₂]. If one is interested in accurately modeling also ionization, then six additional species are required: the ions of the five heavy species composing the air-5 mixture, plus the free-electron species. This mixture is commonly named air-11 – [N, O, NO, N₂, O₂, N⁺, O⁺, NO⁺, N₂⁺, O₂⁺, e⁻].

The choice of the species composing the gas mixture is not sufficient to ensure the correct modeling of their chemical interaction. An appropriate list of chemical reactions must also be employed in order to accurately model the gas chemistry. Most chemical reaction rates are modeled using Arrhenius-like expressions (see § 4.3), and thus require a series of reaction-rate constants. The accurate choice of these constants remains a very active field of research, with most of the effort over

the last years being done by quantum chemists [14–18]. The use of one or another source of reaction-rate constants can lead to major differences in the predicted gas behavior (see § 10.1). For this reason, the name assigned to a given gas mixture comprises the identification of the species conforming it (air-5, air-11, etc) as well as the bibliographic reference from which the set of reactions and the reaction-rate constants were obtained. For instance, the air-5-Park85 mixture has the five species required to model dissociating air [N, O, NO, N₂, O₂], and uses the reaction-rate constants proposed by Park [19] in his 1985 article.

A series of non-reacting mixtures are also employed in this work. It is the case for example of the air-2-He mixture, which includes the two non-reacting air species and Helium – [N₂, O₂, He]. In such mixtures, the interest resides in the accurate modeling of the mixture thermodynamic and transport properties for the various states of species interdiffusion.

A full list of the mixtures considered within this dissertation, together with the reaction rate constants they employ may be found in app. J.

2.3 Flow equations

The motion of a compressible fluid can be described with the Navier-Stokes equations, together with the necessary mass- and energy-conservation equations. Depending on the thermodynamic flow assumption used (see table 2.1), these expressions vary slightly.

Equations are presented in their invariant form, making them valid with independence of the coordinate system, and featuring the metric tensor g_{ij} . It allows to keep track, not only of the variable value changes, but also of the modification of the space itself due to such basis changes. It is defined as:

$$g_{ij} = \sum_{k=1}^3 \frac{\partial \mathcal{X}^k}{\partial x^i} \frac{\partial \mathcal{X}^k}{\partial x^j}, \quad (2.1)$$

where \mathcal{X}^i corresponds to the Cartesian coordinates, and x^i to the actual coordinate system to be employed. Examples of the metric tensor for various coordinate systems are:

$$\text{Cartesian: } g_{ij} = \begin{pmatrix} 1 & 0 & 0 \\ 0 & 1 & 0 \\ 0 & 0 & 1 \end{pmatrix}, \quad (2.2a)$$

$$\text{cylindrical: } g_{ij} = \begin{pmatrix} 1 & 0 & 0 \\ 0 & r^2 & 0 \\ 0 & 0 & 1 \end{pmatrix}, \quad (2.2b)$$

$$\text{spherical: } g_{ij} = \begin{pmatrix} 1 & 0 & 0 \\ 0 & r^2 & 0 \\ 0 & 0 & r^2 \sin^2(\theta) \end{pmatrix}, \quad (2.2c)$$

$$\text{orthocurvilinear: } g_{ij} = \begin{pmatrix} h_1^2 & 0 & 0 \\ 0 & h_2^2 & 0 \\ 0 & 0 & h_3^2 \end{pmatrix}. \quad (2.2d)$$

The orthocurvilinear coordinate system, for instance, defined by the three stretching parameters (h_1 , h_2 , and h_3) is equivalent to that used by many authors [9, 20–22] in the stability and transition community. These parameters are, in general, to be treated as arbitrary functions of the spatial coordinates x^i .

The superscript/subscript notation refers to contravariant/covariant vectorial variables. A vectorial variable is contravariant q^i when its components vary with the inverse transformation with respect to the basis change, i.e. they “contra-vary”. On the other hand, it is covariant q_i if its components vary with the same transformation, i.e. they “co-vary”. A spatial covariant derivative is expressed with a coma followed by an index corresponding to the spatial direction with respect to which one is deriving: $q_{,j}^i$.^a The evaluation of covariant derivatives must be done also taking into consideration the curving of the space itself:

$$q_{,k}^j = \frac{\partial q^j}{\partial x^k} + \Gamma_{ik}^j q^i, \quad (2.3)$$

which features the Christoffel symbol of the second kind:

$$\Gamma_{ik}^j = \sum_{l=1}^3 \frac{1}{2g^{jl}} \left(\frac{\partial g_{li}}{\partial x^k} + \frac{\partial g_{lk}}{\partial x^i} - \frac{\partial g_{ik}}{\partial x^l} \right). \quad (2.4)$$

The contravariant metric tensor is simply the inverse of the covariant tensor defined in Eq. 2.2:

$$[g^{ij}] = [g_{ij}]^{-1}. \quad (2.5)$$

One must also note that the expressions presented in this dissertation feature velocities (u^i) in the non-Cartesian reference frame (x^i rather than \mathcal{X}^i). In order to have them in terms of the velocities in the Cartesian reference frame (\mathcal{U}^i), one must replace them through:

$$u^i = \frac{1}{\sqrt{g_{ii}}} \mathcal{U}^i, \quad \forall i \in [1, 2, 3]. \quad (2.6)$$

For instance, when working with an orthocurvilinear coordinate system (Eq. 2.2d), one is usually interested in the flow equations in terms of the velocities in the

^aThe comma derivative notation is restricted to spatial derivatives. For the sake of notation simplicity the spatial subindices are strictly kept to be i , j , k and l throughout the text. Therefore, variable subindices containing commas followed by other symbols are not to be regarded as derivatives.

Cartesian directions (x, y, z), rather than in the curvilinear ones (h_1x, h_2y, h_3z). This requires that one substitutes the velocity components with Eq. 2.6.

A short introduction to the tensorial algebra can be found in Pinna & Groot [23]. For more details, one should refer to the work of Brillouin [24] and Aris [25].

The state variables for the different flow assumptions are:

- TCNE: (u^i, ρ_s, T, T_v) ,
- CNE: (u^i, ρ_s, T) ,
- TNE and TCFG: (u^i, ρ, T, T_v) ,
- LTEED: (u^i, ρ_E, T) ,
- TPG, LTE and CPG: (u^i, ρ, T) .

Expressions for all variables appearing in this section other than the state ones – the dependent variables, can be found in § 4 and in app. A.

2.3.1 Thermo-chemical non-equilibrium (TCNE)

An N_s -species gas mixture in TCNE can be modeled using N_s species-mass-, three momentum-, and two energy-conservation equations:

$$\frac{\partial \rho_s}{\partial t} + (u^j \rho_s)_{,j} = -J_{s,j}^j + \dot{\omega}_s, \quad \forall s \in \mathcal{S}, \quad (2.7a)$$

$$\rho \frac{\partial u^i}{\partial t} + \rho u^j u_{,j}^i = -g^{ij} p_{,j} + \mathbb{T}_{,j}^{ij}, \quad \forall i \in [1, 2, 3], \quad (2.7b)$$

$$\begin{aligned} \rho \frac{\partial h}{\partial t} + \rho u^j h_{,j} &= \frac{\partial p}{\partial t} + u^j p_{,j} + (\kappa_{tr} g^{ij} T_{,i})_{,j} + (\kappa_v g^{ij} T_{v,i})_{,j} + \\ &\quad - \mathcal{J}_{,j}^j + g_{ik} \mathbb{T}^{kj} u_{,j}^i, \end{aligned} \quad (2.7c)$$

$$\begin{aligned} \rho \frac{\partial h_v}{\partial t} + \rho u^j h_{v,j} &= \frac{\partial p_e}{\partial t} + u^j p_{e,j} + (\kappa_v g^{ij} T_{v,i})_{,j} - \mathcal{J}_{v,j}^j + \\ &\quad + Q_{TV} + \sum_{s \in \mathcal{S}_{\text{mol}}} h_{vs} \dot{\omega}_s, \end{aligned} \quad (2.7d)$$

where the work of the electron pressure p_e is obviously zero for non-ionized mixtures, and where radiation has been neglected.

Alternatively, since the sum of the diffusion fluxes (J_s^j) must be equal to zero, one may substitute the mass-conservation equation of one of the species^b with the mixture continuity equation:

$$\frac{\partial \rho}{\partial t} + (u^j \rho)_{,j} = 0. \quad (2.8)$$

^bPreferably the bath species – the one with the largest mass fraction.

This improves the numerical behavior of the system.

In Eqs. 2.7 and 2.8, J_s^j , \mathcal{J}^j and \mathcal{J}_v^j are the diffusion species mass, total energy, and vibrational-electronic-electron energy fluxes respectively, \mathbb{T}^{ij} is the viscous stress tensor:

$$\mathbb{T}^{ij} = \lambda g^{ij} u_{,k}^k + \mu \left(g^{jk} u_{,k}^i + g^{ik} u_{,k}^j \right), \quad (2.9)$$

ω_s are the species source terms, Q_{TV} is the vibrational-electronic-electron energy relaxation source term, μ and λ are the first and second dynamic viscosity coefficients, κ_{tr} and κ_v are the frozen thermal conductivities due to the translational-rotational and the vibrational-electronic-electron energy, h is the mixture static enthalpy, h_v is the mixture enthalpy due to the vibrational-electronic-electron energy. A Maxwellian reactive regime is assumed, [26] justifying the absence of a reactive pressure term in Eq. 2.7b.

The energy diffusion fluxes are defined as:

$$\mathcal{J}^j = \sum_{s \in S} h_s J_s^j, \quad (2.10)$$

$$\mathcal{J}_v^j = \sum_{s \in S_{\text{mol}}} h_{vs} J_s^j, \quad (2.11)$$

and the species mass diffusion fluxes J_s^j , in their most general form, are defined as:

$$\begin{aligned} J_s^j &= - \sum_{\ell \in S} \rho_s \mathcal{D}_{s\ell} d_\ell^j = \\ &= - \sum_{\ell \in S} g^{ij} \rho_s \mathcal{D}_{s\ell} \left(\frac{p}{n k_B T} \psi_{\ell,i} + \frac{\psi_\ell - Y_\ell}{n k_B T} p_{,i} + \frac{\zeta_\ell}{T} T_{,i} + \right. \\ &\quad \left. + \frac{\zeta_{v\ell}}{T_v} T_{v,i} - \kappa_\ell^E E_i \right), \end{aligned} \quad (2.12)$$

where $\mathcal{D}_{s\ell}$ are the multicomponent diffusion coefficients of species s in species ℓ , Y_ℓ are the species mass fractions, d_ℓ^j are the diffusion driving forces, ψ_ℓ are the species pressure fractions, ζ_ℓ are the species thermal diffusion ratios, $\zeta_{v\ell}$ are the species vibrational-electronic-electron thermal diffusion ratios, which are zero for all species except electrons, E_i is the electric field, ^c n is the mixture number density, k_B is the Boltzmann constant, κ_ℓ^E is a grouping parameter:

$$\kappa_\ell^E = \frac{X_\ell Z_\ell q_e}{k_B T} - \frac{Y_\ell}{k_B T} \sum_{s \in S} X_s Z_s q_e, \quad (2.13)$$

q_e is the electron charge, and Z_s are the species unitary charges.

^cIn non-ionized mixtures, the electric field is obviously zero, and does not contribute to the diffusion fluxes.

The implicit definition of the diffusion driving forces (d_s^j) in Eq. 2.12 corresponds to the dependent form of the driving forces, which is necessary [26] in order to solve the Stefan-Maxwell equations (see § 4.2.2). One must also bear in mind that this dependent form also satisfies that:

$$\sum_{s \in \mathcal{S}} d_s^j = 0^j, \quad (2.14a)$$

$$\sum_{s \in \mathcal{S}} \rho_s \mathcal{D}_{s\ell} = 0, \quad \forall \ell \in \mathcal{S}. \quad (2.14b)$$

For plasma flows around hypersonic vehicles, the low values of the Debye length ($< 10 \mu\text{m}$ ^d) compared to the vehicles', allow to assume ambipolar diffusion.^e In such scenarios the influence of the electric field can be absorbed into the diffusion coefficients (see § 4.2.2), making Eq. 2.12 become:

$$J_s^j = - \sum_{\ell \in \mathcal{S}} g^{ij} \rho_s \mathcal{D}_{s\ell} \left(\frac{p}{n k_B T} \psi_{\ell,i} + \frac{\psi_{\ell} - Y_{\ell}}{n k_B T} p_{,i} + \frac{\zeta_{\ell}}{T} T_{,i} + \frac{\zeta_{v\ell}}{T_v} T_{v,i} \right). \quad (2.15)$$

Thermo- and barodiffusion are oftentimes neglected (three last addends in the right-hand side of Eq. 2.15), leading to diffusion forces driven exclusively by pressure-fraction gradients:

$$d_s^j = g^{ij} \frac{p}{n k_B T} \psi_{s,i}. \quad (2.16)$$

For non-ionized mixtures, $\psi_s = X_s$ and $p = n k_B T$ (see app. A), leading to diffusion forces driven by the mole fraction gradients:

$$d_s^j = g^{ij} X_{s,i}. \quad (2.17)$$

Authors [7, 11, 28] often express the diffusion fluxes with the mass concentration gradients $Y_{\ell,j}$ as their driving force. Such a formulation requires an appropriate modification of the multicomponent diffusion coefficients $\mathcal{D}_{s\ell}$.

Alternatively, one may also model the diffusion fluxes in a simplified fashion using effective diffusion coefficients (see § 4.2.2):

$$J_s^j = -\rho \mathcal{D}_{\text{eff},s} d_s^j. \quad (2.18)$$

Note that the vibrational-electronic-electron energy source term due to the production of molecules (last addend in the right-hand-side of Eq. 2.7d) assumes non-preferential dissociation/recombination. This implies that the dissociated molecules are generally in the vibrational state of the average molecule^f.

^dThis value corresponds to the maximum Debye length obtained for the most aggressive test case under consideration – the Mach-45 trajectory point in § 10.4.

^eFor other plasma flows, featuring low pressures and large Debye lengths, the electric field is either prescribed (plasma wind tunnels) or it is obtained from the resolution of the Poisson equation. Alternatively, it can be obtained making a series of simplifying hypotheses on the order of magnitude of the different flow magnitudes like in Ref. 27.

^fSee footnote w in page 4-31.

2.3.2 Chemical non-equilibrium (CNE) yet in thermal equilibrium

Assuming thermal equilibrium, the thermal state of the gas can be described with a sole temperature T for all energy modes. This eliminates the need of having a second energy-conservation equation for the vibrational-electronic-electron energy (Eq. 2.7d). The total-energy-conservation equation is also simplified by unifying the thermal conduction terms due to the two temperatures into a single addend:

$$\rho \frac{\partial h}{\partial t} + \rho u^j h_{,j} = \frac{\partial p}{\partial t} + w^j p_{,j} + (\kappa^{Fr} g^{ij} T_{,i})_{,j} - \mathcal{J}_{,j}^j + g_{ik} \mathbb{T}^{kj} u_{,j}^i, \quad (2.19)$$

where the frozen thermal conductivity (κ^{Fr}) is the sum of the translational-rotational and vibrational-electronic-electron thermal conductivities appearing in Eq. 2.7c.

The species-mass-, mixture-mass- and momentum-conservation equations remain unchanged (Eqs. 2.7a, 2.7b and 2.8). The dependencies of the dependent variables in them, however, do change, since CNE assumes all energy modes to behave with a unique temperature T . This is further analyzed in § 4.

Regarding the diffusion driving forces, in CNE one has that $\psi_s = X_s$ and $p = n k_B T$. Therefore, if one neglects thermo- and barodiffusion, the driving forces can be simplified to Eq. 2.17 for both ionized and non-ionized mixtures.

2.3.3 Local thermo-chemical equilibrium with elemental demixing (LTEED)

Assuming chemical equilibrium, the molar concentration of the various species can be obtained from solving the equilibrium system. Examples of equilibrium systems for the air-5 and air-11 mixtures can be found in app. B. Such systems essentially establish a functional dependency of the species concentrations on temperature, pressure, and the elemental fractions: $X_s = X_s(p, T, \mathcal{X}_E)$. These elemental fractions can be obtained from specific elemental-mass-conservation equations. In order to reach them, it is necessary to introduce the elemental stoichiometric matrix \mathcal{E}_{Es}^* , containing the number of atoms of element E in species s . For example, for an air-5 mixture with $s \in [\text{N}, \text{O}, \text{NO}, \text{N}_2, \text{O}_2]$ and $E \in [\text{N}, \text{O}]$, the elemental stoichiometric matrix contains:

$$\mathcal{E}_{Es}^* = \begin{bmatrix} \text{N} & \text{O} & \text{NO} & \text{N}_2 & \text{O}_2 \\ 1 & 0 & 1 & 2 & 0 \\ 0 & 1 & 1 & 0 & 2 \end{bmatrix} \begin{matrix} \text{N} \\ \text{O} \end{matrix}. \quad (2.20)$$

Ionized mixtures where charge neutrality is not imposed require a special treatment. Electrons are also considered as an element, yet with negative stoichiometry

for the ion particles, since they are actually missing an electron from one of their atoms. This leads to a few particularities, that are laid out at the end of app. A. Therefore, for an air-11 mixture with $s \in [N, O, NO, N_2, O_2, N^+, O^+, NO^+, N_2^+, O_2^+, e^-]$ and $E \in [N, O, e^-]$, the elemental stoichiometric matrix contains:

$$\mathcal{E}_{Es}^* = \begin{bmatrix} N & O & NO & N_2 & O_2 & N^+ & O^+ & NO^+ & N_2^+ & O_2^+ & e^- \\ 1 & 0 & 1 & 2 & 0 & 1 & 0 & 1 & 2 & 0 & 0 \\ 0 & 1 & 1 & 0 & 2 & 0 & 1 & 1 & 0 & 2 & 0 \\ 0 & 0 & 0 & 0 & 0 & -1 & -1 & -1 & -1 & -1 & 1 \end{bmatrix} \begin{matrix} N \\ O \\ e^- \end{matrix} . \quad (2.21)$$

Similarly to what is done by Scoggins [3], one may add all the species-mass-conservation equations multiplied by the corresponding corrected elemental stoichiometric coefficient:

$$\mathcal{E}_{Es} = \mathcal{E}_{Es}^* \frac{\mathcal{M}_E}{\mathcal{M}_s}, \quad \forall s \in \mathcal{S}, \quad \forall E \in \mathcal{E}, \quad (2.22)$$

with the objective of having a mass balance for each element. This yields:

$$\sum_{s \in \mathcal{S}} \left(\mathcal{E}_{Es} \frac{\partial \rho_s}{\partial t} + \mathcal{E}_{Es} (u^i \rho_s)_{,i} \right) = - \sum_{s \in \mathcal{S}} \mathcal{E}_{Es} J_{s,j}^j, \quad (2.23)$$

where the species source terms ($\dot{\omega}_s$) have been dropped because they are identically zero in chemical equilibrium. Since in thermal equilibrium $\psi_s = X_s$, and $p = n k_B T$, the diffusion fluxes from Eq. 2.15 can be simplified to:

$$J_s^j = - \sum_{\ell \in \mathcal{S}} g^{ij} \rho_s \mathcal{D}_{s\ell} \left(X_{\ell,i} + \frac{X_\ell - Y_\ell}{p} p_{,i} + \frac{\zeta_\ell + \zeta_{v\ell}}{T} T_{,i} \right). \quad (2.24)$$

Exploiting the functional dependency of the species mole fractions established by the equilibrium system $X_s = X_s(p, T, \mathcal{Y}_E)$ ^g, one may expand the mole-fraction gradient using the chain rule:

$$X_{\ell,i} = \frac{\partial X_\ell}{\partial p} p_{,i} + \frac{\partial X_\ell}{\partial T} T_{,i} + \sum_{F \in \mathcal{E}} \frac{\partial X_\ell}{\partial \mathcal{Y}_F} \mathcal{Y}_{F,i}. \quad (2.25)$$

One may then operate with Eq. 2.23 to reach the **elemental-mass-conservation equations**:

$$\frac{\partial \rho_E}{\partial t} + (u^i \rho_E)_{,i} = - J_{E,j}^j, \quad \forall E \in \mathcal{E}, \quad (2.26)$$

which has the same morphology as the species-mass-conservation equation (Eq. 2.7a), without production terms. In Eq. 2.26 the elemental partial densities are defined as:

$$\rho_E = \sum_{s \in \mathcal{S}} \mathcal{E}_{Es} \rho_s = \mathcal{Y}_E \rho, \quad \forall E \in \mathcal{E}. \quad (2.27)$$

^gThe equilibrium system in app. B actually establishes $X_s = X_s(p, T, \mathcal{X}_E)$, but employing the definitions at the end of app. A it is simple to reach $X_s = X_s(p, T, \mathcal{Y}_E)$.

The elemental diffusion fluxes are obtained from substituting Eq. 2.24 into the first summation in the right-hand side of Eq. 2.23:

$$\begin{aligned} J_E^j &= \sum_{s \in \mathcal{S}} \mathcal{E}_{Es} J_s^j = \\ &= -g^{ij} \left(\sum_{F \in \mathcal{E}} \mathcal{C}_{EF} \mathcal{Y}_{F,i} + \mathcal{B}_E p_{,i} + \mathcal{A}_E T_{,i} \right), \quad \forall E \in \mathcal{E}, \end{aligned} \quad (2.28)$$

where:

$$\mathcal{A}_E = \sum_{s \in \mathcal{S}} \sum_{\ell \in \mathcal{S}} \mathcal{E}_{Es} \rho_s \mathcal{D}_{s\ell} \left(\frac{\partial X_\ell}{\partial T} + \frac{\zeta_\ell + \zeta_{v\ell}}{T} \right), \quad \forall E \in \mathcal{E}, \quad (2.29a)$$

$$\mathcal{B}_E = \sum_{s \in \mathcal{S}} \sum_{\ell \in \mathcal{S}} \mathcal{E}_{Es} \rho_s \mathcal{D}_{s\ell} \left(\frac{\partial X_\ell}{\partial p} + \frac{X_\ell - Y_\ell}{p} \right), \quad \forall E \in \mathcal{E}, \quad (2.29b)$$

$$\mathcal{C}_{EF} = \sum_{s \in \mathcal{S}} \sum_{\ell \in \mathcal{S}} \mathcal{E}_{Es} \rho_s \mathcal{D}_{s\ell} \frac{\partial X_\ell}{\partial \mathcal{Y}_F}, \quad \forall E, F \in \mathcal{E}. \quad (2.29c)$$

Note that Eq. 2.15 and consequently Eqs. 2.24 and 2.28 assume ambipolar diffusion. In the absence of the ambipolar assumption, the electric field E_i must be either imposed, or obtained from Poisson's equation. This implies that the contribution of the electric field is no longer to be absorbed by the diffusion coefficients $\mathcal{D}_{s\ell}$. Consequently, the elemental diffusion fluxes in Eq. 2.28 include an additional term accounting for the effect of the electric field on the elemental composition:

$$J_E^j = -g^{ij} \left(\sum_{F \in \mathcal{E}} \mathcal{C}_{EF} \mathcal{Y}_{F,i} + \mathcal{B}_E p_{,i} + \mathcal{A}_E T_{,i} + \mathcal{D}_E E_i \right), \quad \forall E \in \mathcal{E}, \quad (2.30)$$

where:

$$\mathcal{D}_E = - \sum_{s \in \mathcal{S}} \sum_{\ell \in \mathcal{S}} \mathcal{E}_{Es} \rho_s \mathcal{D}_{s\ell} \kappa_\ell^E, \quad \forall E \in \mathcal{E}. \quad (2.31)$$

However, as was already pointed out, plasma flows around hypersonic reentry applications have sufficiently small Debye lengths (Eq. 4.54) to assume ambipolar diffusion.

Alternatively, if one employs a simplified diffusion theory based on effective diffusion coefficients (Eq. 2.18), the coefficients appearing in Eqs. 2.28 and 2.30,

defined by Eqs. 2.29 and 2.31, become:

$$\mathcal{A}_E = \sum_{s \in \mathcal{S}} \mathcal{E}_{Es} \rho \mathcal{D}_{\text{eff}\,s} \left(\frac{\partial X_s}{\partial T} + \frac{\zeta_s}{T} \right), \quad \forall E \in \mathcal{E}, \quad (2.32a)$$

$$\mathcal{B}_E = \sum_{s \in \mathcal{S}} \mathcal{E}_{Es} \rho \mathcal{D}_{\text{eff}\,s} \left(\frac{\partial X_s}{\partial p} + \frac{X_s - Y_s}{p} \right), \quad \forall E \in \mathcal{E}, \quad (2.32b)$$

$$\mathcal{C}_{EF} = \sum_{s \in \mathcal{S}} \mathcal{E}_{Es} \rho \mathcal{D}_{\text{eff}\,s} \frac{\partial X_s}{\partial \mathcal{Y}_F}, \quad \forall E, F \in \mathcal{E}, \quad (2.32c)$$

$$\mathcal{D}_E = - \sum_{s \in \mathcal{S}} \mathcal{E}_{Es} \rho \mathcal{D}_{\text{eff}\,s} \kappa_s^E, \quad \forall E \in \mathcal{E}. \quad (2.32d)$$

The mixture-mass-, momentum-, and energy-conservation equations remain unchanged in form with respect to their CNE version – Eqs. 2.8, 2.7b and 2.19. The functional dependency of the dependent variables on the state quantities (ρ_s, T) is the same as in CNE. The difference being that the species partial densities, when assuming a flow in LTEED, can be expressed as a function of elemental partial densities and temperature $\rho_s = \rho_s(\rho_E, T)$. This functional relation is established through the equilibrium system (app. B) which establishes $X_s = X_s(p, T, \mathcal{Y}_E)^g$, the definitions of the mass and mole fractions of both species and elements (Eqs. A.1 and A.11), and the definitions of the mixture density (Eq. A.5) and pressure (Eq. A.4) in thermal equilibrium. The full system of equations to solve in LTEED is thus composed of Eqs. 2.7b, 2.26 and 2.19, alternatively substituting Eq. 2.26 of the bath element for Eq. 2.8.

2.3.4 Local thermo-chemical equilibrium with constant elemental composition (LTE)

A very common additional hypothesis [1, 3] that greatly simplifies the governing equations in local thermo-chemical equilibrium, is neglecting elemental demixing [12]: $\mathcal{X}_E = \text{cst}$. This leads to the equilibrium concentrations being exclusively a function of pressure and temperature $X_s = X_s(p, T)$. If the elemental concentrations are assumed constant, their individual conservation equations (Eq. 2.26) are no longer needed for the problem to have closure. Hence only the mixture continuity equation (Eq. 2.8) is required. Moreover, the energy-conservation equation (Eq. 2.19) can be further simplified by neglecting both frozen and reactive baro-diffusion, assuming ambipolar diffusion, and grouping the remaining terms into a reactive thermal conductivity. Substituting Eq. 2.24 in Eq. 2.10, together with

Eq. 2.25 with $\partial X_\ell / \partial \mathcal{Y}_F = 0$:

$$\begin{aligned} \mathcal{J}^j &= - \sum_{s,\ell \in \mathcal{S}} h_s g^{ij} \rho_s \mathcal{D}_{s\ell} \left(\left(\frac{\partial X_\ell}{\partial p} + \frac{X_\ell - Y_\ell}{p} \right) p_{,i} + \left(\frac{\partial X_\ell}{\partial T} + \frac{\zeta_\ell + \zeta_{v\ell}}{T} \right) T_{,i} \right) = \\ &= g^{ij} \kappa^{Reac} T_{,i}. \end{aligned} \quad (2.33)$$

The energy equation in LTE can thus be expressed as:

$$\rho \frac{\partial h}{\partial t} + \rho u^j h_{,j} = \frac{\partial p}{\partial t} + u^j p_{,j} + (\kappa g^{ij} T_{,i})_{,j} + g_{ik} \mathbb{T}^{kj} u^i_{,j}, \quad (2.34)$$

where the thermal conductivity includes both the frozen and reactive addends:

$$\kappa = \kappa^{eq} = \kappa^{Fr} + \kappa^{Reac} = \kappa^{Fr} + \sum_{s,\ell \in \mathcal{S}} h_s \rho_s \mathcal{D}_{s\ell} \left(\frac{\partial X_\ell}{\partial T} + \frac{\zeta_\ell + \zeta_{v\ell}}{T} \right). \quad (2.35)$$

It is trivial that for simplified diffusion fluxes based on effective diffusion coefficients (Eq. 2.18), Eq. 2.35 becomes:

$$\kappa = \kappa^{eq} = \kappa^{Fr} + \kappa^{Reac} = \kappa^{Fr} + \sum_{s \in \mathcal{S}} h_s \rho \mathcal{D}_{eff,s} \left(\frac{\partial X_s}{\partial T} + \frac{\zeta_s}{T} \right). \quad (2.36)$$

The frozen thermodiffusion is oftentimes also neglected ($\zeta_s \approx 0$), further simplifying the expression of the reactive thermal conductivity. In ionized mixtures the effect of the electric field is absorbed into the computation of the multicomponent diffusion coefficients $\mathcal{D}_{s\ell}$ appearing in Eq. 2.35 (see § 4.2.2).

Like in LTEED, the mixture-mass- and momentum-conservation equations remain unchanged (Eqs. 2.8 and 2.7b). Once again, it is only the dependencies of the dependent quantities that implicitly do, through the change in dependency of the equilibrium composition $X_s = X_s(p, T)$.

It is important to point out that the simplification of neglecting elemental demixing is not acceptable when analyzing environments in thermo-chemical equilibrium with a wall injection of gases different to the test gas. Take for instance an air flow over an ablating wall – the elemental fraction of carbon at the wall is very high, since all ablation subproducts are carbon-based. However, in the freestream there is a negligible amount of carbon species, and thus a near-zero elemental fraction of carbon. Such a scenario thus requires an LTEED assumption rather than the simpler LTE.

2.3.5 Thermal non-equilibrium yet chemically frozen (TNE)

A gas in TNE must be modeled with the same equation system as one in TCNE, only neglecting the chemical source terms ($\dot{\omega}_s \approx 0$). However, in the absence of

surface mass injection of dissimilar gas species, the diffusion fluxes are zero, and consequently the mass fractions (Y_s) remain constant. This allows to describe a gas in TNE without species inter-diffusion with one mixture-mass-, three momentum- and two energy-conservation equations. The mixture-mass- and momentum-conservation equations are identical to those in TCNE in form (Eqs. 2.8 and 2.7b). The two energy-conservation equations are similar to those in TCNE (Eqs. 2.7c and 2.7d), yet without species mass source terms and energy diffusion fluxes. The total-energy and vibrational-electronic-electron-energy equations in TNE are thus:

$$\rho \frac{\partial h}{\partial t} + \rho u^j h_{,j} = \frac{\partial p}{\partial t} + u^j p_{,j} + (\kappa_{tr} g^{ij} T_{,i})_{,j} + (\kappa_v g^{ij} T_{v,i})_{,j} + g_{ik} \mathbb{T}^{kj} u^i_{,j}, \quad (2.37a)$$

$$\rho \frac{\partial h_v}{\partial t} + \rho u^j h_{v,j} = \frac{\partial p_e}{\partial t} + u^j p_{e,j} + (\kappa_v g^{ij} T_{v,i})_{,j} + Q_{TV}. \quad (2.37b)$$

The functional dependency of all dependent variables involved in these equations (explored in chapter 4) is identical to that in TCNE, only that the species concentrations Y_s remain constant (frozen).

2.3.6 Thermo-chemically frozen gas (TCFG)

Similarly to the TNE case, a TCFG in general requires the same equation set as one in TCNE, neglecting both chemical and energy-relaxation source terms ($\dot{\omega}_s \approx 0$ and $Q_{TV} \approx 0$). However, in the absence of wall blowing of dissimilar gas mixtures, diffusion fluxes can be neglected making the mass fractions constant. In such a scenario, the flow can be described with Eqs. 2.8, 2.7b), 2.37a, and 2.37b. The functional dependency of all dependent variables involved in these equations is identical to that in TNE or TCNE (explored in chapter 4), only that the species concentrations Y_s and the vibrational-electronic-electron temperature T_v remain constant (frozen).

2.3.7 Thermally perfect and chemically frozen gas (TPG)

A TPG, in general, requires the same equation set as a gas in CNE, yet neglecting the species source term ($\dot{\omega} \approx 0$). However, similarly to what was commented for the TNE and TCFG assumptions, when there is no surface injection of dissimilar gases, one can simplify the equation set to simply Eqs. 2.8, 2.7b and 2.34. The only difference is that the thermal conductivity appearing in the energy equation must be the frozen one $\kappa = \kappa^{Fr}$. The functional dependencies of the dependent quantities appearing in them is the same as for TCNE. The difference is that all energy modes are described with a single temperature T , and the mass-fractions Y_s are constant.

2.3.8 Calorically perfect gas (CPG)

When one refers to a CPG, it is implied that the composition remains unchanged, and therefore it can be described with Eqs. 2.8, 2.7b and 2.34, featuring the frozen thermal conductivity $\kappa = \kappa^{Fr}$. As mentioned in § 2.1, the difference between a TPG and a CPG, is the assumption made on the vibrational and electronic energy modes – neglected in CPG.

References

- [1] J. D. Anderson Jr. *Hypersonic and High Temperature Gas Dynamics*. American Institute of Aeronautics and Astronautics, Reston VA, second edition, 2006.
- [2] J. B. Scoggins and T. E. Magin. *Development of Mutation++: Multicomponent Thermodynamics And Transport properties for IONized gases library in C++*. AIAA paper, [2014-2966](#), 2014.
- [3] J. B. Scoggins. *Development of numerical methods and study of coupled flow, radiation, and ablation phenomena for atmospheric entry*. PhD thesis, Université Paris-Saclay and VKI, 2017.
- [4] T. E. Schwartzentruber, M. S. Grover, and P. Valentini. *Direct molecular simulation of nonequilibrium dilute gases*. Journal of Thermophysics and Heat Transfer, [32\(4\):892–903](#), 2018.
- [5] M. P. Clarey and R. B. Greendyke. *Three-Temperature Models for Thermochemical Non-Equilibrium in Compression and Expansion*. AIAA paper, [2018-0743](#), 2018.
- [6] G. Bellas-Chatzigeorgis. *Development of Advanced Gas-Surface Interaction Models for Chemically Reacting Flows for Re-Entry Conditions*. PhD thesis, von Karman Institute and Politecnico di Milano, 2018.
- [7] M. L. Hudson, N. Chokani, and G. V. Candler. *Linear stability of hypersonic flow in thermochemical nonequilibrium*. AIAA Journal, [35\(6\):958–964](#), 1997.
- [8] C. Park. *Non-Equilibrium Hypersonic Aerodynamics*. John Wiley & sons, New York, 1990.
- [9] C. Mortensen and X. Zhong. *Real-Gas and Surface-Ablation Effects on Hypersonic Boundary-Layer Instability over a Blunt Cone*. AIAA Journal, [54\(3\):980–998](#), 2016.
- [10] H. B. Johnson, T. G. Seipp, and G. V. Candler. *Numerical study of hypersonic reacting boundary layer transition on cones*. Physics of Fluids, [10\(10\):2676–2685](#), 1998.
- [11] H. L. Kline, C.-L. Chang, and F. Li. *Hypersonic Chemically Reacting Boundary-Layer Stability using LASTRAC*. AIAA paper, [2018-3699](#), 2018.

- [12] A. Lani, J. Molnar, D. Vanden Abeele, P. Rini, and T. E. Magin. *Numerical Study of Elemental Demixing in Atmospheric Entry Flow Regimes Near Local*. In E. O. P. Wesseling and J. Périaux, editors, ECOMASS CFD, Delft, the Netherlands, 2006.
- [13] A. Munafò. *Multi-Scale Models and Computational Methods for Aerothermodynamics*. PhD thesis, École Centrale Paris and von Karman Institute for Fluid Dynamics, 2014.
- [14] D. Bose and G. V. Candler. *Thermal rate constants of the N₂+O<>NO+N reaction using ab initio 3A” and 3A’ potential energy surfaces*. Journal of Chemical Physics, [104\(8\):2825–2833](#), 1996.
- [15] D. Bose and G. V. Candler. *Thermal rate constants of the O₂+N <> NO+O reaction based on the 2A’ and 4A’ potential-energy surfaces*. The Journal of Chemical Physics, [107\(16\):6136–6145](#), 1997.
- [16] R. S. Chaudhry, M. S. Grover, J. D. Bender, T. E. Schwartzentruber, and G. V. Candler. *Quasiclassical trajectory analysis of oxygen dissociation via O₂, O, and N₂*. AIAA paper, [2018-0237](#), 2018.
- [17] R. S. Chaudhry, J. D. Bender, T. E. Schwartzentruber, and G. V. Candler. *Quasiclassical trajectory analysis of nitrogen for high-temperature chemical kinetics*. Journal of Thermophysics and Heat Transfer, [32\(4\):833–845](#), 2018.
- [18] M. S. Grover, T. E. Schwartzentruber, Z. Varga, and D. G. Truhlar. *Vibrational energy transfer and collision-induced dissociation in O + O₂ collisions*. Journal of Thermophysics and Heat Transfer, [33\(3\):797–807](#), 2019.
- [19] C. Park. *On convergence of computation of chemically reacting flows*. AIAA paper, [85-0247](#), 1985.
- [20] G. K. Stuckert. *Linear Stability Theory of Hypersonic, Chemically Reacting Viscous Flows*. PhD thesis, Arizona State University, 1991.
- [21] N. B. Oliviero. *EPIC: a New and Advanced Nonlinear Parabolized Stability Equation Solver*. PhD thesis, Texas A&M University, 2015.
- [22] C. P. Knisely and X. Zhong. *An Investigation of Sound Radiation by Supersonic Unstable Modes in Hypersonic Boundary Layers*. AIAA paper, [2017-4516](#), 2017.
- [23] F. Pinna and K. J. Groot. *Automatic derivation of stability equations in arbitrary coordinates and different flow regimes*. AIAA paper, [2014-2634](#), 2014.
- [24] L. Brillouin. *Tensors in Mechanics and Elasticity*. Academic Press, 1964.

- [25] R. Aris. *Vectors, Tensors, and the Basic Equations of Fluid Mechanics.* Dover - Prentice Hall, New York, 2nd edition, 1962.
- [26] V. Giovangigli. *Multicomponent Flow Modeling.* 3Island Press, 1999.
- [27] G. V. Candler and R. W. MacCormack. *Computation of weakly ionized hypersonic flows in thermochemical nonequilibrium.* Journal of Thermophysics and Heat Transfer, [5\(3\):266–273](#), 1991.
- [28] J. Klentzman and A. Tumin. *Stability and receptivity of high speed boundary layers in oxygen.* AIAA paper, [2013-2882](#), 2013.

3

Stability and transition

A boundary layer transitions from laminar to turbulent due to the appearance and subsequent growth of flow perturbations within it. This can occur through a variety of paths – Fig. 3.1 displays the steps that build up to turbulent breakdown for the various disturbance levels, as well as a sketch of the transitioning boundary layer in path A. After forcing environmental instabilities enter the flow through receptivity mechanisms, they can follow one of five paths: [1]

- (A) In low-disturbance environments, the most unstable perturbation experiences modal exponential growth. After reaching a certain amplitude, parametric instabilities appear and modes begin to interact with one-another.
- (B) For higher disturbance levels, several perturbations can have significantly large amplitudes. The superposition of these perturbations may display algebraic transient growth preceding modal growth.
- (C) Even higher disturbance environments lead to a transient growth that leads directly to parametric instabilities and mode interactions.
- (D) When the environment has high disturbance levels, the modal growth and modal interactions are bypassed, leading directly to breakdown.
- (E) Very high disturbance levels produce a bypass of all perturbation growth mechanisms, and directly produce breakdown.

It is important to note that perturbations can have a variety of origins: acoustic waves, surface irregularities, structural vibrations, etc. Lord Rayleigh [3] was the

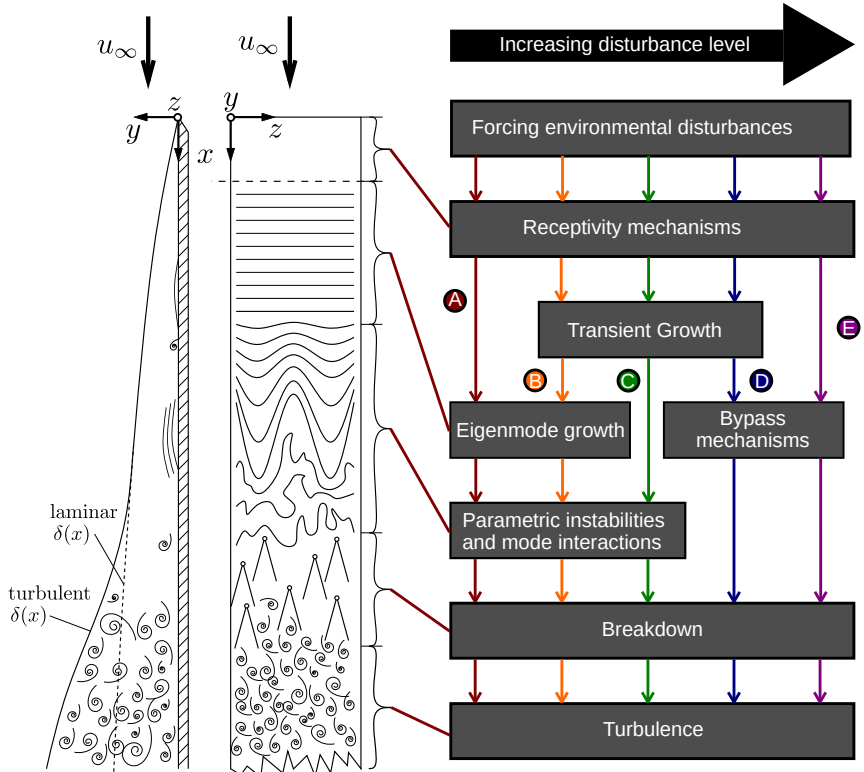


Figure 3.1: Paths to transition for different disturbance levels (right), and sketch of a transitioning boundary layer following path A (left). Originals from White [2] (left) and Reshotko [1] (right).

first to apply perturbation theory to the study of fluid motion in 1880. However, the technique was not very successful during its early days, and as Noether [4] concluded in his 1921 review article, at the time “*the method of small disturbances (...) has led to no useful results concerning the origins of turbulence*”. The main issue was that the analyses were based on inflectional instability. Since such instabilities are stabilized by viscosity, the theoretical framework predicted stable flows that were experimentally observed to be unstable. Despite the initial lack of success, Taylor [5], and later on Prandtl [6] discovered that viscosity can destabilize the flow, and led to the developments that established the viscous theory of Tollmien [7] and Schlichting [8]. This theory was later confirmed by the experimental studies of Schubauer & Skramstad [9], which were actually performed in the early 1940’s, but could not be published until 1947 due to wartime censorship [10].

The development of perturbations within a laminar base flowfield can be mathematically modeled by perturbing the system’s governing equations (see § 2.3). This is achieved by decomposing all the flow variables into a steady laminar base-flow, and a perturbation quantity:

$$q(x^i, t) = \bar{q}(x^i) + q'(x^i, t) . \quad (3.1)$$

This treatment is in appearance very similar to that commonly taken when studying turbulent flows [11], where the flow variables are decomposed into a mean-flow and a fluctuation component. However, when studying turbulent flows, the mean-flow quantity corresponds to a time average, with the fluctuation being the quantity’s instantaneous deviation from this average. This is not the case in the stability framework, where the base-flow quantity corresponds to the value of a certain variable in the absence of instabilities, and the perturbation quantity models the instability itself. Therefore, whilst in the turbulence framework, q' is a statistical deviation, in the stability framework it is an actual physical perturbation. However, stability studies performed on mean flows obtained from the time-averaging of PIV measurements [12] suggest that the concepts of mean- and base-flow are strongly related. Even though in the literature the laminar base flow is often indistinctively referred to as the *base* or the *mean* flow, it is important to understand the differences.

With the evaluation of the different stability ansatz, one reaches the various stability theories, capable of capturing distinct ranges of the transition process – see Fig. 3.2. The major distinction to be done between stability theories regards their linearity – linear theories effectively linearize the system equations by neglecting high-order perturbation terms ($q'_1 q'_2 \approx 0$). This implies that their range of validity is restricted to the parametric region in the vicinity of the base-flow solution. A good visualization and explanation of the solution manifolds in laminar-

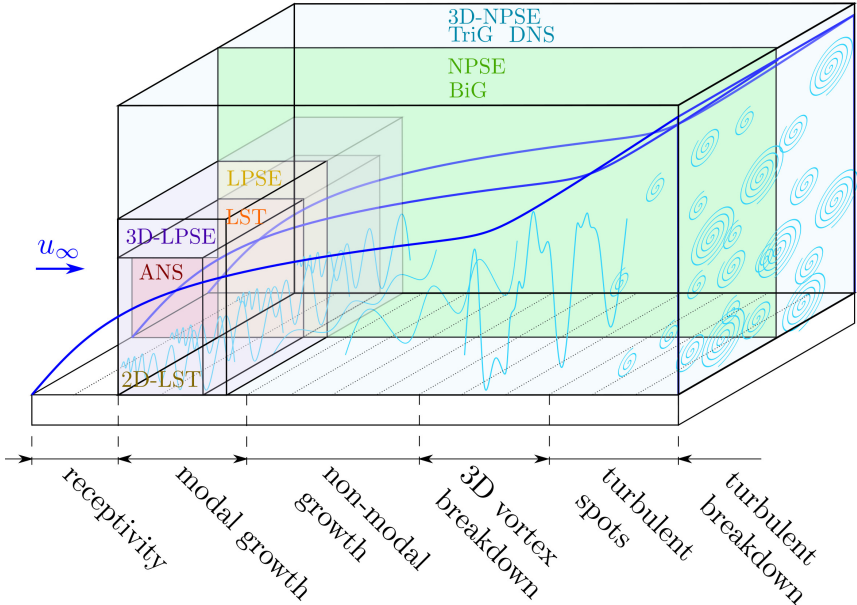


Figure 3.2: Stages of the transition process considered by the various stability theories.

to-turbulent transition problems can be found in Schmid & Henningson [13, Ch. 4] or in Groot [14, Ch. 2].

3.1 Linear theories

This section reviews the most common linearized theories used to investigate the development of instabilities in transitioning flows. However, new theories [15, 16] other than the ones herein detailed are constantly being developed, in order to tailor the mathematical framework for the particular problem of interest.

3.1.1 LDNS

The most physically-general of the linearized theories is what is commonly referred to in the literature as linearized direct numerical simulations (LDNS) [17]. In LDNS, no assumption is done on the shape or periodicity of the perturbation quantities, that can be arbitrary functions of the spatial position and time. Likewise, no assumption is done on the laminar base-flow quantities, other than assuming it to be steady. This leads to the LDNS ansatz:

$$\bar{q} = \bar{q}(x^j), \quad \forall j \in [1, 2, 3], \quad (3.2a)$$

$$q' = \tilde{q}(x^j, t), \quad \forall j \in [1, 2, 3]. \quad (3.2b)$$

3.1.2 Tri-global stability

The four-dimensional perturbation-amplitude function assumed in LDNS (Eq. 3.2b) comes with a high computational cost. A way to slightly relieve such cost is by assuming the amplitude function to be periodic in time. This is known as tri-global stability (TriG) [18–20], and it features the following ansatz:

$$\bar{q} = \bar{q}(x^j), \quad \forall j \in [1, 2, 3], \quad (3.3a)$$

$$q' = \tilde{q}(x^j) \cdot \exp(-i\omega t) + \text{c.c.}, \quad \forall j \in [1, 2, 3], \quad (3.3b)$$

where ω is the temporal frequency of the perturbations and c.c. stands for complex conjugate. Substituting Eq. 3.3 into the system equations presented in § 2.3 results in an eigenvalue problem on the perturbation frequency ω :

$$(\underline{\mathcal{A}} - \omega \underline{\mathcal{B}}) \tilde{q} = \underline{0}, \quad (3.4)$$

where the $\underline{\mathcal{A}}$ and $\underline{\mathcal{B}}$ are the matrices resulting from the discretization of the TriG equations, and \tilde{q} is the vector of discrete perturbation amplitudes of the state variables.^a The eigenvectors associated to the various eigenvalues correspond to the shape of the perturbation amplitude function \tilde{q} .

Like LDNS, this theory makes no assumption on the spatial behavior of instabilities, and is therefore capable of capturing the entire perturbation-growth range of the transition region. However, the development of such theories is still at an early stage, and as presented by Gómez *et al.* [19]:

“It is clear that the instability of (laminar) flows with three inhomogeneous spatial directions is by and large unexplored from a global theory point of view. Order-of-magnitude improvements of the flexibility and the efficiency of the numerical methods used in this context is needed to achieve this target.”

Moreover, as pointed out by Groot [21, Ch. 8], analyses featuring perturbation-amplitude functions that are inhomogeneous in the streamwise direction “are potentially critically tainted by numerical overflow errors, caused by the advection-induced imaginary part of the solution’s wave number that represents a very real spatial growth”.

3.1.3 Bi-global stability or 2D-LST

A further simplification of the stability problem is achieved by assuming the perturbation-amplitude function to be periodic in one of the spatial directions,

^aFor instance, for a CNE flow assumption it would contain $\tilde{q} = [\tilde{u}, \tilde{v}, \tilde{w}, \tilde{T}, \tilde{\rho}_s]$.

and inhomogeneous in the other two. Moreover, the base-flow quantities are assumed to vary negligibly in the perturbation amplitude's periodic direction. Authors [18, 22] initially referred to any such stability theory as bi-global stability (BiG). However, later authors [12, 23, 24] have argued that when the inhomogeneous directions are both in the plane normal to the streamwise direction, it is more appropriate to name the theory 2D-LST (previously [18, 22] referred to as spanwise BiG) since it remains linear in the direction of convective advancement of the instabilities. The BiG qualifier can therefore be reserved to a choice of inhomogeneous directions where one of them corresponds to the streamwise (also [18, 22] referred to as streamwise bi-global stability), since the resulting instability modes are indeed *global* to the flow motion in its convective direction. For the reasons laid out above, attending to the physical nature of the modes investigated by the two approaches, this dissertation employs the naming convention with 2D-LST and BiG. The reader must, however, remain aware that they can be referred to in the literature as spanwise- and streamwise-BiG respectively.

The ansatz for 2D-LST is:

$$\bar{q} = \bar{q}(x^2, x^3), \quad (3.5a)$$

$$q' = \tilde{q}(x^2, x^3) \cdot \exp(i(\alpha x^1 - \omega t)) + \text{c.c.}, \quad (3.5b)$$

where α is the streamwise perturbation wave number. For BiG it assumes:

$$\bar{q} = \bar{q}(x^1, x^2), \quad (3.6a)$$

$$q' = \tilde{q}(x^1, x^2) \cdot \exp(i(\beta x^3 - \omega t)) + \text{c.c.}, \quad (3.6b)$$

where β is the spanwise perturbation wave number.

As one can observe in Fig. 3.2, these choices have implications as to the range of applicability of the resulting theories. 2D-LST's is restricted to the region of streamwise linear development of planar instabilities, since it assumes the flow to be locally parallel in the streamwise direction. It is therefore the equivalent to linear stability theory (see § 3.1.4), yet with the added capability of considering arbitrary shapes for the instabilities in the plane normal to the streamwise coordinate. BiG on the other hand, neglects all spanwise non-periodic variation of the perturbations, yet allowing for their arbitrary streamwise evolution. Similarly to TriG, it is capable of capturing the entire perturbation-growth range of the transition region. However, it shares the same limitations of the mathematical framework presented by Groot [21] and mentioned in § 3.1.2 due to the advection intrinsic to the problem.

The 2D-LST and BiG ansatz (Eq. 3.5 and 3.6) also transform the system equations into a generalized eigenvalue problem. However, the duality of wave parameters in the perturbation term requires choices to be made on one of them. In BiG analyses one typically fixes the value of the spanwise wave number β , and then

solves the eigenvalue problem on the frequency ω :

$$(\underline{\mathcal{A}}(\beta) - \omega \underline{\mathcal{B}}) \underline{\tilde{q}} = \underline{0}. \quad (3.7)$$

In 2D-LST analyses, one can either fix the streamwise wave number α and solve the temporal eigenvalue problem on the frequency ω :

$$(\underline{\mathcal{A}}(\alpha) - \omega \underline{\mathcal{B}}) \underline{\tilde{q}} = \underline{0}, \quad (3.8)$$

or fix the perturbation frequency ω and solve the non-linear spatial problem on the wave number α :

$$(\underline{\mathcal{C}}_0 \alpha^2 + \underline{\mathcal{C}}_1 \alpha + \underline{\mathcal{C}}_2(\omega)) \underline{\tilde{q}} = \underline{0}, \quad (3.9)$$

which can be restructured into a generalized eigenvalue problem by doubling the size of the system matrices and the state vector:

$$(\underline{\mathcal{A}}^* - \alpha \underline{\mathcal{B}}^*) \underline{\tilde{q}}^* = \underline{0}, \quad (3.10a)$$

$$\underline{\mathcal{A}}^* = \begin{pmatrix} -\underline{\mathcal{C}}_1 & -\underline{\mathcal{C}}_2(\omega) \\ \underline{\mathcal{I}} & \underline{\underline{0}} \end{pmatrix}, \quad \underline{\mathcal{B}}^* = \begin{pmatrix} \underline{\mathcal{C}}_0 & \underline{0} \\ \underline{\underline{0}} & \underline{\mathcal{I}} \end{pmatrix}, \quad \underline{\tilde{q}}^* = \begin{pmatrix} \underline{\tilde{q}} \\ \alpha \underline{\tilde{q}} \end{pmatrix}. \quad (3.10b)$$

3.1.4 Linear stability theory

Assuming the perturbation amplitude to be solely dependent on one spatial direction and periodic in all others, one reaches linear stability theory (LST) [10, 25, 26]. It also assumes the flow to be locally parallel, which implies that the base-flow quantities' streamwise and spanwise variation is neglected. This leads to the well-known LST ansatz:

$$\bar{q} = \bar{q}(x^2), \quad (3.11a)$$

$$q' = \tilde{q}(x^2) \cdot \exp(i(\alpha x^1 + \beta x^3 - \omega t)) + \text{c.c.} \quad (3.11b)$$

Similarly to 2D-LST, the LST ansatz transforms the system equations into one of two generalized eigenvalue problems, depending on which wave parameter is fixed and which is left as an unknown. The spanwise wave number β is typically fixed. One may then distinguish between the temporal problem, where the streamwise wave number α is fixed and the frequency ω is the unknown:

$$(\underline{\mathcal{A}}(\alpha, \beta) - \omega \underline{\mathcal{B}}) \underline{\tilde{q}} = \underline{0}, \quad (3.12)$$

and the spatial problem, where the frequency ω is fixed and the streamwise wave number α is the unknown:

$$(\underline{\mathcal{C}}_0 \alpha^2 + \underline{\mathcal{C}}_1 \alpha + \underline{\mathcal{C}}_2(\omega, \beta)) \underline{\tilde{q}} = \underline{0}. \quad (3.13)$$

Eq. 3.12 and 3.13 are identical in shape to their 2D-LST counterparts (Eq. 3.8 and 3.9), except for the wave parameters that the $\underline{\mathcal{A}}$ and $\underline{\mathcal{C}}_2$ matrices depend on. Therefore, the same restructuring of Eq. 3.10 can be performed on Eq. 3.13.

One of the implications of the parallel flow assumption, and the consequent assumption of the base-flow quantities being exclusive functions of the wall-normal coordinate, is that the base-flow wall-normal velocity must be neglected ($\bar{u}^2 \approx 0$). This corollary is reached from the evaluation of the base-flow mixture continuity equation (Eq. 2.8) with Eq. 3.11a.

Due to its simplicity and its low computational requirements when compared to the aforementioned global methods, LST was the first of the stability theories to be developed. It was initially theoretically proposed by Tollmien [7] and Schlichting [8], and then expanded by the work of Lees, Lin, Dunn and Reshotko [27–30]. One can find a good summary of the theory’s initial developments and investigations in Schlichting’s book [31]. The theory reached maturity, including its expansion to hypersonic speeds and the discovery of second-mode instabilities through the extensive work of Mack [32–43]. An excellent review of the theory and its historical development can be found in Mack’s 1984 reference article [10], which as stated by Reed *et al.* [26] “should be considered required reading for those interested in all aspects of boundary-layer stability theory, including all the basic details for deriving, analyzing, and solving the stability equations for 2-D flows, compressible flows, and 3-D flows”.

3.1.5 Linear parabolized stability

In order to relax the parallel flow assumption made by the theories assuming periodic perturbations in the streamwise direction (LST and 2D-LST), one can parabolize the stability equations by assuming the flow quantities to be “weakly varying” in that direction.^b This leads to the parabolized version of these theories – linear parabolized stability equations (LPSE) [44, 45] and its three-dimensional plane-marching homologous theory (3D-LPSE) [46]. In LPSE, one assumes:

$$\frac{\partial}{\partial x^1} \ll \frac{\partial}{\partial x^2}, \quad (3.14)$$

together with the LPSE ansatz:

$$\bar{q} = \bar{q}(x^1, x^2), \quad (3.15a)$$

$$q' = \tilde{q}(x^1, x^2) \cdot \exp \left(i \left(\int_{x_0^1}^{x^1} \alpha(\xi^1) d\xi^1 + \beta x^3 - \omega t \right) \right) + \text{c.c.} \quad (3.15b)$$

^bOne must not confuse “parabolized” with “parabolic”, since the PSE system retains a weak ellipticity [44].

Analogously, in 3D-LPSE, one assumes:

$$\frac{\partial}{\partial x^1} \ll \frac{\partial}{\partial x^2}, \frac{\partial}{\partial x^3}, \quad (3.16)$$

together with the 3D-LPSE ansatz:

$$\bar{q} = \bar{q}(x^1, x^2, x^3), \quad (3.17a)$$

$$q' = \tilde{q}(x^1, x^2, x^3) \cdot \exp \left(i \left(\int_{x_0^1}^{x^1} \alpha(\xi^1) d\xi^1 - \omega t \right) \right) + \text{c.c.} \quad (3.17b)$$

Conditions in Eqs. 3.14 and 3.16 imply that second-order derivatives with respect to the streamwise direction x^1 of both base-flow and perturbation-amplitude variables are neglected. Substituting Eq. 3.15 or 3.17 into the system equations leads to a marching problem of the type:

$$\underline{\mathcal{L}} \tilde{q} + \underline{\mathcal{M}} \frac{\partial \tilde{q}}{\partial x^1} + \frac{\partial \alpha}{\partial x^1} \underline{\mathcal{N}} \tilde{q} = 0, \quad (3.18)$$

where $\underline{\mathcal{L}} = \underline{\mathcal{L}}(\beta, \omega)$ and $\underline{\mathcal{M}} = \underline{\mathcal{M}}(\beta)$ in LPSE and $\underline{\mathcal{L}} = \underline{\mathcal{L}}(\omega)$ in 3D-LPSE.

The LPSE and 3D-LPSE ansatz (Eq. 3.15 and 3.17) feature a streamwise dependency of both the perturbation-amplitude function \tilde{q} and the wave function. Therefore, a normalization condition is required:

$$\int_{\Omega^j} \tilde{q}^\dagger \frac{\partial \tilde{q}}{\partial x^1} dx^j = 0, \quad (3.19)$$

where the integration domain Ω^j corresponds to the spatial region in which the perturbation amplitude is strongly inhomogeneous – the wall-normal direction x^2 in LPSE, and the wall-normal-spanwise plane $[x^2, x^3]$ in 3D-LPSE. Chang *et al.* [47] showed that the stability results are basically independent of the normalization condition.

The relaxation from a parallel to a quasi-parallel flow assumption intrinsic to parabolized theories implies that they can accurately model the propagation of perturbations over a slightly larger region within the transition range. This is sketched in Fig. 3.2.

3.2 e^N method

The mathematical treatment of linear theories restricts them to the early stages of instability development. However, it is possible to relate the amplitude that perturbations would reach if they were to continue developing linearly, with the experimentally-found transition-onset location. This method is known as the e^N method, which was parallely developed by Smith & Gamberoni [48] and van Ingen [49]. It consists in assuming that, in equivalent disturbance environments,

transition occurs when the natural logarithm of the non-dimensional perturbation amplitude is increased by a certain factor – the so-called N-factor:

$$N(x^1) = \int_{x_0^1}^{x^1} \frac{1}{A} \frac{dA}{d\xi^1} d\xi^1 = \ln \left(\frac{A(x^1)}{A(x_0^1)} \right) = - \int_{x_0^1}^{x^1} \Im(\alpha)(\xi^1) d\xi^1, \quad (3.20)$$

where $A(x^1)$ is the amplitude of a given instability as a function of the streamwise position.

3.3 Non-linear theories

Despite the surprising prediction accuracy of linear methods combined with the e^N method for certain conditions and geometries [50, 51], in some occasions one must take into consideration the non-linear interactions of perturbations in order to make a precise estimation of the transition-onset location. Non-linear theories do not drop higher-order perturbation terms $q'_1 q'_2 \approx 0$. Moreover, the perturbation quantities are modeled as a sum of modes that are consequently permitted to interact with one-another, making such theories non-modal. The non-linear versions of LPSE and 3D-LPSE are commonly referred to as NPSE [52] and 3D-NPSE [53]. NPSE features the same assumption on the streamwise gradients as LPSE (Eq. 3.14) and the same dependencies for base-flow quantities (Eq. 3.15a) yet with a different ansatz:

$$\begin{aligned} q' = & \sum_{m \in \mathbb{M}_\beta} \sum_{n \in \mathbb{M}_\omega} A_{(m,n)}^0 \tilde{q}_{(m,n)}(x^1, x^2) \cdot \\ & \cdot \exp \left(i \left(\int_{x_0^1}^{x^1} \alpha_{(m,n)}(\xi^1) d\xi^1 + m\beta x^3 - n\omega t \right) \right) + \text{c.c.}, \end{aligned} \quad (3.21)$$

where $A_{(m,n)}^0$ is the initial amplitude of each mode, and m and n are integer values used to identify the harmonics considered. Analogously, in 3D-LPSE, one still simplifies according to Eq. 3.16 and 3.17a yet with a different ansatz for the perturbation quantities:

$$q' = \sum_{n \in \mathbb{M}_\omega} A_{(n)}^0 \tilde{q}_{(n)}(x^1, x^2, x^3) \cdot \exp \left(i \left(\int_{x_0^1}^{x^1} \alpha_{(n)}(\xi^1) d\xi^1 + n\omega t \right) \right) + \text{c.c.} \quad (3.22)$$

The equation system for each mode (m,n) in NPSE consequently becomes:

$$\left. \left(\underline{\mathcal{L}} \tilde{q} + \underline{\mathcal{M}} \frac{\partial \tilde{q}}{\partial x^1} + \frac{\partial \alpha}{\partial x^1} \underline{\mathcal{N}} \tilde{q} \right) \right|_{(m,n)} = \underline{\mathcal{F}}_{(m,n)}, \quad \forall m \in \mathbb{M}_\beta, n \in \mathbb{M}_\omega, \quad (3.23)$$

where $\mathcal{F}_{(m,n)}$ is the forcing vector for mode (m,n) . Similarly, the equation system for each mode (n) in 3D-NPSE becomes:

$$\left(\underline{\mathcal{L}} \tilde{q} + \underline{\mathcal{M}} \frac{\partial \tilde{q}}{\partial x^1} + \frac{\partial \alpha}{\partial x^1} \underline{\mathcal{N}} \tilde{q} \right) \Big|_{(n)} = \mathcal{F}_{(n)}, \quad \forall n \in \mathbb{M}_\omega. \quad (3.24)$$

Normalization conditions are also required for each mode. In NPSE it reads:

$$\int_{\Omega^2} \tilde{q}_{(m,n)}^\dagger \frac{\partial \tilde{q}_{(m,n)}}{\partial x^1} dx^2 = 0, \quad (3.25)$$

whilst for 3D-NPSE it is:

$$\int_{\Omega^j} \tilde{q}_{(n)}^\dagger \frac{\partial \tilde{q}_{(n)}}{\partial x^1} dx^j = 0, \quad (3.26)$$

where Ω^j is the same domain mentioned in § 3.1.5.

The forcing terms acting on each mode ($\mathcal{F}_{(m,n)}$ and $\mathcal{F}_{(n)}$) are obtained from performing a Fourier decomposition of the non-linear terms in the system equations.

3.4 Adjoint theories

All theories presented in § 3.1 and 3.3 deal with the development of instabilities once they have entered the boundary layer. However, oftentimes one is interested in the inverse problem – determining how sensitive the boundary layer is at a certain location to instabilities appearing upstream from it. This is known as the receptivity problem, and it is commonly studied with adjoint methods [54, 55]. With them, one can, for instance, determine the roughness height at a certain location, that leads to perturbations reaching a critical amplitude at another location of interest [56]. The adjoint formulation can be applied to whichever of the linear theories described in § 3.1, and they can thus provide information on the earliest stages of the transition process (see the region in Fig. 3.2 marked as ADNS – adjoint direct numerical simulations). Such theories however are out of the scope of this thesis, and hence the reader is referred to the work of Tumin & Fedorov [54] and Hill [55] for the full mathematical treatment.

3.5 Physical implications of the choice of the wave parameters

In the most-general case, all wave parameters α , β and ω appearing in the expressions of the theories presented in § 3.1 can be complex numbers. Their real

part characterizes the oscillatory behavior of the instabilities in their associated direction or time, and their imaginary part the exponentially growing or decreasing behavior. However, making different choices on these variables, one is capable of investigating different physical phenomena. In non-parabolized theories where the wave function of the perturbation variable features a streamwise wave number α and a frequency ω (like 2D-LST or LST), the modeling choice made for these wave parameters can distinguish convective from absolute instabilities [57, 58]. The latter are characterized by both a complex α and a complex ω , since they grow simultaneously both in space and time. Contrarily, the former grow only in time (real α and complex ω) or in space (real ω and complex α). Convective instabilities are indeed convected away by the flow, and hence develop only downstream from where they appear. Absolute instabilities, on the other hand, develop both in the upstream and the downstream direction, and are normally caused by punctual impulses or physical steps.

Similarly, assuming β to be a complex number implies that the corresponding perturbation also grows or decays in the spanwise direction. This implies that the direction of maximum growth of the instabilities is not the streamwise. Such a situation modifies the way the integration path should be taken when performing an e^N -analysis [25, § 3.3].

3.6 Instability mechanisms

The aforementioned theoretical framework enables the investigation of the development of the flow instabilities that ultimately lead to transition. However, there exist a variety of instability mechanisms that develop within the flowfields of interest:

- **Tollmien-Schlichting (TS) waves** [7–9] are two-dimensional ($\beta = 0$) vorticity waves that are destabilized by viscosity. They are dominant in incompressible and subsonic flows. As they advance and amplify, they start interacting non-modally in a three-dimensional fashion.
- **First-mode (M1) waves** [30] become dominant at transonic and supersonic Mach numbers. They are not two-dimensional, and instead have wave angles (ϕ) of about 60° . As stated by Reed & Saric [26]: “*this phenomenon is due to decreased cross-stream mutual interaction between disturbances and decreased upstream influence, both of which are compensated by a lower effective 2-D Mach number*”.
- **Second-mode (M2) waves** [10], also called Mack mode waves, are the most unstable at hypersonic speeds. They are acoustic instabilities that are “trapped” inside of [59] or “synchronized” with [60] the boundary layer,

specifically in its region of relative supersonic speed [26]. In 2-D boundary layers they are most unstable when two-dimensional ($\beta = 0$), since “*it is then that the relative supersonic region is of maximum extent*” [26]. In 3-D boundary layers however, the most-unstable M2 waves are slightly 3-D – Balakumar & Reed [61] reported wave angles of $\phi = 5^\circ$ and $\phi = 9^\circ$ in rotating cones at Mach 5 and 8 respectively.

- **Supersonic-mode (SSM) waves** [62] share most of their features with M2 waves. However, unlike M2 waves, they have wave speeds (c) such that they propagate supersonically with respect to the edge velocity. Moreover, unlike TS, M1 and M2 waves, they radiate energy into the freestream, and therefore exhibit a non-exponentially decaying perturbation amplitude. They are commonly encountered in highly-cooled flows [63].
- **Crossflow (CF) waves** [40, 64] appear in regions of pressure gradient on swept surfaces or on rotating disks. Such flowfields have a secondary flow in the boundary layer that is perpendicular to the direction of the inviscid streamline [65]. This results in an inflection point in the crossflow velocity profile, that originates the instabilities. CF waves can be stationary ($\omega = 0$) or traveling ($\omega \neq 0$).
- **Görtler vortices (GV)** [66–68] are induced by concave wall curvature, which generates steady ($\omega = 0$), streamwise-oriented, counter-rotating vortices. The inability of the local pressure gradient to restrain an excess in angular momentum of a particle undergoing an outward virtual displacement, leads to the instability [69].

Referring to the supersonic modes as different from the second mode is notably incorrect. From a mathematical standpoint, so-called “supersonic modes” are in fact Mack’s second mode, after reaching a relative supersonic speed with respect to the free stream whilst remaining unstable. Such a naming inconsistency is not new to the stability field – as pointed out by Fedorov & Tumin [70], the so-called second mode is oftentimes mathematically the same mode as the first. Despite this lack of rigor in the naming, the common labeling distinction between first, second and supersonic “modes” found in the literature is adopted in this dissertation.

An excellent visualization of the mode shapes for most of the instability mechanisms listed in this section can be found in Ref. 71. That is, with the exception of Görtler vortices and supersonic second-mode waves. For a visualization of the former, the reader is referred to the extensive review by Saric [69], and for the latter, to the recent work by Knisely and Zhong [72, 73].

References

- [1] E. Reshotko. *Paths to Transition in Wall Layers*. In Advances in laminar-turbulent transition modeling, pages 1–8. von Karman Institute for Fluid Dynamics, 2008.
- [2] F. M. White. *Viscous Fluid Flow*. McGraw-Hill, 2nd edition, 1991.
- [3] L. Rayleigh. *On the Stability, or Instability, of certain Fluid Motions*. Proceedings of the London Mathematical Society, **s1-11(1):57–72**, 1879.
- [4] F. Noether. *Das Turbulenzproblem*. ZAMM - Journal of Applied Mathematics and Mechanics / Zeitschrift für Angewandte Mathematik und Mechanik, **1(2):125–138**, 1921.
- [5] G. I. Taylor. *Eddy Motion in the Atmosphere*. Philosophical Transactions of the Royal Society A: Mathematical, Physical and Engineering Sciences, **215:1–26**, 1915.
- [6] L. Prandtl. *Bemerkungen über die Entstehung der Turbulenz (in German)*. ZAMM, 1:431–436, 1921.
- [7] W. Tollmien. *Über die Entstehung der Turbulenz (in German)*. ZAMM - Journal of Applied Mathematics and Mechanics / Zeitschrift für Angewandte Mathematik und Mechanik, **11(6):407–409**, 1931.
- [8] H. Schlichting. *Zur Entstehung der Turbulenz bei der Plattenströmung (in German)*. Nachrichten von der Gesellschaft der Wissenschaften zu Göttingen, Mathematisch-Physikalische Klasse, pages 181–208, 1933.
- [9] G. Schubauer and H. Skramstad. *Laminar boundary-layer oscillations and transition on a flat plate*. Technical Report 2, NACA, Washington, 1947.
- [10] L. M. Mack. *Boundary-Layer Linear Stability Theory*. In Special Course on Stability and Transition of Laminar Flow, AGARD 709. AGARD, 1984.
- [11] S. B. Pope. *Turbulent Flows*. Cambridge University press, 1st edition, 2000.
- [12] K. J. Groot, J. Serpieri, F. Pinna, and M. Kotsonis. *Secondary crossflow instability through global analysis of measured base flows*. Journal of Fluid Mechanics, **846:605–653**, 2018.
- [13] P. J. Schmid and D. S. Henningson. *Stability and Transition in Shear Flows*, volume 142. Springer, Ney York, Berlin, 2001.
- [14] K. J. Groot. *Derivation of and Simulations with BiGlobal Stability Equations*. Technical Report AE5110, VKI and TU Delft, 2013.

- [15] J. A. Franco Sumariva and S. J. Hein. *Adaptive Harmonic Linearized Navier-Stokes equations used for boundary layer instability analysis in the presence of large streamwise gradients*. AIAA paper, [2018-1548](#), 2018.
- [16] D. A. Cook, J. Thome, J. M. Brock, J. W. Nichols, and G. V. Candler. *Understanding effects of nose-cone bluntness on hypersonic boundary layer transition using input-output analysis*. AIAA paper, [2018-0378](#), 2018.
- [17] X. Zhong and X. Wang. *Direct Numerical Simulation on the Receptivity, Instability, and Transition of Hypersonic Boundary Layers*. Annual Review of Fluid Mechanics, [44\(1\):527–561](#), 2012.
- [18] V. Theofilis. *Advances in global linear instability analysis of nonparallel and three-dimensional flows*. Progress in Aerospace Sciences, [39\(4\):249–315](#), 2003.
- [19] F. Gómez, S. Le Clainche, P. Paredes, M. Hermanns, and V. Theofilis. *Four decades of studying global linear instability: Problems and challenges*. AIAA Journal, [50\(12\):2731–2743](#), 2012.
- [20] M. Brynjell-Rahkola, N. Shahriari, P. Schlatter, A. Hanifi, and D. S. Henningson. *Stability and sensitivity of a cross-flow-dominated Falkner-Skan-Cooke boundary layer with discrete surface roughness*. Journal of Fluid Mechanics, [826:830–850](#), 2017.
- [21] K. J. Groot. *BiGlobal Stability of Shear Flows Spanwise & Streamwise Analyses*. PhD thesis, TU Delft and von Karman Institute for Fluid Dynamics, 2018.
- [22] V. Theofilis. *On the spatial structure of global linear instabilities and their experimental identification*. Aerospace Science and Technology, [4\(4\):249–262](#), 2000.
- [23] S. J. Hein, A. Theiss, A. Di Giovanni, C. Stemmer, T. Schilden, W. Schröder, P. Paredes, M. M. Choudhari, F. Li, and E. Reshotko. *Numerical investigation of roughness effects on transition on spherical capsules*. Journal of Spacecraft and Rockets, [56\(2\):388–404](#), 2019.
- [24] F. Pinna, F. Miró Miró, L. Zanus, I. Padilla Montero, and S. Demange. *Automatic Derivation of Stability Equations and their Application to Hypersonic and High-Enthalpy Shear Flows*. In International Conference for Flight Vehicles, Aerothermodynamics and Re-entry Missions & Engineering, Monopoli, Italy, 2019.

- [25] D. Arnal. *Boundary layer transition: predictions based on linear theory*. In Special Course on Progress in Transition Modelling AGARD 793. AGARD, 1993.
- [26] H. L. Reed, W. S. Saric, and D. Arnal. *Linear Stability Theory Applied to Boundary Layers*. Annual Review of Fluid Mechanics, [28\(1\):389–428](#), 1996.
- [27] L. Lees and C. C. Lin. *Investigation of the stability of the laminar boundary layer in a compressible fluid*. Technical Report TN-1115, NACA, 1946.
- [28] L. Lees. *The Stability of the Laminar Boundary Layer in a Compressible Fluid*. Technical Report TN-876, NACA, 1947.
- [29] D. W. Dunn and C. C. Lin. *On the Stability of the Boundary layer in a Compressible fluid*. Journal of Aeronautical Sciences, [22:455–477](#), 1955.
- [30] L. Lees and E. Reshotko. *Stability of the compressible laminar boundary layer*. Journal of Fluid Mechanics, [12\(4\):555–590](#), 1962.
- [31] H. Schlichting. *Boundary-Layer Theory*. McGraw-Hill Series in Mechanical Engineering, 1979.
- [32] L. M. Mack. *Numerical Calculation of the Stability of the Compressible Laminar Boundary Layer*. Technical Report 20-122, Jet Propulsion Laboratory, 1960.
- [33] L. M. Mack. *The Inviscid Stability of Compressible Laminar Boundary Layer*. Technical Report 37-23, Jet Propulsion Laboratory, 1963.
- [34] L. M. Mack. *The Inviscid Stability of Compressible Laminar Boundary Layer: Part II*. Technical Report 37-26, Jet Propulsion Laboratory, 1964.
- [35] L. M. Mack. *Stability of the compressible boundary layer according to a direct numerical solution*. AGARDograph, [97:329–362](#), 1965.
- [36] L. M. Mack. *Computation of the stability of the laminar compressible boundary layer*. Methods in Computational Physics, [4](#), 1965.
- [37] L. M. Mack. *Boundary Layer Stability Theory*. Jet Propulsion Laboratory, California Institute of Technology, Pasadena, California, 1969.
- [38] L. M. Mack. *Linear stability theory and the problem of supersonic boundary-layer transition*. AIAA Journal, [13\(3\):278–289](#), 1975.
- [39] L. M. Mack. *A numerical study of the temporal eigenvalue spectrum of the Blasius boundary layer*. Journal of Fluid Mechanics, [73\(3\):497–520](#), 1976.

- [40] L. M. Mack. *On the stability of the boundary layer on a transonic swept-wing*. AIAA paper, [79-0264](#), 1979.
- [41] L. M. Mack. *Compressible boundary-layer stability calculations for swept-back wings with suction*. AIAA Journal, [20\(3\):363–369](#), 1982.
- [42] L. M. Mack. *Remarks on disputed numerical results in compressible boundary-layer stability theory*. Physics of Fluids, [27\(2\):342–347](#), 1984.
- [43] L. M. Mack. *Line Sources of Instability Waves in a Blasius Boundary Layer*. AIAA Paper, [84-0168](#), 1984.
- [44] T. Herbert. *Parabolized Stability Equations*. Annual Review of Fluid Mechanics, [29\(1\):245–283](#), 1997.
- [45] T. Herbert and F. P. Bertolotti. *Stability analysis of nonparallel boundary layers*. Bulletin of the American Physical Society, [32:2079–2086](#), 1987.
- [46] N. De Tullio, P. Paredes, N. D. Sandham, and V. Theofilis. *Laminar-turbulent transition induced by a discrete roughness element in a supersonic boundary layer*. Journal of Fluid Mechanics, [735:613–646](#), 2013.
- [47] C.-L. Chang, M. R. Malik, G. Erlebacher, and M. Y. Hussaini. *Compressible stability of growing boundary layers using parabolized stability equations*. AIAA paper, [91-1636](#), 1991.
- [48] A. M. O. Smith and N. Gamberoni. *Transition, pressure gradient and stability theory*. Technical Report ES 26388, Douglas Aircraft Co., El Segundo, California, 1956.
- [49] J. L. van Ingen. *A suggested semi-empirical method for the calculation of the boundary layer transition region*. Technical Report VTH-74, Technische Hogeschool Delft, Vliegtuigbouwkunde, 1956.
- [50] J. L. van Ingen. *Historical review of work at TU Delft*. AIAA paper, [2008-3830](#), 2008.
- [51] P. Paredes, M. M. Choudhari, F. Li, J. S. Jewell, R. L. Kimmel, E. C. Marineau, and G. Grossir. *Nosetip bluntness effects on transition at hypersonic speeds: experimental and numerical analysis under NATO STO AVT-240*. AIAA paper, [2018-0057](#), 2018.
- [52] F. P. Bertolotti, T. Herbert, and P. R. Spalart. *Linear and nonlinear stability of the Blasius boundary layer*. Journal of Fluid Mechanics, [242:441–474](#), 1992.

- [53] P. Paredes, A. Hanifi, V. Theofilis, and D. S. Henningson. *The Nonlinear PSE-3D Concept for Transition Prediction in Flows with a Single Slowly-varying Spatial Direction*. Procedia IUTAM, **14**:36–44, 2015.
- [54] A. Tumin and A. V. Fedorov. *Instability wave excitation by a localized vibrator in the boundary layer*. Journal of Applied Mechanics and Technical Physics, **25**(6):867–873, 1984.
- [55] D. C. Hill. *Adjoint Systems and Their Role in the Receptivity Problem for Boundary Layers*. Journal of Fluid Mechanics, **292**:183–204, 1995.
- [56] C.-L. Chang and M. M. Choudhari. *Boundary-layer receptivity and integrated transition prediction*. AIAA paper, **2005-0526**:2515–2533, 2005.
- [57] A. Bers. *Space-Time Evolution of Plasma Instabilities - Absolute and Convective*. In A. A. Galeev and R. N. Sudan, editors, Handbook of Plasma Physics: Basic plasma physics I, Volume 1, chapter 3.2. North Holland, 1983.
- [58] P. Huerre. *Absolute and convective instabilities in free shear layers*. Journal of Fluid Mechanics, **159**:151–168, 1985.
- [59] A. V. Fedorov. *Transition and Stability of High-Speed Boundary Layers*. Annual Review of Fluid Mechanics, **43**(1):79–95, 2011.
- [60] J. J. Kuehl. *Thermoacoustic Interpretation of Second-Mode Instability*. AIAA Journal, **56**(9):3585–3592, 2018.
- [61] P. Balakumar and H. L. Reed. *Stability of three-dimensional supersonic boundary layers*. Physics of Fluids A, **3**(4):617–632, 1991.
- [62] L. M. Mack. *Review of Linear Compressible Stability Theory*. In D. L. Dwoyer and M. Y. Hussaini, editors, *Stability of Time Dependent and Spatially Varying Flows*, pages 164–187. ICASE NASA LaRC Series. Springer, New York, NY, 1987.
- [63] N. P. Bitter and J. E. Shepherd. *Stability of highly cooled hypervelocity boundary layers*. Journal of Fluid Mechanics, **778**:586–620, 2015.
- [64] H. L. Reed. *Stability Of Three-Dimensional Boundary Layers*. Annual Review of Fluid Mechanics, **21**(1):235–284, 1989.
- [65] W. S. Saric, H. L. Reed, and E. B. White. *Stability and Transition of Three-Dimensional Boundary Layers*. Annual Review of Fluid Mechanics, **35**(1):413–440, 2003.

- [66] L. Rayleigh. *On the Dynamics of Revolving Fluids*. Proceedings of the Royal Society A: Mathematical, Physical and Engineering Sciences, **93(648):148–154**, 1917.
- [67] H. Görtler. *Instabilitä-umt laminarer Grenzschichten an Konkaven Wänden gegenberr gewissen dreedimensionalen Störungen (in German)*. ZAMM, **21:250–252**, 1941.
- [68] Y. P. Tang and M. Z. Chen. *on the Three Dimensional Instability Modes in Boundary Layers*. Technical Report TM-1375, NACA, Washington D.C., 1985.
- [69] W. S. Saric. *Görtler Vortices*. Annual Review of fluid mechanics, **26(2):379–409**, 1994.
- [70] A. V. Fedorov and A. Tumin. *High-Speed Boundary-Layer Instability: Old Terminology and a New Framework*. AIAA Journal, **49(8):1647–1657**, 2011.
- [71] K. J. Groot, F. Miró Miró, E. S. Beyak, A. J. Moyes, F. Pinna, and H. L. Reed. *DEKAF: spectral multi-regime basic-state solver for boundary layer stability*. AIAA paper, **2018-3380**, 2018.
- [72] C. P. Knisely and X. Zhong. *Sound radiation by supersonic unstable modes in hypersonic blunt cone boundary layers. I. Linear stability theory*. Physics of Fluids, **31(2)**, 2019.
- [73] C. P. Knisely and X. Zhong. *Sound radiation by supersonic unstable modes in hypersonic blunt cone boundary layers. II. Direct numerical simulation*. Physics of Fluids, **31(2)**, 2019.

4

Gas properties

For the flow assumptions listed in § 2.3 one requires $N_s + N_T + 3$ system equations, where N_s is the number of species composing the mixture, and N_T is the number of temperatures used to describe the gas' thermal state. However, the number of variables in such equation systems is much larger. Besides the independent state variables, there are a series of dependent variables – the gas' thermodynamic, transport, chemical and energy-relaxation properties. These dependent quantities are indeed a function of the independent ones, thus requiring appropriate models providing functional relations to them.

When a gas remains below its vibrational activation temperature (see Fig. 2.1) it can be considered a CPG. The corresponding governing equations (Eqs. 2.8, 2.7b and 2.34), with the choice of thermodynamic state variables made in § 2.3, require models for the enthalpy h , the pressure p ^a, the thermal conductivity κ , the dynamic viscosity μ and the bulk viscosity λ . The enthalpy is linearly dependent on the temperature, since only the particle's translational and rotational energies are considered:

$$h = c_p T, \quad (4.1a)$$

$$c_p = \left(\frac{5}{2} + \alpha^{Rot} \right) R = \left(\frac{5}{2} + \alpha^{Rot} \right) \frac{\mathcal{R}}{\mathcal{M}}, \quad (4.1b)$$

where α^{Rot} is 0 for mixtures of atomic gases for which rotational energy is ne-

^aFor alternative choices of the state variables, instead of pressure one may require any of the other two thermodynamic state variables (ρ or T).

glected, and $\mathcal{L}_s/2$ for mixtures of molecular gases^b for which it is not neglected, R is the mixture-specific gas constant, \mathcal{R} is the universal gas constant, and \mathcal{M} is the mixture molar mass. The pressure can be obtained from the ideal gas law (Eq. A.10 in app. A). For the CPG range of temperatures, viscosity can be accurately ($\sim 2\%$ [1, Ch. 1]) described by Sutherland's law [2]:

$$\mu = \mu_{\text{ref}} \left(\frac{T}{T_{\text{ref}}} \right)^{3/2} \frac{T_{\mu_{\text{ref}}} + S_\mu}{T + S_\mu}, \quad (4.2)$$

where the coefficients μ_{ref} , S_μ and T_{ref} are obtained from fitting to experimental data – they can be found for various gases in the book of White [1, Ch. 1]. If inelastic collisions are neglected [3–5] the bulk viscosity can be considered zero, making the second viscosity coefficient satisfy Stokes' hypothesis:

$$\lambda = -\frac{2}{3}\mu. \quad (4.3)$$

The thermal conductivity may be obtained either from Sutherland's law with different coefficients [1]:

$$\kappa = \kappa_{\text{ref}} \left(\frac{T}{T_{\kappa_{\text{ref}}}} \right)^{3/2} \frac{T_{\kappa_{\text{ref}}} + S_\kappa}{T + S_\kappa}, \quad (4.4)$$

or from assuming a constant Prandtl number:

$$\text{Pr} = \frac{\mu c_p}{\kappa}, \quad (4.5)$$

typically taken between 0.7 and 0.72 for air.

Unfortunately, there does not exist an equally accepted and accurate set of models as Eqs. 4.1–4.5 for gases at higher temperatures. The mathematical modeling of gas properties at such regimes has remained a very active field of research among the thermophysics community for the past eight decades (see for instance Chapman & Cowling [6], Hirschfelder *et al.* [7], Blottner *et al.* [8], Gupta & Yos [9], Fertig *et al.* [10], McBride *et al.* [11], Magin & Degrez [12], Scoggins [13] or Clarey & Greendyke [14]). Different authors performing boundary-layer stability and transition investigations have therefore used a variety of models to describe the various properties – see Table 4.1.^c A summary of the most common and significant ones are presented in this section.

Expressions are presented as a function of five temperatures to describe the various energies: translational of heavy particles T^{Trans} , translational of electrons

^b \mathcal{L}_s is equal to 2 for linear molecules, and 3 for non-linear ones.

^cIf several investigations were conducted by the same group with the exact same set of models, only one of them is referred to. This is the case with Mortensen & Zhong [15], Knisely & Zhong [16] and Mortensen [17]; Stuckert & Reed [18] and Lyttle & Reed [19]; or Zanus *et al.* [20] and Zanus & Pinna [21].

Reference	Thermal	Transport	Diffusion	Kinetics	Chemistry	Equilibrium
Malik & Anderson [22]	McB	BEW	cstLe	— ^{*2}	Park85	
Stuckert & Reed [18]	McB	Brokaw	SM	Stuckert	RRHO	
Hudson <i>et al.</i> [23]	RRHO	BEW	cstSc	Park90	Park85	
Mortensen & Zhong [15]	RRHO	BEW	cstSc	Park90	Park85	
Franko <i>et al.</i> [24]	RRHO	BEW & CE	cstSc & SM	Park90	Park85 & RRHO	
Klentzman & Tumin [25]	McB	Yos	Binary	Bortner	Arrhenius	
Bitter & Shepherd [26]	RRHO	SEW	— ^{*1}	— ^{*1}	— ^{*1}	
Miró Miró <i>et al.</i> [27]	RRHO	BEW	cstSc	Park01	RRHO	
Miró Miró <i>et al.</i> [28]	RRHO	CE	SCEBD	Park01	RRHO	
Chang <i>et al.</i> [29]	RRHO	BEW	cstLe	Bortner	Arrhenius	
Johnson & Candler [30]	RRHO	BEW	cstSc	Park90	Park85	
Zanus <i>et al.</i> [20]	RRHO	CE	SM	— ^{*2}	RRHO	
Kline <i>et al.</i> [31]	McB	Yos & BEW	EBD	Bortner	Arrhenius	
Marxen <i>et al.</i> [32]	RRHO	CE	SM	Park01	RRHO	

^{*1} frozen flow. ^{*2} equilibrium flow.

Table 4.1: Summary of the thermodynamic and transport models used by the different authors and research groups.

T^e , rotational T^{Rot} , vibrational T^{Vib} and electronic T^{Elec} . One could go further and define multiple temperatures for the different energy modes of the different species T_s^{Mod} (see Armenise & Kustova [33] or Kosareva & Nagnibeda [34]). However, the expressions presented in this section assume a unique temperature for each internal energy mode of all species, and two temperatures for the translational energy modes – one for heavy species T^{Trans} and one for electron species T^e :

$$T_s^{Trans} = \begin{cases} T^{Trans}, & \forall s \in \mathcal{H} \\ T^e, & s = e^- \end{cases}, \quad (4.6a)$$

$$T_s^{Rot} = T^{Rot}, \quad \forall s \in \mathcal{S}_{mol}, \quad (4.6b)$$

$$T_s^{Vib} = T^{Vib}, \quad \forall s \in \mathcal{S}_{mol}, \quad (4.6c)$$

$$T_s^{Elec} = T^{Elec}, \quad \forall s \in \mathcal{H}. \quad (4.6d)$$

Therefore appearances of the term T_s^{Mod} in the text are subject to the conditions in Eq. 4.6.

For the flow assumptions in thermal equilibrium, describing the thermal state of the system with one unique temperature (see Table 2.1), one has that:

$$T^{Trans} = T^{Rot} = T^{Vib} = T^{Elec} = T^e = T. \quad (4.7)$$

Similarly, for flow assumptions in thermal non-equilibrium (see Table 2.1), two temperatures are used to describe the thermal state of the system (T and T_v), leading to:

$$\begin{aligned} T^{Trans} &= T^{Rot} = T, \\ T^{Vib} &= T^{Elec} = T^e = T_v. \end{aligned} \quad (4.8)$$

One can also group the energy modes differently, having a different number of state temperatures (see for instance Bertolotti [5] or Clarey & Greendyke [14]). However, as long as one respects the thermal assumptions of Eq. 4.6, the expressions presented in this section remain valid.

If expressions are presented as a function of a unique temperature T , it is implied that the model was formulated exclusively for thermal equilibrium (Eq. 4.7).

The models are also detailed as a function of the species mass fractions. Depending on the flow assumption, these mass fractions could either be fixed (TPG, TNE or TCFG without species interdiffusion^d), determined by the equilibrium system (LTE or LTEED – see app. B), or be directly obtained from the system state quantities with Eq. A.1a (CNE or TCNE and TPG, TNE or TCFG with species interdiffusion).

^dFor example, if one has a flow of air over a surface through which CO₂ is injected, one must consequently consider the interdiffusion of species, that will render non-constant species mass fractions.

4.1 Thermal properties

A widely used mathematical model for the species' heat capacities and enthalpies are McBride's NASA-7 and NASA-9 curve fits (McB) [11, 35]. Polynomial functions are fitted to the thermal properties of the individual species per unit mol,^e in the form:

$$\frac{C_{ps}(T)}{\mathcal{R}} = \sum_{m=1}^N a_{sm}^{\text{McB}} T^{m-M}, \quad \forall s \in \mathcal{S}, \quad (4.9a)$$

$$\frac{H_s(T)}{\mathcal{R} T} = \frac{b_{s1}^{\text{McB}}}{T} + \frac{1}{\mathcal{R} T} \int_0^T C_{ps}(\tau) d\tau, \quad \forall s \in \mathcal{S}, \quad (4.9b)$$

$$\frac{S_s(T)}{\mathcal{R}} = b_{s2}^{\text{McB}} + \int_0^T \frac{C_{ps}(\tau)}{\mathcal{R} \tau} d\tau, \quad \forall s \in \mathcal{S}, \quad (4.9c)$$

where $N = 5$ and $M = 1$ for the NASA-7 database [35], and $N = 7$ and $M = 3$ for the NASA-9 database [11].

Eqs. 4.9 can be employed in two-temperature models, by defining:

$$\frac{C_{ptrs}}{\mathcal{R}} = \frac{5}{2} + a_s^{Rot}, \quad \forall s \in \mathcal{S}, \quad (4.10a)$$

$$C_{pvs}(T_v) = C_{ps}(T_v) - C_{ptrs}, \quad \forall s \in \mathcal{S}, \quad (4.10b)$$

where $C_{ps}(T_v)$ is defined in Eq. 4.9a. However, the coefficients of these fittings have the inconvenient of being specific to certain ranges of temperatures, which limits their general applicability. Moreover, since the stability equations include also the thermodynamic derivatives of these properties (see § 4.6) this piecewise definition introduces unwanted discontinuities at the limits of these ranges.

Another approach is to use the expressions obtained from differentiating the partition functions of the different energy modes assuming molecules behave like a rigid rotor and a harmonic oscillator (RRHO),^f and assuming species to populate the electronic energy levels according to a Boltzmann distribution [13, 36, 37]:^g

^eProperties per unit mass can be obtained from those per unit mole by simply dividing by the species' molar mass ($h_s = H_s / \mathcal{M}_s$).

^fNote that differentiating Eqs. 4.13a and 4.13b with Eq. 4.11, one reaches that $e_s^{Trans} = \frac{3}{2} R_s T_s^{Trans}$ and $e_s^{Rot} = \frac{L_s}{2} R_s T^{Rot}$. Moreover, Eq. 4.13a corresponds to the volumetric partition function of the translational energy, since it has been divided by the system's volume.

^gThe expression for the partition function of the electron species' internal energy $\mathcal{Q}_{e^+}^{Int}$ (Eq. 4.13e) is formulated to account for the contribution of the spin of the free electron to the species entropy [13, 36].

$$e_s^{Mod} = \frac{\mathcal{R}}{\mathcal{M}_s} (T_s^{Mod})^2 \frac{\partial \ln Q_s^{Mod}}{\partial T_s^{Mod}}, \quad \forall s \in \mathcal{S}, \quad (4.11)$$

$$c_{vs}^{Mod} = \frac{\mathcal{R}}{\mathcal{M}_s} T_s^{Mod} \left(2 \frac{\partial \ln Q_s^{Mod}}{\partial T_s^{Mod}} + T_s^{Mod} \frac{\partial^2 \ln Q_s^{Mod}}{\partial (T_s^{Mod})^2} \right), \quad \forall s \in \mathcal{S}, \quad (4.12)$$

$$Q_s^{TransV} = \left(\frac{2\pi \mathcal{M}_s k_B T_s^{Trans}}{N_A \hbar^2} \right)^{\frac{3}{2}}, \quad \forall s \in \mathcal{S}, \quad (4.13a)$$

$$Q_s^{Rot} = \frac{1}{\sigma_s} \left(\frac{T_s^{Rot}}{\theta_s^{Rot}} \right)^{\mathcal{L}_s/2}, \quad \forall s \in \mathcal{S}_{\text{mol}}, \quad (4.13b)$$

$$Q_s^{Vib} = \sum_{m=1}^{N_{\text{vib}}} \frac{g_{sm}^{Vib}}{1 - e^{-\theta_{sm}^{Vib}/T^{Vib}}}, \quad \forall s \in \mathcal{S}_{\text{mol}}, \quad (4.13c)$$

$$Q_s^{Elec} = \sum_{m=0}^{N_{\text{elec}}} g_{sm}^{Elec} e^{-\theta_{sm}^{Elec}/T^{Elec}}, \quad \forall s \in \mathcal{H}, \quad (4.13d)$$

$$Q_e^{Int} = 2, \quad (4.13e)$$

$$e_s = \sum_{Mod} e_s^{Mod} + h_{f,s}^\circ, \quad \forall s \in \mathcal{S}, \quad (4.14)$$

$$h_s = \sum_{Mod} e_s^{Mod} + h_{f,s}^\circ + \frac{\mathcal{R}}{\mathcal{M}_s} T_s^{Trans}, \quad \forall s \in \mathcal{S}, \quad (4.15)$$

$$c_{vs} = \sum_{Mod} c_{vs}^{Mod}, \quad \forall s \in \mathcal{S}, \quad (4.16)$$

$$c_{ps} = \sum_{Mod} c_{vs}^{Mod} + \frac{\mathcal{R}}{\mathcal{M}_s}, \quad \forall s \in \mathcal{S}, \quad (4.17)$$

where subindex m refers to the various vibrational or electronic modes. Note that the expression of the electronic partition function (Eq. 4.13d) features a summation between zero and the number of electronic modes. In reality there are infinite electronic modes, but the summation must be truncated to avoid a divergence of the degeneracies [13, 38].

The species properties appearing in Eqs. 4.13 (σ_s , \mathcal{L}_s , θ_s^{Rot} , g_{sm}^{Vib} , θ_{sm}^{Vib} , θ_{sm}^{Elec} and g_{sm}) can be found for instance in Gurvich [39] or summarized in app. K.1 (in SI units) for the species considered in this work. The species formation enthalpy per mole at 298 K ($H_{f,s}^{298K}$) is by convention 0 for a series of reference species (N_2 , O_2 , e^- , C(gr), He, Ne, Ar, etc.) and for all other species, it is obtained from a formation reaction. The species formation enthalpies at 0 K can then be obtained using Hess' law.

The mixture enthalpy and heat capacity are obtained by summing over the species quantities weighed with the mass fractions:

$$h = \sum_{s \in \mathcal{S}} Y_s h_s, \quad (4.18)$$

$$c_p = \sum_{s \in \mathcal{S}} Y_s c_{ps}. \quad (4.19)$$

Again, one may also obtain the mixture internal energy e and heat capacity at constant volume c_v using analogous expressions.

The RRHO approach was followed by various authors [15, 23, 24, 26, 30] yet neglecting the electronic energy. This is a valid assumption given the temperatures that were reached (< 7500 K) [36]. In general the electronic energy should be included in the analysis, as done by authors using the Mutation⁺⁺ library [20, 24, 32], or by Miró Miró *et al.* [27, 28]. However, when assuming thermal equilibrium, electronic energy may be neglected on the grounds of its very slow relaxation time. In other words, by neglecting the electronic energy, one is essentially assuming an electronically frozen thermal state, which is generally more accurate than assuming it in electronic equilibrium.

The main advantage of McBride's fits is that, for some species,^b they also account for anharmonicity in the vibration of molecules, neglected by the RRHO model. However, with the exception of CO₂, its impact for the temperature ranges of the considered cases is minor [36]. Anharmonic molecule vibration becomes significant for the ranges of temperatures where these molecules are normally already dissociated.ⁱ Only the RRHO model is used for the comparisons in this work.

When assuming thermal non-equilibrium, one must define species enthalpies and heat capacities for the different energy groupings. For instance, for the two-temperature grouping used in this work and explicitized in Eq. 4.8, one may define:

$$h_{tr\ s} = \begin{cases} h_s^{Trans} + h_f^{\circ\ s}, & \forall s \in \mathcal{S}_{atom} \\ h_s^{Trans} + h_s^{Rot} + h_f^{\circ\ s}, & \forall s \in \mathcal{S}_{mol} \\ h_f^{\circ\ s}, & s = e^- \end{cases}, \quad (4.20a)$$

$$h_{v\ s} = \begin{cases} h_s^{Elec}, & \forall s \in \mathcal{S}_{atom} \\ h_s^{Vib} + h_s^{Elec}, & \forall s \in \mathcal{S}_{mol} \\ h_s^{Trans}, & s = e^- \end{cases}, \quad (4.20b)$$

^bFor many of the ablation and pyrolysis species for instance, the database simply includes fits to the RRHO expressions.

ⁱIf considering radiation, or other phenomena where the energy of trace molecular species plays a major role, using the RRHO model may introduce inaccuracies.

$$c_{ptr\ s} = \begin{cases} c_{ps}^{Trans}, & \forall s \in \mathcal{S}_{atom} \\ c_{ps}^{Trans} + c_{ps}^{Rot}, & \forall s \in \mathcal{S}_{mol} \\ 0, & s = e^- \end{cases}, \quad (4.21a)$$

$$c_{pv\ s} = \begin{cases} c_{ps}^{Elec}, & \forall s \in \mathcal{S}_{atom} \\ c_{ps}^{Vib} + c_{ps}^{Elec}, & \forall s \in \mathcal{S}_{mol} \\ c_{ps}^{Trans}, & s = e^- \end{cases}. \quad (4.21b)$$

Analogous splittings can be done for the species internal energy e_s and heat capacity at constant volume $c_{v\ s}$. Similarly, one may also define mixture quantities based on the two-temperature quantities:

$$h_{tr} = \sum_{s \in \mathcal{S}} Y_s h_{tr\ s}, \quad (4.22a)$$

$$h_v = \sum_{s \in \mathcal{S}} Y_s h_{v\ s}, \quad (4.22b)$$

$$c_{ptr} = \sum_{s \in \mathcal{S}} Y_s c_{ptr\ s}, \quad (4.23a)$$

$$c_{pv} = \sum_{s \in \mathcal{S}} Y_s c_{pv\ s}. \quad (4.23b)$$

4.2 Transport properties

Transport properties are those describing the processes whereby mass, energy or momentum are transported from one region to another under the influence of composition, temperature, pressure, electric-field, or velocity gradients [40]. Transport properties include viscosity, thermal conductivity, diffusion and thermal-diffusion coefficients.

4.2.1 Viscosity and thermal conductivity

The importance viscosity has on the development of the dominant instabilities in hypersonic boundary layers [41] makes its accurate modeling properties paramount. Not surprisingly, Lyttle & Reed [19] and Franko *et al.* [24] reported major differences in the stability characteristics depending on the employed transport model.

As long as inelastic collisions can be neglected [3–5], one may obtain the second viscosity coefficient from the Stokes hypothesis (Eq. 4.3).

4.2.1.1 Blottner-Eucken-Wilke model

The most commonly followed approach to modeling viscosity and thermal conductivity in hypersonic stability studies is the combination of Blottner's curve fits [8] with Eucken's relation [42] and Wilke's mixing rule [43] (BEW):

$$\mu_s = \exp \left(A_s^\mu \left(\ln T_s^{Trans} \right)^2 + B_s^\mu \ln T_s^{Trans} + C_s^\mu \right), \quad \forall s \in \mathcal{S}, \quad (4.24)$$

$$\kappa_s^{Fr} = \left(\frac{5}{2} c_{vs}^{Trans} + c_{vs}^{Rot} + c_{vs}^{Vib} + c_{vs}^{Elec} \right) \mu_s, \quad \forall s \in \mathcal{S}, \quad (4.25)$$

$$\phi_s^\mu = \sum_{\ell \in \mathcal{S}} X_\ell \frac{\left(1 + \left(\frac{\mu_s}{\mu_\ell} \right)^{1/2} \left(\frac{\mathcal{M}_\ell}{\mathcal{M}_s} \right)^{1/4} \right)^2}{\left(8 \left(1 + \frac{\mathcal{M}_s}{\mathcal{M}_\ell} \right) \right)^{1/2}}, \quad \forall s \in \mathcal{S}, \quad (4.26)$$

$$Q = \sum_{s \in \mathcal{S}} \frac{X_s Q_s}{\phi_s^\mu}, \quad (4.27)$$

where Q is either μ or κ^{Fr} , and where values for A_s^μ , B_s^μ and C_s^μ are given in Blottner [8] or in Tables K.20, K.21 and K.22 (in SI units).

As it occurred with the energy modes in § 4.1, authors [15, 23, 26, 30] have commonly neglected the thermal conductivity due to the electronic energy, which should in general be included.^j

For thermal non-equilibrium assumptions, one must decompose the thermal conductivity into the contribution of the various energy groups. For instance, for the two-temperature modeling considered in this work, one has:

$$\kappa_{trs}^{Fr} = \begin{cases} \left(\frac{5}{2} c_{vs}^{Trans} + c_{vs}^{Rot} \right) \mu_s, & s \in \mathcal{H}, \\ 0, & s = e^-, \end{cases}, \quad (4.28a)$$

$$\kappa_{vs}^{Fr} = \begin{cases} (c_{vs}^{Vib} + c_{vs}^{Elec}) \mu_s, & s \in \mathcal{H}, \\ \frac{5}{2} c_{vs}^{Trans} \mu_s, & s = e^-. \end{cases}. \quad (4.28b)$$

4.2.1.2 Gupta-Wilke model

Gupta *et al.* [9] proposed curve-fit parameters similar to those of Blottner [8], yet for both the species dynamic viscosity and thermal conductivity, which can also be

^jThe electronic energy in air mixtures reaches a non-negligible level for temperatures larger than 7500 K [36].

assembled with Wilke's mixing rule [43] (GW). The expression for μ_s is identical to Eq. 4.24, whereas that for the thermal conductivity is:

$$\kappa_s^{Fr} = \exp \left(A_s^\kappa (\ln T)^4 + B_s^\kappa (\ln T)^3 + C_s^\kappa (\ln T)^2 + D_s^\kappa \ln T + E_s^\kappa \right), \forall s \in \mathcal{S}, \quad (4.29)$$

The coefficients $A_s^\kappa - E_s^\kappa$ can be found in Gupta *et al.* [9] or in Table K.23 (in SI units). The GW model is only valid for thermal equilibrium.

4.2.1.3 Sutherland-Eucken-Wilke and Sutherland-Wilke models

Alternatively, one may also use Sutherland's law [2] (Eq. 4.2) to approximate the viscosity of each individual species μ_s , as was done by Bitter & Shepherd [26], together with Eucken's correction [42] and Wilke's mixing rule [43] (SEW). The SEW model also allows for thermal non-equilibrium scenarios, where the contributions of the various energy groups to conductivity can be separated similarly to Eq. 4.28.

Another alternative is to also approximate the species thermal conductivities with Sutherland's law Eq. 4.4, rather than with Eucken's relation, and then employ Wilke's mixing rule [43] (SW). However, this restricts its applicability to thermal-equilibrium flow assumptions. Species-specific Sutherland coefficients ($\mu_{ref,s}$, $T_{\mu_{ref,s}}$, $S_{\mu,s}$, $\kappa_{ref,s}$, $T_{\kappa_{ref,s}}$ and $S_{\kappa,s}$), obtained from the CFD++ database [44], can be found in Tables K.18 and K.19.

Sutherland's law is more accurate for lower temperatures, yet its range of applicability is more limited (< 2000 K for N₂ and O₂) [26].

4.2.1.4 Chapman-Enskog model

The most accurate transport model consists of the first and second^k approximation to Chapman & Enskog's molecular theory of gases [6] (CE) using Laguerre-Sonine polynomials [45]:

$$Q = - \begin{vmatrix} G_{s\ell}^Q & X_s \\ X_\ell & 0 \end{vmatrix} \Big/ |G_{s\ell}^Q|, \forall s, \ell \in \mathcal{H}, \quad (4.30)$$

where Q can be the viscosity μ or the heavy-particle translational thermal conductivity κ_H^{Trans} . The elements of the matrix subsystems $G_{s\ell}^Q$ are detailed in app. C.1. Note that the expression in Eq. 4.30 is not the numerically most efficient way to solve the linear system [4, 45].

The other addends forming the frozen thermal conductivity are the thermal conductivity due to the internal energy modes (κ^{Rot} , κ^{Vib} and κ^{Elec}), and for

^kFirst for viscosity μ and second for the heavy-particle translational thermal conductivity κ_H^{Trans} .

ionized mixtures the electron thermal conductivity κ_e^{Trans} . Expressions for the the former are obtained from Eucken's relation: [12, 42]

$$\kappa^{Rot} = \sum_{s \in S_{mol}} \frac{\mathcal{M}_s}{N_A} \frac{X_s c_{vs}^{Rot}}{\sum_{\ell \in \mathcal{H}} X_\ell / n \mathcal{D}_{s\ell}}, \quad (4.31a)$$

$$\kappa^{Vib} = \sum_{s \in S_{mol}} \frac{\mathcal{M}_s}{N_A} \frac{X_s c_{vs}^{Vib}}{\sum_{\ell \in \mathcal{H}} X_\ell / n \mathcal{D}_{s\ell}}, \quad (4.31b)$$

$$\kappa^{Elec} = \sum_{s \in \mathcal{H}} \frac{\mathcal{M}_s}{N_A} \frac{X_s c_{vs}^{Elec}}{\sum_{\ell \in \mathcal{H}} X_\ell / n \mathcal{D}_{s\ell}}, \quad (4.31c)$$

The electron thermal conductivity κ_e^{Trans} can be obtained from the second or the third (more accurate) approximation to Chapman & Enskog's theory [6, 45]:

$$\kappa_e^{Trans} = \frac{X_e^2}{\Lambda_{ee}^{11}}, \quad 2^{\text{nd}} \text{ approx.}, \quad (4.32a)$$

$$\kappa_e^{Trans} = \frac{X_e^2 \Lambda_{ee}^{22}}{\Lambda_{ee}^{11} \Lambda_{ee}^{22} - (\Lambda_{ee}^{12})^2}, \quad 3^{\text{rd}} \text{ approx.}, \quad (4.32b)$$

where the polynomials Λ_{ee}^{11} , Λ_{ee}^{12} and Λ_{ee}^{22} can be found in app. C.1. The frozen thermal conductivity is thus:¹

$$\kappa^{Fr} = \kappa_H^{Trans} + \kappa^{Rot} + \kappa^{Vib} + \kappa^{Elec} + \kappa_e^{Trans}. \quad (4.33)$$

4.2.1.5 Brokaw and Yos models

The computational requirements of the CE model^m have led authors to develop simplified versions of it. Brokaw [46] proposed to approximate the matrix system 4.30 for μ and κ^{Trans} as:

$$\mu = \sum_{s \in S} \frac{\frac{\mathcal{M}_s}{N_A} X_s}{\sum_{\ell \in S} X_\ell \Delta_{s\ell}^{(2)}}, \quad (4.34a)$$

$$\kappa^{Trans} = \frac{15}{4} k_B \sum_{s \in S} \frac{X_s}{\sum_{\ell \in S} \varphi_{s\ell} X_\ell \Delta_{s\ell}^{(2)}}, \quad (4.34b)$$

and Yos [9, 47] proposed an improvement such that:

$$Q = \frac{\sum_{s \in S} \frac{X_s}{\mathcal{A}_s^Q + \mathcal{A}_{av}^Q}}{1 - \mathcal{A}_{av}^Q \sum_{s \in S} \frac{X_s}{\mathcal{A}_s^Q + \mathcal{A}_{av}^Q}} \quad (4.35)$$

¹For non-ionized mixtures $\kappa_e^{Trans} = 0$.

^mIt requires the resolution of a linear matrix system for each point in the computational domain.

where Q can be μ or κ^{Trans} .ⁿ The different coefficients appearing in Eqs. 4.34 and 4.35 are detailed in app. C.2.

Transport-model accuracy evaluation

All the aforementioned models are compared in Fig. 4.1, taking the result of solving the CE system as a reference and computing the error of the others with respect to it with:

$$\epsilon(Q) = \left| 1 - \frac{Q}{Q^{\text{Ref}}} \right|. \quad (4.36)$$

The collision integrals, when required by the diffusion models, are all obtained using the same expression (Eq. 4.57 fitted onto Wright *et al.*'s [48] collisional data). It is clear that for an air-5 mixture (Fig. 4.1 a), both Brokaw and Yos' simplifications of the CE matrix system are excellently accurate. This is not the case for the models using Wilke's mixing rule, which display an almost constant error of around 10%. It is also worth noting how Gupta's fit for the thermal conductivity (Eq. 4.29) fails out of its range of applicability – at lower temperatures.

The error committed with Brokaw and Yos' simplifications significantly increases when ionization species are considered. Fig. 4.1 b) proves that these simplifications render major inaccuracies at the higher temperatures where ionization becomes significant. Moreover, the models using Wilke's mixing rule reach critically high error levels, being thus strongly non-recommendable to employ them for ionized mixtures.

4.2.2 Diffusion models

The inter-diffusion of species can either be modeled by considering the diffusion of one species into the mixture or the diffusion of each species into each other species forming the mixture. The latter assumes the diffusion fluxes in Eq. 2.12, whereas the former assumes:

$$J_s^j = -\rho \mathcal{D}_{\text{eff},s} d_s^j, \quad (4.37)$$

where $\mathcal{D}_{\text{eff},s}$ is the effective diffusion coefficient of species s within the mixture.

As outlined in § 2.12, in the absence of an electric field, barodiffusion and thermodiffusion, the diffusion driving force is commonly assumed to be either the

ⁿNote that Eq. 4.30 sums only the contribution of heavy species, [45] whereas the approximations in Eqs. 4.34 and 4.35 were calibrated including also electron species. Consequently Eqs. 4.34b and 4.35 refer to the total translational thermal conductivity, which for ionized mixtures will include that of the heavy particles κ_H^{Trans} plus that of the electrons κ_e^{Trans} .

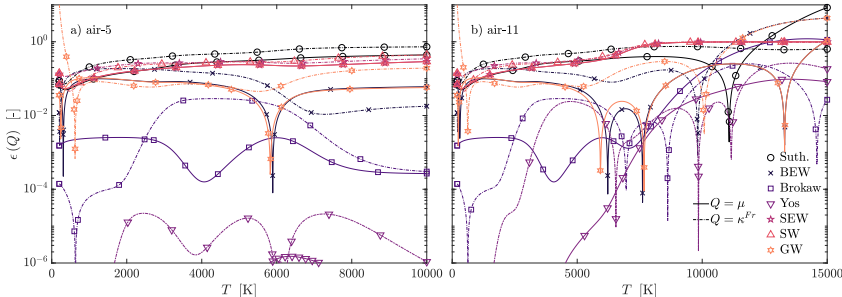


Figure 4.1: Difference between the transport properties computed with mono-species Sutherland with $Pr = 0.7$ (Eqs. 4.2 and 4.5), BEW (Eqs. 4.24, 4.25 and 4.27), Brokaw (Eq. 4.34), Yos (Eq. 4.35), SEW (Eqs. 4.2, 4.25 and 4.27), SW (Eqs. 4.2, 4.4 and 4.27), GW (Eqs. 4.24, 4.29 and 4.27), against the reference CE (Eq. 4.30), for an air mixture in equilibrium at $p = 10 \text{ kPa}$.

mass fraction or the mole fraction gradients ($d_s^j = g^{ij} Y_{s,j}$ or $d_s^j = g^{ij} X_{s,j}$), hereinafter referred to as mass and molar diffusion respectively.^o

An important distinction has to be made between self-consistent and self-inconsistent diffusion models. A self-consistent model returns a null sum of the diffusion fluxes:

$$\sum_{s \in \mathcal{S}} J_s^j = 0, \quad \forall j \in [1, 2, 3]. \quad (4.38)$$

A widely used diffusion model consists in assuming equal the effective diffusion coefficients of all species and such that the Schmidt or the Lewis number are constant throughout the boundary layer. This leads to:

$$\mathcal{D}_{\text{eff } s} = \frac{\mu}{\text{Sc } \rho}, \quad \forall s \in \mathcal{S}, \quad (4.39)$$

or:

$$\mathcal{D}_{\text{eff } s} = \frac{\text{Le } \kappa^{Fr}}{c_p \rho}, \quad \forall s \in \mathcal{S}. \quad (4.40)$$

Since all the diffusion coefficients are the same and since the species concentration gradients sum to zero, these models are self-consistent.

Another alternative is to use the binary diffusion coefficients Eq. C.5 coming from the first approximation to Chapman & Enskog's kinetic theory of gases. These coefficients however are only suitable for binary mixtures of two species with equal concentrations. In order to accurately model multispecies mixtures with varying concentrations, one must use multicomponent diffusion coefficients. The

^oThe expressions of the diffusion coefficients should be modified when changing the driving force (see for instance Sutton & Gnoffo [49]). However, to illustrate the error that would be committed otherwise, results are presented without such modification.

most accurate of the methods to obtain them is the solution of the Stefan-Maxwell (SM) linear system: [7, 45]

$$\sum_{\ell \in \mathcal{S}} \check{G}_{s\ell}^{\mathcal{D}} \frac{J_{\ell}^j}{\rho_{\ell}} = -d_s^j, \quad \forall s \in \mathcal{S}, \quad (4.41)$$

where the diffusion coefficient matrix can consequently be obtained from the inverse of the $\check{G}_{s\ell}^{\mathcal{D}}$ matrix:

$$\underline{\underline{\mathcal{D}}} = \left(\check{G}_{s\ell}^{\mathcal{D}} \right)^{-1}. \quad (4.42)$$

The coefficients in the regularized diffusion matrix ($\check{G}_{s\ell}^{\mathcal{D}}$) can be found in app. C.1.

The resolution of the aforementioned matrix system introduces a significant computational cost, motivating authors to use other diffusion models. For instance, a definition for the effective diffusion coefficients is proposed by Yos: [10, 50]

$$\mathcal{D}_{\text{eff } s} = \frac{1 - X_s}{\sum_{\substack{\ell \in \mathcal{S} \\ \ell \neq s}} X_{\ell} / \mathcal{D}_{s\ell}}, \quad \forall s \in \mathcal{S}. \quad (4.43)$$

This is known as effective binary diffusion (EBD). Ramshaw [51] proposed a correction in order to preserve self-consistency which leads to the self-consistent effective binary diffusion (SCEBD) coefficients:

$$\mathcal{D}_{s\ell} = \frac{\delta_{s\ell} - Y_{\ell}}{X_{\ell}} \frac{1 - Y_{\ell}}{1 - X_{\ell}} \mathcal{D}_{\text{eff } \ell}, \quad \forall s, \ell \in \mathcal{S}. \quad (4.44)$$

Ambipolar diffusion

In ionized mixtures it is common to impose the ambipolar condition, which enforces the net charge flux to be zero:

$$\sum_{s \in \mathcal{S}} \mathcal{Z}_s \frac{J_s^j}{\rho_s} = 0, \quad \forall j \in [1, 2, 3]. \quad (4.45)$$

The effective diffusion coefficients are modified with the condition proposed by Lee [52]:

$$\mathcal{D}_{\text{eff } s}^{\text{ambip.}} \approx \begin{cases} \mathcal{D}_{\text{eff } s}^{\text{non-ambip.}}, & \forall s \notin \mathcal{S}_{\text{ion}} \\ 2\mathcal{D}_{\text{eff } s}^{\text{non-ambip.}}, & \forall s \in \mathcal{S}_{\text{ion}} \end{cases}. \quad (4.46)$$

The resulting model is referred to as effective binary ambipolar diffusion (EBAD). Ramshaw's correction also presents different expressions when assuming ambipolar diffusion [53]:

$$\begin{aligned} \mathcal{D}_{s\ell}^{\text{ambip.}} &= \left(\delta_{s\ell} - Y_{\ell} \left(1 + \mathcal{Z}_{\ell} \frac{\mathcal{M}_e}{\mathcal{M}_{\ell}} \right) \right) \frac{1}{X_{\ell}} \cdot \\ &\quad \cdot \frac{1 - Y_{\ell}}{1 - X_{\ell}} (1 - \delta_{e\ell}) \mathcal{D}_{\text{eff}, \ell}^{\text{ambip.}}, \quad \forall s, \ell \in \mathcal{H}, \end{aligned} \quad (4.47a)$$

$$\begin{aligned} \mathcal{D}_{e\ell}^{\text{ambip.}} &= \left((1 - Y_e) \mathcal{Z}_\ell - Y_e \frac{\mathcal{M}_\ell}{\mathcal{M}_e} \right) \frac{1}{X_e} \\ &\cdot \frac{1 - Y_\ell}{1 - X_\ell} (1 - \delta_{e\ell}) \mathcal{D}_{\text{eff},\ell}^{\text{ambip.}}, \quad \forall \ell \in \mathcal{H}. \end{aligned} \quad (4.47b)$$

hereinafter referred to as self-consistent effective binary ambipolar diffusion (SCEBAD).

One must bear in mind that Ramshaw's correction implicitly assumes that the diffusion fluxes of heavy species is much larger than that of electrons, allowing for a simplified expression of the electric field [45].

When working with ambipolar ionized mixtures, the Stefan-Maxwell system is also slightly modified, since the electric field must also be included in the resolution of the diffusion fluxes. As laid out by Magin & Degrez [45], such a treatment makes Eq. 4.41 become:^p

$$\begin{bmatrix} \check{G}_{sl}^{\mathcal{D}} & -\kappa_s^E / a^\kappa \frac{T_s^{\text{Trans}}}{T_s^{\text{Trans}}} \\ -\kappa_\ell^E / a^\kappa & 0 \end{bmatrix} \begin{bmatrix} \frac{J_s^j}{\rho_s} \\ a^\kappa g^{ij} E_i \end{bmatrix} = \begin{bmatrix} d_s^j \\ 0^j \end{bmatrix}, \quad (4.48)$$

where κ_s^E is the grouping parameter defined in Eq. 2.13, and where a^κ is a scaling parameter equal to the maximum κ_s^E . It is important to note that the electric field is a covariant variable (subindex i notation), and therefore requires the metric matrix g^{ij} so that one can sum it to the diffusion fluxes (see § 2.3). The multicomponent diffusion coefficients thus result from the inversion of the matrix in Eq. 4.48:

$$\begin{bmatrix} \mathcal{D}_{sl} & v_s^{\mathcal{D}} \\ u_\ell^{\mathcal{D}} & w^{\mathcal{D}} \end{bmatrix} = \begin{bmatrix} \check{G}_{sl}^{\mathcal{D}} & -\kappa_s^E / a^\kappa \frac{T_s^{\text{Trans}}}{T_s^{\text{Trans}}} \\ -\kappa_\ell^E / a^\kappa & 0 \end{bmatrix}^{-1}. \quad (4.49)$$

$v_s^{\mathcal{D}}$ and $w^{\mathcal{D}}$ are irrelevant, since when the inverse matrix (Eq. 4.49) multiplies the vector in the right-hand side of Eq. 4.48, they multiply the vectorial 0^j . However, $u_\ell^{\mathcal{D}}$ can be used to retrieve the ambipolar electric field:

$$g^{ij} E_i = \sum_{s \in \mathcal{S}} \frac{u_s^{\mathcal{D}}}{a^\kappa} \frac{J_s^j}{\rho_s}, \quad (4.50)$$

Diffusion-model accuracy evaluation

Figure 4.2 shows the error committed by each of the models with respect to the reference (SM with molar diffusion). In order to avoid singularities in the definition

^pNote that Eq. 4.48 is a linear system of $N_{\text{dim}} (N_s + 1)$ equations, since it must be formulated for each species and the electric field in each spatial direction. One must also recall that, as mentioned in footnote a in § 2.3, the only spatial subindices concerning the tensorial notation are i, j, k and ℓ . The calligraphic subindex ℓ denotes species quantities.

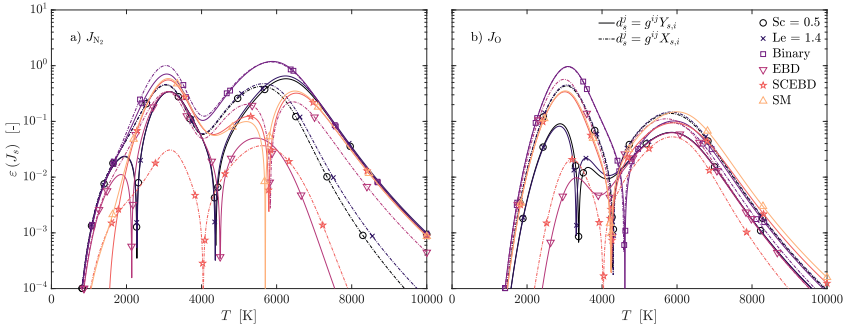


Figure 4.2: Difference between the diffusion fluxes of N_2 and O computed with different diffusion models: constant Sc number (Eq. 4.39), constant Lewis number (Eq. 4.40), binary coefficients (Eq. C.5), EBD (Eq. 4.43), SCEBD (Eq. 4.44); both with mass ($d_s^j = g^{ij} Y_{s,i}$) and molar diffusion ($d_s^j = g^{ij} X_{s,i}$), against the reference SM (Eq. 4.42) with molar diffusion, for an air-5 mixture in equilibrium at $p = 10\text{ kPa}$.

of the error, an alternative to Eq. 4.36 is used:

$$\varepsilon(Q) = \frac{|Q - Q^{\text{Ref}}|}{\max(Q^{\text{Ref}})}. \quad (4.51)$$

The SCEBD model with $d_s^j = g^{ij} X_{s,i}$ is clearly the closest of the simplified models. All the others display a discrepancy that varies between 10 and 100% with respect to the reference.

4.2.3 Collisional models

Certain transport models require expressions for the species pairs' collisional cross-sectional integrals. An excellent review of the physical interpretation of these integrals is given by Hirschfelder *et al.* [7, § 7.4-d]

Data for these collision integrals normally comes from experiments or from computations based on the particles' intermolecular force potentials, and are normally presented in tables as a function of the so-called collisional temperature $T_{s\ell}^{\text{col}}$, defined as [13]:

$$T_{s\ell}^{\text{col}} = \begin{cases} T^{\text{Trans}}, & \forall s, \ell \in \mathcal{H} \\ T^{\text{e}^-}, & s|\ell = \text{e}^- \end{cases}, \quad (4.52)$$

or, for charged collisions, the reduced temperature $T_{s\ell}^*$:

$$T_{s\ell}^* = \frac{\lambda_D k_B T_{s\ell}^{\text{col}}}{q_e^2 / (4\pi\epsilon_0)}, \quad \forall s, \ell \in \mathcal{S}, \quad (4.53)$$

where the Debye shielding length is:⁹

$$\lambda_D = \sqrt{\frac{\epsilon_0 k_B / q_e^2}{\sum_{s \in S} Z_s^2 n_s / T_s^{Trans}}} . \quad (4.54)$$

When performing CFD simulations, it is common practice to simply interpolate between these tabled values. However, for stability analyses it is preferable to fit polynomial expressions to these collisions, thus allowing for an analytical differentiation with respect to temperature (see § 4.6) and avoiding discontinuities in these derivatives.

Some authors [25, 31] used the fitting proposed by Gupta *et al.* [9]:

$$\begin{aligned} \ln(\Omega_{s\ell}^{(i,j)}) &= A_{\Omega_{s\ell}^{(i,j)}} + B_{\Omega_{s\ell}^{(i,j)}} \ln(T_{s\ell}^{\text{col}}) + C_{\Omega_{s\ell}^{(i,j)}} (\ln(T_{s\ell}^{\text{col}}))^2 + \\ &\quad + D_{\Omega_{s\ell}^{(i,j)}} (\ln(T_{s\ell}^{\text{col}}))^3 , \quad \forall s, \ell \in S , \end{aligned} \quad (4.55)$$

where the coefficients^r were obtained from fitting Eq. 4.55 to the different collision integrals obtained with the NATA (Nonequilibrium Arc Tunnel Analysis) code [54]. These coefficients, adapted to SI units and the formulation in Eq. 4.55 can be found in app. K.3.2.

Stuckert & Reed [18, 55] used a different fitting function – on $\Omega_{s\ell}^{(i,j)}$, rather than $\ln(\Omega_{s\ell}^{(i,j)})$:

$$\begin{aligned} \Omega_{s\ell}^{(i,j)} &= A_{\Omega_{s\ell}^{(i,j)}} + B_{\Omega_{s\ell}^{(i,j)}} \ln(T_{s\ell}^{\text{col}}) + C_{\Omega_{s\ell}^{(i,j)}} (\ln(T_{s\ell}^{\text{col}}))^2 + \\ &\quad + D_{\Omega_{s\ell}^{(i,j)}} (\ln(T_{s\ell}^{\text{col}}))^3 , \quad \forall s, \ell \in S . \end{aligned} \quad (4.56)$$

As Stuckert details, [55] the coefficients were obtained from fitting to data from a series of sources [56–59]. These coefficients, adapted to SI units can be found in app. K.3.1.

Additionally, another fitting is proposed consisting in a higher-polynomial-

⁹There exist alternative definitions of the Debye shielding length, since it is not clear whether ions should contribute to the shielding (like in Eq. 4.54) or not [13].

^rNote that the coefficients in Eq. 4.55 are in the inverse order to how they are given by Gupta *et al.* [9]: $A_{\Omega_{s\ell}^{(i,j)}}$ corresponds to the polynomial's independent term and $D_{\Omega_{s\ell}^{(i,j)}}$ to the polynomial's higher order term instead of the opposite. Also, the fitting reported here is on $\ln(\Omega_{s\ell}^{(i,j)})$, rather than $\ln(\pi \Omega_{s\ell}^{(i,j)})$, like Gupta *et al.* [9] did. This implies that the independent term $A_{\Omega_{s\ell}^{(i,j)}}$ has an additional addend $\ln(\pi)$ with respect to Gupta *et al.*'s $D_{\Omega_{s\ell}^{(i,j)}}$.

order version of Eq. 4.55:^s

$$\begin{aligned} \ln \left(\Omega_{s\ell}^{(i,j)} \right) &= A_{\Omega_{s\ell}^{(i,j)}} + B_{\Omega_{s\ell}^{(i,j)}} \ln(T_{s\ell}^{\text{col}}) + \\ &+ C_{\Omega_{s\ell}^{(i,j)}} (\ln(T_{s\ell}^{\text{col}}))^2 + D_{\Omega_{s\ell}^{(i,j)}} (\ln(T_{s\ell}^{\text{col}}))^3 + \\ &+ E_{\Omega_{s\ell}^{(i,j)}} (\ln(T_{s\ell}^{\text{col}}))^4 + F_{\Omega_{s\ell}^{(i,j)}} (\ln(T_{s\ell}^{\text{col}}))^5, \quad \forall s, \ell \in \mathcal{S}, \\ &\quad s|\ell \notin \mathcal{S}_{\text{ion}} \cup e^{-}, \end{aligned} \quad (4.57a)$$

$$\begin{aligned} \ln \left(\left(\frac{T_{s\ell}^*}{\lambda_D} \right)^2 \Omega_{s\ell}^{(i,j)} \right) &= A_{\Omega_{s\ell}^{(i,j)}} + B_{\Omega_{s\ell}^{(i,j)}} \ln(T_{s\ell}^*) + C_{\Omega_{s\ell}^{(i,j)}} (\ln(T_{s\ell}^*))^2 + \\ &+ D_{\Omega_{s\ell}^{(i,j)}} (\ln(T_{s\ell}^*))^3 + E_{\Omega_{s\ell}^{(i,j)}} (\ln(T_{s\ell}^*))^4 + \\ &+ F_{\Omega_{s\ell}^{(i,j)}} (\ln(T_{s\ell}^*))^5, \quad \forall s, \ell \in \mathcal{S}_{\text{ion}} \cup e^{-}. \end{aligned} \quad (4.57b)$$

where Eq. 4.57a applies to collisions between neutral species, or between a neutral and a charged species, and Eq. 4.57b applies to collisions between two charged particles.

Oftentimes authors report the ratios of collision integrals $A_{s\ell}^*$, $B_{s\ell}^*$, $C_{s\ell}^*$, and $E_{s\ell}^*$:

$$A_{s\ell}^* = \frac{\Omega_{s\ell}^{(2,2)}}{\Omega_{s\ell}^{(1,1)}}, \quad \forall s, \ell \in \mathcal{S}, \quad (4.58a)$$

$$B_{s\ell}^* = \frac{5\Omega_{s\ell}^{(1,2)} - 4\Omega_{s\ell}^{(1,3)}}{\Omega_{s\ell}^{(1,1)}}, \quad \forall s, \ell \in \mathcal{S}, \quad (4.58b)$$

$$C_{s\ell}^* = \frac{\Omega_{s\ell}^{(1,2)}}{\Omega_{s\ell}^{(1,1)}}, \quad \forall s, \ell \in \mathcal{S}, \quad (4.58c)$$

$$E_{s\ell}^* = \frac{\Omega_{s\ell}^{(2,3)}}{\Omega_{s\ell}^{(2,2)}}, \quad \forall s, \ell \in \mathcal{S}. \quad (4.58d)$$

For this reason the curve fits are often done on these collision-integral ratios, rather than the integrals themselves. Stuckert [55] followed Brokaw's approach [46] and assumed a constant $B_{s\ell}^* = 1.06$ for all collisions. Gupta *et al.* [9] however, also provided curve-fit parameters for $B_{s\ell}^*$, in the same form:

$$\ln(B_{s\ell}^*) = C_{B_{s\ell}^*} + B_{B_{s\ell}^*} \ln(T_{s\ell}^{\text{col}}) + A_{B_{s\ell}^*} (\ln(T_{s\ell}^{\text{col}}))^2, \quad \forall s, \ell \in \mathcal{S}. \quad (4.59)$$

^sNote that the condition on the species subindices in Eq. 4.57a ($s|\ell \notin \mathcal{S}_{\text{ion}} \cup e^-$) implies that either s or ℓ must not be in the group of charged species ($\mathcal{S}_{\text{ion}} \cup e^-$).

Similarly, novel curve fits are presented here for these collision-integral ratios:

$$\begin{aligned} \ln(B_{s\ell}^*) = & A_{B_{s\ell}^*} + B_{B_{s\ell}^*} \ln(T_{s\ell}^{\text{col}}) + \\ & + C_{B_{s\ell}^*} (\ln(T_{s\ell}^{\text{col}}))^2 + D_{B_{s\ell}^*} (\ln(T_{s\ell}^{\text{col}}))^3 + \\ & + E_{B_{s\ell}^*} (\ln(T_{s\ell}^{\text{col}}))^4 + F_{B_{s\ell}^*} (\ln(T_{s\ell}^{\text{col}}))^5, \quad \forall s, \ell \in \mathcal{S} \\ & s | \ell \notin \mathcal{S}_{\text{ion}} \cup e^-, \end{aligned} \quad (4.60a)$$

$$\begin{aligned} \ln(B_{s\ell}^*) = & A_{B_{s\ell}^*} + B_{B_{s\ell}^*} \ln(T_{s\ell}^*) + \\ & + C_{B_{s\ell}^*} (\ln(T_{s\ell}^*))^2 + D_{B_{s\ell}^*} (\ln(T_{s\ell}^*))^3 + \\ & + E_{B_{s\ell}^*} (\ln(T_{s\ell}^*))^4 + F_{B_{s\ell}^*} (\ln(T_{s\ell}^*))^5, \quad \forall s, \ell \in \mathcal{S}_{\text{ion}} \cup e^-. \end{aligned} \quad (4.60b)$$

Analogous ones are used for $C_{s\ell}^*$ and $E_{s\ell}^*$.

Eqs. 4.57 and 4.60 are fitted to the latest collisional data presented by Wright *et al.* [48, 60] (neutral-neutral and electron-neutral collisions), Levin & Wright [61] (ion-neutral collisions), Mason [62] and Devoto [63] (charged-charged collisions). Bellemans & Magin's [64] more accurate fits are taken for the carbon species whenever necessary, since they have the same form as Eqs. 4.57a and 4.60a. Tables with the coefficients can be found in app. K.3.3 (in SI units) and the curve fits together with the original tabled data is plotted in app. L. A summary of the methodology used to compute the various collision integrals can be found in Table 4.2.

The evaluation of the curve fits outside of the tabled range of temperatures could lead to extrapolation problems. In order to avoid this, additional fictitious points are added, if necessary, to the original set of data points before performing the fitting. For example, $e^- - NO$ collisions are only defined between 2000 and 20000 K [48] (see Figs. L.13c, L.14c, L.15c and L.16c). In order to avoid extrapolation problems when evaluating them at < 2000 K, additional points are added to Wright's dataset [48], such as $[500 \text{ K}; \Omega_{s\ell}^{(i,j)}|_{T=2000 \text{ K}}]$ and $[200 \text{ K}; \Omega_{s\ell}^{(i,j)}|_{T=2000 \text{ K}}]$. Depending on the dataset, the addition points are either “clipped off” (0th-order extrapolation) or extrapolated linearly (1st-order) from the last data points. This is done to preserve eventual clear trends in the data, and to avoid spurious oscillations in the fitting due to radical changes in these trends. The curve fits of all collisions together with the original tabled data can be found in app. L.

Another approach providing continuous expressions for the collision integrals, yet not followed in this dissertation, is to obtain them from Lennard-Jones, Stockmayer, Born-Mayer, Langevin, or Debye-Hückel potentials – see Ref. 13.

Collision-model accuracy evaluation

Figure 4.3 compares the (2,2) collision integrals computed with these three methodologies for an air-5 mixture. $\Omega_{s\ell}^{(2,2)}$ is chosen for comparison due to its

Collision	Computed from
$\Omega_{s\ell}^{(1,1)}$	Curve fits
$\Omega_{s\ell}^{(1,2)}$	$\Omega_{s\ell}^{(1,1)}$ and $C_{s\ell}^*$ curve fits
$\Omega_{s\ell}^{(1,3)}$	$\Omega_{s\ell}^{(1,1)}$, $\Omega_{s\ell}^{(1,2)}$ and $B_{s\ell}^*$ curve fits
$\Omega_{s\ell}^{(1,4)}$	e^- – neut.: equal to $\Omega_{s\ell}^{(1,3)}$ (see Scoggins [13]) e^- – charg.: curve fits
$\Omega_{s\ell}^{(1,5)}$	e^- – neut.: equal to $\Omega_{s\ell}^{(1,3)}$ (see Scoggins [13]) e^- – charg.: curve fits
$\Omega_{s\ell}^{(2,2)}$	Curve fits
$\Omega_{s\ell}^{(2,3)}$	$\Omega_{s\ell}^{(2,2)}$ and $E_{s\ell}^*$ curve fits
$\Omega_{s\ell}^{(2,4)}$	Curve fits

Table 4.2: Methodology to compute the various collision integrals appearing in the transport models.

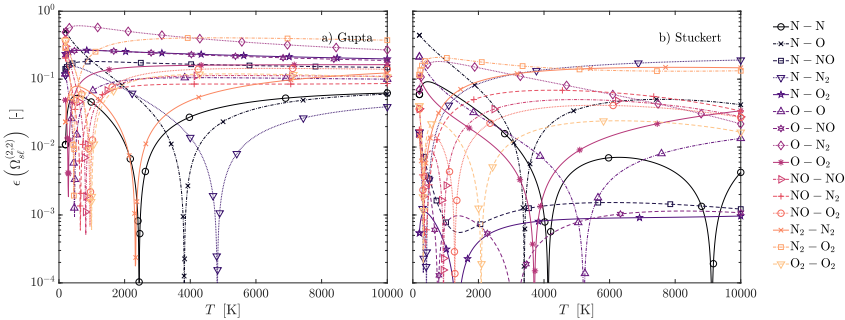


Figure 4.3: Difference between the (2,2) collision integrals computed with Eq. 4.55 and Gupta et al. [9] (a) or with Eq. 4.56 and Stuckert [55] (b) against the reference fittings in Eq. 4.57 and Miró Miró et al. [28] on the data by Wright et al. [48], for an air-5 mixture.

relevance, since it is the one governing the viscosity (see Eq. C.3). The curve fits in Eq. 4.57 are taken as a reference.

Stuckert's fittings generally display a lower error than Gupta's. When interpreting Fig. 4.3 one must bear in mind that, as pointed out by Wright et al. [48], the collisional data have uncertainties that may range from 5 to 50%.

Figure 4.4 presents the error in the transport properties (a) and the diffusion fluxes (b) arising from the use of the different collisional data. By using the same transport model (CE) for all curves in Fig. 4.4 (a) and the same diffusion model (SM with $d_s^j = g^{ij} X_{s,i}$) for all curves in Fig. 4.4 (b), one can isolate the error due to the collisional data from that of the transport and diffusion models themselves. Not surprisingly, the inaccuracies observed in Fig. 4.3 are transferred to the properties depending on them, leading to errors of approximately 10% in both properties.

4.3 Chemical properties

For a set of reactions \mathcal{R} between a set of species \mathcal{S} :

$$\sum_{s \in \mathcal{S}} \nu'_{sr} s \leftrightarrow \sum_{s \in \mathcal{S}} \nu''_{sr} s \quad , \quad \forall r \in \mathcal{R} , \quad (4.61)$$

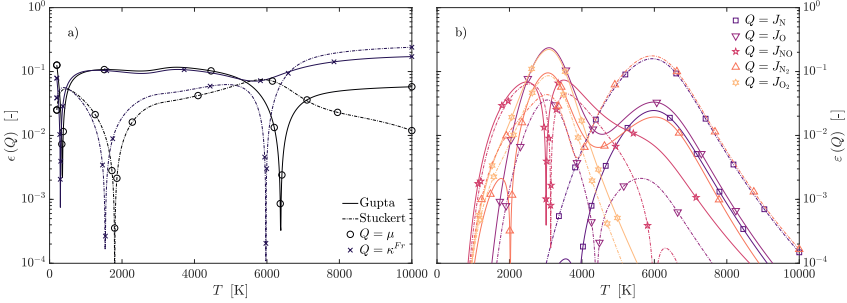


Figure 4.4: Difference between the properties calculated using collision integrals computed with Eq. 4.55 and Gupta et al. [9] or with Eq. 4.56 and Stuckert [55] against the reference fittings in Eq. 4.57 on the data by Wright et al. [48], for an air-5 mixture in equilibrium at $p = 10 \text{ kPa}$. The property models are not changed: CE (Eq. 4.30) and SM (Eq. 4.42) with molar diffusion.

the mass production rate of each species can be approximated by the law of mass action [65]:

$$\begin{aligned} \dot{\omega}_s &= \sum_{r \in \mathcal{R}} \dot{\omega}_{sr} = \\ &= \mathcal{M}_s \sum_{r \in \mathcal{R}} (\nu''_{sr} - \nu'_{sr}) \left(k_{f\,r} \prod_{\ell \in \mathcal{S}} \left(\frac{\rho_\ell}{\mathcal{M}_\ell} \right)^{\nu'_{\ell\,r}} + \right. \\ &\quad \left. - k_{b\,r} \prod_{\ell \in \mathcal{S}} \left(\frac{\rho_\ell}{\mathcal{M}_\ell} \right)^{\nu''_{\ell\,r}} \right), \quad \forall s \in \mathcal{S}, \end{aligned} \quad (4.62)$$

where $k_{f\,r}$ and $k_{b\,r}$ are the forward and backward reaction rates. In order to define them, it is useful to introduce the backward and forward reaction temperatures [14, 52, 66]:

$$T_{f\,r} = \prod_{Mod,s} (T_s^{Mod})^{a_{f\,rs}^{Mod}}, \quad \forall r \in \mathcal{R}, \quad (4.63a)$$

$$T_{b\,r} = \prod_{Mod,s} (T_s^{Mod})^{a_{b\,rs}^{Mod}}, \quad \forall r \in \mathcal{R}, \quad (4.63b)$$

where the weighing coefficients $a_{f\,rs}^{Mod}$ and $a_{b\,rs}^{Mod}$ depend on the nature of each reaction. They may be distinct for the forward and backward rate of one same reaction and must logically sum to one. Despite the barroqueness and verbosity of Eq. 4.63 that ensures its generality – with a product over all energy modes and species, in practice it is reduced to a simple product of however many temperatures define the system. For instance, for the two-temperature thermal model considered

Reaction	$a_{f,r}^{tr}$	$a_{b,r}^{tr}$
Association ionization and dissociative recombination $A + B \leftrightarrow AB^+ + e^-$	1	0
Charge exchange $A^+ + B \leftrightarrow A + B^+$	1	1
Electron impact dissociation and recombination $AB + e^- \leftrightarrow A + B + e^-$	0	0
Electron impact ionization and ion recombination $A + e^- \leftrightarrow A^+ + e^- + e^-$	0	0
Exchange $AB + CD \leftrightarrow AC + BD$	1	1
Heavy particle impact dissociation and recombination $AB + M \leftrightarrow A + B + M$	0.5	1
Heavy particle impact ionization and ion recombination $A + M \leftrightarrow A^+ + e^- + M$	1	1

Table 4.3: Weighing coefficients for the forward and backward reaction temperatures (Eq. 4.63) corresponding to the translational-rotational temperature in a two temperature system (Eq. 4.8). Obtained from Scoggins [13]. The coefficients for the vibrational-electronic-electron temperature T_v are simply $a_{f,r}^v = 1 - a_{f,r}^{tr}$ and $a_{b,r}^v = 1 - a_{b,r}^{tr}$.

in this work (Eq. 4.8), one has:

$$T_{f,r} = T^{a_f^{tr}} T_v^{a_f^v}, \quad \forall r \in \mathcal{R}, \quad (4.64a)$$

$$T_{b,r} = T^{a_b^{tr}} T_v^{a_b^v}, \quad \forall r \in \mathcal{R}, \quad (4.64b)$$

with the corresponding coefficients presented in Table 4.3.

The forward and backward reaction rates can thus be defined as:^t

$$k_{f,r} = A_r^f T_{f,r}^{n_{Tr}^f} e^{-\theta_r^f/T_{f,r}}, \quad \forall r \in \mathcal{R}, \quad (4.65a)$$

$$k_{b,r} = \frac{k_{f,r}(T_{b,r})}{K_{eq,r}}, \quad \forall r \in \mathcal{R}. \quad (4.65b)$$

In simulating the chemical activity of dilute gas mixtures one can make a distinction between the equilibrium state of such activity, and the kinetics of the reactions. Hereinafter, different modeling strategies for the former will consist in using different expressions for the reactions' equilibrium constants $K_{eq,r}$, whereas for the latter they will consist in using different reaction rate constants (A_r , n_{Tr} and θ_r) for the forward reaction rates in Eq. 4.65a.

^tIn order to avoid numerical overflow, it is desirable to evaluate these expressions in their logarithmic form.

$K_{\text{eq } r}$ can be obtained, using kinetic theory, from the partition functions of the different energy modes. Assuming a RRHO model for the species (see § 4.1):

$$K_{\text{eq } r} = \prod_{s \in \mathcal{S}} \left(\frac{\prod_{\text{Mod}} \mathcal{Q}_s^{\text{Mod}}}{N_A} \right)^{\nu''_{sr} - \nu'_{sr}} \cdot \exp \left(-(\nu''_{sr} - \nu'_{sr}) \frac{h_{f,s}^\circ \mathcal{M}_s}{\mathcal{R} T_{br}} \right), \quad \forall r \in \mathcal{R}. \quad (4.66)$$

Alternatively, when using the NASA7 or NASA9 polynomials to determine the thermal properties of the mixture, it is more interesting to express Eq. 4.66 as a function of the species Gibbs free energy at a reference (atmospheric) pressure g_s^{Atm} :

$$K_{\text{eq } r} = \prod_{s \in \mathcal{S}} \left(\frac{p_{\text{Atm}}}{\mathcal{R} T_{br}} \right)^{\nu''_{sr} - \nu'_{sr}} \exp \left(-(\nu''_{sr} - \nu'_{sr}) \frac{g_s^{\text{Atm}} \mathcal{M}_s}{\mathcal{R} T_{br}} \right), \quad \forall r \in \mathcal{R}, \quad (4.67)$$

where the Gibbs free energy of a single species due to a single energy mode is equal to:

$$g_s^{\text{Mod}} = h_s^{\text{Mod}} + s_s^{\text{Mod}} T_s^{\text{Mod}}, \quad \forall s \in \mathcal{S}. \quad (4.68)$$

Park [67] proposed to approximate Eq. 4.66 with a polynomial fitting:

$$K_{\text{eq } r} = \exp \left(\sum_{n=1}^5 A_n^P \left(\frac{10\,000}{T_{br}} \right)^{n-1} \right), \quad \forall r \in \mathcal{R}, \quad (4.69)$$

whereas Bortner [9, 68] proposed to use an Arrhenius-like expression^u like the one used for $k_f r$:

$$K_{\text{eq } r} = A_r^{\text{eq}} T_{br}^{n_{Tr}^{\text{eq}}} e^{-\theta_r^{\text{eq}}/T_{br}}, \quad \forall r \in \mathcal{R}. \quad (4.70)$$

$K_{\text{eq } r}$ plays a major role in the determination of the equilibrium (LTE) composition of the mixture, which is obtained from the resolution of the equilibrium system of equations (see app. B or Anderson [37, Ch. 10]).

One should be cautious when combining the thermal models in § 4.1 with Eqs. (4.66-4.70). The use of inconsistent definitions for the enthalpy and the entropy or Gibbs free energy, which appear implicitly in Eqs. (4.66-4.70), could lead to a violation of the second law of thermodynamics. That is, for thermal equilibrium situations (Eq. 4.7). In thermal non-equilibrium, the use of the two-temperature model presented in Eq. 4.8 already does not satisfy the second law, since its heuristic nature does not allow for an expression for the entropy. Efforts have been made to carry out a rigorous derivation from kinetic theory [69], but they still remain very preliminary.

^uBortner actually presents an Arrhenius-like expression for the backward reaction rate with A_r^b , n_{Tr}^b and θ_r^b . It is however trivial to reach Eq. 4.70 defining $A_r^{\text{eq}} = A_r^f/A_r^b$, $n_{Tr}^{\text{eq}} = n_{Tr}^f - n_{Tr}^b$ and $\theta_r^{\text{eq}} = \theta_r^f - \theta_r^b$.

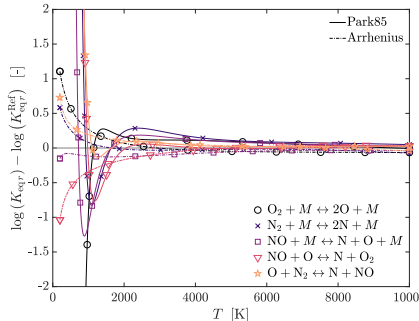


Figure 4.5: Difference between the chemical equilibrium constant computed with either Park85 (Eq. 4.69) or Arrhenius (Eq. 4.70), against the reference RRHO (Eq. 4.66).

Chemical-model accuracy evaluation

Figure 4.5 quantifies the discrepancy between the two fittings (Eqs. 4.69 and 4.70) and the reference (Eq. 4.66), by plotting the order of magnitude of the difference between them. Park [67] affirms the range of applicability of the polynomial fitting to be from 500 to 50,000 K. However, the high error obtained for lower temperatures suggests the lower end of this range to be rather closer to 1,000 K. For temperatures larger than this, both approximations provide results very close to the reference (RRHO), with Bortner's Arrhenius-like expression being slightly closer to it than Park's polynomial fit.

Figure 4.6 plots the order-of-magnitude difference in the forward reaction rate (k_{fr}) when using the reaction rate constants proposed by several authors (Park [67] in 1985 (Table J.3), Park [66] in 1990 (Table J.4), Bortner [9, 68] (Table J.7) or Stuckert [55, 70–77]) (Table J.6) with respect to a reference. This reference is taken to be Park *et al.*'s [78] 2001 constants (Table J.5). The comparison shows broad discrepancies in the reaction rates, which can differ in more than two orders of magnitude in some cases.

4.4 Gas-surface interaction model

In order to model the interaction between the fluid and a graphite surface, three oxidation and three sublimation reactions are considered, similarly to what was proposed by Park [79] and Baker [80] and summarized by Mortensen & Zhong [15]. Nitridation reactions are neglected, but should be accounted for in a modeling framework including the effect of shock-layer radiation on the boundary layer [81, 82]. Surface catalysis is also neglected in order to reduce the, already large, parametric space under investigation. Klentzman & Tumin [25], however, do consider it using a simplified gamma-like model. For an overview of more elab-

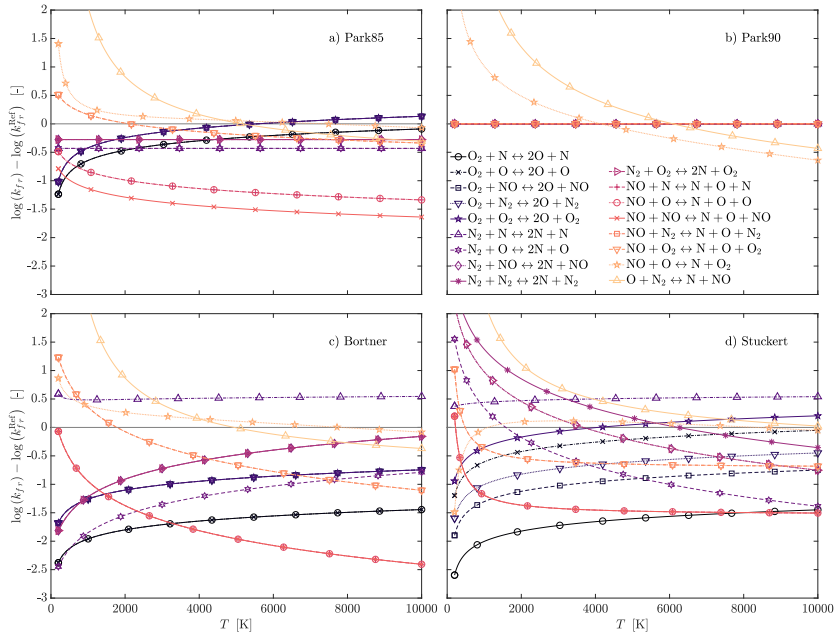
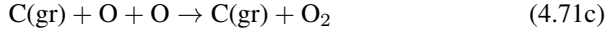


Figure 4.6: Difference between the chemical reaction rates computed with either Park85 [67], Park90 [66], Bortner [9, 68] or Stuckert [55, 70–77], against the reference Park01 [78].

orate gas-surface-interaction modeling strategies please refer to Bellas *et al.* [83], or Turchi *et al.* [84, 85].

The oxidation reactions are:



and based on kinetic theory, one can define the oxidation rates to be:

$$k_r^{\text{Oxid}} = \alpha_r^{\text{Oxid}} \sqrt{\frac{\mathcal{R} T^{\text{Trans}}}{2\pi \mathcal{M}_r^{\text{Oxid}}}}, \quad \forall r \in \mathcal{R}^{\text{Oxid}}, \quad (4.72)$$

where $\mathcal{M}_r^{\text{Oxid}}$ is the molar mass of the oxidizer of each reaction (O_2 for Eq. 4.71a and O for Eqs. 4.71b and 4.71c), and α_r^{Oxid} is the reaction probability of each reaction in Eq. 4.71:

$$\alpha_1^{\text{Oxid}} = \frac{0.00143 + 0.01 \exp(-1450/T^{\text{Trans}})}{1 + 0.0002 \exp(13000/T^{\text{Trans}})}, \quad (4.73\text{a})$$

$$\alpha_2^{\text{Oxid}} = \alpha_3^{\text{Oxid}} = 0.63 \exp(-1160/T^{\text{Trans}}), \quad (4.73\text{b})$$

. If one expresses Eq. 4.71 in a generic form with two stoichiometric matrices like in Eq. 4.61

$$\sum_{s \in \mathcal{S}} \nu'_{sr} s \leftrightarrow \sum_{s \in \mathcal{S}} \nu''_{sr} s, \quad \forall r \in \mathcal{R}^{\text{Oxid}}, \quad (4.74)$$

the mass production/destruction rate of each species due to oxidation reactions can be obtained from the law of mass action neglecting the backward reactions:

$$\dot{m}_{sw}^{\text{Oxid}} = \mathcal{M}_s \sum_{r \in \mathcal{R}^{\text{Oxid}}} (\nu''_{sr} - \nu'_{sr}) k_f^{\text{Oxid}} r \prod_{\ell \in \mathcal{S}} \left(\frac{\rho_\ell}{\mathcal{M}_\ell} \right)^{\nu'_{\ell r}}, \quad \forall s \in \mathcal{S}. \quad (4.75)$$

The three considered sublimation reactions are:



and the mass flux for each reaction is obtained from the Knudsen-Langmuir equation [80]:

$$\dot{m}_{sw}^{\text{Subl}} = \alpha_s^{\text{Subl}} (p_s^{\text{Vap}} - p_s) \sqrt{\frac{\mathcal{M}_s}{2\pi \mathcal{R} T^{\text{Trans}}}}, \quad \forall s \in \mathcal{S}_{\text{Subl}}, \quad (4.77)$$

where the vapor pressure of each species p_s^{Vap} is given by:

$$p_s^{\text{Vap}} = p_{\text{Atm}} \exp \left(\frac{P_s^{\text{Vap}}}{T^{\text{Trans}}} + Q_s^{\text{Vap}} \right), \quad \forall s \in \mathcal{S}_{\text{Subl}}. \quad (4.78)$$

α_s^{Subl} , P_s^{Vap} and Q_s^{Vap} for the three sublimation subproducts are presented in Table 4.4.

The final species mass production rate due to oxidation and sublimation reactions is thus simply:

$$\dot{m}_{sw} = \dot{m}_{sw}^{\text{Oxid}} + \dot{m}_{sw}^{\text{Subl}}, \quad \forall s \in \mathcal{S}, \quad (4.79)$$

and the total surface mass flux due to gas-surface interaction reactions is consequently:

$$\dot{m}_w = \sum_{s \in \mathcal{S}} \dot{m}_{sw}. \quad (4.80)$$

Park & Baker's graphite-ablation model is one of the many developed by various researchers (see for instance Elliott *et al.* [86]). However, it was chosen due to its relative simplicity, and in order to ease eventual verifications against Mortensen & Zhong [15].

Species	α_s^{Subl} [-]	P_s^{Vap} [K]	Q_s^{Vap} [-]
C	0.14	-85715	18.69
C ₂	0.26	-98363	22.2
C ₃	0.03	-93227	23.93

Table 4.4: Species sublimation properties. Obtained from Mortensen & Zhong [15, 87].

4.5 Energy exchange terms

The description of the thermal state of a gas with various energy groups with their corresponding temperatures, inexorably requires the definition of terms accounting for the energy exchange between these groups. For the sake of completeness, distinct source terms are presented for the vibrational, electronic and electron translational energy, similarly to Candler & MacCormack [88] or Clarey & Greendyke [14].

Rotational source terms are not detailed in the present work, however they can be found in the work of Bertolotti [5].

4.5.1 Vibrational source term

The transfer of energy between a molecule's translational and its vibrational energy can be modeled with a Landau-Teller relaxation expression [65, 89]:

$$Q^{Vib} = \sum_{s \in \mathcal{S}_{\text{mol}}} \left(\rho_s \frac{e_{vs}(T^{\text{Trans}}) - e_{vs}(T^{Vib})}{\tau_s^{TR-V}} + \rho_s \frac{e_{vs}(T^{\text{e}^-}) - e_{vs}(T^{Vib})}{\tau_s^{\text{e}^-V}} \right) - Q^{V-E}. \quad (4.81)$$

The first addend in the right-hand-side of Eq. 4.81 accounts for the exchange between the translational-rotational energy of heavy species and the vibrational energy of molecules. The translational-rotational-to-vibrational relaxation time τ_s^{TR-V} is defined with the expression given by Lee [52], with Park's correction [66]:

$$\tau_s^{TR-V} = \frac{\sum_{\ell \in \mathcal{H}} X_{\ell}}{\sum_{\ell \in \mathcal{H}} X_{\ell}/\tau_{s\ell}^{\text{MW}}} + \tau_s^{\text{P}}, \quad \forall s \in \mathcal{S}_{\text{mol}}, \quad (4.82)$$

where $\tau_{s\ell}^{\text{MW}}$ is obtained from Millikan & White's phenomenological formula [90]:

$$\tau_{s\ell}^{\text{MW}} = \frac{p_{\text{Atm}}}{p} \exp \left(a_{s\ell}^{Vib} \left((T^{\text{Trans}})^{-1/3} - b_{s\ell}^{Vib} \right) - 18.42 \right), \quad \forall s \in \mathcal{S}_{\text{mol}}, \quad \forall \ell \in \mathcal{H}, \quad (4.83)$$

with $a_{s\ell}^{Vib}$ and $b_{s\ell}^{Vib}$ obtained either from tables such as those of Park [91, 92] (see Tables K.16 and K.17), or as a function of the activation temperature of the first vibrational mode (θ_{s1}^{Vib}) and the molar masses (as proposed by Millikan & White [90]):

$$a_{s\ell}^{Vib} = 1.16 \cdot 10^{-3} \left(10^3 \frac{\mathcal{M}_s \mathcal{M}_{\ell}}{\mathcal{M}_s + \mathcal{M}_{\ell}} \right)^{1/2} (\theta_{s1}^{Vib})^{4/3}, \quad \forall s \in \mathcal{S}_{\text{mol}}, \quad \forall \ell \in \mathcal{H}, \quad (4.84a)$$

$$b_{s\ell}^{Vib} = 0.015 \left(10^3 \frac{\mathcal{M}_s \mathcal{M}_{\ell}}{\mathcal{M}_s + \mathcal{M}_{\ell}} \right)^{1/4}, \quad \forall s \in \mathcal{S}_{\text{mol}}, \quad \forall \ell \in \mathcal{H}. \quad (4.84b)$$

Park's [67] correction accounts for the underprediction of the relaxation time with Millikan & White's formula, which neglects the limiting of excitation rates due to the finiteness of elastic collision cross-sections. The correction consists in the addend:

$$\tau_s^{\text{P}} = \left(n_s \sqrt{\frac{8 \mathcal{R} T^{\text{Trans}}}{\pi \mathcal{M}_s}} \sigma_s^{Vib} \left(\frac{50\,000}{T^{\text{Trans}}} \right)^2 \right)^{-1}, \quad \forall s \in \mathcal{S}_{\text{mol}}, \quad (4.85)$$

where σ_s^{Vib} is the limiting cross section for vibrational excitation at 50 000 K, which can be found in the work of Park [66, 91, 92] or in Table K.3.^v

^vNote that the term $\sigma_s^{Vib} \left(\frac{50\,000}{T^{\text{Trans}}} \right)^2$ corresponds to the effective cross section for vibrational relaxation, which authors previous to Park had considered to be a simple constant (Gnoffo *et al.* [93])

The second addend in the right-hand-side of Eq. 4.81 accounts for the exchange between the translational energy of electron species and the vibrational energy of molecules [52]. The electron-to-vibrational relaxation time τ_s^{e-V} is defined in Lee [52], or more recent and accurately by Bourdon & Vervisch [94, 95]. The third addend in the right-hand-side of Eq. 4.81 accounts for the loss of vibrational energy in any vibrational-electronic exchange process. This term (Q^{V-E}) is oftentimes neglected [14].

4.5.2 Electronic source term

The source term due to the variation in electronic energy can be expressed as [14]:

$$Q^{Elec} = Q^{V-E} + Q^{e^- im} + Q^{H\text{coll}}. \quad (4.86)$$

The first addend in the right-hand-side of Eq. 4.86 was already identified in Eq. 4.81, accounting for the loss of vibrational energy due to vibrational-electronic exchanges. It logically appears with a positive sign in the source of electronic energy. The second and third addends account for electronic excitation due to electron-impact ($Q^{e^- im}$) and heavy-particle ($Q^{H\text{coll}}$) collisions. The latter can be neglected due to the improbability of such a process, whereas the former is also often dismissed [14].

4.5.3 Electron source term

The source term due to the variation in the translational energy of electrons can be expressed as [13, 14, 88]:

$$\begin{aligned} Q^{e^-} = & -Q^{e^- im} - \sum_{s \in \mathcal{S}_{\text{mol}}} \rho_s \frac{e_{vs}(T^e) - e_{vs}(T^{Vib})}{\tau_s^{e-V}} + \\ & + \sum_{r \in \mathcal{R}_{\text{hpii}} \cup \mathcal{R}_{\text{ai}}} \dot{\omega}_{e^- r} \frac{3 \frac{\mathcal{R} T^e}{\mathcal{M}_e}}{2} - \sum_{\substack{r \in \mathcal{R}_{\text{eii}} \\ s \in \mathcal{S}_{\text{ion}}}} \dot{\omega}_{sr} h_s^{\text{ion}} - \sum_{\substack{r \in \mathcal{R}_{\text{eid}} \\ s \in \mathcal{S}_{\text{mol}}}} \dot{\omega}_{sr} h_s^{\text{diss}} + \\ & + 3\rho_e \frac{\mathcal{R}}{\mathcal{M}_e} \frac{T^{Trans} - T^e}{\tau^{T-e}}. \end{aligned} \quad (4.87)$$

The first two terms in the right-hand-side of Eq. 4.87 appeared also in Eqs. 4.81 and 4.86 with the opposite sign. The third term accounts for the energy with which electrons depart from atoms during ionization due to heavy-particle-impact- or associative-ionization reactions ($r \in \mathcal{R}_{\text{hpii}} \cup \mathcal{R}_{\text{ai}}$). The fourth and fifth terms account for the loss of energy electrons experience when causing electron-impact ionization ($r \in \mathcal{R}_{\text{eii}}$) or dissociation ($r \in \mathcal{R}_{\text{eid}}$). See Table 4.3 for the breakdown

assumed it equal to 10^{-19} m^2). However Park's expression is used in this work, due to its higher accuracy.

of which type each reaction corresponds to. h_s^{ion} and h_s^{diss} are the molar ionization and dissociation energies of each species. The former are presented in Table K.5, whilst the latter, due to vibration-chemistry-vibration coupling [13] and assuming non-preferential dissociation^w may be taken equal to:

$$h_s^{\text{diss}} = h_s^{Vib}, \quad \forall s \in \mathcal{S}_{\text{mol}}. \quad (4.88)$$

Finally, the sixth term accounts for the translational energy exchange between electrons and heavy species. The relaxation time τ^{T-e^-} has been approximated as: [97]

$$\tau^{T-e^-} = \left(\sum_{s \in \mathcal{H}} \nu_{e^-s} \frac{\mathcal{M}_{e^-}}{\mathcal{M}_s} \right)^{-1}, \quad (4.89)$$

where ν_{e^-s} is the effective collision frequency between electrons and species s :

$$\nu_{e^-s} = \frac{8}{3} \left(\frac{\pi N_A}{\mathcal{M}_{e^-}} \right)^{1/2} \frac{n_s q_e^4}{(2k_B T_e^-)^{3/2}} \ln \left(\frac{k_B^3 (T_e^-)^3}{\pi n_{e^-} q_e^6} \right), \quad \forall s \in \mathcal{S}_{\text{ion}}, \quad (4.90a)$$

$$\nu_{e^-s} = n_s \sigma_s^{e^-} \left(\frac{8\mathcal{R} T_e^-}{\pi \mathcal{M}_{e^-}} \right)^{1/2}, \quad \forall s \in \mathcal{S}_{\text{neut}}, \quad (4.90b)$$

where the effective electron-neutral energy exchange cross section can be obtained from the curve fit proposed by Gnoffo *et al.* [93] based on the data by Ali [98]:

$$\sigma_s^{e^-} = a_{e^-s}^\sigma + b_{e^-s}^\sigma T^{e^-} + c_{e^-s}^\sigma (T^{e^-})^2, \quad \forall s \in \mathcal{S}_{\text{neut}}. \quad (4.91)$$

However, Graille *et al.* [99] recently showed that it can be easily obtained from kinetic theory:

$$\tau^{T-e^-} = \left(\sum_{s \in \mathcal{H}} \frac{8}{3} \frac{\mathcal{M}_{e^-}}{\mathcal{M}_s} n_s \sqrt{\frac{8\mathcal{R} T_e^-}{\pi \mathcal{M}_{e^-}}} \Omega_{e^-s}^{(1,1)} \right)^{-1}. \quad (4.92)$$

Eq. 4.92 is thus recommended [13].

Two-temperature model

The present work considers thermal non-equilibrium with a two-temperature model (see Eq. 4.8). In it the vibrational, electronic and electron energies are

^wThe non-preferential assumption implies that the dissociated molecules are generally in the vibrational state of the average molecule. A more accurate assumption is that of preferential dissociation, where the vibrational state is assumed to be higher than that of the average molecule, but need not be near the dissociation energy before a collision in order to dissociate. However this requires the use of a factor in Eq. 4.88 which is highly empirical and case-dependent [93]. Therefore, Eq. 4.88 is oftentimes used [87], even if conservative. This treatment is, however, not appropriate for shock tubes. More elaborate models can be found in § 4.2.6 of Ref. 96.

all modeled with a unique temperature (T_v), and are therefore characterized with one unique energy-conservation equation (Eq. 2.7d). The source term appearing in Eq. 2.7d and accounting for the transfer of energy from the translational and rotational energy modes to the vibrational, electronic and electron is:

$$\begin{aligned} Q_{TV} &= Q^{Vib} + Q^{Elec} + Q^e = \\ &= \sum_{s \in \mathcal{S}_{\text{mol}}} \rho_s \frac{e_{vs}(T^{\text{Trans}}) - e_{vs}(T^{Vib})}{\tau_s^{\text{TR-V}}} + \sum_{r \in \mathcal{R}_{\text{hpii}} \cup \mathcal{R}_{\text{ai}}} \dot{\omega}_{e^r} \frac{3}{2} \frac{\mathcal{R} T^e}{\mathcal{M}_e} + \\ &\quad - \sum_{\substack{r \in \mathcal{R}_{\text{eii}} \\ s \in \mathcal{S}_{\text{ion}}}} \dot{\omega}_{sr} h_s^{\text{ion}} - \sum_{\substack{r \in \mathcal{R}_{\text{eid}} \\ s \in \mathcal{S}_{\text{mol}}}} \dot{\omega}_{sr} h_s^{\text{diss}} + 3\rho_e \frac{\mathcal{R}}{\mathcal{M}_e} \frac{T^{\text{Trans}} - T^e}{\tau^{T-e}}. \end{aligned} \quad (4.93)$$

Note that many of the terms in Eqs. 4.81, 4.86 and 4.87 mutually cancel out and thus do not appear in Eq. 4.93.

The computation of the energy-transfer term at the wall requires additional considerations. The relaxation time is different [81], and phenomena such as vibrational slip may gain importance for highly-cooled walls [100]. However, these are out of the scope of this dissertation.

4.6 Thermodynamic derivatives

When performing stability analyses, one decomposes all flow quantities into their laminar base-flow and perturbation components (Eq. 3.1). This treatment is applied both on the independent state quantities q (detailed in § 2.3 for the various flow assumptions) and on the dependent quantities $Q(q)$, for which expressions are provided in this chapter. The corresponding perturbation terms of the independent quantities q' are the unknowns in the stability equations, for which the system is solved. Those of the dependent quantities Q' must therefore be expressed as a function of q' . This is achieved by performing a Taylor expansion of the dependent perturbation quantities around zero. For a dependent quantity Q depending on a single independent quantity q this is simply:^x

$$Q' = \frac{\partial \bar{Q}}{\partial \bar{q}} q' + \frac{1}{2} \frac{\partial^2 \bar{Q}}{\partial \bar{q}^2} (q')^2 + \dots + \frac{1}{n!} \frac{\partial^n \bar{Q}}{\partial \bar{q}^n} (q')^n. \quad (4.94)$$

In high-enthalpy environments, where one must model the mixture properties with the expressions detailed in this chapter, these properties (the dependent quantities Q) are not a function of a single dependent quantity q , but of several. This implies

^xThis is the case encountered when making a CPG assumption, where viscosity, and thermal conductivity can be considered simply a function of temperature through Sutherland's law (Eqs. 4.2, 4.4 and 4.5).

that one must deploy a multi-variable Taylor expansion instead:

$$Q' = \sum_{a \in \mathcal{V}_Q} \frac{\partial \bar{Q}}{\partial \bar{q}_a} q'_a + \sum_{\substack{a \in \mathcal{V}_Q \\ b \in \mathcal{V}_Q}} \frac{1}{2} \frac{\partial^2 \bar{Q}}{\partial \bar{q}_a \partial \bar{q}_b} q'_a q'_b + \cdots + \sum_{\substack{a_1 \in \mathcal{V}_Q \\ \vdots \\ a_n \in \mathcal{V}_Q}} \frac{1}{n!} \frac{\partial^n \bar{Q}}{\partial \bar{q}_{a_1} \cdots \partial \bar{q}_{a_n}} q'_{a_1} \cdots q'_{a_n}. \quad (4.95)$$

This implies that one must compute derivatives of the thermal, transport and chemical properties presented in this chapter, with respect to the thermodynamic state quantities. Whenever these properties are modeled with analytical functions, one can retrieve their thermodynamic derivatives through the symbolic differentiation of the expressions laid out in this chapter.^y However, for certain dependent quantities and models, one must resolve a linear system of equations, function of the thermodynamic state quantities, in order to retrieve them. This is the case for instance with the viscosity μ and frozen heavy-particle thermal conductivity κ_H^{Froz} when using the CE transport model (Eq. 4.30), or with the multicomponent diffusion coefficients \mathcal{D}_{sl} when using the SM diffusion model (Eq. 4.41). In such scenarios, one must resort to a series of properties of matrix algebra, in order to express the derivatives of the solutions to the matrix systems, as a function of the derivatives of their individual components.

A methodology is presented in this section to compute thermodynamic derivatives of the matrix system defining μ and κ_H^{Froz} with a CE transport model and \mathcal{D}_{sl} with a SM diffusion model. Only expressions for their first- and second-order derivatives are presented, however the methodology can be easily extended to higher orders.

Note that for linear stability theories (LST, LPSE, 3D-LPSE, 2D-LST, BiG or TriG), one must only retain the first addend in the right-hand-side of Eqs. 4.94 and 4.95. In non-linear theories (NPSE or 3D-NPSE), in order to remain consistent in their mathematical treatment, one must retain as many terms as the order of non-linearity considered [101].

^yMost previous authors (see Table 4.1) have either opted for models with expressions that could be “easily” differentiated analytically [15, 23], or have performed a numerical differentiation of precomputed properties tables [20, 21]. The latter is only feasible for LTE scenarios, where a two-dimensional properties table $Q(p, T)$ can be constructed. In the present work the thermodynamic derivatives are computed with an automatic derivation and implementation tool (see § 8.2). This tool effectively differentiates the expressions symbolically and then implements a series of functions for their computation.

4.6.1 Thermodynamic derivatives of the Chapman-Enskog matrix system

The Chapman-Enskog system (Eq. 4.30) for viscosity and frozen heavy-particle thermal conductivity allows to obtain them from the quotient of two determinants:

$$Q = -\mathcal{A}/\mathcal{B} = - \begin{vmatrix} G_{s\ell}^Q & X_s \\ X_\ell & 0 \end{vmatrix} / |G_{s\ell}^Q|, \quad \forall s, \ell \in \mathcal{H}, \quad (4.96)$$

where Q can be either μ or κ_H^{Froz} . Its derivative with respect to an independent thermodynamic variable q_a is therefore:

$$\frac{\partial Q}{\partial q_a} = \frac{1}{\mathcal{B}^2} \left(\frac{\partial \mathcal{B}}{\partial q_a} \mathcal{A} - \mathcal{B} \frac{\partial \mathcal{A}}{\partial q_a} \right), \quad (4.97)$$

and the second derivative with respect to two independent thermodynamic variables q_a and q_b will subsequently be:

$$\begin{aligned} \frac{\partial^2 Q}{\partial q_a \partial q_b} = & - \frac{2}{\mathcal{B}^3} \frac{\partial \mathcal{B}}{\partial q_b} \left(\frac{\partial \mathcal{B}}{\partial q_a} \mathcal{A} - \mathcal{B} \frac{\partial \mathcal{A}}{\partial q_a} \right) + \\ & + \frac{1}{\mathcal{B}^2} \left(\frac{\partial^2 \mathcal{B}}{\partial q_a \partial q_b} \mathcal{A} + \frac{\partial \mathcal{B}}{\partial q_a} \frac{\partial \mathcal{A}}{\partial q_b} - \frac{\partial \mathcal{B}}{\partial q_b} \frac{\partial \mathcal{A}}{\partial q_a} - \mathcal{B} \frac{\partial^2 \mathcal{A}}{\partial q_a \partial q_b} \right). \end{aligned} \quad (4.98)$$

These expressions require first and second derivatives of the two determinants \mathcal{A} and \mathcal{B} . The derivative of the determinant of a matrix $\underline{\underline{A}}$ with respect to a variable q_a can be obtained from Jacobi's formula:

$$\frac{\partial |\underline{\underline{A}}|}{\partial q_a} = |\underline{\underline{A}}| \operatorname{tr} \left(\underline{\underline{A}}^{-1} \frac{\partial \underline{\underline{A}}}{\partial q_a} \right), \quad (4.99)$$

where $\operatorname{tr}(\cdot)$ is the trace operator.

Its second derivative with respect to two distinct variables q_a and q_b comes from differentiating it with the chain rule: ^z

$$\frac{\partial^2 |\underline{\underline{A}}|}{\partial q_a \partial q_b} = \frac{\partial |\underline{\underline{A}}|}{\partial q_b} \operatorname{tr} \left(\underline{\underline{A}}^{-1} \frac{\partial \underline{\underline{A}}}{\partial q_a} \right) + |\underline{\underline{A}}| \operatorname{tr} \left(\frac{\partial \left(\underline{\underline{A}}^{-1} \frac{\partial \underline{\underline{A}}}{\partial q_a} \right)}{\partial q_b} \right). \quad (4.100)$$

Using Jacobi's formula on the first q_b derivative and applying the chain rule on the second:

$$\begin{aligned} \frac{\partial^2 |\underline{\underline{A}}|}{\partial q_a \partial q_b} = & |\underline{\underline{A}}| \operatorname{tr} \left(\underline{\underline{A}}^{-1} \frac{\partial \underline{\underline{A}}}{\partial q_b} \right) \operatorname{tr} \left(\underline{\underline{A}}^{-1} \frac{\partial \underline{\underline{A}}}{\partial q_a} \right) + \\ & + |\underline{\underline{A}}| \operatorname{tr} \left(\frac{\partial \underline{\underline{A}}^{-1}}{\partial q_b} \frac{\partial \underline{\underline{A}}}{\partial q_a} \right) + |\underline{\underline{A}}| \operatorname{tr} \left(\underline{\underline{A}}^{-1} \frac{\partial^2 \underline{\underline{A}}}{\partial q_a \partial q_b} \right), \end{aligned} \quad (4.101)$$

^zNote that the trace and derivative operators can be permuted: $\partial_{q_a} \operatorname{tr}(A) = \operatorname{tr}(\partial_{q_a} A)$.

and finally, factoring out the determinant and applying the relation for the derivative of the inverse:

$$\frac{\partial (\underline{\underline{A}}^{-1})}{\partial q_b} = -\underline{\underline{A}}^{-1} \frac{\partial \underline{\underline{A}}}{\partial q_b} \underline{\underline{A}}^{-1}, \quad (4.102)$$

one reaches:

$$\begin{aligned} \frac{\partial^2 |\underline{\underline{A}}|}{\partial q_a \partial q_b} &= |\underline{\underline{A}}| \left[\text{tr} \left(\underline{\underline{A}}^{-1} \frac{\partial \underline{\underline{A}}}{\partial q_b} \right) \text{tr} \left(\underline{\underline{A}}^{-1} \frac{\partial \underline{\underline{A}}}{\partial q_a} \right) - \text{tr} \left(\underline{\underline{A}}^{-1} \frac{\partial \underline{\underline{A}}}{\partial q_b} \underline{\underline{A}}^{-1} \frac{\partial \underline{\underline{A}}}{\partial q_a} \right) + \right. \\ &\quad \left. + \text{tr} \left(\underline{\underline{A}}^{-1} \frac{\partial^2 \underline{\underline{A}}}{\partial q_a \partial q_b} \right) \right], \end{aligned} \quad (4.103)$$

or grouping $\underline{\underline{A}}^{\text{adj}} = \text{adj}(\underline{\underline{A}}) = |\underline{\underline{A}}| \underline{\underline{A}}^{-1}$:

$$\begin{aligned} \frac{\partial^2 |\underline{\underline{A}}|}{\partial q_a \partial q_b} &= \text{tr} \left(\underline{\underline{A}}^{\text{adj}} \frac{\partial \underline{\underline{A}}}{\partial q_b} \right) \text{tr} \left(\underline{\underline{A}}^{-1} \frac{\partial \underline{\underline{A}}}{\partial q_a} \right) - \text{tr} \left(\underline{\underline{A}}^{\text{adj}} \frac{\partial \underline{\underline{A}}}{\partial q_b} \underline{\underline{A}}^{-1} \frac{\partial \underline{\underline{A}}}{\partial q_a} \right) + \\ &\quad + \text{tr} \left(\underline{\underline{A}}^{\text{adj}} \frac{\partial^2 \underline{\underline{A}}}{\partial q_a \partial q_b} \right). \end{aligned} \quad (4.104)$$

4.6.2 Thermodynamic derivatives of the Stefan-Maxwell matrix system

The Stefan-Maxwell matrix system (Eq. 4.41) can be inverted to obtain the multi-component diffusion coefficients (Eq. 4.42). The first-order thermodynamic derivatives of these diffusion coefficients can therefore be obtained by applying the relation for the derivative of the inverse (Eq. 4.102):

$$\frac{\partial (\underline{\underline{A}}^{-1})}{\partial q_a} = -\underline{\underline{A}}^{-1} \frac{\partial \underline{\underline{A}}}{\partial q_a} \underline{\underline{A}}^{-1}. \quad (4.105)$$

The second-order derivatives, can subsequently be retrieved from applying the chain rule on this relation:

$$\frac{\partial^2 (\underline{\underline{A}}^{-1})}{\partial q_a \partial q_b} = -\frac{\partial (\underline{\underline{A}}^{-1})}{\partial q_b} \frac{\partial \underline{\underline{A}}}{\partial q_a} \underline{\underline{A}}^{-1} - \underline{\underline{A}}^{-1} \frac{\partial^2 \underline{\underline{A}}}{\partial q_a \partial q_b} \underline{\underline{A}}^{-1} - \underline{\underline{A}}^{-1} \frac{\partial \underline{\underline{A}}}{\partial q_a} \frac{\partial (\underline{\underline{A}}^{-1})}{\partial q_b}. \quad (4.106)$$

Substituting $\partial_{q_b}(A^{-1})$ with Eq. 4.102 and factoring out the leading and trailing A^{-1} , one reaches:

$$\frac{\partial (\underline{\underline{A}}^{-1})}{\partial q_a \partial q_b} = \underline{\underline{A}}^{-1} \left[\frac{\partial \underline{\underline{A}}}{\partial q_b} \underline{\underline{A}}^{-1} \frac{\partial \underline{\underline{A}}}{\partial q_a} - \frac{\partial^2 \underline{\underline{A}}}{\partial q_a \partial q_b} + \frac{\partial \underline{\underline{A}}}{\partial q_a} A^{-1} \frac{\partial \underline{\underline{A}}}{\partial q_b} \right] \underline{\underline{A}}^{-1}. \quad (4.107)$$

References

- [1] F. M. White. *Viscous Fluid Flow*. McGraw-Hill, 2nd edition, 1991.
- [2] W. Sutherland. *The viscosity of gases and molecular force*. Philosophical Magazine Series 5, [36\(223\):507–531](#), 1893.
- [3] J. H. Ferziger and H. G. Kaper. *Mathematical theory of transport processes in gases*. North-Holland Publishing Company, Amsterdam, 1st edition, 1972.
- [4] V. Giovangigli. *Multicomponent Flow Modeling*. 3Island Press, 1999.
- [5] F. P. Bertolotti. *The influence of rotational and vibrational energy relaxation on boundary-layer stability*. Journal of Fluid Mechanics, [372\(1998\):93–118](#), 1998.
- [6] S. Chapman and T. Cowling. *The Mathematical Theory of Non-uniform Gases: An Account of the Kinetic Theory of Viscosity, Thermal Conduction, and Diffusion in Gases*. The University Press, 1939.
- [7] J. O. Hirschfelder, C. F. Curtiss, and R. B. Bird. *Molecular theory of gases and liquids*. Wiley, New York, 2 edition, 1954.
- [8] F. G. Blottner, M. Johnson, and M. Ellis. *Chemically Reacting Viscous Flow Program For Multi-Component Gas Mixtures*. Technical Report SC-RR-70-754, Sandia Laboratories, 1971.
- [9] R. N. Gupta, J. M. Yos, R. A. Thompson, and K.-P. Lee. *A review of Reaction Rates and Thermodynamic and Transport Properties for an 11-Species Air Model for Chemical and Thermal Nonequilibrium Calculations to 30000K*. Technical Report RP-1232, NASA, 1990.
- [10] M. Fertig, A. Dohr, and H.-H. Frühauf. *Transport Coefficients for High Temperature Nonequilibrium Air Flows*. Journal of Thermophysics and Heat Transfer, [15\(2\):148–156](#), 2001.
- [11] B. J. McBride, M. J. Zehe, and S. Gordon. *NASA Glenn Coefficients for Calculating Thermodynamic Properties of Individual Species*. Technical Report 2002-21155, NASA, 2002.
- [12] T. E. Magin and G. Degrez. *Transport properties of partially ionized and unmagnetized plasmas*. Physical Review E, [70\(4\)](#), 2004.
- [13] J. B. Scoggins. *Development of numerical methods and study of coupled flow, radiation, and ablation phenomena for atmospheric entry*. PhD thesis, Université Paris-Saclay and VKI, 2017.

- [14] M. P. Clarey and R. B. Greendyke. *Thermochemical nonequilibrium processes in weakly ionized air using three-temperature models*. Journal of Thermophysics and Heat Transfer, [33\(2\):425–440](#), 2019.
- [15] C. Mortensen and X. Zhong. *Real-Gas and Surface-Ablation Effects on Hypersonic Boundary-Layer Instability over a Blunt Cone*. AIAA Journal, [54\(3\):980–998](#), 2016.
- [16] C. P. Knisely and X. Zhong. *Supersonic Modes in Hot-Wall Hypersonic Boundary Layers with Thermochemical Nonequilibrium Effects*. AIAA paper, [2018-2085](#), 2018.
- [17] C. Mortensen. *Toward an understanding of supersonic modes in boundary-layer transition for hypersonic flow over blunt cones*. Journal of Fluid Mechanics, [846:789–814](#), 2018.
- [18] G. Stuckert and H. L. Reed. *Linear Disturbances in Hypersonic, Chemically Reacting Shock Layers*. AIAA Journal, [32\(7\):1384–1393](#), 1994.
- [19] I. Lyttle and H. L. Reed. *Sensitivity of Second-Mode Linear Stability to Constitutive Models within Hypersonic Flow*. AIAA paper, [2005-889](#), 2005.
- [20] L. Zanus, F. Miró Miró, and F. Pinna. *Parabolized stability analysis of chemically reacting boundary layer flows in equilibrium conditions*. In [EU-CASS 2017](#), Milano, Italy, 2017.
- [21] L. Zanus and F. Pinna. *Stability Analysis of Hypersonic Flows in Local Thermodynamic Equilibrium Conditions by Means of Nonlinear PSE*. AIAA paper, [2018-3696](#), 2018.
- [22] M. R. Malik and E. C. Anderson. *Real gas effects on hypersonic boundary-layer stability*. Physics of Fluids, [803\(3\):803–821](#), 1991.
- [23] M. L. Hudson, N. Chokani, and G. V. Candler. *Linear stability of hypersonic flow in thermochemical nonequilibrium*. AIAA Journal, [35\(6\):958–964](#), 1997.
- [24] K. J. Franko, R. W. MacCormack, and S. K. Lele. *Effects of chemistry modeling on hypersonic boundary layer linear stability prediction*. AIAA paper, [2010-4601](#), 2010.
- [25] J. Klentzman and A. Tumin. *Stability and receptivity of high speed boundary layers in oxygen*. AIAA paper, [2013-2882](#), 2013.
- [26] N. P. Bitter and J. E. Shepherd. *Stability of highly cooled hypervelocity boundary layers*. Journal of Fluid Mechanics, [778:586–620](#), 2015.

- [27] F. Miró Miró, F. Pinna, E. S. Beyak, P. Barbante, and H. L. Reed. *Diffusion and chemical non-equilibrium effects on hypersonic boundary-layer stability*. AIAA paper, [2018-1824](#), 2018.
- [28] F. Miró Miró, E. S. Beyak, D. Mullen, F. Pinna, and H. L. Reed. *Ionization and Dissociation Effects on Hypersonic Boundary-Layer Stability*. In 31st ICAS Congress, Belo Horizonte, Brazil, 2018. International Council of the Aeronautical Sciences.
- [29] C.-L. Chang, H. Vinh, and M. R. Malik. *Hypersonic boundary-layer stability with chemical reactions using PSE*. AIAA paper, [1997-2012](#), 1997.
- [30] H. B. Johnson and G. V. Candler. *Hypersonic boundary layer stability analysis using PSE-Chem*. AIAA paper, [2005-5023](#), 2005.
- [31] H. L. Kline, C.-L. Chang, and F. Li. *Hypersonic Chemically Reacting Boundary-Layer Stability using LASTRAC*. AIAA paper, [2018-3699](#), 2018.
- [32] O. Marxen, T. E. Magin, E. S. G. Shaqfeh, and G. Iaccarino. *A method for the direct numerical simulation of hypersonic boundary-layer instability with finite-rate chemistry*. Journal of Computational Physics, [255:572–589](#), 2013.
- [33] I. Armenise and E. Kustova. *Effect of Asymmetric Mode on CO₂ State-to-State Vibrational-Chemical Kinetics*. Journal of Physical Chemistry A, [122\(44\):8709–8721](#), 2018.
- [34] A. A. Kosareva and E. A. Nagnibeda. *Vibrational-Chemical Coupling in mixtures CO₂/CO/O and CO₂/CO/O₂/O/C*. Journal of Physics: Conference Series, [815\(1\)](#), 2017.
- [35] B. J. McBride, S. Heimel, J. G. Ehlers, and S. Gordon. *Thermodynamic Properties To 6000K for 210 substances Involving the First 18 Elements*. Technical Report SP-3001, NASA, 1963.
- [36] J. B. Scoggins and T. E. Magin. *Development of Mutation++: Multicomponent Thermodynamics And Transport properties for IONized gases library in C++*. AIAA paper, [2014-2966](#), 2014.
- [37] J. D. Anderson Jr. *Hypersonic and High Temperature Gas Dynamics*. American Institute of Aeronautics and Astronautics, Reston VA, second edition, 2006.
- [38] G. Bellas-Chatzigeorgis. *Development of Advanced Gas-Surface Interaction Models for Chemically Reacting Flows for Re-Entry Conditions*. PhD thesis, von Karman Institute and Politecnico di Milano, 2018.

- [39] L. Gurvich, I. Veyts, and C. Alcock. *Thermodynamic Properties of Individual Substances. Vol. 1, Elements O, H(D, T), F, Cl, Br, I, He, Ne, Ar, Kr, Xe, Rn, S, N, P and their Compounds. Part Two. Tables.* Hemisphere Publishing Corporation, 4 edition, 1989.
- [40] S. Mylona, M. Assael, and W. Wakeham. *Transport Properties of Fluids.* In [Reference Module in Chemistry, Molecular Sciences and Chemical Engineering](#). UNESCO, 2014.
- [41] L. M. Mack. *Boundary-Layer Linear Stability Theory.* In Special Course on Stability and Transition of Laminar Flow, AGARD 709. AGARD, 1984.
- [42] A. Eucken. *Über das Wärmeleitvermögen, die spezifische Wärme und die innere Reibung der Gase (in german).* Physikalische Zeitschrift, XIV:324–332, 1913.
- [43] C. R. Wilke. *A Viscosity Equation for Gas Mixtures.* The Journal of Chemical Physics, [18\(4\):517–519](#), 1950.
- [44] U. Goldberg, O. Peroomian, S. Chakravarthy, and B. Sekar. *Validation of CFD++ code capability for supersonic combustor flowfields.* AIAA paper, [1997-3271](#), 1997.
- [45] T. E. Magin and G. Degrez. *Transport algorithms for partially ionized and unmagnetized plasmas.* Journal of Computational Physics, [198\(2\):424–449](#), 2004.
- [46] R. S. Brokaw. *Approximate formulas for the viscosity and thermal conductivity of gas mixtures.* The Journal of Chemical Physics, [29\(2\):391–397](#), 1958.
- [47] J. M. Yos. *Approximate equations for the viscosity and translational thermal conductivity of gas mixtures.* Technical Report AVSSD-0112-67-RM, Avco Corporation, 1967.
- [48] M. J. Wright, D. Bose, G. E. Palmer, and E. Levin. *Recommended Collision Integrals for Transport Property Computations Part I: Air Species.* AIAA Journal, [43\(12\):2558–2564](#), 2005.
- [49] K. Sutton and P. A. Gnoffo. *Multi-Component Diffusion with Application to Computational Aerothermodynamics.* AIAA paper, [98-2575](#), 1998.
- [50] J. M. Yos. *Transport properties of nitrogen, hydrogen, oxygen, and air to 30000K.* Technical Report RAD-TM-63-7, Avco Corporation, 1963.

- [51] J. D. Ramshaw. *Hydrodynamic Theory of Multicomponent Diffusion and Thermal Diffusion in Multitemperature Gas Mixtures*. Journal of Non-Equilibrium Thermodynamics, **18**:121–134, 1993.
- [52] J. H. Lee. *Basic governing equations for the flight regimes of aeroassisted orbital transfer vehicles*. In H. F. Nelson, editor, *Progress in Astronautics and Aeronautics: Thermal Design of Aeroassisted Orbital Transfer Vehicles*. AIAA, New York, 1985.
- [53] J. D. Ramshaw and C. H. Chang. *Ambipolar diffusion in multicomponent plasmas*. Plasma Chemistry and Plasma Processing, **13**(3):489–498, 1993.
- [54] W. L. Bade and J. M. Yos. *The NATA Code: Theory and Analysis. Volume 1*. Technical Report CR-2547, NASA, 1975.
- [55] G. K. Stuckert. *Linear Stability Theory of Hypersonic, Chemically Reacting Viscous Flows*. PhD thesis, Arizona State University, 1991.
- [56] S. J. Cubley and E. A. Mason. *Atom-molecule and molecule-molecule potentials and transport collision integrals for high-temperature air species*. Physics of Fluids, **18**:1109, 1975.
- [57] M. Capitelli and E. Ficocelli. *Collision integrals of carbon-oxygen atoms in different electronic states*. Journal of Physics B: Atomic and Molecular Physics, **5**:1819–1823, 1972.
- [58] K. S. Yun and E. A. Mason. *Collision Integrals for the Transport Properties of Dissociating Air at High Temperatures*. Physics of Fluids, **5**:380, 1962.
- [59] J. C. Rainwater, L. Biolsi, K. J. Biolsi, and P. M. Holland. *Transport properties of ground state nitrogen atoms*. The Journal of Chemical Physics, **79**(1462):3203–3210, 1983.
- [60] M. J. Wright, H. H. Hwang, and D. W. Schwenke. *Recommended Collision Integrals for Transport Property Computations Part II: Mars and Venus Entries*. AIAA Journal, **45**(1):281–288, 2007.
- [61] E. Levin and M. J. Wright. *Collision Integrals for Ion-Neutral Interactions of Nitrogen and Oxygen*. Journal of Thermophysics and Heat Transfer, **18**(1):143–147, 2004.
- [62] E. A. Mason. *Transport Coefficients of Ionized Gases*. Physics of Fluids, **10**(8):1827, 1967.
- [63] R. S. Devoto. *Transport coefficients of ionized argon*. Physics of Fluids, **16**(5):616, 1973.

- [64] A. Bellemans and T. E. Magin. *Calculation of Collision Integrals for Ablation Species*. In 8th European Symposium on Aerothermodynamics for Space Vehicles, Lisbon, Portugal, 2015.
- [65] W. G. Vincenti and C. H. Kruger. *Introduction to physical gas dynamics*. Huntington, N.Y. : Krieger, 1967.
- [66] C. Park. *Non-Equilibrium Hypersonic Aerodynamics*. John Wiley & sons, New York, 1990.
- [67] C. Park. *On convergence of computation of chemically reacting flows*. AIAA paper, [85-0247](#), 1985.
- [68] M. H. Bortner. *Suggested Standard Chemical Kinetics for Flow Field Calculations. A consensus Opinion*. In AMRAC Proceedings, Volume XIV, Part I, Doc. No. 4613-135-X (Contract SD-91). Institute of Science and Technology. University of Michigan, April 1966.
- [69] T. E. Magin, B. Graille, and M. Massot. *Kinetic theory derivation of transport equations for gases with internal energy*. AIAA paper, [2011-4034](#), 2011.
- [70] R. K. Hanson and S. S. *Survey of rate constants in the N/H/O system*. In W. C. Gardiner, editor, Combustion Chemistry, chapter 6, pages 361–422. Springer-Verlag, 1984.
- [71] J. P. Monat, R. K. Hanson, and C. H. Kruger. *Shock tube determination of the rate coefficient for the reaction $N_2+O \rightleftharpoons NO+N$* . International Symposium on Combustion, [17\(1\):543–552](#), 1979.
- [72] D. L. Baulch, D. D. Drysdale, D. G. Horne, and A. C. Lloyd. *Evaluated Kinetic Data for High Temperature Reactions. Vol. 2: Homogeneous Gas Phase Reactions of the H₂-N₂-O₂ System*. Butterworth, 1973.
- [73] D. L. Baulch, D. D. Drysdale, J. Duxbury, and S. J. Grant. *Evaluated Kinetic Data for High Temperature Reactions. Vol. 3: Homogeneous Gas Phase Reactions of the O₂-O₃*. Butterworth, 1976.
- [74] S. Byron. *Shock-tube measurement of the rate of dissociation of nitrogen*. The Journal of Chemical Physics, [44\(4\):1378–1388](#), 1966.
- [75] K. Thielen and P. Rothf. *in High-Temperature N₂ Dissociation Kinetics*. AIAA Journal, [24\(7\):1102–1105](#), 1985.
- [76] M. Camac and A. Vaughan. *O₂ dissociation rates in O₂-Ar mixtures*. The Journal of Chemical Physics, [34\(2\):460–470](#), 1961.

- [77] K. L. Wray. *Chemical Kinetics of High Temperature Air*. In F. R. Ridell, editor, *ARS Progress in Astronautics and Rocketry: Hypersonic Flow Research*, volume 7, pages 181–204. Academic Press, New York, 1962.
- [78] C. Park, R. L. Jaffe, and H. Partridge. *Chemical-Kinetic Parameters of Hyperbolic Earth Entry*. *Journal of Thermophysics and Heat Transfer*, **15**(1):76–90, 2001.
- [79] C. Park. *Effects of Atomic Oxygen on Graphite Ablation*. *AIAA Journal*, **14**(11):1640–1642, 1976.
- [80] R. L. Baker. *Graphite sublimation chemistry nonequilibrium effects*. *AIAA Journal*, **15**(10):1391–1397, 1977.
- [81] B. Helber, A. Turchi, J. B. Scoggins, A. Hubin, and T. E. Magin. *Experimental investigation of ablation and pyrolysis processes of carbon-phenolic ablators in atmospheric entry plasmas*. *International Journal of Heat and Mass Transfer*, **100**:810–824, 2016.
- [82] B. Helber, A. Turchi, and T. E. Magin. *Determination of active nitridation reaction efficiency of graphite in inductively coupled plasma flows*. *Carbon*, **125**:582–594, 2017.
- [83] G. Bellas-Chatzigeorgis, A. Turchi, A. Viladegut, O. Chazot, P. Barbante, and T. E. Magin. *Development of catalytic and ablative gas-surface interaction models for the simulation of reacting gas mixtures*. *AIAA paper*, **2017-4499**, 2017.
- [84] A. Turchi, P. M. Congedo, and T. E. Magin. *Thermochemical ablation modeling forward uncertainty analysis—Part I: Numerical methods and effect of model parameters*. *International Journal of Thermal Sciences*, **xxx:497–509**, 2017.
- [85] A. Turchi, P. M. Congedo, B. Helber, and T. E. Magin. *Thermochemical ablation modeling forward uncertainty analysis—Part II: Application to plasma wind-tunnel testing*. *International Journal of Thermal Sciences*, **xxx:510–517**, 2017.
- [86] O. S. Elliott, R. B. Greendyke, J. S. Jewell, and J. R. Komives. *Effect of carbon-based ablation products on hypersonic boundary layer stability*. *AIAA Scitech 2019 Forum*, **2019-0625**, 2019.
- [87] C. Mortensen. *Effects of Thermochemical Nonequilibrium on Hypersonic Boundary-Layer Instability in the Presence of Surface Ablation or Isolated Two-Dimensional Roughness*. PhD thesis, UCLA, 2013.

- [88] G. V. Candler and R. W. MacCormack. *Computation of weakly ionized hypersonic flows in thermochemical nonequilibrium*. Journal of Thermophysics and Heat Transfer, **5**(3):266–273, 1991.
- [89] L. Landau and E. Teller. *on the Theory of Sound Dispersion*. In D. Ter Haar, editor, *Collected Papers of L.D. Landau*, chapter 22, pages 147–153. Pergamon Press, Oxford, 1965.
- [90] R. C. Millikan and D. R. White. *Systematics of vibrational relaxation*. The Journal of Chemical Physics, **39**(12):3209–3213, 1963.
- [91] C. Park. *Review of chemical-kinetic problems of future NASA missions. I - Earth entries*. Journal of Thermophysics and Heat Transfer, **7**(3):385–398, 1993.
- [92] C. Park, J. T. Howe, R. L. Jaffe, and G. V. Candler. *Review of chemical-kinetic problems of future NASA missions. II - Mars entries*. Journal of Thermophysics and Heat Transfer, **8**(1):9–23, 1994.
- [93] P. A. Gnoffo, R. N. Gupta, and J. L. Shinn. *Conservation Equations and Physical Models for Hypersonic Air Flows in Thermal and Chemical Nonequilibrium*. Technical Report TP-2867, NASA, 1989.
- [94] A. Bourdon and P. Vervisch. *Electron-vibration energy exchange models in nitrogen-containing plasma flows*. Physical Review E, **55**(4):4634–4641, 1997.
- [95] A. Bourdon and P. Vervisch. *Analytical Models for Electron-Vibration Coupling*. Journal of Thermophysics and Heat Transfer, **14**(4):489–495, 2000.
- [96] M. Panesi. *Physical models for nonequilibrium plasma flow simulations at high speed re-entry conditions*. PhD thesis, Università degli Studi di Pisa and von Karman Institute for Fluid Dynamics, 2009.
- [97] J. P. Appleton and K. N. C. Bray. *The conservation equations for a non-equilibrium plasma*. Journal of Fluid Mechanics, **20**(4):659–672, 1964.
- [98] A. W. Ali. *The Harmonic and Anharmonic Models for Vibrational Relaxation and Dissociation of the Nitrogen Molecule*. Technical Report NRL-MR-5924, Naval Research Laboratory, Washington D.C., 1986.
- [99] B. Graille, T. E. Magin, and M. Massot. *Kinetic theory of plasmas : translational energy*. Mathematical Models and Methods in Applied Sciences, **19**(4):527–599, 2007.

- [100] I. Nompelis, G. V. Candler, and M. S. Holden. *Effect of vibrational nonequilibrium on hypersonic double-cone experiments.* AIAA Journal, **41**(11):2162–2169, 2003.
- [101] A. J. Moyes, E. S. Beyak, T. S. Kocian, and H. L. Reed. *Accurate and efficient modeling of boundary-layer instabilities.* AIAA paper, **2019-1907**, 2019.

5

Laminar base flow

Flow stability analyses must be preceded by the computation of the unperturbed laminar base-flow solution. This amounts to obtaining the \bar{q} terms, presented in chapter 3. The most accurate way to do so is directly solving the Navier-Stokes equations, detailed in chapter 2 for a variety of flow assumptions. However, certain flows allow a series of simplifying hypotheses, thus reducing the computational expensiveness of the process. Particularly, boundary-layer flows allow simplifications dropping ellipticity, resulting in parabolic equations to be solved with a marching algorithm.

The stability analyses presented in this work are either conducted on the Navier-Stokes solutions obtained with a commercial software (CFD++ [1]), or on boundary-layer solutions obtained with the newly-developed DEKAF flow solver (see chapter 7 or Refs. [2, 3]).

5.1 Boundary-layer equations and their self-similar solutions

A steady flow with stronger variations in the wall-normal direction than in the streamwise, has negligible time and second-order streamwise derivatives:

$$\frac{\partial}{\partial t} = 0, \quad \frac{\partial^2}{\partial x^2} \approx 0. \quad (5.1)$$

Similarly, the quasi-3D assumption implies omitting spanwise derivatives:

$$\frac{\partial}{\partial z} \approx 0. \quad (5.2)$$

The assumption is called *quasi-3D*, because, even if flow variations are ignored, there may be a non-zero flux in the spanwise direction ($\bar{w} \neq 0$). This is the case for instance in swept-wing flows [4].

Applying the aforementioned simplifications onto the TCNE Navier-Stokes equations (Eqs. 2.7 and 2.8) in a cartesian coordinate system, one reaches the TCNE boundary-layer equations:

$$\frac{\partial \bar{\rho} \bar{u}}{\partial x} + \frac{\partial \bar{\rho} \bar{v}}{\partial y} = 0, \quad (5.3a)$$

$$\bar{\rho} \bar{u} \frac{\partial \bar{u}}{\partial x} + \bar{\rho} \bar{v} \frac{\partial \bar{u}}{\partial y} = - \frac{\partial \bar{p}}{\partial x} + \frac{\partial}{\partial y} \left(\bar{\mu} \frac{\partial \bar{u}}{\partial y} \right), \quad (5.3b)$$

$$\frac{\partial \bar{p}}{\partial y} = 0, \quad (5.3c)$$

$$\bar{\rho} \bar{u} \frac{\partial \bar{w}}{\partial x} + \bar{\rho} \bar{v} \frac{\partial \bar{w}}{\partial y} = \frac{\partial}{\partial y} \left(\bar{\mu} \frac{\partial \bar{w}}{\partial y} \right), \quad (5.3d)$$

$$\begin{aligned} \bar{\rho} \bar{u} \frac{\partial \bar{h}^u}{\partial x} + \bar{\rho} \bar{v} \frac{\partial \bar{h}^u}{\partial y} &= \frac{\partial}{\partial y} \left(\bar{\kappa}_{tr} \frac{\partial \bar{T}}{\partial y} + \bar{\kappa}_v \frac{\partial \bar{T}_v}{\partial y} \right) + \frac{\partial}{\partial y} \left(\bar{\mu} \bar{u} \frac{\partial \bar{u}}{\partial y} \right) + \\ &\quad + \bar{\mu} \left(\frac{\partial \bar{w}}{\partial y} \right)^2 - \frac{\partial}{\partial y} \left(\sum_{s \in \mathcal{S}} \bar{h}_s \bar{J}_s \right), \end{aligned} \quad (5.3e)$$

$$\begin{aligned} \bar{c}_{pv} \bar{\rho} \bar{u} \frac{\partial \bar{T}_v}{\partial x} + \bar{c}_{pv} \bar{\rho} \bar{v} \frac{\partial \bar{T}_v}{\partial y} &= \frac{\partial}{\partial y} \left(\bar{\kappa}_v \frac{\partial \bar{T}_v}{\partial y} \right) - \sum_{s \in \mathcal{S}} \bar{c}_{pvs} \frac{\partial \bar{T}_v}{\partial y} \bar{J}_s + \\ &\quad + \bar{u} \frac{\partial \bar{\psi}_e \bar{p}}{\partial x} + \bar{v} \frac{\partial \bar{\psi}_e \bar{p}}{\partial y} + \bar{Q}_{TV}, \end{aligned} \quad (5.3f)$$

$$\bar{\rho} \bar{u} \frac{\partial \bar{Y}_s}{\partial x} + \bar{\rho} \bar{v} \frac{\partial \bar{Y}_s}{\partial y} = - \frac{\partial \bar{J}_s}{\partial y} + \dot{\omega}_s, \quad \forall s \in \mathcal{S}, \quad (5.3g)$$

$$\sum_{s \in \mathcal{S}} \bar{Y}_s = 1, \quad (5.3h)$$

Note that the species-mass-conservation equation (Eq. 5.3g) is expressed in terms of concentrations (Y_s) rather than partial densities (ρ_s). Similarly the energy equation (Eq. 5.3e) features the semi-total enthalpy (h^u) rather than the static (h), since it also includes the contribution of the streamwise kinetic energy ($h^u = h + u^2/2$). The vibrational-electronic-electron energy equation (Eq. 5.3f) also has a slightly different form from that in § 2.3.1 – it is expressed in terms of T_v , rather than h_v . The species concentration condition (Eq. 5.3h) is also included for the sake of

completeness, and can be included in the equation system in substitution of one of the species concentration conservation equations (Eq. 5.3g). The resulting system therefore features $N_s + 6$ equations and unknowns.

The equations can be rearranged into a more convenient form where the marching and self-similar terms are more evident:

$$2\xi \left(\frac{\partial \bar{f}}{\partial \eta} \frac{\partial^2 \bar{f}}{\partial \xi \partial \eta} - \frac{\partial^2 \bar{f}}{\partial \eta^2} \frac{\partial \bar{f}}{\partial \xi} \right) = \frac{\partial}{\partial \eta} \left(\bar{c} \frac{\partial^2 \bar{f}}{\partial \eta^2} \right) + \bar{f} \frac{\partial^2 \bar{f}}{\partial \eta^2} + \beta_H \left(\bar{j} - \left(\frac{\partial \bar{f}}{\partial \eta} \right)^2 \right), \quad (5.4a)$$

$$2\xi \left(\frac{\partial \bar{f}}{\partial \eta} \frac{\partial \bar{k}}{\partial \xi} - \frac{\partial \bar{k}}{\partial \eta} \frac{\partial \bar{f}}{\partial \xi} \right) = \frac{\partial}{\partial \eta} \left(\bar{c} \frac{\partial \bar{k}}{\partial \eta} \right) + \bar{f} \frac{\partial \bar{k}}{\partial \eta}, \quad (5.4b)$$

$$\begin{aligned} 2\xi \left(\frac{\partial \bar{f}}{\partial \eta} \frac{\partial \bar{g}}{\partial \xi} - \frac{\partial \bar{g}}{\partial \eta} \frac{\partial \bar{f}}{\partial \xi} \right) &= \frac{\partial}{\partial \eta} \left(\bar{a}_1 \frac{\partial \bar{g}}{\partial \eta} + \bar{a}_{v2} \frac{\partial \bar{T}_v}{\partial \eta} \right) + \bar{f} \frac{\partial \bar{g}}{\partial \eta} - \Theta_H \frac{\partial \bar{f}}{\partial \eta} \bar{g} + \\ &+ \frac{\partial}{\partial \eta} \left(\bar{a}_2 \frac{\partial \bar{f}}{\partial \eta} \frac{\partial^2 \bar{f}}{\partial \eta^2} \right) + \bar{a}_0 \left(\frac{\partial \bar{k}}{\partial \eta} \right)^2 - \sum_{s \in \mathcal{S}} \frac{\partial}{\partial \eta} \left(\bar{a}_{1s} \frac{\partial \bar{Y}_s}{\partial \eta} \right) + \\ &- \sum_{s \in \mathcal{S}} \frac{\partial (\bar{g}_s \bar{J}_s)}{\partial \eta}, \end{aligned} \quad (5.4c)$$

$$\begin{aligned} 2\xi \left(\frac{\partial \bar{f}}{\partial \eta} \frac{\partial \bar{T}_v}{\partial \xi} - \frac{\partial \bar{T}_v}{\partial \eta} \frac{\partial \bar{f}}{\partial \xi} \right) \bar{c}_{pv} &= \bar{c}_{pv} \bar{f} \frac{\partial \bar{T}_v}{\partial \eta} - \bar{c}_{pv} \theta_{Hv} \bar{T}_v \frac{\partial \bar{f}}{\partial \eta} + \\ + 2\xi \bar{j} \text{Ec}_p \left(\frac{\partial \bar{\psi}_e}{\partial \xi} \frac{\partial \bar{f}}{\partial \eta} - \frac{\partial \bar{\psi}_e}{\partial \eta} \frac{\partial \bar{f}}{\partial \xi} \right) - \bar{j} \text{Ec}_p \frac{\partial \bar{\psi}_e}{\partial \eta} \bar{f} - \bar{j} \text{Ec} \beta_H \bar{\psi}_e \frac{\partial \bar{f}}{\partial \eta} + & \quad (5.4d) \\ - \sum_{s \in \mathcal{S}} \bar{c}_{pvs} \frac{\partial \bar{T}_v}{\partial \eta} \bar{J}_s + \frac{\partial}{\partial \eta} \left(\bar{a}_{v1} \frac{\partial \bar{T}_v}{\partial \eta} \right) + 2\xi \dot{\bar{\Omega}}_v, & \end{aligned}$$

$$2\xi \left(\frac{\partial \bar{f}}{\partial \eta} \frac{\partial \bar{Y}_s}{\partial \xi} - \frac{\partial \bar{Y}_s}{\partial \eta} \frac{\partial \bar{f}}{\partial \xi} \right) = \bar{f} \frac{\partial \bar{Y}_s}{\partial \eta} - \frac{\partial \bar{J}_s}{\partial \eta} + 2\xi \dot{\bar{\Omega}}_s, \quad \forall s \in \mathcal{S}. \quad (5.4e)$$

The concentration condition (Eq. 5.3h) obviously remains unchanged and is still

applicable. Eqs. 5.4 feature the following non-dimensional quantities:

$$\begin{aligned}
\frac{\partial \bar{f}}{\partial \eta} &= \bar{u}/u_e, & \bar{k} &= \bar{w}/w_e, & \bar{g} &= \bar{h}^u/h_e^u, \\
\bar{T}_v &= \bar{T}_v/T_{ve}, & \bar{j} &= \rho_e/\bar{\rho}, & \bar{j}_s &= \frac{\sqrt{2\xi} \bar{J}_s}{\rho_e \mu_e u_e}, \\
\bar{g}_s &= \frac{1}{1 + \text{Ec}/2} \frac{\bar{h}_s}{h_e}, & \bar{c}_{pvs} &= \frac{\bar{c}_{pvs} T_{ve}}{h_e}, & \bar{c}_{pv} &= \frac{\bar{c}_{pv} T_{ve}}{h_e}, \\
\bar{c} &= \frac{\bar{\rho} \bar{\mu}}{\rho_e \mu_e}, & \bar{a}_0 &= \frac{\text{Ec}_w}{1 + \text{Ec}/2} \bar{c}, & \bar{a}_{v1} &= \frac{T_{ve} \bar{\kappa}_v}{h_e \bar{\mu}} \bar{c}, \\
\bar{a}_1 &= \frac{\bar{\kappa}_{tr}}{\bar{c}_{ptr} \bar{\mu}} \bar{c}, & \bar{a}_2 &= \frac{\text{Ec}}{1 + \text{Ec}/2} (\bar{c} - \bar{a}_1), & \bar{a}_{1s} &= \frac{\bar{a}_1}{1 + \text{Ec}/2} \frac{\bar{h}_s}{h_e}, \\
\bar{a}_{v2} &= \left(\frac{\bar{\kappa}_v}{\bar{\mu}} - \frac{\bar{c}_{pv} \bar{\kappa}_{tr}}{\bar{c}_{ptr} \bar{\mu}} \right) \frac{T_{ve}}{h_e} \frac{\bar{c}}{1 + \text{Ec}/2}, & \dot{\Omega}_s &= \frac{\dot{\omega}_s}{\bar{\rho} \rho_e \mu_e u_e^2}, \\
\dot{\Omega}_v &= \frac{\bar{Q}_{TV}}{\bar{\rho} \rho_e \mu_e u_e^2 h_e}, & \theta_{Hv} &= \frac{2\xi}{T_{ve}} \frac{dT_{ve}}{d\xi}, & \Theta_H &= \frac{2\xi}{h_e^u} \frac{dh_e^u}{d\xi}, \\
\beta_H &= \frac{2\xi}{u_e} \frac{du_e}{d\xi}, & \text{Ec} &= \frac{u_e^2}{h_e}, & \text{Ec}_w &= \frac{w_e^2}{h_e}, \\
\text{Ec}_p &= \frac{p_e}{\rho_e h_e}, & & & & \tag{5.5}
\end{aligned}$$

where the subindex e denotes variables at the boundary-layer, which in general are a function of the streamwise coordinate (x). An exception to this is the spanwise velocity (w_e), which must be constant in x such that the quasi-3D assumption (Eq. 5.2) is satisfied. In Eq. 5.4, the Cartesian variables (x and y) were replaced with the self-similar (η) and marching (ξ) variables through the Illingworth transformation:^a

$$d\eta = \frac{u_e}{\sqrt{2\xi}} \bar{\rho} dy, \quad d\xi = \rho_e u_e \mu_e dx. \tag{5.6}$$

Note that Eqs. 5.4 do not include a non-dimensional continuity equation. That is because the choice of the non-dimensional variable \bar{f} is such that it condenses both the wall-normal (\bar{v}) and the streamwise velocity (\bar{u}) through the satisfaction of the continuity equation. The demonstration of this, together with the procedure to obtain the wall-normal velocity from the solution to the non-dimensional boundary-layer equations (Eqs. 5.4) is laid out in app. E.

If the terms highlighted in blue in Eq. 5.4 can be neglected, the boundary-layer equations allow for a self-similar solution. This is the case in the absence of energy

^aThe name of this transformation is referred to differently in different references. We consider what is referred to as the Levy-Lees transformation by Schlichting *et al.* [5, p. 247], the Lees-Dorodnitsyn transformation by Anderson [6, p. 279] and the Illingworth transformation by White [7, p. 511].

and mass source terms, and when all non-dimensional variables defined in Eq. 5.5 are independent of ξ . The implications of these requirements are further explored in app. D. Consequently, out of the flow assumptions laid out in Table 2.1, the ones allowing for a self-similar solution are CPG, TCFG, TNE, TPG, LTE and LTEED.

The expression for the non-dimensional species diffusion flux \bar{J}_s actually drops its explicit dependency on the marching variable ξ when \bar{J}_s is evaluated. For instance, taking J_s as provided by Eqs. 2.17 and 2.18:

$$\bar{J}_s = \frac{\sqrt{2\xi} \bar{J}_s}{\rho_e \mu_e u_e} = -\frac{\bar{\rho} \bar{D}_{\text{eff}} s}{\bar{\mu}} \bar{c} \frac{\partial \bar{X}_s}{\partial \eta}. \quad (5.7)$$

Analogous expressions can be easily obtained for the other expressions of the diffusion fluxes.

The boundary-layer equations (Eqs. 5.3 and 5.4) are simplified for the various flow assumptions in Table 2.1 similarly to how the Navier-Stokes equations are (see § 2.3). For the sake of completeness they are presented in the following subsections.

5.1.1 CNE boundary-layer equations

The thermal-equilibrium assumption implies that the vibrational-electronic-electron-energy equation (Eq. 5.3f and 5.4d) must no longer be solved for, reducing the system to $N_s + 5$ equations and unknowns. The use of a unique temperature, implies that there is only one thermal-conductivity term in the total-energy equation (Eq. 5.3e), rendering:

$$\begin{aligned} \bar{\rho} \bar{u} \frac{\partial \bar{h}^u}{\partial x} + \bar{\rho} \bar{v} \frac{\partial \bar{h}^u}{\partial y} &= \frac{\partial}{\partial y} \left(\bar{\kappa} \frac{\partial \bar{T}}{\partial y} \right) + \frac{\partial}{\partial y} \left(\bar{\mu} \bar{u} \frac{\partial \bar{u}}{\partial y} \right) + \bar{\mu} \left(\frac{\partial \bar{w}}{\partial y} \right)^2 + \\ &\quad - \frac{\partial}{\partial y} \left(\sum_{s \in \mathcal{S}} \bar{h}_s \bar{J}_s \right), \end{aligned} \quad (5.8)$$

or, in non-dimensional form, Eq. 5.4c becomes:

$$\begin{aligned} 2\xi \left(\frac{\partial \bar{f}}{\partial \eta} \frac{\partial \bar{g}}{\partial \xi} - \frac{\partial \bar{g}}{\partial \eta} \frac{\partial \bar{f}}{\partial \xi} \right) &= \frac{\partial}{\partial \eta} \left(\bar{a}_1 \frac{\partial \bar{g}}{\partial \eta} \right) + \bar{f} \frac{\partial \bar{g}}{\partial \eta} - \Theta_H \frac{\partial \bar{f}}{\partial \eta} \bar{g} + \frac{\partial}{\partial \eta} \left(\bar{a}_2 \frac{\partial \bar{f}}{\partial \eta} \frac{\partial^2 \bar{f}}{\partial \eta^2} \right) + \\ &\quad + \bar{a}_0 \left(\frac{\partial \bar{k}}{\partial \eta} \right)^2 - \sum_{s \in \mathcal{S}} \frac{\partial}{\partial \eta} \left(\bar{a}_{1s} \frac{\partial \bar{Y}_s}{\partial \eta} \right) - \sum_{s \in \mathcal{S}} \frac{\partial (\bar{g}_s \bar{J}_s)}{\partial \eta}, \end{aligned} \quad (5.9)$$

where the definition of the non-dimensional \bar{a}_1 variable is different from that in Eq. 5.5:

$$\bar{a}_1 = \frac{\bar{\kappa}}{\bar{c}_p \bar{\mu}} \bar{c}. \quad (5.10)$$

Consequently, \bar{a}_2 and \bar{a}_{1s} , which include \bar{a}_1 in their definition (Eq. 5.5) also change.

The dimensional equation system is completed with Eqs. 5.3a, 5.3b, 5.3c, 5.3d, 5.3g and 5.3h, and the non-dimensional one with Eqs. 5.4a, 5.4b, 5.4e and 5.3h.

5.1.2 LTEED boundary-layer equations

One can apply the same treatment from § 2.3.3 to the boundary-layer equations. Adding all the species-concentration-conservation equations (Eq. 5.3g) multiplied by the corrected elemental stoichiometric coefficient \mathcal{E}_{Es} one reaches the elemental-concentration-conservation equations:

$$\bar{\rho} \bar{u} \frac{\partial \bar{\mathcal{Y}}_E}{\partial x} + \bar{\rho} \bar{v} \frac{\partial \bar{\mathcal{Y}}_E}{\partial y} = - \frac{\partial \bar{J}_E}{\partial y}, \quad \forall E \in \mathcal{E}, \quad (5.11)$$

or in non-dimensional form:

$$2\xi \left(\frac{\partial \bar{f}}{\partial \eta} \frac{\partial \bar{\mathcal{Y}}_E}{\partial \xi} - \frac{\partial \bar{\mathcal{Y}}_E}{\partial \eta} \frac{\partial \bar{f}}{\partial \xi} \right) = \bar{f} \frac{\partial \bar{\mathcal{Y}}_E}{\partial \eta} - \frac{\partial \bar{J}_E}{\partial \eta}, \quad \forall E \in \mathcal{E}, \quad (5.12)$$

where the non-dimensional elemental diffusion mass flux can be decomposed into its various contributions by applying the Illingworth transformation (Eq. 5.6) onto the flux's ambipolar definition in Eq. 2.28:

$$\begin{aligned} \bar{J}_E &= \frac{\sqrt{2\xi} \bar{J}_E}{\rho_e \mu_e u_e} = \\ &= - \left(\sum_{F \in \mathcal{E}} \bar{c}_{EF}^y \frac{\partial \bar{\mathcal{Y}}_F}{\partial \eta} + \bar{a}_E^g \frac{\partial \bar{g}}{\partial \eta} - \sum_{F \in \mathcal{E}} \bar{a}_{EF}^y \frac{\partial \bar{\mathcal{Y}}_F}{\partial \eta} - \bar{a}_E^u \frac{\partial \bar{f}}{\partial \eta} \frac{\partial^2 \bar{f}}{\partial \eta^2} \right), \end{aligned} \quad (5.13)$$

featuring the following non-dimensional quantities:

$$\begin{aligned} \bar{c}_{EF}^y &= \frac{\bar{\rho} \bar{C}_{EF}}{\rho_e \mu_e}, & \bar{a}_E^g &= \frac{\bar{\mathcal{A}}_E \bar{\rho}}{\rho_e \mu_e} \frac{h_e^u}{\bar{c}_p^{\text{eq}}}, \\ \bar{a}_{EF}^y &= \frac{\bar{\mathcal{A}}_E \bar{\rho}}{\rho_e \mu_e} \sum_{s \in \mathcal{S}} \frac{\bar{h}_s}{\bar{c}_p^{\text{eq}}} \frac{\partial \bar{Y}_s}{\partial \bar{\mathcal{Y}}_F}, & \bar{a}_E^u &= \frac{\bar{\mathcal{A}}_E \bar{\rho}}{\rho_e \mu_e} \frac{u_e^2}{\bar{c}_p^{\text{eq}}}, \end{aligned} \quad (5.14)$$

where \mathcal{A}_E and C_{EF} are defined in Eqs. 2.29 or 2.32, and where the equilibrium heat capacity is defined as:

$$c_p^{\text{eq}} = c_p + \sum_{s \in \mathcal{S}} h_s \frac{\partial Y_s}{\partial T}. \quad (5.15)$$

The procedure to obtain the variation of the species mass fractions (Y_s) with temperature (T) and with the elemental mass fractions (\mathcal{Y}_E) in equilibrium conditions is detailed in app. B.

Instead of the species concentration condition (Eq. 5.3h), one must now impose its elemental version:

$$\sum_{E \in \mathcal{E}} \bar{\mathcal{Y}}_E = 1. \quad (5.16)$$

Note that Eq. 5.13 does not include the barodiffusion term, since due to the boundary-layer y -momentum equation (Eq. 5.3c), the wall-normal pressure gradient is zero.

The dimensional energy equation retains the form in Eq. 5.8, but it is convenient to rearrange its non-dimensional version (Eq. 5.9) expanding the species diffusion fluxes (\bar{J}_s defined in Eq. 5.5) with Eq. 2.24, and the mass-fraction gradients taking advantage from the fact that in equilibrium $Y_s = Y_s(p, T, \mathcal{Y}_E)$. This leads to:

$$2\xi \left(\frac{\partial \bar{f}}{\partial \eta} \frac{\partial \bar{g}}{\partial \xi} - \frac{\partial \bar{g}}{\partial \eta} \frac{\partial \bar{f}}{\partial \xi} \right) = \frac{\partial}{\partial \eta} \left(\bar{a}_1 \frac{\partial \bar{g}}{\partial \eta} \right) + \bar{f} \frac{\partial \bar{g}}{\partial \eta} - \Theta_H \frac{\partial \bar{f}}{\partial \eta} \bar{g} + \frac{\partial}{\partial \eta} \left(\bar{a}_2 \frac{\partial \bar{f}}{\partial \eta} \frac{\partial^2 \bar{f}}{\partial \eta^2} \right) + \bar{a}_0 \left(\frac{\partial \bar{\kappa}}{\partial \eta} \right)^2 - \sum_{E \in \mathcal{E}} \frac{\partial}{\partial \eta} \left(\bar{a}_{1E}^{\mathcal{Y}} \frac{\partial \bar{Y}_E}{\partial \eta} \right) + \sum_{E \in \mathcal{E}} \frac{\partial}{\partial \eta} \left(\bar{a}_{2E}^{\mathcal{D}} \frac{\partial \bar{Y}_E}{\partial \eta} \right), \quad (5.17)$$

where the definition of \bar{a}_1 , and consequently that of \bar{a}_2 and \bar{a}_{1s} , differs from that for CNE and TCNE, and where there is an additional non-dimensional variable $\bar{a}_{1E}^{\mathcal{Y}}$ depending on \bar{a}_{1s} :

$$\bar{a}_1 = \frac{\bar{\kappa}^{\text{eq}}}{\bar{c}_p^{\text{eq}} \bar{\mu}} \bar{c}, \quad \bar{a}_{1E}^{\mathcal{Y}} = \sum_{s \in \mathcal{S}} \bar{a}_{1s} \frac{\partial \bar{Y}_s}{\partial \bar{Y}_E}. \quad (5.18)$$

The diffusion variable $\bar{a}_{2E}^{\mathcal{D}}$ depends on the diffusion theory. For multicomponent diffusion models (like in Eq. 2.15), it is defined as:

$$\bar{a}_{2E}^{\mathcal{D}} = \sum_{s, \ell \in \mathcal{S}} \bar{c} \frac{\bar{\rho} \bar{D}_{s\ell}}{\bar{\mu}} \bar{Y}_s \bar{g}_s \frac{\partial \bar{X}_\ell}{\partial \bar{Y}_E}, \quad (5.19)$$

whereas for effective diffusion models (like in Eq. 2.18), it is defined as:

$$\bar{a}_{2E}^{\mathcal{D}} = \sum_{s \in \mathcal{S}} \bar{c} \frac{\bar{\rho} \bar{D}_{\text{eff}\,s}}{\bar{\mu}} \bar{g}_s \frac{\partial \bar{X}_s}{\partial \bar{Y}_E}. \quad (5.20)$$

Attending also to the diffusion model, the equilibrium thermal conductivity (κ^{eq}) in Eq. 5.18 is defined either with Eq. 2.35 or with 2.36.

The dimensional equation system is completed with Eqs. 5.3a, 5.3b, 5.3c, and 5.3d, and the non-dimensional one with Eqs. 5.4a, and 5.4b.

5.1.3 LTE boundary-layer equations

The LTE assumption assumes the elemental mole fractions to be constant throughout the domain, and thus the elemental-concentration-conservation equations (Eq. 5.11 and 5.12) are not required. Moreover, the terms featuring variations of the equilibrium composition with respect to the elemental fractions (\bar{a}_{1E}^Y and \bar{a}_{2E}^D) are zero. Neglecting also barodiffusion, this simplifies the energy equation (Eq. 5.8) to:

$$\bar{\rho} \bar{u} \frac{\partial \bar{h}^u}{\partial x} + \bar{\rho} \bar{v} \frac{\partial \bar{h}^u}{\partial y} = \frac{\partial}{\partial y} \left(\bar{\kappa} \frac{\partial \bar{T}}{\partial y} \right) + \frac{\partial}{\partial y} \left(\bar{\mu} \bar{u} \frac{\partial \bar{u}}{\partial y} \right) + \bar{\mu} \left(\frac{\partial \bar{w}}{\partial y} \right)^2, \quad (5.21)$$

featuring the equilibrium thermal conductivity ($\bar{\kappa} = \bar{\kappa}^{eq}$) defined in Eqs. 2.35 or 2.36. The corresponding non-dimensional form of the energy equation is thus

$$2\xi \left(\frac{\partial \bar{f}}{\partial \eta} \frac{\partial \bar{g}}{\partial \xi} - \frac{\partial \bar{g}}{\partial \eta} \frac{\partial \bar{f}}{\partial \xi} \right) = \frac{\partial}{\partial \eta} \left(\bar{a}_1 \frac{\partial \bar{g}}{\partial \eta} \right) + \bar{f} \frac{\partial \bar{g}}{\partial \eta} - \Theta_H \frac{\partial \bar{f}}{\partial \eta} \bar{g} + \frac{\partial}{\partial \eta} \left(\bar{a}_2 \frac{\partial \bar{f}}{\partial \eta} \frac{\partial^2 \bar{f}}{\partial \eta^2} \right) + \bar{a}_0 \left(\frac{\partial \bar{\kappa}}{\partial \eta} \right)^2, \quad (5.22)$$

where the definition of \bar{a}_1 , and consequently that of \bar{a}_2 , is the same as for LTEED (Eq. 5.18).

The dimensional equation system is completed with Eqs. 5.3a, 5.3b, 5.3c, and 5.3d, and the non-dimensional one with Eqs. 5.4a, and 5.4b.

5.1.4 TNE boundary-layer equations

In general, the modeling of a chemically-frozen boundary layer yet in thermal non-equilibrium, requires the resolution of the same equation system as in TCNE (Eq. 5.4 and 5.3) neglecting the chemical source terms ($\dot{\omega}_s \approx 0$ and $\dot{\Omega}_s \approx 0$). However, in the absence of concentration gradients, the mixture composition is constant and the resolution of the species-concentration-conservation equations is not required. Additionally, the diffusion fluxes can be neglected, since their driving force is identically zero. The remaining equation system includes the vibrational-electronic-electron-energy equation (Eq. 5.3f), after neglecting the diffusion and species production terms:

$$\bar{\rho} \bar{u} \frac{\partial \bar{h}_v}{\partial x} + \bar{\rho} \bar{v} \frac{\partial \bar{h}_v}{\partial y} = \frac{\partial}{\partial y} \left(\bar{\kappa}_v \frac{\partial \bar{T}_v}{\partial y} \right) + \bar{u} \frac{\partial \bar{\psi}_e \bar{p}}{\partial x} + \bar{v} \frac{\partial \bar{\psi}_e \bar{p}}{\partial y} + \bar{Q}_{TV}; \quad (5.23)$$

the total energy equation, simplified from Eq. 5.3e to:

$$\bar{\rho} \bar{u} \frac{\partial \bar{h}^u}{\partial x} + \bar{\rho} \bar{v} \frac{\partial \bar{h}^u}{\partial y} = \frac{\partial}{\partial y} \left(\bar{\kappa}_{tr} \frac{\partial \bar{T}}{\partial y} + \bar{\kappa}_v \frac{\partial \bar{T}_v}{\partial y} \right) + \frac{\partial}{\partial y} \left(\bar{\mu} \bar{u} \frac{\partial \bar{u}}{\partial y} \right) + \bar{\mu} \left(\frac{\partial \bar{w}}{\partial y} \right)^2; \quad (5.24)$$

and the mixture continuity and momentum equations (Eqs. 5.3a, 5.3b, 5.3c, and 5.3d), which remain unchanged.

The non-dimensional equation system is composed of Eqs. 5.4a, and 5.4b, which remain unchanged, together with the non-dimensional form of Eqs. 5.23 and 5.24:

$$2\xi \left(\frac{\partial \bar{f}}{\partial \eta} \frac{\partial \bar{T}_v}{\partial \xi} - \frac{\partial \bar{T}_v}{\partial \eta} \frac{\partial \bar{f}}{\partial \xi} \right) \bar{c}_{pv} = \bar{c}_{pv} \bar{f} \frac{\partial \bar{T}_v}{\partial \eta} - \bar{c}_{pv} \theta_{Hv} \bar{T}_v \frac{\partial \bar{f}}{\partial \eta} + \frac{\partial}{\partial \eta} \left(\bar{a}_{v1} \frac{\partial \bar{T}_v}{\partial \eta} \right) + 2\xi \bar{j} \text{Ec} \left(\frac{\partial \bar{p}_e}{\partial \xi} \frac{\partial \bar{f}}{\partial \eta} - \frac{\partial \bar{p}_e}{\partial \eta} \frac{\partial \bar{f}}{\partial \xi} \right) - \bar{j} \text{Ec} \frac{\partial \bar{p}_e}{\partial \eta} \bar{f} + 2\xi \dot{\bar{\Omega}}_v, \quad (5.25)$$

$$2\xi \left(\frac{\partial \bar{f}}{\partial \eta} \frac{\partial \bar{g}}{\partial \xi} - \frac{\partial \bar{g}}{\partial \eta} \frac{\partial \bar{f}}{\partial \xi} \right) = \frac{\partial}{\partial \eta} \left(\bar{a}_1 \frac{\partial \bar{g}}{\partial \eta} + \bar{a}_{v2} \frac{\partial \bar{T}_v}{\partial \eta} \right) + \bar{f} \frac{\partial \bar{g}}{\partial \eta} - \Theta_H \frac{\partial \bar{f}}{\partial \eta} \bar{g} + \frac{\partial}{\partial \eta} \left(\bar{a}_2 \frac{\partial \bar{f}}{\partial \eta} \frac{\partial^2 \bar{f}}{\partial \eta^2} \right) + \bar{a}_0 \left(\frac{\partial \bar{\kappa}}{\partial \eta} \right)^2, \quad (5.26)$$

All non-dimensional parameters correspond to the definitions in Eq. 5.5.

5.1.5 TCFG boundary-layer equations

A thermo-chemically frozen boundary layer can be described with the same equations of § 5.1.4, yet neglecting the vibrational-electronic-electron-energy source term ($\bar{Q}_{TV} \approx 0$).

5.1.6 TPG and CPG boundary-layer equations

A boundary layer in TPG, in general, requires the same equation system as in CNE (see § 5.1.1), yet neglecting the chemical source terms ($\dot{\bar{\omega}}_s \approx 0$ and $\dot{\bar{\Omega}}_s \approx 0$). However, as it occurs with flows in TNE (see § 5.1.4), the mixture composition remains constant if there are no prescribed concentration gradients.^b The consequences are that one no longer needs to resolve the species-concentration-conservation equations, making the equation system the same as for a gas in LTE (§ 5.1.3). The only difference is that the thermal conductivity appearing in the energy equation

^bThe injection of a dissimilar gas mixture through the wall boundary prescribes such a gradient.

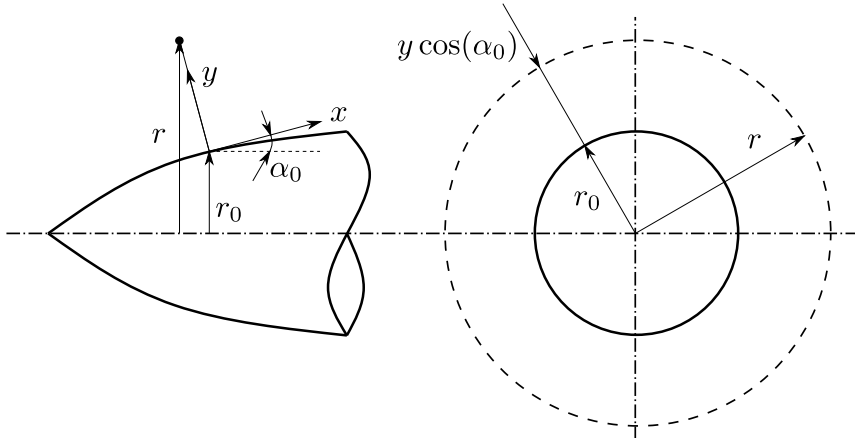


Figure 5.1: Sketch of the relationship between the axisymmetric coordinate system and the Cartesian.

(Eq. 5.21) is not the equilibrium, but rather the frozen one ($\bar{\kappa} = \bar{\kappa}^{Fr}$). Consequently, the non-dimensional equation system is also the same as in LTE (§ 5.1.3), yet with the non-dimensional quantities defined in Eq. 5.10.

The calorically-perfect-gas assumption normally implies a constant mixture composition, and therefore the system equations are the same listed for constant-composition TPG. The only difference is the treatment of the gas' thermal state (see chapter 4). Nevertheless, one can encounter situations where the operative temperature is low enough to neglect the excitation of internal energy modes (CPG range), yet having a wall injection of a gas with a different composition than the bulk gas. Such a flow may be modeled with a mixture of calorically-perfect species, whose thermal state is defined according to Eq. 4.1, yet are allowed to inter-diffuse. The equation system to solve is also the same as for a gas in CNE (see § 5.1.1) yet neglecting the chemical source terms ($\dot{\omega}_s \approx 0$ and $\dot{\Omega}_s \approx 0$).

5.1.7 Axysymmetric boundary layers – the Probstein-Elliott transformation

The equations detailed in this section are expressed on a Cartesian reference frame. However, hypersonic vehicles oftentimes feature axisymmetric geometries. In such cases, one must solve the boundary-layer equations in cylindrical coordinates. Their explicit form is left out of the present work, but can be found in CPG in the book of White [7], for example. Applying the transformation proposed by Probstein & Elliott [8], and assuming $(y/r_0)^2 \ll 0$, it is possible to transform the cylindrical boundary-layer equations into “*Cartesian-like*” equations that have a very similar form to the equations presented in the preceding sections. The main

difference lies in the source terms ($\dot{\omega}_s$ and $\dot{\omega}_v$) which are multiplied by the factor $(L/r_0)^2$, where r_0 is the cone's surface radius and L is a reference length to preserve dimensionality^c. Besides the scaling of the source terms, the equations are a function of the transformed variables χ and y rather than the physical distances x and y . These transformed variables are defined through:

$$d\chi = \frac{r_0(x)^2}{L^2} dx, \quad dy = \frac{r(x, y)}{L} dy, \quad (5.27)$$

where r is the radial distance in the cylindrical reference frame centered in the axis of the body of revolution. Similarly, the transformed equations feature a transformed wall-normal velocity \bar{v} rather than \bar{v} :

$$\bar{v} = \frac{r L}{r_0^2} \bar{v} + \frac{L^2}{r_0^2} \frac{\partial y}{\partial x} \bar{u}. \quad (5.28)$$

A sketch of the different quantities and how they are related to one another is presented in Fig. 5.1. From it, it is clear that:

$$r(x, y) = r_0(x) + y \cos(\alpha_0(x)). \quad (5.29)$$

Specifically, if the body of revolution is a straight cone of half-angle θ_c , then:

$$\alpha_0(x) = \theta_c = \text{cst}, \quad (5.30a)$$

$$r_0(x) = x \sin(\theta_c). \quad (5.30b)$$

It is important to point out, that the Probstein-Elliott (Eq. 5.27) precedes the Illingworth transformation (Eq. 5.6). Therefore, for conical boundary layers, η and ξ are defined as functions of the transformed χ and y , rather than x and y :

$$d\eta = \frac{u_e}{\sqrt{2\xi}} \bar{\rho} dy, \quad d\xi = \rho_e u_e \mu_e d\chi. \quad (5.31)$$

One can still apply the Probstein-Elliott transformation relaxing the hypothesis that $(y/r_0)^2 \ll 1$, and would like-wise reach the non-dimensional boundary-layer equations presented in this section. However, this implies that an additional factor appears in the expression of the Chapman-Rubesin parameter c (Eq. 5.5), which becomes:

$$\bar{c} = \left(1 + \frac{y \cos(\alpha_0)}{r_0}\right)^2 \frac{\bar{\rho} \bar{\mu}}{\rho_e \mu_e}. \quad (5.32)$$

A clear consequence of not assuming $(y/r_0)^2 \ll 1$ is that the boundary-layer equations no longer have a self-similar solution. The reason being that r_0 is an explicit function of the streamwise coordinate and y cannot be obtained from η independently from the streamwise position. In other words, if $(y/r_0)^2 \sim 1$,

^c L can be risklessly assumed in general to be equal to 1 m.

the spanwise curvature affects the boundary-layer profiles in a non-similar fashion at the different streamwise locations. All axisymmetric boundary-layer analyses presented in this work assume $(y/r_0)^2 \ll 1$.

Another important consideration regarding axisymmetric boundary layers is that the Probstein-Elliott transformation is restricted to flows with zero spanwise velocity $w = 0$. Other authors [9–12] have also investigated boundary-layers around vehicles with non-zero rotation speeds around the symmetry axis, but it is out of the scope of this dissertation.

5.2 Base-flow and stability hypotheses

When applying simplifying hypotheses in the pursuit of a mathematical model of reality with reduced complexity, it is important to carry out such simplifications in a coherent manner. If one assumes that the order of magnitude of a certain non-dimensional parameter, proxy of the balance of two groups of physical phenomena, is such that certain terms can be safely neglected, this should be applied across the entire theoretical framework.

In particular, in boundary-layer theory, the assumption that gradients in the wall-normal direction are much larger than in the others [7], amounts to neglecting terms of the order of $1/\text{Re}_x = 1/\text{Re}^2$.^d The parabolized Navier-Stokes (PNS) equations share many simplifying hypotheses with boundary-layer theory, since terms of $\mathcal{O}(1/\text{Re}^2)$ are also dropped, assuming that variations in the plane normal to the streamwise direction are much more significant. A full insight into this simplified subset of equations is left out of this doctoral research, since no such base flow is employed in the presented numerical studies. However, more information can be found in Prabhu *et al.* [13], in Paredes *et al.* [14], or in Anderson's book [6, Ch. 8.3]. Obviously this is not the case with DNS, where all the terms in the Navier-Stokes equations are retained.

Regarding the stability theories laid out in chapter 3, the hypotheses assumed by the parabolized ones (LPSE, 3D-LPSE, NPSE and 3D-NPSE) translate into neglecting terms of $\mathcal{O}(1/\text{Re}^2)$.^e The local theories, such as LST or 2D-LST, due to the parallel flow assumption, effectively drop terms of $\mathcal{O}(1/\text{Re})$ [15]. Streamwise global theories, such as BiG or TriG do not make any of these assumptions, and retain all terms [16] up to $\mathcal{O}(1/\text{Re}^5)$.

It is therefore natural to deploy PSE (both linear and non-linear) on boundary-layer flows [17–20], or 3D-PSE on PNS base flows [21], since they share the same order of simplification in their core hypotheses. Performing LST or 2D-LST anal-

^dThe Reynolds number based on the streamwise location $\text{Re}_x = \rho_e u_e x / \mu_e$, is equal to the square of that based on the Blasius length $\text{Re} = \rho_e u_e \ell_e / \mu_e$, since $\ell_e = \sqrt{\frac{\mu_e x}{\rho_e u_e}}$.

^eNote that the small/large o notation is implied: o denotes “order lower than”, whilst \mathcal{O} translates to “order lower than or equal to”.

yses on boundary-layer laminar base-flow solutions is not so straightforward in its coherence, since the boundary-layer equations neglect terms of $\mathcal{O}(1/\text{Re}^2)$, whilst LST or 2D-LST simplifies the stability equations up to $\mathcal{O}(1/\text{Re})$. This is actually due to the additional parallel flow assumption, which implies that the propagation of instabilities is much more affected by base-flow variations in the wall-normal direction, than it is by those in the streamwise. The same chain of reasoning is implicit when performing LST or 2D-LST on Navier-Stokes base flows. In other words, the use of LST or 2D-LST introduces an additional simplifying hypothesis which is not general to the flow quantities (q), but that rather relates the perturbation (q') with the base-flow quantities (\bar{q}).

Another important remark, is that streamwise global theories, such as BiG or TriG, which retain terms of $\mathcal{O}(1/\text{Re}^5)$, cannot be deployed on boundary-layer or PNS base flows. In other words, the base-flow solutions employed for such analyses must satisfy the Navier-Stokes equations [22].

Note that all the aforementioned base-flow and stability theories which effectively drop terms of $\mathcal{O}(1/\text{Re})$ or $\mathcal{O}(1/\text{Re}^2)$, are consequently largely inaccurate in the vicinity of the leading edge, where there is a singularity as $\text{Re} \rightarrow 0$.

5.3 Base-flow inaccuracy propagation to stability predictions

Stability analyses effectively investigate the propagation of small perturbations inside a laminar basic-state flow field. Performing such analyses on under-resolved base flows can lead to the involuntary consideration of the numerical inaccuracies as instabilities themselves. Theofilis [22] states in this regard that: “*if numerical residuals exist in the basic state (at $\mathcal{O}(1)$) they will act as forcing terms in the $\mathcal{O}(\epsilon)$ disturbance equations and result in erroneous instability predictions*”. Achieving a laminar basic-state solution that is sufficiently well resolved is therefore paramount to avoid such numerical forcing terms. The question subsequently arising is: how well resolved must such base flow be in order to achieve the desired level of numerical accuracy?

In order to clarify this matter, an investigation is carried out on the propagation of base-flow inaccuracies into the ultimate instability predictions. Five simple cases are chosen, representing the major instability mechanisms described in § 3.6 – Tollmien-Schlichting waves (TS), Mack’s first and second mode (M1 and M2), and cross-flow instabilities (CF).

Basic-state flow fields are obtained from solving the boundary-layer equations, which have a self-similar solution for such simplified cases (see § 5.1). The test conditions are summarized in Table 5.1. All cases assume the test gas to be air and to behave like a CPG with Sutherland’s law for viscosity (Eq. 4.2) and a constant

case	M_e [-]	type	Λ_{swp} [deg]	β_H [-]	Re_1 [1/m]
I	10^{-3}	CF	45	0.2	1e7
II	10^{-3}	TS	0	0	5.8e2
III	0.8	M1	0	0	2.0e3
IV	2.5	M1	0	0	5.0e6
V	10	M2	0	0	9.8425e6

case	T_e [K]	\bar{T}_w [K]	Re [-]	$\omega u_e / \ell_e$ [-]	β / ℓ_e [-]
I	220	220	$1000\sqrt{2}$	0	$\pi\sqrt{2}/15$
II	300	adiab.	580	0.06	0
III	215	adiab.	580	0.04	0.1
IV	600/4.05	adiab.	3000	0.04	0.1
V	278	adiab.	2000	0.075	0

Table 5.1: Conditions of the test cases used to investigate the propagation of base-flow inaccuracies into the stability predictions.

Pr [-]	γ [-]	c_p [J/kg-K]	R [J/kg-K]	μ_{ref} [kg/m-s]	T_{ref} [K]	S_μ [K]
0.70	1.4	1004.5	287	1.716e-5	273.15	110.6

Table 5.2: Fixed thermotransport parameters for the analyses in § 5.3.

Prandtl number (Eq. 4.5). The values of the necessary thermotransport parameters employed are detailed in Table 5.2.^f The base-flow self-similar solutions are obtained with the DEKAF flow solver (see chapter 7). The full study can be found in Ref. 2.

5.3.1 Base-flow grid convergence

The first step is to determine the accuracy of the base-flow solution as a function of the grid resolution (\bar{N}). To that end, paired base-flow computations are performed with \bar{N} and $2\bar{N} - 1$ nodes. Both grids will therefore share the \bar{N} grid points of the primary grid. The error of the solution is then evaluated as the ∞ -norm of the difference between the primary and the better-resolved auxiliary solution, noted as $|\epsilon(\bar{q}_{2N-1}, \bar{q}_N)|_\infty$. The flow variable chosen to evaluate the accuracy of the solution is the second derivative of the non-dimensional parameter \bar{f} with the self-similar wall-normal quantity η , representative of the shear in the flow.

In Fig. 5.2 one can observe how, the linear increase in \bar{N} results in an exponential convergence of the solution, thanks to the spectral of the numerical method employed in DEKAF (see chapter 7). The figure also shows that all profiles are

^fNote that R , c_p and γ are not independent from one-another, since $\gamma = 1/(1 - R/c_p)$. However, all three are reported for the sake of completeness.

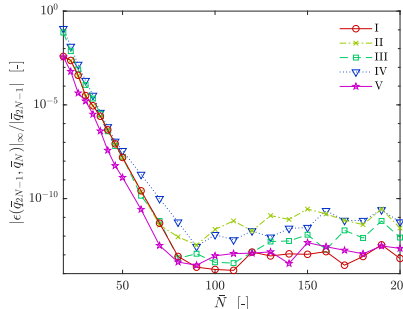


Figure 5.2: Relative base-flow error based on $\partial^2 \bar{f} / \partial \eta^2$ as a function of the number of nodes for all cases in Table 5.1.

numerically converged for $\bar{N} > 90$.

5.3.2 Interpolation errors

The resolution of the stability problem is usually performed in a different grid than that of the base flow. It is therefore necessary to perform an interpolation from the former to the latter, which can be a source of numerical inaccuracy. Such numerical inaccuracy is evaluated using a primary grid of size \bar{N} and an auxiliary one of size $2\bar{N} - 1$. The solution on the primary grid is then interpolated onto the auxiliary one using various interpolation techniques:

- Linear: first-order interpolation.
- Spline: third-order interpolation.
- GICM: Groot-Illingworth-Chebyshev-Malik interpolation detailed in § 7.4.

The aforementioned techniques are compared to the non-interpolated base-flow error, obtained in § 5.3.1 and presented in Fig. 5.2. By comparing the error of the non-interpolated solution to that of the interpolated one, it is possible to determine the error associated to the interpolation itself. In Fig. 5.3 one can observe how the linear and spline interpolations result in linearly-decreasing errors in the log-log scale, which a slope corresponding to the order of their interpolation. Moreover, the GICM method is seen to introduce no interpolation error, profiting of the spectral accuracy of the Chebyshev polynomials (see § 7.4).

5.3.3 Stability grid convergence

Fixing the base-flow resolution to $\bar{N} = 100$, which was observed in § 5.3.1 to be sufficiently converged, one can then proceed to analyze the error introduced by the

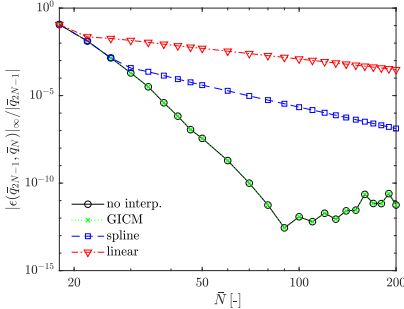


Figure 5.3: Relative interpolation error based on $\partial^2 \tilde{f} / \partial n^2$ as a function of the number of nodes for case IV in Table 5.1, and for various interpolation methods.

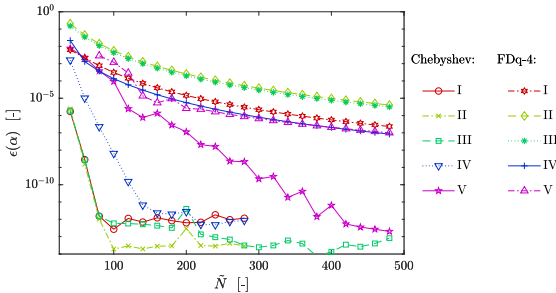


Figure 5.4: Eigenvalue error as a function of the number of stability nodes for all cases in Table 5.1, and for the two numerical methods. The base-flow grid size is fixed to $\bar{N} = 100$.

use of various stability grids. Following the observations made in § 5.3.2, the base-flow solutions are projected onto the stability grid using the spectrally-accurate GICM interpolation. The LST problem is subsequently resolved employing two numerical methods – with pseudo-spectral Chebyshev collocation points [23, 24], or with fourth-order finite-differences on a non-uniform grid. The differentiation matrices required for the latter are computed with the FDq library [25, 26], kindly provided by Dr. Hermanns, and available in the VESTA toolkit^g. The fourth-order finite-difference method is commonly used in the stability community, being the one featured in the studies carried out at Texas A & M University with EPIC [27, 28].

Figure 5.4 displays the evolution of the relative error in the perturbation complex wave number as a function of the number of nodes conforming the stability grid, for the Chebyshev and FDq-4 methods. The reference α value is taken as that at the maximum stability-grid resolution. The exponential decrease in the er-

^gVESTA stands for VKI extensible stability and transition analysis.

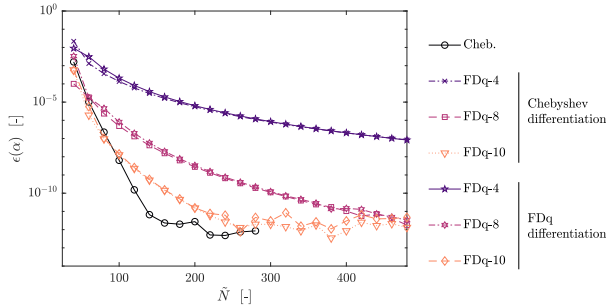


Figure 5.5: Eigenvalue error as a function of the number of stability nodes for case IV in Table 5.1, and for various numerical methods and base-flow differentiation methodologies. The base-flow grid size is fixed to $\bar{N} = 100$.

rors corresponding to the Chebyshev method highlights its spectral-convergence capabilities. Contrarily, the FDq-4 method displays a significantly slower linear convergence, characteristic of such techniques. Analyzing solely the results corresponding to the Chebyshev method, it is worth highlighting the slower convergence displayed by case V with respect to the others.

The large difference in the convergence characteristics of the Chebyshev and the FDq-4 methods observed in Fig. 5.4 is in agreement with the observations of Paredes *et al.* [26] and De Tullio *et al.* [29]. The authors reported that the best compromise between accuracy and computational cost was achieved with FDq-8 or FDq-10. In order to corroborate this claim, various analyses are performed at different finite-difference orders for case IV. Figure 5.5 shows that indeed using FDq-8 or FDq-10 improves the convergence behavior, bringing it close to the spectral convergence of the Chebyshev method.

Figure 5.5 also compares two different methodologies for the computation of the base-flow spatial gradients. They are either computed with the Chebyshev differentiation matrices used to obtain the base-flow solution, or with the FDq matrices used for the stability problem. One can observe that there is a very small difference in the associated convergence behavior.

5.3.4 Base-flow-induced errors

In order to evaluate how the inaccuracies associated to under-resolved base flows propagate to the stability predictions, a parametric study is performed independently varying both the base-flow and stability resolution (\bar{N} and \tilde{N}). The Chebyshev method is used for all base-flow computations, and both the Chebyshev and FDq-4 methods are used for the stability studies. The laminar base-flow profiles are projected onto the stability grid using the GICM interpolation, which was ob-

served in § 5.3.2 to introduce an inappreciable interpolation error. The reference α value is taken as that corresponding to the best base-flow and stability resolution, using the Chebyshev method for the stability computations.

The relationship between the base-flow accuracy and the associated error in the stability characteristics is obtained by pairing each base-flow resolution \bar{N} to the corresponding base-flow accuracy $\epsilon(\bar{q})$ obtained in § 5.3.1. This methodology leads to Fig. 5.6, which presents base-flow-stability error maps, with the base-flow error on the vertical axis, and the corresponding eigenvalue error on the horizontal one. Different markers/colors correspond to different stability grid resolutions \tilde{N} . Fig. 5.6 displays certain recognizable trends reported in § 5.3.3, such as the slower numerical convergence of the FDq-4 method compared to the Chebyshev one. This is visible in the progression of the spacing of $\epsilon(\alpha)$ for the two different methods. Furthermore, the clustering of the solutions obtained with the Chebyshev method represent well the pseudo-spectral convergence property of this method. Another trend in Fig. 5.6 recognizable in § 5.3.3 is the large resolution of the stability grid required by case V to achieve machine-precision accuracy even with the Chebyshev method.

Additionally, one can observe how the use of an insufficient stability resolution (blue-most markers) leads to a stagnation of the wave-number error when improving the base-flow accuracy. The vertical lines of identical markers (same \tilde{N}), appearing in all subfigures represents the stagnation of the wave number error when impairing the base-flow accuracy. A similar stagnation is observed when increasing the stability resolution for a fixed base-flow accuracy. This is deduced from the agglomeration of the different markers (corresponding to different \tilde{N}) at the various levels of base-flow inaccuracy (vertical axis). In other words, for a fixed horizontal position (base-flow accuracy), increasing the stability resolution (going from blue-most to red-most markers) results in an improved eigenvalue accuracy (farther right position) up to a certain limit. The emptiness of the top-left corners of all subplots indeed indicates the existence of a lower limit to the accuracy in the stability predictions for a given base-flow resolution. The most interesting trend observed in Fig. 5.6 is associated to this limit, approximated by the black dashed and solid lines. The former corresponds to a limit where an error of the base-flow profiles results in an equal minimum error in the perturbation wave number $\epsilon(\alpha)|_{\min} = \epsilon(\bar{q})$. Similarly, the latter corresponds to a limit where an error of the base-flow profiles amounts to a minimum error in the perturbation wave number that is one order of magnitude lower $\epsilon(\alpha)|_{\min} = 0.1 \epsilon(\bar{q})$. One can observe how the actual limit of the markers' locations is closer to the latter (solid) than to the former (dashed). The implication of this is that the estimation done by Theofilis [22], of $O(1)$ base-flow errors resulting in $O(1)$ inaccuracies in the stability characteristics, is overly conservative. Instead, base-flow errors appear to generally lead to instability inaccuracies that are one order of magnitude lower than them.

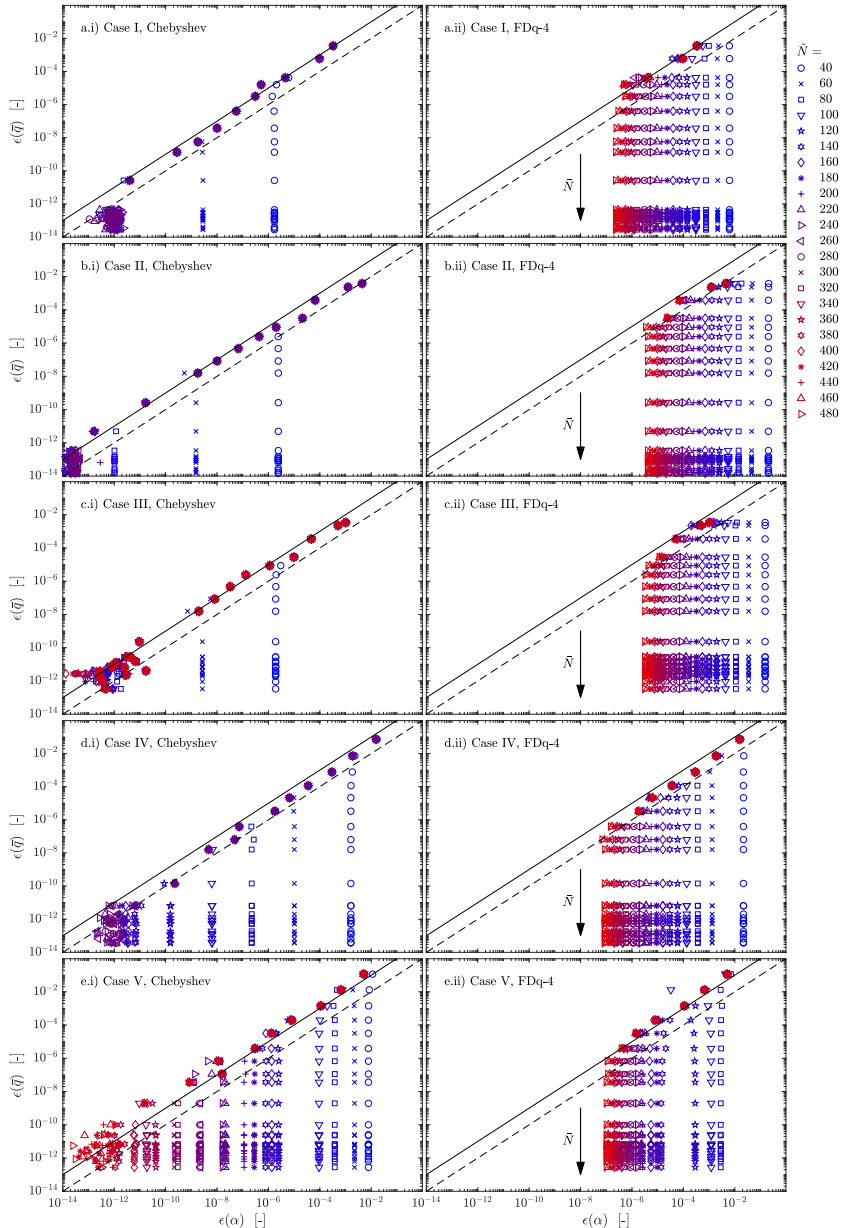


Figure 5.6: Eigenvalue relative error as a function of the base-flow error for all cases in Table 5.1, and for the Chebyshev and FDq-4 numerical methods. Dashed line: $\epsilon(\bar{q}) = \epsilon(\alpha)$. Solid line: $\epsilon(\bar{q}) = 10\epsilon(\alpha)$. Different markers correspond to different stability resolutions (\tilde{N}).

It is important to recall that such under-resolution errors are to be added to the epistemic modeling error associated to boundary-layer and linear-stability theory, outlined in § 5.2.

5.3.5 The importance of performing joint base-flow-stability grid convergence studies

Reed *et al.* [30] highlighted that one should also perform convergence studies evaluating the effect of varying the base-flow resolution on the ultimate stability predictions. If one exclusively varies the stability resolution, keeping the base-flow unchanged, it is possible to reach a fictitious seemingly-converged solution. This is very clearly portrayed in Fig. 5.7. In it, the error in the perturbation wave number is plotted as a function of the stability resolution (\tilde{N}) for various base-flow grids (\bar{N}). The two subplots correspond to computing the relative error with different reference wave numbers – Fig. 5.7a) takes:

$$\alpha^{\text{Ref}}(\bar{N}, \tilde{N}) = \alpha(\bar{N}_{\max}, \tilde{N}_{\max}), \quad (5.33)$$

whereas Fig. 5.7b) takes:

$$\alpha^{\text{Ref}}(\bar{N}, \tilde{N}) = \alpha(\bar{N}, \tilde{N}_{\max}). \quad (5.34)$$

Both the base-flow solution and the stability characteristics are obtained using the Chebyshev method and with the GICM interpolation.

The results obtained with Eq. 5.33 correspond to performing a simultaneous convergence study on both the stability (\tilde{N}) and base-flow (\bar{N}) resolutions, whereas those obtained with Eq. 5.34 correspond to performing a convergence test exclusively on the stability mesh size. Performing the latter, like in Fig. 5.7b), one reaches apparent convergence independently from the base-flow resolution. This convergence is manifestly fictitious, since the companion convergence study in Fig. 5.7a), spanning also various base-flow resolutions, proves that the solution does not converge to the eigenvalue solver's error (ϵ_{eig}) for $\bar{N} < 70$.

Figure 5.7 therefore confirms Reed *et al.*'s [30] statement that stability convergence studies should be performed on both the stability and the base-flow grid size.

5.3.6 Conclusions

The error-propagation investigation carried out in this section allows to draw significant conclusions on the nature of the LST operator in CPG conditions. The most important one is that base-flow inaccuracies of a certain order of magnitude ϵ appear to lead to errors in the predicted stability characteristics that are one order of magnitude lower $\epsilon/10$. This suggests that Theofilis' estimation [22] on the

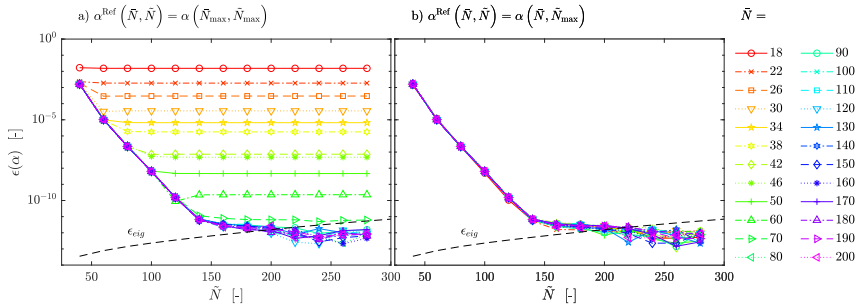


Figure 5.7: Eigenvalue relative error as a function of the stability grid size (\tilde{N}) for various base-flow resolutions (\bar{N}) for case IV in Table 5.1.

base-flow accuracy requirements, when pursuing a certain level of precision in the stability predictions, was actually overly conservative. Moreover, the base-flow-stability error map presented in Fig. 5.4 constitutes an excellent guideline to be used by future researchers when evaluating what level of base-flow inaccuracies are acceptable for a desired final accuracy in the stability predictions.

The evolution of the convergence of wave-number predictions when varying the stability grid size, for a fixed base-flow resolution, appears to be very similar for all considered instabilities; only the hypersonic second-mode case (V) requires a significantly larger stability resolution to achieve machine-precision convergence. Preliminary Reynolds-Orr analyses [31, 32], not included in the present work, suggest that it is associated to the contribution of the temperature perturbation to α . However, results are, at this stage, not sufficiently conclusive so as to elaborate upon them.

The FDq-8 or FDq-10 numerical methods were seen to have similar convergence behavior to the Chebyshev pseudo-spectral method. This is in agreement with what was observed by Paredes *et al.* [26] and De Tullio *et al.* [29].

Similar to the observations of Paredes *et al.* [26] and De Tullio *et al.* [29], the FDq-8 and FDq-10 schemes exhibit a convergence behavior similar to the Chebyshev pseudo-spectral method.

The numerical convergence behavior was seen to vary negligibly if the spatial gradients are obtained with FDq differentiation, rather than Chebyshev. However, one should beware from extrapolating such observations to other base-flow solutions and stability discretizations. Specifically, if the base flow is computed with a method of a lower order of accuracy than that used for the stability computations, one could introduce spurious oscillations in the spatial gradients due to the Gibbs phenomenon [33].

Finally, the importance of performing simultaneous base-flow-stability grid-convergence studies was showcased by changing the reference wave number in

the convergence studies. Not varying the base-flow resolution can reportedly lead to error progressions that appear converged when they are not. In a nutshell: *a solution that is converged to an erroneous base flow remains an erroneous solution.*

References

- [1] U. Goldberg, O. Peroomian, S. Chakravarthy, and B. Sekar. *Validation of CFD++ code capability for supersonic combustor flowfields*. AIAA paper, [1997-3271](#), 1997.
- [2] K. J. Groot, F. Miró Miró, E. S. Beyak, A. J. Moyes, F. Pinna, and H. L. Reed. *DEKAF: spectral multi-regime basic-state solver for boundary layer stability*. AIAA paper, [2018-3380](#), 2018.
- [3] F. Miró Miró, E. S. Beyak, D. Mullen, F. Pinna, and H. L. Reed. *Ionization and Dissociation Effects on Hypersonic Boundary-Layer Stability*. In 31st ICAS Congress, Belo Horizonte, Brazil, 2018. International Council of the Aeronautical Sciences.
- [4] J. C. Cooke. *The Boundary Layer of a Class of Infinite Yawed Cylinders*. Mathematical Proceedings of the Cambridge Philosophical Society, [46\(2\):645–648](#), 1950.
- [5] H. Schlichting. *Boundary-Layer Theory*. McGraw-Hill Series in Mechanical Engineering, 1979.
- [6] J. D. Anderson Jr. *Hypersonic and High Temperature Gas Dynamics*. American Institute of Aeronautics and Astronautics, Reston VA, second edition, 2006.
- [7] F. M. White. *Viscous Fluid Flow*. McGraw-Hill, 2nd edition, 1991.
- [8] R. F. Probstein and D. Elliott. *The Transverse Curvature Effect in Compressible Axially Symmetric Laminar Boundary-Layer Flow*. Journal of Aeronautical Sciences, [23\(3\):208–224](#), 1956.
- [9] I. Nakamura, S. Yamashita, and T. Watanabe. *An effect of sudden circumferential strain on the laminar boundary layer on a rotating cylinder in an axial flow*. Acta Mechanica, [57\(1-2\):69–83](#), 1985.
- [10] E. Truckenbrodt. *Ein Quadraturverfahren zur Berechnung der Reibungsschicht an axial angeströmten rotierenden Drehkörpern*. Ingenieur-Archiv, [22\(1\):21–35](#), 1954.
- [11] A. N. Pokrovskii, V. N. Shmanenkov, and V. M. Shchuchinov. *Determination of the parameters of the boundary layer on rotating axisymmetric cones*. Fluid Dynamics, [19\(3\):367–372](#), 1984.
- [12] T. Watanabe and I. Pop. *Laminar boundary layers on rotating axisymmetric surfaces with suction or injection*. Applied Scientific Research, [52\(2\):101–114](#), 1994.

- [13] D. K. Prabhu, J. C. Tannehill, and J. G. Marvin. *A new PNS code for chemical nonequilibrium flows*. AIAA Journal, **26**(7):808–815, 1988.
- [14] P. Paredes and V. Theofilis. *Accurate parabolic Navier-Stokes solutions of the supersonic flow around an elliptic cone*. 51st AIAA Aerospace Sciences Meeting including the New Horizons Forum and Aerospace Exposition 2013, **2013-0670**, 2013.
- [15] K. J. Groot. *Derivation of and Simulations with BiGlobal Stability Equations*. Technical Report AE5110, VKI and TU Delft, 2013.
- [16] F. Pinna and K. J. Groot. *Automatic derivation of stability equations in arbitrary coordinates and different flow regimes*. AIAA paper, **2014-2634**, 2014.
- [17] C.-L. Chang, H. Vinh, and M. R. Malik. *Hypersonic boundary-layer stability with chemical reactions using PSE*. AIAA paper, **1997-2012**, 1997.
- [18] H. L. Kline, C.-L. Chang, and F. Li. *Hypersonic Chemically Reacting Boundary-Layer Stability using LASTRAC*. AIAA paper, **2018-3699**, 2018.
- [19] A. J. Moyes, E. S. Beyak, T. S. Kocian, and H. L. Reed. *Accurate and efficient modeling of boundary-layer instabilities*. AIAA paper, **2019-1907**, 2019.
- [20] L. Zanus, F. Miró Miró, and F. Pinna. *Parabolized stability analysis of chemically reacting boundary layer flows in equilibrium conditions*. Proceedings of the Institution of Mechanical Engineers, Part G: Journal of Aerospace Engineering, **234**(1):79–95, 2020.
- [21] P. Paredes. *Advances in global instability computations: From incompressible to hypersonic flow*. PhD thesis, 2014.
- [22] V. Theofilis. *Advances in global linear instability analysis of nonparallel and three-dimensional flows*. Progress in Aerospace Sciences, **39**(4):249–315, 2003.
- [23] L. N. Trefethen. *Spectral Methods in MATLAB*. SIAM, 2000.
- [24] F. Pinna. *Numerical study of stability of flows from low to high Mach number*. PhD thesis, Università degli Studi di Roma La Sapienza, 2012.
- [25] M. Hermanns and J. A. Hernández. *Stable high-order finite-difference methods based on non-uniform grid point distributions*. International Journal for Numerical Methods in Fluids, **56**:233–255, 2008.
- [26] P. Paredes, M. Hermanns, S. Le Clainche, and V. Theofilis. *Order 10^4 speedup in global linear instability analysis using matrix formation*. Computer Methods in Applied Mechanics and Engineering, **253**:287–304, 2013.

- [27] N. B. Oliviero, T. S. Kocian, A. J. Moyes, and H. L. Reed. *EPIC: NPSE Analysis of Hypersonic Crossflow Instability on Yawed Straight Circular Cone*. AIAA paper, [2015-2772](#), 2015.
- [28] N. B. Oliviero. *EPIC: a New and Advanced Nonlinear Parabolized Stability Equation Solver*. PhD thesis, Texas A&M University, 2015.
- [29] N. De Tullio, P. Paredes, N. D. Sandham, and V. Theofilis. *Laminar-turbulent transition induced by a discrete roughness element in a supersonic boundary layer*. Journal of Fluid Mechanics, [735:613–646](#), 2013.
- [30] H. L. Reed, W. S. Saric, and D. Arnal. *Linear Stability Theory Applied to Boundary Layers*. Annual Review of Fluid Mechanics, [28\(1\):389–428](#), 1996.
- [31] M. R. Malik, F. Li, M. M. Choudhari, and C.-L. Chang. *Secondary instability of crossflow vortices and swept-wing boundary-layer transition*. Journal of Fluid Mechanics, [399:85–115](#), 1999.
- [32] P. J. Schmid and D. S. Henningson. *Stability and Transition in Shear Flows*, volume 142. Springer, Ney York, Berlin, 2001.
- [33] E. Hewitt and R. E. Hewitt. *The Gibbs-Wilbraham phenomenon: An episode in fourier analysis*. Archive for History of Exact Sciences, [21\(2\):129–160](#), 1979.

6

Boundary conditions

The systems of partial differential equations in § 2.3 and 5, governing perturbation and base-flow quantities need additional conditions at the boundaries of the spatial computational domain. Such boundary conditions are explored in the present section.

When fixing boundary conditions on the perturbation quantities, it is important that they preserve the mathematical character of the ultimate stability problem (see chapter 3). For instance, if working with LST, 2D-LST, BiG or TriG, the boundary conditions must retain the mathematical homogeneity of the generalized eigenvalue problem. This implies that the boundary conditions must relate the various perturbation amplitude variables \tilde{q} , without external forcing terms. This mathematical homogeneity of the eigenvalue problem must not be confused with assuming homogeneous perturbations in one or another boundary. The latter refers to the strict form of the equation system, which must by all means remain an eigenvalue problem without a forcing term, whereas the former simply states that one or another perturbation is zero in one of the spatial limits of the computational domain (E.g.: $\tilde{q}_w = 0$).

6.1 Wall boundary

The wall boundary of the computational domain around atmospheric entry or hypersonic-cruise vehicles corresponds to its surface. An accurate modeling of the problem at stake must therefore account for the physical phenomena occurring

on it. The vehicle surface may be injecting mass or impenetrable, depending on whether the TPS is ablative or not. The decomposition of the TPS also leads to a wide range of porous-layer configurations. Ground tests attempting to partially reproduce the physical phenomena found in flight, typically feature other particularities that must be correctly modeled, such as a regular porous surface, or various mass injection distributions. In order to accurately model all such scenarios, a series of blowing, thermal, and concentration boundary conditions are employed, all of which are laid out in this section.

Most wall boundary conditions can be applied indistinctly to the laminar base-flow problem and to the perturbation problem, after the application of the appropriate ansatz and simplifying hypotheses (see chapter 3). However, others are exclusive to the perturbation quantities, such as the porous (§ 6.1.1.1) or the ablation-mimicking (§ 6.1.1.2) conditions.

All analyses comprised in this dissertation share the no-slip-wall boundary condition, which implies that:^a

$$\bar{u}_w = \bar{w}_w = \tilde{u}_w = \tilde{w}_w = 0. \quad (6.1)$$

On the contrary, wall boundary conditions on the wall-normal velocity, temperature(s), and pressure or partial densities can be imposed in various ways. That is, both for the base-flow (\bar{v} , \bar{T} , \bar{T}_v and $\bar{\rho}$ or $\bar{\rho}_s$) and the perturbation quantities (\tilde{v} , \tilde{T} , \tilde{T}_v and $\tilde{\rho}$ or $\tilde{\rho}_s$).

6.1.1 Blowing boundary condition

In order to model the injection of mass through the wall, one may impose one of the following conditions on the wall-normal base-flow velocity \bar{v}_w :

1. **Impenetrability condition:** there is no mass injection through the surface, and therefore:

$$\bar{v}_w = 0. \quad (6.2)$$

2. **Self-similar blowing:** there is a mass injection such that the self-similar parameter remains constant (see app. D):^b

$$f_w = -\frac{\bar{v}_w \bar{\rho}_w \sqrt{2\xi}}{\rho_e u_e \mu_e}, \quad (6.3)$$

where q_e are the boundary-layer edge quantities, and ξ is the marching variable (Eq. 5.6).

^aFedorov & Malmuth [1] did explore a non-homogeneous boundary condition on the streamwise velocity perturbation due to porous walls. They reported negligible differences on the stability characteristics and N-factor curves.

^bNote that for conical boundary layers, Eq. 6.3 features the transformed wall-normal velocity \bar{v} (Eq. 5.28) rather than \bar{v} .

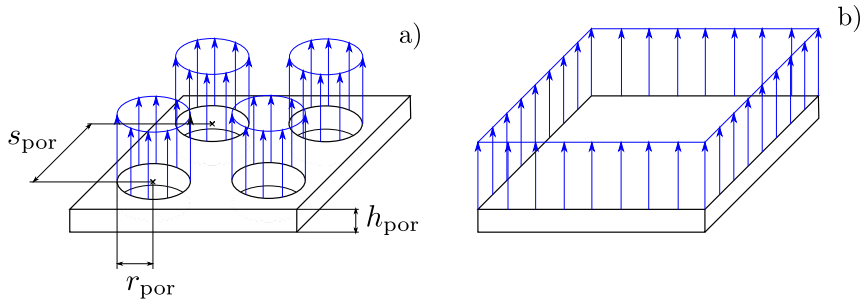


Figure 6.1: Sketch of the blowing assumed by the porous (a) and the ablation-mimicking (b) stability boundary conditions.

3. Mass-flow profile: imposes a surface mass flow $\dot{\bar{m}}_w$ such that:

$$\bar{\rho}_w \bar{v}_w = \dot{\bar{m}}_w , \quad (6.4)$$

where $\dot{\bar{m}}_w$ can either be a prescribed function of the streamwise coordinate, or come from a gas-surface interaction model (see § 4.4).

The investigation of perturbation propagation in wall-blowing configurations also requires the modeling of the wall-normal velocity perturbation at the wall. Authors performing such studies in the past [2–6] have assumed an ideal blowing, with:

$$\tilde{v}_w = 0 . \quad (6.5)$$

However, it is also possible to relax such assumption and relate \tilde{v}_w with the other wall perturbation variables [7]. Two options are presented here:

1. A porous stability boundary condition (PSBC)
2. An ablation-mimicking continuously-blowing stability boundary condition (AMSBC)

The major difference between them lies in the assumption made on the morphology of the surface blowing (see Fig. 6.1). Whilst the PSBC assumes the blowing to be performed through individual discrete whorls, the AMSBC assumes a continuous blowing over the entire surface.

6.1.1.1 Porous stability boundary condition (PSBC)

Gaponov *et al.* [8] and Fedorov *et al.*'s [9] acoustic porous boundary condition links the wall-normal velocity and the pressure perturbation through an admittance K_{por} :

$$\tilde{v}_w = K_{\text{por}} \tilde{p}_w . \quad (6.6)$$

Assuming the porous surface to be composed of regular cylindrical pores, the admittance is a function of the surface porosity n_{por} , the pore radius r_{por} and the porous-layer height h_{por} through [9]:

$$K_{\text{por}} = -\frac{n_{\text{por}}}{Z_0^{\text{por}}} \tanh(\Lambda_{\text{prop}} h_{\text{por}}), \quad (6.7)$$

where the characteristic impedance of the porous wall is defined as:

$$Z_0^{\text{por}} = \sqrt{\frac{Z_1^{\text{por}}}{Y_1^{\text{por}}}}, \quad (6.8)$$

with the impedance of the transmission line (Z_1^{por}) and the shunt admittance (Y_1^{por}) being:

$$Z_1^{\text{por}} = i \omega \bar{\rho}_w \frac{J_0(k_\nu^{\text{por}})}{J_2(k_\nu^{\text{por}})}, \quad (6.9a)$$

$$Y_1^{\text{por}} = -\frac{i \omega}{\bar{\rho}_w \bar{T}_w \bar{R}_w \bar{\gamma}_w} \left(\bar{\gamma}_w + (\bar{\gamma}_w - 1) \frac{J_2(k_\nu^{\text{por}} \sqrt{\bar{\text{Pr}}_w})}{J_0(k_\nu^{\text{por}} \sqrt{\bar{\text{Pr}}_w})} \right), \quad (6.9b)$$

featuring the density, temperature, specific gas constant, Prandtl number and the heat capacity ratio at the wall,^c as well as the 0th- and 2nd-order Bessel functions (J_0 and J_2). The propagation constant is defined as:

$$\Lambda_{\text{prop}} = \sqrt{Z_1^{\text{por}} Y_1^{\text{por}}}, \quad (6.10)$$

the grouping parameter k_ν^{por} is:

$$k_\nu^{\text{por}} = r_{\text{por}} \sqrt{\frac{i \omega \bar{\rho}_w}{\bar{\mu}_w}}, \quad (6.11)$$

and the surface porosity is the surface fraction that is perforated by the pores. For circular pores (Fig. 6.1) this is identically:

$$n_{\text{por}} = \frac{\pi r_{\text{por}}^2}{s_{\text{por}}^2}. \quad (6.12)$$

It is important to note that Eqs. 6.7 - 6.12 are presented as a function of **dimensional** quantities, and are therefore valid with independence of the non-dimensionalization convention. They also do not implicitly assume the base-flow

^cNote that \bar{R} , $\bar{\gamma}$ and $\bar{\text{Pr}}$ are constant over the whole boundary layer in CPG conditions when obtaining the thermal conductivity with Eq. 4.5. These were the assumptions made by Gaponov *et al.* [8] and Fedorov *et al.* [9] when formulating the acoustic boundary condition.

quantities \bar{q} to correspond to a boundary-layer solution, nor do they assume constant \bar{R} , $\bar{\gamma}$ and \bar{Pr} across the boundary layer. They are therefore more general than those presented by Fedorov *et al.* [9], who did make such assumptions. They do, however, assume that the wall temperature is low enough (see Fig. 2.1) so as to have the gas behave as calorically perfect within the pore.

Gaponov *et al.* [8] and Fedorov *et al.* [9] formulated Eq. 6.6 for passive porous surfaces, without mass injection. However, as shown in § 9.1, it can also be successfully employed for blowing surfaces.

It is also important to point out that the porous boundary condition exclusively concerns the **perturbation quantities** (\tilde{q}). The base-flow computation is performed neglecting the discreteness of the blowing pores, thus using a continuously blowing boundary condition in all cases.

The expression for the porous-wall admittance K_{por} is a non-linear function of the perturbation frequency ω . This implies that, if solving the temporal eigenvalue problem (see § 3.1), one must iterate on the value of ω . Moreover, the matrix decomposition laid out in app. H, strongly facilitating the computation of stability neutral curves, cannot be performed.

The expressions for the porous-wall admittance presented in this section are only valid for surfaces with cylindrical evenly-spaced pores. Other expressions have been developed for mesh [10] or random [11] microstructures, and are summarized by Michael & Stephen [12]. Moreover, there is also an ongoing work regarding the characterization of DLR's C/C porous material [13].

There also exists an extensive body of experimental work on porous surfaces of various configurations [10, 14, 15], due to the attenuation of second-mode instabilities achieved with such micro-perforated coatings. Such attenuation and its dependency on the flow condition is explored in § 9.3.

6.1.1.2 Ablation-mimicking continuously-blowing stability boundary condition (AMSBC)

In ablation scenarios, the outgassing does not occur through a series of regularly arranged pores, but rather, it is the entire surface that blows at once (see Fig. 6.1). This motivated the development [16] of a perturbation boundary condition obtained from imposing mass continuity (eq. 2.8) at the wall.

Imposing continuity at the wall is similar to what was done by Mortensen & Zhong [17] when studying chemically reacting flows with TPS ablation. In that case, a mass balance for every species was enforced at the wall.

A special treatment of the wall-normal base-flow velocity appearing in the stability equations is necessary in LST. This treatment is developed in app. F.

6.1.2 Thermal boundary conditions

The thermal wall boundary condition results from imposing one of the following:

1. **Adiabatic wall:** the temperature is considered to be such that the heat-flux is zero at the wall.^d

$$g^{ij} h_{,j}|_w = 0, \quad i = 2. \quad (6.13)$$

2. **Isothermal wall:** the temperature is considered to be constant and equal to a fixed value T_w for all streamwise locations:

$$T_w = \text{cst}. \quad (6.14)$$

3. **Wall temperature profile:** a profile is imposed such that the wall temperature is a function of the streamwise coordinate:

$$T_w = T_w(x). \quad (6.15)$$

4. **Radiative equilibrium:** imposes the radiative equilibrium condition at the surface assuming one-way radiation from the surface to infinity, and thus neglecting flow radiation:

$$g^{ij} \kappa T_{,j} - \dot{\omega}_{\text{rad}} = 0, \quad i = 2, \quad (6.16)$$

or, for TCNE conditions with two temperatures:

$$g^{ij} (\kappa_{tr} T_{,j} + \kappa_v T_{v,j}) - \dot{\omega}_{\text{rad}} = 0, \quad i = 2, \quad (6.17)$$

where $\dot{\omega}_{\text{rad}}$ corresponds to the surface's radiative heat flux:

$$\dot{\omega}_{\text{rad}} = \sigma^{\text{SB}} \epsilon_C T^4, \quad (6.18)$$

and where catalysis has been neglected^e.

5. **Ablative surface energy balance:** imposes the ablative surface energy balance, [17] which for a graphite surface can be simplified to:^f

$$g^{ij} \kappa T_{,j} - \dot{\omega}_{\text{rad}} - \sum_{s \in \mathcal{S}} h_s \dot{m}_{s,w} = 0, \quad i = 2, \quad (6.19)$$

or, for TCNE conditions with two temperatures:

$$g^{ij} (\kappa_{tr} T_{,j} + \kappa_v T_{v,j}) - \dot{\omega}_{\text{rad}} - \sum_{s \in \mathcal{S}} h_s \dot{m}_{s,w} = 0, \quad i = 2, \quad (6.20)$$

^dNote that $g^{ij} h_{,j}|_w$ with $i = 2$, in Cartesian coordinates is equivalent to $\partial h / \partial y|_w$.

^ePlease refer to the work of Bellas *et al.* [18] for further details on how to model catalysis, or to Klentzman & Tumin [19] for its application to boundary-layer stability.

^fThis is the result of simplifying Eq. 21 in Mortensen & Zhong [17] by summing all the species conservation equations (Eq. 23 in Mortensen & Zhong [17]) multiplied by the species enthalpy h_s .

where the surface's radiative heat flux is given by Eq. 6.18, and where catalysis has been neglected^e. Both Eq. 6.19 and 6.20 assume that the wall recession is much lower than the blowing^g.

The use of the three first in the base-flow computation (\tilde{q}), is usually complemented with a homogeneous boundary condition on the temperature perturbation at the wall:

$$\tilde{T}_w = 0. \quad (6.21)$$

This is due to the high thermal inertia of the wall, that cannot adapt to the rapid oscillations of the instabilities, making the wall temperature remain unperturbed. An exception to this [20], are stationary instabilities (like stationary cross-flow) developing in the presence of an adiabatic wall (Eq. 6.13). In such a situation it is recommendable to use an adiabatic stability boundary condition, similar to Eq. 6.13.

The use of the ablative surface energy balance (Eq. 6.19) in the base-flow computation, can either be combined with the homogeneous perturbation condition in Eq. 6.21, if one neglects the effect of the energy mass balance on the temperature perturbation, or with the linearized version of Eq. 6.19 after evaluating the appropriate ansatz (see chapter 3).

For multi-temperature flow assumptions (see § 2.1) it is common [17, 21–23] to assume thermal equilibrium of the perturbations at the wall, thus rendering:

$$\tilde{T}_v = \tilde{T}. \quad (6.22)$$

However, it is a rather simplifying hypothesis. Alternatively, one may impose the gradient of T_v to be zero, the wall to be vibrationally frozen ($T_v = \text{cst.}$), or governed by an energy-transfer equation [24, 25].

6.1.3 Concentration boundary conditions

For those gas mixtures modeling the movement of the various species separately, the wall boundary condition on the species concentrations can be obtained from one of the following mathematical treatments:

1. **Non-catalytic** condition: assumes that no reactions occur at the wall, and that consequently the concentration gradient is zero.^h

$$g^{ij} Y_{s,j} \Big|_w = 0, \quad \begin{cases} \forall s \in \mathcal{S} \\ i = 2 \end{cases}. \quad (6.23)$$

^eOtherwise, an additional term must be added accounting for the wall-normal displacement of the reference frame.

^hNote that $g^{ij} Y_{s,j} \Big|_w$ with $i = 2$, in Cartesian coordinates is equivalent to $\partial Y_s / \partial y \Big|_w$.

2. **Mass fraction profile:** imposes a surface mass-fraction profile as a function of the streamwise direction, such that:

$$Y_{sw} = Y_{sw}(x), \quad \forall s \in \mathcal{S}. \quad (6.24)$$

3. **Ablative surface mass balance:** imposes individual mass conservation equations [17] for the various species at the wall:

$$\rho_s u^i + J_s^i - \dot{m}_{sw} = 0, \quad \forall s \in \mathcal{S}, \quad i = 2, \quad (6.25)$$

where the diffusion fluxes J_s^i are the evaluation of either Eq. 2.12 or 2.18 at the wall, where the species surface source terms \dot{m}_{sw} can be obtained using the gas-surface interaction model described in § 4.4, and where catalysis has been neglected^e. Also note that ρ_s and Y_s are related through Eq. A.1a. Eq. 6.25 also assumes that the wall recession is much lower than the blowing^g. Surface catalysis is also neglected.

These conditions can be imposed on the base-flow quantities (\bar{Y}_s or $\bar{\rho}_s$) without major complication. Similarly, Eqs. 6.23 - 6.25 can also be simplified using the ansatz corresponding to the stability theory of interest (see chapter 3), thus reaching boundary conditions on the perturbation amplitudes (\tilde{Y}_s or $\tilde{\rho}_s$). However, the use of the linearized non-catalytic condition can lead to an ill-conditioning of the stability system matrices. For this reason, it is oftentimes preferable to substitute it for the linearized species-wall-normal-momentum-conservation equation, presented in the following subsection (§ 6.1.4).

6.1.4 Perturbation compatibility boundary conditions

Independently from the boundary condition used on the base-flow pressure perturbation at the wall \bar{p}_w , the perturbation wall pressure will generally not be zero $\tilde{p}_w \neq 0$. This implies that a compatibility condition must be enforced in such boundary. When working with flow assumptions that do not require the species concentrations be among the system state variables (see § 2.1), this condition is commonly [20] taken as the linearized continuity (Eq. 2.8) or wall-normal-momentum-conservation equation (Eq. 2.7b with $i = 2$).

For flow assumptions including the species concentrations among the system state variables, one needs compatibility conditions for each of the species concentration or partial-density perturbations.ⁱ As mentioned in the previous subsection (§ 6.1.3), this is oftentimes done by linearizing the corresponding boundary condition employed on the base-flow quantities (Eqs. 6.23 - 6.25), and for the non-catalytic condition (Eq. 6.23) it leads to an ill-conditioning of the system matrices.

ⁱFor the remaining of the text, only partial-density perturbations will be referred to. However, such references can be indistinctly applied to species-concentration perturbations.

In order to cure such problem, a simplified version of the species-momentum-conservation equation is proposed as a compatibility condition for the various species partial-density perturbations in such mixtures:

$$\rho_s \frac{\partial u^i}{\partial t} + \rho_s u^j u_{,j}^i = -g^{ij} p_{s,j} + \mathbb{T}_{,j}^{ij}, \quad \forall s \in \mathcal{S} \quad \forall i \in [1, 2, 3]. \quad (6.26)$$

The contributions of species interdiffusion and momentum exchange to the momentum balance have been neglected in Eq. 6.26. This may seem like an overly restrictive simplification, but this restriction is already implicit to the usage of mixture momentum equations (Eq. 2.7b) to describe the motion of all species. There is therefore no loss in generality in enforcing Eq. 6.26. The viscous stress tensor \mathbb{T}^{ij} acting on each species is obtained from Eq. 2.9, featuring the mixture (μ), rather than the species viscosity, since there does not exist an accurate mixture rule for viscosity [26].

It is important to note, that it is numerically preferable to employ N_s-1 , instead of N_s , species-wall-normal-momentum equations, together with the mixture-wall-normal-momentum equation. Similarly to what is done with the species continuity equations, it is recommended [27, 28] to let the bath species be the one without a dedicated momentum equation, letting it be accounted for by the mixture momentum equation.

The difference in employing the non-catalytic (Eq. 6.23) or the species-wall-normal-momentum equation (Eq. 6.26) as a compatibility condition was explored in Ref [29]. The use of the species momentum compatibility condition was seen to improve the matrices' condition number in four orders of magnitude, not modifying the stability characteristics. Moreover, it was seen to cure the oscillations appearing on the perturbation mode shape, previously reported by Stuckert & Reed [27].

6.2 Freestream boundary

When solving the laminar Navier-Stokes equations with a shock-capturing numerical scheme in two dimensions^j, the domain limits are similar to those displayed in Fig. 6.2. The inflow typically has all the quantities of interest prescribed (velocities, temperatures, pressure and concentrations), whilst, for the problems of interest in this work, the outflow is supersonic and thus requires no additional conditions. Similarly, when solving the boundary-layer equations (§ 5.1) the freestream conditions to be imposed correspond to the values of the different flow variables on the inviscid wall. This effectively imposes a zeroth-order viscous-inviscid coupling. More elaborate methods, with first- and second-order couplings can be

^jThis includes both cartesian and cylindrical symmetry in the third dimension.

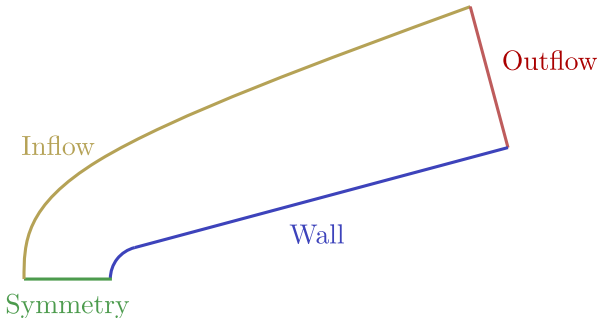


Figure 6.2: Sketch of the main computational limits when solving the 2-D Navier-Stokes equations with a shock-capturing numerical scheme.

found in the work of Brazier *et al.* [30], however, they are out of the scope of this dissertation.

The imposition of boundary conditions on the perturbation quantities (\tilde{q}) is not so straight-forward. In general, perturbations decay exponentially in the inviscid flow region, and it is therefore fair to impose either a Dirichlet:

$$\tilde{q}(y_{\max}) = 0, \quad (6.27)$$

or a Neumann condition on them.^k

$$\left. \frac{\partial \tilde{q}}{\partial y} \right|_{y_{\max}} = 0. \quad (6.28)$$

In general, Neumann conditions are less restrictive on the perturbation shape [20, 31]. However they lead to worse matrix conditioning than Dirichlet conditions. Neumann conditions are therefore preferred in situations with a limited domain extension, such as situations where the shock is very close to the surface.

When imposing Dirichlet conditions, in order to account for the finite size of the computational domain, it is common to free the perturbation amplitude of one of the flow variables, thus not requiring it to be identically zero [20]. In the present work, this is achieved by either liberating the pressure perturbation (\tilde{p}) and imposing wall-normal momentum conservation (Eq. 2.7b with $i = 2$), [20, 32] or by liberating the wall-normal velocity and imposing mixture continuity (Eq. 2.8) [21, 27]. The former approach is taken for CPG and LTE flow assumptions, and the latter for all the others.

^kFor the sake of simplicity, the condition is presented for a Cartesian coordinate system. However, it can be easily generalized to an arbitrary one using tensorial notation: $g^{ij} \tilde{q}_{,j} = 0$, with $i = 2$ (wall-normal direction).

6.2.1 Shock boundary condition

Close to the leading edge, and in high-Mach-number flows over sharp bodies, one encounters shocks that are very close to the vehicle's surface. In such scenarios one can no longer faultlessly assume perturbations to spatially decay fast enough so as to impose Dirichlet or Neumann conditions in the freestream limit of the computational domain. Shocks affect the receptivity problem, and therefore influence the amplitude with which disturbances enter the boundary layer. Waves interacting with a shock generate acoustic, vortical and entropic modes [33, 34]. However, they also affect the stability problem through shock vibration. This led several authors [27, 35–39] to linearize the Rankine-Hugoniot shock-jump relationships, in order to achieve an appropriate perturbation boundary condition to be imposed at the shock boundary.

The Rankine-Hugoniot relations can be expressed in their invariant form as:

$$\frac{\partial y_{\text{sh}}}{\partial t} (\rho_{\text{sh}} - \rho_{\infty}) + y_{\text{sh},j} \left(\rho_{\text{sh}} u_{\text{sh}}^j - \rho_{\infty} u_{\infty}^j \right) = 0, \quad (6.29\text{a})$$

$$\begin{aligned} \frac{\partial y_{\text{sh}}}{\partial t} (\rho_{\text{sh}} u_{\text{sh}}^i - \rho_{\infty} u_{\infty}^i) + y_{\text{sh},j} \left(\rho_{\text{sh}} u_{\text{sh}}^i u_{\text{sh}}^j - \rho_{\infty} u_{\infty}^i u_{\infty}^j \right) + \\ + g^{ij} y_{\text{sh},j} (p_{\text{sh}} - p_{\infty}) = 0, \quad \forall i \in [1, 2, 3], \end{aligned} \quad (6.29\text{b})$$

$$\frac{\partial y_{\text{sh}}}{\partial t} (\rho_{\text{sh}} e_{\text{sh}}^{uvw} - \rho_{\infty} e_{\infty}^{uvw}) + y_{\text{sh},j} \left(\rho_{\text{sh}} u_{\text{sh}}^j h_{\text{sh}}^{uvw} - \rho_{\infty} u_{\infty}^j h_{\infty}^{uvw} \right) = 0, \quad (6.29\text{c})$$

$$Y_{s\text{ sh}} = Y_{s\infty}, \quad (6.29\text{d})$$

$$e_{v\text{ sh}} = e_{v\infty}, \quad (6.29\text{e})$$

where the “sh” and “∞” subindices denote the postshock and preshock quantities, y_{sh} is the instantaneous wall-normal shock position, e^{uvw} and h^{uvw} are the total internal energy and enthalpy:

$$e^{uvw} = e + \frac{1}{2} \sum_{i=1}^3 (u^i)^2 = h - \frac{p}{\rho} + \frac{1}{2} \sum_{i=1}^3 (u^i)^2, \quad (6.30\text{a})$$

$$h^{uvw} = h + \frac{1}{2} \sum_{i=1}^3 (u^i)^2, \quad (6.30\text{b})$$

and where the species concentrations and vibrational-electronic-electron energy are assumed frozen across the shock.¹ Eqs. 6.29 in non-tensorial notation can be found in Pinna [32, Ch. 5] for a Cartesian reference frame. Shock-layer radiation is neglected from the energy balance in Eq. 6.29c.

¹One must note that in scenarios featuring non-zero electron concentrations upstream of the shock, the vibrational-electronic-electron energy can no longer be considered frozen through a shock. Solving the non-conservative product existing due to the electron pressure in such cases is an open research problem [40]. However, non-zero preshock electron concentrations are only present in scenarios with preshock ionization due to strong radiation, which are out of the scope of this dissertation.

It is important to note that the derivative of the wall-normal shock position y_{sh} in the wall-normal direction is by convention: [32]

$$y_{\text{sh},2} = -1. \quad (6.31)$$

Eqs. 6.29 may be linearized by decomposing also the shock position into its mean and perturbed components:

$$y_{\text{sh}} = y_{\text{sh}}(x^i, t) = \bar{y}_{\text{sh}}(x^i) + y'_{\text{sh}}(x^i, t), \quad (6.32)$$

and subsequently applying the appropriate stability ansatz (see chapter 3). In order to eliminate \tilde{y}_{sh} from the list of unknowns, it is typically isolated from the mass shock-jump relation (Eq. 6.29a) and then substituted into the momentum and energy relations (Eq. 6.29b and 6.29c). The perturbation equation system at the shock boundary is completed by the mixture wall-normal momentum conservation equation (Eq. 2.7b with $i = 2$).

One must note that the ansatz applied on the base-flow shock position \bar{y}_{sh} may differ from that applied on the other base-flow quantities, since the dependency on the streamwise and spanwise directions (x and z in Cartesian coordinates) are retained for all stability assumptions. This is done in order to retain the slope of the shock in the equations, following the work of previous authors [27, 35–37, 39].

References

- [1] A. V. Fedorov and N. D. Malmuth. *Parametric Studies of Hypersonic Laminar Flow Control Using a Porous Coating of Regular Microstructure*. AIAA paper, [2008-588](#), 2008.
- [2] M. R. Malik. *Prediction and control of transition in supersonic and hypersonic boundary layers*. AIAA Journal, [27\(11\):1487–1493](#), 1989.
- [3] H. B. Johnson, J. E. Gronvall, and G. V. Candler. *Reacting hypersonic boundary layer stability with blowing and suction*. AIAA paper, [2009-938](#), 2009.
- [4] S. Ghaffari, O. Marxen, G. Iaccarino, and E. S. G. Shaqfeh. *Numerical simulations of hypersonic boundary-layer instability with wall blowing*. AIAA paper, [2010-706](#), 2010.
- [5] F. Li, M. M. Choudhari, C.-L. Chang, and J. White. *Effects of injection on the instability of boundary layers over hypersonic configurations*. Physics of Fluids, [25\(10\)](#), 2013.
- [6] A. V. Fedorov and V. G. Soudakov. *Stability analysis of high-speed boundary-layer flow with gas injection*. AIAA paper, [2014-2498](#), 2014.
- [7] F. Miró Miró. *Numerical Study of the Stability of a Hypersonic Boundary Layer in the presence of Blowing*. Technical Report TR 2015-28, von Karman Institute for Fluid Dynamics, Brussels, Belgium, 2015.
- [8] S. A. Gaponov. *Effect of the Properties of a Porous Coating on Boundary Layer Stability*. Technical Report TM 75235, NASA, Santa Barbara, CA, 1978.
- [9] A. V. Fedorov, N. D. Malmuth, A. Rasheed, and H. G. Hornung. *Stabilization of hypersonic boundary layers by porous coatings*. AIAA Journal, [39\(4\):605–610](#), 2001.
- [10] S. V. Lukashevich, A. A. Maslov, A. N. Shiplyuk, A. V. Fedorov, and V. G. Soudakov. *Stabilization of High-Speed Boundary Layer Using Porous Coatings of Various Thicknesses*. AIAA Journal, [50\(9\):1897–1904](#), 2012.
- [11] A. V. Fedorov, A. N. Shiplyuk, A. A. Maslov, E. Burov, and N. D. Malmuth. *Stabilization of a hypersonic boundary layer using an ultrasonically absorptive coating*. Journal of Fluid Mechanics, [479\(479\):99–124](#), 2003.
- [12] V. Michael and S. O. Stephen. *Nonlinear stability of hypersonic flow over a cone with passive porous walls*. Journal of Fluid Mechanics, [713:528–563](#), 2012.

- [13] V. C. Sousa, D. Patel, J. B. Chapelier, V. Wartemann, A. Wagner, and C. Scalo. *Numerical investigation of second-mode attenuation over carbon/carbon porous surfaces*. Journal of Spacecraft and Rockets, **56**(2):319–332, 2019.
- [14] S. Willems and A. Gühan. *Damping of the Second Mode Instability with Regular and Random Porous Surfaces on Slender Cone in Hypersonic Flow*. In NATO RTO-MP-AVT-200, 2012.
- [15] A. Wagner, M. Kuhn, J. Martinez Schramm, and K. Hannemann. *Experiments on passive hypersonic boundary layer control using ultrasonically absorptive carbon-carbon material with random microstructure*. Experiments in Fluids, **54**(10), 2013.
- [16] F. Miró Miró and F. Pinna. *Effect of uneven wall blowing on hypersonic boundary-layer stability and transition*. Physics of Fluids, **30**(084106), 2018.
- [17] C. Mortensen and X. Zhong. *Real-Gas and Surface-Ablation Effects on Hypersonic Boundary-Layer Instability over a Blunt Cone*. AIAA Journal, **54**(3):980–998, 2016.
- [18] G. Bellas-Chatzigeorgis, A. Turchi, A. Viladegut, O. Chazot, P. Barbante, and T. E. Magin. *Development of catalytic and ablative gas-surface interaction models for the simulation of reacting gas mixtures*. AIAA paper, **2017-4499**, 2017.
- [19] J. Klentzman and A. Tumin. *Stability and receptivity of high speed boundary layers in oxygen*. AIAA paper, **2013-2882**, 2013.
- [20] L. M. Mack. *Boundary-Layer Linear Stability Theory*. In Special Course on Stability and Transition of Laminar Flow, AGARD 709. AGARD, 1984.
- [21] M. L. Hudson, N. Chokani, and G. V. Candler. *Linear stability of hypersonic flow in thermochemical nonequilibrium*. AIAA Journal, **35**(6):958–964, 1997.
- [22] H. B. Johnson and G. V. Candler. *Hypersonic boundary layer stability analysis using PSE-Chem*. AIAA paper, **2005-5023**, 2005.
- [23] H. L. Kline, C.-L. Chang, and F. Li. *Hypersonic Chemically Reacting Boundary-Layer Stability using LASTRAC*. AIAA paper, **2018-3699**, 2018.
- [24] G. Bellas-Chatzigeorgis. *Development of Advanced Gas-Surface Interaction Models for Chemically Reacting Flows for Re-Entry Conditions*. PhD thesis, von Karman Institute and Politecnico di Milano, 2018.

- [25] I. Nompelis, G. V. Candler, and M. S. Holden. *Effect of vibrational nonequilibrium on hypersonic double-cone experiments.* AIAA Journal, **41**(11):2162–2169, 2003.
- [26] V. M. Zhdanov. *Transport phenomena in a partly ionized gas.* Journal of Applied Mathematics and Mechanics, **26**(2):401–413, 1962.
- [27] G. Stuckert and H. L. Reed. *Linear Disturbances in Hypersonic, Chemically Reacting Shock Layers.* AIAA Journal, **32**(7):1384–1393, 1994.
- [28] G. K. Stuckert. *Linear Stability Theory of Hypersonic, Chemically Reacting Viscous Flows.* PhD thesis, Arizona State University, 1991.
- [29] F. Miró Miró and F. Pinna. *Linear Stability Analysis of a Hypersonic Boundary Layer in Equilibrium and Non-Equilibrium.* AIAA paper, **2017-4518**, 2017.
- [30] J. P. Brazier, B. Aupoix, and J. Cousteix. *Second-Order Effects in Hypersonic Laminar Boundary Layers.* In T. Murthy, editor, Computational Methods in Hypersonic Aerodynamics. Kluwer Academic, 1991.
- [31] H. L. Reed, W. S. Saric, and D. Arnal. *Linear Stability Theory Applied to Boundary Layers.* Annual Review of Fluid Mechanics, **28**(1):389–428, 1996.
- [32] F. Pinna. *Numerical study of stability of flows from low to high Mach number.* PhD thesis, Università degli Studi di Roma La Sapienza, 2012.
- [33] A. V. Fedorov. *Transition and Stability of High-Speed Boundary Layers.* Annual Review of Fluid Mechanics, **43**(1):79–95, 2011.
- [34] P. Balakumar and L. R. Owens. *Stability of hypersonic boundary layers on a cone at an angle of attack.* 40th AIAA Fluid Dynamics Conference, **2009-3555**, 2010.
- [35] G. V. Petrov. *Stability of thin Viscous Shock Layer on a Wedge in Hypersonic Flow of a Perfect Gas.* In V. V. Kozlov, editor, Laminar-Turbulent Transition. International Union of Theoretical and Applied Mechanics., pages 487–493. Springer-Verlag, 1985.
- [36] S. Cowley and P. Hall. *On the instability of hypersonic flow past a wedge.* Journal of Fluid Mechanics, **214**:17–42, 1990.
- [37] C.-L. Chang, M. R. Malik, and M. Y. Hussaini. *Effects of shock on the stability of hypersonic boundary layers.* AIAA paper, **90-1448**, 1990.
- [38] F. Pinna and P. Rambaud. *Effects of shock on hypersonic boundary layer stability.* Progress in Flight Physics, **5**:93–106, 2013.

- [39] S. O. Seddougui. *Stability of Hypersonic Flow Over a Cone*. In P. R. B. Du-jarric and C., editors, AGARD CP-541, chapter 28, pages 245–254. NATO, Neuilly sur Seine, France, 1994.
- [40] Q. Wagnier, S. Faure, B. Graille, T. E. Magin, and M. Massot. *Numerical treatment of the nonconservative product in a multiscale fluid model for plasmas in thermal nonequilibrium: application to solar physics*. (in Revision), 2018.

Part II

Tools

7

DEKAF flow solver

The instability spectrum and the ultimate transition predictions are very sensitive to the accuracy and smoothness of the laminar base-flow field. Achieving a laminar solution to the Navier-Stokes equations with the necessary numerical convergence (see § 5.3) normally requires large mesh sizes and computational resources. This is even more so when modeling highly complex physical phenomena like those featuring in flows around atmospheric reentry vehicles (see chapter 2), which require high-fidelity thermophysical modeling (see chapter 4). Moreover, as argued in § 5.2, stability theories such as LST or PSE, have an intrinsic model error with respect to that of the Navier-Stokes equations, that justifies the use of simplified base-flow fields.

These considerations motivated the development of the DEKAF flow solver (Digits^a by Ethan, Koen, Alex and Fernando). The tool is the result of a collaboration between Texas A&M University, the von Karman Institute, and the TU Delft. It consists of a boundary-layer solver, coupled^b with inviscid solvers (shock-jump relations and a 1-D Euler solver) for simple geometries. It uses a spectral method in the wall-normal direction, thus maximizing the accuracy obtained from each mesh node. A variable-order forward finite-difference (FD) scheme is deployed in the marching direction. The solution at each marching station is obtained through a Newton-Raphson method on the linearized non-dimensional boundary-layer equations (see § 5.1).

^aThe initial word “Digits” highlights the design motivation of the tool – the pursuit of high numerical convergence of the base-flow solutions.

^bThe inviscid and visous regions are linked through a zeroth-order coupling [1].

Regarding its thermophysical modeling capabilities, DEKAF can resolve boundary layers in CPG, TPG, CNE, LTE, TCFG, TNE, and TCNE conditions. The only flow assumption of those summarized in Table 2.1 that is not currently supported is LTEED. It includes all mixtures presented in app. J, all base-flow boundary conditions in chapter 5, and all thermodynamic, transport and chemical models presented in chapter 4.

Authorship disclaimer. The DEKAF flow solver is the result of a joined effort of the author together with Ethan S. Beyak^c, Koen J. Groot^d and Alexander J. Moyes^c, under the supervision of Helen L. Reed^c. The contribution of Daniel Mullen^c must also be acknowledged, since he performed the simulations with DPLR used to verify the implementation in DEKAF. The theoretical and technical work collected into this chapter and in app. G is therefore not an exclusive development of the author.

7.1 Shock-jump relations

The shock jump relations are evaluated for both wedge and conical surfaces. The shock characteristics vary with the flow assumption (see Table 2.1). However, the equations to satisfy are in all cases the normal shock relations:

$$\rho_\infty U_\infty = \rho_{\text{sh}} U_{\text{sh}}, \quad (7.1a)$$

$$p_\infty + \rho_\infty U_\infty^2 = p_{\text{sh}} + \rho_{\text{sh}} U_{\text{sh}}^2, \quad (7.1b)$$

$$h_\infty + U_\infty^2/2 = h_{\text{sh}} + U_{\text{sh}}^2/2, \quad (7.1c)$$

which relate the preshock (q_∞) and postshock (q_{sh}) conditions, where the U velocity is oriented in the direction normal to the shock.

Depending on the flow assumption, one can distinguish between three types of shock jumps:

1. Chemically and vibrationally frozen. It is used for CPG, TCFG, TNE and TCNE conditions, and across the shock $c_{p\infty} = c_{p\text{sh}}$ and $Y_{s\infty} = Y_{s\text{sh}}$.
2. Chemically frozen yet in vibrational equilibrium. It is used for TPG and CNE conditions, and across the shock $Y_{s\infty} = Y_{s\text{sh}}$, with the enthalpies being non-linear functions of T: $h_\infty = h_\infty(T_\infty)$ and $h_{\text{sh}} = h_{\text{sh}}(T_{\text{sh}})$, following the RRHO model detailed in § 4.1.

^cAt the time affiliated with Texas A&M University.

^dAt the time affiliated with TU Delft.

3. Chemically and vibrationally in equilibrium. It is used in LTE and LTEED conditions. The composition depends on the pre-shock and post-shock pressure and temperature $Y_{s\infty} = Y_{s\infty}(p_\infty, T_\infty)$ and $Y_{s\text{sh}} = Y_{s\text{sh}}(p_{\text{sh}}, T_{\text{sh}})$, through the equilibrium systems detailed in app. B. The enthalpy therefore depends explicitly on T and implicitly on T and p through the equilibrium system $h_\infty = h_\infty(T_\infty, Y_{s\infty}(p_\infty, T_\infty))$ and $h_{\text{sh}} = h_{\text{sh}}(T_{\text{sh}}, Y_{s\text{sh}}(p_{\text{sh}}, T_{\text{sh}}))$.

Shocks in non-equilibrium conditions (TNE, CNE or TCNE) notably have an inclination angle that varies with the streamwise position. Such a variation is not taken into consideration by the solver. Only chemical and vibrational-relaxation dynamics along the inviscid-wall streamline can be accounted for through the 1-D inviscid solver (see § 7.2). However, the modification of the shock position due to such streamwise variations is neglected. Nevertheless, as observed with the Mach-35 verification case against DPLR (§ 7.6.9), neglecting the variation of the shock inclination is an acceptable simplification for the cases of interest.

Two different shock geometries are supported – an oblique shock, such as that produced by an infinitely-sharp wedge, and a conical shock, such as that induced by an infinitely-sharp cone. For oblique shocks, of type 2 and 3, Eqs. 7.1 are solved with the iterative method proposed by Anderson [2, § 14.3]. The difference between type 2 (TPG or CNE) and 3 (LTE or LTEED) lies in the composition used for the evaluation of the enthalpy and the equation of state. For type 1 shocks (CPG, TCFG, TNE, and TCNE), Eqs. 7.1 conveniently simplify to the so-called “ θ - β -M relation” (θ_{wd} - θ_{sh} - M_∞ following the dissertation’s nomenclature):

$$\tan(\theta_{wd}) = 2 \cot(\theta_{\text{sh}}) \frac{M_\infty^2 \sin^2(\theta_{wd}) - 1}{M_\infty^2 (\gamma + \cos(2\theta_{\text{sh}})) + 2}, \quad (7.2)$$

where θ_{wd} is the wedge inclination angle, θ_{sh} is the shock angle, and γ corresponds to the frozen heat capacity ratio:

$$\gamma^{Fr} = \frac{c_p}{c_v}. \quad (7.3)$$

where the heat capacities c_p and c_v are defined in § 4.1.

The resolution of conical shock jumps and the inviscid flow field contained therein is slightly more complex. For shocks of type 1, one must solve the Taylor-Maccoll [3] equation:

$$\begin{aligned} \frac{\gamma - 1}{2} \left[1 - u_*^2 - \left(\frac{du_*}{d\theta} \right)^2 \right] \left[2u_* + \frac{du_*}{d\theta} \cot(\theta) + \frac{d^2 u_*}{d\theta^2} \right] + \\ - \frac{du_*}{d\theta} \left[u_* \frac{du_*}{d\theta} + \frac{du_*}{d\theta} \frac{d^2 u_*}{d\theta^2} \right] = 0, \end{aligned} \quad (7.4)$$

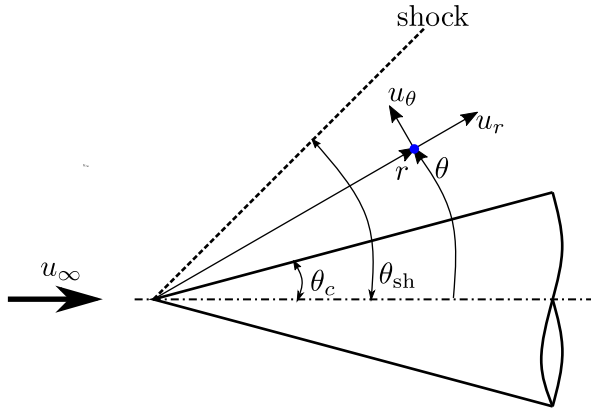


Figure 7.1: Sketch of the coordinate system employed in the resolution of conical inviscid flow fields.

where the coordinate system and the variables are those involved in Fig. 7.1, with:

$$u_* = \frac{u_r}{h_\infty + u_\infty^2/2}, \quad (7.5)$$

and γ corresponds to the frozen heat capacity ratio (Eq. 7.3). Eq. 7.4 is solved with the iterative procedure proposed by Anderson [4, § 10.4]. Conical shock types of types 2 and 3, one must solve a system of three ordinary differential equations (ODE) [2, § 14.8]:

$$\frac{du_\theta}{d\theta} = \frac{a^2}{u_\theta^2 - a^2} \left(2u_r + u_\theta \cot(\theta) - \frac{u_r u_\theta^2}{a^2} \right), \quad (7.6a)$$

$$\frac{dp}{d\theta} = -\frac{\rho u_\theta a^2}{u_\theta^2 - a^2} (u_r + u_\theta \cot(\theta)), \quad (7.6b)$$

$$u_\theta = \frac{du_r}{d\theta}, \quad (7.6c)$$

where a is the speed of sound. If one is solving chemically frozen shocks (type 2), then a is the frozen speed of sound:

$$a^{Fr} = \sqrt{\frac{c_p}{c_v} R T}. \quad (7.7)$$

where the heat capacities c_p and c_v are defined in § 4.1. However, the resolution of shocks in chemical equilibrium (type 3) claims for the use of the equilibrium speed of sound [5, Ch. 2]:

$$a^{eq} = \sqrt{\frac{c_p^{eq}}{c_v^{eq}} R T \left(1 - p \mathcal{M} \sum_{s \in S} \frac{1}{\mathcal{M}_s} \frac{\partial Y_s}{\partial p} \right)^{-1}}. \quad (7.8)$$

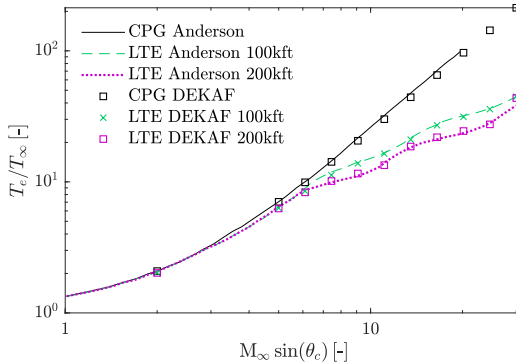


Figure 7.2: Temperature jump between the preshock and the inviscid wall for a conical flowfield in CPG and LTE conditions. Verification against Anderson [2, § 14.8] for two different altitudes (100 and 200 kft).

where the bracketed term accounts for the variation of density with pressure at constant temperature, and where the equilibrium heat capacities also account for the variation of the enthalpy due to composition changes:

$$c_p^{\text{eq}} = c_p + \sum_{s \in S} h_s \frac{\partial Y_s}{\partial T}, \quad (7.9a)$$

$$c_v^{\text{eq}} = c_v + \sum_{s \in S} e_s \frac{\partial Y_s}{\partial T}. \quad (7.9b)$$

The derivative of the equilibrium composition is obtained as presented in app. B. Eqs. 7.6 are solved with the iterative method proposed by Anderson [2, § 14.8]. Figure 7.2 shows a verification of the aforementioned implementation for equilibrium shock by comparing against the data presented by Anderson.

7.2 Inviscid non-equilibrium 1-D solver

The inviscid region of a flow in chemical and/or vibrational non-equilibrium experiences a variation of its composition and/or thermal energy partitioning due to finite-rate chemical reactions and internal-energy-mode relaxation. Fully accounting for these phenomena requires a two-dimensional Euler solver with shock capturing. However, a valid approximation consists in considering the shock to be chemically and/or vibrationally frozen, and then account for the non-equilibrium processes exclusively through a one-dimensional variation along the wall inviscid streamline^e.

^eNote that the wall inviscid streamline coincides with the boundary-layer edge when using a zeroth-order viscous-inviscid coupling. For this reason variables with the e subindex are employed in this

u_e [m/s]	T_e [K]	$T_{v,e}$ [K]	p_e [Pa]	$Y_{N_2,e}$ [-]	$Y_{O_2,e}$ [-]
10 000	10 000	300	28 819	0.7671	0.2329

Table 7.1: Summary of the values of the various flow variables at $x = 0$ for the verification of DEKAF's inviscid solver against DPLR.

To that end, the 1-D Euler equations are solved along the streamline:

$$\frac{d(\rho_e u_e)}{dx} = 0, \quad (7.10a)$$

$$\rho_e u_e \frac{du_e}{dx} = -\frac{dp_e}{dx}, \quad (7.10b)$$

$$\frac{dh_e^u}{dx} = 0, \quad (7.10c)$$

$$\rho_e u_e \frac{dY_{s,e}}{dx} = \dot{\omega}_{s,e}, \quad \forall s \in \mathcal{S}, \quad (7.10d)$$

$$\rho_e u_e \frac{de_{v,e}}{dx} = Q_{TV,e} + \sum_{s \in \mathcal{S}_{mol}} e_{vs,e} \dot{\omega}_{s,e}. \quad (7.10e)$$

Note that Eq. 7.10e assumes Candler's [6] vibration-chemistry-vibration non-preferential coupling. However, it is not recommended for shock tubes – see § 4.2.6 in Ref. 7 for more accurate and elaborate models.

The equations are solved using a variable-order explicit marching scheme matching the finite-difference order with which the boundary-layer solution is later marched (see § 7.3). Note that in order to ensure that the sum of all concentrations remains equal to one, only $N_s - 1$ concentration equations (Eq. 7.10d) are solved, substituting the N_s^{th} for the concentration condition (Eq. 5.3h). Inviscid flows in CNE do not require Eq. 7.10e, since thermal equilibrium is assumed, and similarly flows in TNE are solved without Eq. 7.10d.

Figure 7.3 presents a verification of DEKAF's inviscid 1-D solver against NASA's DPLR (Data-parallel line relaxation) code [8]. For that purpose, DPLR was run on a simple 2-D mesh, with periodic conditions at both limits of the vertical axis, and solving the steady Euler equations in the horizontal direction (x). The conditions prescribed at $x = 0$ are those presented in Table 7.1.

7.3 Numerical method

One of the strongest features in DEKAF lies in its wall-normal spectral accuracy. It deploys a Chebyshev-collocation method based on Chebyshev-Gauss-Lobatto (CGL) point, with a differentiation matrix that uses the complete node stencil to compute the derivatives at each point. More information on spectral methods in section.

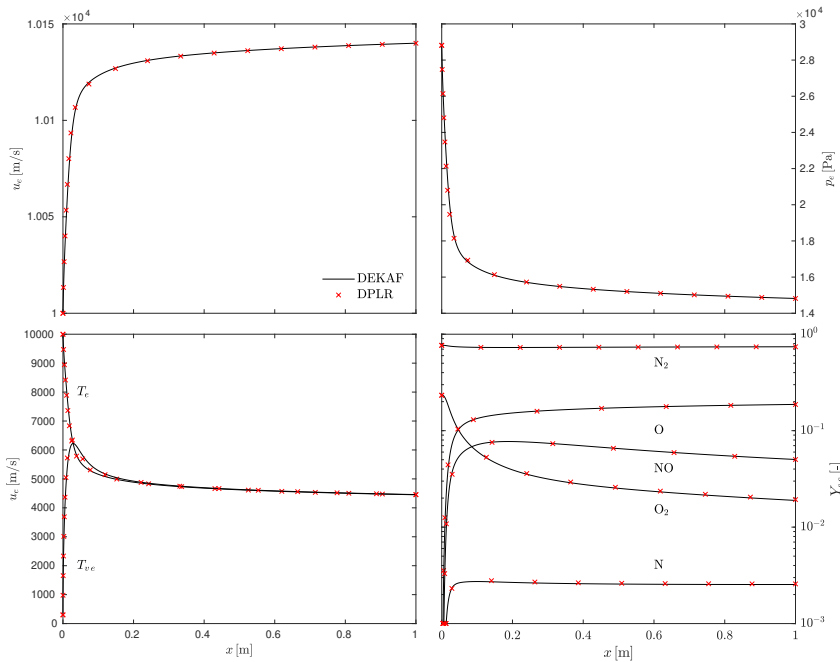


Figure 7.3: Verification of DEKAF's inviscid 1-D TCNE solver against DPLR. The conditions prescribed at $x = 0$ are presented in Table 7.1.

general and Chebyshev-collocation in particular may be found in Trefethen [9], Canuto *et al.* [10] or Burden & Faires [11].

The boundary-layer equations are solved in their non-dimensional form (Eq. 5.4 for TCNE). First the quasi-self-similar equations are solved – dropping the terms explicitly including the marching ξ variable, shown in blue in the non-dimensional equations in § 5.1. As argued in app. D, this solution will only be actually self-similar if it satisfies a series of additional conditions. The equation system is linearized, decomposing the flow variables^f into a *pseudo*-basic-state component \bar{q} and an update \hat{q} :

$$q = \bar{q} + \hat{q}. \quad (7.11)$$

The resulting matrix system can be expressed as:^g

$$\underline{\underline{\mathcal{A}}} \cdot \underline{\hat{\mathcal{F}}} = -\underline{\underline{\mathcal{G}}}, \quad (7.12)$$

where $\underline{\hat{\mathcal{F}}}$ includes the updates of the flow variables^f, $\underline{\underline{\mathcal{A}}}$ is the matrix of coefficients resulting from the linearization of the equations, and $\underline{\underline{\mathcal{G}}}$ is the residual of the equations. $\underline{\underline{\mathcal{A}}}$ and $\underline{\underline{\mathcal{G}}}$ are therefore exclusive functions of the pseudo-basic-state quantities $\underline{\hat{\mathcal{F}}}$. The equation system 7.12 can thus be solved iteratively with a Newton-Raphson method, successively updating the pseudo-basic-state quantities:

$$\underline{\hat{\mathcal{F}}}_k = -\left[\underline{\underline{\mathcal{A}}}\left(\underline{\hat{\mathcal{F}}}_k\right)\right]^{-1} \cdot \underline{\underline{\mathcal{G}}}\left(\underline{\hat{\mathcal{F}}}_k\right), \quad (7.13a)$$

$$\underline{\hat{\mathcal{F}}}_{k+1} = \underline{\hat{\mathcal{F}}}_k + \underline{\hat{\mathcal{F}}}_k. \quad (7.13b)$$

If necessary, the solution is then marched in the ξ direction, by incorporating the terms explicitly containing ξ into the matrix system, which at a given marching station i becomes.^h

$$\left(\underline{\underline{\mathcal{A}}}^i + \xi \underline{\underline{\mathcal{B}}}^i + \xi \underline{\underline{\mathcal{C}}}^i D_1^{\text{FDn}}\right) \cdot \underline{\hat{\mathcal{F}}}^i = -\left(\underline{\underline{\mathcal{G}}}^i + \xi \underline{\underline{\mathcal{H}}}^i + \xi \underline{\underline{\mathcal{C}}}^i \sum_{j=i-n}^{i-1} D_j^{\text{FDn}} \cdot \underline{\hat{\mathcal{F}}}^j\right). \quad (7.14)$$

^fThe list of system variables obviously depends on the flow assumption (see § 5.1). \bar{f} and \bar{g} are always present, and additionally so are: \bar{k} if there is a span-wise velocity component, \bar{Y}_s if species interdiffusion is not neglected (CNE, TCNE, and TPG, TCFG, and TNE with non-constant compositions), \bar{Y}_E if elemental diffusion is allowed for (LTEED), or \bar{T}_v if the thermodynamic state of the mixture is described with two temperatures (TCNE or TNE). Moreover, $\partial \bar{f} / \partial \eta$ is also considered as a computational variable, in order to maintain a maximum differentiation order of 2, after which the Chebyshev matrices are known to lose accuracy [9].

^gRecall that double underlines denote matrix quantities, and single double lines identify vectorial ones.

^hNote that the i, j, k numerical indices do not correspond to the spatial ones (i, j, k) in the invariant notation (§ 2.3).

The terms in blue ($\underline{\mathcal{B}}$ and $\underline{\mathcal{H}}$) are equivalent to $\underline{\mathcal{A}}$ and $\underline{\mathcal{G}}$ yet for the marching terms in the system equations (also in blue in § 5.1). Regarding the terms in green, they are the result of the discretization of the streamwise derivative of $\underline{\mathcal{F}}$ with an n^{th} -order finite-difference method:

$$\frac{\partial}{\partial \xi} \left(\underline{\mathcal{F}}^i \right) = \sum_{j=i-n}^i D_j^{\text{FDn}} \cdot \underline{\mathcal{F}}^j. \quad (7.15)$$

Notedly $\underline{\mathcal{F}}^j$ for all j stations before the current one i should be below the accepted numerical tolerance. However, terms with $j < i$ are kept in the right-hand-side forcing term to avoid the accumulation of numerical inaccuracies throughout the marching. The $\underline{\mathcal{C}}^i$ matrix includes the terms premultiplying $\partial \underline{\mathcal{F}}^i / \partial \xi$ in the linearized equations.

The marching system (Eq. 7.14) is solved at each i station using a Newton-Raphson iteration, analogous to that in Eq. 7.13.

7.3.1 Mappings

In order to increase the resolution in the boundary layer, Malik's [12] mapping is employed to determine the η point distribution from the $X_{\text{CGL}} \in [-1, 1]$ points:

$$\eta = \frac{a^{\text{Mk}} X_{\text{CGL}}}{b^{\text{Mk}} - X_{\text{CGL}}}, \quad (7.16a)$$

$$a^{\text{Mk}} = \frac{\eta_{\max} \eta_i}{\eta_{\max} - 2\eta_i}, \quad (7.16b)$$

$$b^{\text{Mk}} = 1 + \frac{a^{\text{Mk}}}{\eta_{\max}}, \quad (7.16c)$$

where η_i denotes the value of η for which the same number of computational points are located below and over it.

Similarly, in order to have a point distribution in the marching ξ direction that is suited for the particular problem at stake, one must map the equispaced grid points $X_{\text{ES}} \in [0, 1]$ on which the forward finite-differences discretization is applied, onto the ξ points of interest. To this end, three different streamwise mappings are employed:

1. Linear spacing. ξ and X_{ES} are related through a linear equation:

$$\xi = \xi_{\min} + (\xi_{\max} - \xi_{\min}) X_{\text{ES}}. \quad (7.17)$$

2. Logarithmic spacing. ξ and X_{ES} are related through an exponential-logarithmic equation:

$$\xi = \exp(\ln(\xi_{\min}) + (\ln(\xi_{\max}) - \ln(\xi_{\min})) X_{\text{ES}}). \quad (7.18)$$

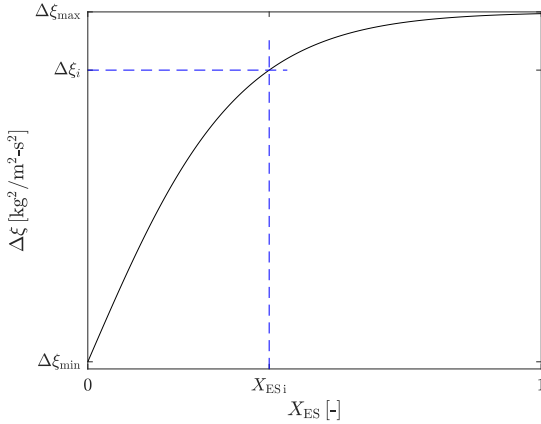


Figure 7.4: Sketch of the tanh ξ mapping's step.

3. Tanh spacing. A hybrid between linear and logarithmic spacing, that allows to cluster points close to the leading edge, where there is a stronger chemical activity and energy relaxation, yet maintaining a constant step at the downstream locations. This ensures also an appropriate point distribution for the relatively slower, yet non-zero, chemistry and energy relaxation occurring in the boundary-layer edge. The mapping imposes a tanh-evolution of the streamwise step $\Delta\xi \propto \tanh(X_{\text{ES}})$, sketched in Fig. 7.4, which leads to:

$$\xi(X_{\text{ES}}) = \xi_{\min} + A_{\xi} X_{\text{ES}} + B_{\xi} \ln(\cosh(a_{\xi} X_{\text{ES}})) , \quad (7.19)$$

where A_{ξ} , B_{ξ} and a_{ξ} depend on the domain size, and the point clustering fixed through $\Delta\xi_{\min}$, $X_{\text{ES}i}$ and the $\Delta\xi_i/\Delta\xi_{\max}$ ratio:

$$A_{\xi} = \Delta\xi_{\min} (N_{\xi} - 1) \quad , \quad a_{\xi} = \frac{1}{X_{\text{ES}i}} \tanh^{-1} \left(\frac{\Delta\xi_i}{\Delta\xi_{\max}} \right) , \quad (7.20)$$

$$B_{\xi} = \frac{\xi_{\max} - \xi_{\min} - \Delta\xi_{\min} (N_{\xi} - 1)}{\ln(\cosh(a_{\xi}))} .$$

Figure 7.5 shows a comparison of the three ξ mappings for a domain with $\xi_{\min} = 1 \text{ mm}$, $\xi_{\max} = 10 \text{ m}$, and a tanh defined by $\Delta\xi_{\min} = (\xi_{\max} - \xi_{\min})/(100(N_{\xi} - 1))$, $X_{\text{ES}i} = 0.5$, and $\Delta\xi_i/\Delta\xi_{\max} = 0.8$. This combination of parameters was heuristically found to provide a good numerical behavior for a wide variety of conditions. It is clear how the point distribution provided by the tanh mapping lies between the linear and logarithmic mapping.

The three mapping presented and displayed in Fig. 7.5 are evaluated on the marching ξ variable. The ultimate distribution of points in the physical domain (in x) is conditioned by the inverse Illingworth transformation (Eq. 5.6) and, for

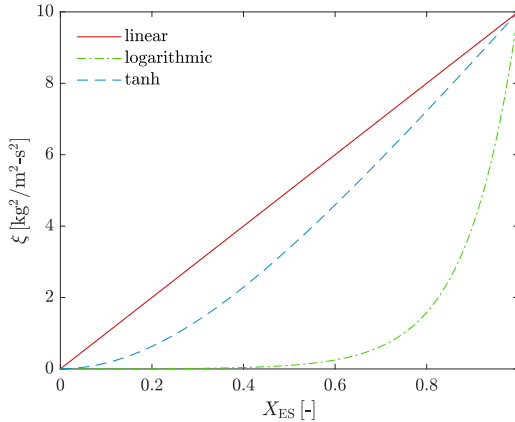


Figure 7.5: Comparison of the three ξ mappings, with $\xi_{\min} = 0.001 \text{ kg}^2/\text{m}^2\cdot\text{s}^2$, $\xi_{\max} = 10 \text{ kg}^2/\text{m}^2\cdot\text{s}^2$, and a tanh defined by $\Delta\xi_{\min} = (\xi_{\max} - \xi_{\min})/(100(N_{\xi} - 1))$, $X_{ESi} = 0.5$, and $\Delta\xi_i/\Delta\xi_{\max} = 0.8$.

conical boundary layers, by the Probstein-Elliott one (Eq. 5.27). These transformations, especially the latter, may significantly distort the point distribution visualized in Fig. 7.5, making the eventual $x - X_{ES}$ relation very different from the $\xi - X_{ES}$ one. For this reason, an additional functionality was implemented, where an arbitrary distribution of points in the physical x domain can be input by the user. After applying the necessary transformations, one reaches the point distribution on the computational ξ domain. The differentiation matrices on this arbitrary ξ point distribution are obtained using a methodology similar to that of Fornberg [13].

7.3.2 Initial guess

In order to apply the Newton-Raphson method described in Eq. 7.13, it is necessary to make an initial guess for the pseudo-basic-state quantities $\bar{\mathcal{F}}_0$. The convergence characteristics of the system were seen to strongly depend on the quality of this initial guess. If the initial guess is too far from the final solution, the method may converge to local solutions, which are spuriously oscillatory.

To this end, the initial guess of the computational variables $\partial\bar{f}/\partial\eta$, \bar{g} and \bar{k} is based on the shape of boundary-layer profiles through the canonical polynomial-exponential function:

$$\bar{\mathcal{F}}_0(\eta) = 1 + (a_1^{IG}\eta^3 + a_2^{IG}\eta^2 + a_3^{IG}\eta + a_4^{IG}) \exp(-a_5^{IG}\eta^2 + a_6^{IG}\eta) , \quad (7.21)$$

where a_1^{IG} - a_6^{IG} are parameters. $a_5^{IG} \neq 0$ in all cases, meaning that the function $\bar{\mathcal{F}}_0(\eta)$ approaches unity (super-)exponentially as $\eta \rightarrow \infty$, automatically satisfying the freestream behavior and boundary condition.

M_e	a_2^{IG}	a_4^{IG}	a_6^{IG}	$\partial^2 f / \partial \eta^2 _w$
0.01	4.07811e-2	9.44090e-2	5.19947e-1	4.69601e-1
0.5	4.05977e-2	9.00186e-2	5.20458e-1	4.72501e-1
1	4.00238e-2	7.62938e-2	5.21708e-1	4.81145e-1
2	3.86102e-3	-1.35885e-1	5.71351e-1	5.13780e-1
3	2.37842e-3	-2.61074e-1	5.59809e-1	5.60286e-1
4	-1.02949e-1	-8.57249e-1	5.06635e-1	6.12808e-1
5	-3.53516e-1	-1.42533e0	4.20244e-1	6.66609e-1
6	-7.14969e-1	-1.84294e0	3.33674e-1	7.19491e-1
7	-1.17384e0	-2.18697e0	2.31696e-1	7.70581e-1
8	-1.71532e0	-2.48439e0	3.01678e-2	8.19618e-1
9	-2.37924e0	-2.68122e0	-3.32850e-3	8.66601e-1
10	-2.91426e0	-2.83399e0	-3.78514e-3	9.11637e-1
15	-4.57399e0	-3.35100e0	-1.25733e-3	1.11264e0
20	1.24255e-1	1.46899e0	7.00088e-1	1.28412e0
25	-6.80627e0	-4.06865e0	-8.83011e-4	1.43566e0

Table 7.2: Sample of coefficients for the initial guess function (Eq. 7.21) for $\partial \bar{f} / \partial \eta$ for adiabatic wall conditions and for several edge Mach numbers. Values of $\partial^2 \bar{f} / \partial \eta^2|_w$, used to obtain a_2^{IG} , a_4^{IG} , and a_6^{IG} are also listed. $\partial^3 \bar{f} / \partial \eta^3|_w$ and \bar{f}_w values are omitted since $\partial^3 \bar{f} / \partial \eta^3|_w = \bar{f}_w = 0$ for a non-blowing adiabatic wall with $\beta_H = \Theta_H = 0$, and $w_e = 0$.

The parameters a_2^{IG} , a_4^{IG} , and a_6^{IG} are fixed by the wall boundary condition on the function value and derivatives, while the complementary parameters a_1^{IG} , a_2^{IG} , and a_5^{IG} are obtained by fitting Eq. 7.21 to several boundary-layer solutions for a larger range of different Mach numbers and wall temperature ratios. To this end, VESTA's fourth-order Runge-Kutta boundary-layer CPG solver [14] was used to obtain $\partial \bar{f} / \partial \eta$, and \bar{g} profiles, keeping $\beta_H = \Theta_H = 0$, and $w_e = 0$. The initial condition for \bar{k} is taken identical to that for $\partial \bar{f} / \partial \eta$.

A sample of the parameters a_1^{IG} , a_2^{IG} , and a_5^{IG} is presented in Tables 7.2 and 7.3. For test conditions other than the computed ones, the set of parameters corresponding to the closest *lower* Mach number is taken. For instance, to run $M = 5.8$, the parameter set corresponding to $M = 5$ is used. This demonstrated to yield better convergence rates than when interpolating the reported values.ⁱ Despite the initial guesses being the result of fittings to profiles corresponding to CPG conditions, they proved to be a sufficiently good approximation for the remaining flow assumptions.

Regarding the other two possible system variables (\bar{Y}_s , \bar{Y}_E , and \bar{T}_v), the initial guess for the mass-fraction profiles are obtained with one of two methods. When

ⁱExperience shows that using \bar{g} profiles attaining values lower than the final profile is beneficial for the convergence behavior.

M_e	a_2^{IG}	a_4^{IG}	a_6^{IG}	\mathcal{J}_w	$\partial^2 \bar{g} / \partial \eta^2 _w$
1	4.00238e-2	7.62938e-2	5.21708e-1	9.72390e-1	2.31501e-2
2	3.86102e-3	-1.35885e-1	5.71351e-1	9.25487e-1	7.03919e-2
3	2.37842e-3	-2.61074e-1	5.59809e-1	8.90527e-1	1.21084e-1
4	-1.02949e-1	-8.57249e-1	5.06635e-1	8.68205e-1	1.71673e-1
5	-3.53516e-1	-1.42533e0	4.20244e-1	8.53808e-1	2.22184e-1
6	-7.14969e-1	-1.84294e0	3.33674e-1	8.44094e-1	2.72722e-1
7	-1.17384e0	-2.18697e0	2.31696e-1	8.37231e-1	3.23289e-1
8	-1.71532e0	-2.48439e0	3.01678e-2	8.32186e-1	3.73857e-1
9	-2.37924e0	-2.68122e0	-3.32850e-3	8.28353e-1	4.24401e-1
10	-2.91426e0	-2.83399e0	-3.78514e-3	8.25358e-1	4.74904e-1
15	-4.57399e0	-3.35100e0	-1.25733e-3	8.16894e-1	7.26630e-1
20	1.24255e-1	1.46899e0	7.00088e-1	8.13037e-1	9.77168e-1
25	-6.80627e0	-4.06865e0	-8.83011e-4	8.10866e-1	1.22686e0

Table 7.3: Sample of coefficients for the initial guess function (Eq. 7.21) for \bar{g} for adiabatic wall conditions and for several edge Mach numbers. Values of \mathcal{J}_w and $\partial^2 \bar{g} / \partial \eta^2|_w$, used to obtain a_2^{IG} , a_4^{IG} , and a_6^{IG} are also listed. $\partial \bar{g} / \partial \eta|_w$ values are omitted since $\partial \bar{g} / \partial \eta|_w = 0$ for adiabatic conditions.

employing a non-catalytic wall boundary condition (Eq. 6.23), the initial \bar{Y}_s is estimated to be constant and equal to the value prescribed at the edge. Contrarily, when employing a constant-mass-fraction boundary condition (Eq. 6.24), the initial guess for the mass fractions is obtained from:

$$\bar{\bar{Y}}_{s0} = Y_{se} + (Y_{sw} - Y_{se}) \exp(-2\eta), \quad \forall s \in \mathcal{S}, \quad (7.22)$$

which was seen to be sufficiently close to the concentration distribution arising from self-similar diffusion. The same strategy is followed to initialize the elemental mass fractions (\bar{Y}_E).

Finally, the initial guess for the non-dimensional vibrational-electronic-electron temperature \bar{T}_v is obtained from solving the vibrational-electronic-electron energy equation (Eq. 5.4d) in a decoupled fashion, provided the initial guesses for all other variables.

7.4 Exploiting spectral accuracy through the GICM interpolation

As put by Burden & Faires [11], CGL nodes feature “an optimal placing of interpolating points to minimize the error in Lagrange interpolation”. Seeking to benefit from this, a methodology is proposed to maintain the spectral accuracy in an arbitrary point distribution, to be used for the stability analyses. Since the

minimal interpolation error is achieved when the interpolation is performed on the CGL nodes, it is necessary to undo the successive transformations that are applied on it before reaching the physical y -domain. These transformations are:

$$X_{\text{CGL}} \in [-1 \ 0 \ 1] \xrightarrow{\text{Malik}} \eta \in [0 \ \eta_i \ \eta_{\max}] \xrightarrow{\text{Illingworth}} y \in [0 \ y_i \ y_{\max}].$$

Additionally, if an axisymmetric boundary layer is being solved, one must incorporate the Probstein-Elliott transformation (see § 5.1.7):

$$X_{\text{CGL}} \in [-1 \ 0 \ 1] \xrightarrow{\text{Malik}} \eta \in [0 \ \eta_i \ \eta_{\max}] \xrightarrow{\text{Illingworth}} y \in [0 \ y_i \ y_{\max}] \xrightarrow{\text{Probstein-Elliott}} y \in [0 \ y_i \ y_{\max}].$$

In order to pass from the stability point distribution y^{stab} to the X -space, one must perform these transformations in the opposite direction. The problem arises from the fact that undoing the Illingworth transformation requires knowledge of the density field $\bar{\rho}$ in the objective grid y^{stab} . $\bar{\rho}(y^{\text{stab}})$ is unknown *a-priori*, since itself must be interpolated using the technique that requires it.

To bypass this limitation, an iterative interpolation methodology is proposed, hereinafter referred as the GICM (Groot-Illingworth-Chebyshev-Malik) interpolation:

1. The density field is interpolated onto the stability y^{stab} grid with a spline (third-order) interpolation. This initial low-order-accuracy interpolation is a matter of first guess.
2. The necessary transformations (Illingworth and Malik or Probstein-Elliott, Illingworth, and Malik) are undone using $\bar{\rho}(y^{\text{stab}})$, to obtain the stability grid distribution in the X -space ($X_{\text{CGL}}^{\text{stab}}$).
3. The density field is interpolated onto the stability grid in the X -space, using high-order Lagrangian interpolation. Specifically, the function suite of Weideman & Reddy [15] is employed.
4. Steps 2-3 are repeated until the density field on the stability grid is numerically converged.
5. Having $\bar{\rho}(y^{\text{stab}})$ numerically converged, and therefore an accurate $X_{\text{CGL}}^{\text{stab}}$ distribution, all field variables of interest are interpolated in the X -space using high-order Lagrangian interpolation.

In order to ensure that the accuracy of the system is not compromised, the integration of the density field in the stability grid that is necessary to undo the Illingworth transformation, must have the same order of accuracy as the scheme to be used for the stability analysis. Integration matrices of arbitrary-order accuracy may be obtained from the corresponding differentiation matrices through the

method presented in app. G. This implies that in order to perform the GICM interpolation, one must provide not only the ultimate stability grid y^{stab} , but also the associated differentiation matrix.

7.5 Implementation

Figure 7.6 presents a sketch of DEKAF’s functional tree. The DEKAF flow solver is fully implemented in MATLAB, and benefits of a series of external functions such as those of Weideman & Reddy [15] providing differentiation and interpolation capabilities on CGL nodes, that of Lassaline [16] solving the CPG Taylor-Maccoll equation (Eq. 7.4), or that of Tursa [17] (`mtimesx`) allowing for matrix multiplications of N-dimensional matrices.

The main work flow is the following: first `setDefaults` fills the non-defined options with their defaults. Second the self-similar solver is called (`DEKAF_FSC`), and if a streamwise marching is to be carried out so is the marching solver (`DEKAF_BL`). Finally, the dimensional variables are retrieved from the computational ones with `eval_dim_vars`. Besides the main function `DEKAF`, the user must also invoke the `GICM_interp` function to perform the GICM interpolation (see § 7.4) before using the solution for a stability analysis.

Several functions are called both within the self-similar and the marching solver. Both of them initially retrieve the wall-normal η point distribution with `build_mapping_vars` (see § 7.3.1), and then obtain all the boundary-layer-edge quantities using `build_edge_values`. In it, first the shock-jump relations (see § 7.1) are solved, followed by the call to the inviscid solver (see § 7.2) for non-equilibrium flows^j, and finally the construction of the computational ξ vector^j (see § 7.3.1). After obtaining the boundary-layer-edge quantities, an initial guess is done on the profiles of the non-dimensional quantities^k (see § 7.3.2). Then the thermodynamic properties are evaluated in `eval_thermo` using the various models presented in chapter 4, and ultimately constructing the remaining non-dimensional variables appearing in the system equations (see § 5.1). Having all the necessary fields, the next steps are to build the elements in the matrix system (Eq. 7.12 for the self-similar solver and Eq. 7.14 for the marching one) with `build_mat`, solve it, and update the solution (see Eq. 7.13) with `update_solution`. The last steps are repeated until the Newton-Raphson method converges. Then, if the solution is to be marched, one advances to the next ξ station and performs these last steps again with the corresponding edge quantities.

^jThis step is only necessary in the marching solver.

^kThis step is only necessary in the self-similar solver.

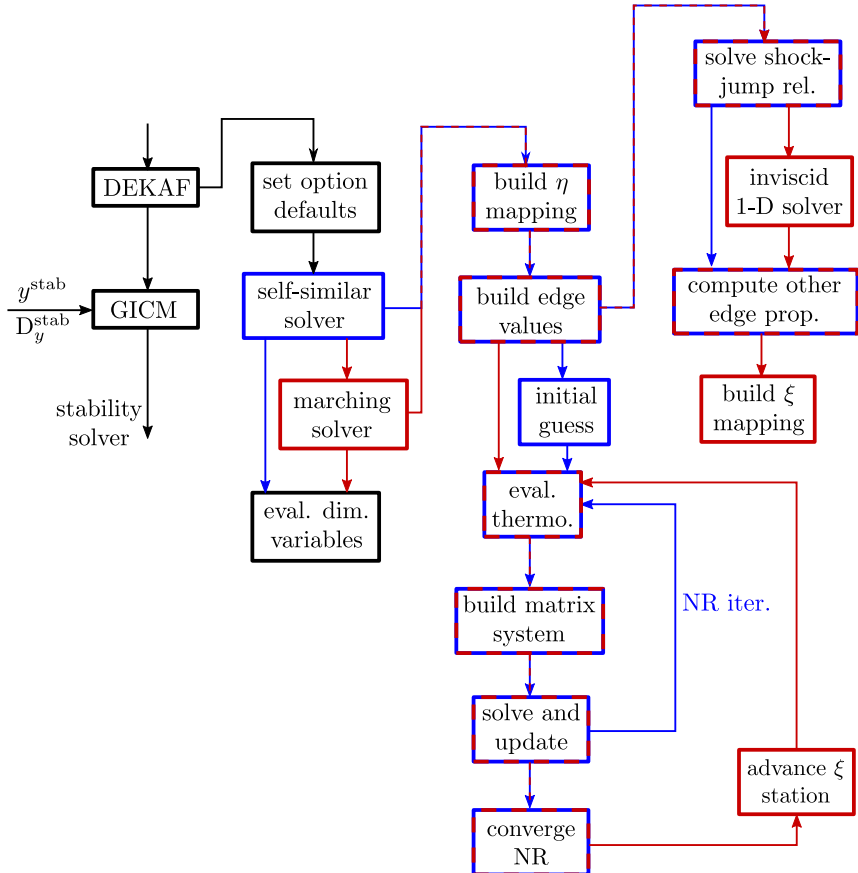


Figure 7.6: Sketch of DEKAF's functional tree. Blue identifies the self-similar solver, and red the marching one.

Case	M_e [-]	Re [-]	T_e [K]	$\bar{T}_w/T_{\text{adiab}}$
1	0.5	2000	252.52	1
2	10^{-6}	580	277.78	1
3	2.5	3000	95.24	1
4	10	2000	56.91	0.1
5	10	1000	56.91	1
6	4.5	1500	67.16	1

Table 7.4: Test conditions for the verification of the CPG non-bleeding flat-plate cases. Cases previously studied by Malik [12].

7.6 Verification

A collection of verification cases against various boundary-layer or Navier-Stokes solvers is presented in this section. The choice of test cases is done so as to cover as thoroughly as possible the range of operating conditions of the solver.

7.6.1 CPG non-bleeding flat-plates

The perfect-gas solver is verified against VESTA's compressible boundary-layer (CBL) solver [14, app. B] for non-bleeding flat plates with various Mach numbers and thermal wall boundary conditions. VESTA's CBL solver uses a shooting RK4 method, combined with a Newton-Raphson iteration on the shooting parameter. The flow conditions of the various tests are summarized in Table 7.4, and correspond to cases originally investigated by Malik [12], and later by Pinna [14]. Note that the provided Reynolds number is based on the Blasius-length ℓ_e . However, the unit Reynolds number (Re_{1e}) is taken such that $\ell_e = 1$ m, making the numerical values of Re and Re_{1e} (in m^{-1}) the same. One must also note that the original reference [12] provides dynamic temperature values in Rankine degrees, thus explaining the non-integer values of T_e . Regarding the flow properties, they are obtained from using Sutherland's law (Eq. 4.2) with a constant Prandtl number (Eq. 4.5). The values of the gas constants of interest are summarized in Table 5.2. The dimensional velocity and temperature profiles presented in Fig. 7.7 present an excellent match for all conditions.

7.6.2 CPG bleeding flat-plates

The self-similar wall-blowing boundary condition is evaluated by reproducing a series of tests previously investigated by Malik [18], Johnson *et al.* [19] and Ghafari *et al.* [20]. The test conditions are those in Table 7.5, with the gas constants in Table 5.2 except for the Prandtl number $Pr = 0.72$. The dimensional streamwise position corresponding to $Re = 1500$ is $x = 0.6855$ m. Figure 7.8 presents the excellent agreement of the velocity and temperature profiles for three values of the

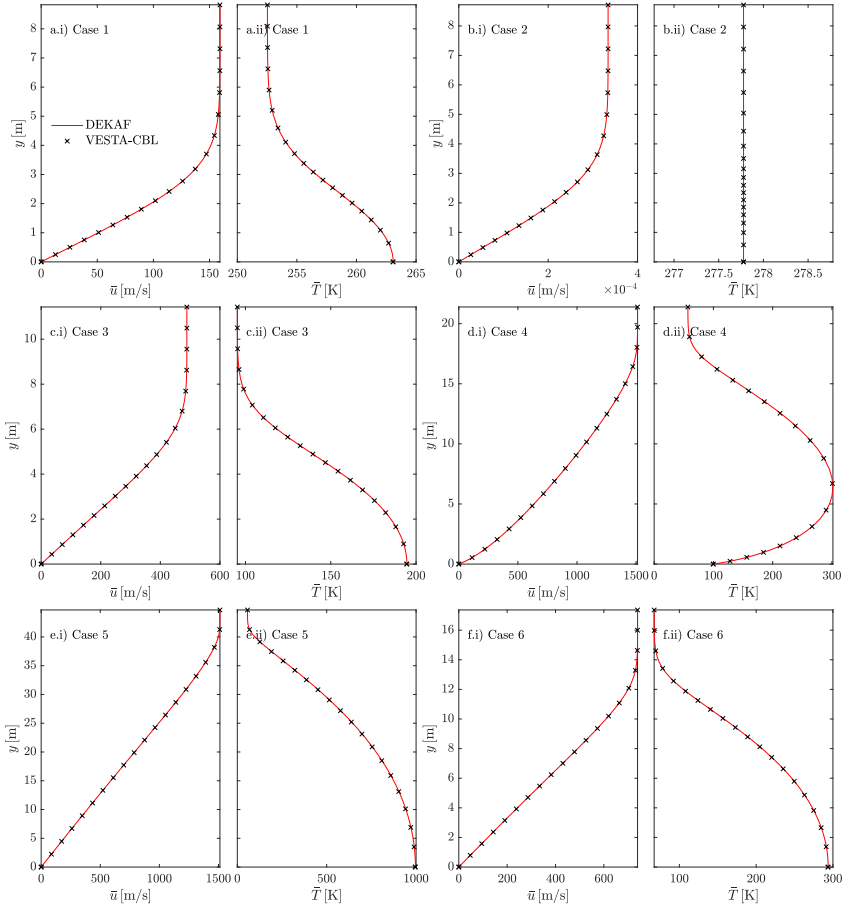


Figure 7.7: DEKAF verification against VESTA's CBL solver for the CPG non-bleeding flat-plate cases in Table 7.4.

$M_e [-]$	$\text{Re} [-]$	$\rho_e [\text{kg/m}^3]$	$T_e [\text{K}]$	$\bar{T}_w [\text{K}]$
4.5	1500	0.01899	61.61	311

Table 7.5: Test conditions for the verification of the CPG bleeding flat-plate cases. Case previously studied by Malik [18], Johnson et al. [19] and Ghaffari et al. [20].

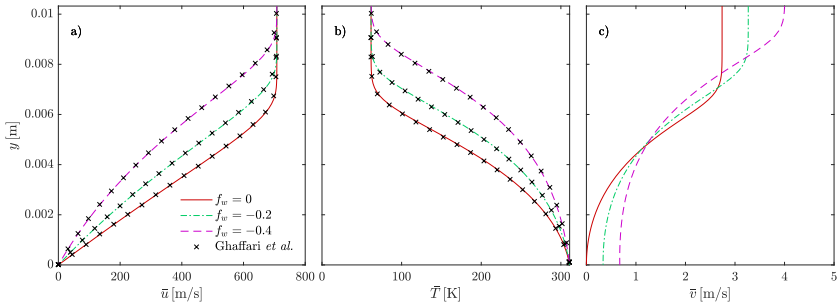


Figure 7.8: DEKAF verification against Ghaffari et al.'s [20] Navier-Stokes solver for the CPG bleeding flat-plate cases in Table 7.5, and for three different values of the blowing parameter f_w (Eq. 6.3).

blowing parameter f_w (Eq. 6.3): 0, -0.2, and -0.4, corresponding to successively higher levels of mass injection. The wall-normal velocity v is also presented for illustration purposes, showing how it increases as f_w becomes more negative.

7.6.3 Incompressible Falkner-Skan-Cooke equation

The implementation of the spanwise momentum equation (Eq. 5.4b) is verified by comparing its solution obtained with DEKAF against the values obtained analytically by Cooke [21] in his original article. For incompressible flow regimes, where $\bar{c} = \bar{j} = 1$, with $\beta_H = \text{cst}$ (see Eq. 5.5), the non-dimensional boundary-layer equations (see § 5.1) are reduced to the Falkner-Skan-Cooke equations:

$$\frac{\partial^3 \bar{f}}{\partial \eta^3} + \bar{f} \frac{\partial^2 \bar{f}}{\partial \eta^2} + \beta_H \left(1 - \left(\frac{\partial \bar{f}}{\partial \eta} \right)^2 \right) = 0, \quad (7.23a)$$

$$\frac{\partial^2 \bar{k}}{\partial \eta^2} + \bar{f} \frac{\partial \bar{k}}{\partial \eta} = 0. \quad (7.23b)$$

Figure 7.9 displays the solution of the solution obtained with DEKAF compared to the values reported by Cooke, as a function of the self-similar wall-normal variable η (Eq. 5.6). The different curves correspond to various values of the streamwise-pressure-gradient Hartree parameter β_H (Eq. 5.5), since it is the only parameter modulating the solution to Eq. 7.23. The agreement with the analytical solution is excellent.

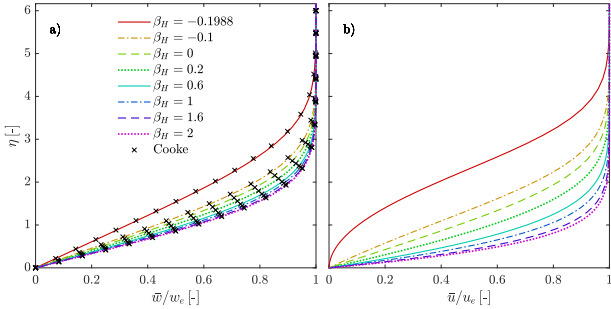


Figure 7.9: DEKAF verification against Cooke’s [21] analytical solution for incompressible flow and for different values of the streamwise-pressure-gradient parameter β_H (Eq. 5.5).

As laid out in § D.8, the evaluation of the self-similar solution at a given streamwise position, when $\beta_H \neq 0$, requires the integration of the streamwise evolution of the edge profiles in order to retrieve ξ for a given x . ξ ultimately affects the conversion from the η - to the y -space, and thus the spacing in the physical y grid. In order to verify this implementation, the solution for $\beta_H = 1/3$ of the Falkner-Skan-Cooke equations (Eq. 7.23) is evaluated at $Re = 227.94$, with a sweep angle¹ of $\Lambda_{\text{swp}} = 45^\circ$, and compared against the results obtained by Tempelmann [22, Ch. 3]. Tempelmann actually reports the value of the Reynolds number based on the displacement thickness and the streamwise velocity u_e . Instead, the value of $Re = 227.94$ corresponds to the Reynolds number based on the Blasius length ℓ_e and the velocity in the direction aligned with the inviscid streamline u^{SL} . The Blasius length is itself also based on u^{SL} :

$$Re = Re_{1e} \ell_e = \frac{\rho_e u_e^{\text{SL}} \ell_e}{\mu_e}, \quad \ell_e = \sqrt{\frac{\mu_e x}{\rho_e u_e^{\text{SL}}}}. \quad (7.24)$$

The choice of the edge unit Reynolds number Re_{1e} does not modify the solution, but it is taken such that its numerical value in m^{-1} coincides with that of Re . This implies that the Blasius length is $\ell_e = 1 \text{ m}$, like in the verification cases in § 7.6.1. The resulting profiles, aligned with the inviscid streamline, are reported in Fig. 7.10 together with Tempelmann’s^m, displaying an excellent agreement.

¹Note that the solution to the Falkner-Skan-Cooke equations (Eq. 7.23) is actually independent of the sweep angle. In other words, \bar{u} and \bar{w} obtain their relative weight with respect to each other through the value of the edge quantities (u_e and w_e), which are related through Λ_{swp} .

^mTempelmann’s results were modified with respect to their original form, in order to normalize the velocities with respect to u_e^{SL} , rather than u_e , and to dimensionalize y with the displacement thickness for the mentioned choice of the unit Reynolds number Re_{1e} . The value of the displacement thickness for $Re_{1e} = 227.94 \text{ m}^{-1}$ and $Re = 227.94 \text{ m}$ is 1.365 m.

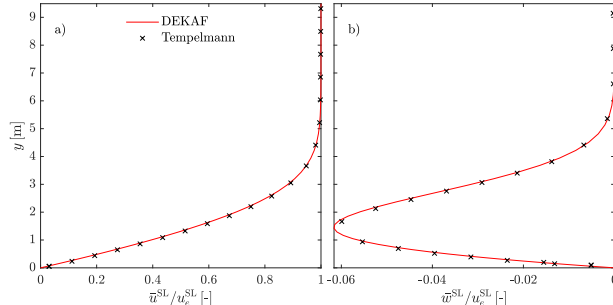


Figure 7.10: DEKAF verification against Tempelmann’s [22] self-similar solution, with $\beta_H = 1/3$, $\Lambda_{\text{swe}} = 45^\circ$ and $Re = 227.94$

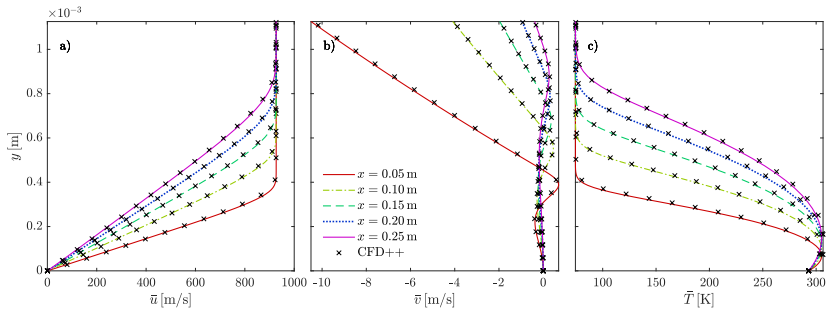


Figure 7.11: DEKAF verification against a Navier-Stokes solution obtained with CFD++ for a 7-degree cone at Mach 6, and at various locations on the cone surface. The exact conditions correspond to case 15B0 in Table 9.1.

7.6.4 CPG cone

The implementation of the Probstein-Elliott transformation (§ 5.1.7) is verified by comparing the results obtained from solving the CPG non-dimensional boundary-layer equations (see § 5.1.6), for the same 7-degree cone configuration studied in § 9.1. Specifically, for case 15B0 in Table 9.1, which features a preshock unit Reynolds number of $15.28 \cdot 10^6 \text{ m}^{-1}$, and a Mach number of 6. This test case also allows for a verification of the implementation of the conical shock-jump relations for shocks of type 1 (see § 7.1). The comparison of the temperature and velocity profiles in Fig. 7.11 to those obtained with CFD++ displays an outstanding agreement, despite the non-zero nose-bluntness radius of 0.164 mm present in the geometry solved with CFD++.

$M_e [-]$	$Re_{1e} [1/m]$	$T_e [K]$	wall	$Y_{N_2 e} [-]$	$Y_{O_2 e} [-]$
10	$9.8425 \cdot 10^6$	278	adiab.	0.78	0.22

Table 7.6: Test conditions for the verification with Hudson’s CNE case. Case previously studied by Hudson *et al.* [23, 24], Stuckert & Reed [26, 27], Franko *et al.* [28], and several others.

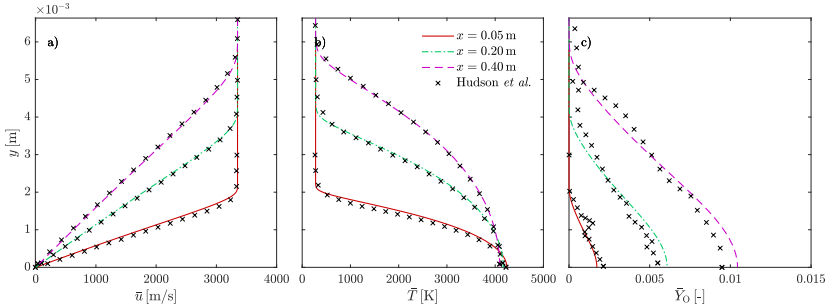


Figure 7.12: DEKAF verification against a Navier-Stokes solution obtained by Hudson *et al.* [23] for an adiabatic Mach 10 flat plate. The exact conditions are summarized in Table 7.6.

7.6.5 CNE Mach 10 flat plate

A first verification for the implementation of DEKAF in CNE conditions is performed by comparing against the Navier-Stokes solution obtained by Hudson *et al.* [23, 24]. The case features an adiabatic Mach 10 flat plate with the conditions laid out in Table 7.6. Regarding the thermophysical modeling, the test case employs the BEW transport model (§ 4.2.1.1), with a constant-Schmidt-number diffusion (Eq. 4.39 with $Sc = 0.5$), and Park’s 1985 [25] chemical reaction-rate constants (Table J.3) for a 5-species air mixture. The thermal properties are obtained assuming a RRHO model (see § 4.1 and Eq. 4.66). Figure 7.12 displays the boundary-layer profiles for various streamwise positions, showing good agreement with the reference data. The dispersion observed in Hudson’s O-mass-fraction profiles is due to the bad quality of the original image from which the data was digitized.

7.6.6 CNE Oxygen mixture

Another verification is carried out on the CNE solver, yet with a different gas mixture (binary oxygen: O and O_2) and with different transport (Brokaw – § 4.2.1.5) and diffusion models (Binary diffusion – Eq. C.5). The collisional data is obtained using Gupta *et al.*’s [29] polynomial curve fittings (Eqs. 4.55 and 4.59 and tables in § K.3.2). The chemical source terms are obtained using Bortner’s [29, 30] reaction-

Case	M_e [-]	p_e [Pa]	T_e [K]	\bar{T}_w [K]	x [m]	$Y_{O_2\ e}$ [-]
1	10.545	4387	278	adiab.	0.4	1
2			556			
3			834			
5a	10.545	4387	834	adiab.	1.1695	1
5b				3000		
5c				2000		
5d				1000		

Table 7.7: Test conditions for the verification with Klentzman & Tumin's CNE cases.

rate constants (Table J.1), yet with an enhancement factor of 9 or 25 for the oxygen dissociation rate depending on whether O₂ or O is the third body, and Arrhenius coefficients (Table J.2) for the equilibrium constant obtained with Eq. 4.70. The thermal properties of the gas are obtained assuming that the individual species behave like a RRHO (see § 4.1). The various cases presented were originally investigated by Klentzman & Tumin [31]. The same naming convention used by the authors is preserved in this comparison. Figure 7.13 presents a good agreement with the reference data for all the analyzed conditions.

7.6.7 6-degree CPG, CNE, and LTE wedge

In order to verify the joint implementation of the various oblique-shock jumps with the boundary-layer solver, a 6-degree wedge is tested for three different flow assumptions: CPG, CNE, and LTE. The test case, originally investigated by Chang *et al.* [32], features a free-stream Mach number of 20, a temperature of 236.67 K, and a unit Reynolds number of $2.953 \cdot 10^6 \text{ m}^{-1}$. The wall is imposed to be isothermal, at 0.1 times the adiabatic temperature for each flow assumption. The free-stream composition is not provided, so it is taken as 76.71% nitrogen and 23.29% oxygen in mass. The remaining thermophysical models employed are: the BEW transport model (§ 4.2.1.1), the SCEBD diffusion model (Eq. 4.44), the RRHO thermal model (§ 4.1), and Bortner's reaction-rate and Arrhenius-equilibrium constants for a 5-species air mixture (Tables J.7 and J.8). The chemical equilibrium constant is thus obtained from Eq. 4.70. The boundary-layer solutions obtained with DEKAF are compared to Chang *et al.*'s boundary-layer and PNS solutions, for three different streamwise locations. There exists good agreement between DEKAF's solutions and those coming from the various the boundary-layer solvers [12, 33]. The comparison in Fig. 7.14 is also a verification of the implementation of the rebuilding of the wall-normal velocity for self-similar solutions (see § E). The discrepancy with the PNS solutions was also reported and commented by Chang *et al.* [32].

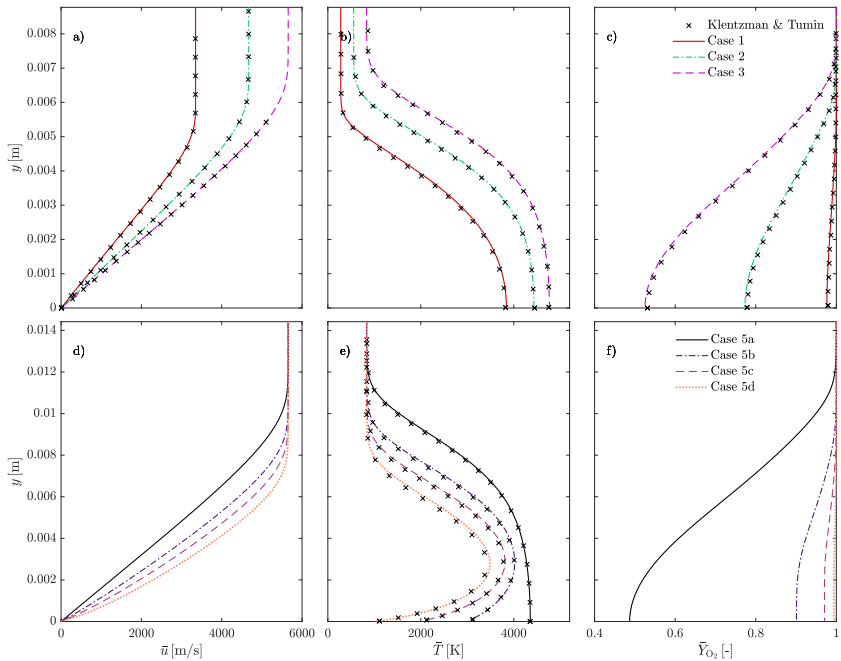


Figure 7.13: DEKAF verification against boundary-layer solutions obtained by Klentzman & Tumin [31] for a Mach 10 flat plate with a binary oxygen mixture. The exact conditions are summarized in Table 7.7.

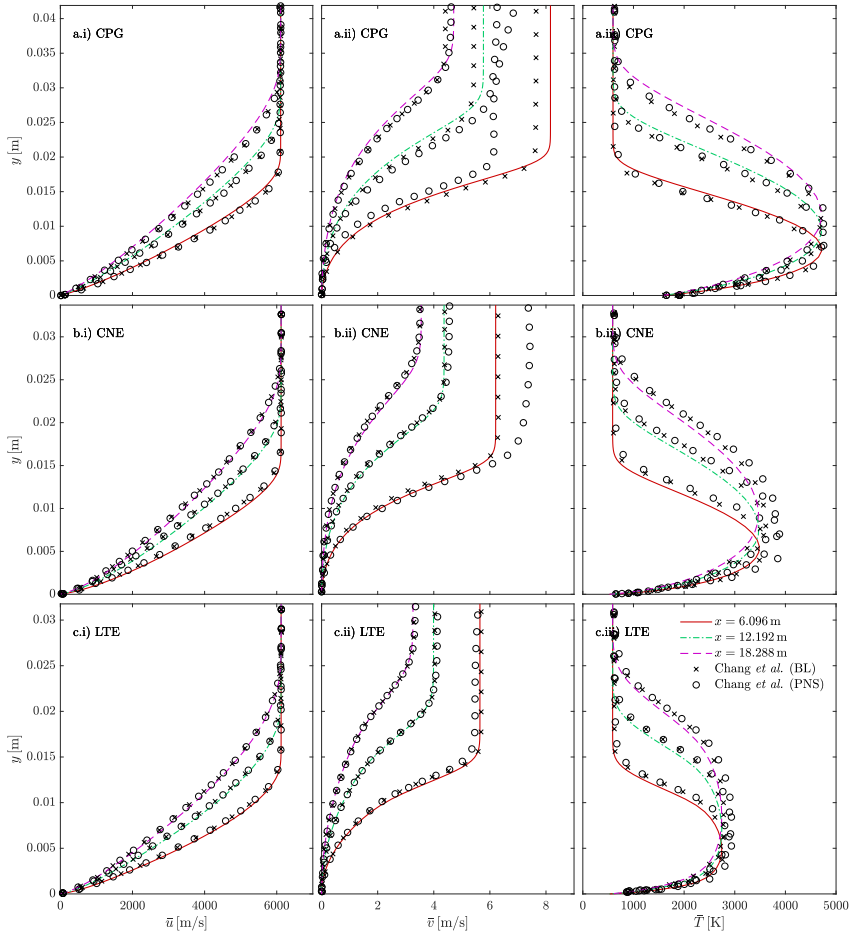


Figure 7.14: DEKAF verification against boundary-layer and PNS solutions obtained by Chang et al. [31] for a Mach-20, 6-degree wedge, and for various flow assumptions.

M_∞ [-]	p_∞ [Pa]	T_∞ [K]	\bar{T}_w [K]	$Y_{O_2\infty}$ [-]	$Y_{N_2\infty}$ [-]
18	10	231.45	1900	0.233	0.767

Table 7.8: Test conditions for the 20-degree-wedge verification with CFD++.

7.6.8 20-degree CPG, TPG, and CNE wedge at Mach 18

A similar verification to the previous one is performed, yet for a much blunter wedge of 20 degreesⁿ. DEKAF’s solution (solving the shock jump and the boundary-layer equations) is compared to the Navier-Stokes solution obtained with CFD++. The flow assumptions are also different to those employed in the comparison with Chang *et al.*, presenting results in CPG, TPG, and CNE. Moreover, two different transport models are compared in CPG conditions: Sutherland’s law (Eq. 4.2) with a constant Prandtl number (Eq. 4.5), and the GW model (§ 4.2.1.2), which is also used in TPG and CNE conditions. The freestream conditions are those employed for the shuttle-reentry case investigated in Ref. 34, and summarized in Table 7.8. The test gas is air, modeled with the air-5-Park01 mixture (see § J.9), with the chemical equilibrium constants obtained from assuming species to behave as a RRHO (Eq. 4.66). The diffusion fluxes are obtained imposing a constant Schmidt number (Eq. 4.39) of 0.7. Thermal properties in the CFD++ and DEKAF solutions are obtained differently – CFD++ employs the NASA7 polynomial fits, whilst DEKAF uses the RRHO model (see § 4.1). The comparison in Fig. 7.15 shows good agreement for the three considered flow assumptions, thus further verifying the implementation, and justifying the use of DEKAF baseflows also for highly-inclined wedges. The agreement of the solutions also reinforces the observation made by Scoggins & Magin [35] that the NASA7 and RRHO models present negligible differences.

7.6.9 15-degree CNE wedge at Mach 35

Seeking to encounter the limits of applicability of the inviscid-viscous-region decoupled approach followed in DEKAF, a more extreme wedge case is investigated. The solution obtained for a 15-degree wedge at Mach 35 is compared against the Navier-Stokes solution obtained with NASA’s DPLR tool [8]. Air is modeled with the air-5-Park01 mixture (§ J.9), with the BEW transport model (§ 4.2.1.1), constant-Schmidt diffusion (Eq. 4.39). Thermal properties in the DPLR and DEKAF solutions are obtained differently – DPLR employs the NASA9 polynomial fits, whilst DEKAF uses the RRHO model (see § 4.1). The freestream conditions are summarized in Table 7.9. The comparison of the profiles presented

ⁿThe word “blunt” refers here to the magnitude of the wedge’s half angle, and not to the radius of the wedge’s tip. All considered wedges have an infinitely-sharp tip, such that the shock relations laid out in § 7.1 are valid.

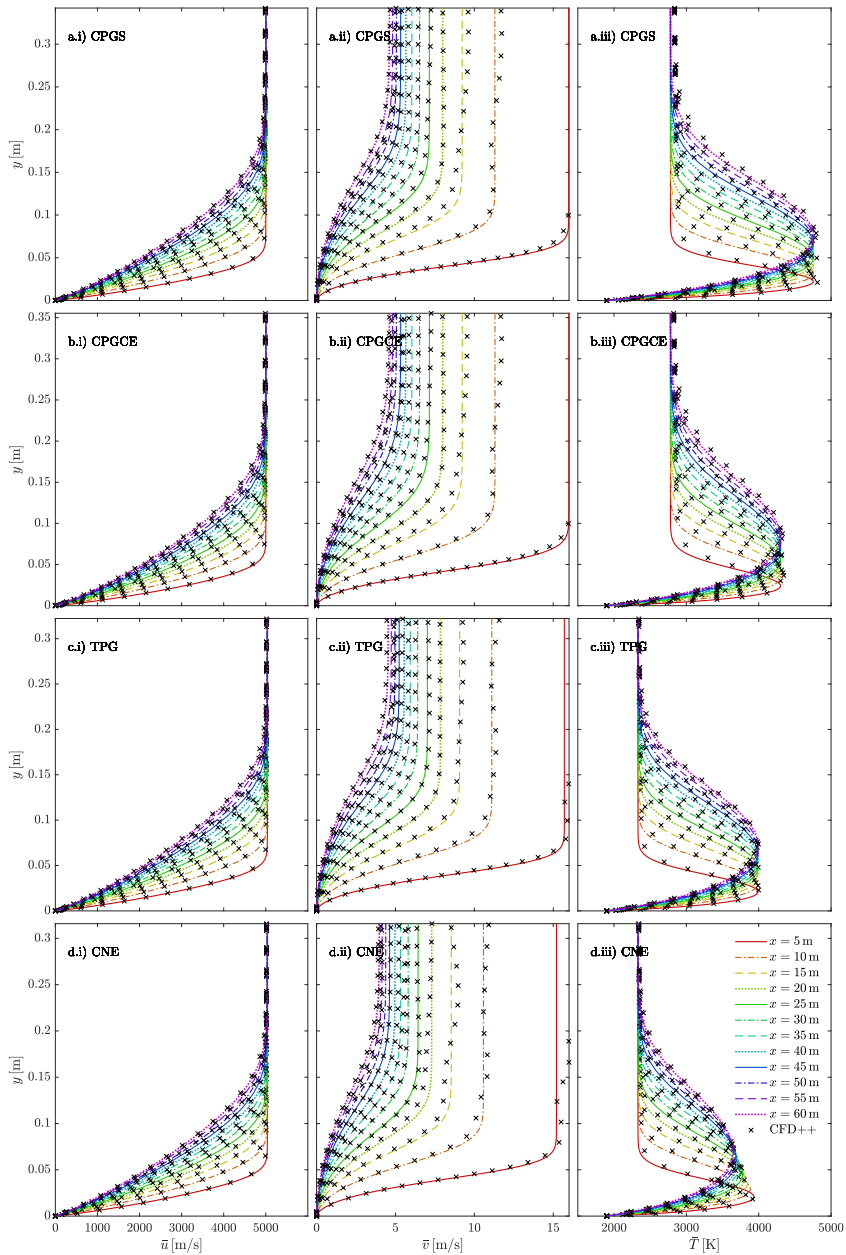


Figure 7.15: DEKAF verification against Navier-Stokes solutions obtained with CFD++ for a 20-degree wedge at Mach 18, and for various flow assumptions. The exact test conditions are reported in Table 7.8.

$M_\infty [-]$	$\rho_\infty [\text{kg/m}^3]$	$T_\infty [\text{K}]$	$\bar{T}_w [\text{K}]$	$Y_{\text{N}_2 e} [-]$	$Y_{\text{O}_2 e} [-]$
35	0.001	220	4000	0.767	0.233

Table 7.9: Test conditions for the verification with the 15-degree wedge at Mach 35.

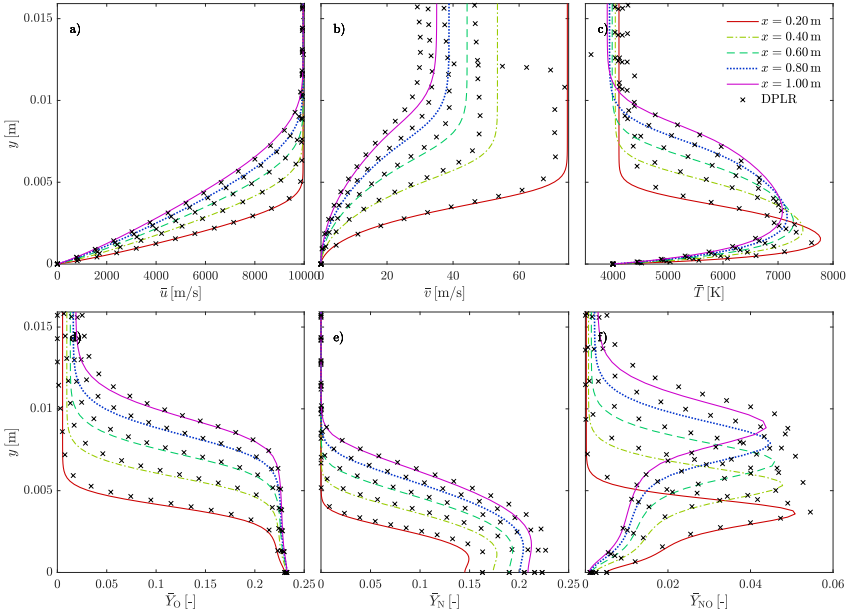


Figure 7.16: DEKAF verification against a Navier-Stokes solution obtained with DPLR for a 15-degree wedge at Mach 35 in CNE. The exact test conditions are reported in Table 7.9.

in Fig. 7.16 presents a worse agreement than in the previous cases, suggesting that viscous-inviscid interactions have a larger weight in this configuration. However, profiles remain sufficiently close to justify the use of DEKAF's solution as a first and rapid approximation to the actual flow field.

7.6.10 TNE flat plate

In order to verify the implementation in TNE, a Mach-5 flat plate previously studied by Bitter & Shepherd [36] is investigated. The test gas is air with 78% N_2 and 22% O_2 in mass, and the test conditions for the three considered cases are summarized in Table 7.10. The freestream and the wall are considered in thermal equilibrium, such that $T_e = T_{v e}$ and $\bar{T}_w = \bar{T}_{v w}$. The vibrational activation temperatures for N_2 and O_2 are the same as Bitter & Shepherd's, originally obtained from Vincenti & Kruger [37], and summarized in Table K.2. The transport model employed for the DEKAF simulation (BEW) differs from that used by Bit-

Case	$M_e [-]$	p_e [kPa]	T_e [K]	\bar{T}_w [K]	x [m]
1	5	5	300	300	0.42
2		5	1500		0.7
3		20	2500		1.2

Table 7.10: Test conditions for the verification with Bitter & Shepherd's Mach-5 flat plates in TNE.

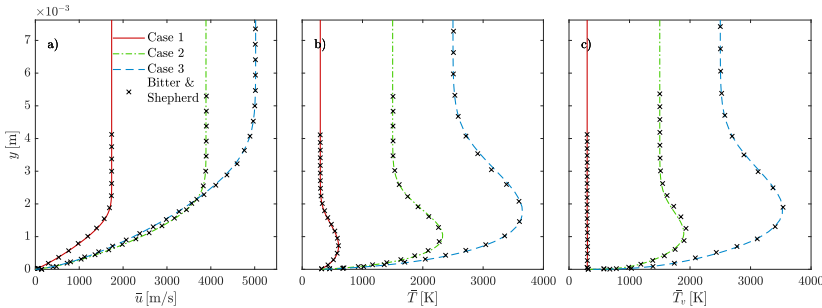


Figure 7.17: DEKAF verification against boundary-layer solutions obtained by Bitter & Shepherd [36] for a flat plate at Mach 5. The exact test conditions are reported in Table 7.10.

ter & Shepherd (SEW). However, the excellent agreement in Fig. 7.17 suggests that both models are very close for the considered flow regimes.

7.6.11 10-degree CPG, CNE and LTE cone at Mach 25

The conical implementation in reacting conditions is verified by investigating a 10-degree cone at Mach 25, previously studied by Stuckert [27] with a PNS solver. The exact test conditions are summarized in Table 7.11, and the gas properties are obtained employing Brokaw's transport model (§ 4.2.1.5), the SM diffusion model (Eq. 4.42), the RRHO model for thermal properties (§ 4.1) and the chemical-equilibrium constant (Eq. 4.66), and the reaction-rate constants collected by Stuckert [27] from a variety of sources [38–45]. The collision integrals are obtained from the fittings proposed by Stuckert (Eq. 4.56 and § K.3.1) to a variety of sources [46–49], and with a B_{sl}^* of 1.06 for all species. The comparison in Figs. 7.18 and 7.19 displays a very good agreement for all flow assumptions. There exists a certain discrepancy, but it is similar to that observed in the comparison with Chang *et al.*'s [32] PNS (§ 7.6.7), suggesting that it is due to the viscous-inviscid interaction considered by the PNS equations, but not by the boundary-layer ones.

$M_\infty [-]$	$p_\infty [\text{Pa}]$	$T_\infty [\text{K}]$	$\bar{T}_w [\text{K}]$	$Y_{\text{N}_2 \infty} [-]$	$Y_{\text{O}_2 \infty} [-]$
25	20.35	252.6	1200	0.79	0.21

Table 7.11: Test conditions for the verification with Stuckert's Mach-25 cone in CPG, CNE and LTE.

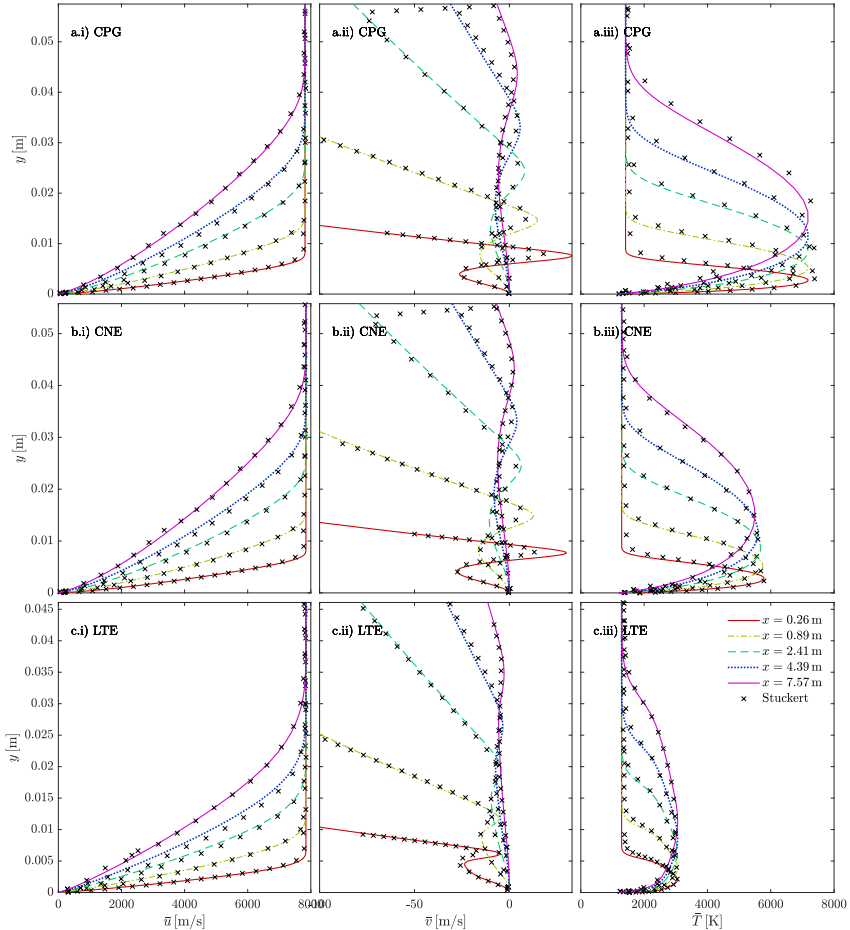


Figure 7.18: DEKAF verification against PNS solutions obtained by Stuckert [27] in CPG, CNE and LTE conditions. \bar{u} , \bar{v} and \bar{T} are compared. The exact test conditions are reported in Table 7.11.

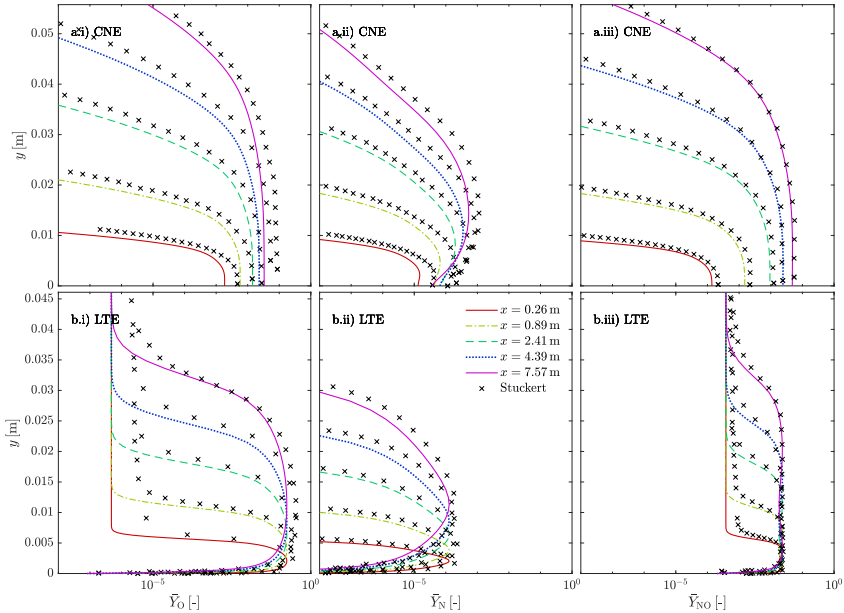


Figure 7.19: DEKAF verification against PNS solutions obtained by Stuckert [27] in CPG, CNE and LTE conditions. The mass fractions of N, O and NO are compared. The exact test conditions are reported in Table 7.11.

7.6.12 State-of-the-art properties

The implementation of the state-of-the-art thermodynamic and transport models is verified by comparison against mutation⁺⁺ [35, 50], for both a 5- and 11-species air mixture. The models in question are the CE transport, the SM diffusion, and the RRHO thermal model. The properties compared are the static enthalpy, frozen heat capacity, viscosity, and frozen and reactive thermal conductivity. The definition of the reactive thermal conductivity (Eq. 2.35) allows one to employ it for the verification of the diffusion coefficients. Figure 7.20 presents a comparison of the aforementioned properties with the composition obtained from assuming LTE conditions (see Fig. B.1) as a function of temperature for various pressures.

7.7 Summary

The capabilities and implementation of the DEKAF flow solver have been presented. A wide variety of test cases have been reproduced in order to carry out a thorough verification of the implementation. The comparisons against higher-fidelity models justify the use of the solver for simplified geometries such as sharp flat plates, wedges and cones. However, one should beware from extrapolating the agreement to more complex geometries. For instance, blunt leading edges, and the entropy layer existing near them is a viscous-inviscid interaction that cannot be considered with a boundary-layer code with zeroth-order coupling. Considering such phenomena requires the use of first- or second-order coupling [1].

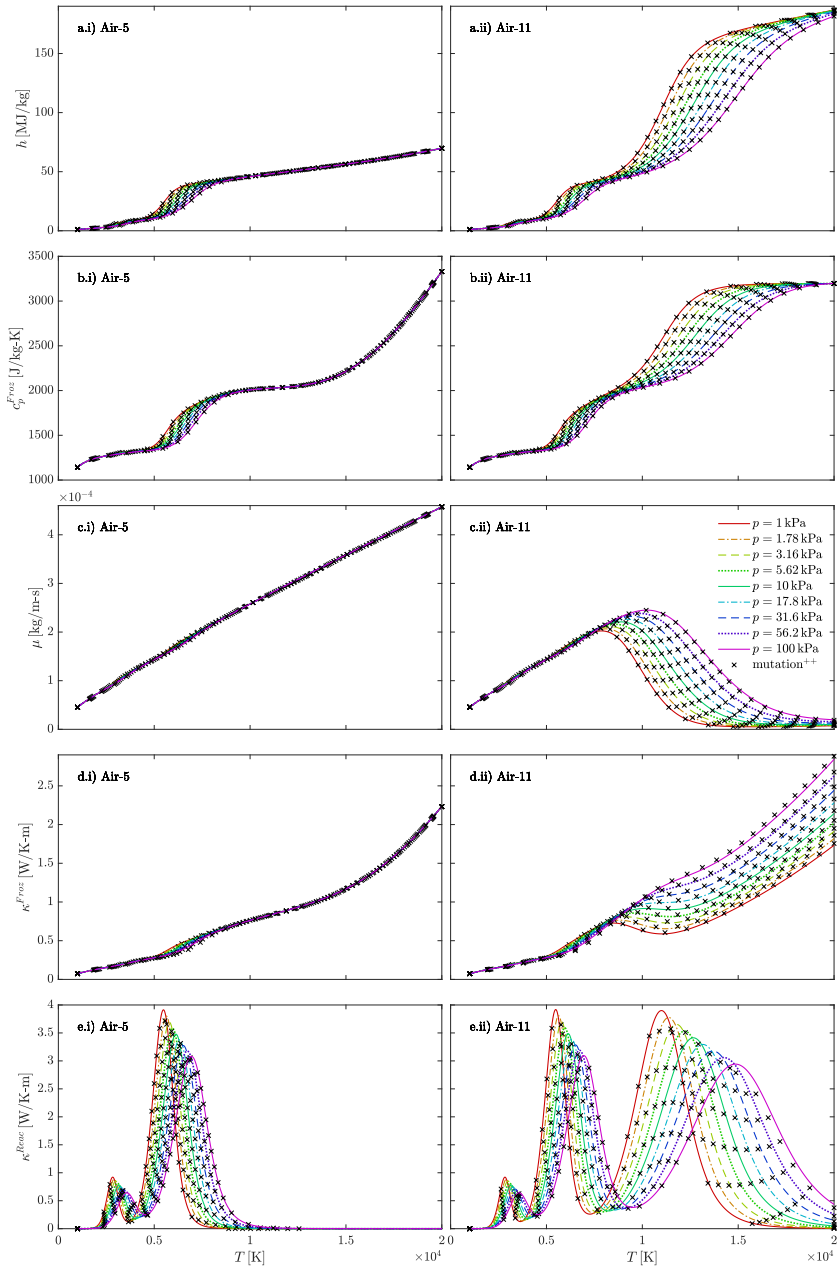


Figure 7.20: Verification of the state-of-the-art thermodynamic and transport properties against mutation⁺⁺ [35, 50]. Properties with the equilibrium concentrations (see Fig. B.1) as a function of temperature for various pressures.

References

- [1] J. P. Brazier, B. Aupoix, and J. Cousteix. *Second-Order Effects in Hypersonic Laminar Boundary Layers*. In T. Murthy, editor, Computational Methods in Hypersonic Aerodynamics. Kluwer Academic, 1991.
- [2] J. D. Anderson Jr. *Hypersonic and High Temperature Gas Dynamics*. American Institute of Aeronautics and Astronautics, Reston VA, second edition, 2006.
- [3] G. I. Taylor and J. W. Maccoll. *The Air Pressure on a Cone Moving at High Speeds. II*. Proceedings of the Royal Society A: Mathematical, Physical and Engineering Sciences, [139\(838\):298–311](#), 1933.
- [4] J. D. Anderson Jr. *Modern compressible flow*. McGraw-Hill, 3rd edition, 1983.
- [5] T. E. Magin. *A Model for Inductive Plasma Wind Tunnels*. PhD thesis, ULB and VKI, 2004.
- [6] G. V. Candler and R. W. MacCormack. *Computation of weakly ionized hypersonic flows in thermochemical nonequilibrium*. Journal of Thermophysics and Heat Transfer, [5\(3\):266–273](#), 1991.
- [7] M. Panesi. *Physical models for nonequilibrium plasma flow simulations at high speed re-entry conditions*. PhD thesis, Università degli Studi di Pisa and von Karman Institute for Fluid Dynamics, 2009.
- [8] M. J. Wright, G. V. Candler, and D. Bose. *Data-Parallel Line Relaxation Method for the Navier-Stokes Equations*. AIAA Journal, [36\(9\):1603–1609](#), 1998.
- [9] L. N. Trefethen. *Spectral Methods in MATLAB*. SIAM, 2000.
- [10] C. Canuto, M. Y. Hussaini, A. Quarteroni, and T. A. Zang. *Spectral Methods: Fundamentals in Single Domain*. Springer Verlag, Berlin, 2006.
- [11] L. Lorig and P. Varona. *Numerical analysis*. Brooks/Cole CENGAGE Learning, 9th edition, 2017.
- [12] M. R. Malik. *Numerical methods for hypersonic boundary layer stability*. Journal of Computational Physics, [86\(2\):376–413](#), 1990.
- [13] B. Fornberg. *Generation of Finite Difference Formulas on Arbitrarily Spaced Grids*. Mathematics of Computation, [51\(184\):699](#), 1988.

- [14] F. Pinna. *Numerical study of stability of flows from low to high Mach number.* PhD thesis, Università degli Studi di Roma La Sapienza, 2012.
- [15] J. A. Weideman and S. C. Reddy. *A MATLAB differentiation matrix suite.* ACM Transactions on Mathematical Software, [26\(4\):465–519](#), 2000.
- [16] J. V. Lassaline. *Supersonic Right Circular Cone at Zero Angle of Attack.* Technical Report AE8121, Ryerson University, 2009.
- [17] J. Tursa. *MTIMESX - Fast Matrix Multiply with Multi-Dimensional Support.* <https://nl.mathworks.com/matlabcentral/>. [Published online on Feb 23rd, 2011].
- [18] M. R. Malik. *Prediction and control of transition in supersonic and hypersonic boundary layers.* AIAA Journal, [27\(11\):1487–1493](#), 1989.
- [19] H. B. Johnson, J. E. Gronvall, and G. V. Candler. *Reacting hypersonic boundary layer stability with blowing and suction.* AIAA paper, [2009-938](#), 2009.
- [20] S. Ghaffari, O. Marxen, G. Iaccarino, and E. S. G. Shaqfeh. *Numerical simulations of hypersonic boundary-layer instability with wall blowing.* AIAA paper, [2010-706](#), 2010.
- [21] J. C. Cooke. *The Boundary Layer of a Class of Infinite Yawed Cylinders.* Mathematical Proceedings of the Cambridge Philosophical Society, [46\(2\):645–648](#), 1950.
- [22] D. Tempelmann. *Receptivity of crossflow-dominated boundary layers.* PhD thesis, Royal Institute of Technology, Stockholm, 2011.
- [23] M. L. Hudson, N. Chokani, and G. V. Candler. *Linear stability of hypersonic flow in thermochemical nonequilibrium.* AIAA Journal, [35\(6\):958–964](#), 1997.
- [24] M. L. Hudson. *Linear Stability of Hypersonic Flows in Thermal and Chemical Nonequilibrium.* PhD thesis, North Carolina State University, 1996.
- [25] C. Park. *On convergence of computation of chemically reacting flows.* AIAA paper, [85-0247](#), 1985.
- [26] G. Stuckert and H. L. Reed. *Linear Disturbances in Hypersonic, Chemically Reacting Shock Layers.* AIAA Journal, [32\(7\):1384–1393](#), 1994.
- [27] G. K. Stuckert. *Linear Stability Theory of Hypersonic, Chemically Reacting Viscous Flows.* PhD thesis, Arizona State University, 1991.

- [28] K. J. Franko, R. W. MacCormack, and S. K. Lele. *Effects of chemistry modeling on hypersonic boundary layer linear stability prediction*. AIAA paper, [2010-4601](#), 2010.
- [29] R. N. Gupta, J. M. Yos, R. A. Thompson, and K.-P. Lee. *A review of Reaction Rates and Thermodynamic and Transport Properties for an 11-Species Air Model for Chemical and Thermal Nonequilibrium Calculations to 30000K*. Technical Report RP-1232, NASA, 1990.
- [30] M. H. Bortner. *Suggested Standard Chemical Kinetics for Flow Field Calculations. A consensus Opinion*. In AMRAC Proceedings, Volume XIV, Part I, Doc. No. 4613-135-X (Contract SD-91). Institute of Science and Technology. University of Michigan, April 1966.
- [31] J. Klentzman and A. Tumin. *Stability and receptivity of high speed boundary layers in oxygen*. AIAA paper, [2013-2882](#), 2013.
- [32] C.-L. Chang, H. Vinh, and M. R. Malik. *Hypersonic boundary-layer stability with chemical reactions using PSE*. AIAA paper, [1997-2012](#), 1997.
- [33] F. G. Blottner, M. Johnson, and M. Ellis. *Chemically Reacting Viscous Flow Program For Multi-Component Gas Mixtures*. Technical Report SC-RR-70-754, Sandia Laboratories, 1971.
- [34] I. Padilla, F. Miró Miró, and F. Pinna. *Influence of High-Temperature Effects on the Stability of the Wake Behind an Isolated Roughness Element in Hypersonic Flow*. In Proceedings of the 2019 IUTAM Symposium on Laminar-Turbulent Transition, London, UK, September 2019.
- [35] J. B. Scoggins and T. E. Magin. *Development of Mutation++: Multicomponent Thermodynamics And Transport properties for IONized gases library in C++*. AIAA paper, [2014-2966](#), 2014.
- [36] N. P. Bitter and J. E. Shepherd. *Stability of highly cooled hypervelocity boundary layers*. Journal of Fluid Mechanics, [778:586–620](#), 2015.
- [37] W. G. Vincenti and C. H. Kruger. *Introduction to physical gas dynamics*. Huntington, N.Y. : Krieger, 1967.
- [38] R. K. Hanson and S. S. *Survey of rate constants in the N/H/O system*. In W. C. Gardiner, editor, Combustion Chemistry, chapter 6, pages 361–422. Springer-Verlag, 1984.
- [39] J. P. Monat, R. K. Hanson, and C. H. Kruger. *Shock tube determination of the rate coefficient for the reaction $N_2 + O \rightleftharpoons NO + N$* . International Symposium on Combustion, [17\(1\):543–552](#), 1979.

- [40] D. L. Baulch, D. D. Drysdale, D. G. Horne, and A. C. Lloyd. *Evaluated Kinetic Data for High Temperature Reactions. Vol. 2: Homogeneous Gas Phase Reactions of the H₂-N₂-O₂ System*. Butterworth, 1973.
- [41] D. L. Baulch, D. D. Drysdale, J. Duxbury, and S. J. Grant. *Evaluated Kinetic Data for High Temperature Reactions. Vol. 3: Homogeneous Gas Phase Reactions of the O₂-O₃*. Butterworth, 1976.
- [42] S. Byron. *Shock-tube measurement of the rate of dissociation of nitrogen*. The Journal of Chemical Physics, [44\(4\):1378–1388](#), 1966.
- [43] K. Thielen and P. Rothf. *in High-Temperature N₂ Dissociation Kinetics*. AIAA Journal, [24\(7\):1102–1105](#), 1985.
- [44] M. Camac and A. Vaughan. *O₂ dissociation rates in O₂-Ar mixtures*. The Journal of Chemical Physics, [34\(2\):460–470](#), 1961.
- [45] K. L. Wray. *Chemical Kinetics of High Temperature Air*. In F. R. Ridell, editor, *ARS Progress in Astronautics and Rocketry: Hypersonic Flow Research*, volume 7, pages 181–204. Academic Press, New York, 1962.
- [46] S. J. Cubley and E. A. Mason. *Atom-molecule and molecule-molecule potentials and transport collision integrals for high-temperature air species*. Physics of Fluids, [18:1109](#), 1975.
- [47] M. Capitelli and E. Ficocelli. *Collision integrals of carbon-oxygen atoms in different electronic states*. Journal of Physics B: Atomic and Molecular Physics, [5:1819–1823](#), 1972.
- [48] K. S. Yun and E. A. Mason. *Collision Integrals for the Transport Properties of Dissociating Air at High Temperatures*. Physics of Fluids, [5:380](#), 1962.
- [49] J. C. Rainwater, L. Biolsi, K. J. Biolsi, and P. M. Holland. *Transport properties of ground state nitrogen atoms*. The Journal of Chemical Physics, [79\(1462\):3203–3210](#), 1983.
- [50] T. E. Magin and G. Degrez. *Transport algorithms for partially ionized and unmagnetized plasmas*. Journal of Computational Physics, [198\(2\):424–449](#), 2004.

8

VESTA's Automatic Derivation and Implementation Tool

The previous chapters gave a sufficiently detailed portrait of the complexity of the mathematical models describing the high-enthalpy flows in atmospheric entry and in hypersonic cruise flights. The subsequent manipulation of these equations that is required in order to perform stability analyses, is thus largely prone to human error. Several examples of such errors were displayed by Pinna & Groot [1, 2] for published 2D-LST, BiG, LPSE, and LST equations. The reported errors concerned equations in CPG conditions. The additional complicatedness of the equations modeling vibrationally-excited, chemically-reacting, or thermally-non-equilibrated flow therefore further increases the likelihood of such misderivations.

Within this frame, the use of computer algebra systems (CAS) that can perform such symbolic manipulations in an automatic fashion is highly recommended. There exist two main derivations to carry out prior to performing stability analyses in high-enthalpy environments. The first is the derivation of the stability (or perturbation) equations themselves, by deploying the various ansatz and simplifications laid out in chapter 3 on the flow equations presented in § 2.3. The second concerns the derivation of the thermodynamic derivatives of the gas properties introduced in chapter 4. The process was presented in § 4.6, and it is necessary, due to the Taylor expansion around 0 of the perturbation dependent quantities (Eqs. 4.94 and 4.95).

The present chapter presents VESTA's automatic derivation and implementation tool (ADIT) – a suite of functions written in Maxima and MATLAB, which

effectively perform the aforementioned operations symbolically, and implement the resulting expressions into functions that can then be employed by the remainder of the code for the numerical analysis. The first section (§ 8.1) concerns the module dealing with the stability equations (ADIT-stab), and the second (§ 8.2) covers the treatment of the thermodynamic and transport properties and their thermodynamic derivatives (ADIT-TTP).

A distinction worth clarifying, between dependent (Q) and independent (q) quantities, is made throughout this chapter. The latter (q) refer to the system's state quantities – the minimal list of variables required to uniquely define its velocity, composition and thermodynamic state. The state variables used in this work are introduced at the beginning of § 2.3, but other combinations are possible. Dependent quantities (Q) are all other flow-field variables appearing in the equations and that can be obtained as a function of the independent. Examples of these are the thermodynamic, transport, chemical, and energy-transfer properties detailed in chapter 4.

8.1 Stability equations

The process one must follow in order to retrieve the stability equations is rather simple:

1. Evaluate the flow equations in function of the total independent and dependent quantities (q and Q), for the chosen coordinate system.
2. Substitute the total with the base-flow quantities (\bar{q} and \bar{Q}) to obtain the laminar flow equations.
3. Separately, substitute the total with the laminar plus the perturbation quantities ($\bar{q} + q'$ and $\bar{Q} + Q'$), leading to the laminar + perturbation equations.
4. Subtract the laminar base-flow equations (step 2) from the laminar + perturbation equations (step 3) to obtain the perturbation equations.
5. Drop the terms with a perturbation order higher than the necessary one - for linear theories it is 1, whilst for non-linear it is equal to the level of nonlinearities to be retained.
6. Expand the dependent perturbation quantities (Q') around 0, as outlined in § 4.6.
7. Substitute the remaining base-flow (\bar{q} and \bar{Q}) and (independent) perturbation quantities (q') with the ansatz corresponding to the stability theory (see chapter 3).

Variable	Reference	Variable	Reference
x^i	ℓ_e	α, β	$1/\ell_e$
t	ℓ_e/u_e	ω	u_e/ℓ_e
u^i	u_e	T, T_v	T_e
p, p_s, p_E	$\rho_e u_e^2$	ρ, ρ_s, ρ_E	ρ_e
μ, λ	μ_e	κ	κ_e
κ_{tr}	κ_{tre}	k_v	k_{ve}
$\mathcal{M}, \mathcal{M}_s$	\mathcal{M}_e	$\mathcal{M}, \mathcal{M}_E$	\mathcal{M}_e
h, h_s	h_e	h_v, h_{vs}	h_e
$\mathcal{D}_{sl}, \mathcal{D}_{eff\,s}$	\mathcal{D}_e	J_s^j, J_E^j	$\rho_e \mathcal{D}_e/\ell_e$
$\dot{\omega}_s$	ρ_e/τ_{chem}	Q_{TV}	$\rho_e h_e/\tau_{vib}$
$\dot{m}_w, \dot{m}_w s$	$\rho_e u_e$	$\dot{\omega}_{rad}$	$\rho_e u_e h_e$

Table 8.1: Nondimensionalization convention used in VESTA. Eqs. 8.1-8.5, and app. I, are the only instances of this dissertation that feature non-dimensional quantities.

8. Remove the factor that is common to all terms – the wave function.^a
9. For parabolized stability theories, perform an order-of-magnitude analysis to account for the slow/fast varying of the different quantities (see 3.1.5).

The flow equations are implemented in their invariant form (§ 2.3), such that they are independent of the coordinate system. They are then evaluated in the coordinate system of interest through the choice of the metric tensor g_{ij} (Eq. 2.1).

The tool presented in this section is based on the one developed by Pinna & Groot [1, 2]. However, it was almost completely rewritten with the goal of generalizing the process for arbitrary flow equations, independent and dependent variables, and flow assumptions. This section is structured as follows: the non-dimensionalization convention and following non-dimensional equations are introduced in § 8.1.1; the potential treatments of the spatial gradients of dependent perturbation quantities ($\partial Q'/\partial x^i$) are commented in § 8.1.2; the implementation of the tool is presented in § 8.1.3; and finally a series of verification cases are shown in § 8.1.4.

8.1.1 Non-dimensionalization convention

In order to appropriately scale the different flow quantities, the equations are implemented in their non-dimensional form. This also allows for the appearance of relevant non-dimensional parameters, that display the relative importance of some of the physical phenomena. The non-dimensionalization convention is summarized in Table 8.1, and leads to the non-dimensional version of the flow equations

^aFor instance, for LST the wave function is: $\exp(i(\alpha x + \beta z - \omega t))$.

presented in § 2.3. It is important to note that the equations in this section, together with app. I, are the **only instances in this dissertation** where variables correspond to their **non-dimensional form**, following the convention summarized in Table 8.1. No distinctive identifier is employed to differentiate them from their dimensional counterparts, in order to simplify the (already sufficiently complex) nomenclature. In TCNE, the non-dimensional flow equations read:

$$\frac{\partial \rho_s}{\partial t} + (u^j \rho_s)_{,j} = -\frac{1}{\text{Sc Re}} J_{s,j}^j + \text{Da} \dot{\omega}_s, \quad \forall s \in \mathcal{S}, \quad (8.1a)$$

$$\rho \frac{\partial u^i}{\partial t} + \rho u^j u_{,j}^i = -g^{ij} p_{,j} + \frac{1}{\text{Re}} \mathbb{T}_{,j}^{ij}, \quad \forall i \in [1, 2, 3], \quad (8.1b)$$

$$\begin{aligned} \rho \frac{\partial h}{\partial t} + \rho u^j h_{,j} &= \text{Ec} \left(\frac{\partial p}{\partial t} + u^j p_{,j} \right) + \frac{1}{\text{Re Pr}_{tr}} (\kappa_{tr} g^{ij} T_{,i})_{,j} + \\ &+ \frac{1}{\text{Re Pr}_v} (\kappa_v g^{ij} T_{v,i})_{,j} - \frac{1}{\text{Re Sc}} \mathcal{J}_{,j}^j + \frac{\text{Ec}}{\text{Re}} g_{ik} \mathbb{T}^{kj} u_{,j}^i, \end{aligned} \quad (8.1c)$$

$$\begin{aligned} \rho \frac{\partial h_v}{\partial t} + \rho u^j h_{v,j} &= \text{Ec} \left(\frac{\partial p_e}{\partial t} + u^j p_{e,j} \right) + \frac{1}{\text{Re Pr}_v} (\kappa_v g^{ij} T_{v,i})_{,j} + \\ &- \frac{1}{\text{Re Sc}} \mathcal{J}_{v,j}^j + \text{Da}_v Q_{TV} + \text{Da} \sum_{s \in \mathcal{S}_{\text{mol}}} \dot{\omega}_s h_{vs}, \end{aligned} \quad (8.1d)$$

where the expressions for the elemental diffusion fluxes can be found in § 2.3. One of the species continuity equations (Eq. 8.1a) can be substituted for the mixture continuity equation^b:

$$\frac{\partial \rho_s}{\partial t} + (u^j \rho_s)_{,j} = 0. \quad (8.2)$$

In CNE, Eq. 8.1d is no longer necessary, and Eq. 8.1c is simplified to:

$$\begin{aligned} \rho \frac{\partial h}{\partial t} + \rho u^j h_{,j} &= \text{Ec} \left(\frac{\partial p}{\partial t} + u^j p_{,j} \right) + \frac{1}{\text{Re Pr}} (\kappa g^{ij} T_{,i})_{,j} + \\ &- \frac{1}{\text{Re Sc}} \mathcal{J}_{,j}^j + \frac{\text{Ec}}{\text{Re}} g_{ik} \mathbb{T}^{kj} u_{,j}^i. \end{aligned} \quad (8.3)$$

Similarly, in LTEED, one must not solve the species continuity, but rather the elemental continuity equations:

$$\frac{\partial \rho_E}{\partial t} + (u^j \rho_E)_{,j} = -\frac{1}{\text{Sc Re}} J_{E,j}^j, \quad \forall E \in \mathcal{E}, \quad (8.4)$$

where the expressions for the elemental diffusion fluxes can be found in § 2.3.3.

The equation system in TPG conditions with species interdiffusion is identical to that in CNE, only setting the chemical source terms ($\dot{\omega}_s$) to zero.

^bIt is generally preferable to replace the bath species' continuity equation by the mixture one [3].

In LTE, CPG, or TPG without species interdiffusion, it is not necessary to solve the species continuity equations (Eq. 8.1a), being the mixture continuity equation (Eq. 8.2) sufficient. The energy equation is also simplified, since the energy diffusion fluxes are either absorbed into the thermal conductivity (LTE - see § 2.3.4) or identically zero (CPG and TPG):

$$\rho \frac{\partial h}{\partial t} + \rho u^j h_{,j} = \text{Ec} \left(\frac{\partial p}{\partial t} + u^j p_{,j} \right) + \frac{1}{\text{Re} \text{Pr}} (\kappa g^{ij} T_{,i})_{,j} + \frac{\text{Ec}}{\text{Re}} g_{ik} \mathbb{T}^{kj} u^i_{,j}. \quad (8.5)$$

The non-dimensional form of the various boundary conditions presented in chapter 6 may be found in app. I.

The non-dimensionalization convention used in VESTA (Table 8.1) differs from the one used by authors like Stuckert [3] in the past. Unlike in Stuckert's work, in VESTA equations are non-dimensionalized using three different time scales for the flow motion (ℓ_e/u_e), the chemical activity (τ_{chem}), and the energy transfer between energy modes (τ_{vib}). Similarly, the diffusion coefficients are non-dimensionalized with a reference edge diffusion coefficient \mathcal{D}_e . This is done in order to have non-dimensional parameters in the equations serving as proxys of the importance of the various physical phenomena within the flow. These non-dimensional parameters, appearing in Eqs. 8.1-8.5, together with the ratio of magnitudes they quantify are:

$$\text{Re} = \frac{\rho_e u_e \ell_e}{\mu_e} \rightarrow \frac{\text{inertial forces}}{\text{viscous forces}}, \quad (8.6a)$$

$$\text{Ec} = \frac{u_e^2}{h_e} \rightarrow \frac{\text{kinetic energy}}{\text{internal energy}}, \quad (8.6b)$$

$$\text{Sc} = \frac{\mu_e}{\rho_e \mathcal{D}_e} \rightarrow \frac{\text{viscous diffusion}}{\text{molar diffusion}}, \quad (8.6c)$$

$$\text{Da} = \frac{\ell_e}{u_e \tau_{chem}} \rightarrow \frac{\text{chemical speed}}{\text{flow speed}}, \quad (8.6d)$$

$$\text{Da}_v = \frac{\ell_e}{u_e \tau_{vib}} \rightarrow \frac{\text{energy relaxation speed}}{\text{flow speed}}, \quad (8.6e)$$

$$\text{Pr} = \frac{h_e \mu_e}{\kappa_e T_e} \rightarrow \frac{\text{viscous energy diffusion}}{\text{conductive energy diffusion}}, \quad (8.6f)$$

$$\text{Pr}_{tr} = \frac{h_e \mu_e}{\kappa_{tr e} T_e} \rightarrow \frac{\text{viscous energy diffusion}}{\text{conductive trans.-rot. energy diffusion}}, \quad (8.6g)$$

$$\text{Pr}_v = \frac{h_e \mu_e}{\kappa_{v e} T_e} \rightarrow \frac{\text{viscous energy diffusion}}{\text{conductive vib.-elec.-el. energy diffusion}}. \quad (8.6h)$$

It is important to note that the definition of the reference Prandtl numbers is somewhat different from the traditional one (Eq. 4.5). This is a direct consequence of

the choice of reference quantities summarized in Table 8.1. The two definitions (Eqs. 4.5 and 8.6f) do however coincide for CPG conditions, where $h_e/T_e = c_p$. Similarly, in CPG, the Eckert number is related to the Mach number through:

$$\text{Ec} = (\gamma - 1) M^2, \quad (8.7)$$

which leads to a form of the energy equation (Eq. 8.5) commonly found in literature [1]. Also note that in CPG the non-dimensional enthalpy and temperature are equivalent, so Eq. 8.5 can be effortlessly expressed in terms of T alone.

The reference chemical time scale is associated to the fastest production or destruction of any species anywhere in the domain:

$$\tau_{chem} = \min_{\substack{\forall s \in S \\ \forall x^i \in \Omega^i}} \left(\frac{|\dot{\omega}_s|}{\rho} \right)^{-1}, \quad (8.8)$$

where the domain over which the minimum is searched (Ω^i) corresponds to the entire spatial domain of interest: $y \in [0, y_{\max}]$ for LST, $y \in [0, y_{\max}]$, $x \in [x_{\min}, x_{\max}]$ for PSE, etc. Similarly, the reference energy-relaxation time scale is defined as:

$$\tau_{vib} = \min_{\forall x^i \in \Omega^i} \left(\frac{|Q_{TV}|}{\rho} \right)^{-1}. \quad (8.9)$$

This is a rather pragmatic approach to scaling the equations, but it can lead to problems as the system tends to equilibrium and $\dot{\omega}_s$ and Q_{TV} tend to zero. A more robust and accurate study of the chemical and thermal-relaxation system dynamics therefore requires using the eigenvalues of the source-term Jacobian [4, App. C.6].

Finally, the reference diffusion coefficient \mathcal{D}_e is defined differently for diffusion models accounting for the diffusion of each species within each other species (see § 4.2.2) through diffusion coefficients for each species pair (\mathcal{D}_{se}), and for diffusion models accounting for the diffusion of each species within the mixture through a unique effective diffusion coefficient per species ($\mathcal{D}_{eff\,s}$). For the former, \mathcal{D}_e is taken as the \mathcal{D}_{se} between the two species with a higher concentration at the boundary-layer edge. For the latter, \mathcal{D}_e is taken as the $\mathcal{D}_{eff\,s}$ corresponding to the species with the highest concentration at the edge.

8.1.2 Treatment of the spatial derivatives of the dependent perturbation quantities Q'

Two different manipulations of the stability equations can be performed regarding the derivatives of the dependent perturbation quantities Q' . These two manipulations are presented for a truncation of the Taylor expansion of Q' (Eq. 4.95) at the first term, as is the case for linear stability theories. Its generalization for the

higher-order truncation needed for non-linear theories is straightforward. Differentiating Eq. 4.95 with respect to a spatial direction x^i , and truncating the expansion on the first term, one reaches:

$$\frac{\partial Q'}{\partial x^i} = \frac{\partial}{\partial x^i} \left[\sum_{a \in \mathcal{V}_Q} \frac{\partial \bar{Q}}{\partial \bar{q}_a} q'_a \right] = \sum_{a \in \mathcal{V}_Q} \left[\frac{\partial}{\partial x^i} \left(\frac{\partial \bar{Q}}{\partial \bar{q}_a} \right) q'_a + \frac{\partial \bar{Q}}{\partial \bar{q}_a} \frac{\partial q'_a}{\partial x^i} \right]. \quad (8.10)$$

One can then operate the spatial derivative in the first addend in two ways:

1. Maintain it as it is, thus considering the thermodynamic **derivatives** of **dependent variables** ($\partial \bar{Q}/\partial \bar{q}_a$) as **spatially-varying quantities** (DDVS).
2. Expand the functional dependency of \bar{Q} with the chain rule, such that:

$$\frac{\partial}{\partial x^i} \left(\frac{\partial \bar{Q}}{\partial \bar{q}_a} \right) = \sum_{b \in \mathcal{V}_Q} \frac{\partial^2 \bar{Q}}{\partial \bar{q}_a \partial \bar{q}_b} \frac{\partial \bar{q}_b}{\partial x^i}. \quad (8.11)$$

The advantage of path 1 is that it reduces the maximum thermodynamic differentiation order that is necessary. However, one must compute additional spatial gradients for the thermodynamic derivatives. Spatial gradients are normally computed numerically, and can therefore increase the numerical error of the ultimate solution. The advantage of path 2 is that the thermodynamic derivatives can be computed analytically, employing the tools presented in § 8.2, and thus avoiding such numerical error. However, the maximum thermodynamic differentiation order required is higher. Path 2 also increases the number of terms appearing in the equations, thus making the computation of the system matrices heavier.

In general, whenever possible, it is preferable to follow path 2. However, if the model corresponding to variable Q features an overly complex expression, computing high-order thermodynamic derivatives becomes largely demanding^c. In such scenarios, it is recommended to follow path 1. This work follows path 2 for the CPG cases, and path 1 for all other flow assumptions. The numerical error associated to the spatial differentiation of the thermodynamic derivatives of the dependent quantities ($\partial \bar{Q}/\partial \bar{q}_a$) is minimized when working with base-flows obtained with the DEKAF solver (chapter 7) thanks to its spectral accuracy.

8.1.3 Implementation

The ADIT-stab module consists of two main blocks - the derivation and the implementation tool. Figure 8.1 presents a sketch of the functional structure composing both of these blocks.

The first step is to impose the defaults to the various available options for the derivation (see § 8.1.3.1). The nine steps outlined at the beginning of

^cThe required computational time can increase by up to an order of magnitude.

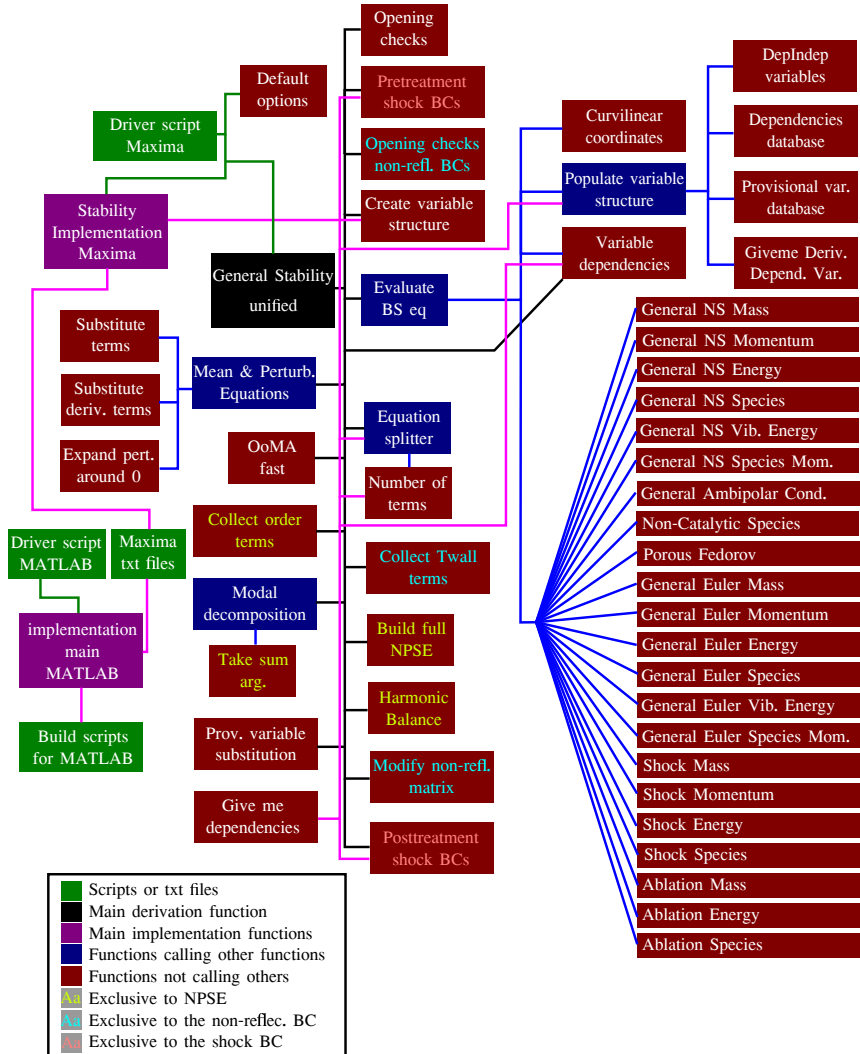


Figure 8.1: Functional structure of VESTA's ADIT for stability equations.

this section are all undertaken by the derivation tool, whose central function is `General_Stability_Unified`. After the necessary preprocessing for certain boundary conditions (for instance appending the shock continuity equation to the list of needed equations when requesting any of the other shock conditions – see § 6.2.1), the central function calls `EvaluateBSeq`. This function acts as a hub, subsequently calling the specific functions storing the various equations in their non-dimensional invariant form (see § 8.1.1). The detailed section of operations performed starts by obtaining the metric tensor, based on the requested coordinate system (see Eqs 2.1 and 2.2); then populating the structure containing the different dependent, independent and provisional variables (see § 8.1.3.2); and then imposing the dependencies of the various variables based on the chosen flow assumption, coordinate system, and stability theory.

The central function (`General_Stability_Unified`) then carries out the nine aforementioned steps, including a splitting of the equation into a series of blocks of terms, in order to avoid memory allocation problems. Finally, the provisional variables are substituted with the final ones, a series of post-treatments are done on certain equations, and the stability equations are outputted.

These equations are then inputted to the implementation tool’s central Maxima function `StabilityImplementation`, where the various terms appearing in the equations are grouped according to the independent perturbation-amplitude quantity (\tilde{q}), and the wave parameter (α, β, ω). This subdivision determines in which computational matrix and submatrix they are implemented at a later stage, and it varies for each different stability theory (see chapter 3). The groups of terms corresponding to different matrices and submatrices, are then written into individual text files that serve as a means of communication between the Maxima and the MATLAB functions. An additional text file is also outputted, containing lists of independent and dependent variables, non-dimensional and wave parameters, spatial coordinates, and other important information concerning the hypotheses defining the derivation. The MATLAB implementation function (`implementation_main`) subsequently reads those files and implements them into the scripts building the various matrices and submatrices constituting the computational problem. The implementation of the derivatives of the laminar quantities can be done using in-line derivatives or not (see § 8.1.3.3).

8.1.3.1 Derivation options

The ADIT-stab module requires five main inputs, and a series of additional options that, if not specified are assigned to their default value. The five main inputs are:

- The **equation list**. It contains the identifiers of the various equations conforming the system. The available equations can be found in Fig. 8.1.
- The **coordinate system**. It can either be Cartesian (Eq. 2.2a), cylindrical

(Eq. 2.2b), spherical (Eq. 2.2c), or orthocurvilinear (Eq. 2.2d).

- The **flow assumption**. Currently supported assumptions are CPG, TPG, LTE, LTEED, CNE and TCNE^d.
- The **stability theory**. The tool currently supports LST, 2D-LST, BiG, LPSE, or NPSE^e. The extension to 3D-LPSE is in development [7].
- The type of **analysis**. It defines^f whether the matrices are for a spatial^g or temporal^h analysis, or if they are wave-parameter-independentⁱ.

Aside from the five main inputs, there are several options conditioning the derivation of the flow equations. The most interesting of them are:

- Eckert or Mach number^j: allows to substitute (or not) the Eckert number with Eq. 8.7.
- Form of the energy equation^{jk}: allows to express the energy equation in terms of temperature, internal energy, static enthalpy, or total enthalpy (see Ref. 2).
- Thermodynamic state quantities^{jk}: allows to choose which thermodynamic quantities define the system.
- Evaluation (or not) of the equation of state^{jk} (Eq. A.10).
- Application (or not) of the Stokes Hypothesis (Eq. 4.3).
- Eigenfunction and spectral directions in theories with two inhomogeneous directions: this distinguishes between 2D-LST and BiG.
- Constant p ^j substitutes the pressure for $1/(\gamma M^2)$, assuming the boundary-layer hypothesis (Eq. 5.3c).
- Number of species or elements^l.

^dNote that the only remaining flow assumption of those summarized in Table 2.1 is the TCFG assumption, which can be easily achieved from employing the TCNE equation system with null chemical and energy-relaxation source terms.

^e**Authorship disclaimer:** the NPSE extension was not developed by the author of this dissertation, but by Zanus [5, 6].

^fThat is of course, for the stability theories that allow for it (see chapter 3).

^gObtaining α for a fixed ω .

^hObtaining ω for a fixed α .

ⁱAnalysis-independent matrices do not include the wave parameters (α, β, ω). This is required to obtain the neutral curve with the procedure presented in app. H.

^jOnly available for CPG conditions.

^kOnly available for LTE conditions.

^lOnly concerning TCNE, CNE and LTEED conditions.

- Diffusion assumption^l: either species-species^m, species-mixtureⁿ, or constant-Schmidt (see Eq. 4.39).
- DDVS: if path 1 or 2 must be followed to deal with $\partial \bar{Q} / \partial \bar{q}_a$ (see § 8.1.2).
- Assume $1/\text{Re}$ to be slowly varying^o
- Order of non-linearity^p and truncation of the Taylor expansion of the dependent perturbation quantities (Eq. 4.95).
- In-line or precomputed spatial derivatives (see § 8.1.3.3).

The presented options therefore uniquely identify the (matrix) build scripts that are generated with the tool. A database system is employed, where each build script is assigned a unique 14-digit identification code. This code is then associated to a specific combination of all the aforementioned options.

8.1.3.2 Provisional variables

Out of the nine steps outlined at the beginning of this section, step 4 would not lead to homogeneous equations of the perturbation quantities, if they featured quotients of flow variables. This can be clearly seen with an example – the diffusion flux in the species continuity equations (Eq. 8.1a). In a Cartesian coordinate system, for a diffusion model leading to Eqs. 2.18 and 2.17, and substituting X_s with Eq. A.7b the diffusion flux becomes:

$$J_s^i = \rho \mathcal{D}_{\text{eff } s} \left(\frac{\mathcal{M}}{\mathcal{M}_s} \frac{\rho_s}{\rho} \right)_{,i}. \quad (8.12)$$

After steps 2 and 3 one reaches the laminar equation, which includes a term such as:

$$\bar{J}_s^i = \bar{\rho} \bar{\mathcal{D}}_{\text{eff } s} \left(\frac{\bar{\mathcal{M}}}{\mathcal{M}_s} \frac{\bar{\rho}_s}{\bar{\rho}} \right)_{,i}, \quad (8.13)$$

and the laminar + perturbation equation, which features:

$$\bar{J}_s^i + (J_s^i)' = (\bar{\rho} + \rho') (\bar{\mathcal{D}}_{\text{eff } s} + \mathcal{D}'_{\text{eff } s}) \left(\frac{\bar{\mathcal{M}} + \mathcal{M}'}{\mathcal{M}_s} \frac{\bar{\rho}_s + \rho'_s}{\bar{\rho} + \rho'} \right)_{,i}. \quad (8.14)$$

The result of subtracting Eq. 8.13 from Eq. 8.14 should have all addends with at least one perturbation quantity among its factors. Otherwise, there would exist a non-homogeneous forcing term, which is not compatible with stability theories

^mWith a diffusion coefficient for each species pair $\mathcal{D}_{s\ell}$.

ⁿWith a unique effective diffusion coefficient for each species $\mathcal{D}_{\text{eff } s}$.

^oOnly concerns PSE.

^pOnly for NPSE.

such as LST, 2D-LST or BiG (see chapter 3). The appearance of $\bar{\rho} + \rho'$ in the denominator of Eq. 8.14 makes it impossible to reach such homogeneity on the perturbation quantities.

If instead, one defines the molar volume \mathcal{V} :

$$\mathcal{V} = \frac{\mathcal{M}}{\rho}, \quad (8.15)$$

as a provisional variable and then carries out steps 2 and 3, rather than reaching Eqs. 8.13 and 8.14 one has:

$$\bar{J}_s^i = \bar{\rho} \bar{\mathcal{D}}_{\text{eff } s} \left(\bar{\rho}_s \frac{\bar{\mathcal{V}}}{\mathcal{M}_s} \right)_{,i}, \quad (8.16)$$

and:

$$\bar{J}_s^i + (J_s^i)' = (\bar{\rho} + \rho') (\bar{\mathcal{D}}_{\text{eff } s} + \mathcal{D}'_{\text{eff } s}) \left((\bar{\rho}_s + \rho'_s) \frac{\bar{\mathcal{V}} + \mathcal{V}'}{\mathcal{M}_s} \right)_{,i}. \quad (8.17)$$

Subtracting Eq. 8.16 from Eq. 8.17, one reaches:

$$\begin{aligned} (J_s^i)' &= \rho' \bar{\mathcal{D}}_{\text{eff } s} \left(\bar{\rho}_s \frac{\bar{\mathcal{V}}}{\mathcal{M}_s} \right)_{,i} + \bar{\rho} \mathcal{D}'_{\text{eff } s} \left(\bar{\rho}_s \frac{\bar{\mathcal{V}}}{\mathcal{M}_s} \right)_{,i} + \\ &\quad + \bar{\rho} \bar{\mathcal{D}}_{\text{eff } s} \left(\rho'_s \frac{\bar{\mathcal{V}}}{\mathcal{M}_s} \right)_{,i} + \bar{\rho} \bar{\mathcal{D}}_{\text{eff } s} \left(\bar{\rho}_s \frac{\mathcal{V}'}{\mathcal{M}_s} \right)_{,i} + \dots, \end{aligned} \quad (8.18)$$

which is indeed homogeneous on the perturbation variables.

One can then proceed with the following steps – Taylor-expanding \mathcal{V}' around 0 (Eq. 4.95), substituting the stability ansatz, and so on, and at the end substitute the provisional variable for the actual variables of interest (or final variables) by evaluating Eq. 8.15. One must substitute not only the laminar provisional variables ($\bar{\mathcal{V}}$ in the example), but also their thermodynamic derivatives ($\partial \bar{\mathcal{V}} / \partial \bar{q}_a$), which must be expressed as a function of those of the final variables.

In general, one has a provisional variable Q^P which depends on several other variables Q_b through a specific function \mathcal{Q}^P :

$$Q^P = \mathcal{Q}^P(Q_b), \quad \forall b \in \mathcal{V}_{Q^P}. \quad (8.19)$$

After following the nine steps laid out at the beginning of this section, one must evaluate Eq. 8.19 on the laminar base-flow quantities:

$$\bar{Q}^P = \bar{\mathcal{Q}}^P(\bar{Q}_b), \quad \forall b \in \mathcal{V}_{Q^P}, \quad (8.20)$$

and also its thermodynamic derivatives, which are obtained applying the chain rule:

$$\frac{\partial \bar{Q}^P}{\partial \bar{q}_a} = \sum_{b \in \mathcal{V}_{Q^P}} \frac{\partial \bar{\mathcal{Q}}^P}{\partial \bar{Q}_b} \frac{\partial \bar{Q}_b}{\partial \bar{q}_a}, \quad \forall a \in \mathcal{V}_{Q_b}, \quad \forall b \in \mathcal{V}_{Q^P}. \quad (8.21)$$

The double condition for all a and all b must be interpreted as all Q_b variables the provisional one Q^P depends on, and all independent quantities q_a that all these Q_b depend on.

In the presented example, one has that:

$$Q^P = \mathcal{V}, \quad (8.22a)$$

$$Q_b = [\mathcal{M}, \rho], \quad (8.22b)$$

$$\mathcal{D}^P(Q_b) = \frac{\mathcal{M}}{\rho}, \quad (8.22c)$$

$$q_a = [\rho_s], \quad \forall s \in \mathcal{S}, \quad (8.22d)$$

since $\mathcal{V} = \mathcal{V}(\mathcal{M}, \rho) = \mathcal{V}(\mathcal{M}(\rho_s), \rho(\rho_s))$ through Eqs. 8.15, A.8 and A.5.

8.1.3.3 In-line derivatives

The current implementation provides two ways to build the spatial derivatives of the base-flow quantities. One can either keep the spatial gradients as distinct inputs to the function, or compute them in-line. The former has the inconvenient of requiring a previous computation of such gradients. Contrarily, the latter requires no such calculation, since it is performed by the build script itself in line. Moreover, since the derivatives are computed with the same differentiation matrices that define the derivatives of the perturbation quantities, the order of accuracy is consistent across all (laminar or perturbation) variables. However, if the original laminar base flow was obtained using an approximation of the derivatives of a lower order than the one featured in the differentiation matrices used in the build script, one could encounter spurious oscillations of the derivatives due to the gibbs phenomenon [8].

Both of these implementations are possible with the ADIT-stab module. The cases presented in this thesis mostly employ build scripts with the in-line computation of the derivatives, since the spectral accuracy of the laminar base flows obtained with DEKAF eliminates the possibility of the Gibbs phenomenon.

8.1.4 Verification

A series of cases are revisited in order to verify various of the flow assumptions, boundary conditions, and coordinate systems incorporated in the ADIT-stab module. The verification carried out in this section concerns the LST solver exclusively. However, partial verification has also been performed for the LPSE [9, 10], 2D-LST [2, 11, 12], or NPSE [5, 6, 13] implementations.

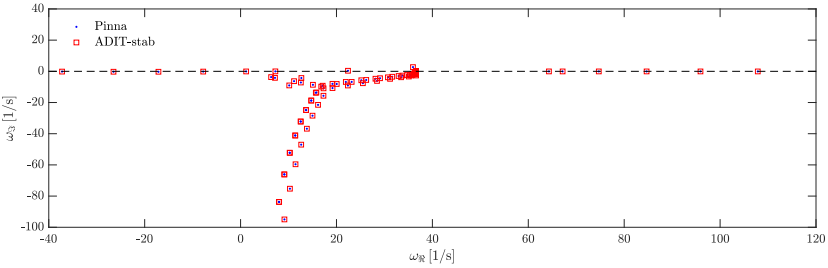


Figure 8.2: Instability spectrum obtained with the automatically-implemented CPG build scripts retrieved with the ADIT-stab module, and with Pinna's [14] manually-implemented solver in CPG conditions. Test conditions correspond to case 3 in Table 7.4, with $\alpha = 0.06 \text{ m}^{-1}$ and $\beta = 0.1 \text{ m}^{-1}$.

8.1.4.1 CPG flow assumption

The implementation of build scripts for a CPG flow assumption is verified by revisiting a test case previously studied by Pinna [14] and Malik [15]. The test conditions correspond to case 3 in Table 7.4, with $\alpha = 0.06 \text{ m}^{-1}$ and $\beta = 0.1 \text{ m}^{-1}$. Note that the edge unit Reynolds number is numerically equal to the Reynolds number based on the Blasius length, and consequently $\ell_e = 1 \text{ m}$. The gas properties are obtained with the conditions in Table 5.2. The baseflow is obtained with VESTA's CBL solver [14]. A Chebyshev discretization with 61 points in the wall-normal direction is used in solving the temporal LST problem. Figure 8.2 presents excellent agreement between the instability spectrum obtained with the manually-implemented compressible LST solver developed by Pinna [14], and that obtained with the one employing the scripts generated by the ADIT-stab module.

8.1.4.2 Porous boundary condition

The implementation of the porous boundary condition (§ 6.1.1.1) is verified by comparison against the manually-implementation previously done by the author [16]. The test conditions correspond to a conical boundary layer previously investigated by Lukashevich & Fedorov [17], and are summarized in Table 8.2. The gas properties are obtained with the conditions in Table 5.2 except for the Prandtl number, which is fixed to $\text{Pr} = 0.72$. The baseflow is obtained with VESTA's CBL solver [14]. A Chebyshev discretization with 150 points in the wall-normal direction is used in solving the spatial LST problem. The excellent agreement observable in Fig. 8.3 verifies the implementation of the boundary condition.

$M_e [-]$	$Re [-]$	$Re_{1,e} [1/m]$	$T_e [K]$	$\bar{T}_w [K]$	$\beta [1/m]$	$\omega [1/s]$
5.37	2000	2000	52.5	290	0	351.4

Table 8.2: Test conditions for the verification of the porous boundary condition in the ADIT-stab module. Case previously studied by Lukashevich & Fedorov [17].

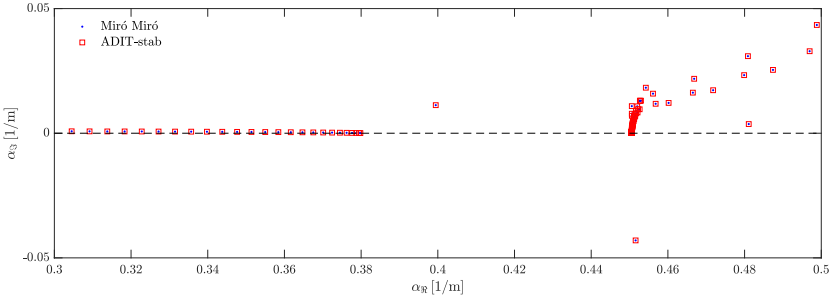


Figure 8.3: Instability spectrum obtained with the automatically-implemented CPG build scripts with a porous boundary condition retrieved with the ADIT-stab module, and with the author's [16] manually-implemented solver. Test conditions correspond to those in Table 8.2.

8.1.4.3 LTE flow assumption

The implementation of the LTE flow assumption is verified by revisiting a test case previously investigated by Malik & Anderson [18]. The test conditions are summarized in Table 8.4. The instability spectrum obtained with Pinna's [14] manually implemented LTE solver is compared to the one obtained with the ADIT-stab's automatically-implemented solvers with and without substituting the equation of state in the flow equations. The gas properties are obtained with look-up tables obtained with the mutation⁺⁺ [19, 20] library, which employs the RRHO thermal model (§ 4.1), the CE transport model (§ 4.2.1.4), the SM diffusion model (Eq. 4.41), and Wright *et al.*'s [21] collisional data. The baseflow is obtained with VESTA's CBL solver [14]. A Chebyshev discretization with 240 points in the wall-normal direction is used in solving the spatial LST problem. All three spectrums presented in Fig. 8.4 display excellent agreement.

A second verification of the LTE solver is performed by reproducing a test

$M_e [-]$	$Re [-]$	$p_e [Pa]$	$T_e [K]$	$\bar{T}_w [K]$	$\beta [1/m]$	$\omega [1/s]$
10	2000	3600	350	adiab.	0	842.4

Table 8.3: Test conditions for the verification of the LTE flow assumption in the ADIT-stab module. Case previously studied by Malik & Anderson [18].

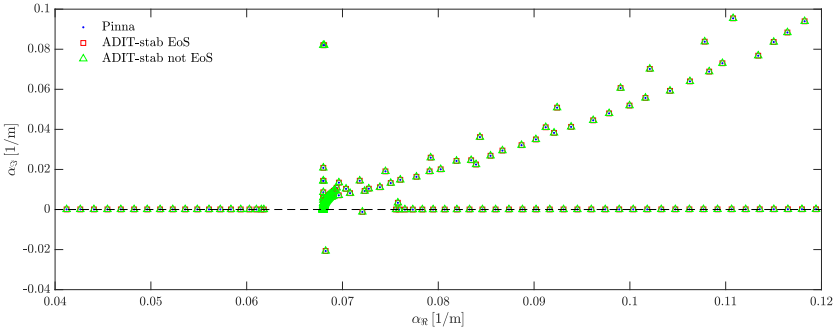


Figure 8.4: Instability spectrum obtained with the automatically-implemented LTE build scripts retrieved with the ADIT-stab module, and with Pinna's [14] manually-implemented solver. Test conditions correspond to those in Table 8.3.

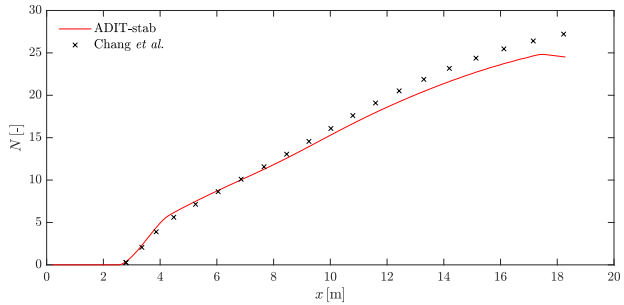


Figure 8.5: Second-mode N factor obtained with the automatically-implemented LTE build scripts retrieved with the ADIT-stab module, and that reported by Chang et al. [22]. Test conditions correspond to those in § 7.6.7, for a perturbation frequency of 100 kHz.

case previously investigated by Chang *et al.* [22]. The test conditions are detailed in § 7.6.7, and the baseflow is obtained with the DEKAF flow solver (see § 7.6.7). Figure 8.5 displays a good agreement between the second-mode N factors for an instability with a frequency of 100 kHz. There is a good agreement for the largest part of the streamwise range. However, the supersonic nature of the mode in the downstream region complicates its accurate reproduction, especially close to the neutral point ($\alpha_3 = 0$). This is due to the interaction of supersonic modes with the continuous branch of the spectrum [9, 23].

8.1.4.4 Shock boundary condition

The implementation of the shock boundary condition (§ 6.2.1) is verified by revisiting a 5-degree wedge case in CPG previously investigated by Esfahanian [24]

M_∞ [-]	p_∞ [Pa]	T_∞ [K]	x [mm]	wall	β [1/m]
8	4000	54.3	3.036	adiab.	0

Table 8.4: Test conditions for the verification of the shock boundary condition in the ADIT-stab module. Case previously studied by Esfahanian [24] and Pinna [25].

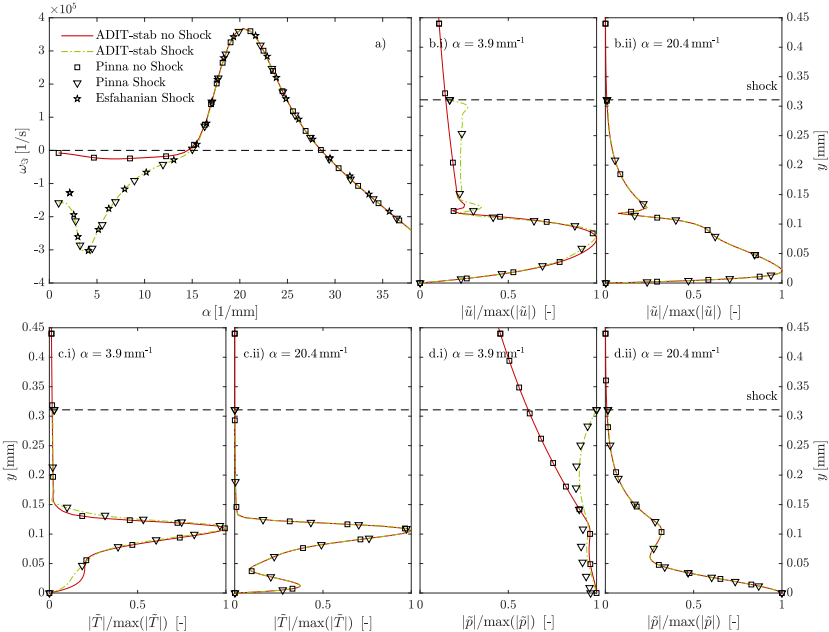


Figure 8.6: Second-mode growth rates and mode shapes obtained with the automatically-implemented CPG build scripts retrieved with the ADIT-stab module, with the manually implemented ones by Pinna [25], and that reported by Esfahanian [24]. Both a shock (§ 6.2.1) and Dirichlet boundary condition on the perturbation amplitudes are compared. Test conditions correspond to those in Table 8.4.

and Pinna [25]. The test conditions are summarized in Table 8.4, and the gas constants are those in Table 5.2. The base-flow solution is obtained with VESTA's CBL solver [14]. Figure 8.6a compares the growth rates obtained with the ADIT-stab module's automatically implemented functions, as well as with Pinna's [25] manually-implemented ones, and those reported by Esfahanian [24]. The growth rates for both the case with and without the shock boundary condition are displayed. Figures 8.6b-d present the mode shapes for two values of the streamwise wave number. It is clear that the shock boundary condition modifies both the instability mode shape and its growth rate more for lower wave numbers. The agreement in all cases is excellent.

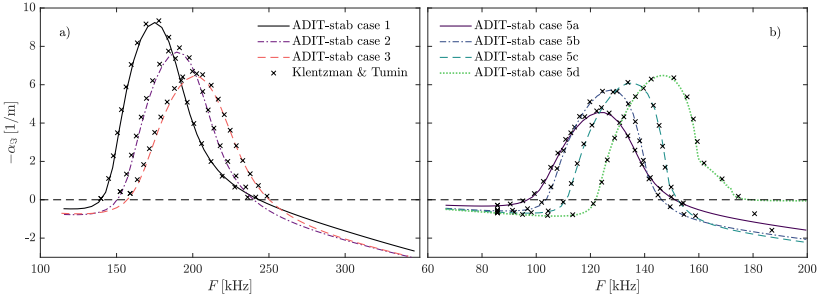


Figure 8.7: Second-mode perturbation growth rates obtained with the automatically-implemented 2-species CNE build scripts retrieved with the ADIT-stab module, and that reported by Klentzman & Tumin [26]. Test conditions correspond to those in Table 7.7, and the gas models to those detailed in § 7.6.6.

8.1.4.5 CNE flow assumption for 2 species

The implementation of the CNE flow assumption for a 2-species mixture in the ADIT-stab module is verified by reproducing a series of test cases previously investigated by Klentzman & Tumin [26]. The test conditions correspond to those in Table 7.7, and the gas models to those detailed in § 7.6.6. The base flow is obtained with the DEKAF flow solver, with the laminar boundary-layer profiles corresponding to those in Fig. 7.13. Figure 8.7 displays an excellent agreement for all the tests.

8.1.4.6 TCNE and CNE flow assumption for 5 species

The CNE and TCNE flow-assumption implementations are verified for a 5-species mixture by reproducing the test case previously investigated by Stuckert & Reed [3, 27], Hudson *et al.* [28, 29], Malik [30], and Franko *et al.* [31], among others. The test conditions correspond to those in Table 7.6 at a streamwise position of $x = 0.4$ m. Two different transport models are compared – the BEW (§ 4.2.1.1), and the Brokaw model (§ 4.2.1.5). The latter requires collisional cross-sectional data for the computation of the transport properties. This data is obtained from the curve fits proposed by Stuckert [3] (Eq. 4.56 and § K.3.1). All laminar base-flow profiles are obtained with the DEKAF flow solver, and correspond to those reported in Fig. 7.12.

Figure 8.8 presents a good agreement for both the CNE and TCNE flow assumptions, and for the two transport models. There is a slight mismatch for the high-frequency content between the various sources. The fact that results present a better match with Malik's, suggests that the mismatch could be related to the numerical method, since Malik employed the same as in this work - a Chebyshev

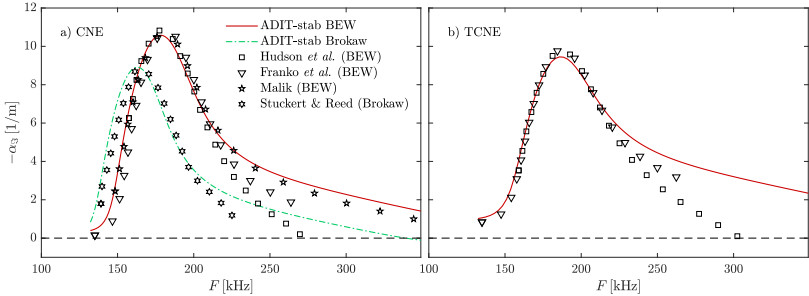


Figure 8.8: Second-mode perturbation growth rates obtained with the automatically-implemented 5-species CNE and TCNE build scripts retrieved with the ADIT-stab module, and that reported by Stuckert & Reed [3, 27], Hudson et al. [28, 29], Malik [30], and Franko et al. [31]. Test conditions correspond to those in Table 7.6 at $x = 0.4\text{ m}$, with two different transport models – the BEW (§ 4.2.1.1), and the Brokaw model (§ 4.2.1.5).

u_∞ [m/s]	p_∞ [kPa]	T_∞ [K]	\bar{T}_w [K]	β [1/m]	$Y_{N_2 \infty}$ [-]	$Y_{O_2 \infty}$ [-]
3882.42	10	1500	300	0	0.78	0.22

Table 8.5: Test conditions for the verification of the TCNE flow assumption in the ADIT-stab module. Case previously studied by Knisely & Zhong [32].

discretization.

8.1.4.7 TCNE flow assumption for 5 species

An additional verification for the implementation of the TCNE flow assumption is performed through a comparison with the results obtained by Knisely & Zhong [32]. The test conditions are summarized in Table 8.5, and the laminar base-flow solution was kindly provided by Dr. Knisely in the framework of a collaboration. The models employed are: the RRHO thermal model (§ 4.1), the BEW transport model (§ 4.2.1.1), the constant-Schmidt-number diffusion model (Eq. 4.39), and the air-5-Park90 mixture (§ J.8). Figure 8.9 displays an excellent agreement in the growth rates, N factors, and mode shapes for all considered frequencies. There exists a slight discrepancy in the behavior of the supersonic modes close to their neutral point ($\alpha_{\mathfrak{Q}} = 0$) similar to what was mentioned in § 8.1.4.3 for Fig. 8.5.

8.1.4.8 Orthocurvilinear coordinate system

The implementation of the orthocurvilinear coordinate system (Eq. 2.2d) is verified by exploring a test case previously investigated by Oliviero *et al.* [33], Balakumar

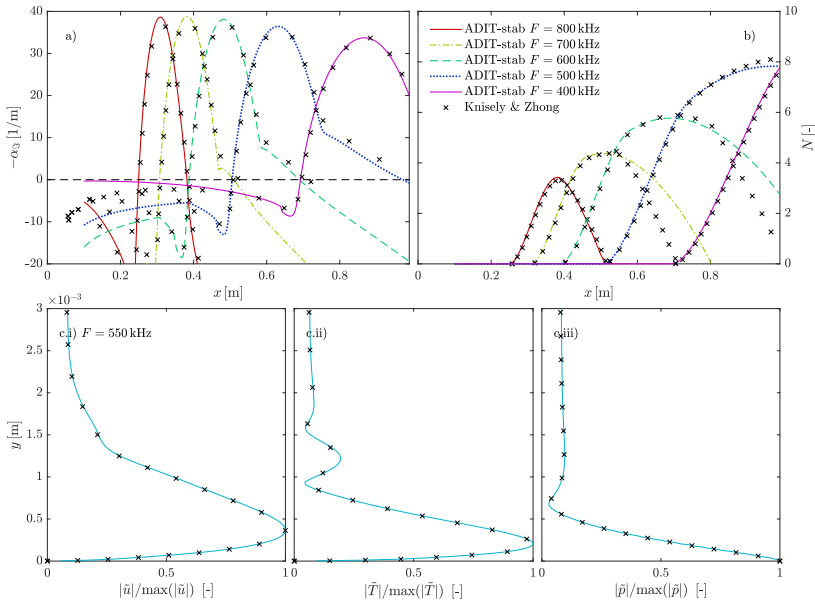


Figure 8.9: Second-mode perturbation growth rates, N factors, and mode shapes obtained with the automatically-implemented 5-species TCNE build scripts retrieved with the ADIT-stab module, and those reported by Knisely & Zhong [32]. Test conditions correspond to those in Table 8.5.

M_∞ [-]	$\text{Re}_{1\infty}$ [1/m]	T_∞ [K]	\bar{T}_w [K]	$r_k \beta$ [-]
6	$10.09 \cdot 10^6$	53.42	300	40

Table 8.6: Test conditions for the verification of the orthocurvilinear coordinate system in the ADIT-stab module. Case previously studied by Oliviero et al. [33], Balakumar & Owens [34], or Craig & Saric [35].

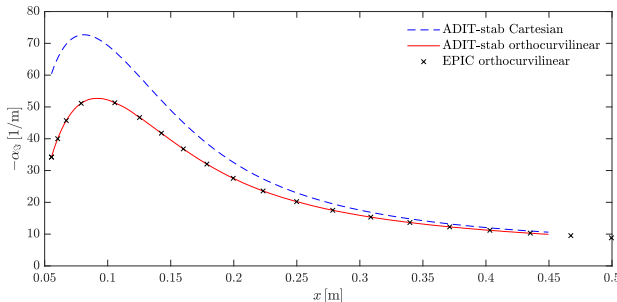


Figure 8.10: Crossflow perturbation growth rates, obtained with the automatically-implemented CPG build scripts with an orthocurvilinear coordinate system retrieved with the ADIT-stab module, and that obtained with EPIC [33]. Test conditions correspond to those in Table 8.6.

& Owens [34], or Craig & Saric [35]. It is a 7-degree cone at an angle of attack of 6 degrees, with the free-stream conditions collected in Table 8.6. The test gas is air, which is modeled with the properties detailed in Table 5.2, yet with a Prandtl number of $\text{Pr} = 0.72$. The base-flow profiles, together with the vortex path, the curvilinear stretching parameters (h_1 , h_2 , and h_3), and the growth rates obtained with EPIC were kindly provided by Dr. Alex Moyes. The streamwise marching is performed along a vortex path, keeping the number of azimuthal waves constant [36]. The number of waves is equal to the local surface radius of curvature in the direction normal to the marching path (r_k) times the azimuthal wave number (β). The excellent agreement observable in Fig. 8.10 of the crossflow growth rates obtained with both tools, verifies the aforementioned implementation. The growth rates obtained neglecting curvature effects are also presented for the sake of completion, and to highlight the influence of such curvature effects in this particular test case.

8.2 Gas properties

In order to carry out the analytical differentiation of all the thermodynamic, transport, chemical, and energy-exchange properties presented in chapter 4, a new module of VESTA's ADIT was developed – the ADIT-TTP.

The symbolic derivation steps followed by the ADIT-TTP module are comparatively simpler than those of the ADIT-stab. The various expressions detailed in chapter 4 are implemented as functions of the species partial densities (ρ_s) and temperature (T) or temperatures (T and T_v). The models are implemented without making assumptions as of the number of species forming the mixture. The Kronecker delta function is therefore used to evaluate the derivative of an arbitrary species partial density ρ_s with respect to another ρ_ℓ :

$$\frac{\partial \rho_s}{\partial \rho_\ell} = \delta_{s\ell}, \quad \forall s, \ell \in \mathcal{S}. \quad (8.23)$$

The expressions for the various properties are differentiated analytically with a series of Maxima functions, and written to several text files that act as a communication channel with the implementation functions in the MATLAB block.

The implementation block is substantially more complex due to three main considerations. First, the expressions presented in chapter 4 feature many summations and products over species, reactions, vibrational modes, energy levels, etc. These summations and products must therefore be identified within the symbolic expressions, and ultimately translated to loops when implemented in the actual functions.

Second, the CE transport model (§ 4.2.1.4) and the SM diffusion model (Eqs. 4.41 and 4.48) require for the resolution of linear systems on the species quantities at each spatial location. As presented in § 4.6, the thermodynamic derivatives of these systems can be obtained from the derivatives of the individual components of the matrix system, and employing a series of matrix-algebra properties. Such matrix operations on the derivative quantities are performed by a function external to those automatically generated by the ADIT-TTP. This implies that the automatically generated scripts must first obtain the thermodynamic derivatives of all the matrix components, then call the external function taking care of the matrix operations, and finally compute any subsequent properties that require as inputs the outputs of the matrix systems. An example of this is the thermal conductivity, which includes a heavy-particle translational component, obtained from solving the matrix system in Eq. 4.30, and internal-energy and electron components (Eqs. 4.31 and 4.32).

Finally, not all the properties require the same order of thermodynamic differentiation. For this reason, a set of functions was developed in order to identify the thermodynamic derivatives required by a given matrix build script generated with the ADIT-stab module. The ADIT-TTP module then goes ahead and implements only these derivatives. In other words, a set of functions generated with ADIT-TTP module can be tailored for a particular matrix build script generated with the ADIT-stab module.

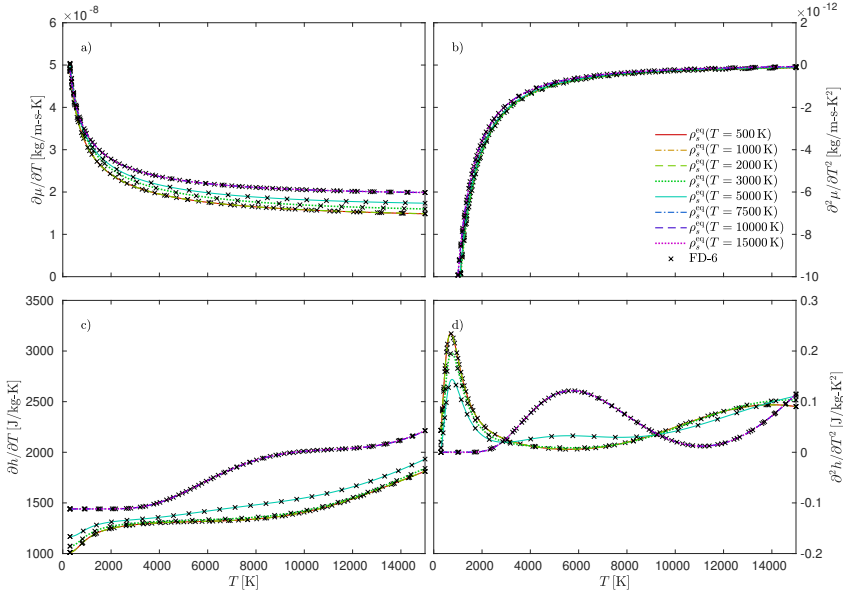


Figure 8.11: Temperature derivatives computed with the ADIT-TTP (analytical) and with a 6th-order FD scheme for an air-11-Park93 mixture. Species densities are constant and equal to their equilibrium values at $p = 1000 \text{ Pa}$ and various temperatures. Properties computed using the CE transport and the RRHO thermal model.

Verification

The implementation of the thermodynamic derivatives with the ADIT-TTP module is verified by comparing the first and second derivative of viscosity and enthalpy with respect to temperature in Fig. 8.11. The analytical derivative, computed with the automatically-implemented functions is compared against the one computed with a 6th-order central finite-difference scheme. The properties' derivatives are computed using the CE transport model, the RRHO thermal model, and the air-11-Park93 mixture (§ J.12). In order to have temperature be the only varying unknown and thus be able to use the aforementioned FD scheme, the species densities remain fixed and equal to their equilibrium values at 1000 Pa and various temperatures (see Fig. B.1). The process to obtain derivatives with respect to ρ_s or T_v is equivalent to that for T -derivatives, thus considering the agreement observable in Fig. 8.11 sufficient for the verification of the tool.

8.3 Summary

This chapter has introduced a series of tools aiding in the complex and highly error-prone process of deriving and implementing the expressions describing the stability of high-speed and/or high-enthalpy boundary layers. The presented ADIT-stab and ADIT-TTP modules, developed within the framework of the VESTA toolkit, are capable of automatically deriving and subsequently implementing, the flow stability equations and the thermodynamic derivatives of the various gas properties. The new tools have been extensively verified, thus providing a solid ground on which to build the following stability and transition analyses.

References

- [1] F. Pinna and K. J. Groot. *Automatic derivation of stability equations in arbitrary coordinates and different flow regimes*. AIAA paper, [2014-2634](#), 2014.
- [2] K. J. Groot. *Derivation of and Simulations with BiGlobal Stability Equations*. Technical Report AE5110, VKI and TU Delft, 2013.
- [3] G. K. Stuckert. *Linear Stability Theory of Hypersonic, Chemically Reacting Viscous Flows*. PhD thesis, Arizona State University, 1991.
- [4] J. B. Scoggins. *Development of numerical methods and study of coupled flow, radiation, and ablation phenomena for atmospheric entry*. PhD thesis, Université Paris-Saclay and VKI, 2017.
- [5] L. Zanus, F. Miró Miró, and F. Pinna. *Nonlinear Parabolized Stability Analysis of Hypersonic Flows in Presence of Curvature Effects*. AIAA paper, [2018-2087](#), 2018.
- [6] L. Zanus and F. Pinna. *Stability Analysis of Hypersonic Flows in Local Thermodynamic Equilibrium Conditions by Means of Nonlinear PSE*. AIAA paper, [2018-3696](#), 2018.
- [7] G. Zuccarino. *Development and implementation of a 3D solver for Parabolized Stability Equations*. Technical Report PR 2019-32, von Karman Institute for Fluid Dynamics, Brussels, Belgium, 2019.
- [8] E. Hewitt and R. E. Hewitt. *The Gibbs-Wilbraham phenomenon: An episode in Fourier analysis*. Archive for History of Exact Sciences, [21\(2\):129–160](#), 1979.
- [9] L. Zanus, F. Miró Miró, and F. Pinna. *Parabolized stability analysis of chemically reacting boundary layer flows in equilibrium conditions*. Proceedings of the Institution of Mechanical Engineers, Part G: Journal of Aerospace Engineering, [234\(1\):79–95](#), 2020.
- [10] L. Zanus, F. Miró Miró, and F. Pinna. *Weak Non-Parallel Effects on Chemically Reacting Hypersonic Boundary Layer Stability*. AIAA paper, [2019-2853](#), 2019.
- [11] I. Padilla Montero and F. Pinna. *Correction: Stability Analysis of the Boundary Layer Developing on a Flat Plate with Discrete Roughness Elements in Hypersonic Flow*. AIAA paper, [2018-1079](#), 2018.
- [12] I. Padilla, F. Miró Miró, and F. Pinna. *Influence of High-Temperature Effects on the Stability of the Wake Behind an Isolated Roughness Element*

- in Hypersonic Flow.* In Proceedings of the 2019 IUTAM Symposium on Laminar-Turbulent Transition, London, UK, September 2019.
- [13] L. Zanus, F. Miró Miró, and F. Pinna. *Nonlinear PSE Transition Predictions in Hypersonic Boundary Layers with Finite Rate Chemical Reactions*. In Proceedings of the 2019 IUTAM Symposium on Laminar-Turbulent Transition, London, UK, September 2019.
 - [14] F. Pinna. *Numerical study of stability of flows from low to high Mach number*. PhD thesis, Università degli Studi di Roma La Sapienza, 2012.
 - [15] M. R. Malik. *Numerical methods for hypersonic boundary layer stability*. Journal of Computational Physics, [86\(2\):376–413](#), 1990.
 - [16] F. Miró Miró. *Numerical Study of the Stability of a Hypersonic Boundary Layer in the presence of Blowing*. Technical Report TR 2015-28, von Karman Institute for Fluid Dynamics, Brussels, Belgium, 2015.
 - [17] S. V. Lukashevich, A. A. Maslov, A. N. Shiplyuk, A. V. Fedorov, and V. G. Soudakov. *Stabilization of High-Speed Boundary Layer Using Porous Coatings of Various Thicknesses*. AIAA Journal, [50\(9\):1897–1904](#), 2012.
 - [18] M. R. Malik and E. C. Anderson. *Real gas effects on hypersonic boundary-layer stability*. Physics of Fluids, [803\(3\):803–821](#), 1991.
 - [19] T. E. Magin and G. Degrez. *Transport algorithms for partially ionized and unmagnetized plasmas*. Journal of Computational Physics, [198\(2\):424–449](#), 2004.
 - [20] J. B. Scoggins and T. E. Magin. *Development of Mutation++: Multicomponent Thermodynamics And Transport properties for IONized gases library in C++*. AIAA paper, [2014-2966](#), 2014.
 - [21] M. J. Wright, D. Bose, G. E. Palmer, and E. Levin. *Recommended Collision Integrals for Transport Property Computations Part I: Air Species*. AIAA Journal, [43\(12\):2558–2564](#), 2005.
 - [22] C.-L. Chang, H. Vinh, and M. R. Malik. *Hypersonic boundary-layer stability with chemical reactions using PSE*. AIAA paper, [1997-2012](#), 1997.
 - [23] C.-L. Chang, H. L. Kline, and F. Li. *Effects of Wall Cooling on Supersonic Modes in High- Enthalpy Hypersonic Boundary Layers over a Cone*. AIAA paper, [2019-2852](#), 2019.
 - [24] V. Esfahanian. *Computation and stability analysis of laminar flow over a blunt cone in hypersonic flow*. PhD thesis, Ohio State University, 1991.

- [25] F. Pinna and P. Rambaud. *Effects of shock on hypersonic boundary layer stability*. Progress in Flight Physics, [5:93–106](#), 2013.
- [26] J. Klentzman and A. Tumin. *Stability and receptivity of high speed boundary layers in oxygen*. AIAA paper, [2013-2882](#), 2013.
- [27] G. Stuckert and H. L. Reed. *Linear Disturbances in Hypersonic, Chemically Reacting Shock Layers*. AIAA Journal, [32\(7\):1384–1393](#), 1994.
- [28] M. L. Hudson, N. Chokani, and G. V. Candler. *Linear stability of hypersonic flow in thermochemical nonequilibrium*. AIAA Journal, [35\(6\):958–964](#), 1997.
- [29] M. L. Hudson. *Linear Stability of Hypersonic Flows in Thermal and Chemical Nonequilibrium*. PhD thesis, North Carolina State University, 1996.
- [30] M. R. Malik. *Hypersonic Flight Transition Data Analysis Using Parabolized Stability Equations with Chemistry Effects*. Journal of Spacecraft and Rockets, [40\(3\):332–344](#), 2003.
- [31] K. J. Franko, R. W. MacCormack, and S. K. Lele. *Effects of chemistry modeling on hypersonic boundary layer linear stability prediction*. AIAA paper, [2010-4601](#), 2010.
- [32] C. P. Knisely and X. Zhong. *Sound radiation by supersonic unstable modes in hypersonic blunt cone boundary layers. I. Linear stability theory*. Physics of Fluids, [31\(2\)](#), 2019.
- [33] N. B. Oliviero, T. S. Kocian, A. J. Moyes, and H. L. Reed. *EPIC: NPSE Analysis of Hypersonic Crossflow Instability on Yawed Straight Circular Cone*. AIAA paper, [2015-2772](#), 2015.
- [34] P. Balakumar and L. R. Owens. *Stability of hypersonic boundary layers on a cone at an angle of attack*. 40th AIAA Fluid Dynamics Conference, [2010-4718](#), 2010.
- [35] S. A. Craig and W. S. Saric. *Crossflow Instability on a Yawed Cone at Mach 6*. Procedia IUTAM, [14:15–25](#), 2015.
- [36] T. S. Kocian. *Computational Hypersonic Boundary-Layer Stability and the Validation and Verification of EPIC*. Ph.d. dissertation, Texas A&M University, 2018.

Part III

Results

9

Surface outgassing and transition

This chapter explores the modification of the transition dynamics due to one of the ablation-caused phenomena – surface outgassing. As briefly mentioned in § 1.4, there exists a significant body of both numerical and experimental research [1–7] showing that the injection of mass into the boundary layer through the surface generally destabilizes it and ultimately leads to an earlier transition.^a

These observations provide a good qualitative insight into the consequences of surface outgassing. However, its modeling remains far from being able to provide reliable quantitative analyses and ultimately predictions. A major limitation of existing models concerns the wall-normal velocity perturbation v'_w . All previous analyses feature a homogeneous condition on the wall-normal velocity perturbation amplitude ($\bar{v}_w = 0$). This implies that the mass injection is assumed to be such that the injection velocity does not experience any fluctuations. Such an assumption appears to be an oversimplification of the underlying physics.

The aforementioned modeling limitations are stronger when accounting for the injection of distinct gasses. The injected-gas composition was experimentally reported [2] to have a large influence on the transition-onset predictions. Despite this, not many investigations have inquired about the causality underlying the observed correlations.

The present chapter addresses some of these issues by extending the previously-existing theoretical and modeling framework. First, the usage of the

^aAn exception to this trend is the stabilization observed by Leyva, Jewell *et al.* [8, 9] when injecting CO₂ at high temperatures. In such instances, the three vibrational modes of the CO₂ molecule were seen to stabilize the flow and lead to a later transition.

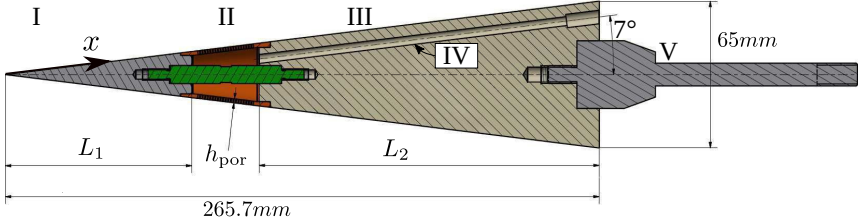


Figure 9.1: Symmetry plane cut of the cones. 1st cone: $L_1 = 82.1 \text{ mm}$, $L_2 = 150.6 \text{ mm}$ and $h_{\text{por}} = 2 \text{ mm}$. 2nd cone: $L_1 = 83.1 \text{ mm}$, $L_2 = 151.6 \text{ mm}$ and $h_{\text{por}} = 1.75 \text{ mm}$.

porous boundary condition (PSBC – see § 6.1.1.1) developed by Fedorov, Gaponov and others [10, 11] for passive walls is validated for blowing configurations. This is done through a joint numerical-experimental campaign carried out at the VKI [12]. Besides validating the models, the investigation also sheds light onto the physical mechanisms underlying the experimental observations. Second, an analysis of the influence of the boundary condition on \tilde{v}_w is performed. The predictions made with the commonly-employed homogeneous condition are compared to those made with the porous condition under various porous-layer configurations, and with the ablation-mimicking condition (AMSCB) developed by the author [13]. Finally, an investigation is carried out on the influence of the injected-gas composition, thus advancing towards identifying the mechanisms involved in Marvin & Akin's [2] experimental work.

9.1 Experimental-numerical investigation of an outgassing cone at Mach 6

9.1.1 Experimental setup

Two experimental campaigns [14, 15] were performed at the VKI-H3 wind tunnel [16, 17]. It is an open-loop blow-down-to-vacuum wind tunnel that provides a uniform 12 cm diameter jet at Mach 6. The free-stream unit Reynolds number is variable, and during the campaigns it was kept between $13.3\text{-}18.4 \cdot 10^6 \text{ m}^{-1}$. The free-stream temperature is around 60 K, and due to the short run time ($< 10 \text{ s}$) the model's surface temperature remains mostly constant and equal to the ambient ($\approx 296 \text{ K}$). Further details about this facility are reported by Simeonides [18].

Figure 9.1 displays a sketch of the cone, with the geometries used for the first and second experimental campaigns (1st and 2nd cone respectively). Both geometries employed the same stainless-steel nose, with a tip radius of 0.1265 mm. The blowing section featured a regular porous layer, with a porosity of 0.37, a pore-radius of about 0.8 mm, and a porous-layer height of 2 and 1.75 mm for the first

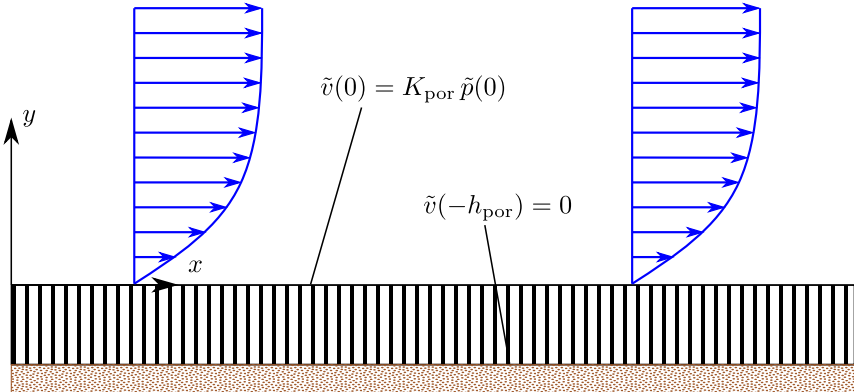


Figure 9.2: Sketch of the various porous layers of the cone and the assumptions made on the wall-normal velocity perturbation.

and second cone respectively. It also included a finer interior porous layer, in order to achieve acoustic decoupling between the plenum's ambient and the wind-tunnel's low-pressure conditions. This precise porous layer, justifies the use of Fedorov and Gaponov's porous boundary condition (see § 6.1.1.1), since one of its requirements is that perturbations must have a zero amplitude at the end of the (regular) porous layer. The configuration of porous layers, together with the requirements for the boundary condition are sketched in Fig. 9.2.

The two different manufacturing techniques employed for the first and second cone (selective laser melting and drilling respectively) lead to substantially different injection profiles (see Ref. 12). In order to compare results with equivalent mass injection, a non-dimensional mass flow rate is introduced, hereinafter referred to as the blowing parameter B :

$$B = \frac{1}{\rho_e u_e S_{\text{base}0}} \int_{x_p0}^{x_p1} 2\pi x \sin(\theta_c) \dot{m}_w^{\text{CL}}(x) dx, \quad (9.1)$$

where $S_{\text{base}0}$ is the cone cross-sectional area at the beginning of the porous section, x_p0 and x_p1 are the positions along the cone surface at which the porous section begins and ends, θ_c is the cone's half-angle, and $\dot{m}_w^{\text{CL}}(x)$ is the injected mass flow along the centerline of the visible area of the cone. This centerline corresponds to the azimuthal position of $\theta = 0$ deg. The injection map is obtained at ambient pressure, and then scaled according to the pressure in the wind tunnel during the test. The boundary-layer-edge density and velocity (ρ_e and u_e) employed for the computation of the experimental B values, are retrieved from solving the Taylor-Maccoll equation (Eq. 7.4). Note that the definition of the B parameter is very similar to the one employed by Marvin & Akin [2], which is also similar to the quantity employed in the ablation community [19, 20].

Case	$M_\infty [-]$	$Re_{1\infty} [1/m]$	$p_\infty [\text{Pa}]$	$T_\infty [\text{K}]$	$\bar{T}_w [\text{K}]$	$\bar{v}_w [\text{m/s}]$
15B0						0
15B4	6	$15.28 \cdot 10^6$	1140.1	61.18	293	0.7
15B7						1.4
15B15						2.7
18B0						0
18B4	6	$18.07 \cdot 10^6$	1293.6	59.67	295.3	0.7
18B7						1.4
18B15						2.7

Table 9.1: Test conditions for the LST analyses in the joint numerical-experimental investigation of surface outgassing.

The experimental transition-onset locations were obtained employing infrared thermography, whilst the perturbation wave numbers of the most amplified waves were retrieved from planar laser-induced fluorescence (PLIF) images.

Further information on the experimental setup, the computation of B , and the post-processing of the infrared and PLIF images can be found in Ref. 12.

9.1.2 Numerical setup

A series of numerical tests are performed in similar conditions to the experiments. Table 9.1 collects the flow conditions employed for the various tests. The preshock unit Reynolds number, pressure and temperature are the result of averaging the two groups of Reynolds numbers (≈ 15.3 and $18.1 \cdot 10^6 \text{ m}^{-1}$) for which experiments were conducted. The low temperatures of the test allow to employ a CPG flow assumption together with Sutherland's law for viscosity (Eq. 4.2) and a constant Prandtl number (Eq. 4.5) of 0.72. Aside from the Prandtl number, the parameters employed for the computation of the thermodynamic and transport properties are those reported in Table 5.2.

The choice of the injection velocities is done in order to accommodate the numerical analysis within the theoretical limitations of boundary-layer theory and LST with mass injection: [21]

$$\bar{v}_w/u_e \sim 1/\text{Re}. \quad (9.2)$$

The laminar base-flow solutions are obtained with the commercial software CFD++ [22], solving the Navier-Stokes equations with a second-order finite-volume method with a Harten-Lax-van Leer-Contact approximate Riemann solver. The computational domain contains 500 points in the wall-normal direction, and 2000 in the streamwise. The mesh-resolution choice is based on the outcome of a convergence test on the N-factor envelopes for Masutti *et al.*'s [16] $Re_{1\infty} \approx 18 \cdot 10^6 \text{ m}^{-1}$ case. The refinement around the shock position was performed by

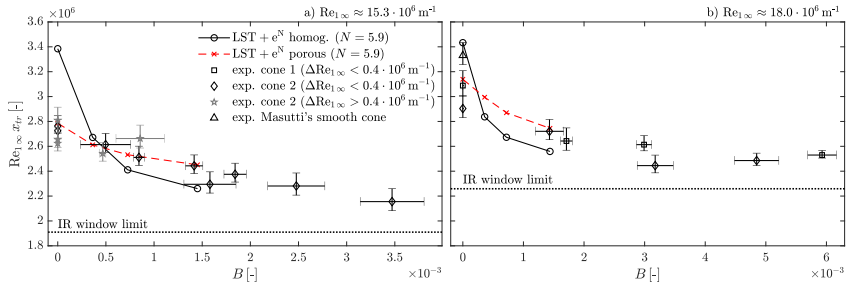


Figure 9.3: Experimental (exp) and predicted transition Reynolds numbers as a function of the blowing parameter B . Masutti et al.'s [10] smooth-cone transition Reynolds number is also included for $Re_{1\infty} = 18.0 \pm 0.4 \cdot 10^6 m^{-1}$.

estimating its position using Billig's experimental correlations for slightly blunt noses [23] and the solution to the Taylor-Maccoll equation (Eq. 7.4). The porous section is treated as a continuous flow inlet. There is no modeling regarding its porosity in the basic-state computation. This approach was shown to be the best option when dealing with porous transpiring surfaces [24].

The transition-onset predictions are performed by employing LST (§ 3.1.4) combined with the e^N method (§ 3.2). Studies are carried out with both the homogeneous boundary condition (Eq. 6.5) and the porous condition (Eq. 6.6). For the cases using the porous condition, the complex perturbation streamwise wave number α is defined in a piecewise fashion:

$$\alpha(x) = \begin{cases} \alpha|_{\text{homog. BC}} & x \notin [x_{p0}, x_{p1}] \\ \alpha|_{\text{porous BC}} & x \in [x_{p0}, x_{p1}] \end{cases} . \quad (9.3)$$

The imaginary component of α is then integrated to obtain the N -curves (§ 3.2). The above piecewise definition is possible because of the parallel-flow hypothesis assumed by LST. However, it is worth mentioning that this very hypothesis actually limits the blowing velocities, which should not be higher than the threshold in Eq. 9.2. The analysis is restricted to second-mode waves, meaning that the spanwise wave number is $\beta = 0$.

9.1.3 Validation of the porous boundary condition

The applicability of the porous boundary condition to wall-blown scenarios is validated by comparing the transition Reynolds numbers, and the wave numbers of the most amplified instabilities, obtained with LST and the e^N method, to those obtained experimentally.

An N factor of $N = 5.9$ is employed for the prediction of the transition-onset locations, in agreement with what was obtained from the aforementioned

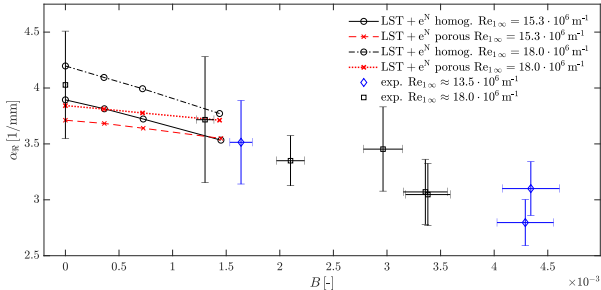


Figure 9.4: Experimental (exp) and predicted second-mode wave numbers of the most amplified disturbances as a function of the blowing parameter B .

grid convergence study on Masutti *et al.*'s [16] case at $\text{Re}_{1\infty} \approx 18 \cdot 10^6 \text{ m}^{-1}$. The experimental results in Fig. 9.3 are restricted to those with $\text{Re}_{1\infty} = 15.3 \pm 0.4 \cdot 10^6 \text{ m}^{-1}$ and $\text{Re}_{1\infty} = 18.0 \pm 0.4 \cdot 10^6 \text{ m}^{-1}$ in order to reduce the scattering of results associated with the dependency of the transition Reynolds number ($\text{Re}_{1\infty} x_{tr}$) on the freestream unit Reynolds number ($\text{Re}_{1\infty}$). The error associated with a higher Reynolds number was previously reported on smooth cones [16], and is observable also from the vertical displacement of the data points in Fig. 9.3a with respect to those in Fig. 9.3b.

Figure 9.3 shows that the piecewise definition of the perturbation growth rates, employing the porous boundary condition on the blowing section (Eq. 9.3), leads to predictions agreeing better with the experimental results than when using the purely homogeneous condition. Moreover, in Fig. 9.3b, at $B = 0$, one observes that whilst the porous boundary condition leads to predictions within the uncertainties of the experiments with a porous section, the homogeneous condition also does so for the experiments with a smooth wall (performed by Masutti *et al.* [16]).

Regarding the trends observed in the experimental results, the transition onset front seems to saturate at around $B = 0.003$. This suggests that some sort of bypass mechanism took over, thus following a different transition path than the one considered by modal theories such as LST – path A in Fig. 3.1. There also appears to be no significant difference between the two considered cone geometries, featuring substantially different mass-injection profiles [12]. An interpretation as to what could be the underlying reason for this is given in the following subsection (§ 9.1.4), based on the LST results.

It is also worth mentioning that the marked IR window limit is different for Figs. 9.3a and 9.3b. This is due to the fact that, while the x range of the IR window is constant across tests, the $\text{Re}_{1\infty}$ is different from Fig. 9.3a to 9.3b, thus displacing the limit vertically on the $\text{Re}_{1\infty} x$ axis.

Profiting of the perturbation spatially-resolved data provided by the PLIF technique, one can also compare the instability-characteristics' predictions made by

LST to the experimental ones. Specifically, one can compare the perturbation wave numbers, characterizing the oscillatory behavior of the perturbations along the spatial direction x . The experimental α_{\Re} values are retrieved by averaging the power-spectral-density (PSD) α_{\Re} -spectrum of each pixel line parallel to the wall in the PLIF image. The resulting experimental α_{\Re} is therefore implicitly averaged over the x range on which the PSD is computed: [156 – 176] mm. For this reason and in order to consistently compare the experimental and numerical results, the wave numbers of the most-amplified perturbations obtained with LST are averaged over this same x range.

The comparison of the experimental and predicted perturbation wave numbers is shown in Fig. 9.4. The good agreement between them suggests that the measured instability characteristics indeed correspond to second-mode waves. Both the experimental and LST wave numbers present a decreasing trend when increasing the value of the blowing parameter. The large uncertainty in the experimental results, however, does not allow to conclude on whether the porous or the homogeneous boundary condition are more suited for the modeling of the particular problem at hand. Moreover, the slightly decreasing trend in the wave numbers when decreasing the unit Reynolds number, that is observable in the LST results, is indistinguishable from the uncertainty of the experimental results.

9.1.4 Interpretation of the experimental results based on the LST analysis

The LST and e^N analyses performed in order to validate the porous boundary condition for wall-blown scenarios (Figs. 9.3 and 9.4), also provide insight into the underlying physical reasons for the observed experimental results. To this end, two cases of those summarized in Table 9.1 are selected (15B0 and 15B15) and compared both with the piece-wise porous and with the homogeneous boundary conditions. The two conditions are identified by the use of the -p (porous) and the -h (homogeneous) suffixes.

Figure 9.5 displays the spatial growth rates of the most amplified perturbations, together with the range of frequencies over which second-mode waves are unstable for the mentioned cases. It is clear that, in the injection region, the growth rates are higher for cases 15B15 than they are for cases 15B0. This is the aforementioned well-known destabilizing effect that mass injection has on boundary layers. The use of the porous boundary condition, however, has the opposite effect – it decreases the amplification rate and stabilizes the flow, as reported by many groups in the past [25–29].^b Regarding the range of unstable frequencies displayed in Fig. 9.5b, mass injection (cases 15B15) is seen to decrease both the maximum and

^bPorous layers do not always stabilize the boundary layer. It actually depends on the size of the pores relative to the boundary-layer height (see Refs. 21, 28 and § 9.3).

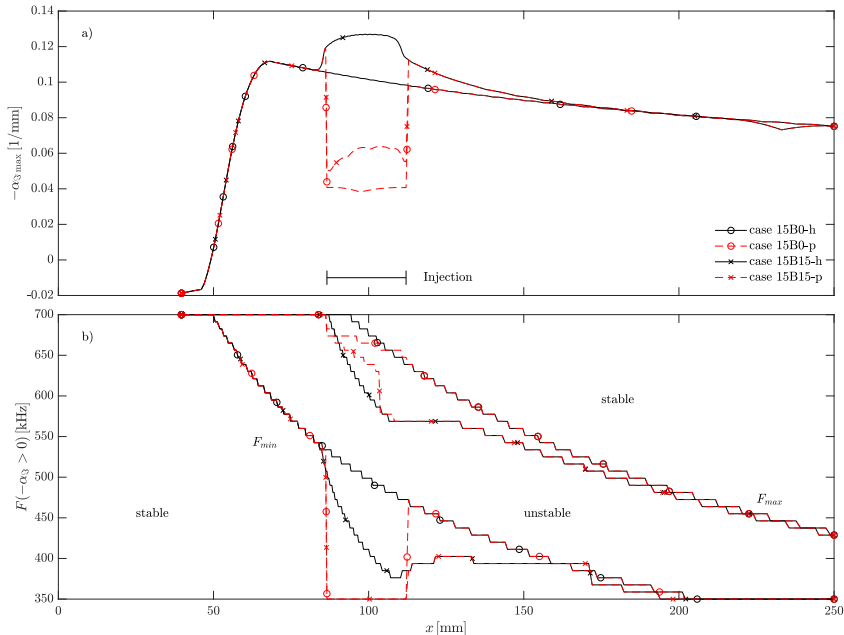


Figure 9.5: Spatial growth rate of the most amplified perturbations (a) and range of unstable frequencies (b) for second-mode instabilities. Case details are summarized in Table 9.1.

the minimum unstable frequencies (with respect to the non-blowing cases 15B0). However, the porous wall exclusively decreases the minimum unstable frequency, thus effectively increasing the range of unstable frequencies. In other words, the problem presents four simultaneously competing effects:

1. The destabilization due to mass injection.
2. The stabilization due to the porous layer.
3. The displacement of the range of unstable frequencies due to mass injection towards lower frequencies.
4. The extension of the range of unstable frequencies due to the porous layer.

One can assess the relative case-dependent importance of the aforementioned effects by integrating the perturbation growth rates for various frequencies (see § 3.2) and comparing the N -factor envelopes. They are displayed in Fig. 9.6 for the four considered cases, including the individual-frequency N -curves for case 15B0-p.

Case 15B0-h (smooth surface) presents a monotonous increasing trend, consistent with what is observed in Fig. 9.5. Case 15B0-p displays the consequences of the mentioned competing effects. At the beginning of the porous region, the N -curves decrease due to the damping that it triggers. However, farther downstream, the lower frequencies that are unstable from an earlier stage than for a smooth wall, consistently increase their magnitude, and eventually reach amplitudes larger than in the smooth case (15B0-h). In fact, they reach the critical transition-onset N -factor ($N = 5.9$) sooner than in the smooth case. In other words, even if the porous layer locally stabilizes the boundary layer, the fact that it also excites a wider range of frequencies, ultimately leads to these frequencies attaining transition-triggering amplitudes sooner than they would in the absence of a porous layer. This is therefore the apparent mechanism-based explanation for the sooner transition observed in the experimental campaigns with a porous surface [14, 15] with respect to Masutti *et al.*'s [16] smooth-cone tests.

Regarding case 15B15-h, in the injection region there is a decrease of the maximum N -factor that is similar to that of case 15B0-p. However, in this case it is not due to the decrease of the maximum amplification rate (blowing actually increases it – Fig. 9.5a), but rather to the decrease of the value of the maximum unstable frequency (Fig. 9.5b). Mass injection stabilizes high-frequency perturbations through the increase in the boundary-layer height. However, similarly to case 15B0-p, at a later streamwise location, the low-frequency waves eventually reach higher amplitude levels than without mass injection, since they have a wider unstable streamwise range. Ultimately the flow reaches the transition-triggering N -factor levels sooner than without mass injection (case 15B0-h).

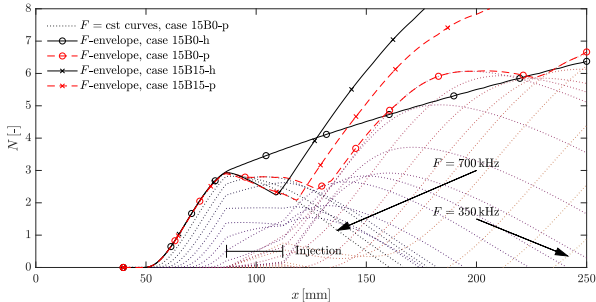


Figure 9.6: Integrated N factors for second-mode instabilities. Case details are summarized in Table 9.1.

When applying the porous condition on case 15B15 (with mass injection), the maximum growth rates are decreased, similarly to what happens with case 15B0. The modification of the range of unstable frequencies, however, is different for case 15B15 than for case 15B0. In case 15B15, the lower limit of the range is already lowered due to mass injection (effect 3 of the previously listed ones), therefore, the marginal decrease in the minimum unstable frequency associated uniquely to the porous condition is less. In other words, the growthrate decrease is similar between the homogeneous and porous conditions is similar for cases 15B0 and 15B15, yet they do not present the same widening of the unstable frequency range. Consequently, the corresponding N -factor envelope for case 15B15-p reaches transition-triggering levels later than case 15B15-h.

To summarize, out of the four competing effects, for case 15B0, number 4 is seen to have a larger importance than number 2, resulting in a sooner transition for the porous case (15B0-p) than for the smooth case (15B0-h). On the contrary, for case 15B15, number 4 is seen to have a minimal impact with respect to number 2. However, the combination of effects 1 and 3 (not present in case 15B0) leads case 15B15-p to transition sooner than any of the non-blowing (15B0) cases.

In spite of everything else, the numerical results suggest that an injection pattern through the surface is not the main defining feature of the considered test cases. Instead, the discontinuity in both the injection and porous wall appears as the driver of instability development. This is a plausible explanation as to why the experimental results were seemingly independent of the injection mapping – very different from the first testing campaign [14] (cone 1) to the second [15] (cone 2).

9.1.5 Evaluation of non-parallel effects

The non-zero wall-blown velocity, together with the discontinuity in the wall boundary condition clearly position the problem on the limit of LST's range of applicability. This is mainly due to the parallel-flow assumption, which assumes

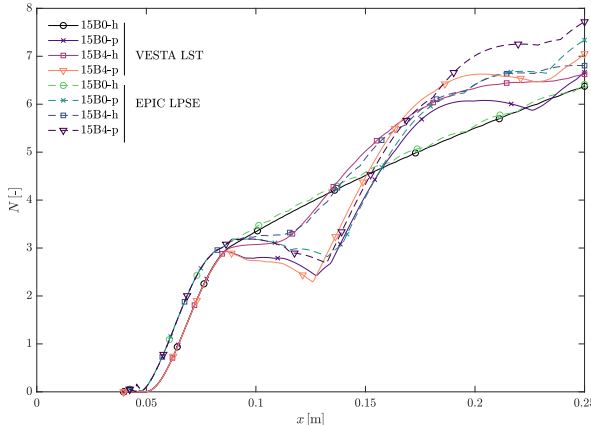


Figure 9.7: Integrated N factors for second-mode instabilities computed with VESTA's LST, and with EPIC's LPSE solvers. Case details are summarized in Table 9.1.

$\bar{q} = \bar{q}(y)$ and $\tilde{q} = \tilde{q}(y)$. In order to assess if such an assumption is still valid under the commented flow conditions, a higher-fidelity analysis is carried out using LPSE, which does consider (weak) streamwise variations. The LPSE analyses were performed by Ethan Beyak, from Texas A&M University, using their in-house tool – EPIC [30].

Figure 9.7 presents very good agreement in the N -factor envelopes obtained with the two codes. There exists a slight discrepancy around the porous injection section, where LPSE does consider the spatial history of instabilities that LST neglects with the piece-wise definition of the growth rates (Eq. 9.3). There is also a discrepancy for the later streamwise locations. However, since the N -factors have already reached transition-triggering levels at that point, the discrepancy is not a major issue. Despite this, the remarkable LST-LPSE agreement further validating the use of LST for the problem at stake.

9.1.6 Conclusions

The use of the porous boundary condition for wall-blown configurations was successfully validated. The predicted transition-onset locations obtained with LST and the e^N method were seen to lie closer to their experimental counterparts when using the porous boundary condition rather than the homogeneous one. Thanks to the perturbation spatially-resolved data provided by the PLIF technique, it was also possible to successfully compare the predicted and measured wave numbers of the most-amplified perturbations. This allows one to affirm that the mechanism leading to transition during the experiments was indeed the development of

second-mode instabilities.

The various computations were then used to investigate which were the underlying mechanisms ultimately leading to the outcome measured in the experiments. The porous layer was seen to advance transition in the non-blowing case, due to the earlier excitation of frequencies that would have otherwise remained stable. The advancement of transition due to this widening of the range of unstable frequencies, was seen to prevail over the delay induced by the local stabilization of the flow above the porous region. In blowing scenarios, the local destabilizing effect of the mass injection was seen to dominate, and therefore lead to a sooner transition onset.

The injection profile through the porous section appears to have a minor influence compared to the wall discontinuity of both mass injection and the porous layer. The latter appears to be the dominant feature of the tested experimental configuration, thus explaining why the two experimental campaigns rendered very similar transition Reynolds numbers whilst featuring radically different injection profiles.

The validity of LST for such a problem was also evaluated by successfully comparing the N -factor envelopes to those obtained with EPIC's LPSE solver.

9.2 Sensitivity of instabilities to the composition of the injection gas

During the decomposition of the TPS, the gas being injected into the boundary layer is obviously not air like in the tests performed in the previous section (§ 9.1), but rather a mixture of various species (see for instance Bhutta & Lewis [31] or Helber *et al.* [32]) resulting from the decomposition of the resin and the fibers. The properties of these species vary significantly from one to another, ranging from those that are overly lighter than air (like H) to those that are much heavier (like CO₂ or C₃). It is therefore important to understand how the transition dynamics vary when injecting gases with different characteristics.

During the 60s and 70s, several groups [2, 33–39] performed experimental campaigns where gases other than air were injected through a porous surface in a slender cone in hypersonic conditions. However, as pointed out by Schneider [1], many of them lacked the necessary control of the test conditions that is required in order to conclude on the implications of such a composition modification. In those campaigns that did feature such rigor [2, 38, 39], a common trend observed was that the injection of lighter gases like He (with a lower molar mass) lead to a sooner transition than with air injection. Heavier gases like CO₂ were seen to have the opposite effect. Marvin & Akin [2] went so far as to develop a correlation weighing in also the molar mass of the injected gas, achieving a remarkable scaling of the

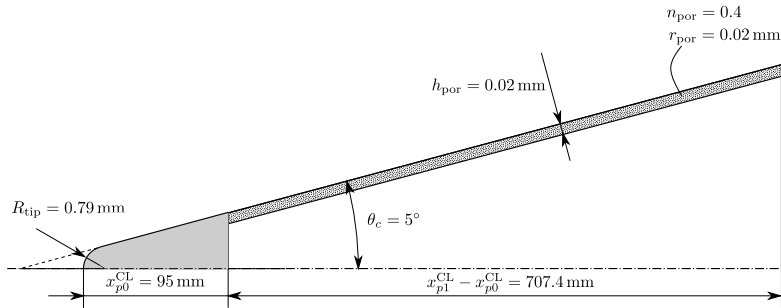


Figure 9.8: Sketch of the cone employed in the investigation of the sensitivity of instabilities to the composition of the injection gas, similar to that of Marvin & Akin [2].

experimental results. Stalmach *et al.* [39] then successfully tested this correlation by applying it to other injected gases different from those employed by Marvin & Akin.

These experimental efforts, however, were not followed by the corresponding physics-based numerical analyses providing insight into the underlying mechanisms establishing the causal link observed in the wind-tunnel tests. The present section addresses this research void by revisiting a configuration similar to that of Marvin & Akin, and performing LST studies on base flows obtained from boundary-layer theory, and the Navier-Stokes equations. The underlying causes for the aforementioned experimentally-observed trend are explored by using simplified models that allow for a decoupling of the coexisting phenomena.

9.2.1 Test conditions and gas modeling

Similarly to Marvin & Akin's [2], the selected geometry is a 5-degree half-angle cone, with the physical characteristics summarized in Fig. 9.8. The total length of the cone is extended, by enlarging the porous injection region to have a length of 707.4 mm along the cone's symmetry axis, rather than 411.2 mm like Marvin & Akin's. Both blunt and infinitely-sharp tips are considered, with the former featuring a nose radius of 0.79 mm equivalent to Marvin & Akin's sharpest tested nose (1/32 in). When employing the PSBC, the porous layer is modeled with the characteristics reported by the authors ($n_{\text{por}} = 0.4$ and $h_{\text{por}} = 0.02 \text{ mm}$) and assuming a pore-radius of also $r_{\text{por}} = 0.02 \text{ mm}$.^c

The test conditions employed for this investigation are summarized in Table 9.2. The test gas is considered to be a non-reacting mixture of N₂, O₂, and

^cThe pore radius is not reported by Marvin & Akin [2]. However, through private communication, Dr. Marvin suggested that the pore size was sufficiently small, so as to have a uniformly-blowing profile. It is therefore taken equal to 20 μm which, as seen in § 9.3.2, leads to a minor modification of the stability characteristics (at least when injecting air).

M_∞ [-]	p_∞ [Pa]	T_∞ [K]	\bar{T}_w [K]	$Y_{N_2 \infty}$ [-]	$Y_{O_2 \infty}$ [-]
7.4	700.85	69.72	293	0.7671	0.2329

Table 9.2: Test conditions for the investigation of the sensitivity of instabilities to the composition of the injection gas.

Case	Tip radius [mm]	$\dot{m}_w(x)$	Eqs.
1	0	cst./ \sqrt{x}	BL
2	0	cst.	BL
3	0	cst.	NS
4	0	cst. $\mathcal{H}(x_{p0})$	NS
5	0.79	cst. $\mathcal{H}(x_{p0})$	NS

Table 9.3: Test matrix for the investigation of the sensitivity of instabilities to the composition of the injection gas. Suffixes “p” and “s” are added to the case identifier to denote the PSBC (§ 6.1.1.1) or the shock boundary condition (§ 6.2.1).

an additional injected gas – He, Ne, Ar or CO₂. They therefore correspond to the air-2-He (§ J.2), the air-2-Ne (§ J.3), the air-2-Ar (§ J.4), and the air-2-CO₂ (§ J.5) mixtures presented in app. J. Due to the low test enthalpy, one can assume thermal equilibrium, with the thermal properties given by the RRHO model (see § 4.1), with the species characteristics detailed in § K.1.

The SW model (§ 4.2.1.3) is employed to retrieve the mixture’s transport properties. The coefficients needed for the evaluation of Sutherland’s law (Eqs. 4.2 and 4.4) for each species are obtained from the CFD++ database [22], and are collected in Tables K.18 and K.19. The diffusion fluxes are computed employing the constant-Schmidt model (Eq. 4.39) with Sc = 0.7.

The laminar base flow is obtained from either solving the one-temperature multi-species boundary-layer (§ 5.1.1) or Navier-Stokes (§ 2.3.2) equations with frozen species chemical source terms ($\dot{\omega}_s = 0$). The BL solutions are obtained with DEKAF (chapter 7), and the NS solutions with CFD++ [22]. The test matrix, summarizing the various geometries, injection profiles and equation systems is presented in Table 9.3, which includes the Heavyside step function $\mathcal{H}(x_0)$:

$$\mathcal{H}(x_0) = \begin{cases} 0, & x < x_0 \\ 1, & x \geq x_0 \end{cases}, \quad (9.4)$$

in order to model a discontinuous mass injection, only through the porous section.

The subsequent LST analyses are performed with the VESTA toolkit [40, 41], exploiting the extended ADIT capabilities (see chapter 8). Suffixes “p” and “s” are respectively added to the case identifier in Table 9.3 in order to denote the use of the PSBC (§ 6.1.1.1) at the wall or the shock boundary condition (§ 6.2.1) at the freestream, rather than the standard HSBC (Eq. 6.5) and Dirichlet conditions

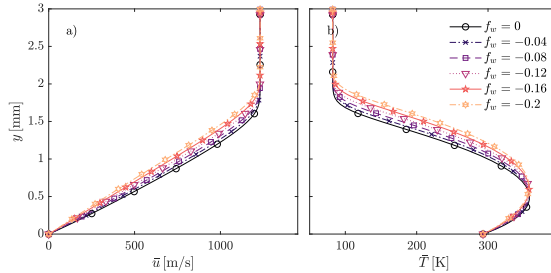


Figure 9.9: Base-flow profiles for case 1 (see Table 9.3) with the air-2 mixture (§ J.1) and self-similar blowing at $x = 508$ mm. Exact test conditions detailed in Table 9.2.

(Eq. 6.27).

9.2.2 Case 1: self-similar multi-species blowing

The multi-species TPG boundary-layer equations (§ 5.1) have a self-similar solution for constant edge quantities and blowing parameter \bar{f}_w (see app. D), thus making an exhaustive parametric study on the influence of the injected gas composition computationally efficient, effective, and inexpensive.

First, the blowing parameter is varied whilst keeping the composition of the injected gas the same as that in the freestream (see Table 9.2) and employing the air-2 mixture (§ J.1). Figure 9.9 presents the boundary-layer velocity and temperature profiles at $x = 508$ mm and for various values of the blowing parameter \bar{f}_w . The mass injection associated to the considered values of \bar{f}_w does not lead to overly enlarged boundary layers when the injected gas is air.

Figure 9.10 displays the corresponding second-mode perturbation growth rates (a) and mode shapes at the most unstable frequency (b). The destabilization of second-mode waves, and the shift of the most unstable mode to lower frequencies, are the expected trends of wall injection, further confirmed in Fig. 9.10a. The mode shapes in Fig. 9.10b are very similar to each other, with the major difference being the vertical shift for larger blowing rates due to the increase in the boundary-layer size.

The integration of the growth rates over the entire x range for various perturbation frequencies, leads to the N -factor envelopes in Fig. 9.11, where the destabilization due to mass injection leads to a slightly-earlier predicted transition onset. Assuming a transition-triggering N factor of 6, according to the findings of § 9.1, the increase in the module of the injection parameter \bar{f}_w from 0 to -0.2^d leads to an advancement of the predicted transition onset location from $x_{tr} = 360$ mm to $x_{tr} = 285.7$ mm.

^dNegative values of \bar{f}_w correspond to mass injection, not suction.

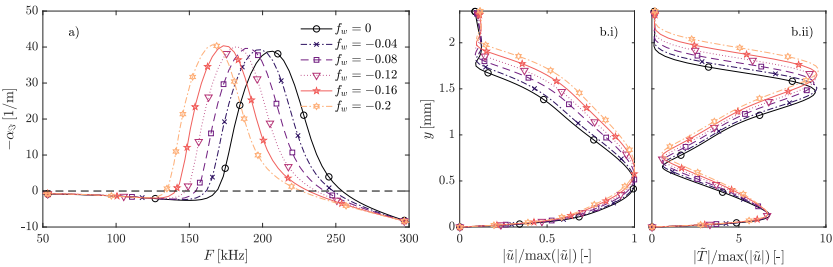


Figure 9.10: Second-mode perturbation growth rates (a) and mode shapes at the most unstable frequency (b) for case I (see Table 9.3) with the air-2 mixture (§ J.1) and self-similar blowing at $x = 508 \text{ mm}$. Exact test conditions detailed in Table 9.2.

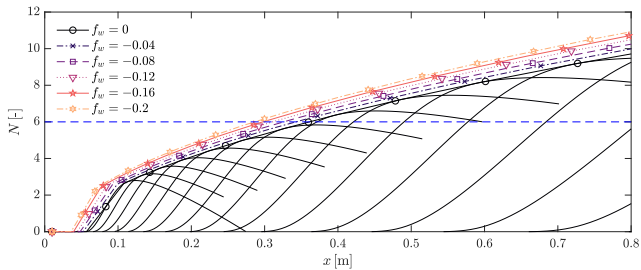


Figure 9.11: Second-mode N -factor envelopes for case I (see Table 9.3) with the air-2 mixture (§ J.1) and self-similar blowing. Exact test conditions detailed in Table 9.2. Single-frequency N -factor curves correspond to $\bar{f}_w = 0$.

For comparison with the preceding and the following sections, a non-dimensional blowing parameter B can be defined analogously to Eq. 9.1, yet for cones with a self-similar blowing:

$$B = \frac{\bar{\rho}_w \bar{v}_w}{\rho_e u_e} = -\sqrt{\frac{3}{2}} \frac{\bar{f}_w}{\text{Re}}. \quad (9.5)$$

The value of B corresponding to the injection levels in Figs. 9.9-9.10 therefore goes from $B = 0$ to $B = 1.05 \cdot 10^{-4}$.

Having established the base-line advancement of the expected transition-onset location when injecting air, one can investigate the isolated influence of the injected gas composition by varying the wall boundary conditions on the mass fractions Y_{sw} . Four different gases are separately mixed with air and injected through the wall: He, Ne, Ar and CO₂. He and Ne have a molar mass (4 and 20.2 g/mol) lower than the average molar mass of air (28.9 g/mol), whilst Ar and CO₂ have a larger one (40 and 44 g/mol). Figure 9.12 presents the velocity, temperature and mass-fraction profiles for six different wall concentrations of each of the injected gases, ranging from 0 to 100% of the mixture. The blowing parameter \bar{f}_w is kept constant for all cases and equal to -0.2. This implies that the injected mass-flow remains constant for all the injection-gas compositions (see definition of \bar{f}_w in Eq. 6.3), similarly to what was done in Marvin & Akin's experiments [2].

The comparison of the boundary-layer profiles in Fig. 9.12 suggests that the injection of lighter species results in an enlargement of the boundary layer, whilst heavier species have the opposite effect. However, the cases with argon injection do not follow this apparent trend. Argon is significantly heavier than air (see Table K.4), yet the boundary-layer height remains unchanged when increasing its concentration in Fig. 9.12c. Instead of the species molar mass, the parameter driving the enlargement or reduction of the boundary-layer size appears to be the thermal diffusivity, defined as:

$$\alpha_s^{\text{diff}} = \frac{\kappa_s}{\rho c_{ps}}, \quad (9.6)$$

and plotted as a function of temperature in Fig. 9.13 for the various injection gases. The gases displaying an enlargement of the boundary layer in Fig. 9.12 (He and Ne), clearly have a higher thermal diffusivity than air, whilst CO₂, which reduced the boundary-layer size in Fig. 9.12d, has a smaller α_s^{diff} than air. Argon, however, has a thermal diffusivity that is practically identical to that of air. This explains why varying the concentration of argon in the injected mixture does not modify the boundary-layer height in Fig. 9.12c.

The thermal diffusivity is a measure of how much energy is conducted away, with respect to the energy that is internally stored by a gas. In other words, for the particular problem at stake, a high thermal diffusivity implies that whatever

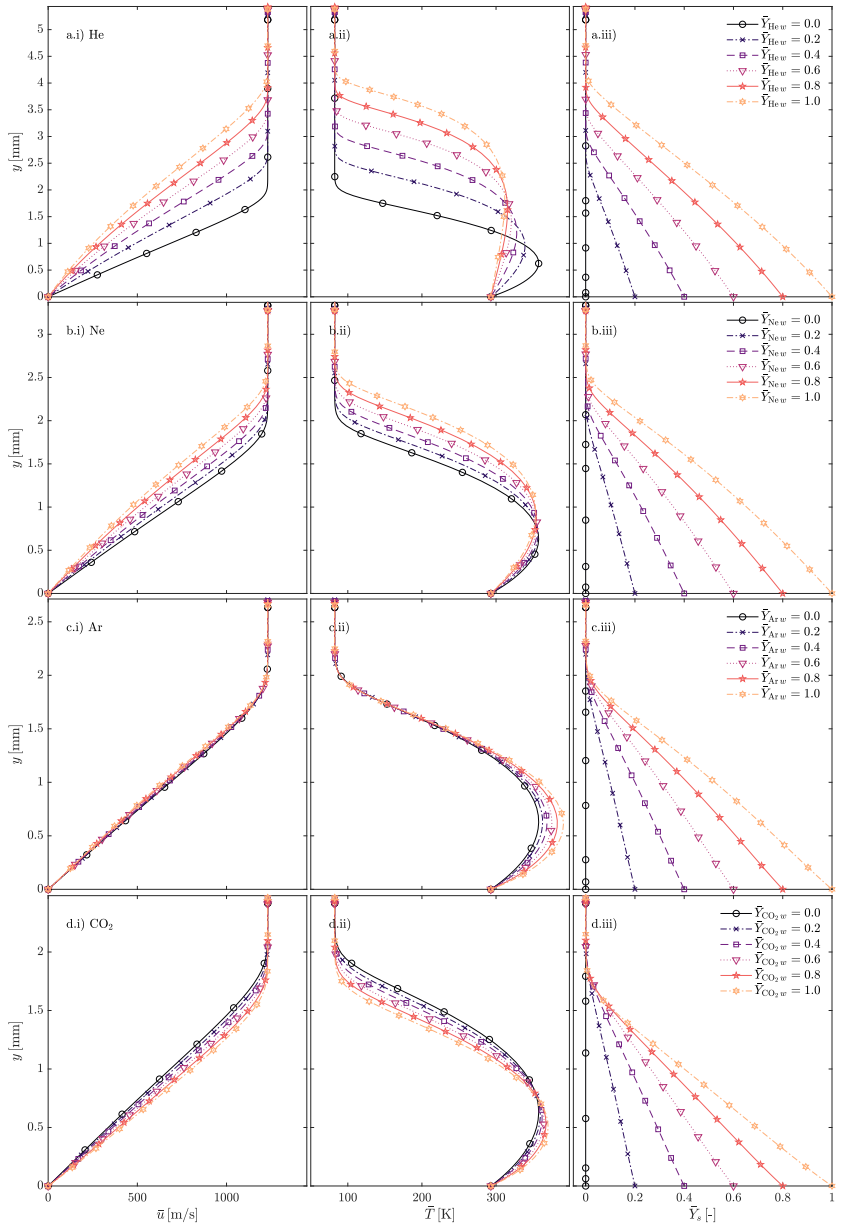


Figure 9.12: Base-flow profiles for case 1 (see Table 9.3) with the air-2-He (a) (§ J.2), the air-2-Ne (b) (§ J.3), the air-2-Ar (c) (§ J.4), and the air-2-CO₂ (d) (§ J.5) mixtures. Self-similar blowing with $f_w = -0.2$ at $x = 508$ mm. Exact test conditions detailed in Table 9.2.

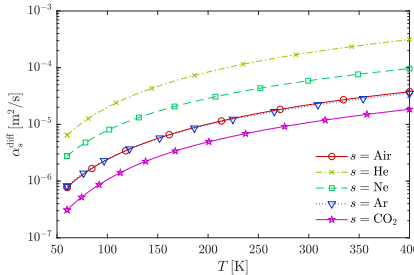


Figure 9.13: Thermal diffusivity as a function of temperature for different gases, computed with the SW transport model (see § 4.2.1.3) and the RRHO thermal model (see § 4.1).

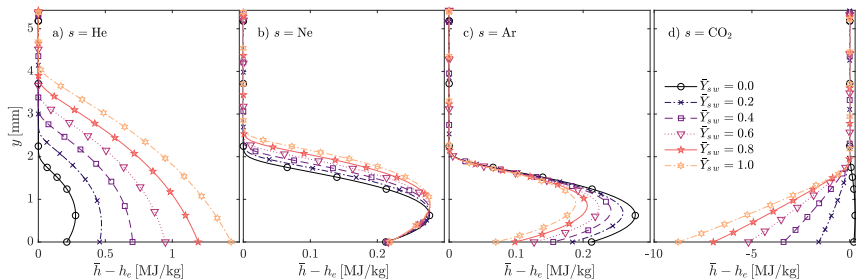


Figure 9.14: Base-flow profiles of the static enthalpy difference for case 1 (see Table 9.3) with the air-2-He (a) (§ J.2), the air-2-Ne (b) (§ J.3), the air-2-Ar (c) (§ J.4), and the air-2-CO₂ (d) (§ J.5) mixtures. Self-similar blowing with \$\bar{f}_w = -0.2\$ at \$x = 508\$ mm. Exact test conditions detailed in Table 9.2.

enthalpy difference arises in the flow as a consequence of the injection of an external species, it is mostly conducted away from the wall. This, in consequence, increases the thermal boundary layer. Similarly, a low thermal diffusivity implies that such an enthalpy difference remains localized close to the surface. These traits are clearly distinguishable in the boundary-layer plots of the static-enthalpy difference for the various injection compositions, presented in Fig. 9.14.

Figure 9.15 displays the second-mode growth rates as a function of frequency for the various laminar flow fields presented in Fig. 9.12. It is interesting to see that the growth rates display the opposite trend to what was experimentally obtained in the experiments [2, 38, 39]. A higher concentration of lighter gases in the injected mixture leads to less unstable perturbations, whilst a higher concentration of heavier gases has the opposite effect. Observing Fig. 9.15a-b, it is clear that besides lowering the maximum amplification rate, a higher helium or neon concentration at the wall also increases the range of unstable frequencies. One could therefore expect the integration of the \$N\$ factors to lead to a sooner transition-onset prediction similar to that observed in the experiments. Figure 9.16 presents the correspond-

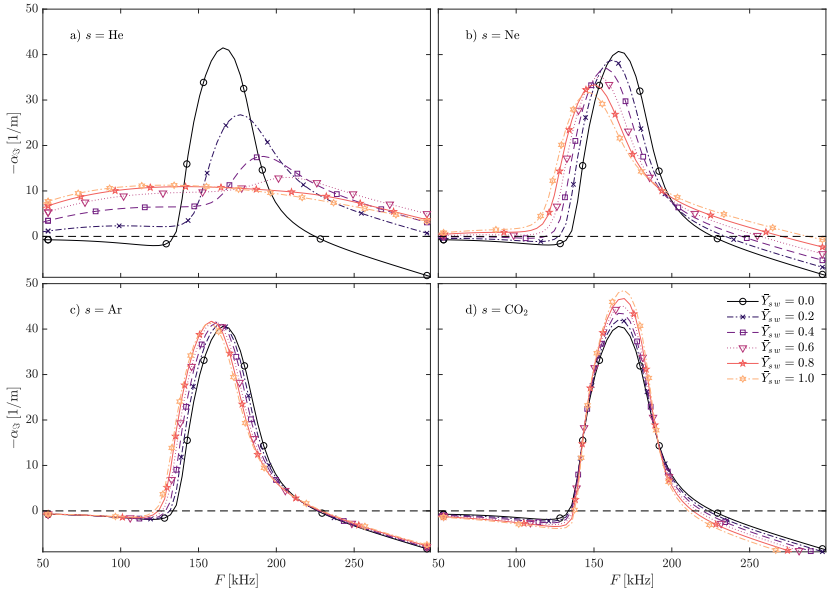


Figure 9.15: Second-mode perturbation growth rates for case 1 (see Table 9.3) with the air-2-He (a) (§ J.2), the air-2-Ne (b) (§ J.3), the air-2-Ar (c) (§ J.4), and the air-2-CO₂ (d) (§ J.5) mixtures. Self-similar blowing with $\bar{f}_w = -0.2$ at $x = 508$ mm. Exact test conditions detailed in Table 9.2.

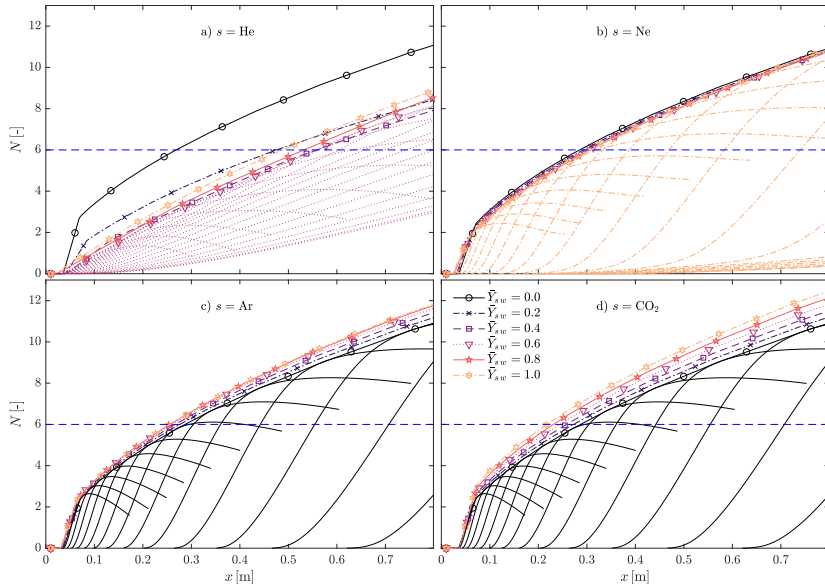


Figure 9.16: Second-mode N -factor envelopes for case 1 (see Table 9.3) with the air-2-He (a) (§ J.2), the air-2-Ne (b) (§ J.3), the air-2-Ar (c) (§ J.4), and the air-2- CO_2 (d) (§ J.5) mixtures. Self-similar blowing with $\bar{f}_w = -0.2$. Exact test conditions detailed in Table 9.2. Single-frequency N -factor curves correspond to $\bar{Y}_{\text{He } w} = 0.6$ (a), $\bar{Y}_{\text{Ne } w} = 1$ (b), $\bar{Y}_{\text{Ar } w} = 0$ (c), and $\bar{Y}_{\text{CO}_2 \, w} = 0$ (d).

	He	Ne	Ar	CO ₂
0 %	285			
20 %	475	293	275	272
40 %	558	299	266	258
60 %	557	304	258	244
80 %	532	307	255	230
100 %	488	307	255	217

Table 9.4: Predicted transition-onset location (in mm) for different compositions of the injection gas mixture obtained from assuming a triggering $N = 6$ on the N -factor envelopes displayed in Fig. 9.16. Test conditions are detailed in Table 9.2 with $\bar{f}_w = -0.2$, and the assumptions are those of case 1 (see Table 9.3).

ing N -factor envelopes, together with a few single-frequency N -factor curves for purely illustrative purposes. The reference transition-triggering N -factor of 6^e is also marked in Fig. 9.16 with a dashed blue line. One can indeed see the competing effect of the decrease in the maximum amplification rate (delaying transition) and the widening of the unstable frequency range (advancing transition) for the lighter-gas cases (Fig. 9.16a-b). The variation of the wall concentration of neon (Fig. 9.16b) displays a balance of these two effects, which ultimately leads to a near-null advancement/delay of the predicted transition-onset location. The N -factor envelopes for scenarios injecting heavier gases (Fig. 9.16c-d) present the same trend observed in the growth rates in Fig. 9.15: a higher concentration of heavier gases ultimately leads to a sooner predicted transition onset. The predicted advancement/delay of transition for a triggering $N = 6$ is summarized in Table 9.4, displaying the expected transition-onset location for all cases.

Overall, the observed trend does not coincide with the experimental findings reported in the experiments [2, 38, 39], being actually opposite to it. This suggests that the advancement/delay of the transition front that they experienced when injecting lighter/heavier gases was not exclusively due to the modification of the injection composition. This in isolation is actually seen to have the opposite effect – delay transition for lighter gases and advance it for heavier ones. It is therefore necessary to progressively question the various simplifying hypotheses made in the preceding analysis, in order to identify which of them actually reverses the observed trend. The hypotheses made are:

1. Dominant second-mode instabilities.
2. SW transport model and constant Schmidt diffusion model.
3. HSBC on the wall velocity perturbation ($\tilde{v}_w = 0$).

^eIt is important to note that such a low N -factor is representative of noisy wind tunnels. In real-flight scenarios, or in quiet wind tunnels, featuring a much lower freestream disturbance level, one typically needs higher N -factor values to trigger transition [42].

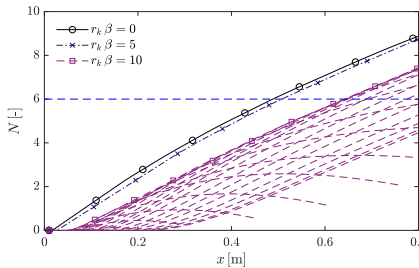


Figure 9.17: N -factor envelopes for case 1 (see Table 9.3) with the air-2-He (\S J.2) mixture and for various numbers of waves in the spanwise direction. Self-similar blowing with $\bar{f}_w = -0.2$. Exact test conditions detailed in Table 9.2. Single-frequency N -factor curves correspond to $r_k \beta = 10$.

4. Self-similar blowing with a constant \bar{f}_w (see Eq. 6.3).
5. Boundary-layer assumptions (see \S 5.1).

The first assumption is questioned in \S 9.2.2.1, the second in \S 9.2.2.2, the third in \S 9.2.2.3, and the fourth and fifth in \S 9.2.3.

9.2.2.1 Span-wise wavenumber sweep

In order to determine if second-mode waves are indeed the most unstable when modifying the composition of the injected gas, the case with the air-2-He mixture (\S J.2) with $Y_{\text{He}w} = 1$ is revisited. Figure 9.17 presents the N -factor envelopes obtained by keeping the number of waves in the spanwise direction ($r_k \beta$) constant. The clear decrease in the N factor envelope for increasing number of waves indicates that first-mode waves (featuring a non-zero β) are not the dominant instabilities in the considered scenarios. One can therefore affirm that hypothesis 1 remains valid.

9.2.2.2 Transport model comparison

The dependency of the observed trends on the thermophysical gas modeling is evaluated by modifying the transport and the diffusion models for three different mixtures: air-2 (\S J.1), air-2-Ar (\S J.4) and air-2-CO₂ (\S J.5). In all cases, the wall composition is assumed to be 100% of either air, argon, or CO₂. Two different sets of models are compared: SW and a constant Sc = 0.7 (like in the rest of the section), and CE and SM. For the latter combination, the necessary collisional data are obtained from fitting Eq. 4.57 to Wright *et al.*'s [43, 44] data. The corresponding curve-fit coefficients are summarized in Tables K.31, K.46, K.47, K.48, and K.49.

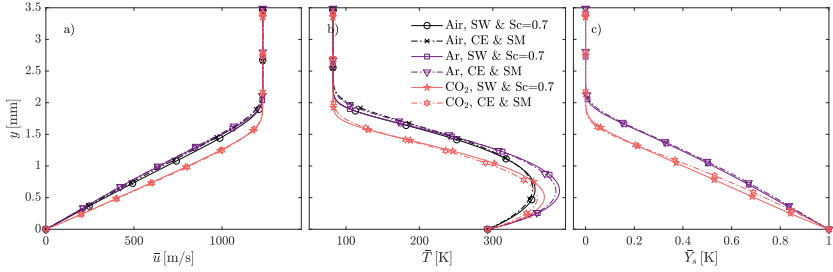


Figure 9.18: Base-flow profiles for case 1 (see Table 9.3) with the air-2 (§ J.1), the air-2-Ar (§ J.4), and the air-2-CO₂ (§ J.5) mixtures, and for two sets of transport and diffusion models. Self-similar blowing with $\bar{f}_w = -0.2$ at $x = 508$ mm. Exact test conditions detailed in Table 9.2.

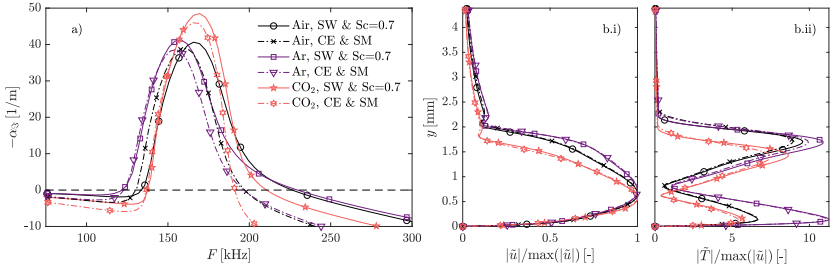


Figure 9.19: Second-mode perturbation growth rates (a) and mode shapes at the most unstable frequency (b) for case 1 (see Table 9.3) with the air-2 (§ J.1), the air-2-Ar (§ J.4), and the air-2-CO₂ (§ J.5) mixtures, and for two sets of transport and diffusion models. Self-similar blowing with $\bar{f}_w = -0.2$ at $x = 508$ mm. Exact test conditions detailed in Table 9.2.

One must note that for the considered temperature range (70-400 K), these curve fits are mostly an extrapolation from the original data points (see app. L). Therefore, the CE and SM models do not offer the higher fidelity, with respect to the SW and the constant Sc = 0.7 models, that they present for high-temperature scenarios (see chapter 4). The comparison displayed in this subsection thus serves as a metric of the sensitivity of the predictions to modeling variations. It is not an evaluation of the accuracy achievable with the employed models.

The base-flow profiles obtained with the two sets of models are presented in Fig. 9.18. The use of one or another set is seen to have a minor impact on the boundary-layer profiles. It is however noteworthy that a stronger cooling and a larger thermal boundary-layer height (visible in Fig. 9.18b) are predicted by the CE and SM models, with respect to the SW and the constant Sc = 0.7 models. This same trend was reported in § 10.1.1 when comparing the CE and the BEW

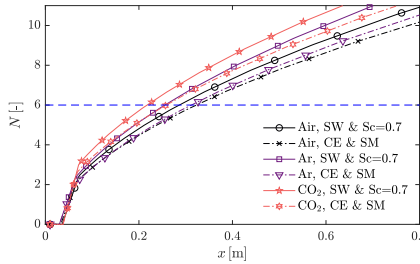


Figure 9.20: Second-mode N -factor envelopes for case 1 (see Table 9.3) with the air-2 (§ J.1), the air-2-Ar (§ J.4), and the air-2-CO₂ (§ J.5) mixtures, and for two sets of transport and diffusion models. Self-similar blowing with $\bar{f}_w = -0.2$. Exact test conditions detailed in Table 9.2.

	Air	Ar	CO ₂
SW & $Sc = 0.7$	285	255	217
CE & SM	322	312	258

Table 9.5: Predicted transition-onset location (in mm) for different compositions of the injection gas mixture and different sets of transport and diffusion models. Locations obtained from assuming a triggering $N = 6$ on the N -factor envelopes displayed in Fig. 9.20. Test conditions are detailed in Table 9.2 with $\bar{f}_w = -0.2$, and the assumptions are those of case 1 (see Table 9.3).

transport models.

Figure 9.19 displays the second-mode growth rates as a function of frequency (a) and the mode shapes for the most-unstable frequency (b) for the laminar base flow presented in Fig. 9.18. The CE and SM models predict lower growth rates than the SW and the constant $Sc = 0.7$ models. This shift, however, is consistent across all mixtures. Blowing heavier gases is seen to destabilize the flow regardless of the transport and diffusion models employed. The mode shapes in Fig 9.19b remain practically unchanged when varying the thermophysical models, aside from a slight vertical shift due to the difference in predicted boundary-layer size. The integrated N -factor envelopes in Fig. 9.20 display the same trend as the growth rates in Fig. 9.19a. The CE and SM models lead to a later predicted transition-onset location than the SW and the constant $Sc = 0.7$ models if assuming a transition-triggering $N = 6$, however the shift is similar for all compositions of the injection gas. Such locations are summarized in Table 9.5.

It is thus clear that the observed destabilizing effect of injecting heavier gases is independent of the transport and diffusion model. Hypothesis 2 therefore appears to not condition the observations reported in this section (Fig. 9.16 and Table 9.4).

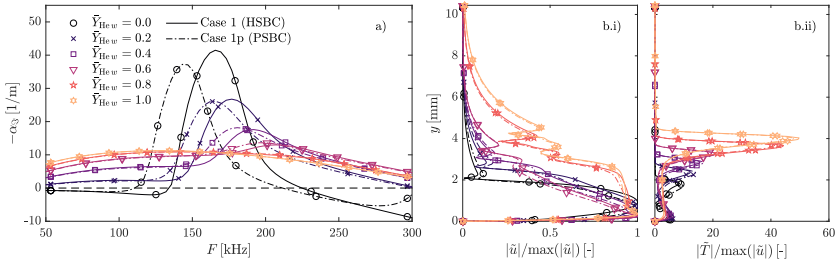


Figure 9.21: Second-mode perturbation growth rates (a) and mode shapes at the most unstable frequency (b) for case 1 (HSBC) and 1p (PSBC) (see Table 9.3) with the air-2-He (§ J.2) mixture. Self-similar blowing with $\bar{f}_w = -0.2$ at $x = 508$ mm. Exact test conditions detailed in Table 9.2.

9.2.2.3 PSBC-HSBC comparison

The influence of the wall-normal-velocity perturbation modeling is investigated by comparing the stability characteristics predicted with the HSBC (used until now) and with the PSBC. Figure 9.21 presents the corresponding second-mode growth rates as a function of frequency (a) and the mode shapes for the most unstable frequency (b), for the air-2-He mixture (§ J.2). The porous layer is seen to stabilize the case with 0% He. As the concentration of helium in the injected gas increases, the marginal effect of the porous wall is to be less stabilizing (see the case with 20% He) and eventually to destabilize slightly (see the case with 60% He). One could therefore expect this effect, if sufficiently meaningful, to ultimately lead to a reversal of the overall stabilizing effect of increasing the wall helium concentration. However, the envelope of the integrated N factors presented in Fig. 9.22 rejects this possibility, displaying a very similar trend for case 1p (PSBC) to that seen for case 1 (HSBC) in Fig. 9.16a. The transition-onset locations predicted with a transition-triggering $N = 6$ are displayed in Table 9.6, where the same trend is shared for cases 1 and 1p.

It is therefore fair to affirm that the use of the PSBC in isolation (hypothesis 3) does not account for the opposite trends observed in the preceding numerical results, and the experimental results [2, 38, 39].

9.2.3 Cases 2-5: non-self-similar He blowing

The influence of self-similar blowing and the boundary-layer assumptions (hypotheses 4 and 5 presented at the beginning of the section) are questioned by examining cases 2-5 in Table 9.3. Hypothesis 3 is also revisited, since the effect of the porous section observed in § 9.2.2.3 counter acts that of the light-gas concentration in the injected mixture. It is therefore reasonable that, under other assumptions,

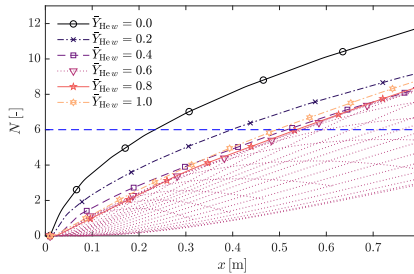


Figure 9.22: Second-mode N -factor envelopes for case 1p (PSBC) (see Table 9.3) with the air-2-He (§ J.2) mixture. Self-similar blowing with $\bar{f}_w = -0.2$. Exact test conditions detailed in Table 9.2. Single-frequency N -factor curves correspond to $\bar{Y}_{He,w} = 0.6$.

	Case 1	Case 1p
0% He	285	233
20% He	475	397
40% He	558	515
60% He	556	543
80% He	532	536
100% He	488	494

Table 9.6: Predicted transition-onset location (in mm) for different compositions of the injection gas mixture and two wall boundary conditions: HSBC (case 1) and PSBC (case 1b). Locations obtained from assuming a triggering $N = 6$ on the N -factor envelopes displayed in Fig. 9.22. Test conditions are detailed in Table 9.2 with $\bar{f}_w = -0.2$, and the assumptions are those of case 1 (see Table 9.3).

the two competing effects could have a different net outcome.

Case 2 features a constant injected mass flux, rather than a constant blowing parameter \bar{f}_w . This implies that the boundary-layer equations (§ 5.1) no longer have a self-similar solution (see app. D), and that the solution must therefore be marched in the streamwise direction. 200 streamwise points, equispaced in x , are taken for the resolution of the boundary-layer equations with DEKAF (see chapter 7). It is important to note that one can achieve mesh convergence of the laminar base flow for such a coarse mesh in the streamwise direction, thanks to the illingworth variable transformation (Eq. 5.6). Most of the streamwise variation of the flow field is due to the enlargement of the boundary layer. Since this variation is absorbed by the self-similar wall-normal variable η , the effective variation in the computational streamwise variable ξ is minor, and does not require such a large amount of points to be properly captured. The constant mass flow per unit surface imposed ($\dot{m}_w = 7.09 \text{ g/s-m}^2$) is such that the total injected mass flow:

$$\dot{m}_w^{\text{tot}}(x) = \int_{x_{p0}}^x 2\pi x \sin(\theta_c) \dot{m}_w(x) \, dx \quad [\text{kg/s}], \quad (9.7)$$

is equal to that with a self-similar injection with constant $\bar{f}_w = -0.2$ at $x = 775 \text{ mm}$.

Case 3 solves the Navier-Stokes equations, rather than the simplified boundary-layer equations, whilst retaining all other conditions identical to case 2. The NS solution is obtained with CFD++ [22], employing 3300 points in the streamwise direction, and 350 in the wall-normal. This resolution was seen to be sufficient to achieve mesh convergence of the N -factor envelopes.

Cases 4 and 5 also solve the Navier-Stokes equations, yet they feature a step-wise injection profile. The mass-flux is slightly higher ($\dot{m}_w = 7.35 \text{ g/s-m}^2$) than in cases 2 and 3, such that the same total mass-flow (Eq. 9.7) is reached at $x = 508 \text{ mm}$ (the end of Marvin & Akin's cone [2]). The difference between cases 4 and 5 lies in the tip of the cone: infinitely sharp for case 4, and blunt with a nose radius of 0.79 mm for case 5 (the same as in Marvin & Akin's sharpest cone – see Fig. 9.8).

The injection velocity profiles of the five considered cases and with 100% He in the injected mixture are displayed in Fig. 9.23. For all other helium concentrations, the velocity profiles are scaled such that the mass-flow per unit surface (\dot{m}_w) remains constant. The corresponding boundary-layer profiles are also presented in Fig. 9.24. Aside from minor differences in the temperature profile, all considered injection distributions and tip geometries lead to very similar base-flow profiles at a later streamwise location.

A differentiating feature of the cases with a discontinuous mass injection (cases 4 and 5) is the appearance of a weak shocklet at the injection point ($x = x_{p0} =$

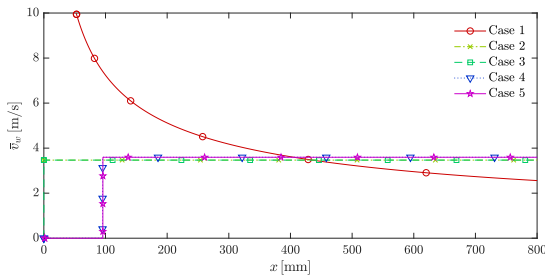


Figure 9.23: Wall injection velocity profiles for the five considered cases (see Table 9.3) and for $\bar{Y}_{He\,w} = 1$.

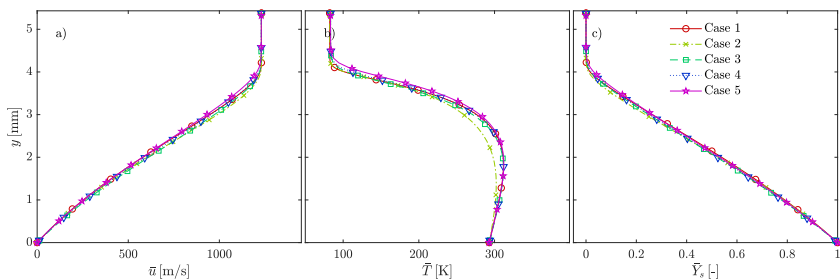


Figure 9.24: Laminar base-flow profiles for the five considered cases (see Table 9.3) and for $\bar{Y}_{He\,w} = 1$ at $x = 508$ mm. Test preshock conditions are detailed in Table 9.2.

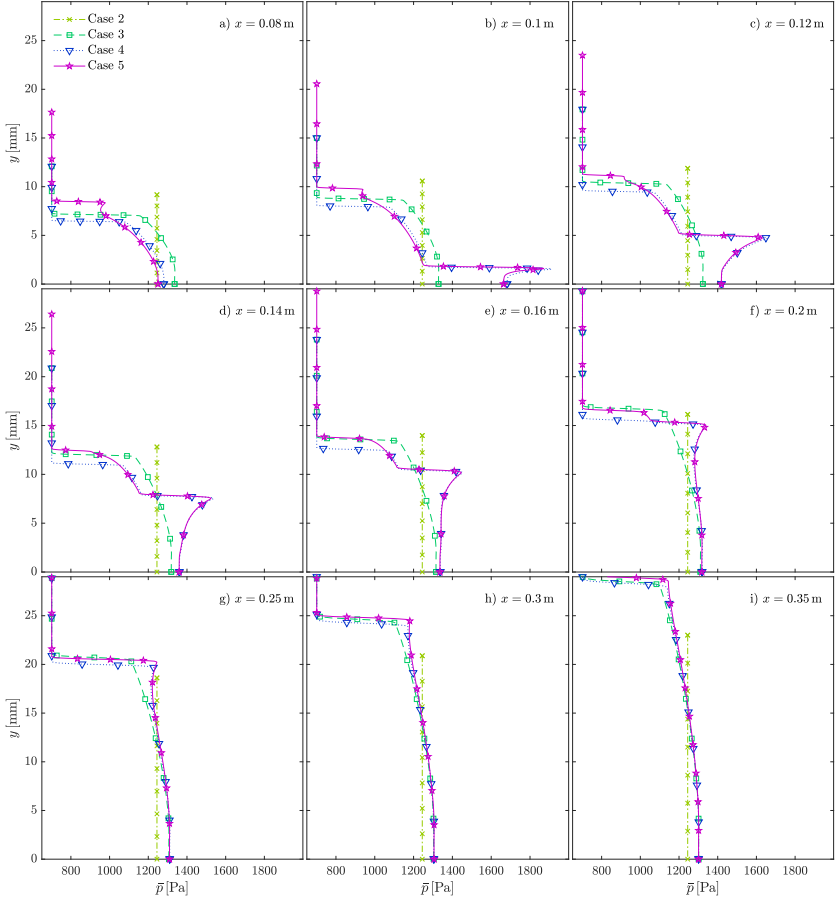


Figure 9.25: Streamwise evolution of the weak shock due to the discontinuous mass injection for cases 2-5 (see Table 9.3) and for $\bar{Y}_{He w} = 1$. Test preshock conditions are detailed in Table 9.2.

95 mm). Figure 9.25 displays the evolution of the shocklet, which dissipates and is ultimately absorbed by the main shock.

The intensity of the injection shocklet is dependent on the concentration of He in the injected mixture. Figure 9.26 displays the shocklet intensity for case 5 and for various helium concentrations in the blowing mixture, shortly after it appears ($x = 100$ mm). It is clear that decreasing the helium concentrations weakens the shocklet, which is undetectable when injecting purely air. It is therefore hereinafter referred to as a “concentration shocklet”.

The existence of this concentration shocklet arises a question regarding how one should go about its modeling when performing stability analyses. Since it is

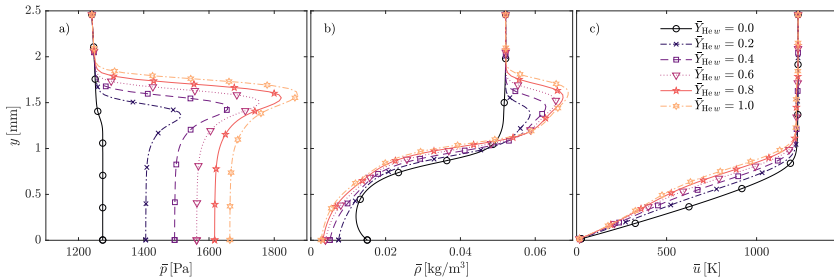


Figure 9.26: Boundary-layer profiles at $x = 0.1\text{ m}$ showing the intensity of the shocklet due to the discontinuous mass injection for cases 5 (see Table 9.3) and for various helium concentrations in the injected mixture. Test preshock conditions are detailed in Table 9.2.

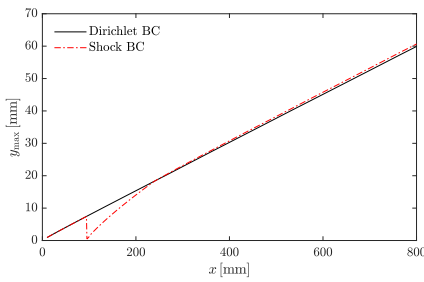


Figure 9.27: Wall-normal position of the top limit of the computational domain for stability analyses when employing the Dirichlet (case 5) or the shock boundary condition (case 5s). Test preshock conditions are detailed in Table 9.2.

a weak shocklet, one could simply keep it within the computational wall-normal domain, and impose a Dirichlet condition (Eq. 6.27) at y_{\max} as done in all the other analyses in this section. Another possibility is to restrict the computational domain to the region within the concentration shocklet, and employ the shock perturbation boundary condition on it (§ 6.2.1). The down-side to the latter approach, is that it neglects the perturbation propagation after the concentration shocklet ($y > y_{\max}$), since the shock boundary condition assumes $\tilde{q} = 0$ in that wall-normal range. The evolution of the top boundary of the domain for the two approaches is displayed in Fig. 9.27. The shock-boundary-condition approach is denoted with the suffix s on the case identifier (for instance case 5 and 5s).

The N -factor envelopes corresponding to the base flows of cases 2-5, with the two treatments of the concentration shocklet for cases 4-5, are presented in Fig. 9.28a-f. Figure 9.28g-h also presents cases 5 and 5s, yet with the PSBC at the wall (cases 5p and 5ps). As seen in § 9.1, the combination of the porous boundary condition with a discontinuous blowing can lead to unexpected outcomes of competing stabilizing and destabilizing effects. The present analysis incorporates

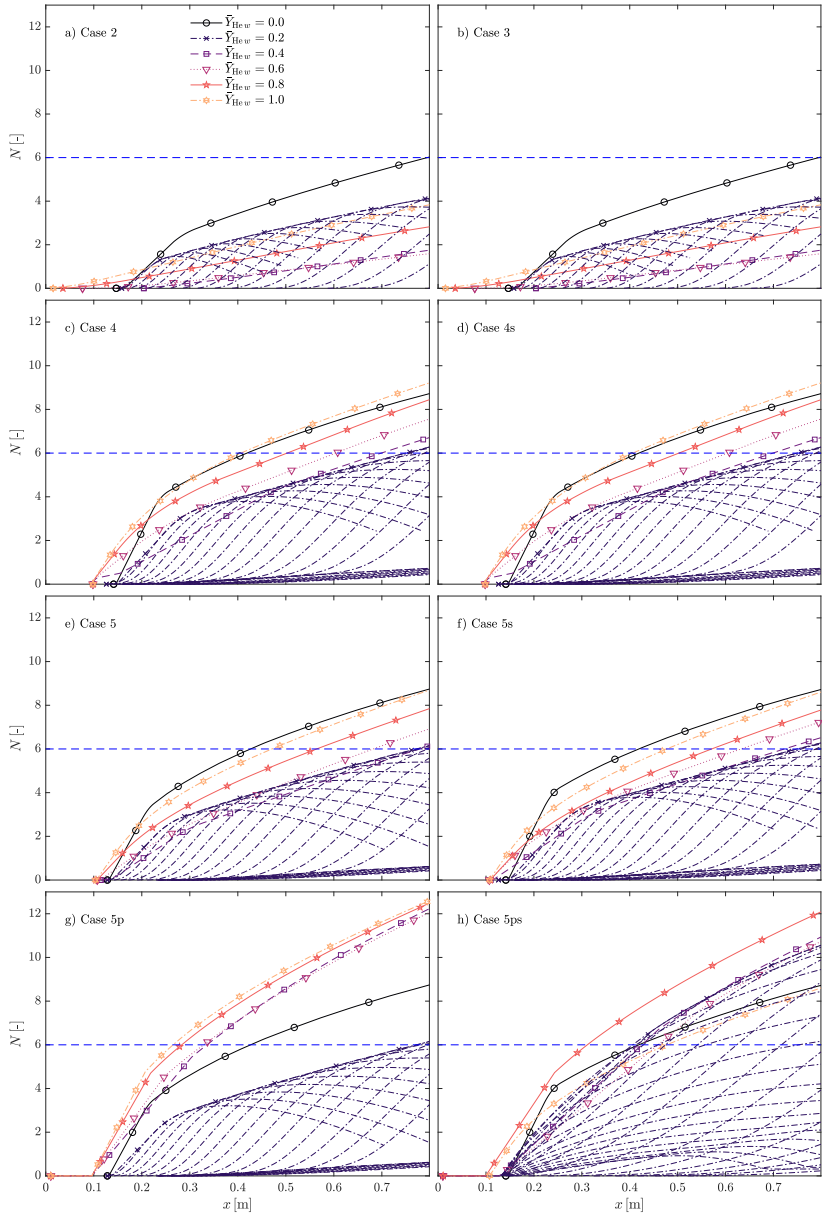


Figure 9.28: Second-mode N -factor envelopes for various cases (see Table 9.3) with the air-2-He (§ J.2) mixture. Exact test conditions detailed in Table 9.2. Single-frequency N -factor curves correspond to $\bar{Y}_{He\,w} = 0.2$.

the influence of the concentration-shocklet modeling, thus further increasing the coupling possibilities.

Cases 2 and 3 (Fig. 9.28a-b) present very similar trends to case 1 (Fig. 9.16a) and case 1p (Fig. 9.22). This suggests that, as long as the injection is done continuously across the surface, it does not significantly affect the stability characteristics. The gradual increase in the concentration of the lighter species (He) appears to trigger first a major delay of transition, and then a slight advancement.

The discontinuous injection of mass through the surface does, however, lead to a substantially different scenario. Cases 4 and 5 (Fig. 9.28c and e) present a much larger advancement of the transition front when increasing $Y_{He w}$, after the initial delay. This advancement is large enough to have the N -factor curve for 100% He be practically coinciding with that of 0% He. This trend is also practically independent of the strategy employed to deal with the concentration shocklet, since cases 4s and 5s (Fig. 9.28d and f) present practically identical N -factor envelopes in cases 4 and 5 (Fig. 9.28c and e). Moreover, the similarity between the predictions of cases 4 and 5 suggests that the cone's bluntness ($R_{tip} = 0.79$ mm) is not sufficient so as to modify the dynamics of instability development. One can therefore affirm that the discontinuous wall injection has an effect contrary to that of decreasing the mixture molar mass^f, since it advances transition more when the injected gas is lighter.

The complete reversal of the trend observed for continuously-blowing scenarios with the HSBC, occurs when one considers simultaneously a discontinuous blowing and a PSBC (case 5p). This is similar to what was observed in § 9.1, and also follows from the unequal effect that the porous layer was reported to have in Fig. 9.21a depending on the injected gas composition: stabilizing for 0% He, gradually decreasing its stabilizing effect for increasing He concentration, and ultimately destabilizing for large mass fractions of He.

It is interesting, however, to observe that case 5ps in Fig. 9.28h does not predict such a reversal. Case 5ps simultaneously employs the shock boundary condition, truncating the domain at the concentration shocklet (see Fig. 9.27), and the porous (PSBC). A possible explanation for this can be given based on the thermoacoustic interpretation of the second mode recently formulated by Kuehl [45]. According to it, the second mode must not be interpreted as a wave trapped in the relatively supersonic pocket between the relative sonic line and the wall, but rather confined to it by the thermoacoustic impedance that is the large density gradient at the top of the boundary layer. Using it, Sakakeeny *et al.* [46] proceeded to explain how bluntness suppresses second-mode instabilities by the weakening of this gradient that the entropy layer causes.

For the case being investigated in this section, the concentration shocklet arises

^fA higher concentration of lighter gases like He lead to a lower mixture molar mass – see definition in Eq. A.8.

ing after the injection region (see Figs. 9.25 and 9.26) is indeed one of such thermoacoustic impedances. This impedance is considered by case 5p, maintaining the concentration shocklet within the computational domain (using the Dirichlet condition at the main shock height), but not by case 5ps, cutting the domain at the concentration shocklet and employing the shock stability boundary condition. The use of the shock boundary condition therefore imposes a different impedance, coming from the linearization of the Rankine-Hugoniot relations. The thermoacoustic coupling of the porous wall and the concentration shocklet, appears to increase the growth rates after the injection for lighter gases, and ultimately shifts the corresponding N -factor curves vertically.

The fact that the shock stability boundary condition (§ 6.2.1) seemingly fails to reach an appropriate acoustic impedance for the concentration shocklet should not refrain one from employing it in other scenarios. It remains the best existing methodology to model the vibration of strong shocks. In the case at stake, it appears that neglecting the traveling of instabilities through the shocklet is an oversimplification that effectively neglects the mentioned porous-concentration shocklet coupling.

In essence, judging by the observations made in Fig. 9.28, it appears as if the discontinuous injection of mass through the surface, and the subsequent coupling between the porous wall admittance and the concentration shocklet's thermoacoustic impedance (case 5p in Fig. 9.28g), are indeed responsible for the sooner transition-onset location observed experimentally when injecting lighter gases.

9.2.4 Case 5p with Ar blowing

Case 5p (discontinuous blowing with a blunt nose and with the PSBC) is also investigated for Argon injection – the other test gas different than air injected in Marvin & Akin's [2] experiments. The mass flow per unit surface through the porous section is also kept constant and equal to $\dot{m}_w = 7.35 \text{ g/s-m}^2$. The corresponding N -factor envelopes, for 6 different Argon concentrations are displayed in Fig. 9.29. Similarly to what was observed experimentally [2] the injection of Argon rather than air practically does not change the predicted transition-onset location. There appears to be a minor advancement associated to higher argon concentrations in the injected mixture. However, this subtle difference could have been inappreciable in the experiments due to the measurement uncertainty.

9.2.5 Conclusions

A thorough investigation was carried out on the sensitivity to the composition of the injected gas of the stability characteristics of wall-bleeding boundary layers, and the ultimately predicted transition-onset location. When injecting mass through the surface in a continuous fashion, lighter gases were seen to increase

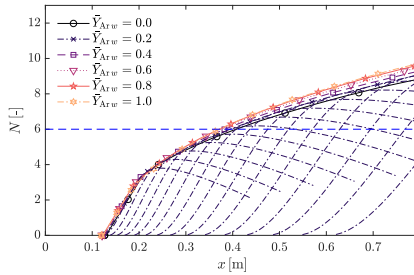


Figure 9.29: Second-mode N -factor envelopes for various case 5p in Table 9.3 with the air-2-Ar (§ J.4) mixture. Exact test conditions detailed in Table 9.2. Single-frequency N -factor curves correspond to $\bar{Y}_{Ar\,w} = 0.2$.

the boundary-layer size, stabilize the second mode, and ultimately lead to a later transition. Heavier gases were seen to have the opposite effect.

Actual wind-tunnel tests [2, 38, 39], however, do not feature continuously-blowing surfaces, but rather a step-wise blowing – zero near the tip and constant after a certain streamwise distance x_{p0} . Experiments in such conditions were actually seen to display the opposite trend – lighter injection gases led to a sooner transition than heavier gases.

The analysis presented in this section suggests that the reason for the reversal of the trend observed for continuously-outgassing surfaces is a combination of several factors. The discontinuous blowing originates a weak shocklet, that is stronger the more different the mixture molar weights of the incoming and the bled gases is. This concentration shocklet acts as a thermoacoustic impedance at a certain height in the domain, and coupled with the admittance of the porous wall, leads to a stronger destabilization when injecting lighter gases. This destabilization ultimately leads to a sooner transition.

Before reaching this mechanisms-based explanation for the experimental observations, several potential causes for the aforementioned reversal were rejected. Specifically the possibility of first-mode waves being most unstable was rejected by comparing analyses with non-zero spanwise wave numbers. Moreover, the comparison of the predictions made with two distinct sets of transport and diffusion models dismissed the possibility of the heavy-gas destabilization obtained in the numerical analysis to be an artifact of the thermophysical modeling.

Applying the same model to a different injection gas (Argon) also lead to transition-onset predictions in agreement with the experimental trends.

9.3 Sensitivity of instabilities to the wall boundary condition

Having successfully validated the porous boundary condition for outgassing hypersonic boundary layers, and subsequently exploited it to unravel the competing physical mechanisms in experimental configurations with a regular porous surface, the next question that arises is: what is the best way to model surfaces in ablation scenarios? Is such a porous boundary condition appropriate to model the pyrolysis and ablation of a TPS? And if so, how is the boundary layer affected by modifications in the porous structure under it?

During the decomposition of the TPS [20, 47], first the polymeric resin pyrolyses, releasing hydrocarbon products through the remaining porous fiber matrix. In such instances, it does seem appropriate to employ a porous-wall boundary condition for the companion stability and transition analyses. As the TPS continues to decompose, depending on the value of the Thiele number [48, 49], either surface or volume ablation follows. The latter, occurs when diffusion through the fiber matrix occurs at a faster rate than the reactions (low Thiele number). Its surface modeling therefore shares resemblance with pyrolysis – it requires a porous surface through which the ablation products diffuse and ultimately enter the boundary layer. The characteristics of the porous material however, vary as ablation advances, decomposing the fibers and increasing the porosity. The former (surface ablation) occurs when the fiber decomposition is faster than the diffusion of the ablation products (large Thiele number). It is therefore referred to as a surface phenomenon, where the outgassing does not occur through a porous matrix, but rather continuously across the entire surface. It is for such an instance that the ablation-mimicking stability boundary condition (AMSCB) was developed (§ 6.1.1.2 and Refs. 13, 21).

Notedly, the porous boundary condition presented in § 6.1.1.1, developed for regularly-shaped and spaced pores, seems overly simplistic for the complex fibrous structure featuring in TPS. However, it can be taken as a first approximation, reducing the multiple and shape-varying cavities in a real porous material to an equivalent pore-radius r_{por} , porous-layer height h_{por} and surface porosity n_{por} . More elaborate boundary conditions have been developed by other researchers [28, 50–52], however the work in this dissertation is restricted to the regularly-cylindrical-pores condition due to the easily-identifiable parameters it depends on.

The present section explores the implications of employing these boundary conditions on the stability characteristics of the boundary layer, and on the ultimate transition-onset predictions. The analysis is centered exclusively on the boundary condition, and therefore features only air as a test gas, with a sufficiently low temperature so as to assume CPG conditions. A baseline case (O) is considered (Mach-6 adiabatic flat plate), followed by an exploration of the effect of modifying the Mach number (M^- and M^+) and the surface temperature ratio (T^- and T^+).

$M_e [-]$	$p_e [\text{Pa}]$	$T_e [\text{K}]$	wall	$\text{Re} [-]$	$x [\text{m}]$	$\bar{f}_w [-]$	$\beta [1/\text{m}]$
6	4000	70	adiab.	2000	0.0945	-0.04	0

Table 9.7: Test conditions for the baseline case for the analysis of the various wall-blowing boundary conditions.

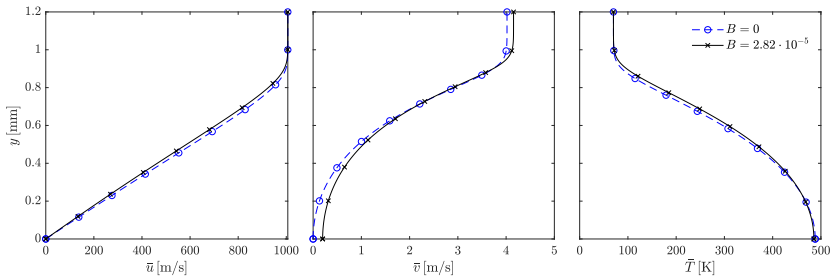


Figure 9.30: Laminar base-flow profiles for the baseline case summarized in Table 9.7 and for the non-blowing case.

9.3.1 Baseline case – homogeneous condition

The baseline case studied in this section is a flat-plate boundary-layer flow field with the characteristics summarized in Table 9.7. The test gas is air in CPG conditions, with the transport properties modeled using Sutherland's law (Eq. 4.2) and with a constant Prandtl number (Eq. 4.5). The corresponding gas constants are summarized in Table 5.2. The wall blowing is obtained from assuming a self-similar blowing (Eq. 6.3), with a blowing parameter \bar{f}_w of -0.04. The non-dimensional parameter B can therefore be defined analogously to Eq. 9.1, yet for flat plates with a self-similar blowing:

$$B = \frac{\bar{\rho}_w \bar{v}_w}{\rho_e u_e} = -\sqrt{2} \frac{\bar{f}_w}{\text{Re}}. \quad (9.8)$$

The value of B corresponding to the conditions in Table 9.7 is therefore $B = 2.82 \cdot 10^{-5}$. The base-flow solution is obtained using VESTA's CBL [40] solver, leading to the profiles displayed in Fig. 9.30. It is clear from them that the amount of mass injection corresponding to $B = 2.82 \cdot 10^{-5}$ does not lead to a significant modification of the base-flow profiles.

The corresponding perturbation growth rates obtained with the homogeneous stability boundary condition (HSBC) are displayed in Fig. 9.31. As expected, the modification of the laminar base flow due to the blowing leads to an increase of the maximum amplification rate, and a displacement of this maximum towards lower frequencies.

Before exploring the implications of modifying the wall stability boundary condition, a parametric study is performed on the effect of varying the free-stream

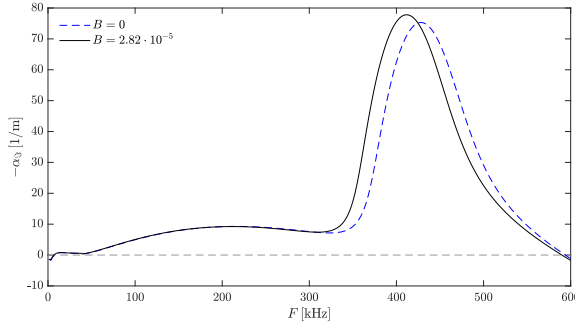


Figure 9.31: Perturbation growth rates for the baseline case in Table 9.7 and for the non-blowing case, employing the HSBC.

Mach number and the wall-temperature ratio, yet employing the HSBC. Figure 9.32 displays the corresponding contours of the maximum amplification rate (a) and the frequency at which this maximum occurs (b). Increasing Mach numbers with a fixed surface temperature ratio display a destabilizing behavior until a certain point, and then become stabilizing, similarly to what was observed by Bitter & Shepherd [53]. This is retrieved by transversing Fig. 9.32a for a constant M_e . Increasing Mach numbers and wall cooling both increase the most unstable mode's frequency. This is once again due to the associated shrinking of the boundary layer. Another interesting observable phenomenon is the most unstable mode shifting from the first to the second mode. In the top-left corner of Fig. 9.32b, one can see the contour lines getting very close together. In this region, with low Mach numbers and hot walls, the first mode dominates over the second. Note that only 2D waves are analyzed, including a maximization of the amplification rate over the different spanwise wave numbers β would make the switch from second to first mode occur sooner [53]. Complementary to wall cooling, wall heating is well known to stabilize the second mode, and destabilize the first [3].

In order to address the combined effect of Mach number and temperature ratio on the boundary-condition, a set of operating points from those detailed in Fig. 9.32 has been chosen. Cases T⁻, O and T⁺ correspond to fixing a Mach number of 6 and varying the wall temperature ratio (0.6, 1 and 1.5), whereas cases M⁻, O and M⁺ correspond to fixing a wall temperature ratio of 1 (adiabatic) and varying the Mach number (4, 6 and 8).

9.3.2 Porous condition for case O

The PSBC is defined by three parameters characterizing the porous layer: the surface porosity n_{por} , the pore radius r_{por} , and the porous-layer height h_{por} (see Fig. 6.1). As mentioned at the beginning of the section, the porous surface of an

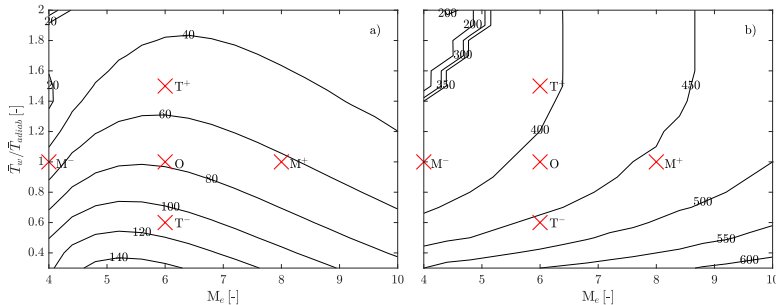


Figure 9.32: Contours of the maximum amplification rate in m^{-1} (a) and perturbation frequency corresponding to that maximum in kHz (b), for the various Mach numbers and surface temperature ratios and for the HSBC. All other test conditions correspond to those in Table 9.7.

ablating TPS can be approximated by equivalent values of these parameters. For instance, the pore radius can be taken as that providing a single-pore area (πr_{por}^2) equal to the average area between the surface fibers. Similarly, the porous-layer height can be taken as the average depth of the cavities. As the TPS decomposition advances these parameters will gradually increase. In order to characterize the influence of these three parameters at various levels of TPS decomposition on the stability characteristics, a parametric study is carried out on the baseline case (Table 9.7).

A preliminary analysis is performed on the effect of porosity in isolation – fixing $r_{\text{por}} = h_{\text{por}} = 0.1$ mm. A higher porosity, for constant r_{por} , effectively means that there is a higher pore concentration on the surface, therefore it would be expectable to have a stronger stabilizing/destabilizing effect of the porous layer with a higher porosity. Figure 9.33 confirms this, showing also its limited role on stability. The surface porosity is therefore fixed to $n_{\text{por}} = 0.8$ for the remainder of this section.

The other two porous parameters, pore radius r_{por} and porous-layer height h_{por} , affect stability in a more complex and non-trivial fashion. Figure 9.34 shows the maximum amplification rate (a) and the frequency for which this maximum is achieved (b), as a function of the pore radius and the porous-layer height. Figure 9.34b shows that both parameters, when increased, move the most unstable mode towards lower frequencies. The maximum amplification rate shows a non trivial behavior – its minimum corresponds to high values of h_{por} and values of r_{por} around 0.1 mm, whereas its maximum corresponds to high values of r_{por} and values of h_{por} around 1 mm.

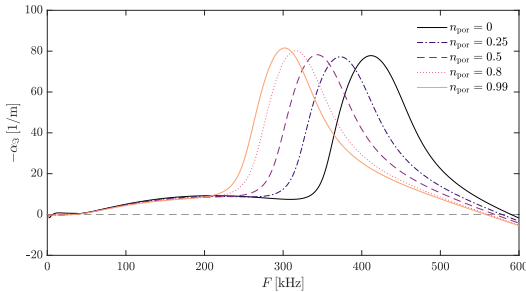


Figure 9.33: Effect of the surface porosity n_{por} on the perturbation growth rate. The flow conditions are those in Table 9.7, and the porous layer has $r_{por} = h_{por} = 0.1$ mm.

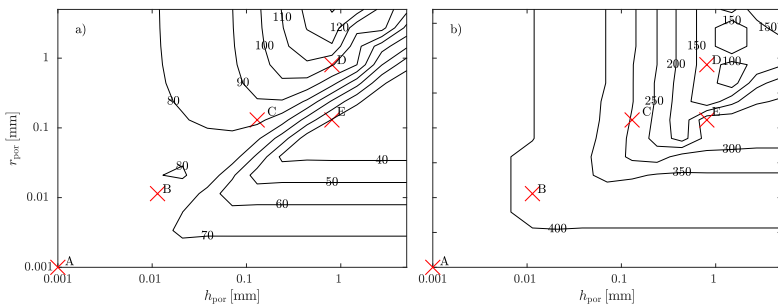


Figure 9.34: Effect of the pore radius r_{por} and the porous-layer height h_{por} on the perturbation maximum amplification rate in m^{-1} (a) and the frequency for which this maximum is achieved in kHz (b). The flow conditions are those in Table 9.7, and the porosity is $n_{por} = 0.8$. Crosses correspond to the combinations of r_{por} and h_{por} for which the Mach number and wall-temperature-ratio effect is studied in Figs. 9.35-9.39.

Case	h_{por} [mm]	r_{por} [mm]
A	0.001	0.001
B	0.014	0.014
C	0.13	0.13
D	0.81	0.81
E	0.81	0.13

Table 9.8: Combinations of the porous parameters analyzed in Figs. 9.35-9.38.

9.3.3 Cases M⁻, M⁺, O, T⁻, and T⁺ for all boundary conditions

In order to further analyze the effect of the porous layer, the growth rates for five combinations of porous conditions (marked as crosses on Fig. 9.34, and detailed in Table 9.8), are taken and compared for different Mach numbers and wall-temperature ratios. Figure 9.35 plots the growth rates for cases A-B in Table 9.8), and for three different Mach numbers (points M⁻, O and M⁺ in Fig. 9.32). It is interesting to see that the destabilizing-stabilizing effect of a growing Mach number commented for Fig. 9.32 can also be seen in Fig. 9.35a, where the Mach 6 curve is more unstable than the Mach 4 curve. However, it disappears for larger pore sizes (Fig. 9.35c-d), where an increasing Mach number is seen to be always stabilizing. Larger pores are seen to excite higher modes, and to bring them closer to the second mode (lower frequencies).

Figure 9.36 shows the comparison between case D (amplified in Fig. 9.34) and E (damped in Fig. 9.34). The damping is seen to be more or less dramatic depending on the Mach number. It also appears to affect Mack's higher acoustic modes, but to a lower extent than the second mode. It is particularly interesting to see that in Fig. 9.36 (b) for $M_e = 6$ and $M_e = 8$, the second and the higher modes are damped in such a way that the first of the higher modes (corresponding to Mack's third mode) actually becomes the most unstable.

Figures 9.37 and 9.38 show the same combinations of r_{por} and h_{por} , but for different wall temperature ratios with a fixed $M_e = 6$ (points T⁻, O and T⁺ in Fig. 9.32). Concerning the maximum amplification rate, the same effect observed in Fig. 9.32 is seen for all values of the porous parameters, that is cooler walls destabilize the second mode. Surfaces with small porous layers see a reduction in the most unstable modes' frequencies caused by warmer walls. The opposite trend is observed in surfaces with large pores. The point where this trend is reversed is captured in Fig. 9.37c. Similarly to the comparison between cases D and E in Fig. 9.36, Fig. 9.38 shows the damping introduced by the porous layer affects all curves, with a bigger impact on the primary modes, rather than the secondary ones.

Figure 9.39 shows an analogous comparison to that of Figs. 9.35-9.38 but for the AMSBC. The trend observed is the same as for the porous cases – a decreasing Mach number and a colder wall both tend to destabilize the flow and move the most

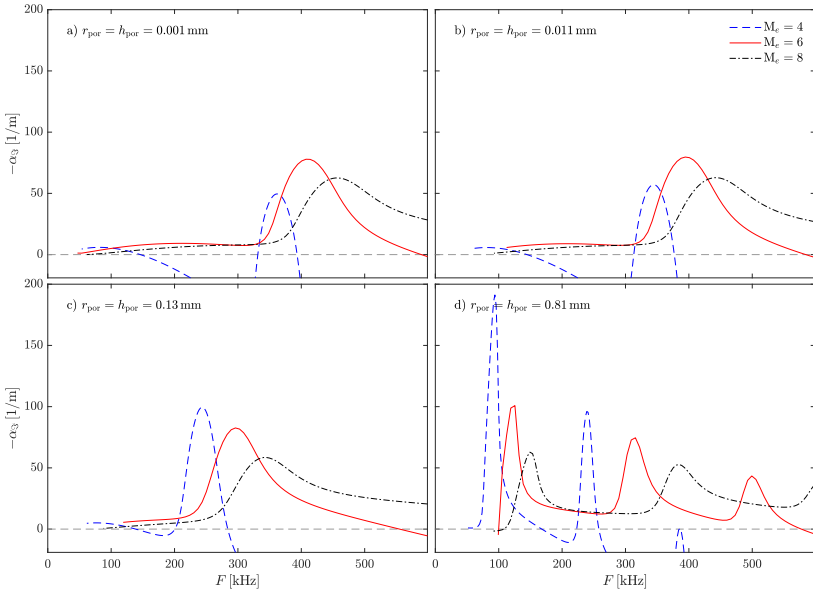


Figure 9.35: Effect of increasing pore radius r_{por} and porous-layer height h_{por} on the growth rate for different Mach numbers. The different plots correspond to the combinations of porous parameters A-D in Table 9.8. All other conditions are those detailed in Table 9.7, with a porosity of $n_{\text{por}} = 0.8$.

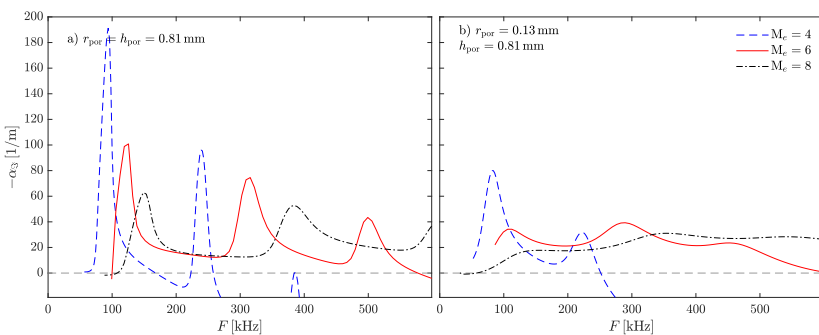


Figure 9.36: Damping effect of the pores on the growth rate for different Mach numbers. The different plots (a) and (b) correspond to cases D and E from Table 9.8. All other conditions are those detailed in Table 9.7, with a porosity of $n_{\text{por}} = 0.8$.

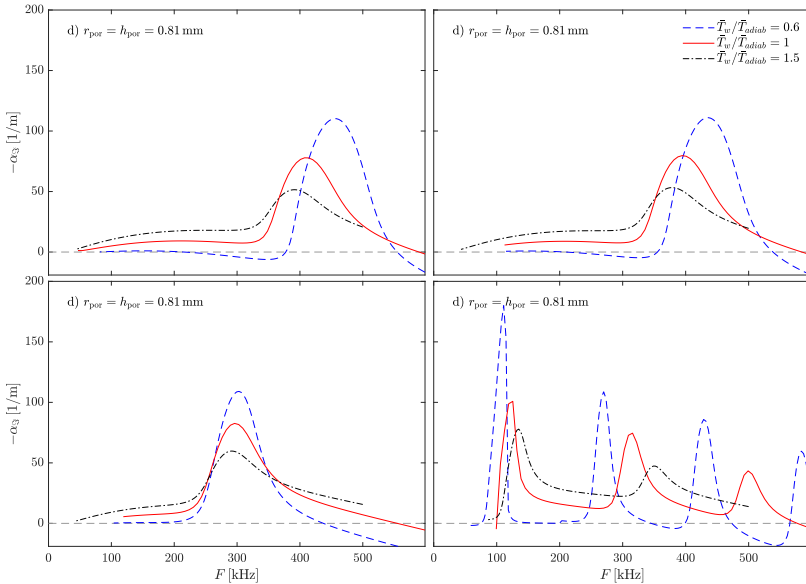


Figure 9.37: Effect of increasing pore radius r_{por} and porous-layer height h_{por} on the growth rate for different wall temperature ratios. The different plots (a)-(d) correspond to cases A-D in Table 9.8. All other conditions are those detailed in Table 9.7, with a porosity of $n_{por} = 0.8$.

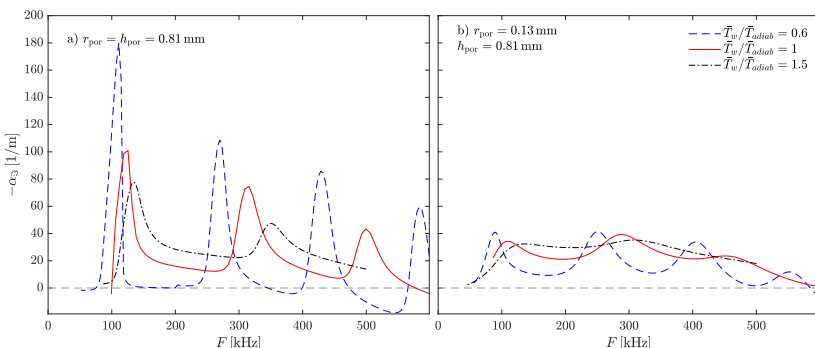


Figure 9.38: Damping effect of the pores on the growth rate for different wall temperature ratios. The different plots (a) and (b) correspond to cases D and E in Table 9.8. All other conditions are those detailed in Table 9.7, with a porosity of $n_{por} = 0.8$.

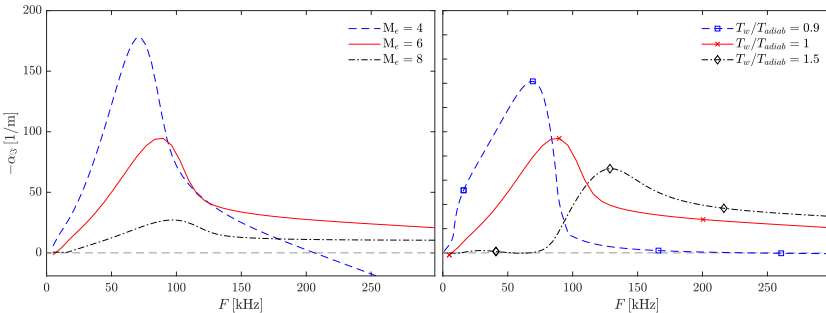


Figure 9.39: Effect of varying the Mach number and wall-temperature ratio with the AMSBC. All other conditions are those detailed in Table 9.7, with a porosity of $n_{\text{por}} = 0.8$.

unstable mode towards lower frequencies. Once again, the “up-down” effect of the Mach number on the growth rate, observable in Fig. 9.32 for the homogeneous boundary condition, does not appear when using the AMSBC.

Figure 9.40 shows a comparison of all the different boundary conditions. It is here where one can see the dramatic effect that the wall-normal velocity perturbation modeling has on the flow stability results. The two curves with a homogeneous boundary condition appear to be significantly close. This shows that, in absence of wall-normal velocity perturbation modeling, the analyzed blowing has very little effect on the boundary layer’s stability. The usage of different porous layers is seen to have the importance stressed in the previous paragraphs. Depending on the values of r_{por} and h_{por} the porous layer can range from having a strongly destabilizing effect ($r_{\text{por}} = h_{\text{por}} = 0.81 \text{ mm}$), passing through a slightly destabilizing effect ($r_{\text{por}} = h_{\text{por}} = 0.13 \text{ mm}$), up to a strongly stabilizing effect ($r_{\text{por}} = 0.13 \text{ mm}$ and $h_{\text{por}} = 0.81 \text{ mm}$). The AMSBC is the one predicting the most unstable boundary layer and the one moving the most unstable mode to the lowest frequencies. One of the most interesting results of this comparison, is that the PSBC, when the pores become very large, predicts a similar behavior to the AMSBC. In other words, having a very large pore, is equivalent to having a surface that is blowing continuously. This is reasonable from a physical perspective, but it is remarkable to observe this when comparing such different models: one coming from an acoustic condition, and another from a mass-conservation approach. These facts clearly show that the outgassing from an ablative boundary layer cannot be experimentally mimicked with an arbitrary pore setup, but their size needs to be carefully considered. They also suggest that, as the decomposition of a TPS advances, one should expect significantly different perturbation development within the boundary layer above it.

The last comparison presented in Fig. 9.41 shows the impact of these boundary conditions on the ultimate prediction of the transition onset location for $M_e = 6$

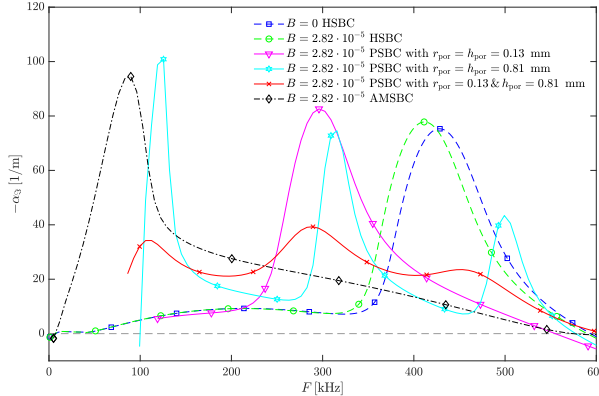


Figure 9.40: Comparison of the different boundary conditions. The flow conditions are those in Table 9.7.

and $\bar{T}_w/\bar{T}_{\text{adiab}} = 1$. By assuming a transition-onset N -factor of 6, similar to what was employed for the experiments in § 9.1, one can estimate the x_{tr} predicted with the different models. The growthrates in Fig. 9.40 anticipated that the cases with $B = 0$ and $B = 2.82 \cdot 10^{-5}$ with a homogeneous boundary condition would return very close predictions of the transition onset location: $x_{tr} = 259.7$ mm and $x_{tr} = 240.4$ mm respectively. However, surprisingly with an apparently weakly destabilizing porous layer ($r_{\text{por}} = h_{\text{por}} = 0.1$ mm in Fig. 9.40), the transition onset location is predicted to be much farther upstream: $x_{tr} = 134.6$ mm. The dominant originator does not lie in the height of the peak, but rather in its larger width. This means that perturbations are unstable for a broader range of frequencies. Accordingly, the integration of these unstable growth rates spans a larger range of x , leading to higher maxima in the N curves. This explains why the e^N contour for the porous condition is significantly higher than its homogeneous counterpart. Finally the AMSBC, due to the extremely broad range of frequencies that are unstable for every x location (see again Fig. 9.40), displays a very steep contour. Mortensen & Zhong [54] reported similar N -factor envelopes when studying the stability of chemically reacting flows with wall ablation. The result, is that transition onset is predicted to occur even farther upstream – at $x_{tr} = 95.7$ mm.

9.3.4 Porous stabilizing/destabilizing maps and experimental result analysis

As shown in the previous subsection, porous layers can enhance or reduce the growth rate for a perturbation traveling in a hypersonic boundary layer. The combination of r_{por} and h_{por} producing these behaviors is summarized in Fig. 9.42.

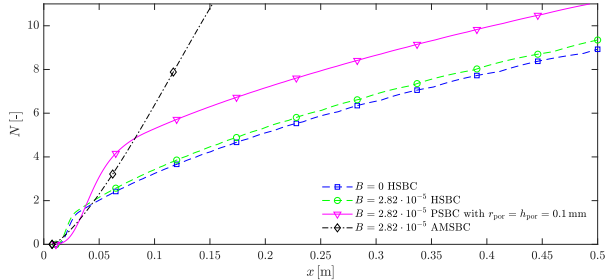


Figure 9.41: e^N contours for the different boundary conditions. The flow conditions are those in Table 9.7.

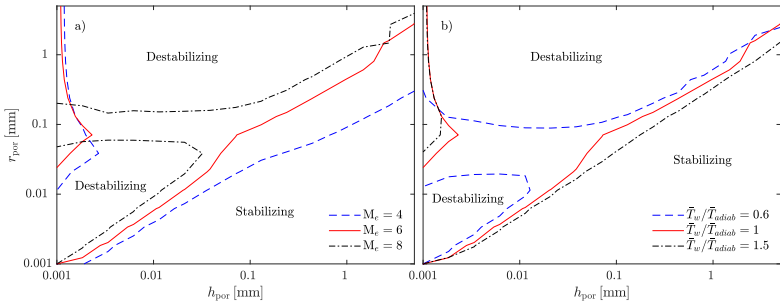


Figure 9.42: Zones of porous-layer stabilization and destabilization for different Mach numbers (a) and wall temperature ratios (b) on the porous-conditions map. All other conditions are those detailed in Table 9.7, with a porosity of $n_{por} = 0.8$.

This map permits an *a-priori* assessment of whether a particular porous layer will amplify or damp instabilities.

The appearance of stabilizing regions for blowing surfaces (generally destabilizing) may seem somewhat surprising. However, these stabilizing regions are not with respect to the corresponding non-blowing configuration, but rather to the blowing non-porous (blowing introduced through infinitely small pores). Nevertheless, one could indeed find a porous surface damping the perturbations more than the blowing amplifies them, leading to a stabilizing blowing wall.

Assuming that the mappings in Fig. 9.42 are not affected by the weak blowing, but rather by the porous nature of the wall, one can attempt to explain the various effects porous surfaces have reported to have on transition in different experimental campaigns. Three investigations performed in different wind tunnels are analyzed: DLR's HEG [55], DLR's H2K [27], and the ITAM TRANZIT-M [28].

The HEG features high-enthalpy flows, which, in absence of sample heat-

ing, leads to highly cooled walls. The wall-temperature ratio can be approximated to around 0.1-0.15 and the post-shock Mach number to around 6.35. The lower left amplification region in Fig. 9.42 appears to shrink with decreasing wall-temperature ratios and with increasing Mach numbers. It seems therefore reasonable to assume that with $\bar{T}_w/\bar{T}_{adiab} \approx 0.1$, with $M_e \approx 6.35$ and with the reported pore-radius ($\sim 10\mu\text{m}$) [55], whatever the porous-layer height may be, the porous surface will stabilize the boundary layer. This is indeed what has been observed experimentally, but one should beware from extrapolating this conclusion to other flow regimes. Figure 9.42 shows that the damping region is highly dependent on the wall-temperature ratio and the Mach number.

The H2K is a low-enthalpy tunnel, and was operated [27] with a temperature ratio of $\bar{T}_w/\bar{T}_{adiab} \approx 0.7$ and a post-shock Mach number of 5.8. Figure 9.42 predicts that for these conditions the lower-left amplification region will not have disappeared. The experiments tested the same porous material as in the HEG case ($r_{por} \sim 10\mu\text{m}$). Assuming the material is homogeneous in volume would make $h_{por} \sim r_{por} \sim 10\mu\text{m}$. This would fall on the marginal amplification-damping line in Fig. 9.42, justifying why the experiments revealed no effect of the porous layer on the transition front [27].

The ITAM TRANZIT-M is also a low-enthalpy tunnel, with operative wall-temperature ratios of $\bar{T}_w/\bar{T}_{adiab} \approx 0.9$ and post-shock Mach numbers of around 5.35. The experiments are carried out with a constant porous radius of around 0.05 mm, and with several porous-layer heights. This region of Fig. 9.42 does not show a clear trend, which explains the varied damping/amplifying effect observed with different perturbation frequencies and porous-layer heights. The same authors [28] report also a parametric study with a much cooler wall $\bar{T}_w/\bar{T}_{adiab} \approx 0.35$, which shows a very clear stabilization. This behavior can be deduced from the trend commented for the HEG wind tunnel.

Note that the aforementioned experiments were conducted on cones rather than flat plates. Flat-plate and conical boundary layers can be related through the Mangler or the Probstein-Elliott transformation [56], resulting in the conical Reynolds number being $\sqrt{3}$ times the flat-plate one [57]. The map in Fig. 9.42 could vary with the Reynolds number. However, the e^N computations presented in Fig. 9.41 suggest that the trend is most-likely preserved.

9.3.5 Conclusions

An exhaustive parameter study was carried out on the influence of the characteristics of the surface blowing on the stability features of hypersonic boundary layers. A baseline test case with a small surface mass injection was selected, subsequently exploring how its behavior was affected by the surface boundary condition. The homogeneous condition was seen to predict only a mild destabilization of the flow.

However, the porous and the ablation-mimicking continuously-blowing boundary conditions predicted radically different instability development. Depending on the characteristics of the surface through which the blowing was introduced, predictions ranged from strongly stabilized (large h_{por} and small r_{por}), to strongly destabilized (large h_{por} and r_{por} , or continuous injection). The trends observed for the baseline case were then explored for different Mach numbers and surface temperature ratios, which displayed very similar trends.

Transition-onset predictions were also performed, using the e^N method, in order to quantify how the variation of the stability characteristics ultimately affects the advancement or delay of the transition front. The trends observed for a single streamwise location were seen to prevail when integrating instability growth along x .

The combinations of h_{por} and r_{por} were mapped out for various flow conditions, in order to obtain the regions of porous-layer stabilization and destabilization. These maps were then employed to analyze a series of non-blowing experiments with passive porous walls and explain the results arising from them.

Overall, the results displayed in this section highlight the high sensitivity of the boundary-layer stability characteristics and ultimately the transition-onset location to variations in the features of the porous layer that is a TPS in decomposition.

References

- [1] S. P. Schneider. *Hypersonic Boundary-Layer Transition with Ablation and Blowing*. Journal of Spacecraft and Rockets, **47**(2):225–237, 2010.
- [2] J. G. Marvin and C. M. Akin. *Combined effects of mass addition and nose bluntness on boundary-layer transition*. AIAA Journal, **8**(5):857–863, 1970.
- [3] M. R. Malik. *Prediction and control of transition in supersonic and hypersonic boundary layers*. AIAA Journal, **27**(11):1487–1493, 1989.
- [4] H. B. Johnson, J. E. Gronvall, and G. V. Candler. *Reacting hypersonic boundary layer stability with blowing and suction*. AIAA paper, **2009-938**, 2009.
- [5] S. Ghaffari, O. Marxen, G. Iaccarino, and E. S. G. Shaqfeh. *Numerical simulations of hypersonic boundary-layer instability with wall blowing*. AIAA paper, **2010-706**, 2010.
- [6] F. Li, M. M. Choudhari, C.-L. Chang, and J. White. *Effects of injection on the instability of boundary layers over hypersonic configurations*. Physics of Fluids, **25**(10), 2013.
- [7] A. V. Fedorov and V. G. Soudakov. *Stability analysis of high-speed boundary-layer flow with gas injection*. AIAA paper, **2014-2498**, 2014.
- [8] I. A. Leyva, S. J. Laurence, A. W.-K. Beierholm, H. G. Hornung, R. M. Wagnild, and G. V. Candler. *Transition delay in hypervelocity boundary layers by means of CO₂/acoustic instability interactions*. AIAA paper, **2009-1287**, 2009.
- [9] J. S. Jewell, R. M. Wagnild, I. A. Leyva, G. V. Candler, and J. E. Shepherd. *Transition Within a Hypervelocity Boundary Layer on a 5-Degree Half-Angle Cone in Air/CO₂ Mixtures*. AIAA paper, **2013-0523**, 2013.
- [10] A. V. Fedorov, A. N. Shiplyuk, A. A. Maslov, E. Burov, and N. D. Malmuth. *Stabilization of high speed boundary layer using a porous coating*. In **41st Aerospace Sciences Meeting and Exhibit**, number January, 2003.
- [11] S. A. Gaponov. *Effect of the Properties of a Porous Coating on Boundary Layer Stability*. Technical Report TM 75235, NASA, Santa Barbara, CA, 1978.
- [12] F. Miró Miró, P. Dehairs, F. Pinna, M. Gkolia, D. Masutti, T. Regert, and O. Chazot. *Effect of wall blowing on hypersonic boundary-layer transition*. AIAA Journal, **57**(4):1567–1578, 2019.

- [13] F. Miró Miró. *Numerical Study of the Stability of a Hypersonic Boundary Layer in the presence of Blowing*. Technical Report TR 2015-28, von Karman Institute for Fluid Dynamics, Brussels, Belgium, 2015.
- [14] M. K. Gkolia. *Development of testing strategy for study of Ablation-Transition Phenomena in Hypersonic Flow*. Technical Report PR 2015-18, von Karman Institute for Fluid Dynamics, Rhode Saint-Genèse, 2015.
- [15] P. Dehairs. *Interaction of Ablation Pyrolysis Gases with the Boundary Layer in Hypersonic Regime*. Technical Report PR 2016-08, von Karman Institute for Fluid Dynamics, 2016.
- [16] D. Masutti, F. Pinna, E. Gunaydinoglu, T. Sopek, and O. Chazot. *Natural and Induced Transition on a 7deg Half-Cone at Mach 6*. In RTO-AVT-200. NATO-RTO, 2012.
- [17] T. Regert, Y. Babou, O. Marxen, M. A. Camarinha, and O. Chazot. *Investigation of flat plate transitional boundary layer in hypersonic flow by means of naphthalene based PLIF*. In 5th European Conference for Aeronautics and Space Sciences (EUCASS). EUCASS organization, 2013.
- [18] G. Simeonides. *The VKI hypersonic wind tunnels and associated measurement techniques*. Technical Report TM 46, von Karman Institute for Fluid Dynamics, Rhode Saint-Genèse, 1990.
- [19] D. B. Spalding. *Convective mass transfer: an introduction*. McGraw-Hill Book Company Inc., New York City, USA, 1963.
- [20] J. H. Koo, D. W. H. Ho, and O. A. Ezekoye. *A review of numerical and experimental characterization of thermal protection materials - Part I. Numerical modeling*. AIAA paper, [2006-4936](#), 2006.
- [21] F. Miró Miró and F. Pinna. *Effect of uneven wall blowing on hypersonic boundary-layer stability and transition*. Physics of Fluids, [30\(084106\)](#), 2018.
- [22] U. Goldberg, O. Peroomian, S. Chakravarthy, and B. Sekar. *Validation of CFD++ code capability for supersonic combustor flowfields*. AIAA paper, [1997-3271](#), 1997.
- [23] F. S. Billig. *Shock-wave shapes around spherical-and cylindrical-nosed bodies*. Journal of Spacecraft and Rockets, [4\(6\):822–823](#), 1967.
- [24] D. Prokein and J. von Wolfersdorf. *Numerical Simulation of Turbulent Boundary Layers with Foreign Gas Transpiration using OpenFOAM*. In [7th European Conference for Aeronautics and Space Sciences](#), Milano, Italy, 2017.

- [25] A. V. Fedorov, N. D. Malmuth, A. Rasheed, and H. G. Hornung. *Stabilization of hypersonic boundary layers by porous coatings*. AIAA Journal, **39**(4):605–610, 2001.
- [26] A. V. Fedorov, V. F. Kozlov, A. N. Shiplyuk, A. A. Maslov, and N. D. Malmuth. *Stability of hypersonic boundary layer on porous wall with regular microstructure*. AIAA Journal, **44**(8):1866–1871, 2006.
- [27] S. Willems and A. Gühan. *Damping of the Second Mode Instability with Regular and Random Porous Surfaces on Slender Cone in Hypersonic Flow*. In NATO RTO-MP-AVT-200, 2012.
- [28] S. V. Lukashevich, A. A. Maslov, A. N. Shiplyuk, A. V. Fedorov, and V. G. Soudakov. *Stabilization of High-Speed Boundary Layer Using Porous Coatings of Various Thicknesses*. AIAA Journal, **50**(9):1897–1904, 2012.
- [29] X. Wang and X. Zhong. *Effect of porous coating on boundary-layer instability*. 48th AIAA Aerospace Sciences Meeting Including the New Horizons Forum and Aerospace Exposition, **2010-1243**, 2010.
- [30] N. B. Oliviero, T. S. Kocian, A. J. Moyes, and H. L. Reed. *EPIC: NPSE Analysis of Hypersonic Crossflow Instability on Yawed Straight Circular Cone*. AIAA paper, **2015-2772**, 2015.
- [31] B. A. Bhutta and C. H. Lewis. *Low-To-High Altitude Predictions of Three-Dimensional Ablative Reentry Flowfields*. AIAA paper, 92-0366, 1992.
- [32] B. Helber, A. Turchi, J. B. Scoggins, A. Hubin, and T. E. Magin. *Experimental investigation of ablation and pyrolysis processes of carbon-phenolic ablators in atmospheric entry plasmas*. International Journal of Heat and Mass Transfer, **100**:810–824, 2016.
- [33] J. C. Dunavant and P. E. Everhart. *Exploratory heat-transfer measurements at mach 10 on a 7.5-deg total-angle cone downstream of a region of air and helium transpiration cooling*. Technical report, NASA, 1969.
- [34] G. G. Mateer and H. K. Larson. *Unusual boundary-layer transition results on cones in hypersonic flow*. AIAA Journal, **7**(4):660–664, 1969.
- [35] C. R. Wimberly, F. K. McGinnis, and J. J. Bertin. *Transpiration and film cooling effects for a slender cone in hypersonic flow*. AIAA Journal, **8**(6):1032–1038, 1970.
- [36] M. C. Fischer. *An experimental investigation of boundary layer transition on a 10 degree half-angle cone at Mach 6.9*. Technical Report TN D-5766, NASA, 1970.

- [37] V. DiCristina. *Three-dimensional laminar boundary-layer transition on a sharp 8-deg cone at Mach 10*. AIAA Journal, **8**(5):852–856, 1970.
- [38] C. J. Scott. *Experimental Investigations of Laminar Heat Transfer and Transition with Foreign Gas Injection of a 16-deg Porous Cone at M=5*. Technical Report UMRAL RR 174, University of Minnesota, Institute of Technology, Rosemont Aeronautical Laboratories, Minneapolis, MN, 1960.
- [39] C. J. J. Stalmach, J. J. Bertin, T. C. Pope, and M. H. McCloskey. *A Study of Boundary Layer Transition on Outgassing Cones in Hypersonic Flow*. Technical Report CR-1908, NASA, 1971.
- [40] F. Pinna. *Numerical study of stability of flows from low to high Mach number*. PhD thesis, Università degli Studi di Roma La Sapienza, 2012.
- [41] F. Pinna. *VESTA toolkit: a Software to Compute Transition and Stability of Boundary Layers*. AIAA paper, **2013-2616**, 2013.
- [42] K. M. Casper, H. B. Johnson, and S. P. Schneider. *Effect of Freestream Noise on Roughness-Induced Transition for a Slender Cone*. Journal of Spacecraft and Rockets, **48**(3):406–413, 2011.
- [43] M. J. Wright, D. Bose, G. E. Palmer, and E. Levin. *Recommended Collision Integrals for Transport Property Computations Part I: Air Species*. AIAA Journal, **43**(12):2558–2564, 2005.
- [44] M. J. Wright, H. H. Hwang, and D. W. Schwenke. *Recommended Collision Integrals for Transport Property Computations Part II: Mars and Venus Entries*. AIAA Journal, **45**(1):281–288, 2007.
- [45] J. J. Kuehl. *Thermoacoustic Interpretation of Second-Mode Instability*. AIAA Journal, **56**(9):3585–3592, 2018.
- [46] J. Sakakeeny, A. Batista, and J. J. Kuehl. *How nose bluntness suppresses second-mode growth*. AIAA paper, **2019-3083**, 2019.
- [47] J. H. Koo, W. Ho, M. Bruns, and O. A. Ezekoye. *A Review of Numerical and Experimental Characterization of Thermal Protection Materials Part II: Properties Characterization*. AIAA paper, **2007-2131**, 2007.
- [48] J. Lachaud, I. Cozmuta, and N. N. Mansour. *Multiscale approach to ablation modeling of phenolic impregnated carbon ablators*. Journal of Spacecraft and Rockets, **47**(6):910–921, 2010.
- [49] E. W. Thiele. *Relation between Catalytic Activity and Size of Particle*. Industrial and Engineering Chemistry, **31**(7):916–920, 1939.

- [50] A. V. Fedorov, A. N. Shiplyuk, A. A. Maslov, E. Burov, and N. D. Malmuth. *Stabilization of a hypersonic boundary layer using an ultrasonically absorptive coating*. Journal of Fluid Mechanics, [479\(479\):99–124](#), 2003.
- [51] V. Michael and S. O. Stephen. *Nonlinear stability of hypersonic flow over a cone with passive porous walls*. Journal of Fluid Mechanics, [713:528–563](#), 2012.
- [52] V. C. Sousa, D. Patel, J. B. Chaperon, V. Wartemann, A. Wagner, and C. Scalo. *Numerical investigation of second-mode attenuation over carbon/carbon porous surfaces*. Journal of Spacecraft and Rockets, [56\(2\):319–332](#), 2019.
- [53] N. P. Bitter and J. E. Shepherd. *Stability of highly cooled hypervelocity boundary layers*. Journal of Fluid Mechanics, [778:586–620](#), 2015.
- [54] C. Mortensen and X. Zhong. *Real-Gas and Surface-Ablation Effects on Hypersonic Boundary-Layer Instability over a Blunt Cone*. AIAA Journal, [54\(3\):980–998](#), 2016.
- [55] A. Wagner, M. Kuhn, J. Martinez Schramm, and K. Hannemann. *Experiments on passive hypersonic boundary layer control using ultrasonically absorptive carbon-carbon material with random microstructure*. Experiments in Fluids, [54\(10\)](#), 2013.
- [56] R. F. Probstein and D. Elliott. *The Transverse Curvature Effect in Compressible Axially Symmetric Laminar Boundary-Layer Flow*. Journal of Aeronautical Sciences, [23\(3\):208–224](#), 1956.
- [57] F. M. White. *Viscous Fluid Flow*. McGraw-Hill, 2nd edition, 1991.

10

High-enthalpy effects and transition

The pyrolysis and ablation of the TPS occurs as a consequence of the high temperature of air surrounding the vehicle during atmospheric entry. Besides the decomposition of the TPS, high temperatures also trigger a series of physical phenomena, such as the vibrational excitation of molecular species, dissociation, species inter-diffusion, or ionization (see chapter 2). The present chapter analyzes how these phenomena affect boundary-layer stability and transition in the absence of surface ablation. The methodology is thus similar to that of chapter 9: approaching one of the coupled phenomena in wall-ablating scenarios in isolation.

The first section (§ 10.1) quantifies the dispersion in the results that one can expect due to the different modeling choices. The second (§ 10.2) deepens on the sensitivity of stability predictions to diffusion fluxes, by enhancing or weakening such fluxes. The third section (§ 10.3) carries out a parametric study on the adequacy of various flow assumptions in atmospheric entry flow regimes. Finally, an investigation of ionization effects on stability is carried out in § 10.4.

10.1 Gas modeling influence on stability predictions

As discussed in chapter 4, the modeling of gas properties at high temperatures has been in and of itself a very active field of research for decades [1–9], and authors investigating the stability and transition of flows under such conditions have employed a variety of different thermophysical models (see Table 4.1). This high modeling variance largely complicates the comparison of results obtained by

different groups. Very often it is unclear if the discrepancies are due to actual physical phenomena, or rather are an artifact of the distinct modeling choices (see for instance Stuckert & Reed [10] and Hudson *et al.* [11]).

Within this frame, the present section quantifies the propagation of high-temperature modeling inaccuracies into the boundary-layer stability and transition predictions. A series of representative literature test cases are revisited, in order to study the sensibility of the basic-state flowfields, stability features and transition-onset locations, to transport, diffusion, collision, equilibrium and chemical-kinetic modeling errors. All simulations are carried out with the DEKAF flow solver (see chapter 7) and the VESTA toolkit (see chapter 8), using the Chebyshev pseudo-spectral collocation method.

It is important to note that the models and the analyses presented in this section are restricted to thermal equilibrium. Many authors [11–16] used two-temperature models. However they all featured the same modeling strategy for the energy-relaxation terms (see § 4.5), thus making a model comparison such as the one hereinafter presented unnecessary.

Four literature cases, summarized in Table 10.1, are revisited. They all analyze second-mode instabilities (known to be dominant in such flow regimes in the absence of cross-flow [17]), and therefore feature a zero spanwise wavenumber ($\beta = 0$). All estimations of the effect on transition-onset location will be in a comparative sense and will be performed by assuming that it will occur when the N -factor envelope reaches an $N = 9$. That is, flow conditions reaching an N of 9 before will be presumed to accelerate transition relative to others. A blue horizontal dashed line marks this limit in all N -factor-envelope plots. The perturbation mode shapes are not observed to be strongly modified by the model variations. However, for the sake of completeness, they are presented in § 10.1.7.

Given the negligible discrepancy [18] between the RRHO and McB thermal models, all presented results assumed the RRHO one (§ 4.1).

10.1.1 Case 1 – influence of the transport model

The effect of the transport model is analyzed through the test case previously investigated by Stuckert & Reed [10] and Hudson *et al.* [11], amongst others [14, 19]. It consists of a Mach 10 flat plate (FP), with a unit Reynolds number of $9.8425 \cdot 10^6 \text{ m}^{-1}$, an edge temperature of 278 K, and an adiabatic wall. Previous studies [22] demonstrated that the chemical activity is small enough to neglect it and assume the flow to be frozen (TPG). The test gas (air) is therefore approximated using two species (N_2 and O_2), whose mass concentrations at the boundary-layer edge are 0.78 and 0.22 respectively. This test case is excellent to analyze the influence of the transport model, since diffusion and chemical activity are neglected when assuming TPG conditions. The collision integrals are obtained using

Case	Geometry	M_e	$Re_1 [\text{m}^{-1}]$	$u_e [\text{m/s}]$	$T_e [\text{K}]$	Wall
1	FP	10	$9.8425 \cdot 10^6$	3348.2	278	adiabatic
2	FP	10.545	$2.555 \cdot 10^6$	5655.2	834	adiabatic
3	6°-wedge	12.66	$6.381 \cdot 10^6$	6121.1	588.7	529.04 [K]
4	FP	10	$6.6 \cdot 10^6$	4877.6	600	adiabatic

Case	Flow assumption	Mixture	References
1	TPG	N_2, O_2	10, 11, 14, 19
2	CNE	O, O_2	20
3	LTE	$\text{N}, \text{O}, \text{NO}, \text{N}_2, \text{O}_2$	16, 21
4	CNE	$\text{N}, \text{O}, \text{NO}, \text{N}_2, \text{O}_2$	22

Table 10.1: Summary of the analyzed cases.

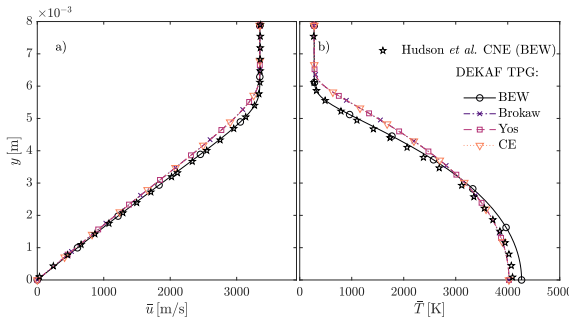


Figure 10.1: Basic-state profiles at $x = 0.4 \text{ m}$ employing the various transport models on case 1 from Table 10.1.

Stuckert's [23] curve fits (Eq. 4.56) on the collisional data collected from various sources [24–27].

Figure 10.1 shows the self-similar boundary-layer velocity and temperature profiles for each of the considered transport models, evaluated 0.4 m away from the tip. The agreement of the BEW curve with Hudson *et al.*'s results is considerably good. One can clearly observe that the use of the BEW model (§ 4.2.1.1) results in a smaller prediction for the boundary-layer height. Figure 10.2 shows the perturbation growth rate ($-\alpha_3$) as a function of the perturbation frequency (F), for the four considered models for viscosity and frozen thermal conductivity, together with the reference literature cases. The fact that the results match the various authors when changing the transport model demonstrates that the disagreement between Stuckert & Reed's [10] growth rates and those of the other authors [11, 14, 19] is indeed due to the modeling of the transport properties. The major difference in the stability characteristics, when using the less accurate BEW

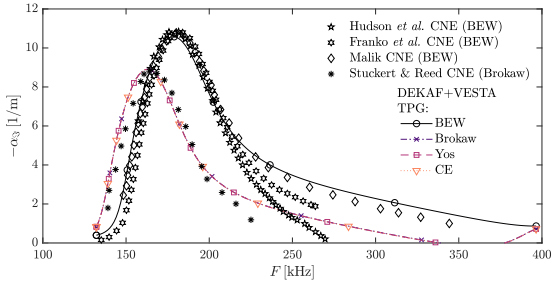


Figure 10.2: Second-mode perturbation growth rates at $x = 0.4\text{ m}$ employing the various transport models on case 1 from Table 10.1.

model instead of any of the others, also coincides with what was previously reported by other authors [14, 28]. The BEW model predicts a larger growth rate and a wider range of unstable frequencies than the others. This is presumably linked to the smaller boundary-layer height forecasted with this model (Fig. 10.1).

Integrating along the streamwise direction the growth rates of perturbations with constant frequency F , one retrieves the N -factor curves [29]. The envelopes of these curves for frequencies ranging from 30 to 300 kHz, for each of the transport models are presented in Fig. 10.3(a). Consistently with what was observed in Fig. 10.2, the use of the BEW model results in an overprediction of instability growth, and to predicting the transition-onset location to be at $x = 4.62\text{ m}$. That is, a 38% sooner than where the state-of-the-art model predicts it to occur, at $x = 7.45\text{ m}$. Once again, Brokaw and Yos' models provide results coinciding with those obtained with the CE model.

Figure 10.3(b) presents the neutral-stability curve [30] for all four transport models. The differences in the ranges of unstable frequencies predicted by each model are consistent with what was observed in Fig 10.2. The BEW model predicts a wider range of unstable frequencies than the other models. This is also one of the reasons why it predicted larger N factors in Fig. 10.3(a). Brokaw and Yos' models lead to identical neutral-stability curves to that obtained using the CE model.

It is important to note that the excellent agreement of Brokaw and Yos' with the CE model is subject to the mixture being non-ionized. As observed in Fig. 4.1, even though these two models feature very small errors for the air-5 mixture, these errors increase significantly when ionization appears, reaching, and in some cases surpassing, those of the BEW model. One would therefore expect the subsequent transition-onset-location predictions done at such regimes to have comparable errors to those displayed when using the BEW model in Fig. 10.3(a).

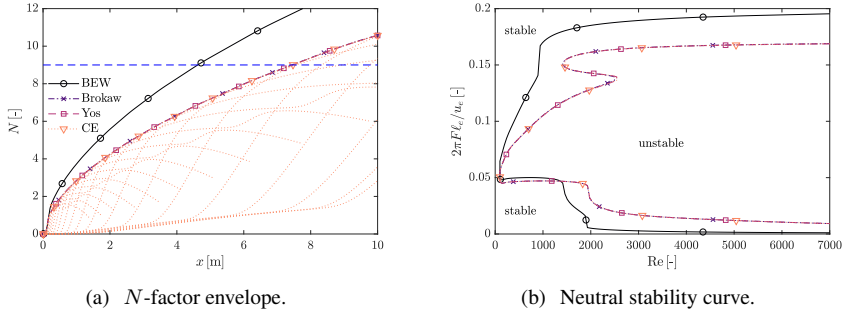


Figure 10.3: Case 1 from Table 10.1 for the various transport models.

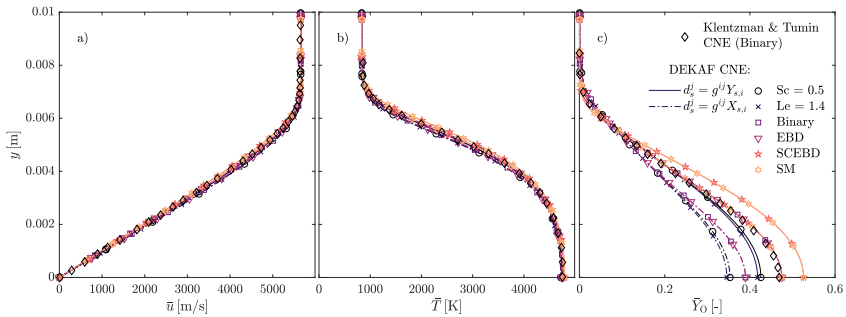


Figure 10.4: Basic-state profiles at $x = 0.4\text{ m}$ employing the various diffusion models on case 2 from Table 10.1.

10.1.2 Case 2 – influence of the diffusion model

The effect of the diffusion model is analyzed through a test case previously investigated by Klentzman & Tumin (case 3 in Ref. 20). It consists in a Mach 10.545 flat plate, with a unit Reynolds number of $2.555 \cdot 10^6 \text{ m}^{-1}$, an edge temperature of 834 K, and an adiabatic wall. The test gas is oxygen, which is approximated using two species (O , and O_2). The employed transport model is Brokaw's (Eq. 4.34) with collisional data coming from Gupta *et al.* [4] (Eq. 4.55). The chemical activity is approximated with Bortner's [4, 31] reaction rate constants enhanced^a similarly to Ref. 20, and with an Arrhenius-like expression for the equilibrium constant (Eq. 4.70).

Figure 10.4 shows the velocity, temperature, and O concentration profiles evaluated 0.4 m away from the tip. The various diffusion models predict similar velocity and temperature profiles, and boundary-layer heights, in excellent agreement

^aThe oxygen dissociation reactions are enhanced by a factor of 25 when O is the third-body, and by a factor of 9 when it is O_2 .

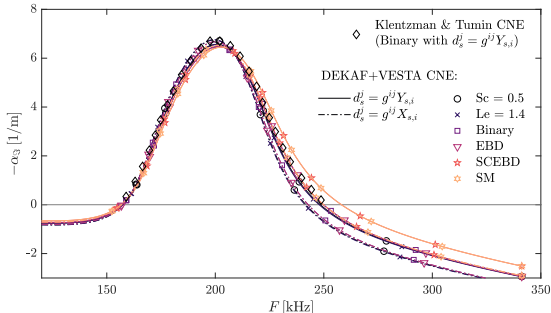


Figure 10.5: Second-mode perturbation growth rates at $x = 0.4\text{ m}$ employing the various diffusion models on case 2 from Table 10.1.

with Klentzman & Tumin's. However, they lead to significantly different concentration profiles, with O wall mass fractions ranging from 0.35 to 0.5. The concentration profile matches Klentzman & Tumin's when using the same model as them^b or when using the state-of-the-art model.^c Despite this, Fig. 10.5 shows that these differences do not affect significantly the predicted stability features – the maximum amplification rate and the low-frequency characteristics remain practically unaltered, displaying only a slight variation of the high-frequency content. This is in agreement with the findings of § 10.2, and suggests that diffusion and its modeling have a minor effect on the predicted stability of the boundary layer. A likely explanation for this is the fact that the boundary-layer size remains unaltered when changing the diffusion model. The use of one or another diffusion driving force was also seen to have a minor effect on the stability characteristics, even if the concentration profiles did vary significantly.

Figure 10.6 presents the N -factor envelopes, obtained with perturbation frequencies between 40 and 350 kHz, together with the neutral-stability curves obtained using the various diffusion models and driving forces. The results suggest that the trends observed in Fig. 10.5 are preserved when integrating the perturbation growth rates along the streamwise direction. The differences in the high-frequency content predicted by the various models are clearly observable in the neutral curves in Fig. 10.6(b), and grow slightly when advancing downstream. There is a scatter in the predicted transition-onset location of approximately $\pm 0.7\text{ m}$ (less than 5%). Possible reasons for this scatter are the aforementioned change in the high-frequency content, promoting instabilities at sooner streamwise positions, or the slight variability of the maximum amplification rate observed in Fig. 10.5. One must note that the neutral stability curves are plotted with the frequency F scaled by the Blasius length ℓ_e . The range of unstable fre-

^bBinary diffusion model with mass-fraction driving forces.

^cStefan-Maxwell diffusion model with molar-fraction driving forces.

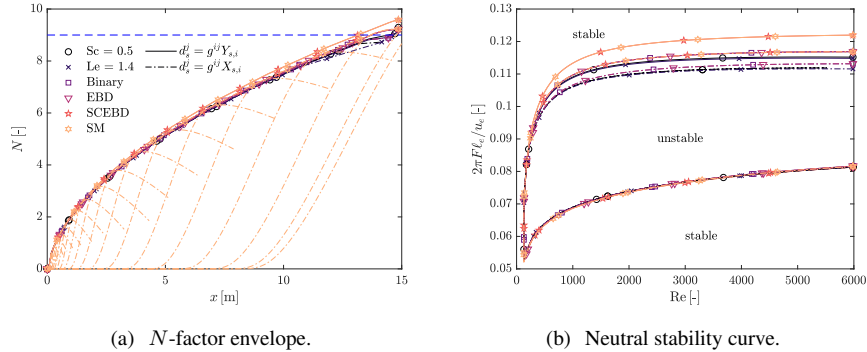


Figure 10.6: Case 2 from Table 10.1 for the various diffusion models.

quencies actually moves towards higher frequencies when reducing the Reynolds number, not to lower ones as it may seem from Fig. 10.6(b).

One should refrain from extending these observations to mixtures of gases with dissimilar features. Such scenarios could introduce strong variations in viscosity and thermal conductivity due to the concentration profiles, and therefore require careful individual examination.

10.1.3 Cases 1 and 2 – influence of the collision model

The influence of the collisional model on the boundary-layer stability characteristics is investigated by revisiting cases 1 and 2, varying solely the source of the collisional data. Case 1 is modeled with the CE transport model and with all the other models being those detailed in § 10.1.1. Similarly, case 2 uses the SM diffusion model with mole-fraction driving forces, with all other models coinciding with those mentioned in § 10.1.2. Looking at the boundary-layer profiles in Figs. 10.7 and 10.8, one may observe that the use of Gupta *et al.*'s [4] collisional data significantly underpredicts the boundary-layer height, whereas using Stuckert's [23] slightly overpredicts it. Since this trend is observed both in Fig. 10.7 and in Fig. 10.8, one may affirm that it is caused by the modification of the transport properties and not that of the diffusion fluxes, which are neglected in Fig. 10.7 because of assuming TPG conditions. Moreover, the differences in the O wall concentration between the various sources of collisional data (Fig 10.8 c) are negligible, suggesting that varying the collisional data used to compute the diffusion fluxes has very little impact on the predicted boundary-layer profiles. It is not surprising that Stuckert's collection of collisional data provides closer results to the state-of-the-art than those computed with Gupta *et al.*'s data. This could be anticipated by the lower error that Stuckert's data displayed in Fig. 4.3.

Figure 10.9 shows the predicted perturbation growth rates as a function of their

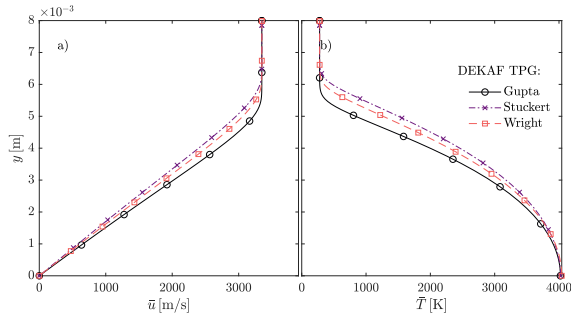


Figure 10.7: Basic-state profiles at $x = 0.4\text{ m}$ employing the various sources of collisional data on case 1 from Table 10.1, and with using the CE transport model. All other models coincide to those detailed in § 10.1.1.

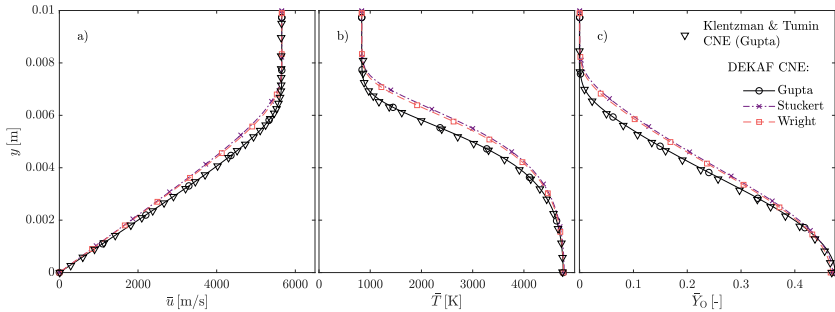


Figure 10.8: Basic-state profiles at $x = 0.4\text{ m}$ employing the various sources of collisional data on case 2 from Table 10.1, and using the SM diffusion model with mole-fraction driving forces. All other models coincide to those detailed in § 10.1.2.

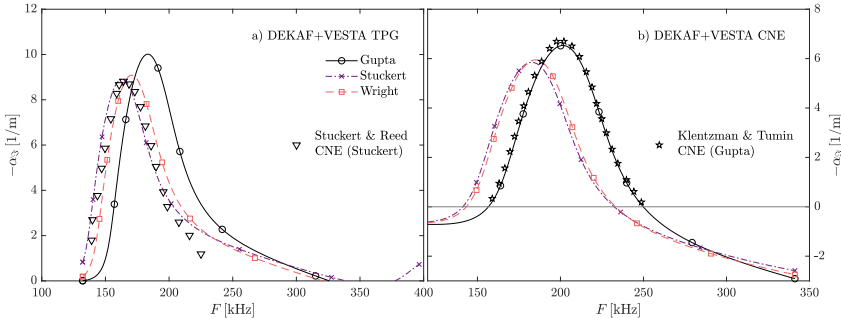


Figure 10.9: Second-mode perturbation growth rates at $x = 0.4\text{ m}$ employing the various sources of collisional data. (a) case 1 with CE transport model and all other models coinciding to those detailed in § 10.1.1. (b) case 2 with SM diffusion model with mole-fraction driving forces and all other models coinciding to those detailed in § 10.1.2. Case details can be found in Table 10.1.

frequency for cases 1 and 2 (see Table 10.1) using the three sources of collisional data. Gupta *et al.*'s collisional data leads to overpredicting the perturbation growth rates, whereas Stuckert's leads to slightly underpredicting them. This is once again consistent with the corresponding boundary-layer heights that were obtained.

Figure 10.10 presents the envelopes of the integrated N factors for the three sources of collisional data, using the same frequency ranges as in Fig. 10.3(a) and 10.6(a) (30 - 300 kHz for Fig. 10.10(a) and 40 - 350 kHz for Fig. 10.10(b)). The trends observed in Fig. 10.10 are coherent with those seen in Fig. 10.9. The use of Gupta *et al.*'s collisional data leads to larger predicted perturbation amplitudes and to a transition-onset location 8% farther upstream, whereas with Stuckert's one predicts the same as with the state-of-the-art data (Wright *et al.*'s [32]).

Fig. 10.11 illustrates the modification of the neutral-stability curves of case 1 and case 2 introduced by the use of different collisional data. The various collisional models affect the predicted high- and low-frequency behavior in case 1. These regions correspond to other instability mechanisms (Mack's first and third mode [17]) different from Mack's second mode with very small growth rates under the considered configuration. Consequently, they do not affect the N -factor envelopes significantly. One should, however, take them into account when investigating situations dominated by Mack's first-mode instabilities. For case 2 there is a consistent shift of the unstable region towards higher frequencies when using Gupta *et al.*'s data. The size of this range however, does remain fairly unchanged with the collisional modeling.

The effect of using Gupta *et al.*'s collisional data rather than the state-of-the-art on the growth rates of case 1 (Fig. 10.9(a)), is comparable to that reported in § 10.1.1 caused by using the BEW transport model instead of the state-of-the-art

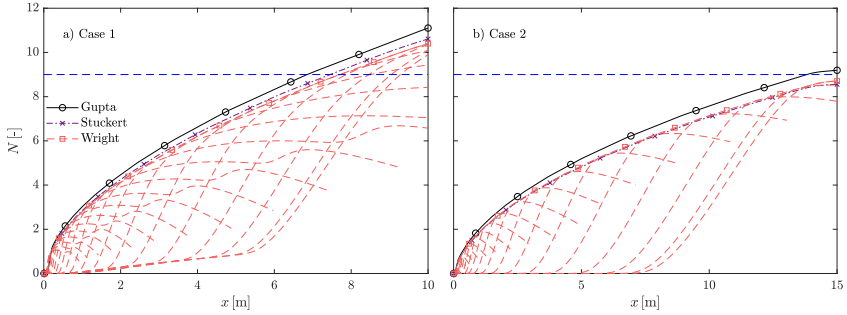


Figure 10.10: Second-mode N -factor envelopes employing the various sources of collisional data. (a) case 1 with CE transport model and all other models coinciding to those detailed in § 10.1.1. (b) case 2 with SM diffusion model with mole-fraction driving forces and all other models coinciding to those detailed in § 10.1.2. Case details can be found in Table 10.1.

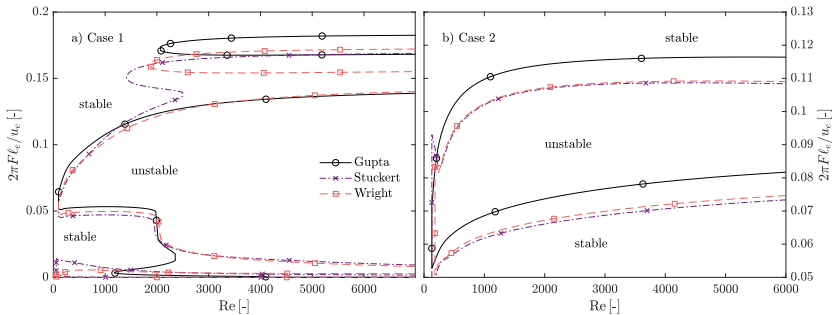


Figure 10.11: Neutral-stability curve employing the various sources of collisional data. (a) case 1 with CE transport model and all other models coinciding to those detailed in § 10.1.1. (b) case 2 with SM diffusion model with mole-fraction driving forces and all other models coinciding to those detailed in § 10.1.2. Case details can be found in Table 10.1.

(Fig. 10.2). Despite this, the artificial advancement of the predicted transition-onset location introduced by both modeling inaccuracies is very different - 8% when using Gupta *et al.*'s collisional data and 38% when using the BEW transport model. A possible explanation for this lies in how the area under the $-\alpha_{\infty}$ vs F curve is modified by one and another modeling error. The $-\alpha_{\infty}$ vs F curve in self-similar problems such as case 1 is typically very similar to the $-\alpha_{\infty}$ vs x curve, after some appropriate scaling. The BEW model leads to a fuller curve than Gupta *et al.*'s collisional data, which, when integrated along the streamwise direction, results in a larger N factor and a sooner predicted transition onset.

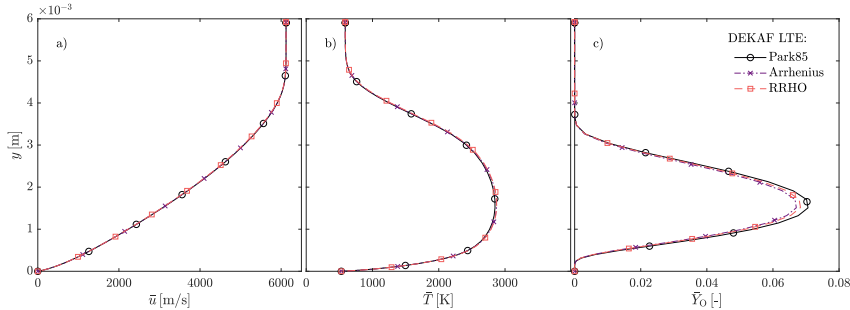


Figure 10.12: Basic-state profiles at $x = 18.29 \text{ m}$ employing the various equilibrium models on case 3 from Table 10.1.

10.1.4 Case 3 – influence of the chemical equilibrium model

The influence of the chemical equilibrium model is investigated through a test case previously studied by Chang *et al.* [21] (LST and PSE) and Kline *et al.* [16] (PSE). It features a 6-degree infinitely-sharp wedge in a flow at Mach 20, with a free-stream unit Reynolds number of $2.953 \cdot 10^6 \text{ m}^{-1}$ ($9 \cdot 10^5 \text{ ft}^{-1}$), a temperature of 236.67 K, and an isothermal wall temperature of 529.04 K (one tenth of the adiabatic wall temperature in equilibrium). The post-shock conditions, which coincide with those at the boundary-layer edge detailed in Table 10.1, are obtained from the TPG shock-jump relations (see § 7.1). The test gas is air, which is approximated using five species (N, O, NO, N₂ and O₂). LTE conditions are assumed, such that the influence of the chemical equilibrium model can be investigated independently from the chemical kinetics. The transport and diffusion models employed are BEW (§ 4.2.1.1) and molar SCEBD (Eq. 4.44), with collisional data coming from Gupta *et al.* [4] (Eq. 4.55), in order to accurately reproduce the literature conditions.

Figure 10.12 displays the basic-state profiles obtained with the various equilibrium models evaluated at $x = 18.29 \text{ m}$ (60 ft). The three models return practically identical profiles, with only a minor difference in the maximum O mass fraction (Fig. 10.12(c)). This difference does not affect the individual N factors for $F = 100 \text{ kHz}$ presented in Fig. 10.13, nor the N -factor envelopes in Fig. 10.14(a) (with frequencies varying between 50 and 400 kHz), nor the neutral-stability curves in Fig. 10.14(b). The predicted transition-onset location varies less than 2% when changing the modeling of the chemical equilibrium constant.

10.1.5 Case 4 – influence of the chemical kinetic model

Different modelings of the chemical kinetics are compared by recreating a test case previously studied by the author [22]. It features a Mach 10 flow over a flat

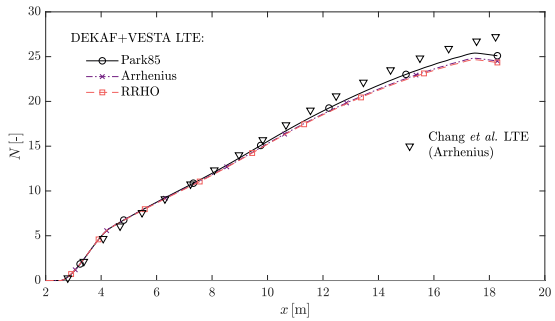


Figure 10.13: Second-mode N factor for $F = 100$ kHz employing the various equilibrium models on case 3 from Table 10.1.

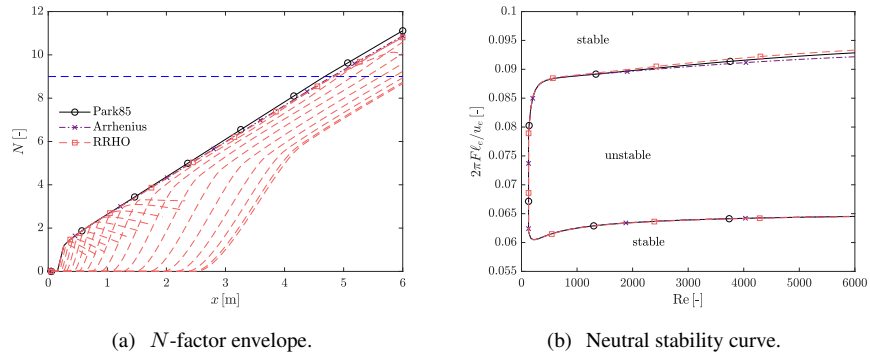


Figure 10.14: Case 3 from Table 10.1 for the various equilibrium models.

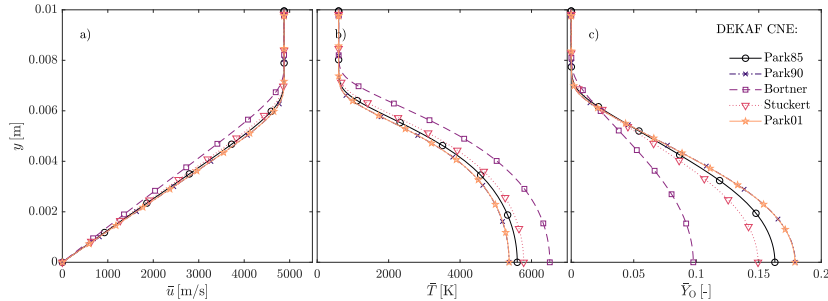


Figure 10.15: Basic-state profiles at $x = 0.6$ m employing the various sources for the reaction-rate constants on case 4 from Table 10.1.

plate, with a unit Reynolds number of $6.6 \cdot 10^6 \text{ m}^{-1}$, an edge temperature of 600 K, and an adiabatic wall, evaluated at 0.6 m from the tip. The test gas is air, which is approximated using five species (N_2 , O_2 , NO , O , and N). The transport and diffusion models employed are BEW (§ 4.2.1.1) and cstSc (Eq. 4.39) with mass-fraction driving forces. The chemical equilibrium constants are obtained assuming a RRHO model (Eq. 4.66).

The laminar basic-state velocity, temperature, and O-mass-fraction profiles obtained with the various chemical kinetic models are presented in Fig. 10.15. The profiles display significant differences – Park’s 1985 [33], Stuckert’s [23] and Bortner’s [31] models predict decreasing levels of dissociation and boundary-layer cooling, all of them lower than that predicted by the state-of-the-art model (Park01 [34]). It is not surprising that Park’s 1990 model provides very close results to his 2001 model, since they use the same reaction-rate constants for the dissociation reactions, and thus only differ in those of the exchange reactions (see Fig. 4.6). The dissociation-induced boundary-layer cooling entails a decrease of the boundary-layer height, being logically more pronounced when using Bortner’s model.

Figure 10.16 presents the corresponding perturbation growth rates, which follow the lines of what one would expect from the basic-state profiles. The use of models predicting less dissociation-induced boundary-layer-size reduction, also leads to lower predicted perturbation growth rates. The differences however, are not as pronounced as one could expect from the basic-state profiles. A possible reason for this are the two competing effects that chemistry has on Mack’s second-mode instabilities: the destabilization of the flow due to basic-state cooling, and the stabilization due to the removal of energy from the perturbations, with the net effect usually being a destabilization.^d The latter would therefore compensate to a certain extent the effects of the former, which are observable in Fig. 10.15.

^dA clear visualization of these competing effects can be found in § 10.4.

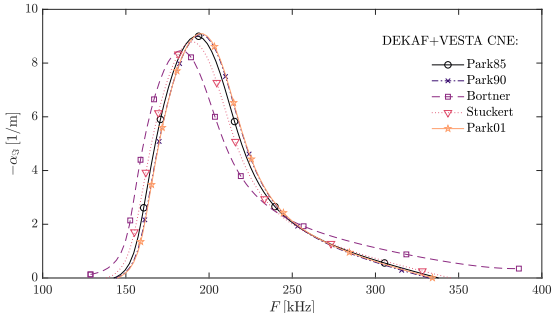


Figure 10.16: Second-mode perturbation growth rates at $x = 0.6\text{ m}$ employing the various sources for the reaction-rate constants on case 4 from Table 10.1.

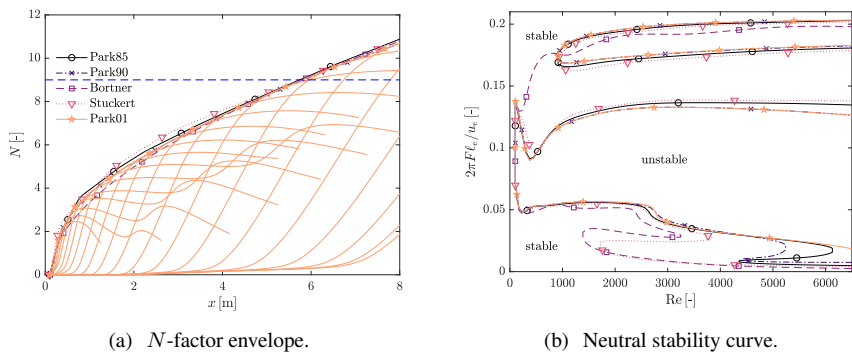


Figure 10.17: Case 4 from Table 10.1 for the various sources for the reaction-rate constants.

The integrated N -factor envelopes for the five chemical kinetic models are displayed in Fig. 10.17(a). The curves of the different models display some differences at the earlier streamwise locations, but they all converge farther downstream. This is reasonable since after sufficient time they all lead to chemical equilibrium, independently from the rate at which chemical reactions take place.

The neutral stability curves retrieved using the various chemical kinetic models are presented in Fig. 10.17(b). All models return similar unstable ranges for the second Mack mode. However, they display notorious differences in the high- and low-frequency region. Bortner's model does not predict a range of stable frequencies between the second and the third mode peaks, whereas all other models do. The discrepancies in the low-frequency region should be further investigated in order to determine whether or not they are also present for three-dimensional waves ($\beta \neq 0$), which are known to be the most unstable first-mode perturbations.

10.1.6 Case 1 – effects of transport modeling on perturbation terms

The analyses presented in § 10.1.1-10.1.5 employed the different models consistently both in the basic-state and stability computations. However, one may encounter situations where the basic-state flowfield has been computed with a given set of thermodynamic and transport models that are different from those used in the stability computations (see for instance Chang *et al.* [21] or Kline *et al.* [16]). Such practices are by all means not recommendable, due to the modeling inconsistencies that they constitute. Nevertheless, in order to quantify the differences in the stability characteristics that distinct perturbation modeling may introduce, case 1 is revisited using the different transport models for the perturbations. The basic state however, is the same for all cases, and is that of the most accurate CE transport model.

Figures 10.18 and 10.19 present the corresponding growth rates, N -factor envelopes, and neutral-stability curves. They suggest similar trends to those observed in § 10.1.1 with consistent sets of models. The BEW model predicts slightly larger growth rates than the other models, however there is no change in the frequency at which the maximum growth rate appears. The influence of the modeling on the perturbations however, is much smaller than on the basic state, reinforcing the idea that the major source of discrepancy when using different models (consistently) is the variation it may introduce in the boundary-layer size. These trends are equally observable in the N -factor curves and the neutral stability curves in Fig. 10.19, with only a 3.4% advancement of the predicted transition onset location when using the BEW model for the perturbations with respect to the others. Repeating the same analyses of § 10.1.2-10.1.5 but with an unchanged basic-state flowfields provides analogous trends to those in Fig. 10.18.

10.1.7 Mode shapes

Figure 10.20 presents the second-mode perturbation amplitude shapes for the various model comparisons performed, normalized with respect to the maximum value of the velocity perturbation amplitude. The conditions are reported in Table 10.2. Aside from the logical scaling of the instabilities attending to the size of the boundary layer, none of the models differences seem to predict strong modifications of the mode shapes.

10.1.8 Conclusions

A thorough analysis was carried out to quantify how inaccuracies due to the different thermophysical models previously used by authors in the community (seen in chapter 4), affect the laminar base flow and the second-mode stability and

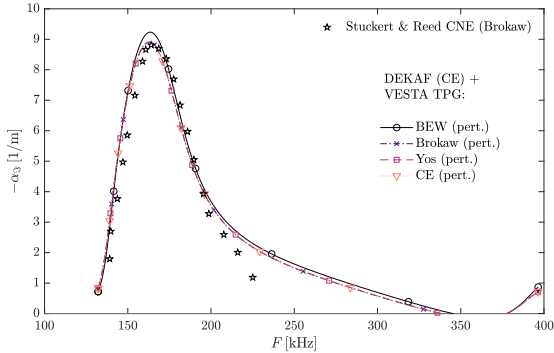


Figure 10.18: Second-mode perturbation growth rates at $x = 0.4\text{ m}$ employing the various transport models on the perturbation terms on case I from Table 10.1. The basic-state flowfield for all cases uses the CE model.

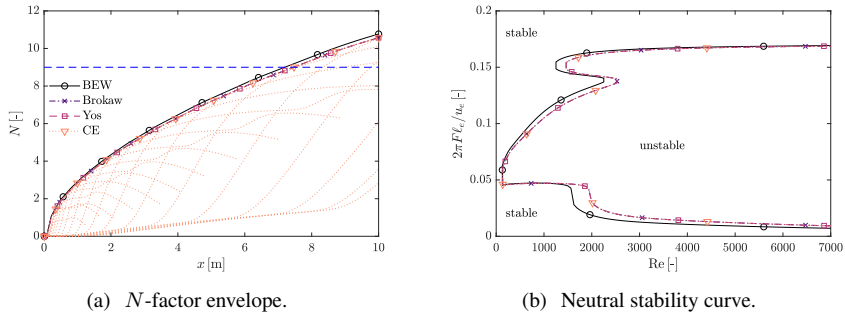


Figure 10.19: Case I from Table 10.1 employing the various transport models on the perturbation terms. The basic-state flowfield for all cases uses the CE model.

Case	$F [\text{kHz}]$	$x [\text{m}]$	$\ell_e [\text{m}]$
1	162.71	0.4	$2.016 \cdot 10^{-4}$
2	201.75	0.4	$3.956 \cdot 10^{-4}$
3	100	3.65	$1.058 \cdot 10^{-3}$
4	196.35	0.6	$3.015 \cdot 10^{-3}$

Table 10.2: Summary of the conditions under which the second-mode perturbation shapes in Fig. 10.20 are obtained.

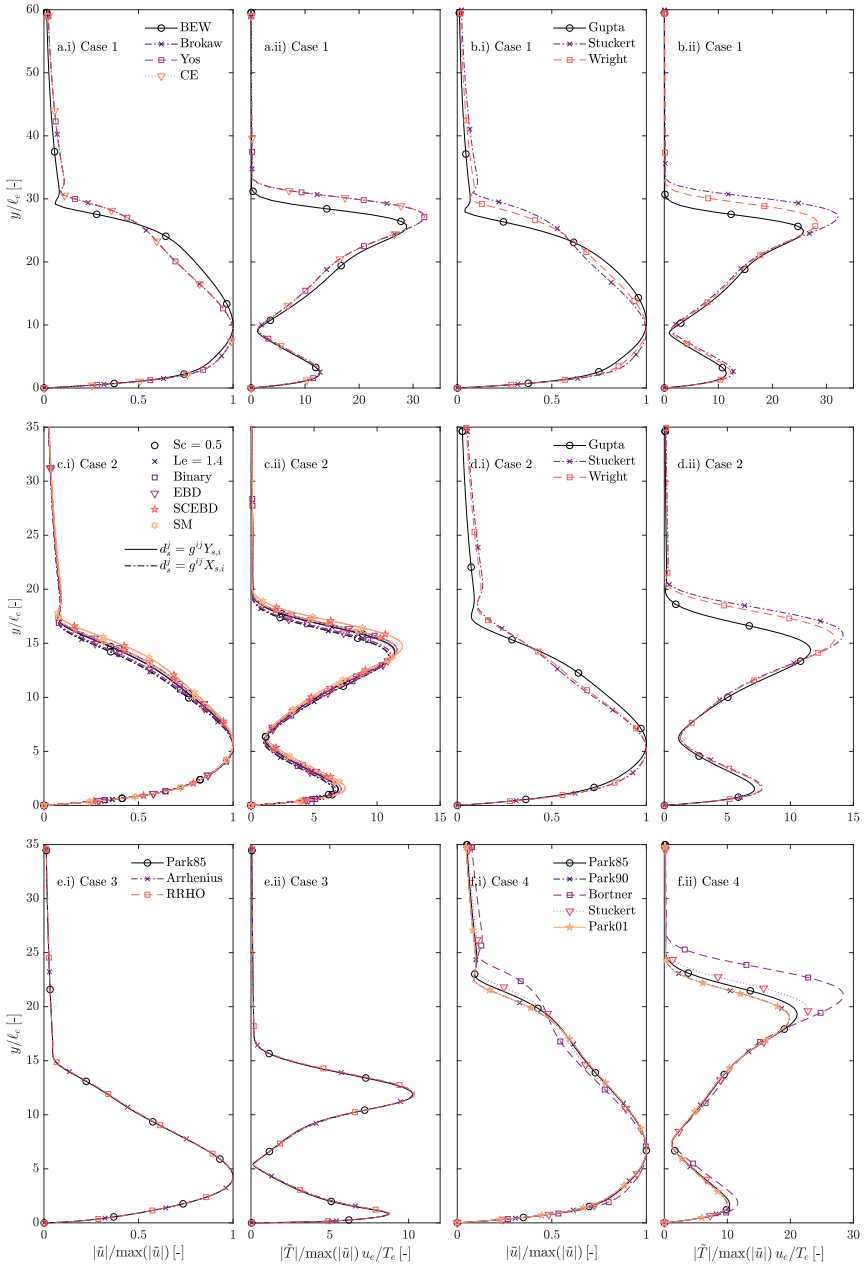


Figure 10.20: Second-mode streamwise velocity (i) and temperature (ii) perturbation amplitude shapes for the various model comparisons: (a) transport (see § 10.1.1), (c) diffusion (see § 10.1.2), (b) and (d) collisional (see § 10.1.3), (e) equilibrium (see § 10.1.4) and (f) chemical kinetics (see § 10.1.5). Conditions are summarized in Table 10.2.

transition-onset estimations. To that end, a series of representative literature cases were revisited.

Stability and transition-onset-location estimations were seen to be most sensitive to the modeling of the transport properties. The use of the BEW transport model, which featured errors in the properties of approximately 10% with respect to the state-of-the-art CE model, lead to estimating the transition onset approximately 38% farther upstream than with the CE model. However, when using the same base flow and varying solely the modeling of the perturbation terms, the estimated transition-onset location was only approximately 3.4% sooner with the BEW model. This suggests that the modeling inaccuracies in the base flow are the ones driving the erroneous estimation. The usage of the BEW model for both base-flow and perturbation terms led to higher perturbation growth rates and a wider range of unstable frequencies, which was clearly observable in the comparison of the neutral stability curves. The adoption of the two other models (Brokaw and Yos') led to negligible differences with respect to the CE model for the considered air-5 mixture. One should however be cautious when extrapolating this observation to ionized mixtures. The properties computed with these two models for an air-11 mixture in § 4.2 featured large errors that would presumably translate into erroneous transition-onset-location estimations.

The use of Gupta *et al.*'s collection of collisional data was reported to under-predict the boundary-layer size and therefore overpredict the perturbation growth rates and N factors. This led to forecasting the transition-onset location to be approximately 8% farther downstream than using Wright *et al.*'s data, which were taken as the state of the art. The adoption of Stuckert's collection of collisional data was seen to return slightly overestimated boundary-layer sizes and underestimated growth rates. However, this led to practically negligible differences in the estimated transition-onset location. The neutral stability curves did display noticeable differences when computed with the different collisional models. These differences affected the high- and low-frequency regions, which feature small perturbation growth rates and consequently have a minor impact on the transition-onset estimations. However, in scenarios of low-frequency instability dominance (Mack's first mode) they may significantly alter the predictions.

The modeling of the diffusion fluxes and the chemical equilibrium constant were observed to have a very small impact on the expected transition-onset location (less than 5 and 2% respectively). The corresponding neutral stability curves were also very similar, with the diffusion models changing only slightly the high-frequency neutral branch. This conclusion must be cautiously extended to other situations, since mixtures featuring gases with dissimilar molar weights will have thermodynamic and transport properties strongly depending on the species concentration. This implies that the diffusion fluxes would have a large impact on these properties, and would therefore significantly condition the predictions. Similarly,

using some of the chemical equilibrium models out of their range of applicability could lead to major inaccuracies – Park’s [33] polynomial expressions were seen in § 4.3 to be largely inaccurate for temperatures below 1000K.

The five investigated sources of chemical-reaction-rate constants returned significant differences in the boundary-layer profiles and perturbation growth rates. However, these did not translate to differences in the estimated transition-onset locations, which varied less than 1%. This is due to the fact that at the streamwise positions where perturbations have reached sufficiently large amplitudes, the flow is close to equilibrium and thus independent from the reaction rates. The corresponding neutral-stability curves displayed similar unstable second-mode regions, but differences in the low- and high-frequency predictions. This variability should be further investigated to determine whether or not it affects the predicted first-mode development.

The features and inaccuracies reported in the present section may be very strongly linked to the test conditions, particularly to temperature. Caution should be taken when extending them to other scenarios. Nevertheless, the current analysis may provide a useful assessment of the error associated to a specific model in other conditions: it suffices to compare the model error at the temperature range of interest (chapter 4) against that found at the temperature range considered in the current study, and to then estimate the performance of interest from the corresponding stability and transition estimations made in this section.

The stability predictions were consistently highly dependent on the boundary-layer size: this was a common trend throughout all of the various analyses, and can be likely extrapolated to other second-mode stability analyses. In general, the models that lead to the largest discrepancies in the forecasted second-mode characteristics also predicted strong differences in the boundary-layer height. Such observations are consistent with the nature of second-mode instabilities – acoustic waves confined to the boundary layer and therefore conditioned by its dimensions. This implies that, to improve the accuracy of future second-mode development predictions, the aerospace community ought to value efforts to more accurately characterize and model the properties strongly governing the boundary-layer size.

10.2 Enhanced and weakened diffusion fluxes

A parametric study is carried out to investigate if the low dependency of the stability growth rates on the diffusion fluxes (§ 10.1.2) is also observed for extremely enhanced or weakend values of these fluxes. The case analyzed was previously investigated by Perraud & Arnal [35], and the conditions are summarized in Table 10.3. The test gas is air, which is modeled with the air-5-Park01 mixture (§ J.9). The

$M_e [-]$	$T_e [K]$	wall	$Re_{1,e} [1/m]$	$x [m]$	$\bar{Y}_{N_2,w} [-]$	$\bar{Y}_{O_2,w} [-]$
10	350	adiab.	$6.6 \cdot 10^6$	0.6	0.78	0.22

Table 10.3: Test conditions for the investigation on the effect of diffusion on stability.

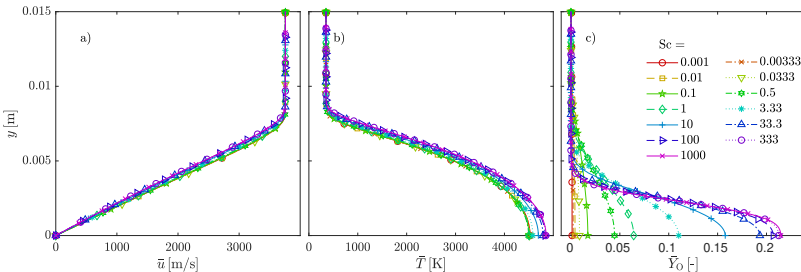


Figure 10.21: Boundary-layer base-flow profiles varying the Schmidt number. Test conditions summarized in Table 10.3.

gas properties are obtained from assuming the BEW transport model^e (§ 4.2.1.1), the RRHO thermal model (§ 4.1 and Eq. 4.66), and the constant-Schmidt-number diffusion model (Eq. 4.39). The analysis is restricted to second-mode instabilities, featuring a $\beta = 0$, and it employs the Chebyshev pseudo-spectral collocation method.

Assuming a constant Schmidt notably leads to inaccurate diffusion fluxes (see Fig. 4.2). However, it allows to reduce all diffusion effects to a single non-dimensional parameter, thus simplifying the analysis. The Schmidt number is a measure of the relative importance of the viscous versus the molecular diffusion (Eq. 8.6c). Large Schmidt numbers are associated with flows with little diffusion due to the gradients in the molar fractions, where it is all driven by viscous shear instead. On the other hand, a very low Schmidt number is associated to flows where the relative movement of the different species is mainly driven by the gradients in their molar fractions. Flows with high Schmidt numbers will therefore feature larger concentration gradients.

Figure 10.21 presents the laminar base-flow profiles for the aforementioned conditions, displaying the commented larger O gradients for higher Schmidt numbers (Fig. 10.21c). Similar curve shapes are observed for the other species. Figures 10.21a and b, also show that larger gradients in the concentrations lead to a slight wall heating, which also causes the boundary-layer thickness to increase.

Regarding the stability behavior of the different cases, Fig. 10.22a shows only minor differences in the growth rate of the most unstable eigenmode, which does

^eThe analysis in § 10.1.1 notably showed the inaccuracy of the BEW model. However, it is nonetheless employed due to its simplicity, and because the focus of this section is not on the transport properties, but rather on the effect of the diffusion fluxes.

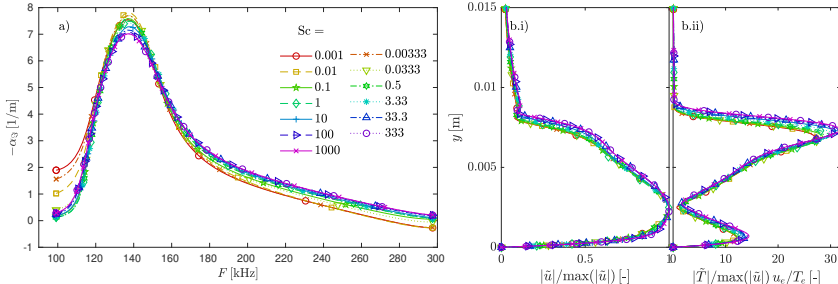


Figure 10.22: Growth rate of the most unstable mode varying the Schmidt number. Test conditions summarized in Table 10.3.

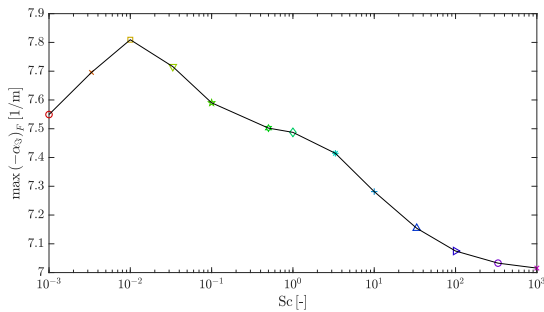


Figure 10.23: Maximum perturbation growth rate as a function of the Schmidt number. Test conditions summarized in Table 10.3.

not vary more than $\pm 10\%$ with respect to the reference $\text{Sc} = 0.5$ case [22]. There seems however to be a trend in the maximum amplification rate that is disproportional with the Schmidt number.

Figure 10.22b compares the shapes of the velocity and temperature perturbation amplitudes for the most unstable frequency. The Schmidt number seems to have practically no effect on this, since all the curve shapes are nearly coinciding.

Reworking the data in Fig. 10.22, it is possible to obtain the evolution of the maximum amplification rate as a function of the Schmidt number, as presented in Fig. 10.23. The most unstable flows, appear to be those for which the Schmidt number is of order 0.01. In other words, the second Mack mode is most unstable when the rate of diffusion due to viscous stresses is 100 times slower than that caused by gradients in the concentrations.

Varying the Schmidt number also has an interesting effect on the spectrum (Fig. 10.24). The vertical continuous branches seem to slant towards larger α_{\Re} for increasing Schmidt numbers. In the extreme, for $\text{Sc} = 1000$, they become prac-

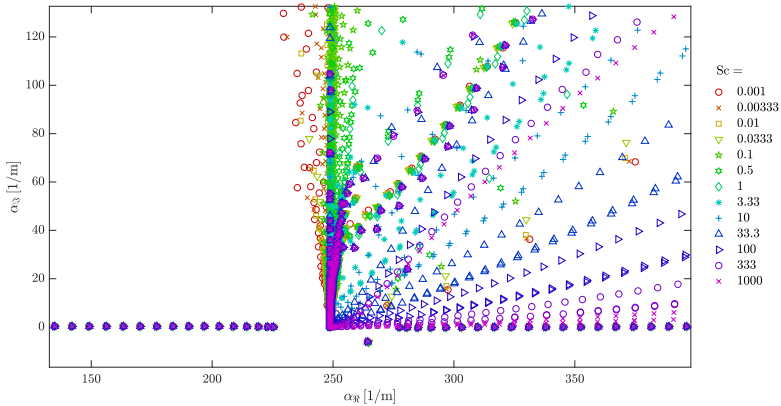


Figure 10.24: Evolution of the stability spectrum for a perturbation frequency of 148.74 kHz varying the Schmidt number. Test conditions summarized in Table 10.3.

$M_\infty [-]$	Altitude [km]	$T_\infty [\text{K}]$	$p_\infty [\text{Pa}]$	$\bar{T}_w [\text{K}]$
25	46.509	269.3	118.0	1400
20	46.565	269.4	117.2	
15	45.904	267.6	127.5	
10	42.327	257.6	203.0	
8	37.567	244.2	388.2	
6	31.655	228.3	914.0	

Table 10.4: Test matrix for the flow-assumption-adequacy study.

tically horizontal, and additional continuous branches separate from the vertical. Further investigation is required in order to determine if this behavior is due to a particular feature of the diffusion mechanisms, or if it is a numerical artifact.

10.3 Flow-assumption adequacy for different earth entry flow regimes

At different points in an atmospheric entry trajectory (see Fig. 1.1) the high-temperature phenomena described in § 2.1 have variable levels of importance. It is therefore very useful to know under what circumstances one can or cannot adopt a more restrictive set of hypotheses, simplifying the problem, and reducing the computational requirements.

To that end, six characteristic flight-envelope points from Fig. 1.1 are investigated. These points, together with the corresponding free-stream static tempera-

ture and pressure^f are summarized in Table 10.4. The assumed free-stream composition is 23.3% O₂ and 76.7% N₂ in mass, and the geometry under consideration is 10-degree wedge of length $L = 5$ m. The wall is assumed to be isothermal for all cases with $T_w = 1400$ K, which is a typical decomposition temperature for ablative TPS [36]. Six different flow assumptions are employed:

1. **CPGS:** CPG with Sutherland's transport law (Eq. 4.2) and a constant Prandtl number (Eq. 4.5).
2. **CPGCE:** CPG with CE transport model (§ 4.2.1.4).
3. **TPG:** frozen TPG with constant composition.
4. **CNETPG:** CNE base flow with TPG perturbations ($J'_s = 0$ and $\dot{\omega}'_s = 0$).
5. **CNE:** five-species CNE.
6. **LTE:** five-species LTE.

The CPGS assumption employs the gas constants in Table 5.2, whilst the CPGCE only assumes the same heat capacity as the CPGS one: 1004.5 J/kg-K. All flow assumptions other than CPGS feature state-of-the-art models: the CE transport model (§ 4.2.1.4), the SM diffusion model (Eq. 4.41), collisional cross sections approximated from the polynomial-bilogarithmic fits (Eq. 4.57) to Wright *et al.*'s [32] data, a RRHO thermal model (§ 4.1 and Eq. 4.66), and reaction-rate constants corresponding to the air-5-Park01 mixture (§ J.9).^g All flow assumptions feature a single temperature to describe the thermodynamic state of the gas.

10.3.1 Laminar base-flow field

The laminar base-flow field is obtained with the DEKAF flow solver (see chapter 7). The boundary-layer profiles at $x = 2.5$ m are displayed in Fig. 10.25. One can clearly observe how at earlier envelope points in the considered earth entry trajectory (higher Mach number), phenomena like vibrational excitation or molecular dissociation are more significant than in the later points. The importance of vibrational excitation is visible from the discrepancy between the CPGCE and the TPG profiles, whilst that of dissociation transcends from the difference between the TPG profiles and the CNE and LTE ones. For the three last envelope points (Figs. 10.25d-f), dissociation appears to have a minor importance, reaching a concentration of less than 0.1% of atomic oxygen even in LTE conditions. The same extends to the third envelope point (Fig. 10.25c) in CNE conditions. At the first

^fISA pressure and temperature values.

^gSome of these models are obviously not necessary for certain flow assumptions – see § 2.3.

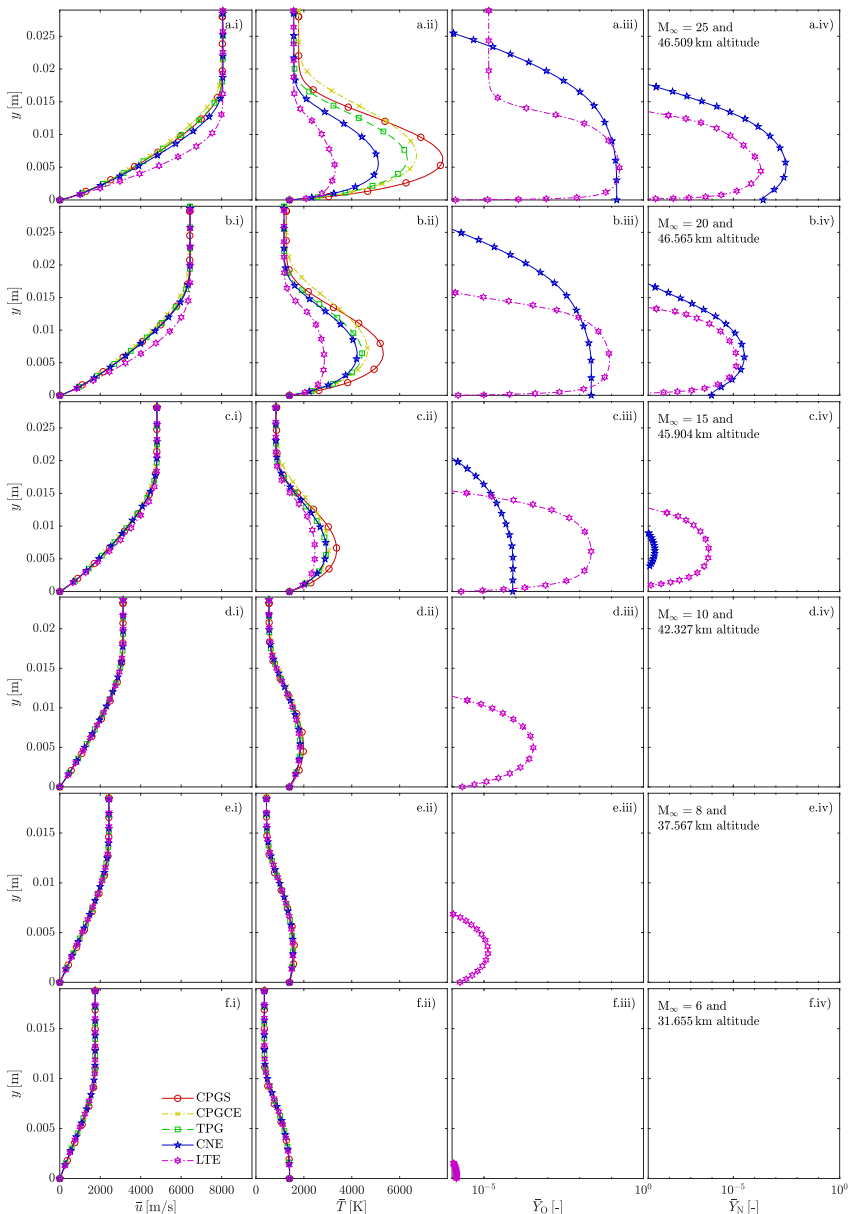


Figure 10.25: Laminar base-flow profiles at $x = 2.5$ m for the cases in Table 10.4 and for various flow assumptions.

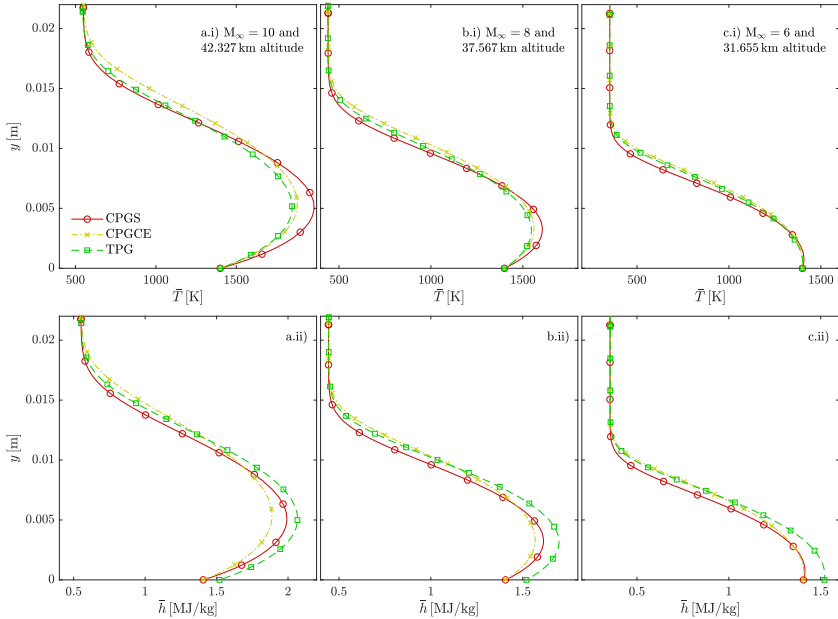


Figure 10.26: Zoom-in of the laminar base-flow profiles at $x = 2.5$ m for the three last cases in Table 10.4 and for various flow assumptions.

point however (Fig. 10.25a), the mass fraction of dissociated oxygen reaches levels of around 10%, whilst that of dissociated nitrogen stays between 0.01 and 1% depending on whether one assumes equilibrium or non-equilibrium.

A stronger chemical activity is associated in all cases with a colder and smaller boundary-layer – for a given flight-envelope point, the BL height and temperature predicted with LTE is always lower than that with CNE, which is likewise lower than that with TPG. Similarly, vibrational excitation also contributes to cool the boundary layer and reduce its size, as visible from the comparison between the TPG and CPGCE curves.

Despite the CPGS and CPGCE flow assumptions having the same thermal model, the use of Sutherland's viscosity law in CPGS predicts overly hot boundary layers, with respect to the more-accurate CE transport model (CPGCE) in Figs. 10.25a-c. The three later flight-envelope points (Figs. 10.25d-f) appear to display a lower sensitivity to the transport model in CPG. However, a closer examination in Fig. 10.26, shows that the same mentioned effects are also observable. Fig. 10.26a-c.ii also displays differences between the TPG and CPGCE enthalpy predictions, suggesting that vibrational excitation has a non-negligible effect, also for the latest flight-envelope points.

Taking a $\text{Pr} = 0.7$ is therefore clearly not recommendable for high-temperature

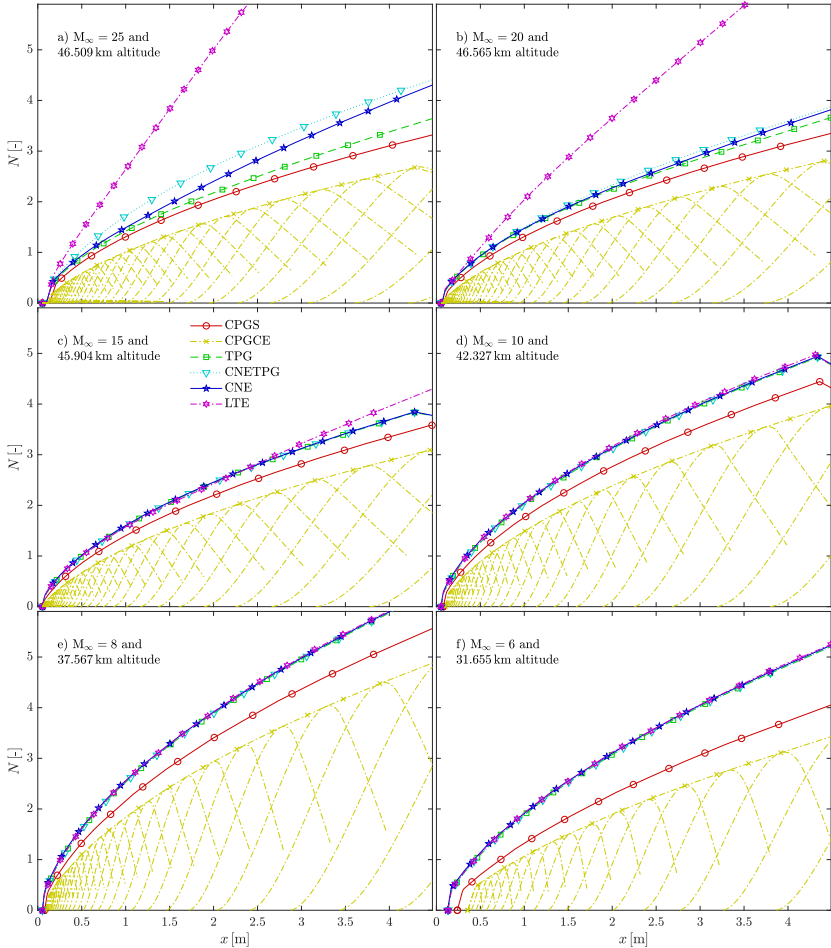


Figure 10.27: LST N -factor envelopes for the cases in Table 10.4 and for various flow assumptions. Single-frequency N curves also included for the CPGCE flow assumption.

scenarios. An interesting feature of the predictions made with Sutherland's law, however, is that, for hotter boundary layers (Figs. 10.25a-c), they feature a boundary-layer size closer to that of the more physically-inclusive assumptions (LTE, CNE, or TPG). Given the importance of the boundary-layer size on the predicted behavior of second-mode instabilities (see § 10.1), this feature could strongly affect the following stability analysis.

10.3.2 LST N -factor curves

LST analyses are performed with the VESTA toolkit [37, 38], exploiting the extended ADIT capabilities (see chapter 8). The wall-normal domain is discretized using the FDq-8 method with 300 points distributed with Malik's mapping [39]. The wall boundary conditions on the perturbation quantities are homogeneous ($\tilde{q}_w = 0$) for \tilde{u} , \tilde{v} , \tilde{w} , and \tilde{T} , and compatibility conditions for either the pressure \tilde{p} (Eq. 2.7b), or the species partial densities $\tilde{\rho}_s$ (Eq. 6.26). In the freestream, Neumann conditions are imposed on all perturbation quantities (Eq. 6.28).

The LST N -factor envelopes corresponding to the base flows presented in Fig. 10.25 and 10.26 are presented in Fig. 10.27, together with single-frequency N curves of the CPGCE cases, for purely illustrative purposes. The stronger chemical activity consequence of assuming LTE conditions in the three first trajectory points is seen to destabilize the flow and lead to larger N factors in Figs. 10.27a-c. As discussed in Ref. 40, this is a consequence of the existence of supersonic unstable modes (see § 3.6) under such circumstances. These modes are fed energy from the continuous branch of the instability spectrum and remain unstable for a longer x range.

The CNE and CNETPG assumptions are seen to return almost identical N -factor envelopes, except for the first flight-envelope point (Fig. 10.27a). This is yet another example showing that the most significant effect of chemical activity is its modification of the laminar base flow. For the case where CNE and CNETPG assumptions do predict different N factors, one sees that the chemically-induced base-flow cooling destabilizes and increases the N factors. This is clearly visible from the difference between the CNETPG and the TPG predictions, which differ only on the base-flow solution. The additional consideration of non-zero diffusion-flux and source-term perturbations (J'_s and $\dot{\omega}'_s$) subsequently stabilizes and decreases the N factors, explaining the difference between the CNE and TPG predictions. This effect is analyzed more in depth in § 10.4.

As one could predict from the base-flow profiles in Figs. 10.25d-f, the lack of chemical activity in the last three flight-envelope points leads to very close N -factor curves in Figs. 10.27d-f.

Vibrational excitation is seen to be significant in all 6 flight-envelope points. The predictions done considering it (TPG) strongly differ with those without it under equivalent transport models (CPGCE). Such a trend could be expected from the base-flow profiles reported in Figs. 10.25 and 10.26.

The relative contribution of the various physical phenomena to the N factor are quantified by comparing the values obtained with the various flow assumptions at $x = 4$ m. The results are displayed in Fig. 10.28, which constitutes a good visual summary of the various trends previously commented.

The choice of the transport model in CPG conditions is seen to largely condition the predictions. The CPGS assumption predicts higher N factors than the

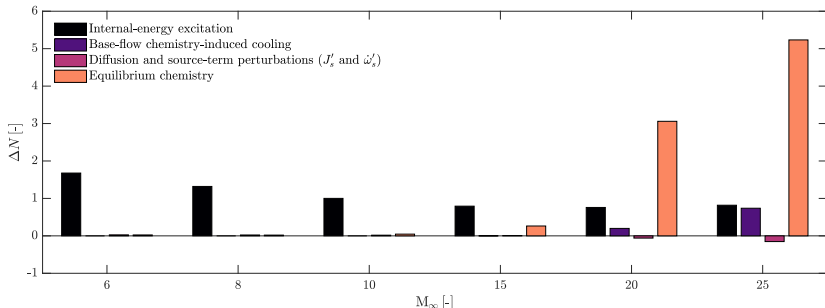


Figure 10.28: Variation in the maximum N factor at $x = 4\text{ m}$ due to the various physical phenomena, for the cases in Table 10.4.

CPGCE, and therefore appears to give a better estimation (closer to that predicted under TPG conditions). However, what is actually occurring is that two modeling inaccuracies – that of the transport and that of the thermal assumption, happen to cancel each other out.

10.3.3 LPSE N -factor curves

In order to evaluate the importance of weak non-parallel effects, a similar analysis is conducted using LPSE instead of LST [40]. The corresponding LPSE N -factor envelopes for a more restricted range of frequencies, kindly provided by Ludovico Zanus, are presented in Fig. 10.29. One can see how the same trends observed with LST in Fig. 10.27 are also present, suggesting that the coupling of non-parallelism with vibrational excitation and molecular dissociation do not modify the underlying mechanisms.

10.3.4 Conclusions

A study was carried out on the adequacy of the various flow assumptions at different points within a typical atmospheric reentry trajectory. The CPG flow assumption was observed to be inadequate, even for the latest point in the flight envelope (Mach 6 and 31.655 km altitude). The use of Sutherland's law rather than the CE transport model (better suited for high temperatures) appeared to lead to better N -factor predictions. However, the observed correlation lacks the necessary causality, since it is the consequence of a casual cancellation of the inaccuracies of the transport and the thermal modeling.

The TPG flow assumption was seen to provide a very good estimation for most flight-envelope points, being only slightly inaccurate for the earliest and fastest (Mach 25 at 46.509 km altitude). This observation, together with the inaccurate predictions associated to the LTE assumption (featuring instantaneous equilibrium

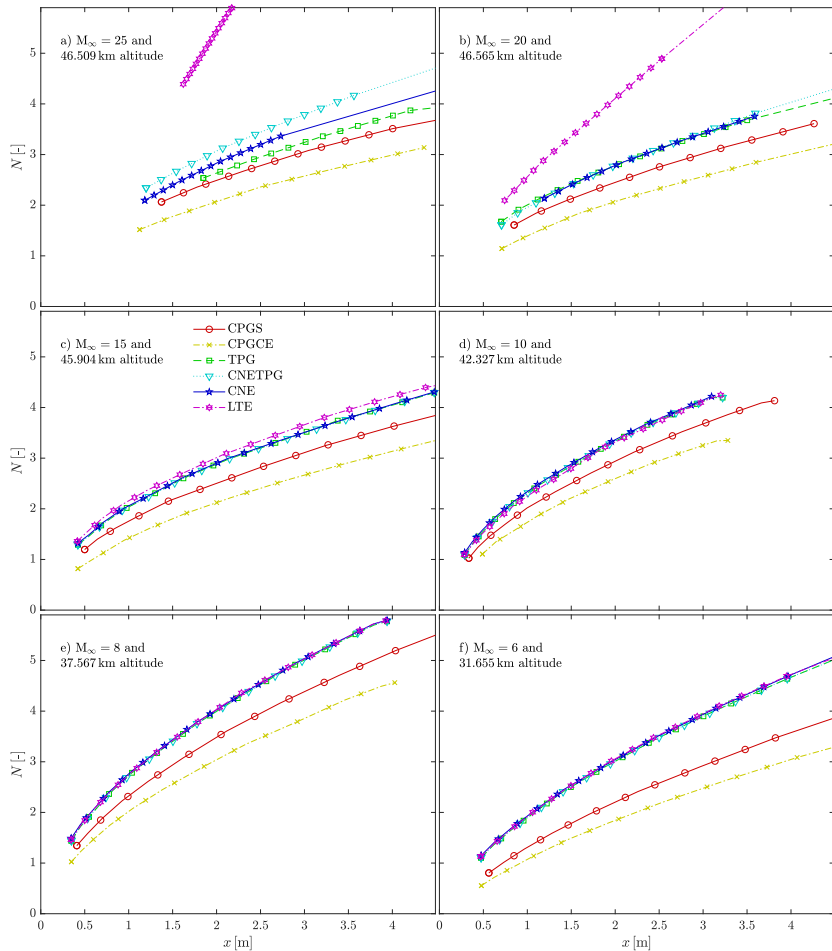


Figure 10.29: LPSE N-factor envelopes for the cases in Table 10.4 and for various flow assumptions.

M_∞ [-]	Altitude [km]	T_∞ [K]	p_∞ [Pa]	\bar{T}_w [K]
45	45	265	143	10000
37.5				7500
30				5000

Table 10.5: Test matrix for the ionization-effect study.

chemistry), suggest that the finite rate at which reactions occur in the considered cases is actually closer to frozen conditions than it is to equilibrium.

The use of the CNETPG assumption lead to very close estimations to those done in CNE conditions. This suggests that the most important chemistry-related effect is the modification of the laminar base flow.

10.4 Ionization and dissociation

The previous sections investigated chemical effects as those arising from the dissociation of molecular species. However, at higher gas temperatures the dissociated atomic species eventually reach sufficiently highly excited electronic states so as to ionize (see Fig. 2.1). This results in a partially ionized plasma, containing neutral species, ions and electrons. The appearance of ions has a dramatic effect on the mixture's viscosity, which drops due to the lower momentum that is exchanged between colliding ion species. This drop in viscosity is clearly visible in Fig. 7.20c.ii. Viscosity is known to have a strong impact on the evolution of the second Mack mode (see Mack [17] or § 10.1.1), and thus a partially ionized mixture is likely to have very different stability features from a non-ionized one.

This section investigates the effects of ionization by reproducing three flight-envelope points on a Martian return mission (see Fig. 1.1), presented in Table 10.5^h. The test gas is air in all cases, with a free-stream composition of 23.3% O₂ and 76.7% N₂ in mass. The considered geometry is the same as in § 10.3 – a 10-degree wedge of length $L = 5$ m. The high wall temperatures (see Table 10.5) are clearly beyond what can be sustained by any existing TPS material. The present analysis must therefore be taken as an extreme case, pursued with the goal of understanding the underlying physics in ionized boundary layers, rather than accurately reproducing an actual engineering problem.

In order to isolate the various coexisting phenomena in an environment at such a high-temperature, a similar yet more thorough flow-assumption division to that considered in § 10.3 is adopted:

1. **CPGS:** CPG with Sutherland's transport law (Eq. 4.2) and a constant Prandtl number (Eq. 4.5).

^hISA pressure and temperature values.

2. **CPGCE**: CPG with CE transport model (§ 4.2.1.4).
3. **TPG**: frozen TPG with constant composition.
4. **CNETPG5**: CNE five-species base flow with frozen, non-diffusing TPG perturbations ($J'_s = 0$ and $\dot{\omega}'_s = 0$).
5. **CNEfroz5**: CNE five-species base flow with frozen perturbations ($\dot{\omega}'_s = 0$).
6. **CNE5**: five-species CNE.
7. **LTECNE5**: five-species LTE base flow, with CNE perturbations.
8. **LTE5**: five-species LTE.
9. **CNETPG11**: CNE eleven-species base flow with frozen, non-diffusing TPG perturbations ($J'_s = 0$ and $\dot{\omega}'_s = 0$).
10. **CNEfroz11**: CNE eleven-species base flow with frozen perturbations ($\dot{\omega}'_s = 0$).
11. **CNEnoIon11**: CNE eleven-species base flow with frozen ionization source-term perturbations ($\dot{\omega}'_{\text{Ion } s} = 0$).
12. **CNE11**: eleven-species CNE.
13. **LTECNE11**: eleven-species LTE base flow, with CNE perturbations.
14. **LTE11**: eleven-species LTE.

The implications of and hypotheses made by the various flow assumptions can be found in chapter 2. Additionally, those assumptions with ionizable (eleven-species) mixtures take the local charge of the flow to be neutral, meaning that:

$$\sum_{s \in S} Z_s X_s = 0. \quad (10.1)$$

where Z_s is the unitary charge and X_s is the mole fraction of each species. Five-species assumptions consider air as a dilute mixture of N, O, NO, N_2 , and O_2 , whilst eleven-species ones incorporate their ion counter parts (N^+ , O^+ , NO^+ , N_2^+ , and O_2^+) and electrons (e^-).

Regarding the thermophysical modeling, the treatment is analogous to that of the previous section (§ 10.3). The CPGS assumption employs the gas constants in Table 5.2, whilst the CPGCE only assumes the same heat capacity as the CPGS one: 1004.5 J/kg-K. All flow assumptions other than CPGS feature state-of-the-art models: the CE transport model (§ 4.2.1.4) with the second approximation to the electron thermal conductivity (Eq. 4.32a), the SCEBAD diffusion

model (Eq. 4.47), collisional cross sections approximated from the polynomial-bilogarithmic fits (Eq. 4.57) to state-of-the-art data [32, 41, 42], a RRHO thermal model (§ 4.1 and Eq. 4.66), and reaction-rate constants corresponding to the air-5-Park01 (§ J.9) or the air-11-Park93 mixture (§ J.12). All flow assumptions feature a single temperature to describe the thermodynamic state of the gas.

The work laid out in this section is an extension of that presented by the author in Ref. 43. It must be noted, that the CNE11 growth rates here differ from those of Ref. 43, which were discovered to be incorrect after the publication of the article.

10.4.1 Laminar base flow

The laminar base-flow field is obtained using the DEKAF solver (see chapter 7). The inviscid flow region is therefore characterized by solving the corresponding shock-jump relation for each flow assumption (see § 7.1), and then employing a one-dimensional Euler solver (see § 7.2) for the CNE cases. This approach notably neglects the shock curving induced by the inviscid chemistry [44, § 15.3]. The values of the different flow-field quantities at the inviscid wall are then used as the free-stream boundary condition for boundary-layer computations, in what is effectively a zeroth-order coupling of the inviscid and viscous regions [45].

The boundary-layer edge (or inviscid-wall) profiles for the first flight-envelope point (see Table 10.5) are displayed in Fig. 10.30. One can clearly see effects of the chemical activity in the inviscid flow region, which progressively dissociates O₂ advancing downstream (Fig. 10.30e), and consequently reduces pressure (d) and temperature (c) and accelerates the flow (b). The result is an increase in the edge Mach number (a), which is computed based on the frozen speed of sound (Eq. 7.7). An interesting feature of Fig. 10.30d is the fact that the non-equilibrium edge pressure undershoots that of the equilibrium case. This artifact is a consequence of neglecting the curvature of the shock due to the chemical activity. In reality, this curving brings the shock closer to the surface, and increases the pressure, therefore avoiding the undershooting. However, the objective of the study is to investigate the implications of ionization as a phenomenon on instability development, rather than truthfully reproducing an engineering problem. The mentioned modeling inaccuracies are therefore accepted, since they do not conflict with such objective.

The other two flight-envelope points ($M_\infty = 37.5$ and $M_\infty = 30$ in Table 10.5) present practically no finite-rate chemical activity in the inviscid flow region. The post-shock (or boundary-layer-edge) values of the quantities of interest are therefore constant in the CNE base flows. The edge values for these two flight-envelope points and all flow assumptions are reported in Table 10.6.

It is also important to note, that the test cases feature shocks that are very close to the surface. This is due to the high free-stream Mach numbers under

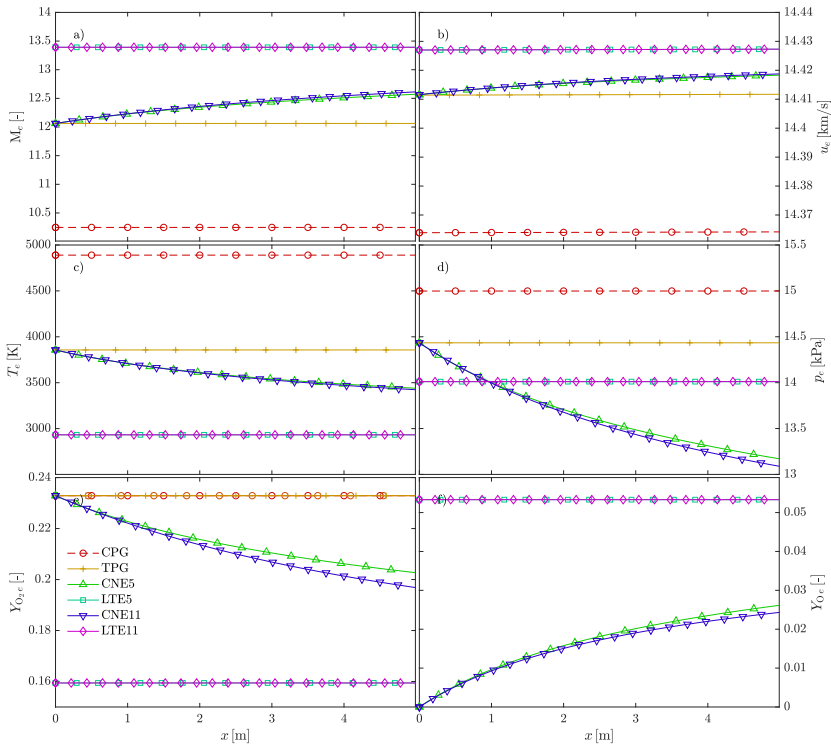


Figure 10.30: Evolution of the boundary-layer edge (or inviscid-wall) profiles for the first flight-envelope point ($M_\infty = 45$) in Table 10.5 and for various flow assumptions.

$M_\infty = 37.5$	$M_e [-]$	$u_e [\text{km/s}]$	$T_e [\text{K}]$	$p_e [\text{kPa}]$	$Y_{\text{O}_2 e} [-]$
CPG	10.09	11.97	3503	10.51	0.233
TPG and CNE	11.63	12.01	2863	10.16	0.233
LTE	12.20	12.01	2555	10.01	0.205

$M_\infty = 30$	$M_e [-]$	$u_e [\text{km/s}]$	$T_e [\text{K}]$	$p_e [\text{kPa}]$	$Y_{\text{O}_2 e} [-]$
CPG	9.81	9.57	2368	6.84	0.233
TPG and CNE	11.01	9.60	2028	6.65	0.233
LTE	11.10	9.60	1993	6.63	0.228

Table 10.6: Post-shock (or boundary-layer-edge) values of the different base-flow quantities of interest for the second and third flight-envelope points in Table 10.5.

$\theta_{\text{sh}} [\text{deg}]$	$M_\infty = 45$	$M_\infty = 37.5$	$M_\infty = 30$
CPG	2.173	2.233	2.342
TPG and CNE	1.712	1.823	2.003
LTE	1.363	1.648	1.970

Table 10.7: Relative shock angle (in degrees) with respect to the 10-degree wedge's surface for the flight-envelope points in Table 10.5 and for the various flow assumptions.

consideration. The corresponding shock angles, relative to the surface of the 10-degree wedge are laid out in Table 10.7.

The boundary-layer profiles at $x = 1 \text{ m}$, corresponding to the aforementioned edge conditions, and with the thermal wall boundary conditions in Table 10.5 are presented in Fig. 10.31. The different levels of flow ionization are clearly visible from the electron mole-concentration profiles (Figs. 10.31#.iv). For the first-flight envelope point, both the LTE11 and CNE11 assumptions predict a maximum ionization of about 10%, which goes down to about 1% for the second and between 0.01 and 0.1% for the third. Aside from ionized, the test gas is also clearly dissociated. Molecular nitrogen is completely dissociated into N close to the wall for the first and second flight-envelope point (Fig. 10.31a-b.iii), whilst approximately half of it ($\bar{X}_N \approx 0.3$) is for the third point (Fig. 10.31c.iii).

As a consequence of the commented ionization levels for the $M_\infty = 45$ case, the temperature profiles for the chemically-reacting flow assumptions that account for ionization (CNE11 and LTE11) differ significantly from those that do not (CNE5 and LTE5). Ionization induces a cooling of the boundary layer, which is clearly visible in Fig. 10.31b.ii. The levels of ionization in the two other flight-envelope points are not sufficient to cause major differences between the five- and the eleven-species temperature predictions (with and without ionization) – the CNE5 and LTE5 temperature profiles in Fig. 10.31b-c.ii are respectively coinciding with the CNE11 and LTE11 profiles.

Neglecting all chemical activity (as done by the CPGS, CPGCE and TPG as-

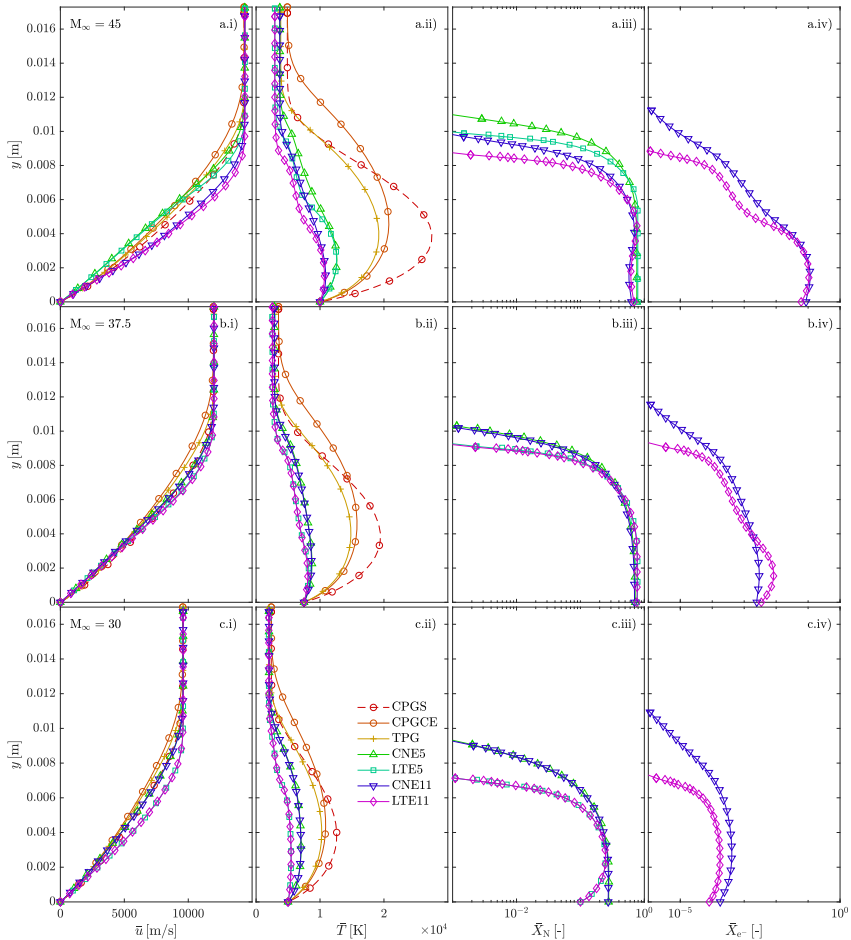


Figure 10.31: Boundary-layer profiles at $x = 1$ m for the flight-envelope points in Table 10.5 and for various flow assumptions.

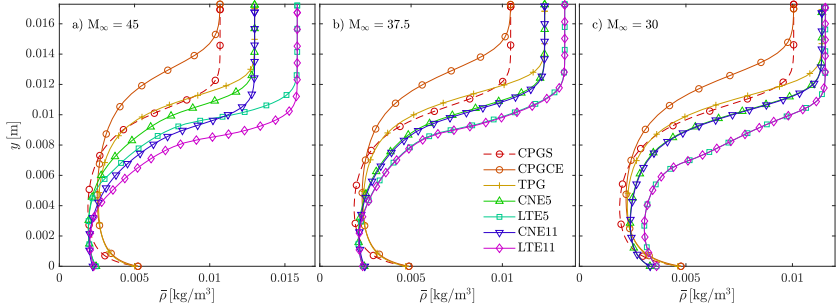


Figure 10.32: Boundary-layer density profiles at $x = 1$ m for the flight-envelope points in Table 10.5 and for various flow assumptions.

sumptions) leads to a clear overestimation of the boundary-layer temperature (see Figs. 10.31a-c.ii). This overestimation is more so when the excitation of internal energy modes is neglected (CPGS and CPGCE). The chemistry- and internal-energy-excitation-related cooling also leads to a decrease in the boundary-layer size.

The use of Sutherland's law with a constant $\text{Pr} = 0.7$, rather than the better-suited CE transport model, leads to a similar behavior to that reported in § 10.3. The CPGS assumption indeed predicts a hotter yet smaller boundary layer than the CPGCE one.

The LST analyses in the following subsection (§ 10.4.2) are focused on second-mode instabilities (see § 3.6). Following Kuehl's recently-formulated thermoacoustic interpretation of such waves [46], it is the density gradient acting as a thermoacoustic impedance close to the boundary layer edge (on the relative sonic line) that confines the instability. For that reason, it is meaningful to also compare the boundary-layer density profiles of the various cases, as done in Fig. 10.32. The smaller boundary layers predicted with the flow assumptions accounting for chemical activity and/or internal-energy excitation logically lead to stronger density gradients. Besides the boundary-layer size, the dissociation of molecules also contributes to increasing this gradient by reducing the value of the mixture density at the wall. The wall density is lowered as a consequence of the decrease of the mixture molar mass (see Eq. A.10) due to the larger mass fraction of lighter dissociated species. Similarly, the larger edge density predicted by the LTE assumptions also contributes to increasing the density gradient in the boundary layer. A stronger density gradient is believed to be associated to a stronger confinement and consequent destabilization of the second mode.

10.4.2 LST analyses

Stability studies are carried out using VESTA's [37, 38] LST solver, exploiting the extended ADIT capabilities (see chapter 8). The wall-normal domain is discretized using the FDq-8 method with 400 points distributed with Malik's mapping [39]. The wall boundary conditions on the perturbation quantities are homogeneous ($\tilde{q}_w = 0$) for \tilde{u} , \tilde{v} , \tilde{w} , and \tilde{T} , and compatibility conditions for either the pressure \tilde{p} (Eq. 2.7b), or the species partial densities $\tilde{\rho}_s$ (Eq. 6.26). In the freestream, the domain is extended vertically and a Dirichlet boundary condition is applied. This is done on all variables except for \tilde{v} , which is allowed to be different than zero in order to account for the finite size of the domain, therefore imposing the linearized continuity equation (Eq. 2.8).

10.4.2.1 Consistent base-flow and perturbation hypotheses

The first comparison features consistent hypotheses for the base-flow and the perturbation quantities. The transport model is also kept the same for all cases, thus reducing the list of flow assumptions presented at the beginning of the section to CPGCE, TPG, CNE5, LTE5, CNE11 and LTE11. The second-mode growth rates (i) and mode shapes (ii-iii) are displayed in Fig. 10.33a-c for the three flight-envelope points in Table 10.5.

All three growth-rate plots display the destabilizing nature of internal-energy-mode excitation – considered by the TPG but not by the CPGCE assumption. The differences in the corresponding density gradient in Fig. 10.32 (stronger for TPG than for CPGCE) suggest that the associated strengthening of the thermoacoustic impedance, and subsequent confinement of the second-mode waves may be the mechanism driving this destabilization. Another trait supporting this claim is the stronger temperature perturbation amplitude in Figs. 10.33#.iii that the TPG cases display with respect to the CPGCE.

Comparing the TPG predictions with those considering finite-rate chemistry (CNE5 and CNE11), the trends vary slightly depending on the flight-envelope point. For the first one (Fig. 10.33a) the differences between the TPG and CNE5 predictions suggest that dissociation is significantly destabilizing the boundary layer and increasing the range of unstable frequencies. This trend is reversed when also accounting for ionization, resulting in the differences that one can observe between the CNE5 and the CNE11 growth-rate curves. The other two flight-envelope points (Figs. 10.33b-c), which feature lower levels of ionization (see Fig. 10.31#.iv), do not display significant differences between the CNE5 and CNE11 growth rates. They are however distinct from the TPG predictions – displaying a slight stabilization and a shift of the most unstable mode to higher frequencies. An interesting difference observable between the TPG and CNE cases concerns the temperature perturbation amplitude (Fig. 10.33#.iii). The clearly

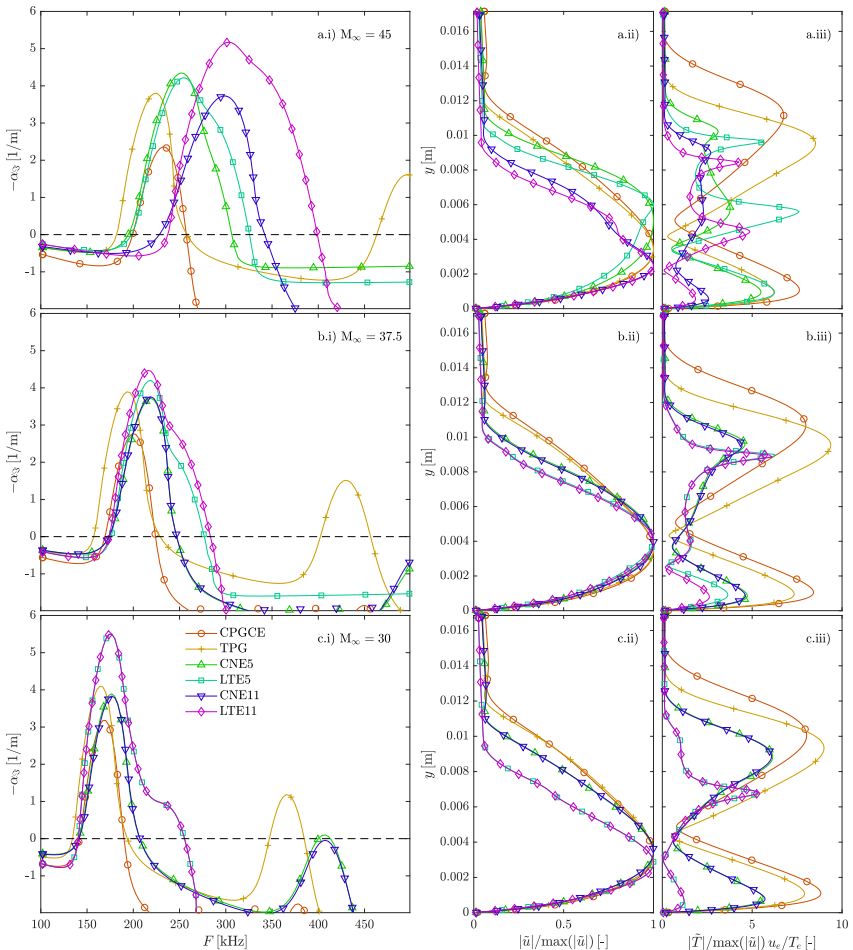


Figure 10.33: Second-mode perturbation growth rates (i) and the mode shapes for the most unstable frequency (ii-iii) at $x = 1 \text{ m}$ for the flight-envelope points in Table 10.5 and for various flow assumptions introduced at the beginning of § 10.4. All assumptions share the base-flow and perturbation hypotheses.

distinctive second peak that is visible for the CPGCE and TPG cases around $y \approx 0.01$ m is also found, yet with a smaller amplitude, for the CNE cases in the third flight-envelope point (Fig. 10.33c.iii). This peak in the CNE temperature perturbation, however, is further weakened for the second flight-envelope point (Fig. 10.33b.iii), and reaches unrecognizable levels in the first (Fig. 10.33a.iii). If the mentioned second temperature-perturbation peak is a consequence of the instability confinement infringed by the thermoacoustic impedance that is a density gradient, one would expect it to be larger for the chemically reacting assumptions, which displayed a stronger density gradient in Fig. 10.32. The fact that this is not the case, suggests that there is another physical mechanism affecting the development of second-mode instabilities in chemically-reacting boundary layers, beyond the confinement caused by the thermoacoustic impedance. This is further investigated in the following subsection (§ 10.4.2.2).

Fig. 10.33 also suggests that when the boundary layer reaches equilibrium conditions (LTE5 or LTET11 assumptions), it is significantly more unstable than under frozen (TPG) or finite-rate chemistry (CNE5 or CNE11). This trend was also observed in the flow-assumption-adequacy investigation carried out in § 10.3. Once again, the distinct levels of ionization featured at the three flight envelope points (see Fig. 10.31#.iv) explain why the LTE5 and LTE11 predictions coincide for the third flight-envelope point (Fig. 10.33c), differ slightly for the second (Fig. 10.33b), and present major differences for the first (Fig. 10.33a). It is also noteworthy that the damping of the second temperature-perturbation peak that the CNE assumptions predicted with respect to the TPG, is even stronger when assuming LTE. This suggests that it is most-likely related to the stronger chemical activity assumed in the LTE and CNE cases with respect to the TPG.

Instead of examining the stability characteristics of a single streamwise station, one can also integrate the growth rates of the various perturbation frequencies in the x direction, thus obtaining the N -factor curves. The envelopes of these curves for frequencies between 50 and 800 kHz are displayed in Fig. 10.34 for the three points of the flight envelope. Individual-frequency curves corresponding to the CPGCE assumption are also displayed for purely illustrative purposes. Fig. 10.34 displays the logical consequences of the trends observed and commented for Fig. 10.33#.i. An interesting additional behavior that one can identify in Fig. 10.34b is the evolution of the CNE envelopes, that coincide with the TPG one close to the leading edge, and eventually depart from it (at around $x = 2$ m). This is most-likely a consequence of the increasing modification of the flow due to finite-rate chemistry while advancing downstream.

In order to offer a better visualization of the mentioned trends, one can quantify the contribution of the various physical phenomena to the ultimate N factor at a given streamwise location. This is done at $x = 4$ m, by computing the increase in N factor when using successively more physically-inclusive assumptions. The re-

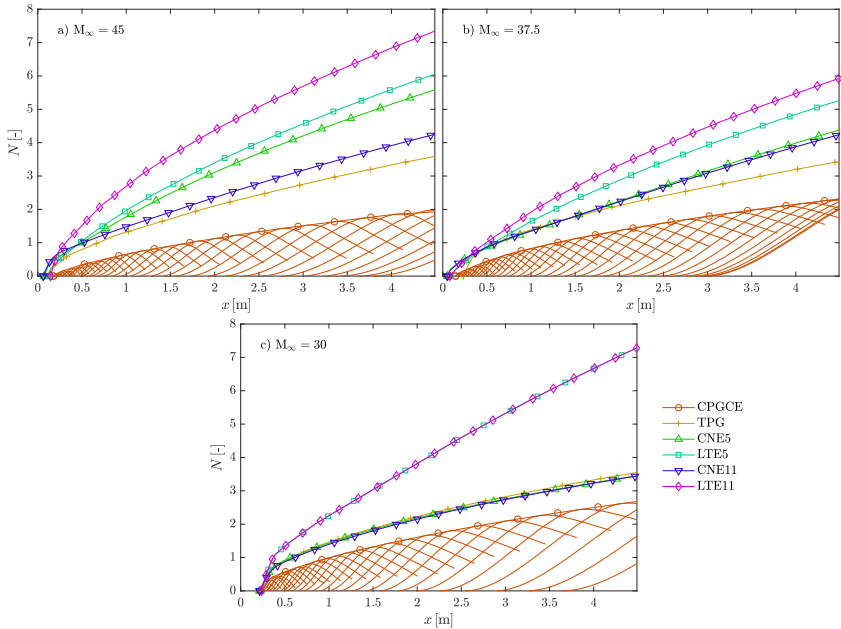


Figure 10.34: Second-mode N -factor envelopes for the flight-envelope points in Table 10.5 and for various flow assumptions introduced at the beginning of § 10.4. All assumptions share the base-flow and perturbation hypotheses. Individual-frequency curves correspond to the CPGCE assumption.

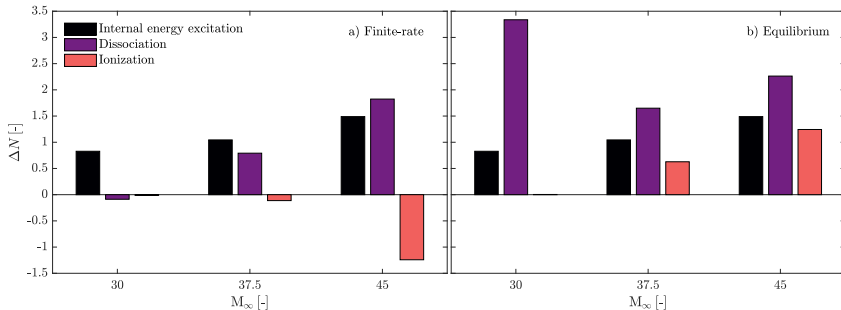


Figure 10.35: Variation in the maximum N factor at $x = 4 \text{ m}$ due to the different physical phenomena affecting simultaneously the base-flow and the perturbation quantities. Case details are summarized in Table 10.5.

sults are displayed in Fig. 10.35, where a distinction is made depending on whether chemical activity is assumed to occur at a finite rate (a), or to correspond to equilibrium conditions (b). Fig. 10.35 displays very clearly a rather counter-intuitive trend observed in Figs. 10.33 and 10.34: ionization is seen to stabilize the flow when considering finite-rate reactions, yet destabilize it under equilibrium conditions. The following subsections analyze various flow assumptions, featuring different hypotheses for the base-flow and perturbation quantities, in order to investigate the underlying reason for this trend reversal.

10.4.2.2 Base-flow cooling, diffusion and chemical source term

The temperature perturbation amplitude shapes in Fig. 10.33#iii suggest that, besides the second-mode waves' confinement as a consequence of the density gradient's thermo-acoustic impedance [46], there are other major actors affecting the development of instabilities. In order to shed light onto what such phenomena may be and how they are interrelated, various combinations of base-flow and perturbation hypotheses are compared. Figure 10.36 compares the TPG against the CNE (5- or 11-species) results, as well as those corresponding to a series of intermediate flow assumptions (see the beginning of the section § 10.4).

Aside from the TPG case, all others feature chemically-reacting basic-state solutions. As mentioned at the beginning of the section, the CNETPG cases assume TPG conditions for the perturbation variables \tilde{q} , thus effectively neglecting the diffusion-flux and source-term perturbations (J'_s and $\dot{\omega}'_s$). The CNEfroz cases simply neglect the source-term perturbations, whilst the CNEnoIon11 case neglects the contribution of ionization reactions to the source-term perturbation.

One can clearly see that, for equivalent mixtures (5- or 11-species) the CNETPG assumption always predicts the largest range of unstable frequencies and the maximum growth-rate value. An exception to this trend is seen for the 5-

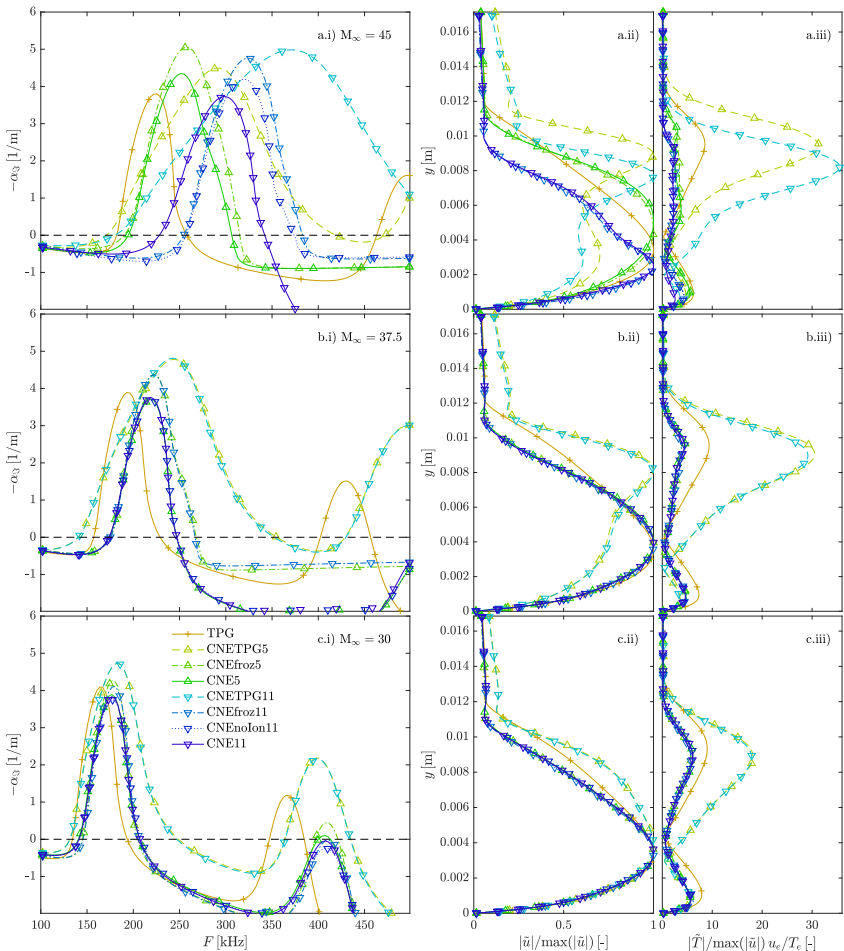


Figure 10.36: Second-mode perturbation growth rates (i) and the mode shapes for the most unstable frequency (ii-iii) at $x = 1$ m for the flight-envelope points in Table 10.5 and for various flow assumptions introduced at the beginning of § 10.4.

species cases in the first flight-envelope point (Fig. 10.36a.i). The CNEfroz5 case actually has a maximum growth that is larger than the CNETPG5 case. However, the range of unstable frequencies is so substantially smaller, that one would expect the CNETPG5 case to still predict a sooner transition. For the remainder of the section, the term “stabilizing” or “destabilizing” is used to refer to how something affects the entire frequency range, and not only the maximum growth rate. The CNETPG5 case is unstable over a larger range of frequencies, and therefore, overall, it is more unstable than the CNEfroz5 case.

Aside from the mentioned exception, gradually accounting for diffusion-flux, dissociation, and ionization contributes to a reduction of the predicted range of unstable frequencies, together with the maximum growth rate. This is a clear example of the two major competing effects in chemically-reacting boundary layers:

1. The destabilization due to the cooling of the base-flow field.
2. The stabilization due to the chemical source terms acting on the perturbations.

The present analysis suggests that there is yet another actor that is actually the most important one in many cases:

3. The stabilization due to the diffusion fluxes acting on the perturbations.

The CNETPG assumptions only experience the first effect, and therefore make the most-unstable of all predictions. The CNEfroz cases also include the third effect, whilst the CNE ones have all three.

These trends can also be analyzed from the thermoacoustic stand point. The CNETPG assumption makes the same hypotheses on the perturbation terms as the TPG one. However, it makes significantly different base-flow hypotheses (CNE), which actually lead to predicting stronger density gradients due to the chemical activity (see Fig. 10.32). The CNETPG perturbations therefore have the same characteristics as the TPG ones, yet they are confined by a significantly stronger thermoacoustic impedance. It is therefore understandable that they display overly larger growth rates. The temperature perturbation shapes in Fig. 10.36#.iii support this interpretation – the second peak, around $y \approx 0.01$ m is indeed much stronger for the CNETPG cases than it is for the TPG ones. This is arguably a consequence of the commented stronger instability confinement. The effect of the diffusion fluxes is to damp this instability peak, as can be seen by the comparison of the CNEfroz and the CNETPG temperature perturbations in Fig. 10.36#.iii. This damping could be the underlying reason for the stabilizing effect of the diffusion fluxes.

It is important to note that, unlike what is observed in § 10.2, the diffusion fluxes are seen to have a major impact on the stability predictions. This suggests

that indeed for strongly-reacting boundary layers such as those under consideration in this section, they can no longer be faultlessly disregarded.

Fig. 10.36 also presents practically coinciding stability predictions with the 5- and 11-species assumptions for the second and last flight-envelope points. This indeed reinforces the idea that the finite-rate ionization occurring in them is sufficiently low so as to neglect it.

Another interesting conclusion to draw from this comparison, is that the reason why the ionizing CNE case (CNE11) predicts a more stable boundary-layer than the non-ionizing one (CNE5) at the first flight-envelope point ($M_\infty = 45$) is not the modification of the mixture viscosity caused by the larger concentration of ions. If this were the case, then the CNETPG equivalents, which feature the same base-flow field as the CNE cases, would also experience such an ionization-related stabilization. Instead, the CNETPG11 case is more unstable and over a wider range of frequencies than the CNETPG5 one. The cooling of the laminar boundary layer, and consequent increase in the thermoacoustic impedance (density gradient) remains the driver of the mentioned destabilization associated to ionization and distinguishing cases CNETPG11 and CNETPG5.

The N -factor envelopes resulting from the integration of the instabilities corresponding to the assumptions compared in Fig. 10.36, are presented in Fig. 10.37. The general trends lie within what was already mentioned for Fig. 10.36, and perfectly display the three mentioned competing effects and their distinct importance for the different points within the flight envelope. By taking the different values of the N -factor envelopes at $x = 4$ m, these effects can be very clearly quantified. The visualization of the different contributions is displayed in Fig. 10.38, where a distinction is made on whether the mixture is assumed to be 5- or 11-species air. An interesting feature that is clearly visible from Fig. 10.38 is that for the first flight-envelope point ($M_\infty = 45$) diffusion is seen to have a much stronger stabilizing effect when the mixture contains ions (11-species) than when it does not (5-species). This is a plausible explanation for the overall stabilizing effect of ionization observed in Fig. 10.35a when assuming finite-rate chemistry.

10.4.2.3 Equilibrium-perturbation hypothesis

The deployment of the LTE assumption on both the laminar base-flow and the perturbation terms is questionable. Oftentimes the characteristic oscillatory timescale of instabilities is too fast to allow them to reach equilibrium. In order to quantify this assumption, the stability characteristics obtained with the same LTE base flow, yet with LTE and CNE perturbations are compared.

The second-mode growth rates (i) and perturbation amplitudes of the streamwise velocity (ii) and temperature (iii) are presented in Fig. 10.39. The stability characteristics predicted with the commented LTCNE assumptions are compared to those obtained with the corresponding CNE and LTE assumptions. Allowing

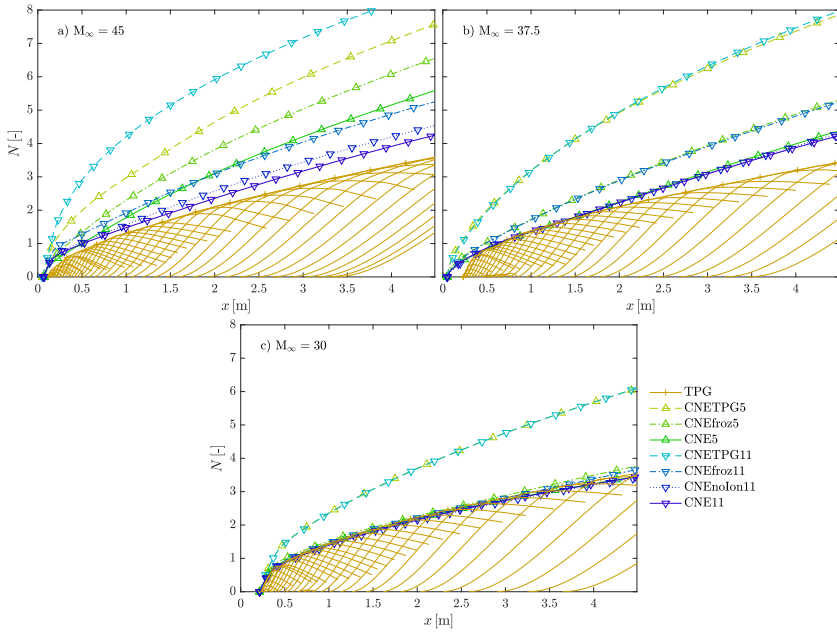


Figure 10.37: Second-mode N -factor envelopes for the flight-envelope points in Table 10.5 and for various flow assumptions introduced at the beginning of § 10.4.

Individual-frequency curves correspond to the TPG assumption.

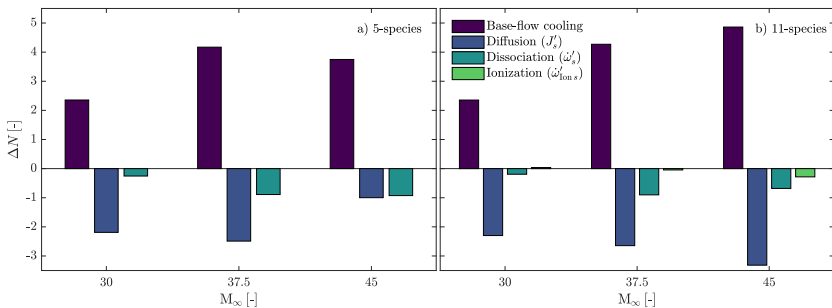


Figure 10.38: Variation in the maximum N factor at $x = 4 \text{ m}$ due to the different physical phenomena. Case details are summarized in Table 10.5.

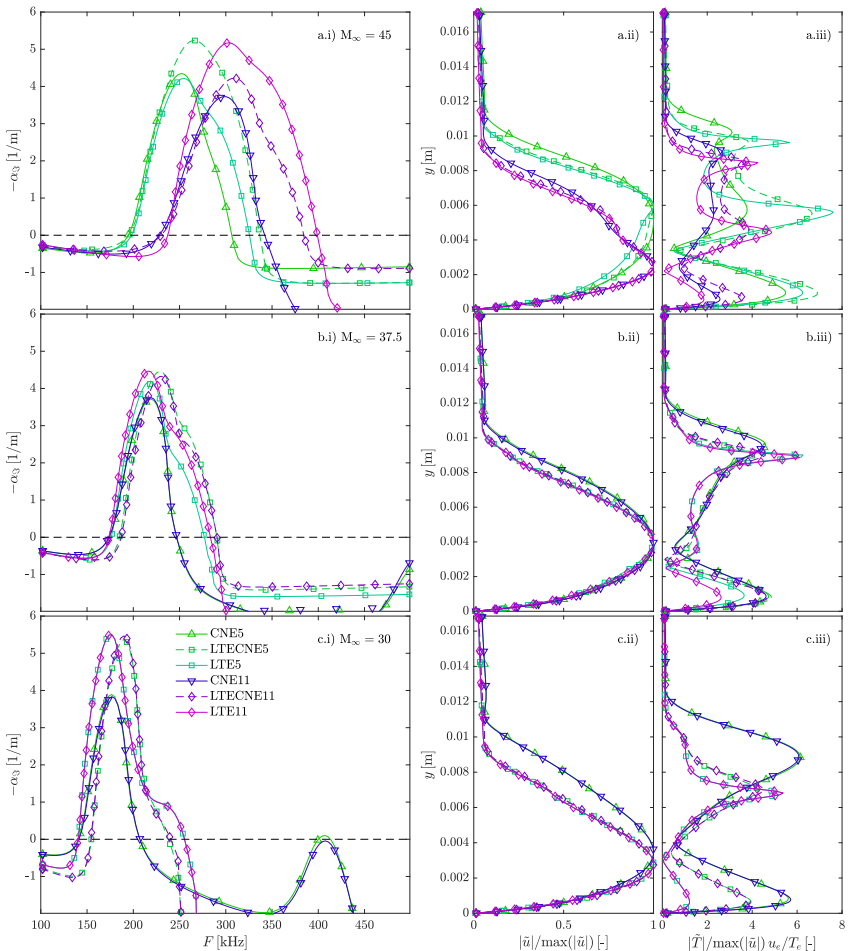


Figure 10.39: Second-mode perturbation growth rates (i) and the mode shapes for the most unstable frequency (ii-iii) at $x = 1 \text{ m}$ for the flight-envelope points in Table 10.5 and for various flow assumptions introduced at the beginning of § 10.4.

for the non-equilibrium behavior of perturbations in the third flight-envelope point (Fig. 10.39c) is seen to have a minor impact on the predictions. This suggests that assuming equilibrium perturbations is indeed acceptable in that case and most-likely also in the flight-envelope points considered in § 10.3. They do, however, present interesting, and by all means non-negligible, differences on the predictions in the first and second flight-envelope points. In both of them (Fig. 10.39a-b) the LTECNE5 prediction is more unstable than the LTE5, yet the LTECNE11 is more stable than the LTE11. This suggests that the non-equilibrium behavior of perturbations is very different if the mixture contains ionized species or not.

The N -factor envelopes presented in Fig. 10.40 confirm that this trend is preserved along the entire streamwise range. One can also proceed in the same way as in § 10.4.2.1, and quantify the differential effect of dissociation and ionization on the N factors at $x = 4\text{ m}$. The result is Fig. 10.41, which displays the same comparison as Fig. 10.35b, yet with perturbations in CNE. The trends presented in Fig. 10.41 are indeed closer to those in Fig. 10.35a than they are to those in Fig. 10.35b. This suggests that the observation made when assuming LTE (Fig. 10.35b), that ionization further destabilizes the flow in equilibrium conditions, is actually an incorrect artifact of assuming the perturbations to be in equilibrium.

10.4.2.4 Supersonic modes

A distinctive feature of second-mode instabilities is related to their wave speed relative to the boundary-layer-edge velocity. If the difference between the former and the latter is supersonic, one refers to them as *supersonic modes* (see § 3.6), which have a series of particular characteristics (see Refs. 15, 47, 48). Supersonic modes receive energy from their “synchronization” with the continuous branch of the instability spectrum, similarly to how the second mode does with either the fast or slow mode (following Fedorov & Tumin’s naming convention [49]). This causes a non-exponential decay of the perturbation amplitude in the free-stream region, as well as an increase in the upper limit of the range of unstable frequencies. The latter can have a strong effect on the ultimate transition-onset predictions, since it effectively shifts the N -factor envelopes vertically [15].

In order to better understand the various trends observed in the preceding sections, the instability growth rates of the first flight-envelope point (Table 10.5) at $x = 1\text{ m}$ are plotted as a function of the wave speed, rather than the wave frequency in Fig. 10.42. In order to effectively compare cases with distinct boundary-layer-edge velocities and Mach numbers (see Fig. 10.30 and Table 10.6), the horizontal axis in Fig. 10.42 is the non-dimensional wave speed relative to the sonic line

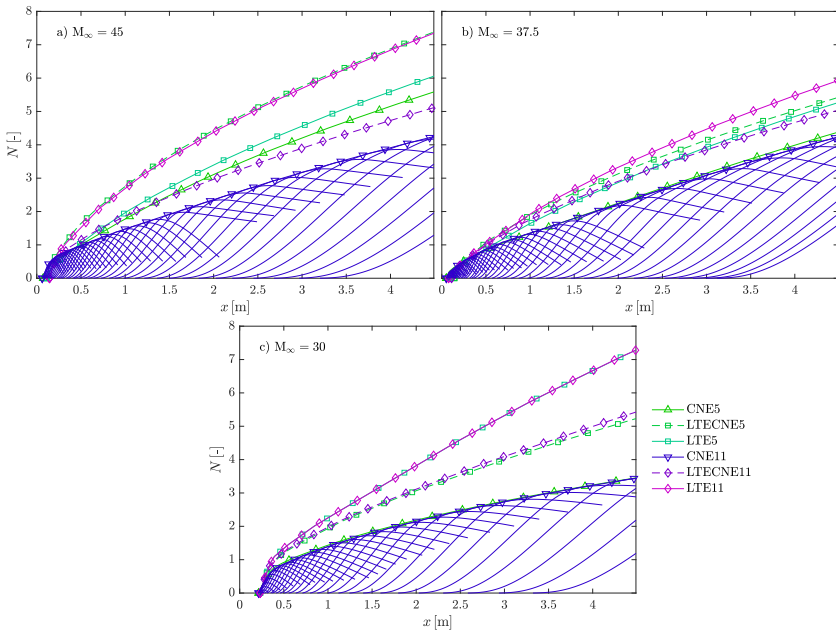


Figure 10.40: Second-mode N -factor envelopes for the flight-envelope points in Table 10.5 and for various flow assumptions introduced at the beginning of § 10.4. Individual-frequency curves correspond to the CNE11 assumption.

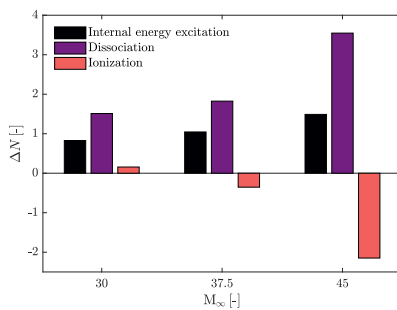


Figure 10.41: Variation in the maximum N factor at $x = 4 \text{ m}$ due to the different physical phenomena. Chemical activity assumed in equilibrium in the base-flow, yet not in the (CNE) perturbations – LTECNE assumptions. Case details are summarized in Table 10.5.

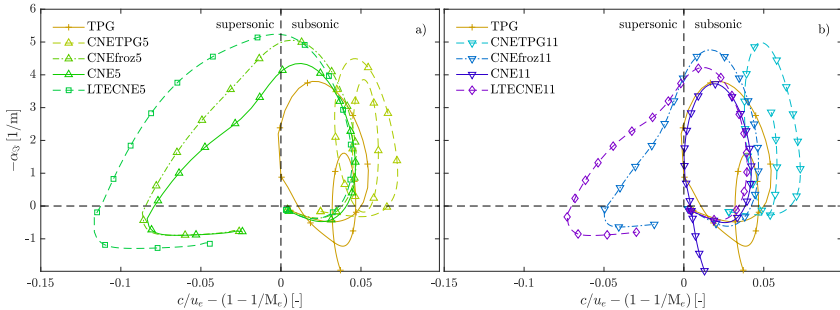


Figure 10.42: Second-mode perturbation growth rates as a function of the non-dimensional wave-speed (ω/α) relative to the sonic line ($1 - 1/M_e$) at $x = 1 \text{ m}$ for the first flight-envelope point in Table 10.5. All assumptions described at the beginning of § 10.4).

based on the frozen speed of sound (Eq. 7.7):

$$\frac{c}{u_e} - \left(1 - \frac{1}{M_e}\right) = \frac{\omega/\alpha_{\Re}}{u_e} - \left(1 - \frac{\sqrt{\frac{c_{p,e}}{c_{v,e}} R_e T_e}}{u_e}\right). \quad (10.2)$$

Therefore, instabilities will be relatively supersonic on the left of 0 in Fig. 10.42, and subsonic on the right. Figure 10.42 compares the flow assumptions that were deemed more significant after the analyses of the previous sections, with their 5-species variant in Fig. 10.42a and their 11-species one in Fig. 10.42b.

Neglecting all chemical activity both in the base-flow and perturbation quantities (TPG assumption) leads to instabilities that remain always subsonic relative to the boundary-layer edge velocity. The inclusion of dissociation and ionization on the base-flow field (CNETPG assumptions) increases the instability wave speed. However, considering the effect of diffusion fluxes on the perturbation terms (CNEfroz assumptions) decreases this wave speed, and makes instabilities relatively supersonic.

The appearance of unstable supersonic modes is usually associated with the boundary-layer cooling induced by either cold wall [15, 17, 47, 48] or strong chemical activity [21, 43, 50]. However, the present results suggest that, in chemically reacting scenarios, it is not the base-flow cooling that causes the modes to become supersonic, but rather the diffusion fluxes acting on the perturbations.

The inclusion of the chemical source-term perturbations ($\dot{\omega}'_s$) has once again a different impact on the predictions made with 5- or with 11-species mixtures. Comparing the CNE to the CNEfroz curves in Fig. 10.42, one observes that non-zero $\dot{\omega}'_s$ lead to a reduction of the range of unstable wave speeds. However, for 11-species assumptions (Fig. 10.42b) this actually makes the instabilities remain relatively subsonic over the entire unstable frequency range.

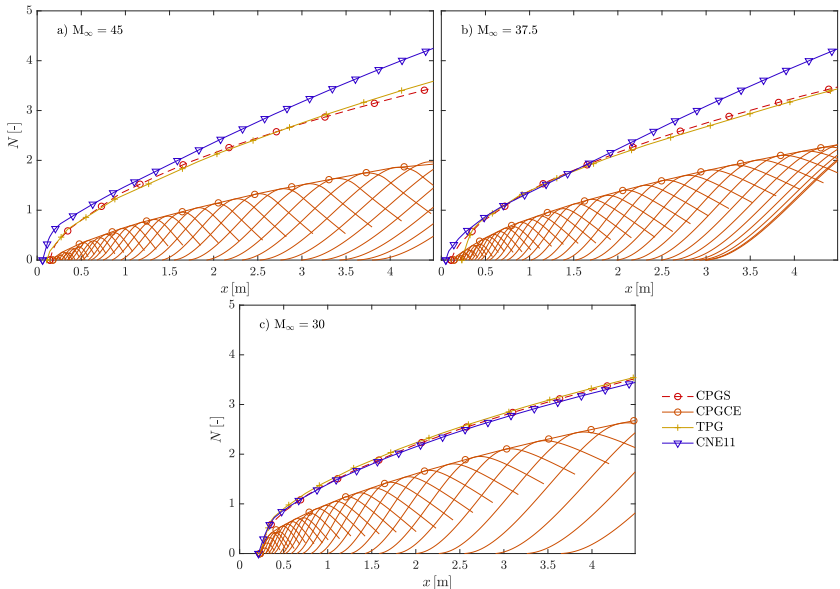


Figure 10.43: Second-mode N -factor envelopes for the flight-envelope points in Table 10.5 and for various flow assumptions introduced at the beginning of § 10.4. Individual-frequency curves correspond to the CPGCE assumption.

Assuming LTE for the base-flow quantities and CNE for the perturbation terms (LTECNE assumptions), one predicts a further extension of the range of wave speeds of unstable perturbations.

Similar trends are obtained when performing the same analysis for the other two flight-envelope points.

10.4.2.5 Transport model in CPG

A rather interesting result is obtained from the comparison of the CPG instability predictions with Sutherland's viscosity law, or with the CE transport model. As discussed in § 10.3, the inaccuracy in the transport modeling associated with the use of Sutherland's law, oftentimes casually counteracts the inaccuracy in the thermodynamic modeling linked to neglecting internal-energy-mode excitation or any form of chemical activity. This is once again observed for the three flight-envelope points under comparison (see Table 10.5). Fig. 10.43 displays the integrated N -factor envelopes as well as the individual-frequency N -factor curves for the CPGCE case. One can indeed see how the CPGS predictions happen to lie very close to the TPG and even the CNE11 ones. As pointed out in § 10.3, however, one should refrain from identifying the CPGS assumption as having any modeling accuracy. It actually poses an excellent example of how one can circumstantially

reach the right answer for the wrong reason.

10.4.3 Free-stream boundary condition

The test cases under consideration feature a shock that is very close to the surface (see § 10.4.1 and Table 10.7). It is therefore reasonable to believe that instabilities do not have a sufficiently large wall-normal stretch so as to fully decay before reaching the shock. Also, as seen in § 10.4.2.4, the most unstable perturbation is a supersonic mode over a large fraction of the streamwise range. Supersonic modes are known to have a non-exponential decay in the freestream region [47, 48, 51], further increasing the amplitude with which they reach the shock.

It is therefore questionable whether one should apply Dirichlet boundary conditions, as was done in the previous sections, or if it is more appropriate to use the linearized Rankine-Hugoniot relations instead (see § 6.2.1). The growth rate and perturbation-amplitude comparisons presented for the Dirichlet boundary condition in Fig. 10.33 are revisited, yet employing the linearized shock condition. The result is presented in Fig. 10.44 for the three flight-envelope points of interest (see Table 10.5). Figs. 10.44a-b.i exhibit a second growth-rate peak for the LTE11 cases which was not predicted with the Dirichlet boundary condition. Despite it, the trend displayed is very similar to that of Fig. 10.33, suggesting that the shock does not introduce a major modification on the instability development. This is confirmed by Fig. 10.45, which displays the variation in the maximum N factor due to the imposition of the shock boundary condition, rather than the Dirichlet. The low values of the shock N -factor difference across all flight-envelope points supports the choice of the free-stream boundary conditions made throughout this section.

10.4.4 Conclusions

An extensive investigation was carried out using LST on boundary-layer laminar base-flow fields to determine how ionization and dissociation affect the development of instabilities within a boundary layer. Three test cases were investigated, approximating the conditions encountered in extreme atmospheric reentry missions (Martian return). Fourteen different flow assumptions, featuring various combinations of base-flow and perturbation hypotheses, were employed in the effective decoupling of the various physical phenomena simultaneously interacting in such scenarios.

The boundary layers of the three flight-envelope points were seen to have maximum ionization levels ranging from 0.01 to 10%. Successively accounting for internal-energy-mode excitation, dissociation, and ionization was seen to reduce the boundary-layer size and cool it. The effect was enhanced when the chemical activity was assumed in equilibrium, rather than accounting for the finite-rate of

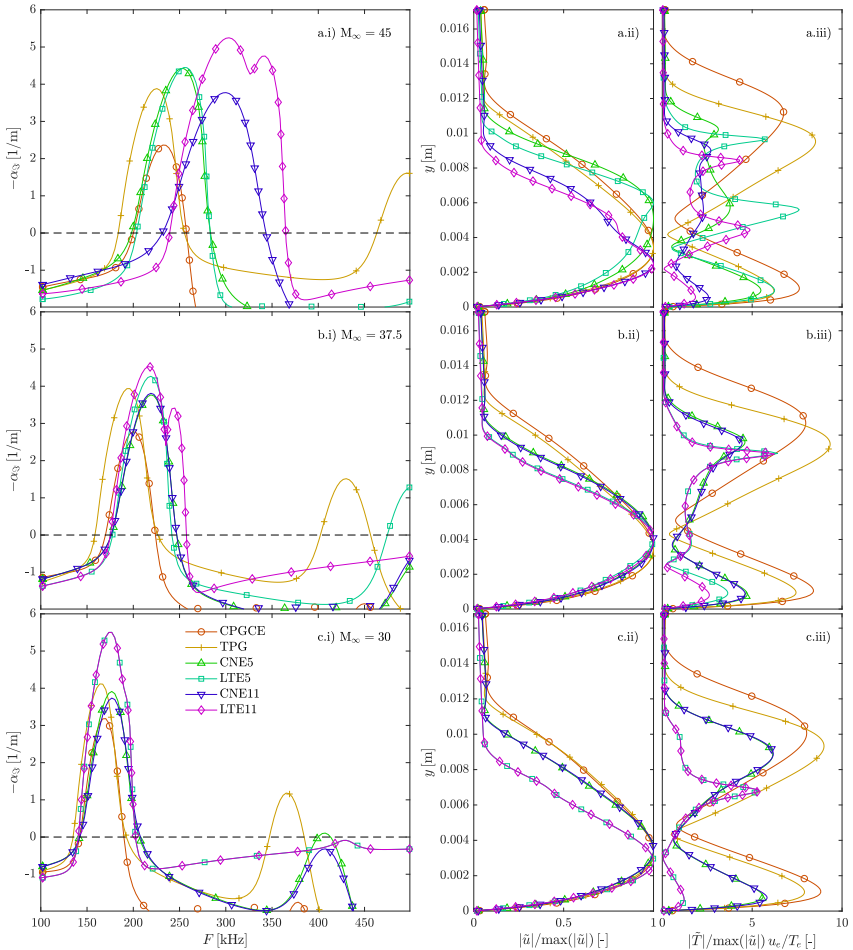


Figure 10.44: Second-mode perturbation growth rates (i) and the mode shapes for the most unstable frequency (ii-iii) at $x = 1 \text{ m}$ for the flight-envelope points in Table 10.5, employing the linearized shock perturbation boundary condition (see § 6.2.1). All assumptions (see the beginning of § 10.4) make the same hypotheses on the base-flow and perturbation quantities.

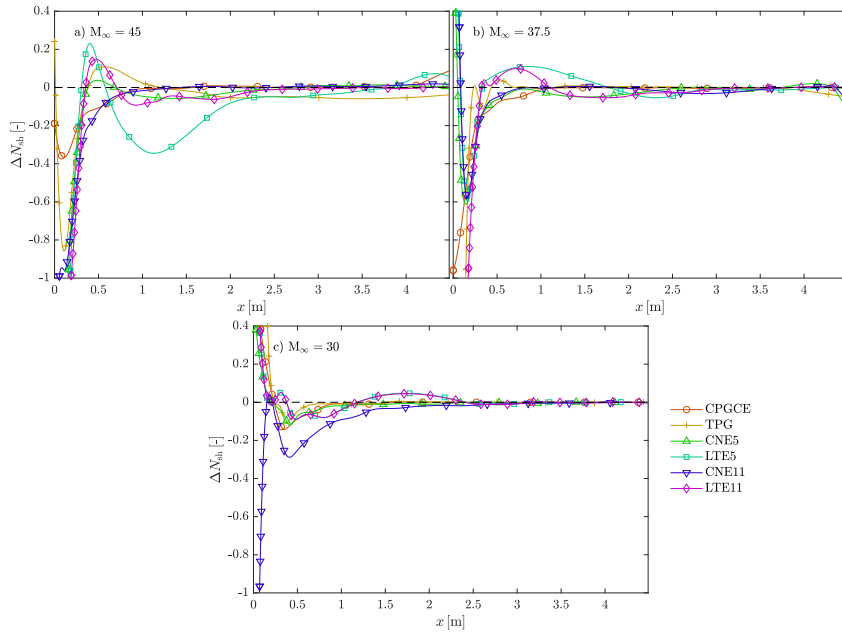


Figure 10.45: Variation in the second-mode maximum N-factor due to the use of the shock boundary condition (see § 6.2.1) rather than the Dirichlet. Test cases correspond to the flight-envelope points in Table 10.5 and feature various flow assumptions introduced at the beginning of § 10.4.

reactions. Dissociation was also seen to introduce an additional drop in the wall density due to the decrease in the mixture molar mass. All these features contributed to increasing the thermoacoustic impedance in the boundary layer that is believed to ultimately confine and destabilize second-mode instabilities.

The excitation of internal energy modes, as well as the dissociation of molecular species, were seen to destabilize the boundary layer and ultimately lead to higher N factors. Conversely, ionization was seen to be mainly stabilizing. Assuming the perturbations to be in equilibrium was seen to erroneously predict a destabilizing effect of ionization.

The various competing effects in instability development linked to chemical activity were identified and quantified for the three considered flight-envelope points:

1. The destabilization due to the base-flow cooling induced by the chemical activity. The driving mechanism appears to be the increase in the thermoacoustic impedance that is the density gradient, and that significantly increases the peak in the temperature perturbation amplitude in the top of the boundary layer.
2. The stabilization introduced by the diffusion fluxes acting on the perturbation terms. They were seen to act on the aforementioned peak in the temperature perturbation amplitude. This damping is believed to be driving the associated stabilization of second-mode instabilities.
3. A further stabilization linked to the chemical source terms acting on the perturbation terms.

Out of these three competing effects, it was the diffusion fluxes that were seen to make second-mode instabilities become supersonic. This contradicts the previously dominating belief that it was the chemistry-induced base-flow cooling that was actually originating supersonic modes in high-enthalpy flows. Previous studies did not decouple these two phenomena, and therefore could only speculate with the base-flow cooling to be the underlying reason for it.

The modification of the predictions linked to using the linearized Rankine-Hugoniot relations on the free-stream perturbation values, rather than Dirichlet conditions, was also investigated. The shock boundary condition was seen to slightly modify the perturbation growth rates, especially for the flow assumptions featuring supersonic modes. However, the ultimate modification of the N factors was seen to be negligible. The fact that this was the case for shocks at such a small distance to the surface (1.3-2.3 degrees) suggests that the effect of the shock for such simple geometries may be disregarded, or that alternative, more physically-accurate methodologies must be found to model the interaction between instabilities and a shock.

References

- [1] S. Chapman and T. Cowling. *The Mathematical Theory of Non-uniform Gases: An Account of the Kinetic Theory of Viscosity, Thermal Conduction, and Diffusion in Gases*. The University Press, 1939.
- [2] J. O. Hirschfelder, C. F. Curtiss, and R. B. Bird. *Molecular theory of gases and liquids*. Wiley, New York, 2 edition, 1954.
- [3] F. G. Blottner, M. Johnson, and M. Ellis. *Chemically Reacting Viscous Flow Program For Multi-Component Gas Mixtures*. Technical Report SC-RR-70-754, Sandia Laboratories, 1971.
- [4] R. N. Gupta, J. M. Yos, R. A. Thompson, and K.-P. Lee. *A review of Reaction Rates and Thermodynamic and Transport Properties for an 11-Species Air Model for Chemical and Thermal Nonequilibrium Calculations to 30000K*. Technical Report RP-1232, NASA, 1990.
- [5] M. Fertig, A. Dohr, and H.-H. Fröhlauf. *Transport Coefficients for High Temperature Nonequilibrium Air Flows*. Journal of Thermophysics and Heat Transfer, [15\(2\):148–156](#), 2001.
- [6] B. J. McBride, M. J. Zehe, and S. Gordon. *NASA Glenn Coefficients for Calculating Thermodynamic Properties of Individual Species*. Technical Report 2002-21155, NASA, 2002.
- [7] T. E. Magin and G. Degrez. *Transport properties of partially ionized and unmagnetized plasmas*. Physical Review E, [70\(4\)](#), 2004.
- [8] J. B. Scoggins. *Development of numerical methods and study of coupled flow, radiation, and ablation phenomena for atmospheric entry*. PhD thesis, Université Paris-Saclay and VKI, 2017.
- [9] M. P. Clarey and R. B. Greendyke. *Thermochemical nonequilibrium processes in weakly ionized air using three-temperature models*. Journal of Thermophysics and Heat Transfer, [33\(2\):425–440](#), 2019.
- [10] G. Stuckert and H. L. Reed. *Linear Disturbances in Hypersonic, Chemically Reacting Shock Layers*. AIAA Journal, [32\(7\):1384–1393](#), 1994.
- [11] M. L. Hudson, N. Chokani, and G. V. Candler. *Linear stability of hypersonic flow in thermochemical nonequilibrium*. AIAA Journal, [35\(6\):958–964](#), 1997.
- [12] H. B. Johnson and G. V. Candler. *Hypersonic boundary layer stability analysis using PSE-Chem*. AIAA paper, [2005-5023](#), 2005.

- [13] C. Mortensen and X. Zhong. *Real-Gas and Surface-Ablation Effects on Hypersonic Boundary-Layer Instability over a Blunt Cone*. AIAA Journal, **54**(3):980–998, 2016.
- [14] K. J. Franko, R. W. MacCormack, and S. K. Lele. *Effects of chemistry modeling on hypersonic boundary layer linear stability prediction*. AIAA paper, **2010-4601**, 2010.
- [15] N. P. Bitter and J. E. Shepherd. *Stability of highly cooled hypervelocity boundary layers*. Journal of Fluid Mechanics, **778**:586–620, 2015.
- [16] H. L. Kline, C.-L. Chang, and F. Li. *Hypersonic Chemically Reacting Boundary-Layer Stability using LASTRAC*. AIAA paper, **2018-3699**, 2018.
- [17] L. M. Mack. *Boundary-Layer Linear Stability Theory*. In Special Course on Stability and Transition of Laminar Flow, AGARD 709. AGARD, 1984.
- [18] J. B. Scoggins and T. E. Magin. *Development of Mutation++: Multicomponent Thermodynamics And Transport properties for IONized gases library in C++*. AIAA paper, **2014-2966**, 2014.
- [19] M. R. Malik. *Hypersonic Flight Transition Data Analysis Using Parabolized Stability Equations with Chemistry Effects*. Journal of Spacecraft and Rockets, **40**(3):332–344, 2003.
- [20] J. Klentzman and A. Tumin. *Stability and receptivity of high speed boundary layers in oxygen*. AIAA paper, **2013-2882**, 2013.
- [21] C.-L. Chang, H. Vinh, and M. R. Malik. *Hypersonic boundary-layer stability with chemical reactions using PSE*. AIAA paper, **1997-2012**, 1997.
- [22] F. Miró Miró, F. Pinna, E. S. Beyak, P. Barbante, and H. L. Reed. *Diffusion and chemical non-equilibrium effects on hypersonic boundary-layer stability*. AIAA paper, **2018-1824**, 2018.
- [23] G. K. Stuckert. *Linear Stability Theory of Hypersonic, Chemically Reacting Viscous Flows*. PhD thesis, Arizona State University, 1991.
- [24] S. J. Cubley and E. A. Mason. *Atom-molecule and molecule-molecule potentials and transport collision integrals for high-temperature air species*. Physics of Fluids, **18**:1109, 1975.
- [25] M. Capitelli and E. Ficocelli. *Collision integrals of carbon-oxygen atoms in different electronic states*. Journal of Physics B: Atomic and Molecular Physics, **5**:1819–1823, 1972.

- [26] K. S. Yun and E. A. Mason. *Collision Integrals for the Transport Properties of Dissociating Air at High Temperatures*. Physics of Fluids, **5**:380, 1962.
- [27] J. C. Rainwater, L. Biolsi, K. J. Biolsi, and P. M. Holland. *Transport properties of ground state nitrogen atoms*. The Journal of Chemical Physics, **79**(1462):3203–3210, 1983.
- [28] I. Lyttle and H. L. Reed. *Sensitivity of Second-Mode Linear Stability to Constitutive Models within Hypersonic Flow*. AIAA paper, **2005-889**, 2005.
- [29] J. L. van Ingen. *A suggested semi-empirical method for the calculation of the boundary layer transition region*. Technical Report VTH-74, Technische Hogeschool Delft, Vliegtuigbouwkunde, 1956.
- [30] D. Arnal. *Boundary layer transition: predictions based on linear theory*. In Special Course on Progress in Transition Modelling AGARD 793. AGARD, 1993.
- [31] M. H. Bortner. *Suggested Standard Chemical Kinetics for Flow Field Calculations. A consensus Opinion*. In AMRAC Proceedings, Volume XIV, Part I, Doc. No. 4613-135-X (Contract SD-91). Institute of Science and Technology. University of Michigan, April 1966.
- [32] M. J. Wright, D. Bose, G. E. Palmer, and E. Levin. *Recommended Collision Integrals for Transport Property Computations Part I: Air Species*. AIAA Journal, **43**(12):2558–2564, 2005.
- [33] C. Park. *On convergence of computation of chemically reacting flows*. AIAA paper, **85-0247**, 1985.
- [34] C. Park, R. L. Jaffe, and H. Partridge. *Chemical-Kinetic Parameters of Hyperbolic Earth Entry*. Journal of Thermophysics and Heat Transfer, **15**(1):76–90, 2001.
- [35] J. Perraud, D. Arnal, L. Dussillols, and F. Thivet. *Studies of Laminar-Turbulent Transition in Hypersonic Boundary Layers at ONERA*. In 3rd European Symposium on Aerothermodynamics for Space Vehicles, 1998.
- [36] S. D. Williams, D. M. Curry, D. C. Chao, and V. T. Pham. *Ablation analysis of the shuttle orbiter oxidation protected reinforced carbon-carbon*. Journal of Thermophysics and Heat Transfer, **9**(3):478–485, 1995.
- [37] F. Pinna. *Numerical study of stability of flows from low to high Mach number*. PhD thesis, Università degli Studi di Roma La Sapienza, 2012.
- [38] F. Pinna. *VESTA toolkit: a Software to Compute Transition and Stability of Boundary Layers*. AIAA paper, **2013-2616**, 2013.

- [39] M. R. Malik. *Numerical methods for hypersonic boundary layer stability*. Journal of Computational Physics, [86\(2\):376–413](#), 1990.
- [40] L. Zanus, F. Miró Miró, and F. Pinna. *Weak Non-Parallel Effects on Chemically Reacting Hypersonic Boundary Layer Stability*. AIAA paper, [2019-2853](#), 2019.
- [41] E. Levin and M. J. Wright. *Collision Integrals for Ion-Neutral Interactions of Nitrogen and Oxygen*. Journal of Thermophysics and Heat Transfer, [18\(1\):143–147](#), 2004.
- [42] E. A. Mason. *Transport Coefficients of Ionized Gases*. Physics of Fluids, [10\(8\):1827](#), 1967.
- [43] F. Miró Miró, E. S. Beyak, D. Mullen, F. Pinna, and H. L. Reed. *Ionization and Dissociation Effects on Hypersonic Boundary-Layer Stability*. In 31st ICAS Congress, Belo Horizonte, Brazil, 2018. International Council of the Aeronautical Sciences.
- [44] J. D. Anderson Jr. *Hypersonic and High Temperature Gas Dynamics*. American Institute of Aeronautics and Astronautics, Reston VA, second edition, 2006.
- [45] J. P. Brazier, B. Aupoix, and J. Cousteix. *Second-Order Effects in Hypersonic Laminar Boundary Layers*. In T. Murthy, editor, *Computational Methods in Hypersonic Aerodynamics*. Kluwer Academic, 1991.
- [46] J. J. Kuehl. *Thermoacoustic Interpretation of Second-Mode Instability*. AIAA Journal, [56\(9\):3585–3592](#), 2018.
- [47] C. P. Knisely and X. Zhong. *Sound radiation by supersonic unstable modes in hypersonic blunt cone boundary layers. I. Linear stability theory*. Physics of Fluids, [31\(2\)](#), 2019.
- [48] C. P. Knisely and X. Zhong. *Sound radiation by supersonic unstable modes in hypersonic blunt cone boundary layers. II. Direct numerical simulation*. Physics of Fluids, [31\(2\)](#), 2019.
- [49] A. V. Fedorov and A. Tumin. *High-Speed Boundary-Layer Instability: Old Terminology and a New Framework*. AIAA Journal, [49\(8\):1647–1657](#), 2011.
- [50] C.-L. Chang, H. L. Kline, and F. Li. *Effects of Wall Cooling on Supersonic Modes in High-Enthalpy Hypersonic Boundary Layers over a Cone*. AIAA paper, [2019-2852](#), 2019.

- [51] C. P. Knisely and X. Zhong. *Significant supersonic modes and the wall temperature effect in hypersonic boundary layers.* AIAA Journal, [57\(4\):1552–1566](#), 2019.

11

Decoupling ablation-transition problems

The present chapter advances towards the effective decoupling of the various physical phenomena that simultaneously coexist and ultimately condition the development of instabilities within a high-enthalpy boundary layer in the presence of ablation. This is achieved by using different flow assumptions and blowing basic-state and stability boundary conditions.

State-of-the-art thermodynamic and transport models (see chapter 4 or Ref. 1) are used to characterize the high-enthalpy flow: the CE transport model (§ 4.2.1.4), the SM diffusion model (Eq. 4.41), a polynomial-bilogarithmic fit (Eq. 4.57) on state-of-the-art collisional data [2–4], the RRHO thermal model (§ 4.1), and the reaction-rate coefficients collected by Mortensen & Zhong [5] (Table J.11). Additionally, another less accurate (see quantifications in chapter 4) combination of transport and diffusion models is compared to the previous: the BEW transport model (§ 4.2.1.1) and the constant $Sc = 0.5$ (Eq. 4.39). This corresponds to the modeling framework adopted by Mortensen & Zhong [5]. The two sets of models are compared in order to establish whether or not the large differences in the predicted stability characteristics stemming from inaccurate transport modeling seen in § 10.1 also manifest themselves in more complex thermophysical scenarios.

The work collected in this chapter is an extension of the work presented in Ref. 6.

11.1 Flow assumptions

A variety of thermodynamic assumptions, transport models, mixtures and wall boundary conditions are employed to decouple the various physical phenomena. The considered sets of flow assumptions arranged in increasing level of physical complexity are:

- CPGS: calorically perfect gas assumption with Sutherland's transport law (Eq. 4.2). It does not include the excitation of internal energy modes, and has a low-temperature model for the transport properties. All other flow assumptions use the Chapman-Enskog transport model (§ 4.2.1.4).
- CPGCE: calorically perfect gas assumption with the Chapman-Enskog transport model (§ 4.2.1.4). It does not include the excitation of internal energy modes, but has a transport model suited for high temperatures.
- TPG1: 1-species (air) thermally-perfect gas. It includes the excitation of the internal energy modes. The mixture has one species, since the chemical activity is frozen and the concentration of N₂ and O₂ in air are assumed constant (23.65% O₂, 76.35% N₂ in mass).
- CNE5: 5-species (N, O, NO, N₂, O₂) gas in chemical non-equilibrium, modeled with the air-5-Park90 mixture (§ J.8). It considers the chemical activity due to the air species, but does not include carbon.
- TPG6: 6-species (CO₂, N, O, NO, N₂, O₂) thermally-perfect chemically-frozen gas, modeled with the airC-6-Mortensen mixture (§ J.13). It allows for the diffusion of CO₂ blown at the wall into the other air species, yet it remains with frozen chemistry.
- CNE6: 6-species (CO₂, N, O, NO, N₂, O₂) gas in chemical non-equilibrium, modeled with the airC-6-Mortensen mixture (§ J.13). It considers the inter-diffusion of CO₂ with the other air species, and how the chemical activity of these air species is modified by the existence of CO₂. However, CO₂ cannot react with the other species.
- TPG11: 11-species (C₃, CO₂, C₂, CO, CN, C, N, O, NO, N₂, O₂) chemically frozen gas, modeled with the airC-11-Mortensen mixture (§ J.14). It considers the diffusion of all carbon species (ablation subproducts), yet chemically frozen.
- CNE11: 11-species (C₃, CO₂, C₂, CO, CN, C, N, O, NO, N₂, O₂) gas in chemical non-equilibrium, modeled with the airC-11-Mortensen mixture (§ J.14). It considers also the chemical activity associated to all carbon species (ablation subproducts).

Note that none of these include charged or electron species. Namely ionization effects on stability [7] are neglected. Thermal non-equilibrium is also neglected in the present work, in order to restrict the coexisting physical phenomena and facilitate the subsequent analysis.

11.2 Boundary conditions

Various combinations of base-flow and stability boundary conditions (presented in chapter 6) are employed in the decoupling of the ablation-related phenomena. Six combinations of base-flow wall conditions are hereinafter presented, named and subsequently employed in the numerical investigation:

1. **noBw**: no blowing. Assumes an impenetrable (Eq. 6.2), isothermal (Eq. 6.14) and non-catalytic (Eq. 6.23) wall.
2. **SSBw**: self-similar blowing. Assumes a blowing wall with a mass injection such that the self-similar blowing parameter f_w (Eq. 6.3) is constant. The wall is assumed isothermal (Eq. 6.14), and either non-catalytic (Eq. 6.23) for mixtures without carbon species, or, for mixtures with carbon species, with an imposed mass-fraction profile (Eq. 6.24) coming from the solution to the Abl case.
3. **AblBwCstT**: prescribed ablation blowing with constant temperature. The mass flux obtained from the Abl case is imposed at the wall (Eq. 6.4). The treatment of the wall temperature and mass fractions is the same as in the SSBw case.
4. **AblTBw**: prescribed ablation temperature and blowing. The wall temperature and blowing mass flow are imposed to be profiles (Eqs. 6.15 and 6.4) obtained from the full Abl case. Similarly to the SSBw case, the wall is assumed either non-catalytic (Eq. 6.23), for mixtures without carbon species, or with an imposed mass-fraction profile (Eq. 6.24) coming from the solution to the Abl case, for mixtures with carbon species.
5. **AblT**: ablation with imposed temperature. A gas-surface interaction model is used to obtain the species mass fractions at the wall (Eq. 6.25) and the injected mass flux 6.4. The temperature profile obtained from the full Abl case is imposed at the wall (Eq. 6.15).
6. **Abl**: full ablation model. Uses the gas-surface interaction model to obtain the species mass fractions (Eq 6.25), the total mass flux (Eq. 6.4) and the temperature (Eq. 6.19) at the wall.

It is important to note that in order for the base-flow treatment to be valid, one must assume steady surface ablation. This implies assuming a flow regime where the ablation rate at the surface can be considered independent of time. Real ablating surfaces are obviously time-evolving. However, as long as the rate of recession is slow enough in comparison to the flow and instability time scale [8] it is fair to assume the surface recession to be steady. One can consequently place the reference frame on the receding ablating surface, and use the equation system presented in this section, together with the stability hypotheses of the subsequent one.

Regarding the boundary conditions on the perturbation quantities, the no-slip condition allows fixing $\tilde{u}_w = \tilde{w}_w = 0$. For all other variables, four different sets of boundary conditions are distinguished:

1. **HSBC:** homogeneous stability boundary condition. One assumes that either there is no wall blowing, or the blowing is done such that there are no wall-normal velocity perturbations (Eq. 6.5). This approach was followed by the majority of authors previously studying wall-blown effects on stability [9–14]. Regarding the temperature perturbation, as laid out in § 6.1.2, the thermal inertia of the wall normally allows to assume it homogeneous (Eq. 6.21). Compatibility conditions are imposed to account for the fact that the pressure or density perturbations at the wall are not necessarily zero. For mono-species flow assumptions (CPG and TPG1) the mixture y-momentum equation (Eq. 2.7b) is linearized and evaluated at the wall [15]. For multi-species assumptions, separate y-momentum equations for each species (Eq. 6.26) are linearized and evaluated at the wall.
2. **RESBC:** radiative-equilibrium stability boundary condition. The assumptions are the same as with the HSBC, with the exception that the boundary condition on the temperature perturbation (\tilde{T}_w) is obtained from the linearization of the surface radiative-equilibrium condition (Eq. 6.16).
3. **ATSBC:** ablation isothermal stability boundary condition. This approach imposes the mixture surface mass balance (Eq. 6.4) and species surface mass balance (Eq. 6.25), linearized and evaluated at the wall, and with the source terms provided by Eqs. 4.79 and 4.80. The ATSBC does however assume homogeneous temperature perturbations (Eq. 6.21). The multi-species character of Eq. 6.25 obviously restricts the use of the ATSBC to 11-species mixtures.
4. **ASBC:** full ablation stability boundary condition. An additional equation is included with respect to ATSBC – the surface energy balance (Eq. 6.19). Eq. 6.19 is linearized and evaluated at the wall. The usage of Eq. 6.19 implies that, unlike in the previous set of boundary conditions, the temperature

perturbation is no longer homogeneous $\tilde{T}_w \neq 0$. Eqs. 6.4 and 6.25, linearized and evaluated at the wall complete the set of boundary conditions. This implies that the wall-normal velocity and species partial-density perturbations are also inhomogeneous at the wall $\tilde{v}_w, \tilde{\rho}_{sw} \neq 0$.

Regarding the freestream boundary conditions, all perturbations but one are assumed to damp out in the inviscid region, and are therefore imposed to be zero at a far enough distance from the wall. One is left inhomogeneous in order to account for the non-infinite size of the computational domain. In CPG and TPG1 flow assumptions it is the mixture pressure or density, which is liberated by enforcing the wall-normal-momentum equation (Eq. 2.7b) linearized and evaluated in the freestream [15]. Similarly, in multi-species flow assumptions, it is the wall-normal velocity \tilde{v} that is non-zero in the freestream. In order to account for it, the mixture continuity equation (Eq. 2.8) is linearized and evaluated in the freestream [16, 17].

11.3 Results

The laminar base flow and the stability features of the flow around a 7-degree wedge of length $L = 20$ m for four flight-envelope points on an aggressive atmospheric reentry mission (see Fig. 1.1) are investigated. The free-stream preshock conditions of these four trajectory points are summarized in Table 11.1, where an international standard atmosphere (ISA) is assumed. Table 11.1 also presents the values of \bar{T}_w and \bar{f}_w obtained from the treatment presented in § 11.3.1, and only enforced whenever they are assumed constant (see § 11.2). The free-stream composition is 76.35% N₂ and 23.65% O₂ in mass. When assuming a CPG, this implies that the heat capacity at constant pressure is $c_p = 1009.3$ J/kg-K and the specific gas constant is $R = 288.37$ J/kg-K. The present analysis is restricted to second-mode instabilities, which are known to be dominant in such speed regimes in the absence of crossflow [15]. The spanwise wave number can therefore be fixed to zero $\beta = 0$ (see § 3.6). Table 11.2 provides a summary of all the combinations of the base-flow-stability boundary conditions (§ 11.2) and flow assumptions (§ 11.1) considered for this chapter.

The basic-state flowfields are obtained using the DEKAF flow solver (see chapter 7). The LST computations are performed with the VESTA toolkit [18, 19], exploiting the capabilities of the ADIT (see chapter 8). The spatial LST generalized eigenvalue problem (Eq. 3.13) is solved using 400 points in the wall-normal direction and an FDq-8 numerical method, employing the FDq library developed and kindly provided by Dr. Hermanns [20, 21].

M_∞ [-]	Altitude [km]	T_∞ [K]	p_∞ [Pa]	\bar{T}_w [K]	\bar{f}_w [-]
30	46.5	269.4	117.2	1498	-0.0559
25				1325	-0.0393
20				1141	-0.0080
15				914	-0.0005

Table 11.1: Test matrix for the ablation-effect study.

	CPGS	CPGCE	TPG1	CNE5	TPG6	CNE6	TPG11	CNE11
noBw-HSBC	✓	✓	✓	✓	—	—	—	—
SSBw-HSBC	✓	✓	✓	✓	✓	✓	—	—
AblBwCstT-HSBC	✓	✓	✓	✓	✓	✓	—	—
AblTBw-HSBC	✓	✓	✓	✓	✓	✓	✓	✓
AblT-HSBC	—	—	—	—	—	—	—	✓
AblT-ATSBC	—	—	—	—	—	—	—	✓
Abl-HSBC	—	—	—	—	—	—	—	✓
Abl-RESBC	—	—	—	—	—	—	—	✓
Abl-ASBC	—	—	—	—	—	—	—	✓

Table 11.2: Summary of the analyzed combinations of boundary conditions and flow assumptions considered.

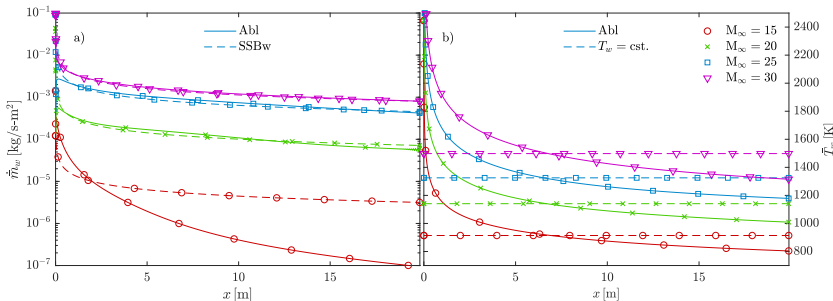


Figure 11.1: Surface mass-flow (a) and temperature (b) profiles for the Abl base-flow assumption for the four flight-envelope points in Table 11.1.

11.3.1 Wall profiles from the CNE11-Abl case

The surface mass-flow, temperature and concentration profiles of the CNE11-Abl case are used for many of the subsequent test cases. It is for this reason that they are presented in the first place. Fig. 11.1a displays the mass flux injected at the wall as a consequence of the gas-surface-interaction reactions presented in § 4.4 (Eqs. 4.71 and 4.76). It also includes the mass flux introduced when assuming a SSBw boundary condition. The value of the self-similar blowing parameter (f_w) presented in Table 11.1 for each flight-envelope point is chosen such that the total mass injection is the same as with the Abl boundary condition:

$$\int_0^L \dot{\bar{m}}_w^{\text{Abl}} dx = \int_0^L \dot{\bar{m}}_w^{\text{SSBw}} dx = \int_0^L -\bar{f}_w \frac{\rho_e u_e \mu_e}{\sqrt{2\xi}} dx. \quad (11.1)$$

Similarly, Fig. 11.1b presents the wall temperature profile obtained with the full Abl boundary condition, together with a constant value used for the isothermal-wall cases and included in Table 11.1. This temperature is such that the average energy of the isothermal surface is the same as the ablating one. Since the heat capacity of the solid graphite surface is constant, this is equivalent to averaging the temperature:

$$\bar{T}^{\text{est}} = \frac{1}{L \bar{c}_{p,w}^{\text{est}}} \int_0^L \bar{h}_w^{\text{Abl}} dx = \frac{1}{L} \int_0^L \bar{T}_w^{\text{Abl}} dx. \quad (11.2)$$

Figure 11.2 displays the wall concentration profiles of the eleven species in the CNE11 flow assumption. It also includes an additional profile for “CO₂ (CNE6)”, corresponding to the concentration of CO₂ that is injected for the flow assumptions featuring only six species. In those cases, the injected mass fraction of CO₂ is taken as the sum of all carbon species predicted to be injected by the CNE11 flow assumption. In other words:

$$(Y_{\text{CO}_2 w})^{\text{CNE6}} = (Y_{\text{CO}_2 w} + Y_{\text{CO } w} + Y_{\text{C } w} + Y_{\text{C}_2 w} + Y_{\text{C}_3 w} + Y_{\text{CN } w})^{\text{CNE11}}. \quad (11.3)$$

The non-reacting counterparts (TPG6 and TPG11) to CNE6 and CNE11 also impose the mass fractions detailed in Fig. 11.2 and Eq. 11.3.

Several flow features of the various flight-envelope points can be distinguished from Figs. 11.1 and 11.2. It is clear that a higher preshock mach number results in a hotter surface (Fig. 11.1b) and a higher mass injection as a consequence of the ablation of graphite (Fig. 11.1a). The stronger ablation existing in the higher-Mach-number cases also results in a higher surface concentration of ablation subproducts (Fig. 11.2). The concentration plots in Fig. 11.2 also display the dominance of the different ablation mechanisms introduced in § 4.4. Sublimation is dominant at higher wall temperatures, and therefore sublimation products such as C₃ and C₂

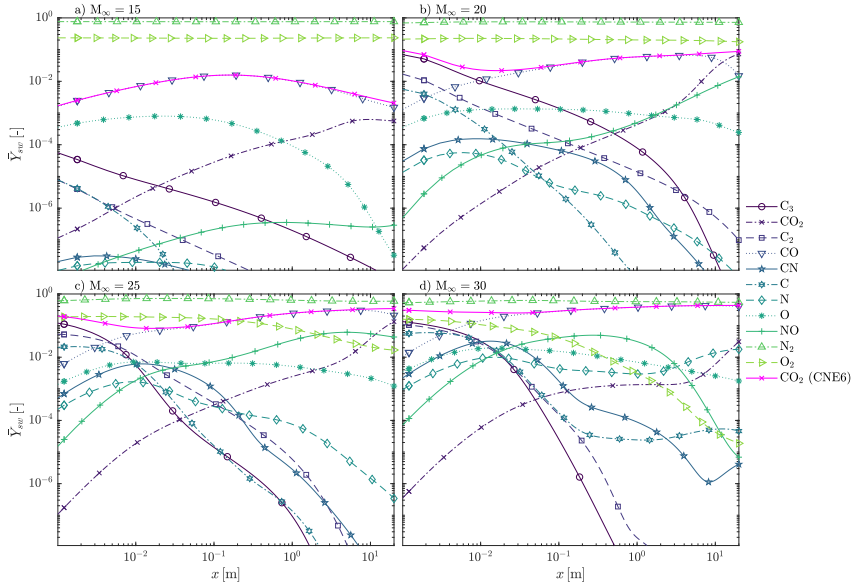


Figure 11.2: Surface concentration profiles for the Abl base-flow assumption for the four flight-envelope points in Table 11.1.

have larger wall concentrations at the streamwise regions close to the leading edge (see Fig. 11.2c for example) where the temperature is higher (see Fig. 11.1b). An exception to this is the last flight-envelope point ($M_\infty = 15$ in Fig. 11.2a), where the wall temperature at the leading edge remains too low to trigger sublimation reactions. Consequently, the concentration of C_3 and C_2 remains at a very low level. At later streamwise locations, where the wall temperature decreases (see Fig. 11.1b) oxidation reactions become dominant, and therefore lead to larger CO concentrations at the wall.

11.3.2 Mass injection effects

The present subsection investigates how mass injection modifies the laminar base flow and the subsequent stability and transition predictions. However, only the consequences of the mass-injection modification of the base flow are considered. All cases employ the same HSBC for the perturbation terms, thus neglecting the influence of the wall-normal velocity perturbation modeling investigated in § 9.3.

Figure 11.3 shows the effect on the base-flow streamwise velocity (i) and temperature (ii) of varying the surface mass-injection boundary condition whilst making a CPGCE assumption for the four flight-envelope points (a-b) in Table 11.1. Besides the increase in free-stream temperature associated to a higher pre-shock

Mach number (Fig. 11.3#i) one can also observe the effects of the decreasing mass flow for the various flight-envelope points (Table 11.1). The case with the lowest Mach number ($M_\infty = 15$), featuring a very low mass injection (see Fig. 11.1a) displays practically coincident velocity and temperature profiles in Fig. 11.3d for all blowing boundary conditions. This suggests that indeed the existing wall blowing is not sufficient to cause a significant boundary-layer displacement.

Gradually increasing the Mach number and the surface mass blowing (see Fig. 11.1a) leads to larger differences between the profiles obtained with the different blowing boundary conditions (Figs. 11.3c-a). Cases with a non-zero mass injection (cases SSBw, AblBwCstT, or AblTBw) result in a larger boundary layer than those with an impenetrable wall (noBw) – see for instance Fig. 11.3a. The SSBw and AblBwCstT boundary conditions appear to underestimate the boundary-layer displacement displayed by the AblTBw condition (closer to the fully-ablating case – Abl). As mentioned in § 11.2, the latter (AblBwCstT) assumes an isothermal wall with a temperature such that the total surface energy is the same as in the Abl case. Looking at Fig. 11.1b, such a constant temperature is lower than the Abl case for $x = 0\text{-}4$ m. Since colder walls lead to smaller boundary layers [15], this difference in the wall temperature justifies why the profiles of the AblBwCstT case (constant \bar{T}_w) in Fig. 11.3a display a smaller boundary layer than the AblTBw case ($\bar{T}_w(x)$ obtained from the Abl case). Similarly, the self-similar mass injection between $x = 0\text{-}4$ m assumed by the SSBw case appears to be smaller than the one obtained from the Abl case (also featured in the AblTBw and AblBwCstT cases). This results in the smaller boundary-layers observed for the SSBw cases in Fig. 11.3 with respect to the AblTBw and AblBwCstT ones.

Figure 11.4#i displays the corresponding second-mode growth rates, obtained from the base-flow profiles in Fig. 11.3. The stronger mass injection in the first flight-envelope points is seen to result in a larger difference between the noBw and the blowing cases. As the Mach number and surface injection decrease, all boundary conditions result in closer predictions of the perturbation growth rates. For the flight-envelope points with a non-negligible mass injection (Fig. 11.4a-c), the increasing surface injection assumed by the different boundary conditions, mentioned in the previous paragraph, results in practically identical maximum growth rates, yet in a displacement of this maximum to lower frequencies. The use of the Abl temperature profile (AblTBw case) rather than a constant wall temperature obtained with Eq. 11.2 (AblBwCstT case) is seen to systematically predict lower perturbation growth rates for all flight-envelope points. This is associated to the well-known destabilizing effect [12, 15] of cooled walls.

The normalized perturbation-amplitude functions for the most unstable frequency (Fig. 11.4#ii-iii) are also practically coincident, displaying only minor vertical displacements associated to the commented variation of the boundary-layer size (see Fig. 11.3).

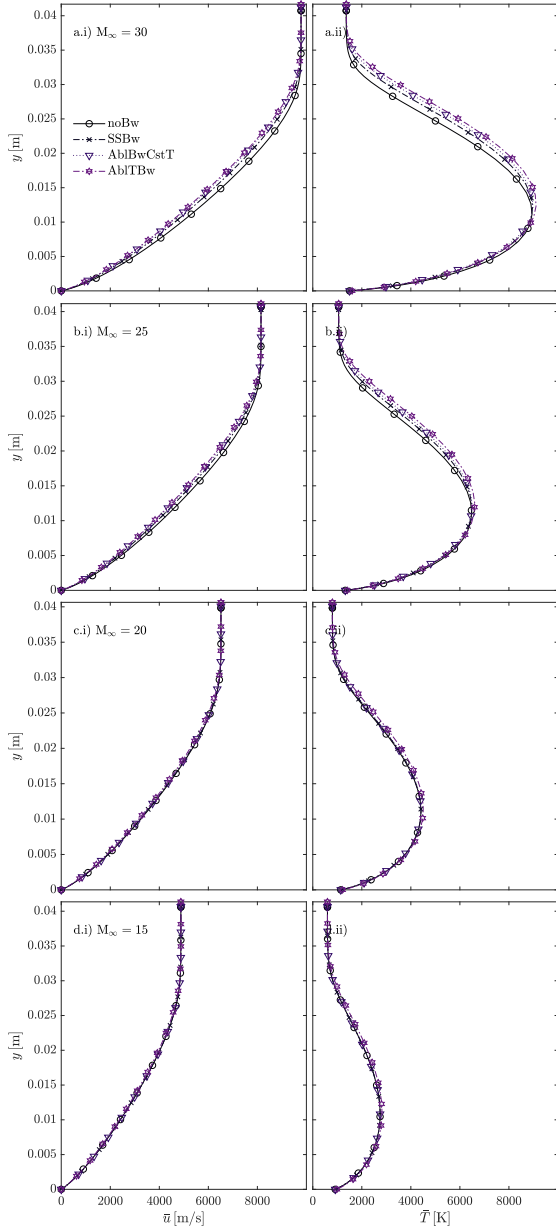


Figure 11.3: Basic-state profiles for cases with a CPGCE flow assumption and various surface boundary conditions at $x = 4$ m. Preshock conditions in a-d correspond to the four flight-envelope points in Table 11.1.

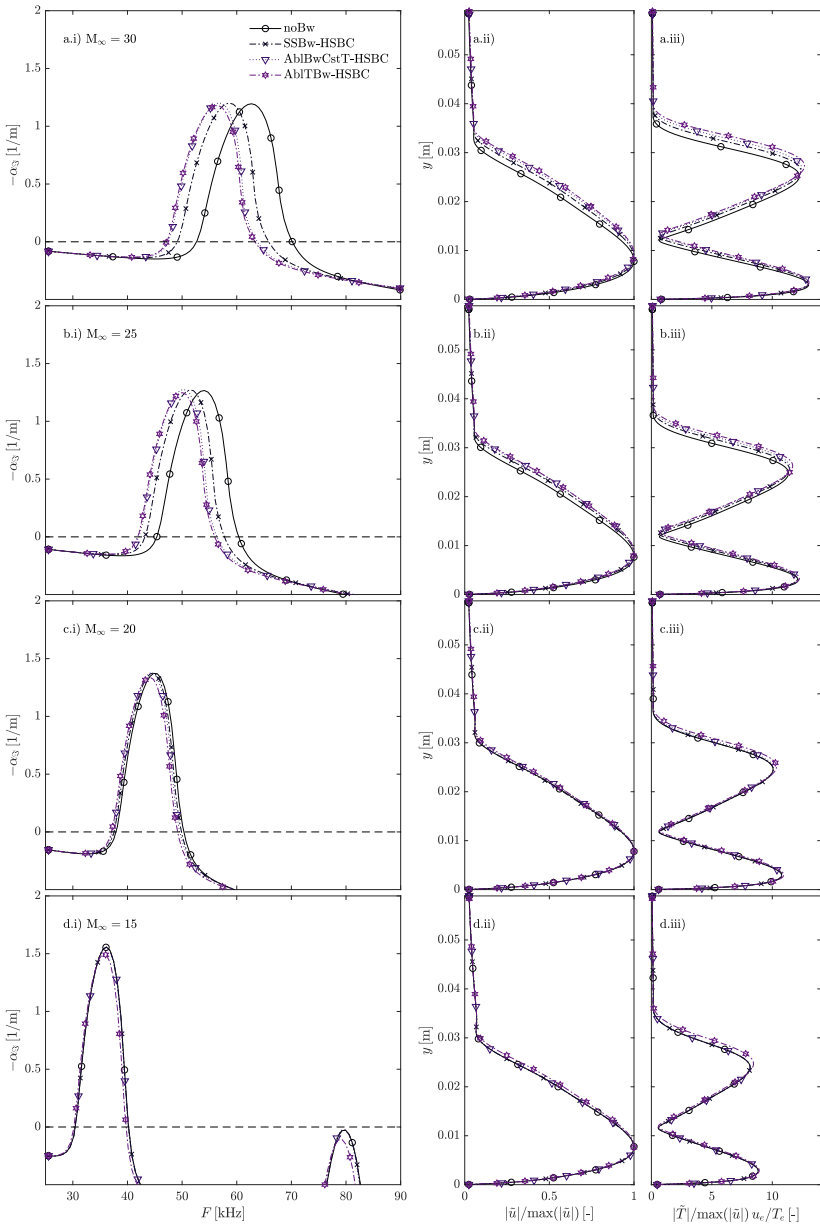


Figure 11.4: Second mode instability characteristics for cases with a CPGCE flow assumption and various surface boundary conditions at $x = 4 \text{ m}$: perturbation growth rates as a function of the perturbation frequency (i), and non-dimensional velocity (ii) and temperature (iii) perturbation amplitude profiles for the most unstable frequency. Preshock conditions in a-d correspond to the four flight-envelope points in Table 11.1.

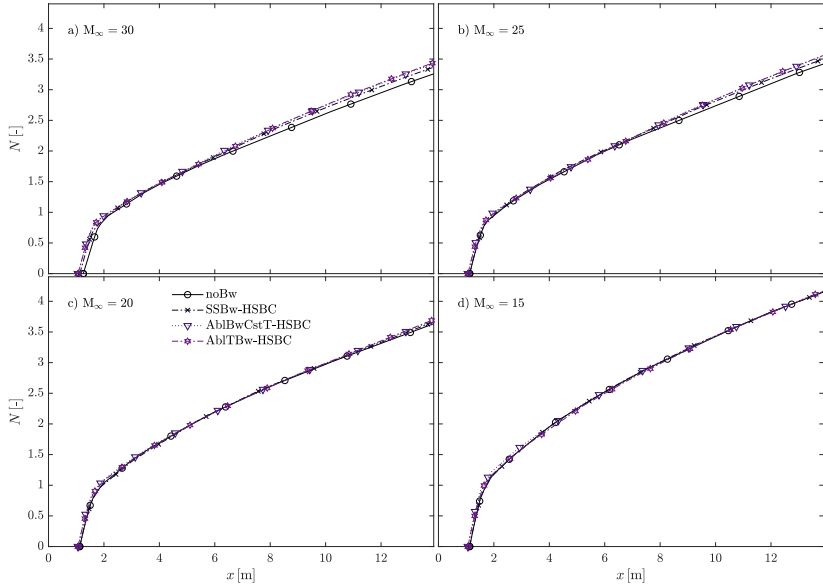


Figure 11.5: Second mode N -factor envelopes for cases with a CPGCE flow assumption and various surface boundary conditions. Preshock conditions in a-d correspond to the four flight-envelope points in Table 11.1.

The corresponding N -factor envelopes, obtained from integrating the perturbation growth rates along the streamwise direction for various constant perturbation frequencies between 10 and 100 kHz are presented in Fig. 11.5. The larger mass injection associated to the flight-envelope points with a higher pre-shock Mach number (Fig. 11.5a-b) is seen to introduce an increase in the N -factor envelopes with respect to the non-blowing cases (noBw). For the flight-envelope points with a lower mass injection, the difference associated to the surface injection of mass is negligible (Fig. 11.5c-d). The differences in the temperature and mass-flow wall profiles imposed by the blowing cases (SSBw, AblBwCstT and AblTBw) are seen to lead to negligible discrepancies in the ultimate N -factor envelopes. This suggests that matching the total injected mass flow and the total surface internal energy is sufficient for the accurate modeling of the development of second-mode instabilities.^a

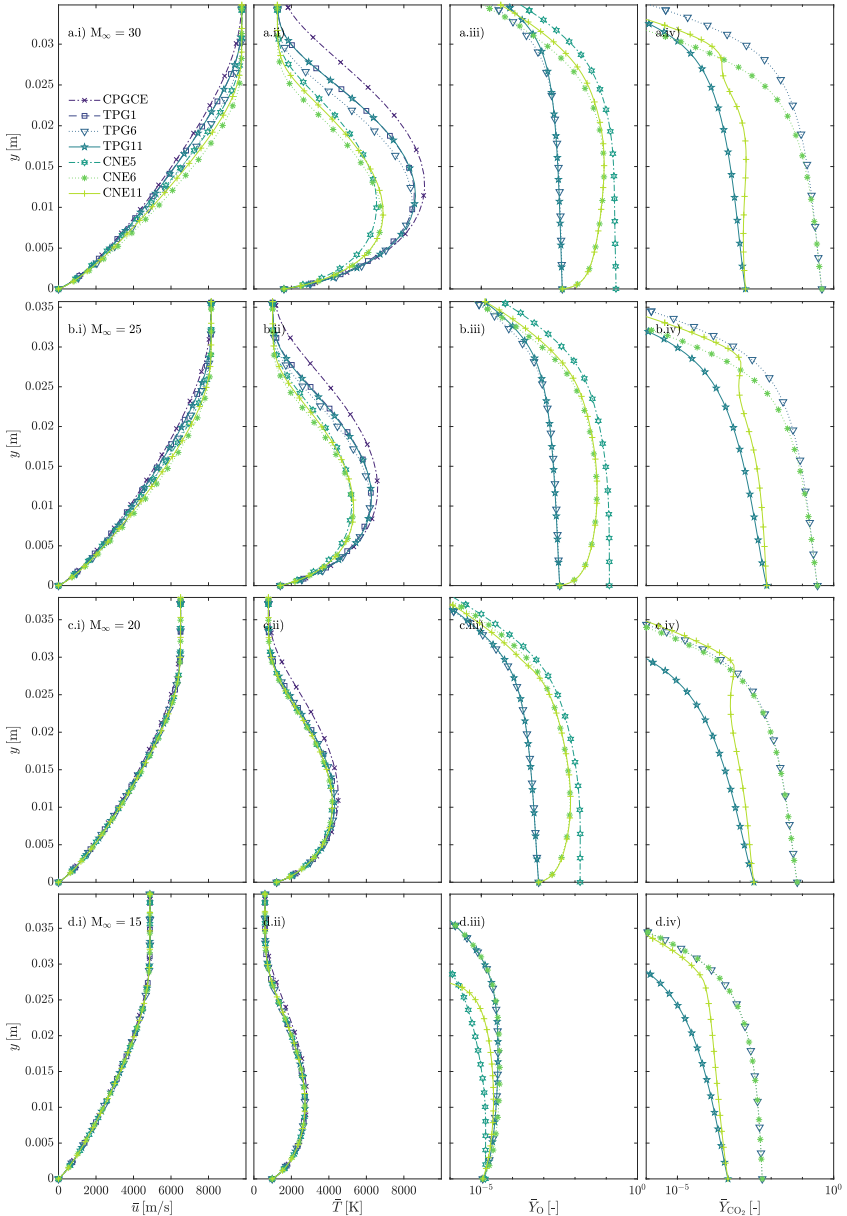


Figure 11.6: Basic-state profiles for cases with an *AblTBw* boundary condition and various flow assumptions with the same transport models at $x = 4$ m. Preshock conditions in a-d correspond to the four flight-envelope points in Table 11.1.

11.3.3 Vibrational excitation and air chemistry effects

Figure 11.6 shows a comparison of the laminar base-flow profiles obtained using the AblTBw boundary condition, which features the same injection and temperature profiles as the Abl case. The various flow assumptions compared share the same transport model (CE) and feature mixtures without carbon species (CPGCE, TPG1, and CNE5), exclusively with CO₂ injected through the wall (TPG6 and CNE6), and with all the ablation-subproducts (TPG11 and CNE11). The wall concentration profiles for the TPG6, CNE6, TPG11 and CNE11 assumptions correspond to those in Fig. 11.2. The different subfigures in Fig. 11.6a-d correspond to the various flight-envelope points detailed in Table 11.1.

Fig. 11.6 suggests that the CPG flow assumption, is not valid for such a range of temperatures, since for all flight-envelope points, it predicts an overly large boundary layer. This implies that the excitation of the internal energy modes cannot be faultlessly neglected. Comparing the results including the excitation of internal energy modes (TPG and CNE), they lead to practically identical velocity and temperature profiles for the two last flight-envelope points (Fig. 11.6c-d). Contrarily, for the two first flight-envelope points (Fig. 11.6a-b), molecular dissociation appears to gain importance, and consequently the boundary layers predicted by the CNE assumptions are cooler than those predicted by their non-reacting counter parts (TPG). Regarding the influence of the gas composition (distinguishing TPG1, TPG6 and TPG11, or CNE5, CNE6 and CNE11) the injection of CO₂ at the wall (TPG6 and CNE6) appears to introduce the largest boundary layer cooling in Figs. 11.6a-b. The other two TPG assumptions (TPG1 and TPG11) present practically identical temperature profiles, whilst they do display a slight difference between the other two CNE assumptions (CNE5 and CNE11). The injection of the ablation subproducts (CNE11) appears to result in a boundary layer that is cooler than that over a non-catalytic wall (CNE5).

The concentration profiles (Figs. 11.6#.iii-iv) present significant differences between the various flow assumptions, but display similar trends for the four flight-envelope points (Figs. 11.6a-d). The concentration of atomic oxygen (O) at the wall is imposed equal for the TPG6, TPG11, CNE6 and CNE11 flow assumptions. The profiles in Figs. 11.6#.#.iii display this, together with an increase in the O concentration in the bulk of the flow when assuming CNE6 or CNE11 with respect to that corresponding to the TPG6 or TPG11 assumptions. This is a consequence of the dissociation that the CNE assumptions consider and the TPG ones neglect. The O concentration obtained with the CNE5 assumption, which features a non-catalytic condition, differs from the others. The CNE5 assumption predicts stronger oxygen dissociation than the CNE6 and CNE11 ones for the three first

^aNote that this remark applies due to the absence of strong discontinuities in the wall boundary condition. As seen in § 9.1 and 9.2, the presence of such discontinuities can have a dramatic effect on the development of instabilities due to the excitation of distinct frequencies.

flight-envelope points (Figs. 11.6a-c.iii). This is not the case for the $M_\infty = 15$ point (Fig. 11.6d.iii) where it is actually lower. However, the low chemical activity present in this point makes the aforementioned difference unimportant.

Regarding the CO_2 concentration profiles in Fig. 11.6#.iv, one can distinguish the distinct values of the CO_2 mass fraction imposed on the 6-species and 11-species mixtures (see Fig. 11.2). This difference then conditions the concentration of CO_2 throughout the boundary layer. Moreover, since the CNE6 assumption neglects all chemical activity involving CO_2 , it can only diffuse into the boundary layer. However, the CNE11 assumption does have several reactions leading to the creation or destruction of CO_2 (see § J.14), thus explaining the profiles in Fig. 11.6#.iv.

Figure 11.7#i presents the corresponding growth rates for the various aforementioned flow assumptions. Overall, the observed trends are what one would expect from what was seen in Fig. 11.6. The difference between the CPGCE and TPG1 growth rates confirms the assertion made after comparing the boundary-layer profiles in Fig. 11.6 – the excitation of internal energy modes cannot be neglected for the four flight-envelope points under consideration. Doing so (CPGCE) results in an underprediction of the perturbation growth rates.

Comparing the flow assumptions accounting for internal-energy-mode excitation (TPG and CNE) they present identical predictions for the two last flight-envelope points (Fig. 11.7c-d.i). This confirms what was hypothesized based on the profiles in Fig. 11.6 – molecular dissociation can be neglected for the two last flight-envelope points. This is not the case for the two first points, where the growth rates present substantial differences depending on the CNE or TPG flow assumption that is employed. The boundary-layer cooling introduced by the chemical activity (accounted for by the CNE assumptions but not the TPG ones) appears to destabilize the boundary layer, resulting in higher perturbation growth rates in Figs. 11.7a-b.i. Regarding the composition of the injected gas, it is clear that modeling the exact ablation sub-product composition (TPG11 and CNE11) or unifying all carbon products into a single species – CO_2 (TPG6 and CNE6) leads to very similar perturbation growth rates, only differing slightly in the high-frequency content. However, neglecting carbon species altogether (TPG1 and CNE5) or imposing a non-catalytic condition (CNE5) are seen to significantly underpredict the perturbation growth rates.

The normalized perturbation-amplitude functions for the most unstable frequency (Fig. 11.7#.ii-iii) do not present major differences in their shape. They display minor vertical displacements associated to the commented variation of the boundary-layer size (see Fig. 11.6). One can therefore state that the stabilizing effect of the perturbation chemical source terms ($\dot{\omega}'_s$), which were seen in § 10.4 to also introduce major differences in the temperature perturbation amplitude, is not very significant for the considered flight-envelope points.

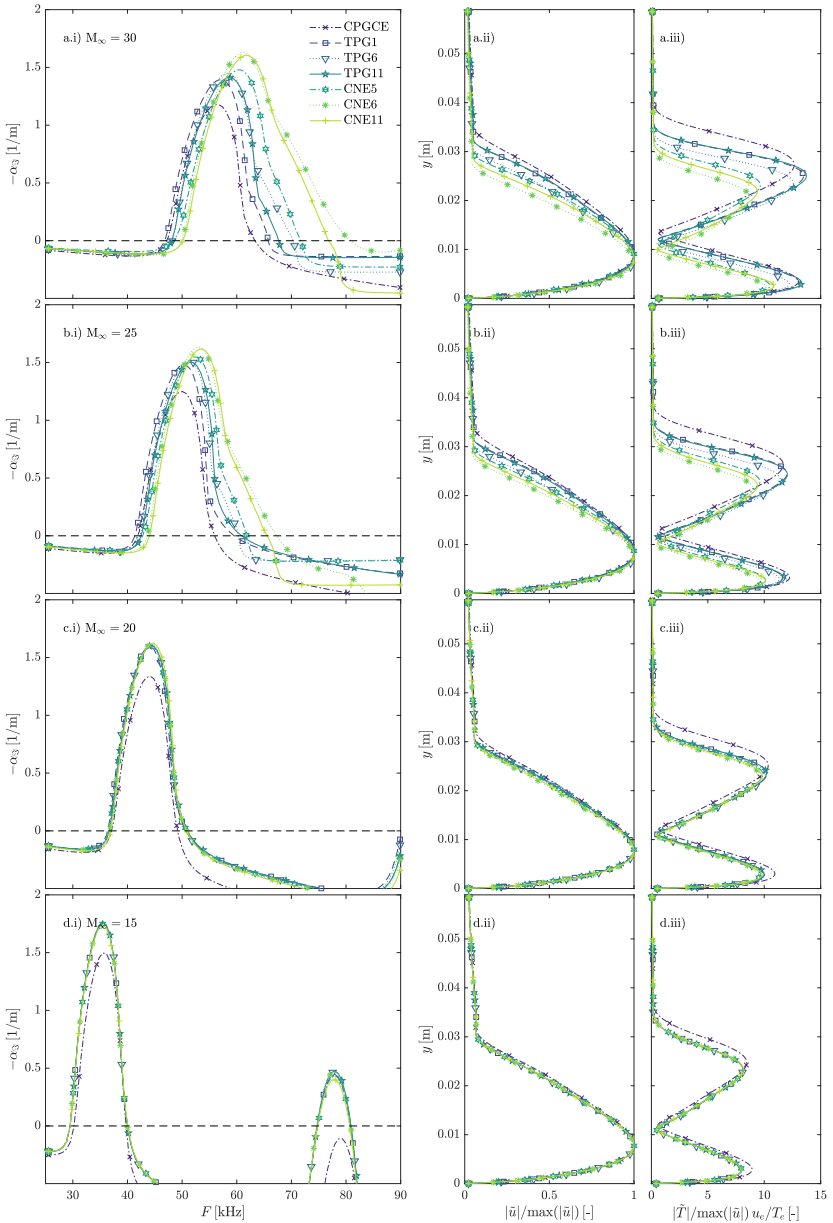


Figure 11.7: Second mode instability characteristics for cases with an AbITBw boundary condition and various flow assumptions with the same transport models at $x = 4\text{ m}$: perturbation growth rates as a function of the perturbation frequency (i), and non-dimensional velocity (ii) and temperature (iii) perturbation amplitude profiles for the most unstable frequency. Preshock conditions in a-d correspond to the four flight-envelope points in Table 11.1.

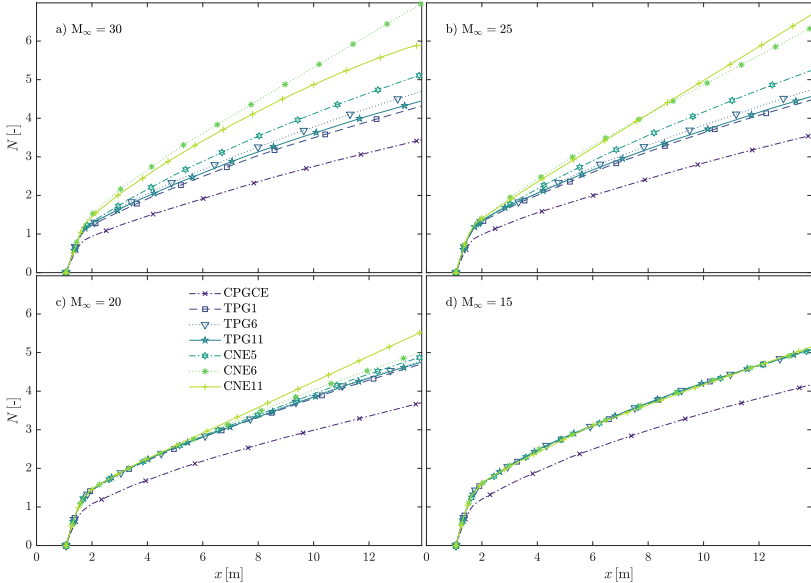


Figure 11.8: Second mode N -factor envelopes for cases with an AblITBw boundary condition and various flow assumptions with the same transport models. Preshock conditions in a-d correspond to the four flight-envelope points in Table 11.1.

The corresponding integrated N -factor envelopes, covering a frequency range between 10 and 100 kHz are presented in Fig. 11.8. Most of the trends that were pointed out for a single streamwise location are preserved when integrating over the entire x range. There are, however, also a few notable differences. For instance, the chemical activity, which was believed to be completely negligible for the third flight-envelope point leads to minor differences in the N -factor envelopes at the later streamwise locations in Fig. 11.8c. The CNE11 assumption is seen to be the one predicting a larger increase in the N factor, suggesting that its cause is the chemical activity occurring between the carbon species and the air species (accounted for by the CNE11 assumption, but not by the others). Additionally Fig. 11.8a displays a large difference in the N -factor envelopes predicted by the flow assumptions injecting a gas with the exact ablation-subproduct composition (TPG11 and CNE11) and those predicted with one injecting a unique carbon species (TPG6 and CNE6). This is contrary to what is observed in Fig. 11.7a.i, suggesting that the minor differences that are patent in Fig. 11.7a.i increase when advancing downstream and ultimately lead to the major differences in the N -factor envelopes displayed in Fig. 11.8a.

Similar trends to those observed in Figs. 11.6-11.8 are also observable for the SSBw and AblBwCstT base-flow boundary conditions. For the sake of compact-

ness, such comparisons are left out of the present analysis.

11.3.4 Surface chemistry effects

Figure 11.9 compares the base flowfield obtained with the chemically-reacting eleven-species flow assumption (CNE11) and with different ablating boundary conditions. The excellent agreement of the profiles between the three sets of boundary conditions for all four flight-envelope points suggests that the prescription of the wall profiles coming from more detailed simulations amounts to very similar results in the ultimately obtained base flow.

Figure 11.10#.*i* presents the corresponding growth-rate comparison, which displays the same trends for the four flight-envelope points (a-d). The use of the various base-flow boundary conditions (AblTBw, AblT or Abl) with the homogeneous stability condition (HSBC) leads to practically coincident instability growth-rate predictions. Similarly, the use the ATSBC (isothermal yet with the linearized species mass balance conditions) does not introduce a significant modification of the predicted growth rates. The employment of a radiative-equilibrium wall condition (RESBC) is seen to predict a larger instability growth rate than the HSBC and the ATSBC. Similarly, imposing the full surface energy balance (ASBC), which also considers the injection of enthalpy as a consequence of the surface ablation, presents a negligible difference from imposing the RESBC. Radiation therefore appears to be the most destabilizing of the phenomena in this subsection.

The non-dimensional perturbation velocity (Fig. 11.10#.*ii*) and temperature (Fig. 11.10#.*iii*) amplitudes at the most unstable frequency present no discernible differences between the various sets of conditions being compared.

The integrated N -factor envelopes, displayed in Fig. 11.11a-d for the various flight-envelope points, present the same trends previously pointed out in the growth-rate plots (Fig. 11.10#.*i*). The use of the RESBC systematically displaces the N -factor envelope vertically for all flight-envelope points. Additionally, the use of the linearized surface species mass balance conditions instead of the species momentum conditions leads to a slight decrease in the N -factor envelope. That is, for the flight-envelope points with a relevant ablation rate – the last point ($M_\infty = 15$) shows a negligible difference between the predictions done by the RESBC and the ASBC.

One may think that the RESBC is more physically-accurate than the HSBC, since it includes a modeling of the surface perturbation energy balance. However, as commented in § 6.1.2 it is also fair to argue that, given the high frequency of second-mode waves, and the high thermal inertia of the graphite wall, temperature instabilities cannot adapt fast enough to satisfy the RESBC. The near-zero reaction time with which radiation occurs, however, suggests that it should, in general, be accounted for in a perturbation energy-balance condition. It is therefore unclear

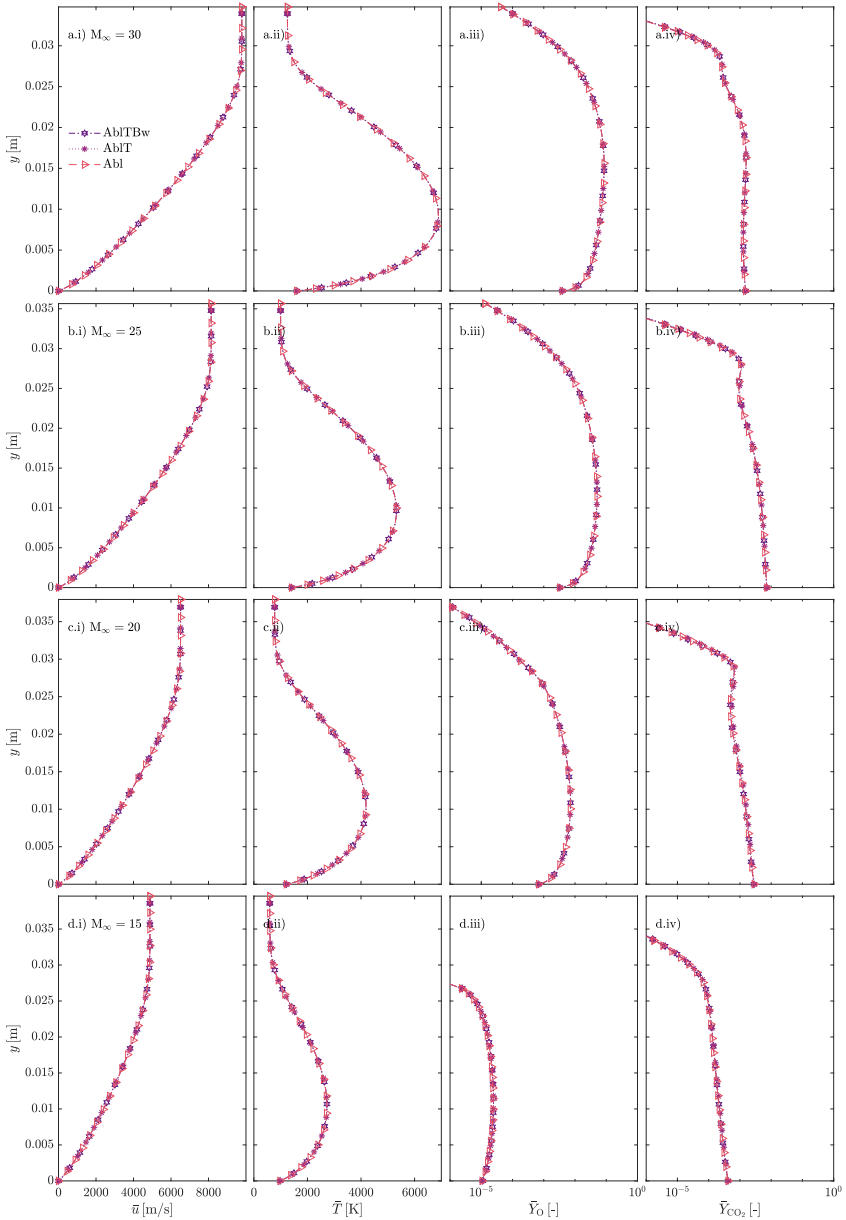


Figure 11.9: Basic-state profiles for cases with a CNE11 flow assumption and various surface boundary conditions at $x = 4\text{ m}$. Preshock conditions in a-d correspond to the four flight-envelope points in Table 11.1.

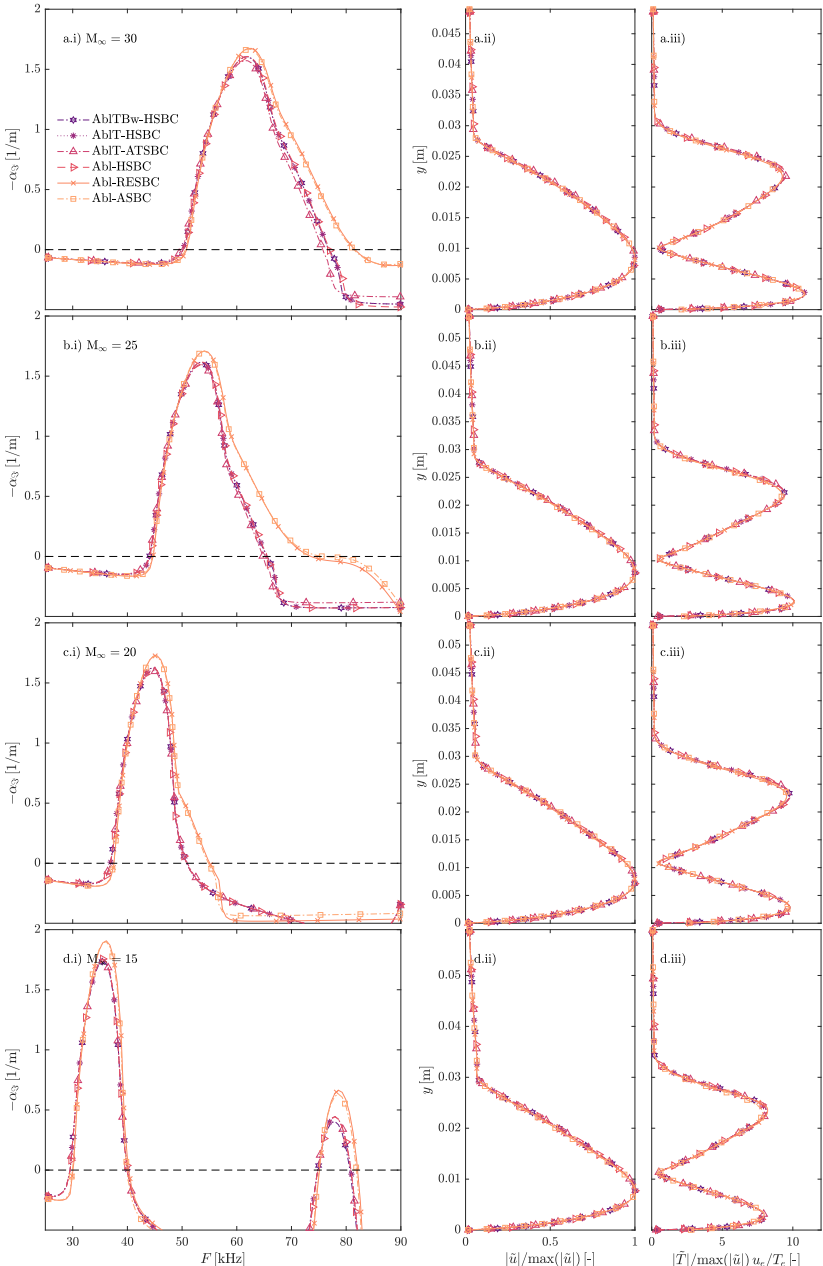


Figure 11.10: Second mode instability characteristics for cases with a CNE11 flow assumption and various surface boundary conditions at $x = 4 \text{ m}$: perturbation growth rates as a function of the perturbation frequency (i), and non-dimensional velocity (ii) and temperature (iii) perturbation amplitude profiles for the most unstable frequency. Preshock conditions in a-d correspond to the four flight-envelope points in Table 11.1.

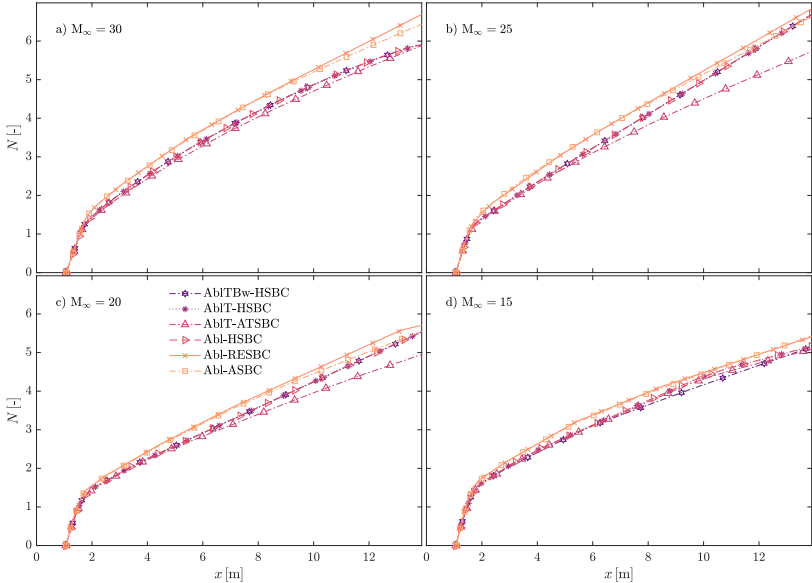


Figure 11.11: Second mode N -factor envelopes for cases with a CNE11 flow assumption and various surface boundary conditions. Preshock conditions in a-d correspond to the four flight-envelope points in Table 11.1.

whether it is preferable to employ the ASBC, the RESBC, or the HSBC.

11.3.5 CPG assumption with different transport models

It is noteworthy to compare the predictions made in CPG conditions with Sutherland's viscosity law (CPGS) and with the CE transport model (CPGCE), better suited for high temperatures. Similarly to what was observed in § 10.3 and 10.4.2.5, the inaccuracies associated to the use of Sutherland's model appear to compensate for those associated to neglecting the excitation of internal energy modes. The result is that the N -factor envelopes obtained with the CPGS assumption and displayed in Fig. 11.12 are closer to those of the TPG1 assumption than those of the CPGCE one. One could therefore be inclined to affirm that Sutherland's law is in fact more accurate than the CE transport model. However, the apparent modeling improvement is purely circumstantial and must not be associated to Sutherland's law providing a more accurate description of the gas physics than Chapman & Enskog's model.

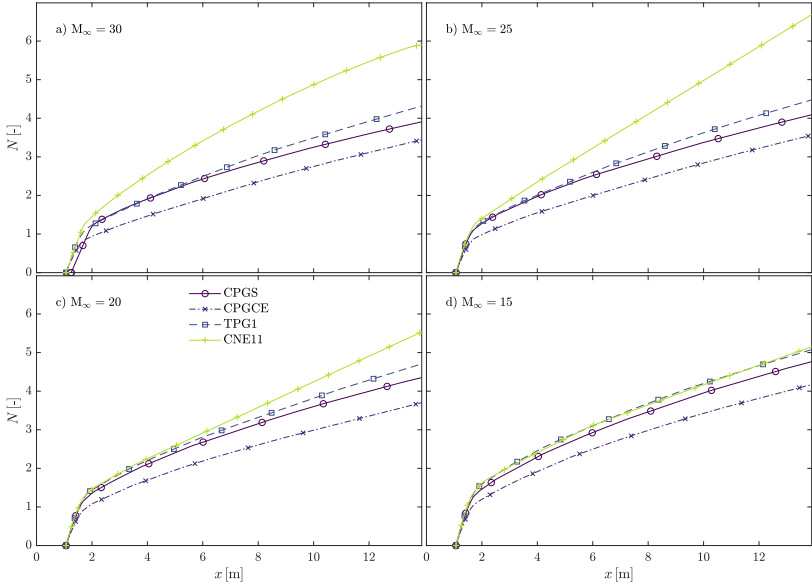


Figure 11.12: Second mode N -factor envelopes for cases with an AbLTBw boundary condition and various flow assumptions. Preshock conditions in a-d correspond to the four flight-envelope points in Table 11.1.

11.3.6 Influence of the transport models on the fully-ablating case

In order to investigate the importance of transport modeling in an ablating boundary layer, the two sets of models mentioned at the beginning of the chapter are compared on an 11-species CNE flow assumption, with the Abl base-flow boundary condition, and the perturbations modeled with the ASBC.

Figure 11.13 shows the base-flow profiles obtained with the BEW+cstSc model with $Sc = 0.5$ compared to those obtained with the state-of-the-art CE+SM models for the four flight-envelope points in Table 11.1. The differences in the temperature profile and the boundary-layer height appear to be less than those reported in § 10.1, where these differences were linked to the major inaccuracies in the stability and transition-onset predictions. These differences also appear to be practically constant across the different flight-envelope points.

The N -factor envelopes are displayed in Fig. 11.14, together with individual constant-frequency N curves for the BEW and $Sc = 0.5$ set of models. The observable differences are significantly lower than what was seen in § 10.1, suggesting that the differences in the growth rates associated to the transport model that were reported in Ref. 6 are not present at all the streamwise stations. The

Phenomenon	Case A	Case B
Mass injection	CPGCE-noBw	CPGCE-AblBwCstT
Wall temperature	CPGCE-AblBwCstT	CPGCE-AblTBw
Internal-energy excitation	CPGCE-AblTBw	TPG1-AblTBw
Ablation-species outgassing	TPG1-AblTBw	TPG11-AblTBw
Air-species chemistry	TPG1-AblTBw	CNE5-AblTBw
Carbon-air-species chemistry*	CNE5-AblTBw	CNE11-AblTBw
Surface radiation \tilde{T} BC	CNE11-AblTBw	CNE11-Abl-RESBC
Surface chemistry \tilde{q} BC	CNE11-Abl-RESBC	CNE11-Abl-ASBC

* the ΔN corresponding to ablation-species outgassing must be subtracted.

Table 11.3: Pairs of cases used to compute the N -factor jump. All cases without a specific stability boundary-condition acronym employ the HSBC.

ultimate result is that the error in the N -factor envelopes committed due to the use of one or another transport model is significantly lower than what was reported in the model comparison of § 10.1 and is therefore assumable.

11.3.7 N -factor budgets of the physical phenomena

Profiting of the decoupling performed with the sets of flow assumptions (§ 11.1) and boundary conditions (§ 11.2) compared in this chapter, it is possible to obtain budgets for the contribution of the various coexisting physical phenomena to the ultimate N -factor envelopes. Table 11.3 presents a summary of the test cases employed to evaluate the relative importance of the different physical mechanisms. By subtracting the N factor of case B to that of case A (see Table 11.3) at $x = 12$ m for the various flight-envelope points (see Table 11.1) one reaches the phenomenon N -factor budgets displayed in Fig. 11.15.

Figure 11.15 constitutes an effective summary of the various trends observed throughout the chapter. Most considered flight-envelope points are seen to have internal-energy excitation as the phenomenon that contributes the most to the N -factor envelope. Mass injection is seen to have an increasing contribution to the N factors as the pre-shock Mach number increases, whilst the wall temperature profile negligibly modifies the envelopes. The relative importance of ablation-species blowing and air-species chemistry is seen to increase with M_∞ . Similarly, the relative contribution of carbon-air-species chemistry is seen to strongly increase between $M_\infty = 15\text{--}25$, and slightly decrease for $M_\infty = 30$. Regarding the modeling of instabilities at the wall, the use of the surface radiative-equilibrium condition, rather than a homogeneous condition on the temperature perturbation amplitude (\tilde{T}), is seen to increase the predicted N -factors. However, as discussed in § 11.3.4 it is unclear whether one should employ one (Eq. 6.16) or the other (Eq. 6.21).

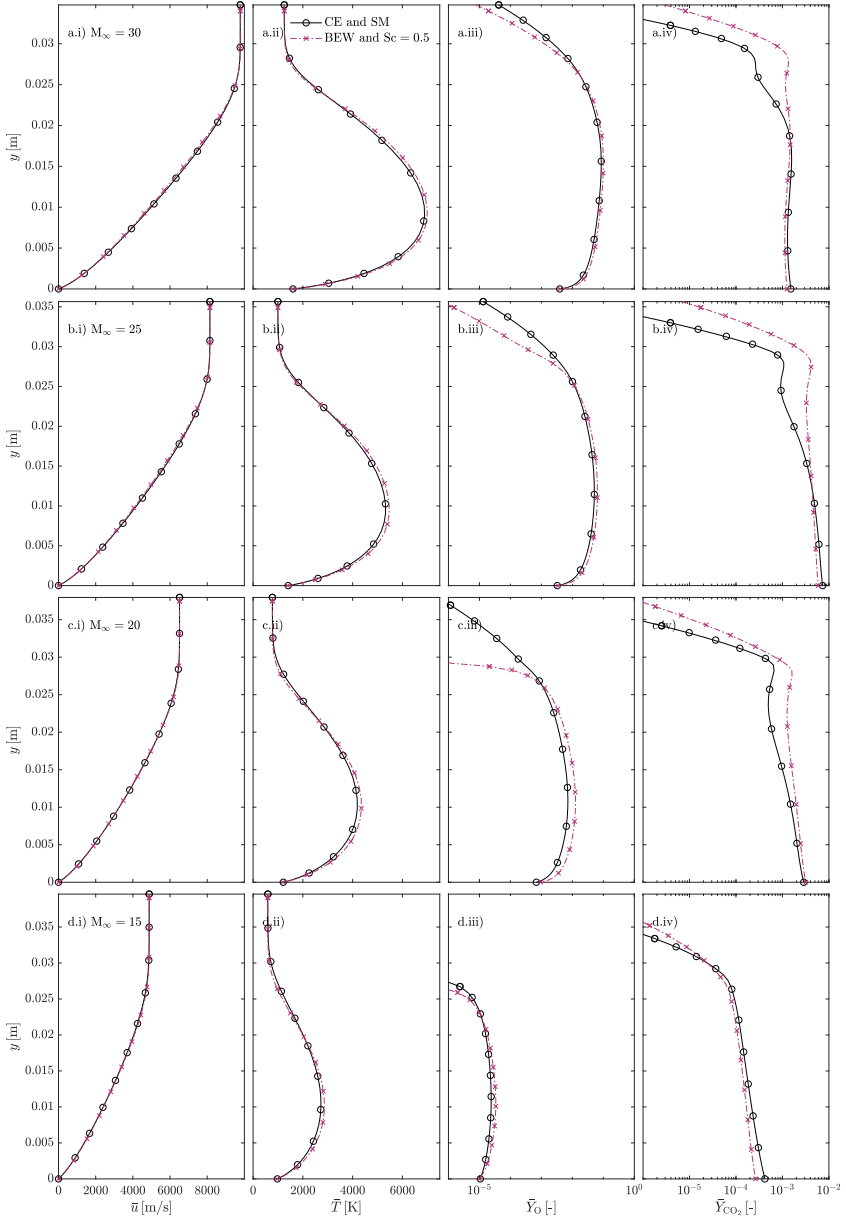


Figure 11.13: Basic-state profiles obtained with the BEW-cstSc or with the more accurate CE-SM transport models at $x = 4\text{ m}$ for the CNE11-Abl-ASBC case, and for the flight-envelope points in Table 11.1.

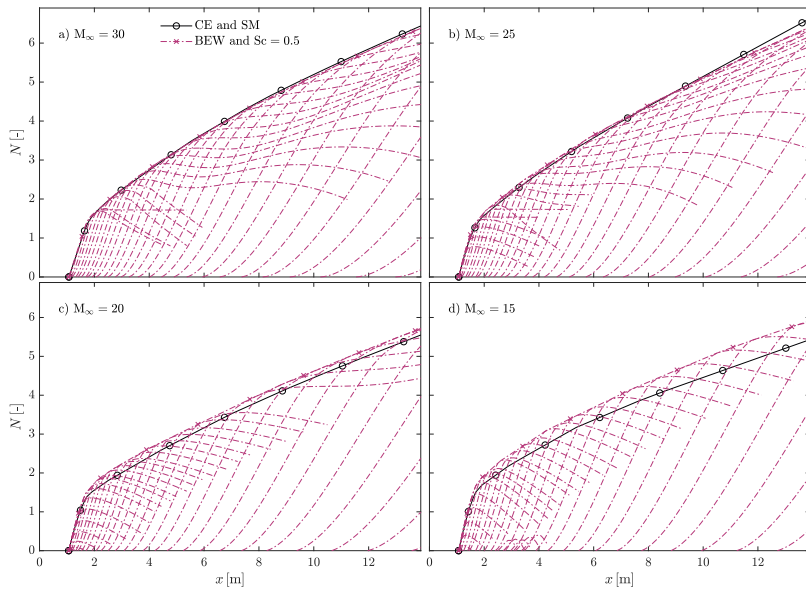


Figure 11.14: Second mode N -factor envelopes obtained with the BEW-cstSc or with the more accurate CE-SM transport models at $x = 4$ m for the CNE11-Abl-ASBC case, and for the flight-envelope points in Table 11.1.

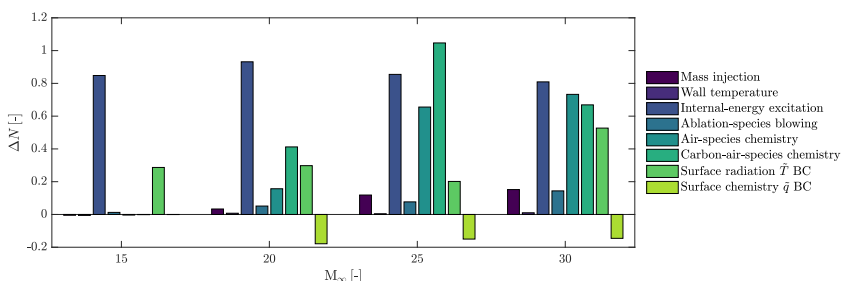


Figure 11.15: Second mode N -factor budgets at $x = 12$ m of the various physical phenomena (see Table 11.3) for the flight-envelope points in Table 11.1.

The inclusion of the surface-mass- and energy-balance conditions on the perturbation amplitudes (\tilde{q}) is seen to have a small yet stabilizing effect on the N -factor envelopes.

11.3.8 Linearized Rankine-Hugoniot relations

Due to the high Mach numbers featured in the presented comparisons, it is questionable whether or not one can faultlessly impose a Dirichlet condition on the freestream boundary. In order to assess this hypothesis, all the cases in the test matrix in Table 11.2 for all the flight-envelope points in Table 11.1 are revisited yet imposing the linearized Rankine-Hugoniot relations (see § 6.2.1) at the free-stream boundary. The resulting modification of the N -factor envelopes is presented in Fig. 11.16. The resulting absolute values of ΔN are mostly small, however, they reach non-negligible levels for the mixture allowing for a stronger chemical activity (CNE11) at the later downstream locations. At such locations, chemistry has been acting on the flow for a longer stretch. A stronger chemical activity, more specifically the subsequent interdiffusion of the various species, is linked with the appearance of supersonic modes (see § 10.4.2.4). These modes do not decay exponentially in the inviscid flow region outside of the boundary layer, having non-negligible amplitudes when reaching the shock boundary. It is therefore understandable that they experience a stronger modulation due to the use of a distinct boundary condition (the linearized Rankine-Hugoniot relation instead of a Dirichlet condition). The marginal effect of the shock is strongly case-dependent – it can either increase or decrease the N factor of the most amplified instability.

Aside from the mentioned outlying cases, linked to the decay of supersonic modes, the overall trend is for higher free-stream mach numbers to result in a bigger shock-related deviation of the N factors. This is understandable, due to the closer position of the shock to the surface in such cases. Having the shock at a lower wall-normal position implies that it will interact with the decaying perturbation when it has a larger amplitude, thus conditioning it in a more significant manner.

11.4 Conclusions

An investigation was carried out in order to effectively decouple the various physical phenomena that coexist in the boundary layer developing around an ablating TPS. Focusing on four points in the flight envelope of a typical aggressive reentry trajectory, laminar boundary-layer simulations were performed, followed by an analysis of the development of second-mode instabilities using LST and the e^N method.

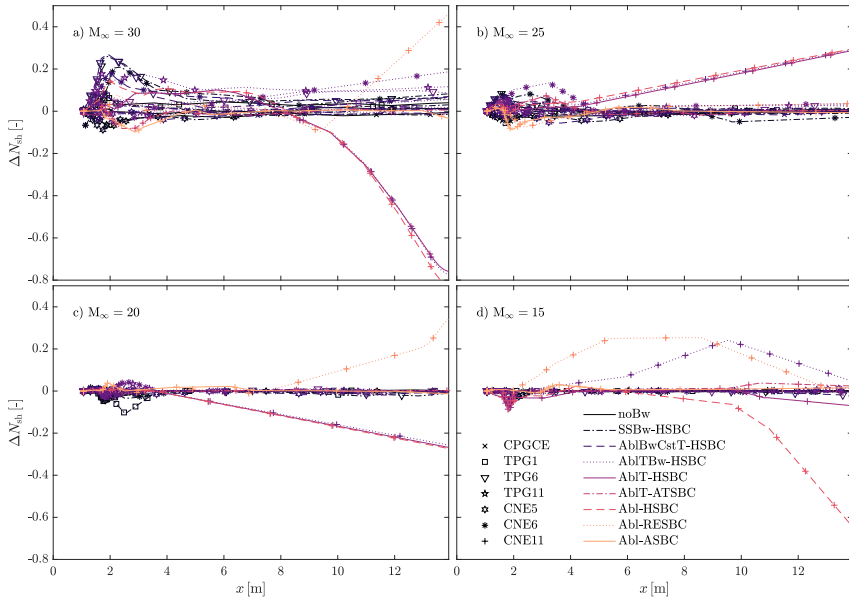


Figure 11.16: Second mode N-factor-envelope differences between using a free-stream shock (§ 6.2.1) or Dirichlet condition (Eq. 6.27). All test cases in Table 11.2 and all flight-envelope points in Table 11.1 are presented together.

The comparison of the CPGCE cases allowed to conclude that the mass injected as a result of the TPS decomposition has an increasing impact on the predictions for increasing pre-shock Mach numbers and the consequently larger ablation rates. The use of various surface mass-flow and temperature profiles, with the same total mass-flow and TPS internal energy respectively, resulted in no substantial differences in the predicted N -factor envelopes. Such a conclusion must, however, be assimilated with caution. The considered injection profiles did not feature discontinuities such as those seen in § 9.1 and 9.2 to significantly modify instability development. Moreover, no modeling was done on the wall-normal velocity perturbation, which was seen in § 9.3 to have a tremendous impact on the predictions.

The comparison of the various flow assumptions with equivalent mass-injection profiles concluded that the excitation of the species' internal energy modes was non-negligible for the four considered flight-envelope points. Its contribution to the N -factor envelope was fairly constant for all points. After internal-energy excitation, the second physical phenomenon mostly contributing to the destabilization and consequent increase in the N factors is the chemistry of air species. Its relative importance also increases with the pre-shock Mach number. Both internal-energy excitation and air-species chemistry were seen to modify the instability characteristics, mostly through the cooling of the laminar boundary-layer profiles.

The injection of the carbon species that result from the ablation of the graphite surface were seen to increase the predicted growth rates and N -factor envelopes. This is once again linked to the relatively smaller boundary layer size that is featured as a consequence of injecting gases that are heavier than air (see § 9.2).

The attempt to substitute all ablation subproducts with a unique non-reacting carbon species (CO_2) was seen to overpredict the N -factor envelopes, despite the good agreement of the perturbation growth rates at a single streamwise location ($x = 4 \text{ m}$).

Using a radiative-equilibrium thermal boundary condition, instead of a homogeneous one, was seen to substantially increase the perturbation growth rates and the subsequent N -factor envelopes. However, it is unclear whether one should employ the former or the latter, due to the high frequency of the instabilities, the high thermal inertia of the graphite wall, and the near-zero activation time required for radiation.

The comparisons performed return better CPG predictions when using Sutherland's law than when using the state-of-the-art Chapman-Enskog transport model. However, such an observation was deemed merely coincidental, since Sutherland's law is well-known to be a more inaccurate model than Chapman & Enskog's at the high temperatures featured in the considered conditions.

Finally, a comparison of the effect of transport modeling on the most

physically-inclusive case (CNE11-Abl-ASBC) was performed. The extensively-used Blottner-Eucken-Wilke viscosity and thermal-conductivity model, together with the constant-Schmidt-number diffusion model, were compared to the state-of-the-art Chapman-Enskog and Stefan-Maxwell models. Less sophisticated models, when compared to the state-of-the-art ones, resulted in negligible differences in the predicted base-flow profiles and N -factor envelopes. This result suggests that the high sensitivity of second-mode instabilities to the transport model, reported in § 10.1 may be more or less dramatic depending on the flow conditions.

The deployment of the shock boundary condition in the free-stream boundary, rather than a homogeneous Dirichlet condition was seen to have a minor impact on the predicted N -factor envelopes. An exception to this being cases with a strong chemistry-related modulation of the flow, and the associated supersonic modes. Such cases displayed non-negligible shock-related deviations in the N factors of the most-amplified instabilities.

References

- [1] F. Miró Miró, E. S. Beyak, F. Pinna, and H. L. Reed. *High-enthalpy models for boundary-layer stability and transition*. Physics of Fluids, [31\(044101\)](#), 2019.
- [2] M. J. Wright, D. Bose, G. E. Palmer, and E. Levin. *Recommended Collision Integrals for Transport Property Computations Part I: Air Species*. AIAA Journal, [43\(12\):2558–2564](#), 2005.
- [3] M. J. Wright, H. H. Hwang, and D. W. Schwenke. *Recommended Collision Integrals for Transport Property Computations Part II: Mars and Venus Entries*. AIAA Journal, [45\(1\):281–288](#), 2007.
- [4] A. Bellemans and T. E. Magin. *Calculation of Collision Integrals for Ablation Species*. In 8th European Symposium on Aerothermodynamics for Space Vehicles, Lisbon, Portugal, 2015.
- [5] C. Mortensen and X. Zhong. *Real-Gas and Surface-Ablation Effects on Hypersonic Boundary-Layer Instability over a Blunt Cone*. AIAA Journal, [54\(3\):980–998](#), 2016.
- [6] F. Miró Miró and F. Pinna. *On Decoupling Ablation Effects on Boundary-Layer Stability and Transition*. AIAA paper, [2019-2854](#), 2019.
- [7] F. Miró Miró, E. S. Beyak, D. Mullen, F. Pinna, and H. L. Reed. *Ionization and Dissociation Effects on Hypersonic Boundary-Layer Stability*. In 31st ICAS Congress, Belo Horizonte, Brazil, 2018. International Council of the Aeronautical Sciences.
- [8] P. Schrooyen. *Numerical simulation of aerothermal flows through ablative thermal protection systems*. PhD thesis, UCL, 2015.
- [9] R. M. Wagnild, G. V. Candler, I. A. Leyva, J. S. Jewell, and H. G. Hornung. *Carbon Dioxide Injection for Hypervelocity Boundary Layer Stability*. AIAA paper, [2010-1244](#), 2010.
- [10] F. Li, M. M. Choudhari, C.-L. Chang, and J. White. *Effects of injection on the instability of boundary layers over hypersonic configurations*. Physics of Fluids, [25\(10\)](#), 2013.
- [11] A. V. Fedorov and V. G. Soudakov. *Stability analysis of high-speed boundary-layer flow with gas injection*. AIAA paper, [2014-2498](#), 2014.
- [12] M. R. Malik. *Prediction and control of transition in supersonic and hypersonic boundary layers*. AIAA Journal, [27\(11\):1487–1493](#), 1989.

- [13] H. B. Johnson, J. E. Gronvall, and G. V. Candler. *Reacting hypersonic boundary layer stability with blowing and suction*. AIAA paper, [2009-938](#), 2009.
- [14] S. Ghaffari, O. Marxen, G. Iaccarino, and E. S. G. Shaqfeh. *Numerical simulations of hypersonic boundary-layer instability with wall blowing*. AIAA paper, [2010-706](#), 2010.
- [15] L. M. Mack. *Boundary-Layer Linear Stability Theory*. In Special Course on Stability and Transition of Laminar Flow, AGARD 709. AGARD, 1984.
- [16] G. Stuckert and H. L. Reed. *Linear Disturbances in Hypersonic, Chemically Reacting Shock Layers*. AIAA Journal, [32\(7\):1384–1393](#), 1994.
- [17] M. L. Hudson, N. Chokani, and G. V. Candler. *Linear stability of hypersonic flow in thermochemical nonequilibrium*. AIAA Journal, [35\(6\):958–964](#), 1997.
- [18] F. Pinna. *VESTA toolkit: a Software to Compute Transition and Stability of Boundary Layers*. AIAA paper, [2013-2616](#), 2013.
- [19] F. Pinna. *Numerical study of stability of flows from low to high Mach number*. PhD thesis, Università degli Studi di Roma La Sapienza, 2012.
- [20] M. Hermanns and J. A. Hernández. *Stable high-order finite-difference methods based on non-uniform grid point distributions*. International Journal for Numerical Methods in Fluids, [56:233–255](#), 2008.
- [21] P. Paredes, M. Hermanns, S. Le Clainche, and V. Theofilis. *Order 10^4 speedup in global linear instability analysis using matrix formation*. Computer Methods in Applied Mechanics and Engineering, [253:287–304](#), 2013.

12

Conclusions

This dissertation constitutes an advancement towards the accurate modeling, and subsequent better understanding, of some of the multiple physical phenomena simultaneously coexisting in ablation-transition problems, crucial for atmospheric entry missions. The transition of high-speed flows from a laminar to a turbulent regime, is investigated through a stability approach, since it is the development of flow instabilities that ultimately leads to turbulence.

The state of the art in the field was reviewed, laying out the various flow assumptions, stability theories, thermophysical models, and boundary conditions, together with their ground hypotheses and their range of applicability (chapters 2–6). This is presented with a unified variable-naming and unit convention, thus gathering the work of many authors, who oftentimes employed very different nomenclatures from one-another.

Two main tools were developed and verified, making the analysis possible – the DEKAF flow solver and VESTA’s ADIT (chapters 7 and 8). The former, a joint development with E. Beyak, K. Groot, and A. Moyes [1, 2], allows to solve laminar base-flow fields with a simplified 0th-order coupling between the inviscid and viscous (boundary-layer) region for simple vehicle geometries. The latter, built upon previous work by Pinna & Groot [3], allows to derive and implement in an automatic manner both the stability equations and the thermodynamic derivatives of the thermophysical gas properties.

The analysis of ablation-transition problems was subdivided into three main sections, tackling the consequences and implications of: surface outgassing (chapter 9), high-enthalpy gas effects like internal-energy-mode excitation, species in-

terdiffusion, dissociation and ionization (chapter 10), and the coupling of both and surface chemistry in gas-surface interaction scenarios (chapter 11). The various questions laid out in § 1.5 were specifically addressed.

How do base-flow inaccuracies propagate to the ultimate stability predictions?

Profiting of the high (spectral) accuracy of the DEKAF flow solver, an investigation was carried out on the propagation of base-flow inaccuracies to the ultimate stability predictions (§ 5.3). Errors in the resolution of the base-flow field of order ϵ appear to lead to errors in the predicted stability characteristics that are an order of magnitude lower. This suggests that Theofilis' estimation [4] on the base-flow accuracy requirements, when pursuing a certain level of precision in the stability predictions, was actually overly conservative. Moreover, the base-flow-stability maps presented for the various instability mechanisms, constitute an excellent guideline to be used by future researchers in the evaluation of the base-flow inaccuracy level that is acceptable for a desired final accuracy in the stability predictions. The analysis presented also highlights the importance of performing simultaneous base-flow-stability grid-convergence studies since a solution to the perturbation equations that is converged to an erroneous base flow remains an erroneous solution.

Can the e^N method be applied to wall-blowing scenarios?

The e^N method was successfully deployed on configurations with mass injection (§ 9.1). The use of the same N factor as in non-blowing scenarios was seen to provide an excellent agreement with the experimental results.

Does the porous-wall boundary condition, developed by Gaponov [5] and Fedorov *et al.* [6] for passive porous walls, present a modeling improvement in scenarios with mass injection?

The porous stability boundary condition (PSBC) was successfully validated against experiments for blowing configurations (§ 9.1). Indeed, the predictions made with LST and the e^N method lied closer to their experimental counter parts when using the porous boundary condition rather than the homogeneous one. The comparison of predicted and measured perturbation wave numbers, benefiting from the spatially-resolved data provided by the PLIF technique, allowed to assert that the underlying mechanism leading to transition in the experiments was the development of second-mode instabilities. The computations performed also shed light onto the various trends observed in the experiments. The porous layer was computationally seen to advance transition in the non-blowing case, due to the earlier excitation of frequencies that would have otherwise remained stable.

The associated advancement of transition was seen to prevail over the local damping of second-mode instabilities on the porous surface, ultimately advancing the transition front, as seen in the experiments. In blowing scenarios, the marginal effect of the porous surface was actually stabilizing. However, the net effect of both the porous surface and the outgassing combined was to advance transition. Non-parallel effects were not seen to introduce a significant modification of the observations made with LST.

What is the underlying reason for the advancement/delay of transition that was experimentally observed when injecting gases lighter/heavier than air [7, 8]?

After validating the porous boundary condition for blowing configurations, an investigation was carried out in § 9.2 on the influence of the injected-gas composition on the development of instabilities. The experimental observations made by Marvin & Akin [7] suggested that injecting lighter gases (with a lower molar mass) lead to a sooner transition than injecting heavier gases. The analysis performed in this work suggests that, instead, this is the consequence of the coupling of the thermoacoustic impedance introduced by the weak concentration shock and the admittance of the porous wall.

How do the boundary-layer-stability characteristics vary as a function of the surface porous arrangement?

A parametric study was performed in § 9.3 to investigate the sensitivity of instabilities to the wall boundary condition. During the decomposition of the TPS, both the arrangement of the porous fibers and the way the ablation products are injected into the boundary layer vary significantly. The characteristics of second-mode waves developing over such different wall configurations also presented major differences. The porous surface is reported to have a wide range of stabilizing or destabilizing effects on second-mode waves depending on the characteristics of the porous surface. The use of a continuously-blowing boundary condition, mimicking the dynamics of surface-ablation scenarios (high Thiele number), was seen to be largely destabilizing, in agreement with the trend observed for increasing pore sizes. Porous-layer destabilization and stabilization regions were mapped and then employed to explain the results obtained in a series of non-blowing experiments with passive porous walls.

How sensitive are the predictions to the use of inaccurate transport, diffusion, collisional, or chemical models?

An investigation was carried out (§ 10.1) on the sensitivity of high-enthalpy stability-and-transition predictions to modeling inaccuracies. The various thermo-

physical models employed by previous authors were compared against the state of the art, thus evaluating their validity. Transition-onset-location estimations were seen to be most sensitive to the modeling of the transport properties. The BEW transport model lead to a prediction of the transition-onset location approximately 38% sooner than the state-of-the-art CE model. This was mostly due to the use of this model on the base-flow computation, since employing it exclusively on the perturbation terms only lead to a transition-onset-location advancement of 3.4% with respect to the state of the art. This sensitivity to the transport model, was seen to be less dramatic in the gas-surface interaction study performed in chapter 11, suggesting a case-dependency of the modeling inaccuracies.

The sensitivity of the transition-onset predictions to the modeling of the diffusion fluxes, the chemical-equilibrium constant, or the chemical-reaction-rate constants was negligible for the considered test cases. The influence of the chemical-reaction-rate constants is of particular interest, since both the stability characteristics at a given streamwise location close to the leading edge, and the neutral stability curve presented noteworthy differences depending on the model. However, as one advances downstream, approaching chemical equilibrium, the differences associated to the finite rate of the reactions become negligible. The ultimate result is therefore a variability smaller than 1% with the choice of the reaction-rate constants.

The largest discrepancies in the predicted second-mode characteristics were consistently linked to high differences in the boundary-layer height for all model comparisons. This is consistent with the nature of the second mode, that is, acoustic waves confined to the boundary layer and therefore conditioned by its dimensions. It is therefore recommendable to place a stronger modeling effort in those properties significantly affecting the boundary-layer size.

What is the isolated effect of molar diffusion on the perturbation growth rates and frequencies?

A parametric study was presented in § 10.2 on the sensitivity of second-mode characteristics to the relative significance of diffusion fluxes, with respect to viscous forces. The increase or decrease of the Schmidt number by up to three orders of magnitude was seen to have a minor influence on the instability features, suggesting that diffusion does not greatly affect the development of second-mode waves.

Which flow assumptions are valid at different trajectory points in an atmospheric entry?

Section 10.3 analyzed the adequacy of various flow assumptions at six different flight-envelope points in typical Earth entry missions, when investigating second-mode-instability development. The CPG flow assumption was seen to be inade-

quate for all flight-envelope points, including the one with the lowest Mach number. Sutherland's viscosity law apparently lead to more accurate predictions than the CE model, better suited for high temperatures. However, the observed correlation lacks the necessary causality, since it is the consequence of the cancellation of the inaccuracies of the transport and the thermal model. This trend was also observed in the study of ionization effects (§ 10.4), and on the gas-surface interaction investigation (chapter 11), presenting an excellent example of how one can “*reach the right result for the wrong reason*”. The TPG flow assumption proved a very good approximation for most flight-envelope points, being only slightly inappropriate for the fastest one. This, combined with how inaccurate the LTE assumption was seen to be, suggests that the considered cases are actually closer to frozen conditions than to equilibrium. One should, however, beware from extrapolating this result to other geometries, since blunt noses feature a region around the stagnation point where the flow is indeed in equilibrium, subsequently evolving toward a non-equilibrium or frozen configuration downstream. Whether one or the other, ultimately depends on the actual geometry.

How do high-enthalpy phenomena such as internal-energy-mode-excitation, dissociation, ionization, shock-perturbation coupling, or ablation-product injection contribute to stabilizing or destabilizing the boundary layer?

Two separate investigations were carried out focusing on the modifications of second-mode instabilities due to ionization (§ 10.4) and graphite ablation (§ 11). This was done by exploring seven flight-envelope points in an extreme planetary return mission. The excitation of internal energy modes and the dissociation of molecular species were seen to destabilize the boundary layer and lead to larger N -factor envelopes. Contrarily, ionization was seen to be mainly stabilizing. However, assuming the perturbations to be in equilibrium was seen to erroneously forecast the opposite effect.

The use of the linearized Rankine-Hugoniot relations as boundary conditions for the perturbation amplitude terms were seen to negligibly modify the N -factor-envelope predictions, even when the base-flow featured shocks extremely close to the surface (1.3-2.3 degrees). A similar trend was also observed in the study presented in chapter 11, with the exception of certain cases featuring supersonic modes.

Ablation-induced mass injection logically demonstrated to increase the N -factor envelopes more for increasing free-stream Mach numbers and consequently larger ablation rates. The relative importance of air-species dissociation develops in a similar fashion. In general, phenomena that contribute to cooling the boundary layer, and therefore reducing the boundary-layer size were seen to increase the N -factor values in consequence.

The injection of a gas with the composition arising from the ablation of

graphite rather than air predicted larger N -factor envelopes. Such cases feature heavier injection gases, which result in a lower boundary-layer height. The associated stronger confinement of the second mode thus destabilizes it and causes the mentioned increase in the N factors. Attempting to substitute all carbon species in the injected mixture by a single inert species (CO_2) lead to overpredicting the N -factor envelopes.

Finally, the use of a radiative-equilibrium thermal boundary condition, instead of a homogeneous one, lead to substantially larger predicted perturbation growth rates and N -factor envelopes. However, it is unclear whether one should employ the former or the latter, due to the high frequency of the instabilities, the high thermal inertia of the graphite wall, and the near-zero activation time required for radiation.

Are these effects mostly due to the modification of the base-flow field, or of the perturbations themselves?

The use of various combinations of base-flow and perturbation hypotheses in § 10.4 allowed to observe the three main competing effects in scenarios with internal-energy-mode excitation, dissociation, and ionization:

1. The destabilization due to the base-flow cooling induced by dissociation and ionization. The driving mechanism appears to be the increase in the thermoacoustic impedance that is the density gradient, and that significantly increases the peak in the temperature perturbation amplitude in the top of the boundary layer.
2. The stabilization introduced by the diffusion fluxes acting on the perturbation terms. They were seen to act on the mentioned peak in the temperature perturbation amplitude. This damping is believed to be driving the associated stabilization of second-mode instabilities.
3. A further stabilization linked to the chemical dissociation and ionization source terms acting on the perturbation terms.

Which phenomenon is the one promoting supersonic modes in high-enthalpy scenarios?

Unstable supersonic modes were first observed in low-enthalpy scenarios with strong wall-cooling. When subsequently observing unstable supersonic modes also in high-enthalpy tests with much lower surface-cooling levels, authors hypothesized that the base-flow cooling due to internal-energy-mode excitation and dissociation acted similarly to wall cooling in low-enthalpy cases and thus promoted unstable supersonic modes. However, the results presented in this dissertation suggest that the decrease in wave speed, ultimately leading to the appearance

of unstable supersonic modes in § 10.4, was seen to be a consequence of the perturbation diffusion fluxes, rather than of the cooling of the laminar base flow

Outlook

In order to perpetuate and continue the advancement laid out in this dissertation, the author believes that there are four main lines of research to pursue:

1. Incorporate thermal non-equilibrium effects to the parametric investigations performed in chapters 10 and 11. Presumably, assuming a finite rate of energy transfer between modes will make predictions between those made with a full excitation of internal energy modes (TPG or CNE for example) and those neglecting it completely (CPG). In this work, this excitation was repeatedly seen to destabilize the flow through the cooling of the laminar base flow, suggesting that in fact these constitute the worse-case scenario.
2. Extend chemically-reacting studies to more complex geometries. The work presented in this dissertation mostly focuses on sharp-tip configurations, where the flow is frozen at the leading edge, and then dissociates as it advances downstream. Blunt noses display a different flow configuration, with equilibrium conditions around the stagnation point in the leading edge, and a finite-rate recombination following as one advances downstream. It is therefore necessary to see if the presented trends persist for such flow scenarios.
3. Extending the high-temperature analyses to more physically-inclusive stability theories. This dissertation focuses on LST, but lays the ground for a relatively simple extension of the methodology to more elaborate theoretical frameworks [9, 10]. Such frameworks will allow to assess if the trends reported here are indeed physical, rather than an artifact of the simplified LST.
4. Detailed budgets for the contribution of the various physical phenomena to the growth rates and mode shapes. Using the high-enthalpy compressible version of the Reynolds-Orr equations [11] it is possible to make a detailed computation of the contribution of the various physical phenomena to the instability growth rates. Such an analysis, combined with the flow-assumption- and boundary-condition-based budget analysis performed in this dissertation, will provide a more clear insight into the physical mechanisms underlying in the complexly-coupled problems of interest.

It is by following the aforementioned pathway that the community will advance towards a better understanding of the potential *mission killer* that is the ablation-transition problem in atmospheric entry missions. The resolution of such

challenges will take humanity a step closer to the safe space exploration that is necessary to mitigate the multiple, imminent, and unpredictable existential threats that we face as a species.

References

- [1] K. J. Groot, F. Miró Miró, E. S. Beyak, A. J. Moyes, F. Pinna, and H. L. Reed. *DEKAF: spectral multi-regime basic-state solver for boundary layer stability*. AIAA paper, [2018-3380](#), 2018.
- [2] F. Miró Miró, E. S. Beyak, D. Mullen, F. Pinna, and H. L. Reed. *Ionization and Dissociation Effects on Hypersonic Boundary-Layer Stability*. In 31st ICAS Congress, Belo Horizonte, Brazil, 2018. International Council of the Aeronautical Sciences.
- [3] F. Pinna and K. J. Groot. *Automatic derivation of stability equations in arbitrary coordinates and different flow regimes*. AIAA paper, [2014-2634](#), 2014.
- [4] V. Theofilis. *Advances in global linear instability analysis of nonparallel and three-dimensional flows*. Progress in Aerospace Sciences, [39\(4\):249–315](#), 2003.
- [5] S. A. Gaponov. *Effect of the Properties of a Porous Coating on Boundary Layer Stability*. Technical Report TM 75235, NASA, Santa Barbara, CA, 1978.
- [6] A. V. Fedorov, N. D. Malmuth, A. Rasheed, and H. G. Hornung. *Stabilization of hypersonic boundary layers by porous coatings*. AIAA Journal, [39\(4\):605–610](#), 2001.
- [7] J. G. Marvin and C. M. Akin. *Combined effects of mass addition and nose bluntness on boundary-layer transition*. AIAA Journal, [8\(5\):857–863](#), 1970.
- [8] C. J. J. Stalmach, J. J. Bertin, T. C. Pope, and M. H. McCloskey. *A Study of Boundary Layer Transition on Outgassing Cones in Hypersonic Flow*. Technical Report CR-1908, NASA, 1971.
- [9] I. Padilla, F. Miró Miró, and F. Pinna. *Influence of High-Temperature Effects on the Stability of the Wake Behind an Isolated Roughness Element in Hypersonic Flow*. In Proceedings of the 2019 IUTAM Symposium on Laminar-Turbulent Transition, London, UK, September 2019.
- [10] L. Zanus, F. Miró Miró, and F. Pinna. *Nonlinear PSE Transition Predictions in Hypersonic Boundary Layers with Finite Rate Chemical Reactions*. In Proceedings of the 2019 IUTAM Symposium on Laminar-Turbulent Transition, London, UK, September 2019.
- [11] K. J. Groot, J. Serpieri, F. Pinna, and M. Kotsonis. *Secondary crossflow instability through global analysis of measured base flows*. Journal of Fluid Mechanics, [846:605–653](#), 2018.

Part IV

Appendices

A

General relations between species and mixture quantities

This section collects a series of relations between various species-specific and mixture quantities. These relations derive from the definitions of the quantities, Dalton's law, and the various forms of the equation of state.

The definitions of the mass, mole, and pressure fractions establish:

$$Y_s = \frac{\rho_s}{\rho}, \quad \forall s \in \mathcal{S}, \quad (\text{A.1a})$$

$$X_s = \frac{n_s}{n}, \quad \forall s \in \mathcal{S}, \quad (\text{A.1b})$$

$$\psi_s = \frac{p_s}{p}, \quad \forall s \in \mathcal{S}. \quad (\text{A.1c})$$

The equation of state for a single species can be expressed in terms of the partial densities or the number density of the species constituting the mixture:

$$p_s = \rho_s \frac{\mathcal{R}}{\mathcal{M}_s} T_s^{Trans} = \rho_s R_s T_s^{Trans} = n_s k_B T_s^{Trans}, \quad \forall s \in \mathcal{S}, \quad (\text{A.2})$$

where R_s is the species-specific gas constant, T_s^{Trans} is the temperature characterizing the translational motion of each species (Eq. 4.6a). In a one-temperature flow assumption it is obviously equal to T for all species (see Eq. 4.7).

From Eq. A.2, it is direct that the number density and mass densities of species and elements are related through their molar mass and Avogadro's number $N_A =$

\mathcal{R}/k_B :

$$n_s = \rho_s \frac{N_A}{\mathcal{M}_s}, \quad \forall s \in \mathcal{S}. \quad (\text{A.3})$$

Dalton's law [1] establishes that the pressure of a mixture is the result of the sum of the partial contributions of the various species forming the mixture:

$$p = \sum_{s \in \mathcal{S}} p_s. \quad (\text{A.4})$$

Similarly, the mixture density ρ and number density n are defined as:

$$\rho = \sum_{s \in \mathcal{S}} \rho_s, \quad (\text{A.5})$$

$$n = \sum_{s \in \mathcal{S}} n_s. \quad (\text{A.6})$$

Operating with Eqs. A.1-A.6, one may reach expressions relating the molar, mass and pressure fractions:

$$Y_s = \frac{\mathcal{M}_s X_s}{\sum_{\ell \in \mathcal{S}} \mathcal{M}_\ell X_\ell} = X_s \frac{\mathcal{M}_s}{\mathcal{M}}, \quad \forall s \in \mathcal{S}, \quad (\text{A.7a})$$

$$X_s = \frac{Y_s / \mathcal{M}_s}{\sum_{\ell \in \mathcal{S}} Y_\ell / \mathcal{M}_\ell} = Y_s \frac{\mathcal{M}}{\mathcal{M}_s}, \quad \forall s \in \mathcal{S}, \quad (\text{A.7b})$$

$$\psi_s = \frac{n T_s^{Trans}}{\sum_{\ell \in \mathcal{S}} n_\ell T_\ell^{Trans}} X_s, \quad \forall s \in \mathcal{S}, \quad (\text{A.7c})$$

where the mixture molar mass \mathcal{M} are introduced:

$$\mathcal{M} = \left(\sum_{s \in \mathcal{S}} \frac{Y_s}{\mathcal{M}_s} \right)^{-1} = \sum_{s \in \mathcal{S}} \mathcal{M}_s X_s, \quad (\text{A.8})$$

An alternative definition of the corrected mixture molar mass:

$$\mathcal{M}^* = \left(\sum_{s \in \mathcal{H}} \frac{Y_s}{\mathcal{M}_s} + \frac{Y_e^-}{\mathcal{M}_e^-} \frac{T^{e^-}}{T^{Trans}} \right)^{-1}, \quad (\text{A.9})$$

allows to express the equation of state for the mixture as:

$$p = \rho \frac{\mathcal{R}}{\mathcal{M}^*} T^{Trans}, \quad (\text{A.10})$$

for all flow assumptions presented in table 2.1.

Note that for non-ionized mixtures, or for flow assumptions in thermal equilibrium ($T^{e^-} = T^{Trans} = T$), the corrected mixture molar mass (Eq. A.9) is equal to the mixture molar mass (Eq. A.8): $\mathcal{M}^* = \mathcal{M}$. In such scenarios, the pressure fraction also coincides with the mole fraction $\psi_s = X_s$.

Elemental quantities

When working with the LTEED flow assumption, it is interesting to define elemental mass and atomic fractions, analogously to the species mass and mole fractions:^a

$$\mathcal{Y}_E = \frac{\rho_E}{\rho}, \quad \forall E \in \mathcal{E}, \quad (\text{A.11a})$$

$$\mathcal{X}_E = \frac{n_E^*}{n^*}, \quad \forall E \in \mathcal{E}, \quad (\text{A.11b})$$

where the elemental partial density is defined as:

$$\rho_E = \sum_{s \in \mathcal{S}} \mathcal{E}_{Es}^* \frac{\mathcal{M}_E}{\mathcal{M}_s} \rho_s = \sum_{s \in \mathcal{S}} \mathcal{E}_{Es} \rho_s, \quad \forall E \in \mathcal{E}. \quad (\text{A.12})$$

featuring the corrected elemental stoichiometric coefficient \mathcal{E}_{Es} (see Eq. 2.22). Similarly the elemental atomic number densities n_E^* are defined as:

$$n_E^* = \sum_{s \in \mathcal{S}} \mathcal{E}_{Es}^* n_s, \quad \forall E \in \mathcal{E}, \quad (\text{A.13a})$$

$$n^* = \sum_{E \in \mathcal{E}} n_E^*. \quad (\text{A.13b})$$

Note that the mixture atomic (n^*) and the molecular (n) number densities are not equivalent. For a gas mixture of pure O₂, for instance, one has that $n^* = 2n$, since there are two atoms of O for every molecule of O₂. It is therefore useful to define the molar average of the number of atoms per molecule:

$$\mathfrak{y} = \frac{n^*}{n} = \frac{\sum_{E \in \mathcal{E}} n_E^*}{\sum_{s \in \mathcal{S}} n_s} = \sum_{\substack{s \in \mathcal{S} \\ E \in \mathcal{E}}} \mathcal{E}_{Es}^* X_s. \quad (\text{A.14})$$

Similarly to Eq. A.3, it also follows from their definitions that the elemental atomic number densities and the elemental partial densities are related through:

$$n_E^* = \frac{N_A}{\mathcal{M}_E} \rho_E, \quad \forall E \in \mathcal{E}. \quad (\text{A.15})$$

Also, analogously to the definition of the mixture molar mass, it is also possible to define the mixture atomic mass:

$$\mathcal{M} = \left(\sum_{E \in \mathcal{E}} \frac{\mathcal{Y}_E}{\mathcal{M}_E} \right)^{-1} = \sum_{E \in \mathcal{E}} \mathcal{M}_E \mathcal{X}_E, \quad (\text{A.16})$$

^aElemental quantities are of interest for the LTEED flow assumption. In it, one assumes thermal equilibrium, and therefore the pressure and mole fractions coincide. For this reason elemental pressure fractions are not introduced.

and operating with Eqs. A.11-A.16:

$$\mathcal{Y}_E = \frac{\mathcal{M}_E \mathcal{X}_E}{\sum_{F \in \mathcal{E}} \mathcal{M}_F \mathcal{X}_F} = \mathcal{X}_E \frac{\mathcal{M}_E}{\mathcal{M}}, \quad \forall E \in \mathcal{E}, \quad (\text{A.17a})$$

$$\mathcal{X}_E = \frac{\mathcal{Y}_E / \mathcal{M}_E}{\sum_{F \in \mathcal{E}} \mathcal{Y}_F / \mathcal{M}_F} = \mathcal{Y}_E \frac{\mathcal{M}}{\mathcal{M}_E}, \quad \forall E \in \mathcal{E}. \quad (\text{A.17b})$$

Operating with the definition of \mathfrak{h} (Eq. A.14), substituting Eq. A.3 and Eq. A.15 into it, and using the definitions of \mathcal{M} (Eq. A.8) and \mathcal{M} (Eq. A.16), one reaches that:

$$\mathfrak{h} = \frac{\mathcal{M}}{\mathcal{M}}, \quad (\text{A.18})$$

which explicitly appears in the equation of state, expressed in terms of the elemental quantities:

$$p = \frac{1}{\mathfrak{h}} \sum_{E \in \mathcal{E}} n_E^* k_B T = \frac{1}{\mathfrak{h}} \sum_{E \in \mathcal{E}} \rho_E \frac{\mathcal{R}}{\mathcal{M}_E} T = \rho \frac{\mathcal{R}}{\mathfrak{h} \mathcal{M}} T. \quad (\text{A.19})$$

An important particularity of the electron “element”^b is that it may present negative values of n_E^* or ρ_E (and therefore also \mathcal{X}_E and \mathcal{Y}_E). If charge neutrality is not enforced, one may encounter situations with a locally positive charge. This implies that there are more particles that have lost electrons (positively-charged ions) than free electrons (negatively charged), thus resulting in an overall lack of electrons – mathematically represented with a negative amount of electron elements. A negative mass is obviously not physical. However, it is the mathematical artifact of the decomposition of the mixture into various elements, one of which (the electron element) is actually a sub-constituent of the others – atoms are made up of several subatomic particles, one of which are electrons. It also has an acceptable physical interpretation, since the negative density corresponds to the mass of the electrons lacking from the other elements in ionized species.

References

- [1] J. Dalton. *Essay IV. On the expansion of elastic fluids by heat*. Memoirs of the Literary and Philosophical Society of Manchester, 5(2):595–602, 1802.

^bElectrons are clearly not an element in the chemical sense – they are actually present in all chemical elements. However, they are treated as such for the sake of the LTEED flow model.

B

Equilibrium system of equations

The retrieval of the mixture composition in chemical equilibrium requires of the resolution of its corresponding equilibrium system. To have closure, it must necessarily have as many equations as species in the mixture. One can express the equilibrium system, as long as the mixture is considered dilute, in a general fashion, taking a set of equilibrium reactions \mathcal{R}^{eq} between a set of species \mathcal{S} :

$$\sum_{s \in \mathcal{S}} \nu'_{sr} s \leftrightarrow \sum_{s \in \mathcal{S}} \nu''_{sr} s, \quad \forall r \in \mathcal{R}^{\text{eq}}, \quad (\text{B.1})$$

one may define a series of equilibrium pressure relations, expressed in terms of the logarithms of the mole fractions:

$$\sum_{s \in \mathcal{S}} \Delta \nu_{sr} \ln(X_s) = \ln(K_{pr}) - \sum_{s \in \mathcal{S}} \Delta \nu_{sr} \ln(p), \quad \forall r \in \mathcal{R}^{\text{eq}}. \quad (\text{B.2})$$

where the equilibrium pressure constants K_{pr} are related to those defined in § 4.3 (Eqs. 4.66, 4.69 or 4.70) through:

$$K_{pr} = K_{eqr} (\mathcal{R} T)^{\sum_{s \in \mathcal{S}} \Delta \nu_{sr}}. \quad (\text{B.3})$$

where the stoichiometric jump is defined as:

$$\Delta \nu_{sr} = \nu''_{sr} - \nu'_{sr}, \quad \forall s \in \mathcal{S}, \quad \forall r \in \mathcal{R}^{\text{eq}}. \quad (\text{B.4})$$

Additionally, from the definitions laid out in app. A one has that the elemental balance requires:

$$\sum_{s \in \mathcal{S}} \mathcal{E}_{Es}^* n_s = n_E^*, \quad \forall E \in \mathcal{E}, \quad (\text{B.5})$$

where the elemental stoichiometric coefficients \mathcal{E}_{Es}^* were introduced in § 2.3.3, \mathcal{E} is the set of all elements, n_E^* is the atomic number density of element E , and n_s is the molecular number density of species s . Operating with Eq. B.5 and the definitions of X_s in thermal equilibrium and \mathcal{X}_E (app. A) it is possible to reach:

$$\sum_{s \in S} \left(\sum_{F \in \mathcal{E}} \mathcal{E}_{Fs}^* \mathcal{X}_E - \mathcal{E}_{Es}^* \right) X_s = 0, \quad \forall E \in \mathcal{E}. \quad (\text{B.6})$$

Note that the elemental balance on one of the elements will be redundant, since it is already satisfied by definition through the stoichiometric elemental matrix \mathcal{E}_{Es}^* . The equilibrium equation system is completed by the relation ensuring that all mole fractions add to one:

$$\sum_{s \in S} X_s = 1. \quad (\text{B.7})$$

In summary: for a mixture of N_s dilute gas species, featuring N_E elements in them, the equilibrium system must include the condition on the mole fractions adding up to one (Eq. B.7), $N_E - 1$ elemental balance relations (Eq. B.6), and $N_s - N_E$ equilibrium pressure relations (Eq. B.2). The equation system is solved on the natural logarithms of the mole fractions to avoid numerical overflow and underflow. The equations are also linearized and solved using a Newton-Raphson iterative method.

Examples of the equilibrium systems for air-5 and air-11 mixtures are found in the following subsections (§ B.2 and B.3).

Multiphase systems pose other challenges in the determination of their equilibrium concentrations, and require another mathematical framework which is out of the scope of the present dissertation [1].

B.1 Equilibrium-composition derivatives with respect to temperature, pressure or elemental fractions

The grouping of certain variables in equilibrium conditions, necessary for the simplification of the flow equations (see § 2.3 and 5.1), requires the computation of the first-order derivatives of the equilibrium concentration with respect to temperature (T), pressure (p) and elemental mass fractions (\mathcal{Y}_E). Such derivatives can be obtained by solving the system resulting from differentiating the equations solved to obtain X_s (Eqs. B.2, B.6 and B.7) with respect to p , T , and \mathcal{Y}_E . The resulting systems are linear in the equilibrium concentration gradients, and can therefore be solved rather effortlessly once X_s is known. For instance, the equation system for

$\partial X_s / \partial T$ is simply:

$$\sum_{s \in \mathcal{S}} \Delta \nu_{sr} \frac{1}{X_s} \frac{\partial X_s}{\partial T} = \frac{\partial \ln(K_{pr})}{\partial T}, \quad \forall r \in \mathcal{R}^{\text{eq}}. \quad (\text{B.8a})$$

$$\sum_{s \in \mathcal{S}} \left(\sum_{F \in \mathcal{E}} \mathcal{E}_{Fs}^* \mathcal{X}_E - \mathcal{E}_{Es}^* \right) \frac{\partial X_s}{\partial T} = 0, \quad \forall E \in \hat{\mathcal{E}}, \quad (\text{B.8b})$$

$$\sum_{s \in \mathcal{S}} \frac{\partial X_s}{\partial T} = 0, \quad (\text{B.8c})$$

where $\hat{\mathcal{E}}$ is the set of all-but-one element. Similarly, the one for $\partial X_s / \partial \mathcal{Y}_F$ is:

$$\sum_{s \in \mathcal{S}} \Delta \nu_{sr} \frac{1}{X_s} \frac{\partial X_s}{\partial \mathcal{Y}_F} = 0, \quad \forall r \in \mathcal{R}^{\text{eq}}. \quad (\text{B.9a})$$

$$\sum_{s \in \mathcal{S}} \left(\sum_{G \in \mathcal{E}} \mathcal{E}_{Gs}^* \mathcal{X}_E - \mathcal{E}_{Es}^* \right) \frac{\partial X_s}{\partial \mathcal{Y}_F} = -\frac{\partial \mathcal{X}_E}{\partial \mathcal{Y}_F} \sum_{s \in \mathcal{S}} \sum_{G \in \mathcal{E}} \mathcal{E}_{Gs}^* X_s, \quad \forall E \in \hat{\mathcal{E}}, \quad (\text{B.9b})$$

$$\sum_{s \in \mathcal{S}} \frac{\partial X_s}{\partial \mathcal{Y}_F} = 0, \quad (\text{B.9c})$$

where the derivative of one elemental mole fraction with respect to another elemental mass fraction is obtained from differentiating the definition of \mathcal{X}_E in Eq. A.17a and that of \mathcal{M} in Eq. A.16:

$$\begin{aligned} \frac{\partial \mathcal{X}_F}{\partial \mathcal{Y}_E} &= \frac{\mathcal{M}}{\mathcal{M}_F} \delta_{EF} + \frac{\mathcal{Y}_F}{\mathcal{M}_F} \frac{\partial \mathcal{M}}{\partial \mathcal{Y}_E} = \\ &= \frac{\mathcal{M}}{\mathcal{M}_F} \delta_{EF} - \frac{\mathcal{Y}_F}{\mathcal{M}_F} \frac{\mathcal{M}^2}{\mathcal{M}_E} = \\ &= \frac{\mathcal{M}}{\mathcal{M}_E} (\delta_{EF} - \mathcal{X}_F), \quad \forall E, F \in \mathcal{E}. \end{aligned} \quad (\text{B.10})$$

Note that the subscript of \mathcal{M}_F in the first addend of the right-hand-side of Eq. B.10 is changed between the second and the third row from F to E . This can be faultlessly done since it is multiplying the Kronecker delta function (δ_{EF}) which is only different than zero for $F = E$.

One must beware from directly differentiating Eqs. B.6 with respect to \mathcal{X}_F instead of \mathcal{Y}_F . The elemental mass (or mole) fractions are interrelated through the concentration conditions – they must all sum up to one. When differentiating with respect to \mathcal{Y}_F this interrelatedness is implicitly accounted for through the derivative of the elemental mole fractions with respect to the mass fractions (Eq. B.10), but this is not the case when differentiating Eqs. B.6 directly with respect to \mathcal{X}_F .

Carrying out stability analyses, featuring an expansion of the derivatives of the system's dependent variables around their laminar base-flow values (see § 4.6), requires the computation of higher-order derivatives of the equilibrium concentrations with respect to p , T , and \mathcal{Y}_E . The process to obtain them is the same as the one laid out for the first-order derivatives, only increasing the differentiation order.

After retrieving the thermodynamic derivatives of the equilibrium composition, one may proceed to assembling the derivatives of the thermodynamic and transport properties. This is done by applying the chain rule:

$$\left. \frac{\partial Q}{\partial q_1} \right|_{\mathcal{S}}^{\text{eq}} = \sum_{s \in \mathcal{S}} \frac{\partial Q}{\partial \rho_s} \frac{\partial \rho_s}{\partial q_1} + \frac{\partial Q}{\partial q_1}, \quad (\text{B.11a})$$

$$\begin{aligned} \left. \frac{\partial^2 Q}{\partial q_1 \partial q_2} \right|_{\mathcal{S}}^{\text{eq}} = & \sum_{s \in \mathcal{S}} \left(\sum_{\ell \in \mathcal{S}} \frac{\partial^2 Q}{\partial \rho_s \partial \rho_\ell} \frac{\partial \rho_s}{\partial q_1} \frac{\partial \rho_\ell}{\partial q_2} + \frac{\partial^2 Q}{\partial \rho_s \partial q_1} \frac{\partial \rho_s}{\partial q_2} + \right. \\ & \left. + \frac{\partial^2 Q}{\partial \rho_s \partial q_2} \frac{\partial \rho_s}{\partial q_1} + \frac{\partial Q}{\partial \rho_s} \frac{\partial^2 \rho_s}{\partial q_1 \partial q_2} \right) + \frac{\partial^2 Q}{\partial q_1 \partial q_2}, \end{aligned} \quad (\text{B.11b})$$

$$\begin{aligned} \left. \frac{\partial^3 Q}{\partial q_1 \partial q_2 \partial q_3} \right|_{\mathcal{S}}^{\text{eq}} = & \sum_{s \in \mathcal{S}} \left(\sum_{\ell \in \mathcal{S}} \left(\sum_{m \in \mathcal{S}} \frac{\partial^3 Q}{\partial \rho_s \partial \rho_\ell \partial \rho_m} \frac{\partial \rho_s}{\partial q_1} \frac{\partial \rho_\ell}{\partial q_2} \frac{\partial \rho_m}{\partial q_3} + \right. \right. \\ & + \frac{\partial^3 Q}{\partial \rho_s \partial \rho_\ell \partial q_1} \frac{\partial \rho_s}{\partial q_2} \frac{\partial \rho_\ell}{\partial q_3} + \frac{\partial^3 Q}{\partial \rho_s \partial \rho_\ell \partial q_2} \frac{\partial \rho_s}{\partial q_1} \frac{\partial \rho_\ell}{\partial q_3} + \\ & + \frac{\partial^3 Q}{\partial \rho_s \partial \rho_\ell \partial q_3} \frac{\partial \rho_s}{\partial q_1} \frac{\partial \rho_\ell}{\partial q_2} + \frac{\partial^2 Q}{\partial \rho_s \partial \rho_\ell} \frac{\partial^2 \rho_s}{\partial q_1 \partial q_2} \frac{\partial \rho_\ell}{\partial q_3} + \\ & + \frac{\partial^2 Q}{\partial \rho_s \partial \rho_\ell} \frac{\partial^2 \rho_s}{\partial q_2 \partial q_3} \frac{\partial \rho_\ell}{\partial q_1} + \frac{\partial^2 Q}{\partial \rho_s \partial \rho_\ell} \frac{\partial^2 \rho_s}{\partial q_1 \partial q_3} \frac{\partial \rho_\ell}{\partial q_2} \right) + \\ & + \frac{\partial^3 Q}{\partial \rho_s \partial q_1 \partial q_2} \frac{\partial \rho_s}{\partial q_3} + \frac{\partial^3 Q}{\partial \rho_s \partial q_2 \partial q_3} \frac{\partial \rho_s}{\partial q_1} + \frac{\partial^3 Q}{\partial \rho_s \partial q_1 \partial q_3} \frac{\partial \rho_s}{\partial q_2} + \\ & + \frac{\partial^2 Q}{\partial \rho_s \partial q_1} \frac{\partial^2 \rho_s}{\partial q_2 \partial q_3} + \frac{\partial^2 Q}{\partial \rho_s \partial q_2} \frac{\partial^2 \rho_s}{\partial q_1 \partial q_3} + \frac{\partial^2 Q}{\partial \rho_s \partial q_3} \frac{\partial^2 \rho_s}{\partial q_1 \partial q_2} + \\ & \left. \left. + \frac{\partial Q}{\partial \rho_s} \frac{\partial^3 \rho_s}{\partial q_1 \partial q_2 \partial q_3} \right) + \frac{\partial^3 Q}{\partial q_1 \partial q_2 \partial q_3}, \right. \end{aligned} \quad (\text{B.11c})$$

where the independent variables (q_1 , q_2 , and q_3) can be either temperature (T), pressure (p), or any of the elemental mass fractions (\mathcal{Y}_E). The thermodynamic derivatives of the equilibrium species partial densities (ρ_s) can be expressed as a function of the derivatives of the equilibrium mole fractions (X_s). Employing the species equation of state (Eq. A.2), and since in equilibrium $p_s = p X_s$, one can express the species partial density as:

$$\rho_s = \frac{p X_s}{R_s T}, \quad (\text{B.12})$$

which can be differentiated with respect to p , T , and \mathcal{Y}_E , reaching the desired relations:

$$\frac{\partial \rho_s}{\partial p} = \frac{X_s}{R_s T} + \frac{p}{R_s T} \frac{\partial X_s}{\partial p}, \quad (\text{B.13a})$$

$$\frac{\partial \rho_s}{\partial T} = -\frac{p X_s}{R_s T^2} + \frac{p}{R_s T} \frac{\partial X_s}{\partial T}, \quad (\text{B.13b})$$

$$\frac{\partial \rho_s}{\partial \mathcal{Y}_E} = \frac{p}{R_s T} \frac{\partial X_s}{\partial \mathcal{Y}_E}, \quad \forall E \in \mathcal{E}, \quad (\text{B.13c})$$

$$\frac{\partial^2 \rho_s}{\partial p^2} = \frac{2}{R_s T} \frac{\partial X_s}{\partial p} + \frac{p}{R_s T} \frac{\partial^2 X_s}{\partial p^2}, \quad (\text{B.13d})$$

$$\frac{\partial^2 \rho_s}{\partial p \partial T} = -\frac{X_s}{R_s T^2} + \frac{1}{R_s T} \frac{\partial X_s}{\partial T} - \frac{p}{R_s T^2} \frac{\partial X_s}{\partial p} + \frac{p}{R_s T} \frac{\partial^2 X_s}{\partial p \partial T}, \quad (\text{B.13e})$$

$$\frac{\partial^2 \rho_s}{\partial p \partial \mathcal{Y}_E} = \frac{1}{R_s T} \frac{\partial X_s}{\partial \mathcal{Y}_E} + \frac{p}{R_s T} \frac{\partial^2 X_s}{\partial p \partial \mathcal{Y}_E}, \quad \forall E \in \mathcal{E}, \quad (\text{B.13f})$$

$$\frac{\partial^2 \rho_s}{\partial T^2} = \frac{2 X_s p}{R_s T^3} - \frac{2 p}{R_s T^2} \frac{\partial X_s}{\partial T} + \frac{p}{R_s T} \frac{\partial^2 X_s}{\partial T^2}, \quad (\text{B.13g})$$

$$\frac{\partial^2 \rho_s}{\partial T \partial \mathcal{Y}_E} = -\frac{p}{R_s T^2} \frac{\partial X_s}{\partial \mathcal{Y}_E} + \frac{p}{R_s T} \frac{\partial^2 X_s}{\partial T \partial \mathcal{Y}_E}, \quad \forall E \in \mathcal{E}, \quad (\text{B.13h})$$

$$\frac{\partial^2 \rho_s}{\partial \mathcal{Y}_E \partial \mathcal{Y}_F} = \frac{p}{R_s T} \frac{\partial^2 X_s}{\partial \mathcal{Y}_E \partial \mathcal{Y}_F}, \quad \forall E, F \in \mathcal{E}, \quad (\text{B.13i})$$

$$\frac{\partial^3 \rho_s}{\partial p^3} = \frac{3}{R_s T} \frac{\partial^2 X_s}{\partial p^2} + \frac{p}{R_s T} \frac{\partial^3 X_s}{\partial p^3}, \quad (\text{B.13j})$$

$$\frac{\partial^3 \rho_s}{\partial p^2 \partial T} = -\frac{2}{R_s T^2} \frac{\partial X_s}{\partial p} + \frac{2}{R_s T} \frac{\partial^2 X_s}{\partial p \partial T} - \frac{p}{R_s T^2} \frac{\partial^2 X_s}{\partial p^2} + \frac{p}{R_s T} \frac{\partial^3 X_s}{\partial p^2 \partial T}, \quad (\text{B.13k})$$

$$\frac{\partial^3 \rho_s}{\partial p^2 \partial \mathcal{Y}_E} = \frac{2}{R_s T} \frac{\partial^2 X_s}{\partial p \partial \mathcal{Y}_E} + \frac{p}{R_s T} \frac{\partial^3 X_s}{\partial p^2 \partial \mathcal{Y}_E}, \quad \forall E \in \mathcal{E}, \quad (\text{B.13l})$$

$$\begin{aligned} \frac{\partial^3 \rho_s}{\partial p \partial T^2} = & \frac{2X_s}{R_s T^3} + \frac{2p}{R_s T^3} \frac{\partial X_s}{\partial p} - \frac{2}{R_s T^2} \frac{\partial X_s}{\partial T} - \frac{2p}{R_s T^2} \frac{\partial^2 X_s}{\partial p \partial T} + \\ & + \frac{1}{R_s T} \frac{\partial^2 X_s}{\partial T^2} + \frac{p}{R_s T} \frac{\partial^3 X_s}{\partial p \partial T^2}, \end{aligned} \quad (\text{B.13m})$$

$$\begin{aligned} \frac{\partial^3 \rho_s}{\partial p \partial T \partial \mathcal{Y}_E} = & -\frac{1}{R_s T^2} \frac{\partial X_s}{\partial \mathcal{Y}_E} + \frac{1}{R_s T} \frac{\partial^2 X_s}{\partial T \partial \mathcal{Y}_E} - \frac{p}{R_s T^2} \frac{\partial^2 X_s}{\partial p \partial \mathcal{Y}_E} + \\ & + \frac{p}{R_s T} \frac{\partial^3 X_s}{\partial p \partial T \partial \mathcal{Y}_E}, \quad \forall E \in \mathcal{E}, \end{aligned} \quad (\text{B.13n})$$

$$\frac{\partial^3 \rho_s}{\partial p \partial \mathcal{Y}_E \partial \mathcal{Y}_F} = \frac{1}{R_s T} \frac{\partial^2 X_s}{\partial \mathcal{Y}_E \partial \mathcal{Y}_F} + \frac{p}{R_s T} \frac{\partial^3 X_s}{\partial p \partial \mathcal{Y}_E \partial \mathcal{Y}_F}, \quad \forall E, F \in \mathcal{E}, \quad (\text{B.13o})$$

$$\frac{\partial^3 \rho_s}{\partial T^3} = -\frac{6X_s p}{R_s T^4} + \frac{6p}{R_s T^3} \frac{\partial X_s}{\partial T} - \frac{3p}{R_s T^2} \frac{\partial^2 X_s}{\partial T^2} + \frac{p}{R_s T} \frac{\partial^3 X_s}{\partial T^3}, \quad (\text{B.13p})$$

$$\frac{\partial^3 \rho_s}{\partial T^2 \partial \mathcal{Y}_E} = \frac{2p}{R_s T^3} \frac{\partial X_s}{\partial \mathcal{Y}_E} - \frac{2p}{R_s T^2} \frac{\partial^2 X_s}{\partial T \partial \mathcal{Y}_E} + \frac{p}{R_s T} \frac{\partial^2 X_s}{\partial T^2 \partial \mathcal{Y}_E}, \quad \forall E \in \mathcal{E}, \quad (\text{B.13q})$$

$$\frac{\partial^3 \rho_s}{\partial T \partial \mathcal{Y}_E \partial \mathcal{Y}_F} = -\frac{p}{R_s T^2} \frac{\partial^2 X_s}{\partial \mathcal{Y}_E \partial \mathcal{Y}_F} + \frac{p}{R_s T} \frac{\partial^3 X_s}{\partial T \partial \mathcal{Y}_E \partial \mathcal{Y}_F}, \quad \forall E, F \in \mathcal{E}, \quad (\text{B.13r})$$

$$\frac{\partial^3 \rho_s}{\partial \mathcal{Y}_E \partial \mathcal{Y}_F \partial \mathcal{Y}_G} = \frac{p}{R_s T} \frac{\partial^3 X_s}{\partial \mathcal{Y}_E \partial \mathcal{Y}_F \partial \mathcal{Y}_G}, \quad \forall E, F, G \in \mathcal{E}. \quad (\text{B.13s})$$

B.2 The air-5 equilibrium system

For the air-5 mixture, three dissociation equilibrium relations are imposed together with the concentration condition, and with the elemental-fraction-ratio condition:

$$p X_{\text{O}}^2 / X_{\text{O}_2} = K_{p \text{O}_2}^{\text{Diss}}(T), \quad (\text{B.14a})$$

$$p X_{\text{N}}^2 / X_{\text{N}_2} = K_{p \text{N}_2}^{\text{Diss}}(T), \quad (\text{B.14b})$$

$$p X_{\text{N}} X_{\text{O}} / X_{\text{NO}} = K_{p \text{NO}}^{\text{Diss}}(T), \quad (\text{B.14c})$$

$$\sum_{s \in \mathcal{S}} X_s = 1, \quad (\text{B.14d})$$

$$\mathcal{X}_O X_N + (\mathcal{X}_O - 1) X_O + (2\mathcal{X}_O - 1) X_{NO} + 2\mathcal{X}_O X_{N_2} + (2\mathcal{X}_O - 2) X_{O_2} = 0. \quad (\text{B.14e})$$

B.3 The air-11 equilibrium system

For the air-11 mixture, one must add the equilibrium relations for ionization reactions, and an additional elemental balance condition:

$$p X_O^2 / X_{O_2} = K_{p O_2}^{\text{Diss}}(T), \quad (\text{B.15a})$$

$$p X_N^2 / X_{N_2} = K_{p N_2}^{\text{Diss}}(T), \quad (\text{B.15b})$$

$$p X_N X_O / X_{NO} = K_{p NO}^{\text{Diss}}(T), \quad (\text{B.15c})$$

$$p X_{O+} X_{e^-} / X_O = K_{p O}^{\text{Ioniz}}(T), \quad (\text{B.15d})$$

$$p X_{O_2^+} X_{e^-} / X_{O_2} = K_{p O_2}^{\text{Ioniz}}(T), \quad (\text{B.15e})$$

$$p X_{N+} X_{e^-} / X_N = K_{p N}^{\text{Ioniz}}(T), \quad (\text{B.15f})$$

$$p X_{N_2^+} X_{e^-} / X_{N_2} = K_{p N_2}^{\text{Ioniz}}(T), \quad (\text{B.15g})$$

$$p X_{NO+} X_{e^-} / X_{NO} = K_{p NO}^{\text{Ioniz}}(T), \quad (\text{B.15h})$$

$$\sum_{s \in \mathcal{S}} X_s = 1, \quad (\text{B.15i})$$

$$\begin{aligned} & \mathcal{X}_O (X_N + X_O + 2X_{NO} + 2X_{N_2} + X_{N_2} + X_{NO+} + X_{N_2^+} + X_{O_2^+} + X_{e^-}) + \\ & + X_O + X_{NO} + 2X_{O_2} + X_{O+} + X_{NO+} + 2X_{O_2^+} = 0, \end{aligned} \quad (\text{B.15j})$$

$$\begin{aligned} & \mathcal{X}_{\text{e}} \left(X_{\text{N}} + X_{\text{O}} + 2X_{\text{NO}} + 2X_{\text{N}_2} + X_{\text{N}_2} + X_{\text{NO}^+} + X_{\text{N}_2^+} + X_{\text{O}_2^+} + X_{\text{e}^-} \right) + \\ & - X_{\text{N}^+} - X_{\text{O}^+} - X_{\text{NO}^+} - X_{\text{N}_2^+} - X_{\text{O}_2^+} + X_{\text{e}^-} = 0, \end{aligned} \quad (\text{B.15k})$$

where the Diss and Ioniz superscripts denote if the reaction is dissociative or ionizing. Note that Eqs. B.15j and B.15k are nothing other than the evaluation of Eq. B.6 with $E = \text{O}$ and $E = \text{e}^-$ respectively. In Eq. B.15k, the term \mathcal{X}_{e} corresponds to the elemental fraction of the electron element. If one assumes charge neutrality, then it is identically zero, and Eq. B.15k is significantly simplified.

B.4 Verification

The implementation of the equilibrium systems (Eqs. B.14 and B.15) is verified by comparing the resulting mole fractions X_s against those obtained with mutation⁺⁺ (Refs. 2, 3). Figure B.1 presents an excellent agreement of both the mole fractions (Fig. B.1a and B.1b) and mole-fraction temperature gradients (Fig. B.1c). Figure B.1b presents the same as Fig. B.1a, yet with a logarithmic scaling, allowing to compare also the concentrations of trace species.

The implementation of the assembling of the thermodynamic derivatives for equilibrium conditions is verified by comparing the derivatives of the equilibrium thermal conductivity (κ^{eq}). The derivatives obtained with the assembly presented in Eqs. B.11 and B.13 is compared against those obtained with a 6th-order central FD stencil. First and second derivatives with respect to temperature can be computed with a FD stencil by keeping the pressure fixed and varying solely the temperature. The same process renders pressure derivatives by keeping the temperature fixed and varying only the pressure. The comparison presented in Fig. B.2 for an air-11-Park93 mixture (see § J.12) displays an excellent agreement.

References

- [1] J. B. Scoggins and T. E. Magin. *Gibbs function continuation for linearly constrained multiphase equilibria*. Combustion and Flame, 162(12):4514–4522, 2015.
- [2] T. E. Magin and G. Degrez. *Transport algorithms for partially ionized and unmagnetized plasmas*. Journal of Computational Physics, 198(2):424–449, 2004.
- [3] J. B. Scoggins and T. E. Magin. *Development of Mutation++: Multicomponent Thermodynamics And Transport properties for IONized gases library in C++*. AIAA paper, 2014-2966, 2014.

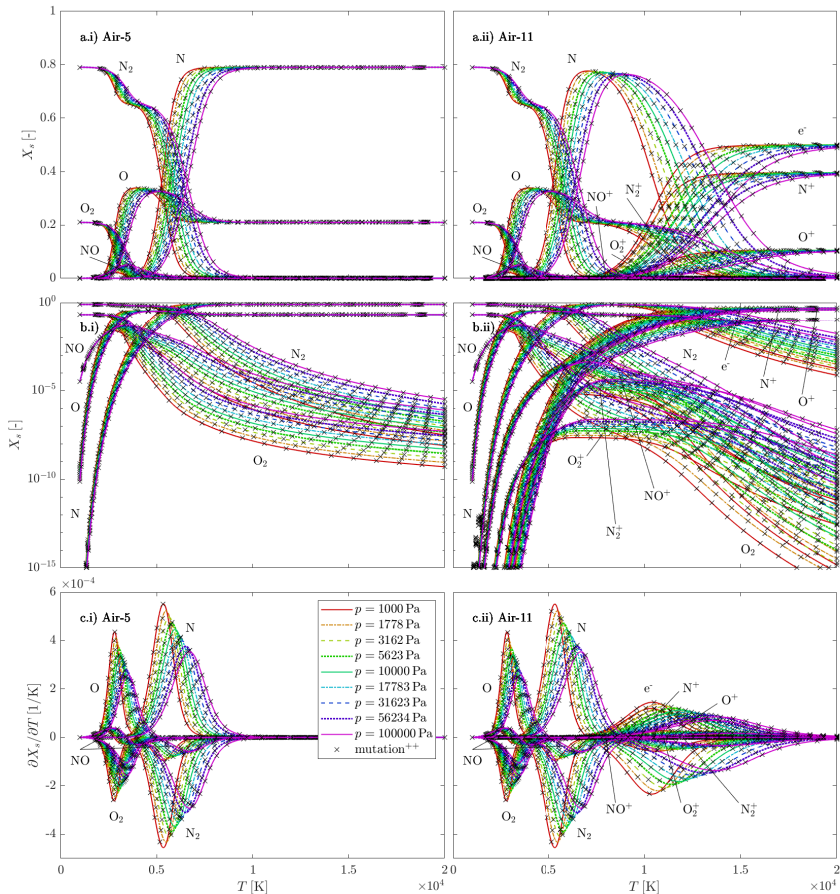


Figure B.I: Verification of the equilibrium-system solver against mutation⁺⁺ [2, 3] for 5- and 11-species air mixtures. Mole fractions and mole-fraction temperature gradients as a function of temperature for various pressures and for $X_N = 0.79$ and $X_O = 0.21$.

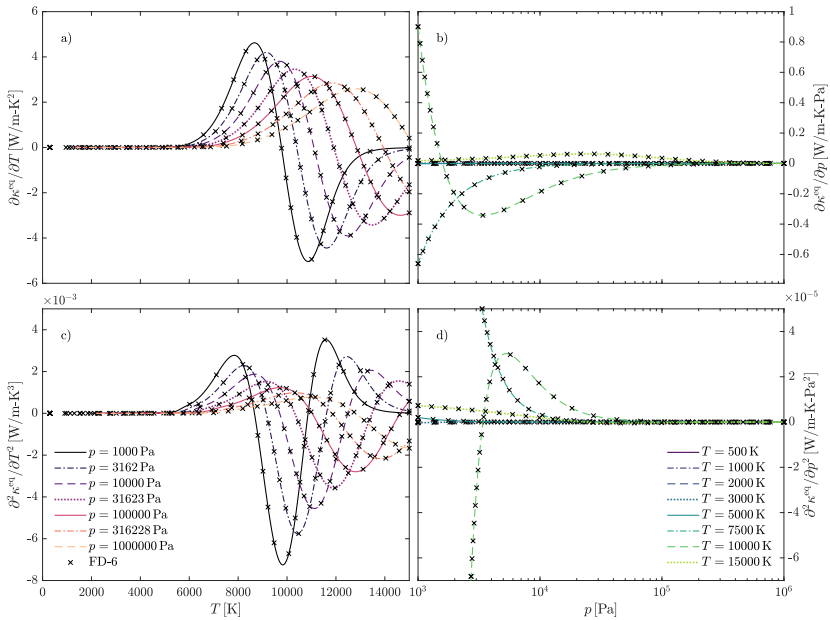


Figure B.2: Verification of the assembly of the thermodynamic derivatives for LTE. Properties for air, modeled with the air-11-Park93 mixture (see § J.12) with $\mathcal{X}_N = 0.79$ and $\mathcal{X}_O = 0.21$.

C

Coefficients for the transport properties

C.1 Coefficients for the polynomial approximation of Chapman-Enskog's theory for transport properties

The elements of the matrix subsystems for the first approximation on μ and the second on κ_H^{Trans} are defined as: [1]

$$G_{s\ell}^\mu = \frac{X_s X_\ell}{n \mathcal{D}_{s\ell}} \frac{N_A}{\mathcal{M}_s + \mathcal{M}_\ell} \left(\frac{6}{5} A_{s\ell}^* - 2 \right), \quad \begin{matrix} \forall s, \ell \in \mathcal{H} \\ s \neq \ell \end{matrix}, \quad (\text{C.1a})$$

$$G_{ss}^\mu = \sum_{\substack{\ell \in \mathcal{H} \\ \ell \neq s}} \frac{X_s X_\ell}{n \mathcal{D}_{s\ell}} \frac{N_A}{\mathcal{M}_s + \mathcal{M}_\ell} \cdot \left(\frac{6\mathcal{M}_\ell}{5\mathcal{M}_s} A_{s\ell}^* + 2 \right) + \frac{X_s^2}{\eta_s^\mu}, \quad \forall s \in \mathcal{H}, \quad (\text{C.1b})$$

$$G_{s\ell}^{\kappa} = \frac{1}{25 k_B} \frac{X_s X_{\ell}}{n \mathcal{D}_{s\ell}} \frac{\mathcal{M}_s \mathcal{M}_{\ell}}{(\mathcal{M}_s + \mathcal{M}_{\ell})^2} (16 A_{s\ell}^* + 12 B_{s\ell}^* - 55), \quad \begin{array}{l} \forall s, \ell \in \mathcal{H} \\ s \neq \ell \end{array}, \quad (C.2a)$$

$$\begin{aligned} G_{ss}^{\kappa} = \frac{1}{25 k_B} \sum_{\substack{\ell \in \mathcal{H} \\ \ell \neq s}} \frac{X_s X_{\ell}}{n \mathcal{D}_{s\ell}} \frac{\mathcal{M}_s \mathcal{M}_{\ell}}{(\mathcal{M}_s + \mathcal{M}_{\ell})^2} \cdot & \left(16 A_{s\ell}^* - 12 \frac{\mathcal{M}_{\ell}}{\mathcal{M}_s} B_{s\ell}^* + \right. \\ & \left. + 25 \frac{\mathcal{M}_{\ell}}{\mathcal{M}_s} + 30 \frac{\mathcal{M}_s}{\mathcal{M}_{\ell}} \right) + \frac{4}{15 k_B} \frac{X_s^2 \mathcal{M}_s}{N_A \eta_s^{\mu}}, \quad \forall s \in \mathcal{H}, \end{aligned} \quad (C.2b)$$

where the mono-species shear viscosity coefficients are defined as:

$$\eta_s^{\mu} = \frac{5}{16} \frac{\sqrt{\pi k_B T \mathcal{M}_s / N_A}}{\pi \Omega_{ss}^{(2,2)}}, \quad \forall s \in \mathcal{S}, \quad (C.3)$$

The polynomials appearing in the expression for the electron thermal conductivity (Eqs. 4.32a and 4.32b) are:

$$\Lambda_{e^- e^-}^{11} = \frac{64 X_{e^-}}{75 k_B} \sqrt{\frac{\pi \mathcal{M}_{e^-}}{2 \mathcal{R} T_{e^-}}} \left(\sum_{\ell \in \mathcal{H}} X_{\ell} \left(\frac{25}{4} \Omega_{e^- \ell}^{(1,1)} - 15 \Omega_{e^- \ell}^{(1,2)} + 12 \Omega_{e^- \ell}^{(1,3)} \right) + \right. \\ \left. + X_{e^-} \sqrt{2} \Omega_{e^- e^-}^{(2,2)} \right), \quad (C.4a)$$

$$\Lambda_{e^- e^-}^{12} = \frac{64 X_{e^-}}{75 k_B} \sqrt{\frac{\pi \mathcal{M}_{e^-}}{2 \mathcal{R} T_{e^-}}} \left(\sum_{\ell \in \mathcal{H}} X_{\ell} \left(\frac{175}{16} \Omega_{e^- \ell}^{(1,1)} - \frac{315}{8} \Omega_{e^- \ell}^{(1,2)} + 57 \Omega_{e^- \ell}^{(1,3)} + \right. \right. \\ \left. \left. - 30 \Omega_{e^- \ell}^{(1,4)} \right) + X_{e^-} \sqrt{2} \left(\frac{7}{4} \Omega_{e^- e^-}^{(2,2)} - 2 \Omega_{e^- e^-}^{(2,3)} \right) \right), \quad (C.4b)$$

$$\Lambda_{e^- e^-}^{22} = \frac{64 X_{e^-}}{75 k_B} \sqrt{\frac{\pi \mathcal{M}_{e^-}}{2 \mathcal{R} T_{e^-}}} \left(\sum_{\ell \in \mathcal{H}} X_{\ell} \left(\frac{1225}{64} \Omega_{e^- \ell}^{(1,1)} - \frac{735}{8} \Omega_{e^- \ell}^{(1,2)} + \frac{399}{2} \Omega_{e^- \ell}^{(1,3)} + \right. \right. \\ \left. \left. - 210 \Omega_{e^- \ell}^{(1,4)} + 90 \Omega_{e^- \ell}^{(1,5)} \right) + X_{e^-} \sqrt{2} \left(\frac{77}{16} \Omega_{e^- e^-}^{(2,2)} - 7 \Omega_{e^- e^-}^{(2,3)} + 5 \Omega_{e^- e^-}^{(2,4)} \right) \right), \quad (C.4c)$$

The binary diffusion coefficients are defined as:

$$\mathcal{D}_{s\ell} = \frac{3}{16} \frac{\sqrt{2\pi\mathcal{R}T^{Trans}}}{n\pi\Omega_{s\ell}^{(1,1)}} \sqrt{\frac{\mathcal{M}_s + \mathcal{M}_\ell}{\mathcal{M}_s \mathcal{M}_\ell}}, \quad \forall s, \ell \in \mathcal{H}, \quad (\text{C.5a})$$

$$\mathcal{D}_{se^*} = \frac{3}{16} \frac{\sqrt{2\pi\mathcal{R}T^e / \mathcal{M}_e^*}}{n\pi\Omega_{se^*}^{(1,1)}}, \quad \forall s \in \mathcal{H}, \quad (\text{C.5b})$$

$$\mathcal{D}_{e^*e^*} = \frac{3}{8} \frac{\sqrt{\pi\mathcal{R}T^e / \mathcal{M}_e^*}}{n\pi\Omega_{e^*e^*}^{(1,1)}}. \quad (\text{C.5c})$$

The matrix subsystem for the first approximation of the diffusion fluxes is:

$$G_{s\ell}^D = -\frac{X_s X_\ell}{\mathcal{D}_{s\ell}}, \quad \begin{matrix} \forall s, \ell \in \mathcal{H} \\ s \neq \ell \end{matrix}, \quad (\text{C.6a})$$

$$G_{ss}^D = \sum_{\substack{\ell \in \mathcal{S} \\ \ell \neq s}} \frac{X_s X_\ell}{\mathcal{D}_{s\ell}} + \left(\frac{T^e}{T^{Trans}} \right)^2 \frac{X_s X_{e^*}}{\mathcal{D}_{se^*}}, \quad \forall s \in \mathcal{H}, \quad (\text{C.6b})$$

$$G_{se^*}^D = -\frac{T^e}{T^{Trans}} \frac{X_s X_{e^*}}{\mathcal{D}_{se^*}}, \quad \forall s \in \mathcal{H}, \quad (\text{C.6c})$$

$$G_{e^*e^*}^D = \sum_{\ell \in \mathcal{H}} \frac{X_{e^*} X_\ell}{\mathcal{D}_{e^*\ell}}, \quad (\text{C.6d})$$

which must be made non-singular by enforcing the regularization condition (Eq. 4.38) through a Lagrange multiplier:

$$\check{G}_{s\ell}^D = G_{s\ell}^D + a_D Y_s Y_\ell, \quad \forall s, \ell \in \mathcal{S}, \quad (\text{C.7})$$

where the choice of a_D does not affect the solution of the problem. In order to preserve the order of magnitude of the problem, as suggested by Magin & Degrez [1], it is taken to be $a_D = 1/\max(\mathcal{D}_{s\ell})$.

C.2 Coefficients for Brokaw and Yos' simplification of Chapman & Enskog's theory for transport properties

The different coefficients appearing in Eqs. (4.34) and (4.35) for Brokaw [2] and Yos' [3, 4] simplification of Chapman & Enskog's theory are:

$$\mathcal{A}_{av}^Q = \frac{\sum_{s,\ell \in \mathcal{S}} X_s X_\ell \left(\frac{1}{\mathcal{A}_s^Q} - \frac{1}{\mathcal{A}_\ell^Q} \right)^2 \psi_{s\ell}^Q}{\sum_{s,\ell \in \mathcal{S}} X_s X_\ell \left(\frac{1}{\mathcal{A}_s^Q} - \frac{1}{\mathcal{A}_\ell^Q} \right)^2}, \quad (\text{C.8a})$$

$$\mathcal{A}_s^Q = \sum_{\ell \in \mathcal{S}} X_\ell \mathcal{B}_{s\ell}^Q, \quad \forall s \in \mathcal{S}, \quad (\text{C.8b})$$

$$\psi_{s\ell}^\mu = \frac{N_A}{\mathcal{M}_s + \mathcal{M}_\ell} \left(2\Delta_{s\ell}^{(1)} - \Delta_{s\ell}^{(2)} \right), \quad \forall s, \ell \in \mathcal{S}, \quad (\text{C.9a})$$

$$\mathcal{B}_{s\ell}^\mu = \frac{N_A}{\mathcal{M}_s} \Delta_{s\ell}^{(2)}, \quad \forall s, \ell \in \mathcal{S}, \quad (\text{C.9b})$$

$$\psi_{s\ell}^\kappa = \frac{2}{15 k_B} \frac{\mathcal{M}_s \mathcal{M}_\ell}{(\mathcal{M}_s + \mathcal{M}_\ell)^2} \left[\left(\frac{33}{2} - \frac{18}{5} B_{s\ell}^* \right) \Delta_{s\ell}^{(1)} - 4 \Delta_{s\ell}^{(2)} \right], \quad \forall s, \ell \in \mathcal{S}, \quad (\text{C.10a})$$

$$\begin{aligned} \mathcal{B}_{s\ell}^\kappa = \frac{1}{15 k_B (\mathcal{M}_s + \mathcal{M}_\ell)^2} & \left[16 \mathcal{M}_s \mathcal{M}_\ell \Delta_{s\ell}^{(2)} + 2 (\mathcal{M}_s - \mathcal{M}_\ell) \cdot \right. \\ & \cdot \left. \left(9 \mathcal{M}_s - \frac{15}{2} \mathcal{M}_\ell + \frac{18}{5} B_{s\ell}^* \mathcal{M}_\ell \right) \right] \cdot \Delta_{s\ell}^{(1)}, \quad \forall s, \ell \in \mathcal{S}, \end{aligned} \quad (\text{C.10b})$$

$$\Delta_{s\ell}^{(1)} = \frac{8}{3} \pi \Omega_{s\ell}^{(1,1)} \sqrt{\frac{2\pi \mathcal{M}_s \mathcal{M}_\ell}{\mathcal{R} T^{Trans} (\mathcal{M}_s + \mathcal{M}_\ell)}}, \quad \forall s, \ell \in \mathcal{S}, \quad (\text{C.11a})$$

$$\Delta_{s\ell}^{(2)} = \frac{16}{5} \pi \Omega_{s\ell}^{(2,2)} \sqrt{\frac{2\pi \mathcal{M}_s \mathcal{M}_\ell}{\mathcal{R} T^{Trans} (\mathcal{M}_s + \mathcal{M}_\ell)}}, \quad \forall s, \ell \in \mathcal{S}, \quad (\text{C.11b})$$

$$\varphi_{s\ell} = 1 + \frac{\left(1 - \frac{\mathcal{M}_s}{\mathcal{M}_\ell}\right) \left(0.45 - 2.54 \frac{\mathcal{M}_s}{\mathcal{M}_\ell}\right)}{\left(1 + \frac{\mathcal{M}_s}{\mathcal{M}_\ell}\right)^2}, \quad \forall s, \ell \in \mathcal{S}. \quad (\text{C.12})$$

References

- [1] T. E. Magin and G. Degrez. *Transport algorithms for partially ionized and unmagnetized plasmas*. Journal of Computational Physics, **198**(2):424–449, 2004.
- [2] R. S. Brokaw. *Approximate formulas for the viscosity and thermal conductivity of gas mixtures*. The Journal of Chemical Physics, **29**(2):391–397, 1958.
- [3] J. M. Yos. *Approximate equations for the viscosity and translational thermal conductivity of gas mixtures*. Technical Report AVSSD-0112-67-RM, Avco Corporation, 1967.

- [4] R. N. Gupta, J. M. Yos, R. A. Thompson, and K.-P. Lee. *A review of Reaction Rates and Thermodynamic and Transport Properties for an 11-Species Air Model for Chemical and Thermal Nonequilibrium Calculations to 30000K.* Technical Report RP-1232, NASA, 1990.

D

Requirements for the existence of self-similar solutions to the boundary-layer equations

As briefly laid out in § 5.1, the boundary-layer equations will have self-similar solutions as long as the variables and coefficients appearing in them are independent of the streamwise coordinate ξ . This requires, for starters, that the chemical and energy-relaxation non-dimensional source terms must be constant:

$$2\xi \dot{\bar{\Omega}}_s = \text{cst}, \quad \forall s \in \mathcal{S}, \quad (\text{D.1a})$$

$$2\xi \dot{\bar{\Omega}}_v = \text{cst}. \quad (\text{D.1b})$$

Recalling the definition of $\dot{\bar{\Omega}}_s$ in Eq. 5.5, constraint D.1a requires the species source terms to have the unlikely shape:

$$\frac{\dot{\bar{\omega}}_s}{\bar{\rho}} = \text{cst} \frac{\rho_e \mu_e u_e^2}{2\xi}, \quad \forall s \in \mathcal{S}. \quad (\text{D.2})$$

Similarly, operating with the definition of $\dot{\bar{\Omega}}_v$ in Eq. 5.5, constraint D.1b requires:

$$\frac{\bar{Q}_{TV}}{\bar{\rho}} = \text{cst} \frac{\rho_e \mu_e u_e^2 h_e}{2\xi}, \quad (\text{D.3a})$$

$$\frac{\dot{\bar{\omega}}_s}{\bar{\rho}} = \text{cst} \frac{\rho_e \mu_e u_e^2}{2\xi} \frac{h_e}{\bar{h}_{vs}}, \quad \forall s \in \mathcal{S}. \quad (\text{D.3b})$$

The condition in Eq. D.3b conflicts with that in Eq. D.2, making it impossible to reach self-similarity in TCNE. Even if only the conditions in Eq. D.2 (CNE) or those in Eq. D.3 (TNE) are required, the source-term shape they impose is highly unlikely. For this reason, the possibility of encountering self-similar solutions assuming a flow in TCNE, CNE, or TNE is directly dismissed.

Regarding the remaining flow assumptions summarized in Table 2.1, if the edge quantities are constant in the streamwise direction $q_e \neq q_e(\xi)$, the boundary-layer equations in CPG, TCFG, TPG, LTE or LTEED conditions will always have a self-similar solution.

For scenarios where the edge quantities do vary, the existence of self-similar solutions is subject to a series of constraints on the distribution of such edge quantities. It is the purpose of this appendix to study the implications of these constraints. First they will be discussed for CPG with a constant Prandtl number (Eq. 4.5) and a power law for viscosity of the type:

$$\mu = \mu_{\text{ref}} \left(\frac{T}{T_{\text{ref}}} \right)^{m_\mu}. \quad (\text{D.4})$$

with m_μ being larger than zero. Second the requirements for the existence of such solutions to exist in CPG with other viscosity laws, TPG, LTE, LTEED, and TCFG conditions will be laid out. Finally, a few remarks are made concerning the surface boundary conditions that allow for self-similar solutions.

D.1 CPG with a viscosity power law and with $q_e = q_e(\xi)$

It is useful to recall the boundary-layer equations in non-dimensional form for CPG conditions (Eqs. 5.4a, 5.4b and 5.22):

$$2\xi \left(\frac{\partial \bar{f}}{\partial \eta} \frac{\partial^2 \bar{f}}{\partial \xi \partial \eta} - \frac{\partial^2 \bar{f}}{\partial \eta^2} \frac{\partial \bar{f}}{\partial \xi} \right) = \frac{\partial}{\partial \eta} \left(\bar{c} \frac{\partial^2 \bar{f}}{\partial \eta^2} \right) + \bar{f} \frac{\partial^2 \bar{f}}{\partial \eta^2} + \beta_H \left(\bar{j} - \left(\frac{\partial \bar{f}}{\partial \eta} \right)^2 \right), \quad (\text{D.5a})$$

$$2\xi \left(\frac{\partial \bar{f}}{\partial \eta} \frac{\partial \bar{k}}{\partial \xi} - \frac{\partial \bar{k}}{\partial \eta} \frac{\partial \bar{f}}{\partial \xi} \right) = \frac{\partial}{\partial \eta} \left(\bar{c} \frac{\partial \bar{k}}{\partial \eta} \right) + \bar{f} \frac{\partial \bar{k}}{\partial \eta}, \quad (\text{D.5b})$$

$$2\xi \left(\frac{\partial \bar{f}}{\partial \eta} \frac{\partial \bar{g}}{\partial \xi} - \frac{\partial \bar{g}}{\partial \eta} \frac{\partial \bar{f}}{\partial \xi} \right) = \frac{\partial}{\partial \eta} \left(\bar{a}_1 \frac{\partial \bar{g}}{\partial \eta} \right) + \bar{f} \frac{\partial \bar{g}}{\partial \eta} - \Theta_H \frac{\partial \bar{f}}{\partial \eta} \bar{g} + \frac{\partial}{\partial \eta} \left(\bar{a}_2 \frac{\partial \bar{f}}{\partial \eta} \frac{\partial^2 \bar{f}}{\partial \eta^2} \right) + \bar{a}_0 \left(\frac{\partial \bar{k}}{\partial \eta} \right)^2, \quad (\text{D.5c})$$

where:

$$\begin{aligned}
 \frac{\partial \bar{f}}{\partial \eta} &= \bar{u}/u_e, & \bar{k} &= \bar{w}/w_e, & \bar{g} &= \bar{h}^u/h_e^u, \\
 \bar{j} &= \rho_e/\bar{\rho}, & \bar{c} &= \frac{\bar{\rho} \bar{\mu}}{\rho_e \mu_e}, & \bar{a}_0 &= \frac{Ec_w}{1 + Ec/2} \bar{c}, \\
 \bar{a}_1 &= \frac{\bar{\kappa}}{\bar{c}_p \bar{\mu}} \bar{c}, & \bar{a}_2 &= \frac{Ec}{1 + Ec/2} (\bar{c} - \bar{a}_1), & \beta_H &= \frac{2\xi}{u_e} \frac{du_e}{d\xi}, \\
 \Theta_H &= \frac{2\xi}{h_e^u} \frac{dh_e^u}{d\xi}, & Ec &= \frac{u_e^2}{h_e}, & Ec_w &= \frac{w_e^2}{h_e}. \tag{D.6}
 \end{aligned}$$

Note that Eqs. D.5, dropping the blue left-hand-side depending on ξ , constitute the compressible version of the Falkner-Skan-Cooke equations [1].

In order for there to be a self-similar solution to Eqs. D.5, the equations themselves must be independent of the marching variable ξ . White [2, §7-2.1] laid out the requirements for the compressible Falkner-Skan equations (omitting Eq. D.5b). Completing such requirements with those derived from including a non-zero spanwise velocity, one has:

1. $\bar{c} = \bar{c}(\bar{f}, \bar{g})$,
2. $\bar{Pr} = \frac{\bar{\kappa}}{\bar{c}_p \bar{\mu}} = \bar{Pr}(\bar{f}, \bar{g})$,
3. $\bar{j} = \bar{j}(\bar{f}, \bar{g})$,
4. $\beta_H = \frac{2\xi}{u_e} \frac{du_e}{d\xi} = \text{cst}$,
5. $Ec = \frac{u_e^2}{h_e} = \text{cst}$,
6. $\Theta_H = \frac{2\xi}{h_e^u} \frac{dh_e^u}{d\xi} = \text{cst}$,
7. $Ec_w = \frac{w_e^2}{h_e} = \text{cst}$.

If these 7 conditions are satisfied, then the solution $\bar{f}, \bar{g}, \bar{k}$ to Eqs. D.5 will be solely dependent on the self-similar variable η . As previously claimed, this is clearly the case if all edge conditions are constant. In such a scenario, $\beta_H = 0$, $\Theta_H = 0$, and Ec and Ec_w are constant. Moreover, the static enthalpy can be obtained as:

$$\frac{\bar{h}}{h_e} = \left(1 + \frac{Ec}{2}\right) \bar{g} - \frac{Ec}{2} \left(\frac{\partial \bar{f}}{\partial \eta}\right)^2, \tag{D.7}$$

where h_e is constant. One may then obtain \bar{T} from \bar{h} , and ultimately compute all the properties in conditions 1-3, solely based on \bar{f} and \bar{g} . Eqs. D.5, and thus the 7 existence requirements are identical in LTE and mono-species TPG conditions. The only difference for LTE is that the properties also depend on p_e through the equilibrium system (app. B). However, if p_e is constant as hypothesized, it does not affect the satisfaction of conditions 1-3. This confirms the previous claim that having constant edge parameters is a sufficient requisite for self-similar solutions to exist to the boundary-layer equations in (at least) CPG, mono-species TPG, and LTE conditions.

Regarding flows with non-constant edge parameters, requirements 1-3 are also satisfied in CPG conditions for a constant Prandtl number and a viscosity power law with the equation of state presented in Eq. A.10, since:

$$\bar{c} = \frac{\bar{\mu} \bar{\rho}}{\mu_e \rho_e} = \left(\frac{\bar{T}}{T_e} \right)^{m_\mu - 1} = \left(\frac{\bar{h}}{h_e} \right)^{m_\mu - 1}, \quad (\text{D.8a})$$

$$\bar{\Pr} = \Pr_e, \quad (\text{D.8b})$$

$$\bar{j} = \frac{\rho_e}{\bar{\rho}} = \frac{\bar{T}}{T_e} = \frac{\bar{h}}{h_e}, \quad (\text{D.8c})$$

where Eq. D.7 relates \bar{h}/h_e to \bar{f} , \bar{g} and Ec. This implies that conditions 1-3 are satisfied if condition 5 also is.

Condition 4 can be satisfied with a non-constant edge velocity with a shape:

$$u_e = u_{e0} \left(\frac{\xi}{\xi_0} \right)^{\beta_H / 2}, \quad (\text{D.9})$$

which is feasible a-priori. However, as illustrated in the following, such a shape is incompatible with simultaneously satisfying conditions 5 and 7. The quasi-3D requirement implies that $w_e \neq w_e(\xi)$, so that conditions 5 and 7 require:

$$5. \rightarrow h_e = \text{cst} \cdot u_e(\xi)^2,$$

$$7. \rightarrow h_e = \text{cst},$$

which are clearly incompatible. This means that there is no general self-similar solution to the compressible Falkner-Skan-Cooke equations. One can therefore only obtain *quasi-self-similar* solutions, where the variation of the Eckert numbers is small enough for it to be neglected. Such a scenario could be found in high-enthalpy, yet low-speed boundary-layers, which are common in plasma wind tunnels and in the proximity to the leading edge of hypersonic vehicles. However, this is generally not the case farther downstream, at the locations where laminar-to-turbulent transition is of interest.

When working with a purely two-dimensional flow, one can remove Eq. D.5b from the equation system and condition 7 from the list of requirements for the existence of a self-similar solution. The remaining system is thus the compressible version of the Falkner-Skan equations [3]. In such instances, condition 6 can be satisfied by having an edge semi-total enthalpy with a shape:

$$h_e^u = h_{e0}^u \left(\frac{\xi}{\xi_0} \right)^{\Theta_H/2}, \quad (\text{D.10})$$

and consequently the edge static enthalpy with a shape:

$$h_e = h_e^u - \frac{u_e^2}{2} = h_{e0}^u \left(\frac{\xi}{\xi_0} \right)^{\Theta_H/2} - \frac{u_{e0}^2}{2} \left(\frac{\xi}{\xi_0} \right)^{\beta_H}. \quad (\text{D.11})$$

In other words, for two-dimensional boundary layers, simultaneously satisfying conditions 4-6 requires a value of $\Theta_H = 2\beta_H$. As White points out, such a situation “*is not very likely*” [2, §7-2.1]. This implies that, like for the compressible Falkner-Skan-Cooke equations, there also does not exist a general realistic self-similar solution to the compressible version of the Falkner-Skan equations.

As mentioned by White, most realistic boundary-layer flows feature a constant total enthalpy at the edge.^a This simplifies Eqs. D.10 and D.11 to:

$$h_e^u = h_{e0}^u, \quad (\text{D.12})$$

$$h_e = h_{e0}^u - \frac{u_{e0}^2}{2} \left(\frac{\xi}{\xi_0} \right)^{\beta_H}. \quad (\text{D.13})$$

Therefore, only realistic quasi-self-similar solutions exist, subject to the same simplifications mentioned for the compressible Falkner-Skan-Cooke equations (Eq. D.5).

D.2 CPG with other viscosity laws and $q_e = q_e(\xi)$

If one employs Sutherland’s law (Eq. 4.2), or any of the high-temperature transport models explored in § 4.2, \bar{c} is not related to \bar{f} , \bar{g} and Ec through Eqs. D.8a and D.7, since:

$$\bar{c} = \frac{\bar{\mu} \bar{\rho}}{\mu_e \rho_e} = \left(\frac{\bar{T}}{T_e} \right)^{1/2} \left(\frac{T_e + S_\mu}{\bar{T} + S_\mu} \right). \quad (\text{D.14})$$

Whilst the first parenthesis in the right-hand-side is related to \bar{f} , \bar{g} and Ec through Eq. D.7, the second one is not. One cannot rearrange it to have as a sole function of \bar{T}/T_e and other constants. In order to satisfy condition 1, it is therefore necessary

^aIn a quasi-3D boundary-layer flow, this also implies that the semi-total enthalpy is constant, since $\partial w_e / \partial \xi = 0$, then $\partial h_e^{uvw} / \partial \xi = \partial h_e^u / \partial \xi$.

to model viscosity with a proportionality law with respect to a certain power of temperature. The departure of the viscosity model from such a proportionality law will result in the quasi-self-similar solution to the boundary-layer equations being a worse representation of reality.

D.3 TPG with $q_e = q_e(\xi)$

Self-similar solutions in mono-species TPG with $q_e = q_e(\xi)$ are subject to the same aforementioned restrictions for CPG. Additionally, since enthalpy is no longer a linear function of temperature, \bar{T}/T_e cannot be obtained from \bar{h}/h_e . Similarly to what was argued for viscosity models other than a power law, the departure from the linear relationship between h and T will result in the quasi-self-similar solutions to the boundary-layer equations being an even worse representation of the real physical system.

In instances where there exists interdiffusion of non-reacting species (multi-species TPG), one must also solve the non-dimensional species-concentration-conservation equations (Eq. 5.4e) in the absence of chemical source terms ($\dot{\Omega}_s = 0$). The only additional variable in such equations is the non-dimensional mass diffusion flux \bar{j}_s , given in Eq. 5.7 for a simple diffusion assumption. Aside from the system unknowns (\bar{Y}_s)^b, \bar{j}_s only features thermotransport properties, which will impose conditions similar to 1-3. Such conditions can be (quasi-)satisfied for TPG, with the same restrictions mentioned for the viscosity law – a departure from proportionality laws with some exponent of the temperature will compromise the self-similarity of the solutions. More elaborate diffusion theories will likewise only feature thermotransport properties in \bar{j}_s , thus sharing the requirements.

D.4 LTE and LTEED with $q_e = q_e(\xi)$

Self-similar solutions in LTE conditions with $q_e = q_e(\xi)$ have an additional restriction to those in TPG. It arises from the fact that the thermodynamic state of the mixture is defined also by p_e , which also varies with ξ . Integrating the Bernoulli equation and substituting the one-temperature equation of state (Eq. A.10) at the edge, one has:^c

$$p_e = p_{e0} \exp \left(\int_0^\xi \frac{u_e(\check{\xi})}{R_e(\check{\xi}) T_e(\check{\xi})} \frac{du_e}{d\check{\xi}} d\check{\xi} \right). \quad (\text{D.15})$$

^bThe general version of conditions 1-3 requires the properties be exclusive functions of the system variables. In multispecies TPG these are \bar{f} , \bar{g} , \bar{k} and \bar{Y}_s .

^cNote that the evaluation of Eq. D.15 must be done iteratively, since $T_e = T_e(h_e, p_e)$ through the equilibrium system. Therefore, one typically makes a guess of p_e , then computes T_e with the equilibrium system (app. B), and then updates the guess of p_e with Eq. D.15, repeating the process until numerical convergence is reached.

Since $p_e = p_e(\xi)$, and \bar{c} , Pr and \bar{j} depend on p_e , conditions 1-3 can no longer be satisfied. However, if the pressure variation is not very large, one can neglect the dependency of the thermo-transport properties on pressure,^d and reach again a quasi-self-similar solution as defined before. However, it is important to bear in mind that such a solution in LTE is an increasingly worse approximation to the full solution with respect to those in CPG or TPG conditions.

Quasi-self-similar solutions to the boundary-layer equations in LTEED conditions with $q_e = q_e(\xi)$ have similar limitations to those in LTE. The only difference between LTEED and LTE is that the thermodynamic state of the mixture also varies with the non-constant elemental fractions \mathcal{Y}_E . However, since these fractions are unknowns in the system of boundary-layer equations (see Eq. 5.12), they will be independent (or quasi-independent) of ξ if the remaining coefficients in the equations are too. The LTEED non-dimensional boundary-layer equations also feature elemental diffusion fluxes (Eq. 5.13). However, the same remarks made for multi-species TPG conditions also apply.

D.5 TCFG with $q_e = q_e(\xi)$

Finally, the boundary-layer equations in TCFG conditions with $q_e = q_e(\xi)$ additionally solve the decoupled vibrational-electronic-electron energy equation (Eq. 5.4d) in the absence of energy-relaxation source terms ($\dot{\Omega}_v = 0$). Due to the unlikelihood of encountering an ionized thermo-chemically frozen boundary layer, the role of the non-dimensional electron pressure (\bar{p}_e) to eventual (quasi-)self-similar solutions is omitted. Since θ_H appears explicitly in Eq. 5.4d, it must also be constant in order to achieve (quasi-)self-similarity. However, this is always the case if both Θ_H and β_H are constant (conditions 4 and 6). The remaining additional parameters in Eq. 5.4d are \bar{c}_{p1} , \bar{c}_{p2} and \bar{a}_{v1} . In order for there to be a (quasi-)self-similar solution in TCFG conditions, these must remain (quasi-)independent from the marching variable ξ . This is an additional constraint with respect to CPG and mono-species TPG cases. It is possible that an alternative grouping of variables relaxes such requirements in TCFG conditions. However, determining it is beyond the scope of this dissertation.

D.6 Surface thermal boundary condition

If the edge parameters are constant, the existence of a self-similar solution to the boundary-layer equations is not affected by the thermal wall boundary condition.

^dTemperature has the largest impact on the properties in LTE. Most of them are explicit functions of temperature (see chapter 4), and implicit functions of both pressure and temperature through the equilibrium system (app. B).

One can thus apply either an isothermal, an adiabatic, or a constant-heat-flux condition. In other words, one can impose:

$$\bar{g}_w = \text{cst}, \quad \text{or} \quad (\text{D.16a})$$

$$\left. \frac{\partial \bar{g}}{\partial \eta} \right|_w = \text{cst}. \quad (\text{D.16b})$$

Eq. D.16a leads to a wall at constant temperature, whilst Eq. D.16b leads to a wall at constant heat flux (0 for adiabatic).

If the edge parameters do change, satisfying the requirements presented in the preceding sections, the accepted boundary conditions are the same (Eq. D.16), but the implications are different. If h_e^u varies but $\bar{g}_w = \text{cst}$, the result is that \bar{h}_w^u and \bar{h}_w (they are equivalent at the wall since $\bar{u}_w = 0$) vary identically to how h_e^u does.

It is important to point out that such implications vary with the choice of system variables. If one were to work with the energy-conservation equation in terms of the static enthalpy h rather than the semi-total enthalpy h^u , one would define $\bar{g} = \bar{h}/h_e$ rather than $\bar{g} = \bar{h}^u/h_e^u$. This implies that the wall static enthalpy, keeping $\bar{g} = \text{cst}$, would vary like $h_e(\xi)$ rather than like $h_e^u(\xi)$. This can be a major difference, since as stated in § D.1, h_e^u normally remains constant, whilst h_e does not. One can therefore wisely choose the form of the energy equation to encounter a self-similar solution that is most adequate for the type of flow of interest.

A similar situation occurs when applying Eq. D.16b rather than Eq. D.16a in situations with $q_e = q_e(\xi)$ – the surface heat flux varies in ξ in the same way as h_e^u (or h_e if one works with the energy equations in terms of the static enthalpy) does.

D.7 Surface mass injection

In order for the boundary-layer equations to have self-similar (or quasi-self-similar) solutions with mass injection at the wall, this injection must be such that the blowing parameter:^e

$$f_w = -\frac{\bar{v}_w \bar{\rho}_w \sqrt{2\xi}}{\rho_e u_e \mu_e}, \quad (\text{D.17})$$

remains constant. The edge profiles can be functions of ξ as long as they satisfy the aforementioned requirements. This parameter corresponds to the value of \bar{f} at the wall.

D.8 y -vector rebuilding for $\beta_H \neq 0$

The treatment required for the undoing of the Illingworth transformation (Eq. 5.6) for quasi-self-similar boundary layers without constant edge properties requires

^eNote that for conical boundary layers, Eq. D.17 features the transformed wall-normal velocity \bar{v} (Eq. 5.28) rather than \bar{v} .

special mention. From Eq. 5.6 one has that:

$$y = \int_0^\eta \frac{\sqrt{2\xi}}{u_e \bar{\rho}} d\check{\eta}, \quad (\text{D.18})$$

where:

$$d\xi = \rho_e u_e \mu_e dx. \quad (\text{D.19})$$

Integrating Eq. D.18 for incompressible flows is rather simple, since ρ_e and μ_e are constant, and u_e is given by Eq. D.9. Operating Eq. D.18 with these considerations one reaches:

$$\xi = (1 - \beta_H/2) \rho_e \mu_e u_e x, \quad (\text{D.20})$$

which is an implicit function, since $u_e = u_e(\xi)$, and can be rearranged to:

$$\xi = \left((1 - \beta_H/2) \rho_e \mu_e \frac{u_{e0}}{\xi_0^{\beta_H/2}} x \right)^{\beta_H/2-1}. \quad (\text{D.21})$$

However, for quasi-self-similar compressible flows, one has that ρ_e , u_e and μ_e are all functions of ξ , and therefore the integration of Eq. D.19 must be done numerically. Specifically, one has that u_e is given by Eq. D.9, and that T_e can be obtained from h_e , which is given by Eq. D.11. With them, one can obtain the pressure p_e through Eq. D.15, and subsequently the density ρ_e with the equation of state (Eq. A.10).^f Finally, μ_e can be obtained applying whichever transport model of those presented in § 4.2.

Having $\mu_e(\xi)$, $\rho_e(\xi)$ and $u_e(\xi)$ one can proceed to integrate Eq. D.19. When evaluating a quasi-self-similar solution, one is typically searching for the value of ξ corresponding to a particular physical streamwise position of interest x . However, the mentioned expressions are functions of ξ . This means that one must discretize the ξ -space, integrate Eq. D.19 numerically to obtain the corresponding values of x , and then interpolate backwards to obtain the ξ value for the particular x of interest.

D.9 Summary

There exist no realistic self-similar solutions to the TCNE, CNE or TNE boundary-layer equations. Purely self-similar solutions to the compressible boundary-layer equations will only exist, in general, in CPG, TPG, LTE, LTEED and TCFG conditions when the edge quantities are constant $q_e \neq q_e(\xi)$.

^fNote that for LTE and LTEED, h_e is a function of T_e and p_e through the equilibrium system (see app. B). This implies that one cannot sequentially obtain T_e from h_e , and then with it and u_e obtain p_e . Instead, one must make a guess for p_e , perform the aforementioned process, and then iterate on the value of p_e , correcting the successive guesses.

If the edge quantities are not constant $q_e = q_e(\xi)$, the solutions to the boundary-layer cannot be anything other than quasi-self-similar. How far these solutions are from self-similarity depends on the flow assumption and the edge conditions. CPG flows with a viscosity power law require the edge Eckert numbers to be sufficiently constant such that they do not modulate the boundary-layer profiles excessively away from self-similarity. If other viscosity laws are employed, their departure from a proportionality law with respect to some exponent of temperature will result in the quasi-self-similar solution to depart farther from self-similarity. This departure is even more so in TPG as the static enthalpy moves away from being linear with temperature. LTE and LTEED assumptions additionally require the edge (and boundary-layer) pressure variation to be small enough not to overly condition the thermotransport properties. Finally, in TCFG conditions, several additional grouping variables must be (quasi-)independent of the marching variable ξ for there to exist (quasi-)self-similar solutions.

Both isothermal and constant-heat-flux wall boundary conditions can be employed without compromising the self-similarity of the solutions. However, the shape of the wall profiles of the physical quantities will vary if the edge quantities do.

Self-similar solutions also exist in scenarios with mass injection, insofar as the blowing parameter f_w remains constant.

References

- [1] J. C. Cooke. *The Boundary Layer of a Class of Infinite Yawed Cylinders*. Mathematical Proceedings of the Cambridge Philosophical Society, **46**(2):645–648, 1950.
- [2] F. M. White. *Viscous Fluid Flow*. McGraw-Hill, 2nd edition, 1991.
- [3] V. M. Falkner and S. W. Skan. *Solutions of the boundary-layer equations*. The London, Edinburgh, and Dublin Philosophical Magazine and Journal of Science, **12**(80):865–896, 1931.

E

Rebuilding of the wall-normal velocity from a boundary-layer solution

The non-dimensional variable \bar{f} appearing in the non-dimensional boundary-layer equations (§ 5.1), is related to the streamfunction Ψ through:

$$\bar{f} = \sqrt{2\xi} \bar{\Psi}, \quad (\text{E.1})$$

such that the continuity equation (Eq. 5.3a) is directly satisfied:

$$\left. \begin{aligned} \bar{\rho} \bar{u} &= \frac{\partial \bar{\Psi}}{\partial y} \\ \bar{\rho} \bar{v} &= -\frac{\partial \bar{\Psi}}{\partial x} \end{aligned} \right\} \frac{\partial \bar{\rho} \bar{u}}{\partial x} + \frac{\partial \bar{\rho} \bar{v}}{\partial y} = \frac{\partial^2 \bar{\Psi}}{\partial x \partial y} - \frac{\partial^2 \bar{\Psi}}{\partial y \partial x} = 0. \quad (\text{E.2})$$

The wall-normal velocity, is therefore:

$$\bar{v} = -\frac{1}{\bar{\rho}} \left(\frac{\partial \eta}{\partial x} \sqrt{2\xi} \frac{\partial \bar{f}}{\partial \eta} + \frac{\mu_e \rho_e u_e}{\sqrt{2\xi}} \bar{f} + \mu_e \rho_e u_e \sqrt{2\xi} \frac{\partial \bar{f}}{\partial \xi} \right). \quad (\text{E.3})$$

Out of all the terms appearing in Eq. E.3, the derivative of η with respect to x requires particular attention. Attending to the definition of η (Eq. 5.6) its derivative can be expressed in integro-differential form as:

$$\frac{\partial \eta}{\partial x} = \frac{\partial}{\partial x} \left(\int_0^y \frac{u_e}{\sqrt{2\xi}} \bar{\rho} d\bar{y} \right). \quad (\text{E.4})$$

Since x and y are orthogonal, one can operate with Eq. E.4 and apply the chain rule such that:

$$\begin{aligned}\frac{\partial \eta}{\partial x} &= \int_0^y \left(\frac{\rho_e \mu_e u_e}{\sqrt{2\xi}} \frac{\partial u_e}{\partial \xi} \bar{\rho} - \frac{u_e}{(2\xi)^{3/2}} \bar{\rho} + \frac{\rho_e \mu_e u_e^2}{\sqrt{2\xi}} \frac{\partial \bar{\rho}}{\partial x} \right) dy = \\ &= \int_0^y \left(\frac{\rho_e \mu_e u_e}{\sqrt{2\xi}} \left(\frac{\partial u_e}{\partial \xi} \bar{\rho} - \frac{u_e}{2\xi} \bar{\rho} \right) + \frac{u_e}{\sqrt{2\xi}} \left(\frac{\partial \eta}{\partial x} \frac{\partial \bar{\rho}}{\partial \eta} + \rho_e \mu_e u_e \frac{\partial \bar{\rho}}{\partial \xi} \right) \right) dy\end{aligned}\quad (\text{E.5})$$

After differentiating with respect to y , Eq. E.5 can be rearranged into a non-linear ordinary differential equation on the x derivative of η :

$$\frac{\partial}{\partial y} \left(\frac{\partial \eta}{\partial x} \right) = \mathcal{M}_1 + \mathcal{M}_2 \frac{\partial \eta}{\partial x}, \quad (\text{E.6})$$

with:

$$\mathcal{M}_1 = \frac{\rho_e \mu_e u_e}{\sqrt{2\xi}} \left(\frac{\partial u_e}{\partial \xi} \bar{\rho} - \frac{u_e}{2\xi} \bar{\rho} + u_e \frac{\partial \bar{\rho}}{\partial \xi} \right), \quad (\text{E.7a})$$

$$\mathcal{M}_2 = \frac{u_e}{\sqrt{2\xi}} \frac{\partial \bar{\rho}}{\partial \eta}, \quad (\text{E.7b})$$

and with the boundary condition that $\partial \eta / \partial x = 0$ at $y = 0$. Eq. E.6 is integrated in order to reach $\partial \eta / \partial x$, which is necessary to obtain the wall-normal velocity \bar{v} .

Note that for axisymmetric boundary layers, where the equations are made “Cartesian-like” with the Probstein-Elliott transformation (§ 5.1.7), the treatment presented in this appendix is the same. The only difference is that the expressions feature the transformed variables χ , y and \bar{v} , instead of the physical ones x , y and \bar{v} .

F

Base-flow wall-normal velocity treatment in LST when using the AMSBC

In LST, the evaluation of the continuity equation (Eq. 2.8) on the base-flow quantities (\bar{q}) with the corresponding ansatz (Eq. 3.11a) leads to the requirement that:^a

$$\frac{\partial(\bar{\rho}\bar{v})}{\partial y} = 0. \quad (\text{F.1})$$

This is usually satisfied (see for instance Refs. 4–6) by imposing:

$$\bar{v} = \frac{\partial \bar{v}}{\partial y} = 0. \quad (\text{F.2})$$

However, this introduces an inconsistency when the blowing velocity in the laminar base flow is not zero. Authors dealing with such inconsistency have argued that since $\bar{v}_w \ll \bar{u}$, it is fair to assume Eq. F.2. Even though this is true when comparing the wall-blowing velocity to the streamwise in the freestream, it is not in the lower region of the boundary layer. As y approaches 0, \bar{u} is reduced until, eventually $\bar{u} \sim \bar{v}$.

A second way of satisfying Eq. F.1 would be imposing:

$$\bar{v} = \text{cst.}/\bar{\rho}. \quad (\text{F.3})$$

^aA Cartesian reference system is employed in this development for the sake of clarity. However, it can very easily be applied to an arbitrary reference frame employing the tensorial notation [1–3].

This path is not free from inconsistencies, since it imposes \bar{v} to be different than zero in the entire domain, when in reality, out of the boundary layer, one has that $\bar{v}(y > \delta_H) = 0$. Even though it respects $\bar{v}_w \neq 0$, and includes a certain decay of the wall-normal velocity throughout the domain, this decay is not physically correct, depending only on the density. Another inconvenience of assuming Eq. F.3 is that it requires a complete rederivation of the stability equations, thus complicating its implementation in existing codes.

The approach proposed in this work when employing the AMSBC defines the wall-normal velocity in a piecewise fashion:

$$\bar{v}(y) = \begin{cases} \bar{v}_w, & y = 0 \\ 0, & y > 0 \end{cases}. \quad (\text{F.4})$$

Its spatial gradients are set equal to zero in the entire domain:

$$\frac{\partial \bar{v}}{\partial y} = 0, \quad \frac{\partial^2 \bar{v}}{\partial y^2} = 0. \quad (\text{F.5})$$

This discontinuous definition allows to respect the desired conditions on both boundaries, having $\bar{v}_w \neq 0$ and $\bar{v}(y_{\max}) = 0$. It also allows the boundary condition to be implemented in traditional LST codes without a major rederivation, since the only terms affected are those at the wall. However, it is not free from error – the continuity equation applied on the mean-flow variables at the wall will not be satisfied.

It is possible to estimate the error introduced by each treatment of the inconsistency by looking at the afflicted regions. The error committed assuming Eq. F.2 can be approximated [7] to be of the order of $\bar{v}_w/u_e \sim 1/\text{Re}$ at $y = 0$. With Eq. F.3, one also introduces an error of $\bar{v}_w/u_e \sim 1/\text{Re}$ but in the entire freestream region $y > \delta_H$. Finally, with Eq. F.4, both boundaries are respected, but in the proximity of $y = 0$ the continuity equation is not. This is estimated to introduce an error of $\bar{v}_w (\partial \bar{v}/\partial y)|_w$. As developed in Ref. 8, typical hypersonic cases lead to an error of around $10^{-4} - 10^{-6}$, which is between one and three orders of magnitude lower than $1/\text{Re}$.

Any other boundary condition evaluated at the wall together with the AMSBC must therefore be consistent with the aforementioned treatment of the wall-normal velocity and its gradients.

More information on the AMSBC and the treatment of the wall-normal velocity can be found in Refs. 8–10.

References

- [1] R. Aris. *Vectors, Tensors, and the Basic Equations of Fluid Mechanics*. Dover - Prentice Hall, New York, 2nd edition, 1962.

- [2] F. Pinna and K. J. Groot. *Automatic derivation of stability equations in arbitrary coordinates and different flow regimes*. AIAA paper, [2014-2634](#), 2014.
- [3] K. J. Groot. *Derivation of and Simulations with BiGlobal Stability Equations*. Technical Report AE5110, VKI and TU Delft, 2013.
- [4] M. R. Malik. *Prediction and control of transition in supersonic and hypersonic boundary layers*. AIAA Journal, [27\(11\):1487–1493](#), 1989.
- [5] H. B. Johnson, J. E. Gronvall, and G. V. Candler. *Reacting hypersonic boundary layer stability with blowing and suction*. AIAA paper, [2009-938](#), 2009.
- [6] S. Ghaffari, O. Marxen, G. Iaccarino, and E. S. G. Shaqfeh. *Numerical simulations of hypersonic boundary-layer instability with wall blowing*. AIAA paper, [2010-706](#), 2010.
- [7] T. Cebeci and J. Cousteix. *Modeling and Computation of Boundary-Layer Flows: Laminar, Turbulent and Transitional Boundary Layers in Incompressible Flows : Solutions Manual and Computer Programs*. Horizons Pub., 2001.
- [8] F. Miró Miró and F. Pinna. *Effect of uneven wall blowing on hypersonic boundary-layer stability and transition*. Physics of Fluids, [30\(084106\)](#), 2018.
- [9] F. Miró Miró. *Numerical Study of the Stability of a Hypersonic Boundary Layer in the presence of Blowing*. Technical Report TR 2015-28, von Karman Institute for Fluid Dynamics, Brussels, Belgium, 2015.
- [10] F. Pinna and F. Miró Miró. *Numerical modeling of continuous blowing surface in hypersonic boundary layers*. In [EUCASS 2017](#), Milano, Italy, 2017.

G

Integration matrices of arbitrary-order accuracy

It is possible to obtain an integration matrix with the same level of accuracy as a differentiation matrix by operating on it three simple steps. For a discretization with the last position of the vector corresponding to the first position in the physical space, like it is the case with Chebyshev [1, 2] and FDq [3, 4] discretizations, one must follow the steps sketched in Fig. 7.5:

1. Substitute the last row for zeros, except for the last point. Using the Kronecker delta function δ_{ab} :

$$D_{Ni}^* = \delta_{Ni}, \quad \forall i \in [1, N]. \quad (\text{G.1})$$

2. Invert the modified matrix:

$$I^* = (D^*)^{-1}. \quad (\text{G.2})$$

3. Subtract 1 from the last column of the inverted matrix I^* :

$$I_{iN} = I_{iN}^* - 1, \quad \forall i \in [1, N]. \quad (\text{G.3})$$

Step 1 annihilates the inherent null-space of the differentiation matrix, thus allowing one to invert the matrix in step 2. Step 3 ensures that the integration effectively starts from 0. This implies that any discrete integration performed with matrix I requires one to additionally sum the value of the integration constant.

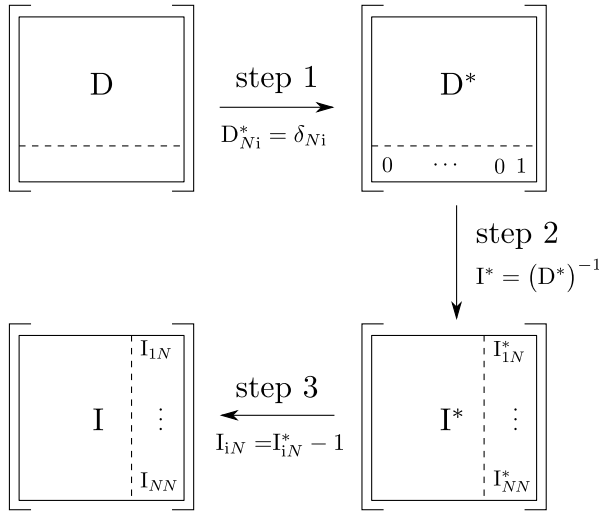


Figure G.1: Sketch of the procedure to obtain an integration matrix I from a differentiation one D . The discretization is assumed to be such that the last position of the vector corresponds to the first position in the physical space, like it is the case with Chebyshev [1, 2] and FDq [3, 4] discretizations.

The three-step procedure sketched in Fig. G.1 may be slightly modified in order to apply it to discretizations with the first vector position corresponding to the first position in the physical space, such as regular FD. One must modify steps 1 and 3 to operate with the first row of D and the first column of I^* , rather than the last. This implies that Eqs. G.1 and G.3 become:

$$D_{1i}^* = \delta_{1i}, \quad \forall i \in [1, N], \quad (\text{G.4a})$$

$$I_{i1} = I_{i1}^* - 1, \quad \forall i \in [1, N]. \quad (\text{G.4b})$$

References

- [1] L. N. Trefethen. *Spectral Methods in MATLAB*. SIAM, 2000.
- [2] C. Canuto, M. Y. Hussaini, A. Quarteroni, and T. A. Zang. *Spectral Methods: Fundamentals in Single Domain*. Springer Verlag, Berlin, 2006.
- [3] M. Hermanns and J. A. Hernández. *Stable high-order finite-difference methods based on non-uniform grid point distributions*. International Journal for Numerical Methods in Fluids, **56**:233–255, 2008.

- [4] P. Paredes, M. Hermanns, S. Le Clainche, and V. Theofilis. *Order 10^4 speedup in global linear instability analysis using matrix formation.* Computer Methods in Applied Mechanics and Engineering, [253:287–304](#), 2013.

H

Neutral curve Newton-Raphson solver

The neutral curve presents the evolution of the perturbation wave number (α) or frequency (ω) that results in purely oscillating perturbations – zero growth/decay [1]. In other words, at a neutral point, the imaginary part of all wave parameters is zero:

$$\Im(\alpha) = \Im(\beta) = \Im(\omega) = 0. \quad (\text{H.1})$$

Even if such curves can also be obtained for other stability theories, they are commonly obtained with LST. A common computational workflow to obtain a neutral point is to guess a real value of ω , solve the spatial LST problem (Eq. 3.13) using a Newton-Raphson local solver (see Ref. [2, App. C]) to obtain a complex α , and iteratively modify ω until the imaginary part of α is below a certain threshold. However, this process, featuring two iterative computations embedded within one-another, can be substantially sped-up by solving a unified Newton-Raphson iterative problem on both α and ω simultaneously.

First one must rearrange the LST generalized eigenvalue problem presented in Eqs. 3.12 or 3.13 into:

$$(\alpha^2 \underline{\mathcal{A}} + \alpha \underline{\mathcal{B}}(\beta) + \underline{\mathcal{C}}(\beta) + \omega \underline{\mathcal{D}}) \tilde{q} = 0. \quad (\text{H.2})$$

Then, one must decompose $\underline{\mathcal{A}}$, $\underline{\mathcal{B}}$, $\underline{\mathcal{C}}$, $\underline{\mathcal{D}}$ and \tilde{q} into their real (q_{\Re}) and imaginary

part (q_{\Im}) :

$$\left[\alpha^2 \left(\underline{\underline{\mathcal{A}}}_{\Re} + i \underline{\underline{\mathcal{A}}}_{\Im} \right) + \alpha \left(\underline{\underline{\mathcal{B}}}_{\Re} + i \underline{\underline{\mathcal{B}}}_{\Im} \right) + \right. \\ \left. + \left(\underline{\underline{\mathcal{C}}}_{\Re} + i \underline{\underline{\mathcal{C}}}_{\Im} \right) + \omega \left(\underline{\underline{\mathcal{D}}}_{\Re} + i \underline{\underline{\mathcal{D}}}_{\Im} \right) \right] \left(\tilde{q}_{\Re} + i \tilde{q}_{\Im} \right) = 0. \quad (\text{H.3})$$

Taking the real and imaginary parts of Eq. H.3, and introducing the two necessary normalization conditions for the eigenmodes \tilde{q} similarly to Pinna [2, App. C]:

$$1 - \underline{\underline{q}}^H \tilde{q} = 1 - \underline{\underline{q}}_{\Re}^T \tilde{q}_{\Re} - \underline{\underline{q}}_{\Im}^T \tilde{q}_{\Im} = 0, \quad (\text{H.4a})$$

$$\underline{\underline{q}}_{\Re}^T \tilde{q}_{\Re} - \underline{\underline{q}}_{\Im}^T \tilde{q}_{\Im} = 0, \quad (\text{H.4b})$$

it is possible to build the following unified Newton-Raphson system:

$$\underline{\underline{x}}_{k+1} = \underline{\underline{x}}_k - \underline{\underline{\mathcal{J}}}^{-1} \underline{\underline{\mathcal{F}}}_k, \quad (\text{H.5})$$

featuring the following vectors:

$$\underline{\underline{x}} = \begin{bmatrix} \tilde{q}_{\Re} \\ \tilde{q}_{\Im} \\ \alpha \\ \omega \end{bmatrix}, \quad \underline{\underline{\mathcal{F}}} = \begin{bmatrix} \underline{\underline{\mathcal{E}}}_{\Re} \tilde{q}_{\Re} - \underline{\underline{\mathcal{E}}}_{\Im} \tilde{q}_{\Im} \\ \underline{\underline{\mathcal{E}}}_{\Re} \tilde{q}_{\Im} + \underline{\underline{\mathcal{E}}}_{\Im} \tilde{q}_{\Re} \\ 1 - \underline{\underline{q}}_{\Re}^T \tilde{q}_{\Re} - \underline{\underline{q}}_{\Im}^T \tilde{q}_{\Im} \\ \underline{\underline{q}}_{\Re}^T \tilde{q}_{\Re} - \underline{\underline{q}}_{\Im}^T \tilde{q}_{\Im} \end{bmatrix}, \quad (\text{H.6a})$$

$$\underline{\underline{\mathcal{J}}} = \frac{\partial \underline{\underline{\mathcal{F}}}}{\partial \underline{\underline{x}}} = \begin{bmatrix} \underline{\underline{\mathcal{E}}}_{\Re} & -\underline{\underline{\mathcal{E}}}_{\Im} & \frac{\partial \underline{\underline{\mathcal{E}}}_{\Re}}{\partial \alpha} \tilde{q}_{\Re} - \frac{\partial \underline{\underline{\mathcal{E}}}_{\Im}}{\partial \alpha} \tilde{q}_{\Im} & \underline{\underline{\mathcal{D}}}_{\Re} \tilde{q}_{\Re} - \underline{\underline{\mathcal{D}}}_{\Im} \tilde{q}_{\Im} \\ \underline{\underline{\mathcal{E}}}_{\Im} & -\underline{\underline{\mathcal{E}}}_{\Re} & \frac{\partial \underline{\underline{\mathcal{E}}}_{\Re}}{\partial \alpha} \tilde{q}_{\Im} + \frac{\partial \underline{\underline{\mathcal{E}}}_{\Im}}{\partial \alpha} \tilde{q}_{\Re} & \underline{\underline{\mathcal{D}}}_{\Re} \tilde{q}_{\Im} - \underline{\underline{\mathcal{D}}}_{\Im} \tilde{q}_{\Re} \\ -2 \underline{\underline{q}}_{\Re}^T & -2 \underline{\underline{q}}_{\Im}^T & 0 & 0 \\ 2 \tilde{q}_{\Re}^T & -2 \tilde{q}_{\Im}^T & 0 & 0 \end{bmatrix} \quad (\text{H.6b})$$

where:

$$\underline{\underline{\mathcal{E}}}_{\Re} = \alpha^2 \underline{\underline{\mathcal{A}}}_{\Re} + \alpha \underline{\underline{\mathcal{B}}}_{\Re} + \underline{\underline{\mathcal{C}}}_{\Re} + \omega \underline{\underline{\mathcal{D}}}_{\Re}, \quad (\text{H.7a})$$

$$\underline{\underline{\mathcal{E}}}_{\Im} = \alpha^2 \underline{\underline{\mathcal{A}}}_{\Im} + \alpha \underline{\underline{\mathcal{B}}}_{\Im} + \underline{\underline{\mathcal{C}}}_{\Im} + \omega \underline{\underline{\mathcal{D}}}_{\Im}, \quad (\text{H.7b})$$

$$\frac{\partial \underline{\underline{\mathcal{E}}}_{\Re}}{\partial \alpha} = \alpha \underline{\underline{\mathcal{A}}}_{\Re} + \underline{\underline{\mathcal{B}}}_{\Re}, \quad (\text{H.7c})$$

$$\frac{\partial \underline{\underline{\mathcal{E}}}_{\Im}}{\partial \alpha} = \alpha \underline{\underline{\mathcal{A}}}_{\Im} + \underline{\underline{\mathcal{B}}}_{\Im}. \quad (\text{H.7d})$$

Note that all coefficients in the aforementioned Newton-Raphson system are real quantities. This implies that the $\alpha - \omega$ pair that is obtained from it also is, thus constituting a neutral point.

References

- [1] D. Arnal. *Boundary layer transition: predictions based on linear theory*. In Special Course on Progress in Transition Modelling AGARD 793. AGARD, 1993.
- [2] F. Pinna. *Numerical study of stability of flows from low to high Mach number*. PhD thesis, Università degli Studi di Roma La Sapienza, 2012.

I

Non-dimensional form of the boundary conditions

For the sake of completeness, the boundary conditions introduced in chapter 6 are presented in this appendix in their non-dimensional form, after applying the convention summarized in table 8.1. This appendix therefore remains, together with Eqs. 8.1-8.5, the only part of the dissertation featuring non-dimensional flow quantities rather than dimensional.

The porous boundary condition (Eq. 6.6) remains the same when non-dimensionalized as long as the porous-wall admittance is scaled with $\rho_e u_e$.

The ablative surface energy balance equations (Eq. 6.19 and 6.20) become:

$$g^{ij} \frac{1}{\text{Re Pr}} \kappa T_{,j} - \dot{\omega}_{\text{rad}} - \sum_{s \in \mathcal{S}} h_s \dot{m}_{sw}, \quad i = 2, \quad (\text{I.1})$$

and:

$$g^{ij} \left(\frac{1}{\text{Re Pr}_{tr}} \kappa_{tr} T_{,j} + \frac{1}{\text{Re Pr}_v} \kappa_v T_{v,j} \right) - \dot{\omega}_{\text{rad}} - \sum_{s \in \mathcal{S}} h_s \dot{m}_{sw}, \quad i = 2. \quad (\text{I.2})$$

Similarly, the species ablative surface mass balance (Eq. 6.25) morphs into:

$$\rho_s u^i - \frac{1}{\text{Re Sc}} J_s^i - \dot{m}_{sw} = 0, \quad \begin{matrix} \forall s \in \mathcal{S} \\ i = 2 \end{matrix}, \quad (\text{I.3})$$

whilst the mixture ablative surface mass balance (Eq. 6.4) maintains the same form.

The species-momentum-conservation equation (Eq. 6.26) becomes:

$$\rho_s \frac{\partial u^i}{\partial t} + \rho_s u^j u_{,j}^i = -g^{ij} p_{s,j} + \frac{1}{\text{Re}} \mathbb{T}_{,j}^{ij}, \quad \forall s \in \mathcal{S} \quad \forall i \in [1, 2, 3]. \quad (\text{I.4})$$

Regarding the freestream boundary, the Rankine-Hugoniot relations (Eq. 6.29) have the same form when non-dimensionalized according to Table 8.1. However, the enthalpy h appearing in Eq 6.30 must be replaced with h/Ec , thus affecting the energy equation (Eq. 6.29c).

J

Gas mixtures and reaction rate constants

J.1 Air-2

Species list: O₂, N₂
Non-reacting mixture.

J.2 Air-2-He

Species list: O₂, N₂, He
Non-reacting mixture.

J.3 Air-2-Ne

Species list: O₂, N₂, Ne
Non-reacting mixture.

J.4 Air-2-Ar

Species list: O₂, N₂, Ar
Non-reacting mixture.

J.5 Air-2-CO₂

Species list: O₂, N₂, CO₂

Non-reacting mixture.

J.6 O-2-Bortner

Species list: O, O₂

Reaction list:

- O₂ + M \leftrightarrow 2O + M

The forward reaction-rate constants in S.I. units are summarized in Table J.1.

Reaction	M	$A_r^f \left[\frac{(\text{m}^3/\text{mol})^{\sum_s \nu'_{sr} - 1}}{\text{s K}^{n_{Tr}^f}} \right]$	n_{Tr}^f [-]	θ_r^f [K]
$\text{O}_2 + M \leftrightarrow 2\text{O} + M$	O	3.61e+12	-1	59400
	O ₂	3.61e+12		

Table J.1: O-2-Bortner forward reaction rate constants (Eq. 4.65a) from Ref. [1].

Reaction	M	$A_r^{\text{eq}} \left[\frac{(\text{m}^3/\text{mol})^{\sum_s \nu'_{sr} - \nu''_{sr}}}{\text{K}^{n_{Tr}^{\text{eq}}}} \right]$	n_{Tr}^{eq} [-]	θ_r^{eq} [K]
$\text{O}_2 + M \leftrightarrow 2\text{O} + M$	O	1.20e+09	-0.5	59400
	O ₂	1.20e+09		

Table J.2: O-2-Bortner Arrhenius coefficients for the equilibrium constant (Eq. 4.70) from Ref. [1].

J.7 Air-5-Park85

Species list: N, O, NO, N₂, O₂

Reaction list:

- O₂ + M \leftrightarrow 2O + M
- N₂ + M \leftrightarrow 2N + M
- NO + M \leftrightarrow N + O + M
- NO + O \leftrightarrow N + O₂
- O + N₂ \leftrightarrow N + NO

The forward reaction-rate constants in S.I. units are summarized in Table J.3.

Reaction	M	$A_r^f \left[\frac{(\text{m}^3/\text{mol})^{\sum_s \nu'_{sr} - 1}}{\text{s K}^{n_{Tr}^f}} \right]$	n_{Tr}^f [-]	θ_r^f [K]
$\text{O}_2 + M \leftrightarrow 2\text{O} + M$	N	8.25e+13	-1	59500
	O	8.25e+13		
	NO	2.75e+13		
	N_2	2.75e+13		
	O_2	2.75e+13		
$\text{N}_2 + M \leftrightarrow 2\text{N} + M$	N	1.11e+16	-1.6	113200
	O	1.11e+16		
	NO	3.70e+15		
	N_2	3.70e+15		
	O_2	3.70e+15		
$\text{NO} + M \leftrightarrow \text{N} + \text{O} + M$	N	4.60e+11	-0.5	75500
	O	4.60e+11		
	NO	2.30e+11		
	N_2	2.30e+11		
	O_2	2.30e+11		
$\text{NO} + \text{O} \leftrightarrow \text{N} + \text{O}_2$		2.16e+02	1.29	19220
$\text{O} + \text{N}_2 \leftrightarrow \text{N} + \text{NO}$		3.18e+07	0.1	37700

Table J.3: Air-5-Park85 forward reaction rate constants (Eq. 4.65a) from Ref. [2].

J.8 Air-5-Park90

Species list: N, O, NO, N_2 , O_2

Reaction list:

- $\text{N}_2 + M \leftrightarrow 2\text{N} + M$
- $\text{O}_2 + M \leftrightarrow 2\text{O} + M$
- $\text{NO} + M \leftrightarrow \text{N} + \text{O} + M$
- $\text{O} + \text{N}_2 \leftrightarrow \text{N} + \text{NO}$
- $\text{NO} + \text{O} \leftrightarrow \text{N} + \text{O}_2$

The forward reaction-rate constants in S.I. units are summarized in Table J.4.

Reaction	M	$A_r^f \left[\frac{(\text{m}^3/\text{mol})^{\sum_s \nu'_{sr}-1}}{\text{s K}^{n_{Tr}^f}} \right]$	n_{Tr}^f [-]	θ_r^f [K]
$\text{N}_2 + M \leftrightarrow 2\text{N} + M$	N	3.00e+16	-1.6	113200
	O	3.00e+16		
	NO	7.00e+15		
	N_2	7.00e+15		
	O_2	7.00e+15		
$\text{O}_2 + M \leftrightarrow 2\text{O} + M$	N	1.00e+16	-1.5	59360
	O	1.00e+16		
	NO	2.00e+15		
	N_2	2.00e+15		
	O_2	2.00e+15		
$\text{NO} + M \leftrightarrow \text{N} + \text{O} + M$	N	1.00e+11	0	75500
	O	1.00e+11		
	NO	1.00e+11		
	N_2	5.00e+09		
	O_2	5.00e+09		
$\text{O} + \text{N}_2 \leftrightarrow \text{N} + \text{NO}$		6.40e+11	-1	38400
$\text{NO} + \text{O} \leftrightarrow \text{N} + \text{O}_2$		8.40e+06	0	19220

Table J.4: Air-5-Park90 forward reaction rate constants (Eq. 4.65a) from Ref. [3].

J.9 Air-5-Park01

Species list: N, O, NO, N_2 , O_2

Reaction list:

- $\text{N}_2 + M \leftrightarrow 2\text{N} + M$
- $\text{O}_2 + M \leftrightarrow 2\text{O} + M$
- $\text{NO} + M \leftrightarrow \text{N} + \text{O} + M$
- $\text{O} + \text{N}_2 \leftrightarrow \text{N} + \text{NO}$
- $\text{N} + \text{O}_2 \leftrightarrow \text{NO} + \text{O}$

The forward reaction-rate constants in S.I. units are summarized in Table J.5.

Reaction	M	$A_r^f \left[\frac{(\text{m}^3/\text{mol})^{\sum_s \nu'_{sr}-1}}{\text{s K}^{n_{Tr}^f}} \right]$	n_{Tr}^f [-]	θ_r^f [K]
$\text{N}_2 + M \leftrightarrow 2\text{N} + M$	N	3.00e+16	-1.6	113200
	O	3.00e+16		
	NO	7.00e+15		
	N_2	7.00e+15		
	O_2	7.00e+15		
$\text{O}_2 + M \leftrightarrow 2\text{O} + M$	N	1.00e+16	-1.5	59360
	O	1.00e+16		
	NO	2.00e+15		
	N_2	2.00e+15		
	O_2	2.00e+15		
$\text{NO} + M \leftrightarrow \text{N} + \text{O} + M$	N	1.00e+11	0	75500
	O	1.00e+11		
	NO	1.00e+11		
	N_2	5.00e+09		
	O_2	5.00e+09		
$\text{O} + \text{N}_2 \leftrightarrow \text{N} + \text{NO}$		5.69e+06	0.42	42938
$\text{N} + \text{O}_2 \leftrightarrow \text{NO} + \text{O}$		2.49e+03	1.18	4005.5

Table J.5: Air-5-Park01 forward reaction rate constants (Eq. 4.65a) from Ref. [4].

J.10 Air-5-Stuckert

Species list: N, O, NO, N_2 , O_2

Reaction list:

- $\text{N}_2 + M \leftrightarrow 2\text{N} + M$
- $\text{O}_2 + M \leftrightarrow 2\text{O} + M$
- $\text{NO} + M \leftrightarrow \text{N} + \text{O} + M$
- $\text{O} + \text{N}_2 \leftrightarrow \text{N} + \text{NO}$
- $\text{NO} + \text{O} \leftrightarrow \text{N} + \text{O}_2$

The forward reaction-rate constants in S.I. units are summarized in Table J.6.

Reaction	M	$A_r^f \left[\frac{(\text{m}^3/\text{mol})^{\sum_s \nu'_{sr}-1}}{\text{s K}^{n_{Tr}^f}} \right]$	n_{Tr}^f [-]	θ_r^f [K]
$\text{N}_2 + M \leftrightarrow 2\text{N} + M$	N	4.15e+16	-1.5	113200
	O	1.03e+22		
	NO	1.03e+22		
	N_2	2.57e+22		
	O_2	1.03e+22		
$\text{O}_2 + M \leftrightarrow 2\text{O} + M$	N	3.61e+12	-1	59500
	O	9.02e+13		
	NO	3.61e+12		
	N_2	7.22e+12		
	O_2	3.25e+13		
$\text{NO} + M \leftrightarrow \text{N} + \text{O} + M$	N	2.89e+09	0	74700
	O	2.89e+09		
	NO	2.89e+09		
	N_2	9.62e+08		
	O_2	9.62e+08		
$\text{O} + \text{N}_2 \leftrightarrow \text{N} + \text{NO}$		1.83e+08	0	38370
$\text{NO} + \text{O} \leftrightarrow \text{N} + \text{O}_2$		3.81e+03	1	20820

Table J.6: Air-5-Stuckert forward reaction rate constants (Eq. 4.65a) from Ref. [5].

J.11 Air-5-Bortner

Species list: N, O, NO, N_2 , O_2

Reaction list:

- $\text{O}_2 + M \leftrightarrow 2\text{O} + M$
- $\text{N}_2 + M \leftrightarrow 2\text{N} + M$
- $\text{NO} + M \leftrightarrow \text{N} + \text{O} + M$
- $\text{NO} + \text{O} \leftrightarrow \text{N} + \text{O}_2$
- $\text{O} + \text{N}_2 \leftrightarrow \text{N} + \text{NO}$

The forward reaction-rate constants in S.I. units are summarized in Table J.7.

Reaction	M	A_r^f	$\left[\frac{(\text{m}^3/\text{mol})^{\sum_s \nu'_{sr} - 1}}{\text{s K}^{n_f^r}} \right]$	n_{Tr}^f [-]	θ_r^f [K]
$\text{O}_2 + M \leftrightarrow 2\text{O} + M$	N	3.61e+12		-1	59400
	O	3.61e+12			
	NO	3.61e+12			
	N ₂	3.61e+12			
	O ₂	3.61e+12			
$\text{N}_2 + M \leftrightarrow 2\text{N} + M$	N	4.15e+16		-1.5	113100
	O	1.92e+11			
	NO	1.92e+11			
	N ₂	1.92e+11			
	O ₂	1.92e+11			
$\text{NO} + M \leftrightarrow \text{N} + \text{O} + M$	N	3.97e+14		-1.5	75600
	O	3.97e+14			
	NO	3.97e+14			
	N ₂	3.97e+14			
	O ₂	3.97e+14			
$\text{NO} + \text{O} \leftrightarrow \text{N} + \text{O}_2$		3.18e+03		1	19700
$\text{O} + \text{N}_2 \leftrightarrow \text{N} + \text{NO}$		6.75e+07		0	37500

Table J.7: Air-5-Bortner forward reaction rate constants (Eq. 4.65a) from Ref. [1].

Reaction	M	A_r^{eq}	$\left[\frac{(\text{m}^3/\text{mol})^{\sum_s \nu'_{sr} - \nu''_{sr}}}{\text{K}^{n_f^r} T_r^{\text{eq}}} \right]$	n_{Tr}^{eq} [-]	θ_r^{eq} [K]
$\text{O}_2 + M \leftrightarrow 2\text{O} + M$	N	1.20e+09		-0.5	59400
	O	1.20e+09			
	NO	1.20e+09			
	N ₂	1.20e+09			
	O ₂	1.20e+09			
$\text{N}_2 + M \leftrightarrow 2\text{N} + M$	N	1.79e+07		0	113100
	O	1.76e+07			
	NO	1.76e+07			
	N ₂	1.76e+07			
	O ₂	1.76e+07			
$\text{NO} + M \leftrightarrow \text{N} + \text{O} + M$	N	3.93e+06		0	75600
	O	3.93e+06			
	NO	3.93e+06			
	N ₂	3.93e+06			
	O ₂	3.93e+06			
$\text{NO} + \text{O} \leftrightarrow \text{N} + \text{O}_2$		3.30e-03		0.5	16100
$\text{O} + \text{N}_2 \leftrightarrow \text{N} + \text{NO}$		4.50e+00		0	37500

Table J.8: Air-5-Bortner Arrhenius coefficients for the equilibrium constant (Eq. 4.70) from Ref. [1].

J.12 Air-11-Park93

Species list: N, O, N₂, O₂, NO, N⁺, O⁺, N₂⁺, O₂⁺, NO⁺, e⁻

Reaction list:

- N₂ + M \leftrightarrow 2N + M
- O₂ + M \leftrightarrow 2O + M
- NO + M \leftrightarrow N + O + M
- NO + O \leftrightarrow N + O₂
- N₂ + O \leftrightarrow NO + N
- N + O \leftrightarrow NO⁺ + e⁻
- O + O \leftrightarrow O₂⁺ + e⁻
- N + N \leftrightarrow N₂⁺ + e⁻
- NO⁺ + O \leftrightarrow N⁺ + O₂
- N⁺ + N₂ \leftrightarrow N₂⁺ + N
- O₂⁺ + N \leftrightarrow N⁺ + O₂
- O⁺ + NO \leftrightarrow N⁺ + O₂
- O₂⁺ + N₂ \leftrightarrow N₂⁺ + O₂
- O₂⁺ + O \leftrightarrow O⁺ + O₂
- NO⁺ + N \leftrightarrow O⁺ + N₂
- NO⁺ + O₂ \leftrightarrow O₂⁺ + NO
- NO⁺ + O \leftrightarrow O₂⁺ + N
- O⁺ + N₂ \leftrightarrow N₂⁺ + O
- NO⁺ + N \leftrightarrow N₂⁺ + O
- O + e⁻ \leftrightarrow O⁺ + 2e⁻
- N + e⁻ \leftrightarrow N⁺ + 2e⁻

The forward reaction-rate constants in S.I. units are summarized in Table J.9.

Reaction	M	A_r^f	$\left[\frac{(\text{m}^3/\text{mol})^{\sum_s \nu'_{sr} - 1}}{\text{s K}^{n_{Tr}^f}} \right]$	n_{Tr}^f [-]	θ_r^f [K]
$\text{N}_2 + M \leftrightarrow 2\text{N} + M$	N	3.00e+16		-1.6	113200
	O	3.00e+16			
	N_2	7.00e+15			
	O_2	7.00e+15			
	NO	7.00e+15			
	N^+	3.00e+16			
	O^+	3.00e+16			
	N_2^+	7.00e+15			
	O_2^+	7.00e+15			
	NO^+	7.00e+15			
	e^-	3.00e+18			
$\text{O}_2 + M \leftrightarrow 2\text{O} + M$	N	1.00e+16		-1.5	59500
	O	1.00e+16			
	N_2	2.00e+15			
	O_2	2.00e+15			
	NO	2.00e+15			
	N^+	1.00e+16			
	O^+	1.00e+16			
	N_2^+	2.00e+15			
	O_2^+	2.00e+15			
	NO^+	2.00e+15			
	e^-	0.00e+00			
$\text{NO} + M \leftrightarrow \text{N} + \text{O} + M$	N	1.10e+11		0	75500
	O	1.10e+11			
	N_2	5.00e+09			
	O_2	5.00e+09			
	NO	1.10e+11			
	N^+	1.10e+11			
	O^+	1.10e+11			
	N_2^+	5.00e+09			
	O_2^+	5.00e+09			
	NO^+	5.00e+09			
	e^-	0.00e+00			
$\text{NO} + \text{O} \leftrightarrow \text{N} + \text{O}_2$		8.40e+06		0	19450
$\text{N}_2 + \text{O} \leftrightarrow \text{NO} + \text{N}$		6.40e+11		-1	38400
$\text{N} + \text{O} \leftrightarrow \text{NO}^+ + \text{e}^-$		8.80e+02		1	31900
$\text{O} + \text{O} \leftrightarrow \text{O}_2^+ + \text{e}^-$		7.10e-04		2.7	80600
$\text{N} + \text{N} \leftrightarrow \text{N}_2^+ + \text{e}^-$		4.40e+01		1.5	67500
$\text{NO}^+ + \text{O} \leftrightarrow \text{N}^+ + \text{O}_2$		1.00e+06		0.5	77200
$\text{N}^+ + \text{N}_2 \leftrightarrow \text{N}_2^+ + \text{N}$		1.00e+06		0.5	12200

Table J.9: Air-11-Park93 forward reaction rate constants (Eq. 4.65a) from Ref. [6].

Reaction	$A_r^f \left[\frac{(m^3/mol)^{\sum_s \nu'_{sr} - 1}}{s K^{n_f}_{Tr}} \right]$	$n_{Tr}^f [-]$	$\theta_r^f [K]$
$O_2^+ + N \leftrightarrow N^+ + O_2$	8.70e+07	0.14	28600
$O^+ + NO \leftrightarrow N^+ + O_2$	1.40e-01	1.9	26600
$O_2^+ + N_2 \leftrightarrow N_2^+ + O_2$	9.90e+06	0	40700
$O_2^+ + O \leftrightarrow O^+ + O_2$	4.00e+06	-0.09	18000
$NO^+ + N \leftrightarrow O^+ + N_2$	3.40e+07	-1.08	12800
$NO^+ + O_2 \leftrightarrow O_2^+ + NO$	2.40e+07	0.41	32600
$NO^+ + O \leftrightarrow O_2^+ + N$	7.20e+06	0.29	48700
$O^+ + N_2 \leftrightarrow N_2^+ + O$	9.10e+05	0.36	22800
$NO^+ + N \leftrightarrow N_2^+ + O$	7.20e+07	0	35500
$O + e^- \leftrightarrow O^+ + 2e^-$	3.90e+27	-3.78	158500
$N + e^- \leftrightarrow N^+ + 2e^-$	2.50e+28	-3.82	168600

Table J.9: (cont) Air-11-Park93 forward reaction rate constants (Eq. 4.65a) from Ref. [6].

J.13 AirC-6-Mortensen

Species list: CO₂, N, O, NO, N₂, O₂

Reaction list:

- N₂ + M \leftrightarrow 2N + M
- O₂ + M \leftrightarrow 2O + M
- NO + M \leftrightarrow N + O + M
- N₂ + O \leftrightarrow NO + N
- NO + O \leftrightarrow N + O₂
- N₂ + O₂ \leftrightarrow 2NO

The forward reaction-rate constants in S.I. units are summarized in Table J.10.

Reaction	M	$A_r^f \left[\frac{(\text{m}^3/\text{mol})^{\sum_s \nu'_{sr}-1}}{\text{s K}^{n_{Tr}^f}} \right]$	$n_{Tr}^f [-]$	$\theta_r^f [\text{K}]$
$\text{N}_2 + M \leftrightarrow 2\text{N} + M$	CO ₂	3.70e+15	-1.6	113200
	N	1.11e+16		
	O	1.11e+16		
	NO	3.70e+15		
	N ₂	3.70e+15		
	O ₂	3.70e+15		
$\text{O}_2 + M \leftrightarrow 2\text{O} + M$	CO ₂	2.75e+13	-1	59500
	N	8.25e+13		
	O	8.25e+13		
	NO	2.75e+13		
	N ₂	2.75e+13		
	O ₂	2.75e+13		
$\text{NO} + M \leftrightarrow \text{N} + \text{O} + M$	CO ₂	2.30e+11	-0.5	75500
	N	4.60e+11		
	O	6.90e+11		
	NO	2.30e+11		
	N ₂	2.30e+11		
	O ₂	2.30e+11		
$\text{N}_2 + \text{O} \leftrightarrow \text{NO} + \text{N}$		3.18e+07	0.1	37700
$\text{NO} + \text{O} \leftrightarrow \text{N} + \text{O}_2$		2.16e+02	1.29	19220
$\text{N}_2 + \text{O}_2 \leftrightarrow 2\text{NO}$		6.69e+03	-2.54	64639

Table J.10: AirC-6-Mortensen forward reaction rate constants (Eq. 4.65a) from Ref. [7, 8].

J.14 AirC-11-Mortensen

Species list: C₃, CO₂, C₂, CO, CN, C, N, O, NO, N₂, O₂

Reaction list:

- N₂ + M \leftrightarrow 2N + M
- O₂ + M \leftrightarrow 2O + M
- NO + M \leftrightarrow N + O + M
- C₃ + M \leftrightarrow C₂ + C + M
- CO₂ + M \leftrightarrow CO + O + M
- C₂ + M \leftrightarrow 2C + M
- CO + M \leftrightarrow C + O + M
- CN + M \leftrightarrow C + N + M
- N₂ + O \leftrightarrow NO + N
- NO + O \leftrightarrow N + O₂
- N₂ + O₂ \leftrightarrow 2NO
- CO + O \leftrightarrow C + O₂
- CN + O \leftrightarrow NO + C
- CO₂ + O \leftrightarrow O₂ + CO
- CO + C \leftrightarrow C₂ + O
- N₂ + C \leftrightarrow CN + N
- CN + C \leftrightarrow C₂ + N
- C₃ + C \leftrightarrow 2C₂
- CO + N \leftrightarrow CN + O
- CO + N \leftrightarrow NO + C
- 2CO \leftrightarrow CO₂ + C
- C₂ + CO \leftrightarrow C₃ + O
- 2CO \leftrightarrow C₂ + O₂
- CO + NO \leftrightarrow CO₂ + N

The forward reaction-rate constants in S.I. units are summarized in Table J.11.

Reaction	M	$A_r^f \left[\frac{(\text{m}^3/\text{mol})^{\sum_s \nu'_{sr} - 1}}{\text{s K}^{n_{Tr}^f}} \right]$	n_{Tr}^f [-]	θ_r^f [K]
$\text{N}_2 + M \leftrightarrow 2\text{N} + M$	C ₃	3.70e+15	-1.6	113200
	CO ₂	3.70e+15		
	C ₂	3.70e+15		
	CO	3.70e+15		
	CN	3.70e+15		
	C	1.11e+16		
	N	1.11e+16		
	O	1.11e+16		
	NO	3.70e+15		
	N ₂	3.70e+15		
	O ₂	3.70e+15		
$\text{O}_2 + M \leftrightarrow 2\text{O} + M$	C ₃	2.75e+13	-1	59500
	CO ₂	2.75e+13		
	C ₂	2.75e+13		
	CO	2.75e+13		
	CN	2.75e+13		
	C	8.25e+13		
	N	8.25e+13		
	O	8.25e+13		
	NO	2.75e+13		
	N ₂	2.75e+13		
	O ₂	2.75e+13		
$\text{NO} + M \leftrightarrow \text{N} + \text{O} + M$	C ₃	2.30e+11	-0.5	75500
	CO ₂	2.30e+11		
	C ₂	2.30e+11		
	CO	2.30e+11		
	CN	2.30e+11		
	C	4.60e+11		
	N	4.60e+11		
	O	4.60e+11		
	NO	2.30e+11		
	N ₂	2.30e+11		
	O ₂	2.30e+11		

Table J.11: AirC-11-Mortensen forward reaction rate constants (Eq. 4.65a) from Ref. [7, 8].

Reaction	M	$A_r^f \left[\frac{(\text{m}^3/\text{mol})^{\sum_s \nu'_{sr} - 1}}{\text{s K}^{n_{Tr}^f}} \right]$	n_{Tr}^f [-]	θ_r^f [K]
$\text{C}_3 + M \leftrightarrow \text{C}_2 + \text{C} + M$	C ₃	1.60e+10	1	87480
	CO ₂	1.60e+10		
	C ₂	1.60e+10		
	CO	1.60e+10		
	CN	1.60e+10		
	C	1.60e+10		
	N	1.60e+10		
	O	1.60e+10		
	NO	1.60e+10		
	N ₂	1.60e+10		
	O ₂	1.60e+10		
$\text{CO}_2 + M \leftrightarrow \text{CO} + \text{O} + M$	C ₃	1.20e+05	0.5	36850
	CO ₂	1.20e+05		
	C ₂	1.20e+05		
	CO	1.20e+05		
	CN	1.20e+05		
	C	1.20e+05		
	N	1.20e+05		
	O	1.20e+05		
	NO	1.20e+05		
	N ₂	1.20e+05		
	O ₂	1.20e+05		
$\text{C}_2 + M \leftrightarrow 2\text{C} + M$	C ₃	4.50e+12	-1	70930
	CO ₂	4.50e+12		
	C ₂	4.50e+12		
	CO	4.50e+12		
	CN	4.50e+12		
	C	4.50e+12		
	N	4.50e+12		
	O	4.50e+12		
	NO	4.50e+12		
	N ₂	4.50e+12		
	O ₂	4.50e+12		

Table J.11: (cont) AirC-11-Mortensen forward reaction rate constants (Eq. 4.65a) from Ref. [7, 8].

Reaction	M	A_r^f	$\left[\frac{(m^3/mol)^{\sum_s \nu_{sr}^f - 1}}{s K^n T_r} \right]$	$n_{Tr}^f [-]$	$\theta_r^f [K]$
CO + M \leftrightarrow C + O + M	C ₃	8.50e+13		-1	129000
	CO ₂	8.50e+13			
	C ₂	8.50e+13			
	CO	8.50e+13			
	CN	8.50e+13			
	C	8.50e+13			
	N	8.50e+13			
	O	8.50e+13			
	NO	8.50e+13			
	N ₂	8.50e+13			
	O ₂	8.50e+13			
CN + M \leftrightarrow C + N + M	C ₃	2.50e+08		0	71000
	CO ₂	2.50e+08			
	C ₂	2.50e+08			
	CO	2.50e+08			
	CN	2.50e+08			
	C	2.50e+08			
	N	2.50e+08			
	O	2.50e+08			
	NO	2.50e+08			
	N ₂	2.50e+08			
	O ₂	2.50e+08			
N ₂ + O \leftrightarrow NO + N		3.18e+07		0.1	37700
NO + O \leftrightarrow N + O ₂		2.16e+02		1.29	19220
N ₂ + O ₂ \leftrightarrow 2NO		6.69e+03		-2.54	64639
CO + O \leftrightarrow C + O ₂		2.00e+04		1	69500
CN + O \leftrightarrow NO + C		1.60e+07		0.1	14600
CO ₂ + O \leftrightarrow O ₂ + CO		3.00e+02		1	18210
CO + C \leftrightarrow C ₂ + O		4.10e+04		0.5	59790
N ₂ + C \leftrightarrow CN + N		2.00e+08		0	23200
CN + C \leftrightarrow C ₂ + N		5.00e+07		0	13000
C ₃ + C \leftrightarrow 2C ₂		1.70e+03		1.5	19580
CO + N \leftrightarrow CN + O		2.00e+08		0	38600
CO + N \leftrightarrow NO + C		9.00e+10		-1	53200
2CO \leftrightarrow CO ₂ + C		1.00e-03		2	72390
C ₂ + CO \leftrightarrow C ₃ + O		1.20e+07		0	43240
2CO \leftrightarrow C ₂ + O ₂		9.20e+05		0.75	163300
CO + NO \leftrightarrow CO ₂ + N		1.00e-03		2	20980

Table J.11: (cont) AirC-11-Mortensen forward reaction rate constants (Eq. 4.65a) from Ref. [7, 8].

References

- [1] M. H. Bortner. *Suggested Standard Chemical Kinetics for Flow Field Calculations. A consensus Opinion.* In AMRAC Proceedings, Volume XIV, Part I, Doc. No. 4613-135-X (Contract SD-91). Institute of Science and Technology. University of Michigan, April 1966.
- [2] C. Park. *On convergence of computation of chemically reacting flows.* AIAA paper, [85-0247](#), 1985.
- [3] C. Park. *Non-Equilibrium Hypersonic Aerodynamics.* John Wiley & sons, New York, 1990.
- [4] C. Park, R. L. Jaffe, and H. Partridge. *Chemical-Kinetic Parameters of Hyperbolic Earth Entry.* Journal of Thermophysics and Heat Transfer, [15\(1\):76–90](#), 2001.
- [5] G. K. Stuckert. *Linear Stability Theory of Hypersonic, Chemically Reacting Viscous Flows.* PhD thesis, Arizona State University, 1991.
- [6] C. Park. *Review of chemical-kinetic problems of future NASA missions. I - Earth entries.* Journal of Thermophysics and Heat Transfer, [7\(3\):385–398](#), 1993.
- [7] C. Mortensen and X. Zhong. *Real-Gas and Surface-Ablation Effects on Hypersonic Boundary-Layer Instability over a Blunt Cone.* AIAA Journal, [54\(3\):980–998](#), 2016.
- [8] C. Mortensen. *Effects of Thermochemical Nonequilibrium on Hypersonic Boundary-Layer Instability in the Presence of Surface Ablation or Isolated Two-Dimensional Roughness.* PhD thesis, UCLA, 2013.

K

Species-parameters tables

K.1 Thermal parameters

Species	\mathcal{L}_s [-]	σ_s [-]	θ_s^{Rot} [K]	g_{sm}^{Vib} [-]	θ_{sm}^{Vib} [K]
NO	2	1	2.4522	1	2739.7189
N ₂	2	2	2.8742	1	3393.4991
O ₂	2	2	2.0794	1	2273.5552
NO ⁺	2	1	2.873	1	3419.1094
N ₂ ⁺	2	2	2.7787	1	3175.3806
O ₂ ⁺	2	2	2.4326	1	2740.4383

Table K.1: Rotational and vibrational properties of the molecular species in an air-11 mixture computed from Park [1].

Species	g_{sm}^{Vib} [-]	θ_{sm}^{Vib} [K]
N ₂	1	3390
O ₂	1	2270

Table K.2: Vibrational properties of the species in an air-2 mixture obtained as in Bitter & Shepherd [2] (originally from Vincenti & Kruger [3]).

Species	\mathcal{L}_s [-]	σ_s [-]	θ_s^{Rot} [K]	g_{sm}^{Vib} [-]	θ_{sm}^{Vib} [K]	σ_s^{Vib} [m^2]
NO	2	1	2.464	1	2759.293	3e-21
N ₂	2	2	2.886	1	3408.464	3e-21
O ₂	2	2	2.086	1	2276.979	3e-21
NO ⁺	2	1	2.892	1	3473.491	3e-21
N ₂ ⁺	2	2	2.818	1	3253.157	3e-21
O ₂ [±]	2	2	2.475	1	2887.139	3e-21
CO ₂	2	2	0.563	2	932.109	1e-20
				1	1914.081	
				1	3373.804	
CO	2	1	2.782	1	3083.452	3e-22
C ₃	2	2	0.607	2	212.582	1e-21
				1	1723.379	
				1	2990.46	
C ₂	2	2	2.579	1	2603.551	1e-21
CN	2	1	2.761	1	2992.786	1e-21

Table K.3: Rotational and vibrational properties of the molecular species considered in this work. Obtained from the mutation++ [4–6] database, which gathers values originally in Gurvich [7], or in Park et al. [1, 8, 9] (values of σ_s^{Vib}).

Species	\mathcal{M}_s [kg/mol]	$H_{f,s}^{298\text{ K}}$ [J/mol]
Air	0.028856	0
Ar	0.03994	0
He	0.004003	0
Ne	0.02018	0
N	0.014007	472440
O	0.015999	249229
NO	0.030006	91089
N ₂	0.028013	0
O ₂	0.031999	0
N ⁺	0.014006	1881903
O ⁺	0.015999	1568841
NO ⁺	0.030006	990653
N ₂ ⁺	0.028013	1509509
O ₂ ⁺	0.031998	1171413
e ⁻	5.5e-07	0
CO ₂	0.04401	-393472
C	0.012011	716680
CO	0.02801	-110530
C ₃	0.036033	823630
C ₂	0.024022	828374
CN	0.026018	439970

Table K.4: Molar mass and formation enthalpy of the species considered in this work. Obtained from the mutation++ [4–6] database, which gathers values originally in Gurvich [7].

Species	h_s^{ion} [J/kg]
N	1.001053e+08
O	8.211252e+07
NO	3.055212e+07
N ₂	5.342854e+07
O ₂	3.769673e+07

Table K.5: First ionization energy of the air neutral species. Obtained from Gnoffo et al. [10].

m	$g_{N,m}^{Elec}$ [-]	N	$g_{O,m}^{Elec}$ [-]	O
		$\theta_{N,m}^{Elec}$ [K]		$\theta_{O,m}^{Elec}$ [K]
0	4	0	9	0
1	10	27665	5	22861
2	6	41497	1	48622
3	12	119898	5	106136
4	6	124018	3	110487
5	12	126802	15	124633
6	2	134648	9	127535
7	20	136458	5	137374
8	12	137422	3	138442
9	4	139209	25	140299
10	10	139324	15	140415
11	6	140705	15	142737
12	10	143397	9	143548
13	12	149188	15	145637
14	6	149919	5	147030
15	6	150535	3	147493
16	28	150673	5	147842
17	26	150859	25	148075
18	20	151092	15	148190
19	10	151266	56	148306
20	2	153204	15	149234
21	20	153703	9	149582
22	12	153969	5	151207
23	10	154271	3	151440
24	4	154597	49	151788
25	6	154840	56	151869
26	12	158100	15	152368
27	6	158379	9	152484
28	90	158739	5	153412
29	126	158901	3	153529
30	24	159181	168	153761
31	2	159795	5	154689
32	38	160050	3	154805
33	4	160422	96	154956
34	10	160979	8	155640
35	6	161593	40	155710
36	18	162104	8	156186
37	60	162324	40	156244
38	126	162452	3	156581
39	32	163091	40	156615

Table K.6: Degeneracies and activation temperatures of the various electronic levels of neutral atomic species N and O. Obtained from the mutation++ [4-6] database, which gathers values originally in Gurvich [7].

m	N		O	
	$g_{N,m}^{Elec}$ [-]	$\theta_{N,m}^{Elec}$ [K]	$g_{O,m}^{Elec}$ [-]	$\theta_{O,m}^{Elec}$ [K]
40	18	164193	0	0
41	90	164321		
42	180	164367		
43	20	164808		
44	108	165481		
45	18	166131		

Table K.6: (cont) Degeneracies and activation temperatures of the various electronic levels of neutral atomic species N and O. Obtained from the mutation++ [4–6] database, which gathers values originally in Gurvich [7].

m	N ⁺		O ⁺	
	$g_{N^+,m}^{Elec}$ [-]	$\theta_{N^+,m}^{Elec}$ [K]	$g_{O^+,m}^{Elec}$ [-]	$\theta_{O^+,m}^{Elec}$ [K]
0	1	0	4	0
1	3	70	6	38571
2	5	188	4	38602
3	5	22037	4	58223
4	1	47032	2	58225
5	5	67313		
6	7	132709		
7	5	132728		
8	3	132730		

Table K.7: Degeneracies and activation temperatures of the various electronic levels of ionic atomic species N⁺ and O⁺. Obtained from the mutation++ [4–6] database, which gathers values originally in Gurvich [7].

m	N ₂		O ₂		NO	
	$g_{N_2,m}^{Elec}$ [-]	$\theta_{N_2,m}^{Elec}$ [K]	$g_{O_2,m}^{Elec}$ [-]	$\theta_{O_2,m}^{Elec}$ [K]	$g_{NO,m}^{Elec}$ [-]	$\theta_{NO,m}^{Elec}$ [K]
0	1	0	3	0	4	0
1	3	72232	2	11392	8	54674
2	6	85779	1	18985		
3	6	86050	1	47560		
4	3	95351	6	49912		
5	1	98057	3	50923		
6	2	99683	3	71640		
7	2	103732				

Table K.8: Degeneracies and activation temperatures of the various electronic levels of neutral air species N₂, O₂ and NO. Obtained from the mutation++ [4–6] database, which gathers values originally in Gurvich [7].

m	$g_{N_2^+,m}^{Elec}$ [-]	N_2^+	$\theta_{N_2^+,m}^{Elec}$ [K]	$g_{O_2^+,m}^{Elec}$ [-]	O_2^+	$\theta_{O_2^+,m}^{Elec}$ [K]	$g_{NO^+,m}^{Elec}$ [-]	NO^+	$\theta_{NO^+,m}^{Elec}$ [K]
0	2		0	4		0	1		0
1	4		13189	8		47354	3		75090
2	2		36633	4		58374	6		85212
3	4		36689	4		58414	6		89036
4	8		59853	6		62299	3		97470
5	8		66184				1		100055
6	4		75989				2		102803
7	4		76255				2		105713
8	4		82010						

Table K.9: Degeneracies and activation temperatures of the various electronic levels of ionic air species N_2^+ , O_2^+ and NO^+ . Obtained from the mutation++ [4–6] database, which gathers values originally in Gurvich [7].

m	$g_{CO_2,m}^{Elec}$ [-]	CO_2	$\theta_{CO_2,m}^{Elec}$ [K]	$g_{CO,m}^{Elec}$ [-]	CO	$\theta_{CO,m}^{Elec}$ [K]	$g_{C_3,m}^{Elec}$ [-]	C_3	$\theta_{C_3,m}^{Elec}$ [K]
0	1		0	1		0	1		0
1	3		43163	6		70049	6		20143
2	6		47480	3		80321	6		30934
3	3		51796	6		87944	3		34243
4	2		64745	3		92413	2		35503
5				2		93630	6		41868
6				1		93642	3		47192
7				2		94856	1		47336
8				10		115102	2		48487
9				5		116541	2		58270

Table K.10: Degeneracies and activation temperatures of the various electronic levels of carbon species CO_2 , CO and C_3 . Obtained from the mutation++ [4–6] database, which gathers values originally in Gurvich [7].

m	C_2		CN		C	
	$g_{C_2,m}^{Elec}$ [-]	$\theta_{C_2,m}^{Elec}$ [K]	$g_{CN,m}^{Elec}$ [-]	$\theta_{CN,m}^{Elec}$ [K]	$g_{C,m}^{Elec}$ [-]	$\theta_{C,m}^{Elec}$ [K]
0	1	0	2	0	1	0
1	6	1030	4	13294	3	24
2	3	9258	2	37051	5	62
3	2	12073	4	46616	5	14665
4	3	13276	8	61867	1	31147
5	2	21841	8	68630	5	48537
6	1	26963	4	77406	7	92207
7	6	28808	4	78393	5	92213
8	10	32372	2	85105	3	92211
9	5	43847	4	86464	3	108274
10	2	49295	4	87988	5	108276
11	6	50177	4	89780	1	108277
12	1	50609	4	91650	5	140825
13	6	55105	4	92404	3	152221
14	2	56637	2	92082	3	172478
15	6	58697	8	99995		
16	6	58990	2	101002		
17	6	61292	4	101722		
18	2	62011				
19	1	62212				
20	3	62515				
21	6	64385				
22	1	74601				
23	2	76039				
24	1	79183				
25	2	79708				
26	2	90787				

Table K.11: Degeneracies and activation temperatures of the various electronic levels of carbon species C_2 and CN . Obtained from the mutation++ [4–6] database, which gathers values originally in Gurvich [7].

m	N		O	
	$g_{N,m}^{Elec}$ [-]	$\theta_{N,m}^{Elec}$ [K]	$g_{O,m}^{Elec}$ [-]	$\theta_{O,m}^{Elec}$ [K]
0	4	0	9	112
1	10	27665	5	22831
2	6	41494	1	48619
3	12	119903	5	106136
4	6	124012	3	110491
5	36	137081	15	124640
6	18	139264	9	127520
7	18	149434	8	137773
8	60	150866	40	140202
9	30	150931	24	142889
10	54	154067	8	147082
11	18	158296	96	148023
12	90	158719	24	149444
13	126	158965	168	151638
14	54	160227	288	153430
15	90	162367	392	154788
16	288	162480	512	155556
17	648	164449	648	156076
18	882	165613	800	156444
19	1152	166367		
20	1458	166885		
21	1800	167255		

Table K.12: Degeneracies and activation temperatures of the various electronic levels of neutral atomic species N and O. Computed from Park [1].

m	N ⁺		O ⁺	
	$g_{N^+,m}^{Elec}$ [-]	$\theta_{N^+,m}^{Elec}$ [K]	$g_{O^+,m}^{Elec}$ [-]	$\theta_{O^+,m}^{Elec}$ [K]
0	9	128	4	0
1	5	22036	10	38582
2	1	47028	6	58223
3	15	132721	12	172557
4	9	157142	10	237097
5	5	207456	18	268482
6	12	214461		

Table K.13: Degeneracies and activation temperatures of the various electronic levels of ionic atomic species N⁺ and O⁺. Computed from Park [1].

m	N_2		O_2		NO	
	$g_{N_2,m}^{Elec}$ [-]	$\theta_{N_2,m}^{Elec}$ [K]	$g_{O_2,m}^{Elec}$ [-]	$\theta_{O_2,m}^{Elec}$ [K]	$g_{NO,m}^{Elec}$ [-]	$\theta_{NO,m}^{Elec}$ [K]
0	1	0	3	0	4	0
1	3	72232	2	11392	8	55835
2	6	85778	1	18985	2	63257
3	6	86050	1	47562	4	66086
4	3	95351	6	49911	4	68989
5	1	98057	3	50930	4	75084
6	2	99683	10	56514	2	76377
7	2	103731	3	71641	4	77172
8	5	109974	3	77739	4	86850
9	6	126468	6	79887	2	87232
10	6	128248	6	82069	4	88916
11			8	97608	2	89885
12			8	99453	2	90518
13			2	104803	4	90700
14			2	107715	4	92194
15			3	108282		
16			1	109478		
17			3	114934		
18			1	118219		

Table K.14: Degeneracies and activation temperatures of the various electronic levels of neutral air species N_2 , O_2 and NO. Computed from Park [1].

m	N_2^+		O_2^+		NO ⁺	
	$g_{N_2^+,m}^{Elec}$ [-]	$\theta_{N_2^+,m}^{Elec}$ [K]	$g_{O_2^+,m}^{Elec}$ [-]	$\theta_{O_2^+,m}^{Elec}$ [K]	$g_{NO^+,m}^{Elec}$ [-]	$\theta_{NO^+,m}^{Elec}$ [K]
0	2	0	4	0	1	0
1	4	13189	8	47428	3	75090
2	4	36633	4	58514	6	85233
3	4	75274	4	71296	6	89032
4	4	92956			3	97434
5					1	100053
6					2	102801
7					2	105710

Table K.15: Degeneracies and activation temperatures of the various electronic levels of ionic air species N_2^+ , O_2^+ and NO⁺. Computed from Park [1].

Vibrator	Partner	a_{sl}^{Vib} [K ^{1/3}]	b_{sl}^{Vib} [K ^{-1/3}]
NO	N	49.5	0.042
	O	49.5	0.042
	NO	49.5	0.042
	N ₂	49.5	0.042
	O ₂	49.5	0.042
	N ⁺	49.5	0.042
	O ⁺	49.5	0.042
	NO ⁺	49.5	0.042
	N ₂ ⁺	49.5	0.042
	O ₂ ⁺	49.5	0.042
N ₂	N	180	0.0262
	O	72.4	0.015
	NO	225	0.0293
	N ₂	221	0.029
	O ₂	229	0.0295
	N ⁺	180	0.0262
	O ⁺	72.4	0.015
	NO ⁺	225	0.0293
	N ₂ ⁺	221	0.029
	O ₂ ⁺	229	0.0295
O ₂	N	72.4	0.015
	O	47.7	0.059
	NO	136	0.0298
	N ₂	134	0.0295
	O ₂	138	0.03
	N ⁺	72.4	0.015
	O ⁺	47.7	0.059
	NO ⁺	136	0.0298
	N ₂ ⁺	134	0.0295
	O ₂ ⁺	138	0.03

Table K.16: Vibrational-relaxation constants for Millikan & White's [11] formula (Eq. 4.83). Values obtained from Park et al. [8] (neutral partners) and from the mutation++ database [4–6] (charged partners).

Vibrator	Partner	a_{sl}^{Vib} [K ^{1/3}]	b_{sl}^{Vib} [K ^{-1/3}]
NO ⁺	N	188	0.0264
	O	197	0.027
	NO	236	0.0295
	N ₂	231	0.0293
	O ₂	239	0.0298
	N ⁺	188	0.0264
	O ⁺	197	0.027
	NO ⁺	236	0.0295
	N ₂ ⁺	231	0.0293
	O ₂ ⁺	239	0.0298
N ₂ ⁺	N	170	0.0262
	O	178	0.0268
	NO	212	0.0293
	N ₂	209	0.029
	O ₂	216	0.0295
	N ⁺	170	0.0262
	O ⁺	178	0.0268
	NO ⁺	212	0.0293
	N ₂ ⁺	209	0.029
	O ₂ ⁺	216	0.0295
O ₂ ⁺	N	148	0.0265
	O	155	0.0271
	NO	187	0.0298
	N ₂	184	0.0295
	O ₂	190	0.03
	N ⁺	148	0.0265
	O ⁺	155	0.0271
	NO ⁺	187	0.0298
	N ₂ ⁺	184	0.0295
	O ₂ ⁺	190	0.03

Table K.17: Vibrational-relaxation constants for Millikan & White's [11] formula (Eq. 4.83). Values obtained from the mutation++ database [4–6].

K.2 Transport parameters

Species	$\mu_{\text{ref } s}$ [kg/m-s]	$S_{\mu s}$ [K]	$T_{\mu_{\text{ref } s}}$ [K]
Ar	2.117e-05	146.3	273.16
He	1.865e-05	72.9	273.16
Ne	2.975e-05	64.1	273.16
N ₂	1.656e-05	104.7	273.16
O ₂	1.919e-05	125	273.16
CO ₂	1.38e-05	253	273.16

Table K.18: Sutherland viscosity coefficients (Eq. 4.2) of the species considered in this work. Obtained from the CFD++ [12] database.

Species	$\kappa_{\text{ref } s}$ [W/K-m]	$S_{\kappa s}$ [K]	$T_{\kappa_{\text{ref } s}}$ [K]
Ar	0.0164	146.3	273.16
He	0.1428	187.4	273.16
Ne	0.0465	88.1	273.16
N ₂	0.02407	178.1	273.16
O ₂	0.02449	268.8	273.16
CO ₂	0.0146	939.8	273.16

Table K.19: Sutherland thermal conductivity coefficients (Eq. 4.4) of the species considered in this work. Obtained from the CFD++ [12] database.

Species	A_s^μ [-]	B_s^μ [-]	C_s^μ [-]
N	0.011572	0.60317	-14.7353
O	0.020314	0.42944	-13.9057
NO	0.043638	-0.033551	-11.8793
N ₂	0.026814	0.31778	-13.6181
O ₂	0.044929	-0.082616	-11.5045
NO ⁺	0.30201	-3.504	-6.0381

Table K.20: Viscosity coefficients for the BEW and GW models (Eq. 4.24) proposed by Blottner [13]. Note that they correspond to SI units without scaling factors, so they may vary from the original source.

Species	A_s^μ [-]	B_s^μ [-]	C_s^μ [-]
CO ₂	-0.019527	1.0478	-16.6247
CO	-0.019527	1.0133	-16.2813
C ₃	-0.0147	0.8811	-15.8077
C ₂	-0.0031	0.692	-14.9153
C	-0.0001	0.7928	-15.718
CN	-0.0025	0.681	-14.794

Table K.21: Viscosity coefficients for the BEW and GW models (Eq. 4.24) proposed by Mortensen [14] for the carbon species. Note that they correspond to SI units without scaling factors, so they may vary from the original source.

Species	A_s^μ [-]	B_s^μ [-]	C_s^μ [-]
N	0.012	0.593	-14.6831
O	0.0205	0.4257	-13.8829
NO	0.0452	-0.0609	-11.7622
N ₂	0.0203	0.4329	-14.1179
O ₂	0.0484	-0.1455	-11.2257
N ⁺		2.5	-34.3479
O ⁺		2.5	-34.6632
NO ⁺		2.5	-34.3479
N ₂ ⁺		2.5	-34.3853
O ₂ ⁺		2.5	-34.3174
e ⁻		2.5	-39.7498

Table K.22: Viscosity coefficients for the BEW and GW models (Eq. 4.24) proposed by Gupta et al. [15]. Note that they correspond to SI units without scaling factors, so they may vary from the original source.

Species	A_s^κ [-]	B_s^κ [-]	C_s^κ [-]	D_s^κ [-]	E_s^κ [-]
N			0.01619	0.55022	-6.8855
O			0.0331	0.22834	-5.5447
NO	0.02792	-0.87133	10.1797	-52.0347	94.707
N ₂	0.03607	-1.075	11.9503	-57.9006	99.2543
O ₂	0.07987	-2.5843	31.2596	-166.7627	327.7346
N ⁺			0.03088	2.0634	-25.4772
O ⁺	-0.4013	1.3247	-16.2209	89.9678	-202.538
NO ⁺	-0.06836	2.5783	-35.7274	219.0922	-512.9662
N ₂ ⁺		-0.03723	0.84192	-3.5904	-12.6198
O ₂ ⁺	-0.08373	2.7546	-33.7453	185.1327	-395.4711
e ⁻			0.00032	2.4937	-21.8616

Table K.23: Thermal conductivity coefficients for the GW model (Eq. 4.29) proposed by Gupta et al. [15]. Note that they correspond to SI units without scaling factors, so they may vary from the original source.

K.3 Collision parameters

K.3.1 Stuckert's [16] curve fits (Eq. 4.56)

Pair	$A^{\Omega_{sl}^{(1,1)}}$	$B^{\Omega_{sl}^{(1,1)}}$	$C^{\Omega_{sl}^{(1,1)}}$	$D^{\Omega_{sl}^{(1,1)}}$
N – N	4.8849e-19	1.2805e-19	1.2968e-20	-4.7993e-22
N – O	9.2060e-19	-2.6293e-19	2.6851e-20	-9.5254e-22
N – NO	2.3853e-19	-3.3056e-20	1.3301e-21	-1.2241e-23
N – N ₂	2.6591e-19	-3.8935e-20	1.6472e-21	-1.5553e-23
N – O ₂	2.0729e-19	-2.7406e-20	1.0566e-21	-9.5056e-24
O – O	8.1401e-20	7.9414e-21	-2.5153e-21	1.1488e-22
O – NO	2.0479e-19	-2.6843e-20	1.0268e-21	-9.1982e-24
O – N ₂	2.2520e-19	-3.0918e-20	1.2335e-21	-1.1301e-23
O – O ₂	1.9032e-19	-2.3897e-20	8.7907e-22	-7.7080e-24
NO – NO	4.4656e-19	-9.0428e-20	7.0358e-21	-2.0472e-22
NO – N ₂	4.7958e-19	-1.0032e-19	7.9982e-21	-2.3681e-22
NO – O ₂	4.1455e-19	-8.1261e-20	6.1693e-21	-1.7640e-22
N ₂ – N ₂	5.1468e-19	-1.1043e-19	8.9745e-21	-2.6937e-22
N ₂ – O ₂	4.4705e-19	-9.0996e-20	7.1076e-21	-2.0739e-22
O ₂ – O ₂	3.8272e-19	-7.1980e-20	5.2957e-21	-1.4809e-22

Table K.24: Curve fit parameters (Eq. 4.56) for $\Omega_{sl}^{(1,1)}$ (in m) of neutral air species proposed by Stuckert [16]. Note that they correspond to SI units without scaling factors, so they may vary from the original source.

Pair	$A_{s\ell}^{\Omega^{(2,2)}}$	$B_{s\ell}^{\Omega^{(2,2)}}$	$C_{s\ell}^{\Omega^{(2,2)}}$
N – N	3.0719e-19	-4.8704e-20	2.1278e-21
N – O	5.0906e-19	-9.3033e-20	4.5565e-21
N – NO	2.5830e-19	-3.2433e-20	1.0181e-21
N – N ₂	2.9141e-19	-3.8833e-20	1.2936e-21
N – O ₂	2.2207e-19	-2.6500e-20	7.9057e-22
O – O	1.7833e-19	-2.0584e-20	5.6591e-22
O – NO	2.1895e-19	-2.5884e-20	7.6500e-22
O – N ₂	2.4336e-19	-3.0248e-20	9.3990e-22
O – O ₂	2.0138e-19	-2.2725e-20	6.4107e-22
NO – NO	3.5499e-19	-5.1484e-20	2.1375e-21
NO – N ₂	3.7201e-19	-5.5124e-20	2.3237e-21
NO – O ₂	3.3826e-19	-4.8069e-20	1.9672e-21
N ₂ – N ₂	3.8543e-19	-5.7634e-20	2.4452e-21
N ₂ – O ₂	3.5989e-19	-5.2705e-20	2.2033e-21
O ₂ – O ₂	3.1695e-19	-4.3579e-20	1.7423e-21

Table K.25: Curve fit parameters (Eq. 4.56) for $\Omega_{s\ell}^{(2,2)}$ (in m) of neutral air species proposed by Stuckert [16]. Note that they correspond to SI units without scaling factors, so they may vary from the original source.

K.3.2 Gupta *et al.*'s [15] curve fits (Eq. 4.55)

Pair	$A_{s\ell}^{\Omega^{(1,1)}}$	$B_{s\ell}^{\Omega^{(1,1)}}$	$C_{s\ell}^{\Omega^{(1,1)}}$
N – N	-4.2151e+01	-5.7200e-02	-3.3000e-03
N – O	-4.1419e+01	-4.1950e-01	4.8000e-03
N – NO	-4.3137e+01	1.1800e-02	-1.8500e-02
N – N ₂	-4.3091e+01	1.1900e-02	-1.9400e-02
N – O ₂	-4.3197e+01	1.5200e-02	-1.7900e-02
O – O	-4.2206e+01	-5.7200e-02	-3.4000e-03
O – NO	-4.3197e+01	1.5200e-02	-1.7900e-02
O – N ₂	-4.2618e+01	-8.2500e-02	-1.3900e-02
O – O ₂	-4.3860e+01	1.3000e-01	-2.2600e-02
NO – NO	-4.4725e+01	3.8250e-01	-3.6400e-02
NO – N ₂	-4.3988e+01	2.3240e-01	-2.9100e-02
NO – O ₂	-4.5471e+01	5.3520e-01	-4.3800e-02
N ₂ – N ₂	-4.2350e+01	-1.1820e-01	-1.1200e-02
N ₂ – O ₂	-4.5578e+01	5.7290e-01	-4.6500e-02
O ₂ – O ₂	-4.5366e+01	4.9770e-01	-4.1000e-02

Table K.26: Curve fit parameters (Eq. 4.55) for $\Omega_{s\ell}^{(1,1)}$ of neutral air species proposed by Gupta *et al.* [15]. Note that they correspond to SI units without scaling factors, so they may vary from the original source.

Pair	$A_{s\ell}^{\Omega^{(2,2)}}$	$B_{s\ell}^{\Omega^{(2,2)}}$	$C_{s\ell}^{\Omega^{(2,2)}}$
N – N	-4.2871e+01	-9.6000e-02	-1.1800e-02
N – O	-4.1154e+01	-4.4670e-01	6.5000e-03
N – NO	-4.3164e+01	4.7800e-02	-1.9600e-02
N – N ₂	-4.3018e+01	2.3900e-02	-1.9000e-02
N – O ₂	-4.3315e+01	7.3000e-02	-2.0300e-02
O – O	-4.3631e+01	7.8000e-02	-2.0700e-02
O – NO	-4.3315e+01	7.3000e-02	-2.0300e-02
O – N ₂	-4.2777e+01	-1.4300e-02	-1.6900e-02
O – O ₂	-4.3945e+01	1.7830e-01	-2.4700e-02
NO – NO	-4.5430e+01	5.6240e-01	-4.5300e-02
NO – N ₂	-4.4746e+01	4.2260e-01	-3.8500e-02
NO – O ₂	-4.6123e+01	7.0450e-01	-5.2200e-02
N ₂ – N ₂	-4.3106e+01	6.8300e-02	-2.0300e-02
N ₂ – O ₂	-4.6301e+01	7.5900e-01	-5.5800e-02
O ₂ – O ₂	-4.5936e+01	6.4750e-01	-4.8500e-02

Table K.27: Curve fit parameters (Eq. 4.55) for $\Omega_{s\ell}^{(2,2)}$ of neutral air species proposed by Gupta et al. [15]. Note that they correspond to SI units without scaling factors, so they may vary from the original source.

Pair	$A_{s\ell}^{B^*}$	$B_{s\ell}^{B^*}$	$C_{s\ell}^{B^*}$
N – N	5.3700e-02	2.0000e-04	2.0000e-04
N – O	1.2943e+00	-2.6280e-01	1.4700e-02
N – NO	2.5740e-01	-4.2500e-02	3.8000e-03
N – N ₂	2.8500e-01	-4.9400e-02	4.3000e-03
N – O ₂	2.3320e-01	-3.6600e-02	3.3000e-03
O – O	5.4900e-02		2.0000e-04
O – NO	2.3320e-01	-3.6600e-02	3.3000e-03
O – N ₂	2.7470e-01	-4.7100e-02	4.2000e-03
O – O ₂	1.8080e-01	-2.4500e-02	2.4000e-03
NO – NO	-2.5530e-01	7.0000e-02	-2.7000e-03
NO – N ₂	-3.8720e-01	1.0100e-01	-4.5000e-03
NO – O ₂	-1.3120e-01	4.1000e-02	-1.0000e-03
N ₂ – N ₂	-5.6250e-01	1.4440e-01	-7.3000e-03
N ₂ – O ₂	-2.1750e-01	6.0200e-02	-1.9000e-03
O ₂ – O ₂	-3.0600e-02	1.8100e-02	1.0000e-04

Table K.28: Curve fit parameters (Eq. 4.59) for $B_{s\ell}^*$ of neutral air species proposed by Gupta et al. [15]. Note that they correspond to SI units without scaling factors, so they may vary from the original source.

K.3.3 Novel curve fits (Eq. 4.57) to recent data

K.3.3.1 Air neutral species (N, O, NO, N₂, O₂)

Pair	$A^{\Omega_{s\ell}^{(1,1)}}$	$B^{\Omega_{s\ell}^{(1,1)}}$	$C^{\Omega_{s\ell}^{(1,1)}}$	$D^{\Omega_{s\ell}^{(1,1)}}$
N – N	-3.9038e+01	-1.7537e+00	2.1127e-01	-9.6851e-03
N – O	-3.9926e+01	-1.3742e+00	1.6071e-01	-7.5128e-03
N – NO	-4.2197e+01	-4.2600e-01	3.7508e-02	-2.2969e-03
N – N ₂	-3.8724e+01	-1.8610e+00	2.3616e-01	-1.1228e-02
N – O ₂	-4.2744e+01	-2.6369e-01	1.7422e-02	-1.3345e-03
O – O	-3.9584e+01	-1.3768e+00	1.4468e-01	-6.3322e-03
O – NO	-4.2468e+01	-3.6840e-01	3.0304e-02	-1.8378e-03
O – N ₂	-3.7564e+01	-2.3100e+00	2.7639e-01	-1.1946e-02
O – O ₂	-4.0757e+01	-9.7101e-01	1.0277e-01	-4.8121e-03
NO – NO	-4.2358e+01	-2.8044e-01	1.8121e-02	-1.2700e-03
NO – N ₂	-4.1948e+01	-4.7267e-01	4.8809e-02	-2.8408e-03
NO – O ₂	-4.2201e+01	-3.3644e-01	2.2289e-02	-1.2450e-03
N ₂ – N ₂	-4.0494e+01	-1.0583e+00	1.2580e-01	-5.9892e-03
N ₂ – O ₂	-3.8991e+01	-1.5849e+00	1.7307e-01	-7.1877e-03
O ₂ – O ₂	-4.2101e+01	-3.7136e-01	2.3946e-02	-1.1232e-03

Table K.29: Curve fit parameters (Eq. 4.57a) for $\Omega_{s\ell}^{(1,1)}$ onto the data collected by Wright et al. [17] for neutral air species. Units in SI.

Pair	$A^{\Omega_{s\ell}^{(2,2)}}$	$B^{\Omega_{s\ell}^{(2,2)}}$	$C^{\Omega_{s\ell}^{(2,2)}}$	$D^{\Omega_{s\ell}^{(2,2)}}$
N – N	-3.9544e+01	-1.4745e+00	1.7016e-01	-7.6824e-03
N – O	-4.1206e+01	-8.5985e-01	9.7252e-02	-4.8372e-03
N – NO	-4.2196e+01	-3.7564e-01	3.1628e-02	-1.9878e-03
N – N ₂	-3.9525e+01	-1.4870e+00	1.8326e-01	-8.5684e-03
N – O ₂	-4.2785e+01	-2.0080e-01	1.0094e-02	-9.8152e-04
O – O	-4.0393e+01	-1.0303e+00	1.0124e-01	-4.4392e-03
O – NO	-4.2376e+01	-3.5586e-01	2.9098e-02	-1.7302e-03
O – N ₂	-3.8745e+01	-1.7766e+00	2.0368e-01	-8.6395e-03
O – O ₂	-4.1346e+01	-7.2951e-01	7.5403e-02	-3.6865e-03
NO – NO	-3.8671e+01	-1.7290e+00	2.0907e-01	-9.3898e-03
NO – N ₂	-3.9328e+01	-1.4954e+00	1.8442e-01	-8.6334e-03
NO – O ₂	-3.8881e+01	-1.6391e+00	1.9446e-01	-8.5899e-03
N ₂ – N ₂	-3.9501e+01	-1.3977e+00	1.6674e-01	-7.4713e-03
N ₂ – O ₂	-3.8863e+01	-1.6253e+00	1.8175e-01	-7.6114e-03
O ₂ – O ₂	-3.9060e+01	-1.5600e+00	1.8101e-01	-7.8269e-03

Table K.30: Curve fit parameters (Eq. 4.57a) for $\Omega_{s\ell}^{(2,2)}$ onto the data collected by Wright et al. [17] for neutral air species. Units in SI.

Pair	$A^{B_{s\ell}^*}$	$A^{C_{s\ell}^*}$
Neutral-neutral	1.3976e-01	-8.3382e-02
Ion-neutral	1.8232e-01	-1.6252e-01

Table K.31: Curve fit parameters (Eq. 4.60a) for $B_{s\ell}^*$ and $C_{s\ell}^*$ for ion-neutral and neutral-neutral collisions based on the data by Wright et al. [17]. These values apply both to the carbon and air species.

K.3.3.2 Air neutral (N , O , NO , N_2 , O_2) and charged species (N^+ , O^+ , NO^+ , N_2^+ , O_2^+)

Pair	$A_{s\ell}^{\Omega^{(1,1)}}$	$B_{s\ell}^{\Omega^{(1,1)}}$	$C_{s\ell}^{\Omega^{(1,1)}}$
Rep.	-1.3932e+00	7.9810e-01	-9.7037e-02
Att.	-8.2711e-01	5.9677e-01	-7.3910e-02
Pair	$D_{s\ell}^{\Omega^{(1,1)}}$	$E_{s\ell}^{\Omega^{(1,1)}}$	$F_{s\ell}^{\Omega^{(1,1)}}$
Rep.	6.6179e-03	-2.2314e-04	2.9119e-06
Att.	5.5810e-03	-2.0870e-04	2.9711e-06

Table K.32: Curve fit parameters (Eq. 4.57b) for $(T^*)^2 \Omega_{s\ell}^{(1,1)}$ onto the data collected by Mason [18] for charged air species. Units in SI.

Pair	$A_{s\ell}^{\Omega^{(2,2)}}$	$B_{s\ell}^{\Omega^{(2,2)}}$	$C_{s\ell}^{\Omega^{(2,2)}}$
Rep.	-1.1120e+00	7.6882e-01	-1.0084e-01
Att.	-8.5890e-01	7.1315e-01	-1.0346e-01
Pair	$D_{s\ell}^{\Omega^{(2,2)}}$	$E_{s\ell}^{\Omega^{(2,2)}}$	$F_{s\ell}^{\Omega^{(2,2)}}$
Rep.	7.3631e-03	-2.6143e-04	3.5427e-06
Att.	8.4181e-03	-3.2525e-04	4.6921e-06

Table K.33: Curve fit parameters (Eq. 4.57b) for $(T^*)^2 \Omega_{s\ell}^{(2,2)}$ onto the data collected by Mason [18] for charged air species. Units in SI.

Pair	$A_{s\ell}^{\Omega^{(1,4)}}$	$B_{s\ell}^{\Omega^{(1,4)}}$	$C_{s\ell}^{\Omega^{(1,4)}}$
Rep.	-2.6226e+00	5.7907e-01	-8.3198e-02
Att.	-2.3192e+00	3.9669e-01	-4.5284e-02
Pair	$D_{s\ell}^{\Omega^{(1,4)}}$	$E_{s\ell}^{\Omega^{(1,4)}}$	$F_{s\ell}^{\Omega^{(1,4)}}$
Rep.	6.8149e-03	-2.5892e-04	3.6671e-06
Att.	3.3917e-03	-1.2133e-04	1.6513e-06

Table K.34: Curve fit parameters (Eq. 4.57b) for $(T^*)^2 \Omega_{s\ell}^{(1,4)}$ onto the data collected by Devoto [19] for charged air species. Units in SI.

Pair	$A^{\Omega_{s\ell}^{(1,5)}}$	$B^{\Omega_{s\ell}^{(1,5)}}$	$C^{\Omega_{s\ell}^{(1,5)}}$
Rep.	-2.8950e+00	5.4232e-01	-7.8387e-02
Att.	-2.6317e+00	3.7310e-01	-4.1459e-02
Pair	$D^{\Omega_{s\ell}^{(1,5)}}$	$E^{\Omega_{s\ell}^{(1,5)}}$	$F^{\Omega_{s\ell}^{(1,5)}}$
Rep.	6.5109e-03	-2.5020e-04	3.5750e-06
Att.	3.0628e-03	-1.0831e-04	1.4609e-06

Table K.35: Curve fit parameters (Eq. 4.57b) for $(T^*)^2 \Omega_{s\ell}^{(1,5)}$ onto the data collected by Devoto [19] for charged air species. Units in SI.

Pair	$A^{\Omega_{s\ell}^{(2,4)}}$	$B^{\Omega_{s\ell}^{(2,4)}}$	$C^{\Omega_{s\ell}^{(2,4)}}$
Rep.	-1.7799e+00	6.4828e-01	-9.2679e-02
Att.	-1.5686e+00	5.7290e-01	-8.5787e-02
Pair	$D^{\Omega_{s\ell}^{(2,4)}}$	$E^{\Omega_{s\ell}^{(2,4)}}$	$F^{\Omega_{s\ell}^{(2,4)}}$
Rep.	7.4672e-03	-2.7990e-04	3.9226e-06
Att.	7.4392e-03	-2.9632e-04	4.3538e-06

Table K.36: Curve fit parameters (Eq. 4.57b) for $(T^*)^2 \Omega_{s\ell}^{(2,4)}$ onto the data collected by Devoto [19] for charged air species. Units in SI.

Pair	$A^{B_{s\ell}^*}$	$B^{B_{s\ell}^*}$	$C^{B_{s\ell}^*}$
Rep.	3.1749e-01	-2.2843e-02	-6.3770e-03
Att.	2.8246e-01	-4.4648e-02	2.7386e-03
Pair	$D^{B_{s\ell}^*}$	$E^{B_{s\ell}^*}$	$F^{B_{s\ell}^*}$
Rep.	1.0084e-03	-4.9226e-05	7.9185e-07
Att.	-5.5317e-05		

Table K.37: Curve fit parameters (Eq. 4.60b) for $B_{s\ell}^*$ onto the data collected by Mason [18] for charged air species. Units in SI.

Pair	$A^{C_{s\ell}^*}$	$B^{C_{s\ell}^*}$	$C^{C_{s\ell}^*}$
Rep.	-5.1464e-01	-1.0303e-01	4.3466e-03
Att.	-6.4017e-01	-1.0876e-01	1.5360e-02
Pair	$D^{C_{s\ell}^*}$	$E^{C_{s\ell}^*}$	$F^{C_{s\ell}^*}$
Rep.	3.1379e-04	-2.7816e-05	5.3969e-07
Att.	-1.1785e-03	4.3987e-05	-6.2213e-07

Table K.38: Curve fit parameters (Eq. 4.60b) for $C_{s\ell}^*$ onto the data collected by Mason [18] for charged air species. Units in SI.

Pair	$A^{E_{s\ell}^*}$	$B^{E_{s\ell}^*}$	$C^{E_{s\ell}^*}$
Rep.	-3.7044e-01	-7.0048e-02	5.3942e-03
Att.	-3.9500e-01	-8.2138e-02	1.1150e-02
Pair	$D^{E_{s\ell}^*}$	$E^{E_{s\ell}^*}$	$F^{E_{s\ell}^*}$
Rep.	-7.9598e-05	-6.1127e-06	1.7463e-07
Att.	-7.5783e-04	2.4741e-05	-3.0924e-07

Table K.39: Curve fit parameters (Eq. 4.60b) for $E_{s\ell}^*$ onto the data collected by Mason [18] for charged air species. Units in SI.

Pair	$A^{\Omega_{s\ell}^{(1,1)}}$	$B^{\Omega_{s\ell}^{(1,1)}}$	$C^{\Omega_{s\ell}^{(1,1)}}$
e ⁻ – N	3.2281e+02	-2.4904e+02	6.7663e+01
e ⁻ – O	-4.7782e+01	7.3464e-02	3.3446e-02
e ⁻ – NO	-3.0735e+02	1.8481e+02	-5.1335e+01
e ⁻ – N ₂	-4.2406e+01	-2.4665e+00	4.6503e-01
e ⁻ – O ₂	-4.6532e+01	-7.1295e-01	2.0169e-01
Pair	$D^{\Omega_{s\ell}^{(1,1)}}$	$E^{\Omega_{s\ell}^{(1,1)}}$	$F^{\Omega_{s\ell}^{(1,1)}}$
e ⁻ – N	-9.0938e+00	6.0146e-01	-1.5649e-02
e ⁻ – O	-2.1165e-03		
e ⁻ – NO	7.0356e+00	-4.7545e-01	1.2666e-02
e ⁻ – N ₂	-2.4338e-02		
e ⁻ – O ₂	-1.1934e-02		

Table K.40: Curve fit parameters (Eq. 4.57a) for $\Omega_{s\ell}^{(1,1)}$ onto the data collected by Wright et al. [17] for electron-neutral collisions. Units in SI.

Pair	$A^{\Omega_{s\ell}^{(2,2)}}$	$B^{\Omega_{s\ell}^{(2,2)}}$	$C^{\Omega_{s\ell}^{(2,2)}}$
e ⁻ – N	2.8065e+02	-2.2550e+02	6.2339e+01
e ⁻ – O	-4.5517e+01	-1.0845e+00	2.1308e-01
e ⁻ – NO	-2.5538e+01	-9.7678e+00	2.0119e+00
e ⁻ – N ₂	-3.9455e+01	-3.8924e+00	6.8042e-01
e ⁻ – O ₂	-4.6161e+01	-8.7392e-01	2.1951e-01
Pair	$D^{\Omega_{s\ell}^{(2,2)}}$	$E^{\Omega_{s\ell}^{(2,2)}}$	$F^{\Omega_{s\ell}^{(2,2)}}$
e ⁻ – N	-8.5260e+00	5.7519e-01	-1.5306e-02
e ⁻ – O	-1.0341e-02		
e ⁻ – NO	-1.8704e-01	6.4026e-03	
e ⁻ – N ₂	-3.4670e-02		
e ⁻ – O ₂	-1.2297e-02		

Table K.41: Curve fit parameters (Eq. 4.57a) for $\Omega_{s\ell}^{(2,2)}$ onto the data collected by Wright et al. [17] for electron-neutral collisions. Units in SI.

Pair	$A^{B_{sl}^*}$	$B^{B_{sl}^*}$	$C^{B_{sl}^*}$
e ⁻ – N	1.8060e+02	-1.2272e+02	3.3368e+01
e ⁻ – O	1.2037e+00	-7.9615e-01	1.2980e-01
e ⁻ – NO	-3.3553e+02	2.3468e+02	-6.5098e+01
e ⁻ – N ₂	3.4135e+01	-2.5033e+01	7.5405e+00
e ⁻ – O ₂	2.7998e-01	-1.1538e+00	2.4472e-01
Pair	$D^{B_{sl}^*}$	$E^{B_{sl}^*}$	$F^{B_{sl}^*}$
e ⁻ – N	-4.4778e+00	2.9474e-01	-7.5949e-03
e ⁻ – O	-6.3897e-03		
e ⁻ – NO	8.9211e+00	-6.0286e-01	1.6062e-02
e ⁻ – N ₂	-1.1607e+00	8.9734e-02	-2.7440e-03
e ⁻ – O ₂	-1.3242e-02		

Table K.42: Curve fit parameters (Eq. 4.60a) for B_{sl}^* onto the data collected by Wright et al. [17] for electron-neutral collisions. Units in SI.

Pair	$A^{C_{sl}^*}$	$B^{C_{sl}^*}$	$C^{C_{sl}^*}$
e ⁻ – N	1.3920e+02	-1.0077e+02	2.8664e+01
e ⁻ – O	-6.3155e-01	3.3775e-01	-4.9419e-02
e ⁻ – NO	-2.9473e+00	2.3549e+00	-4.1738e-01
e ⁻ – N ₂	3.4658e-01	-1.0124e-01	2.2365e-02
e ⁻ – O ₂	-5.1691e-01	4.5219e-01	-7.6554e-02
Pair	$D^{C_{sl}^*}$	$E^{C_{sl}^*}$	$F^{C_{sl}^*}$
e ⁻ – N	-4.0256e+00	2.7923e-01	-7.6490e-03
e ⁻ – O	2.2542e-03		
e ⁻ – NO	2.1115e-02		
e ⁻ – N ₂	-1.7057e-03		
e ⁻ – O ₂	3.6272e-03		

Table K.43: Curve fit parameters (Eq. 4.60a) for C_{sl}^* onto the data collected by Wright et al. [17] for electron-neutral collisions. Units in SI.

Pair	$A^{\Omega_{s\ell}^{(1,1)}}$	$B^{\Omega_{s\ell}^{(1,1)}}$	$C^{\Omega_{s\ell}^{(1,1)}}$	$D^{\Omega_{s\ell}^{(1,1)}}$
N – N ⁺	-3.7581e+01	-1.6448e+00	1.8683e-01	-7.5578e-03
N – O ⁺	-2.4775e+01	-6.7148e+00	8.1943e-01	-3.4978e-02
N – NO ⁺	-3.1961e+01	-3.2668e+00	2.8783e-01	-8.5854e-03
N – N ₂ ⁺	-3.0760e+01	-3.9510e+00	4.0191e-01	-1.4068e-02
N – O ₂ ⁺	-3.9579e+01	-1.2054e-01	-1.3596e-01	9.6694e-03
O – N ⁺	-2.7402e+01	-5.7465e+00	7.0483e-01	-3.0935e-02
O – O ⁺	-3.8131e+01	-1.5362e+00	1.7325e-01	-6.9344e-03
O – NO ⁺	-2.9685e+01	-4.2924e+00	4.2837e-01	-1.4818e-02
O – N ₂ ⁺	-3.0158e+01	-4.3173e+00	4.5831e-01	-1.6786e-02
O – O ₂ ⁺	-3.6448e+01	-1.4838e+00	4.6679e-02	1.7505e-03
NO – N ⁺	-3.9487e+01	-1.2764e-03	-1.5636e-01	1.0702e-02
NO – O ⁺	-4.1206e+01	7.2851e-01	-2.5547e-01	1.4921e-02
NO – NO ⁺	-3.6146e+01	-2.0148e+00	2.1474e-01	-8.1158e-03
NO – N ₂ ⁺	-3.3071e+01	-2.7592e+00	2.2605e-01	-6.0142e-03
NO – O ₂ ⁺	-4.3769e+01	1.7367e+00	-3.8451e-01	2.0239e-02
N ₂ – N ⁺	-4.0019e+01	1.7359e-01	-1.7473e-01	1.1292e-02
N ₂ – O ⁺	-4.2235e+01	1.1468e+00	-3.0975e-01	1.7178e-02
N ₂ – NO ⁺	-3.7508e+01	-7.4474e-01	-6.2442e-02	6.8725e-03
N ₂ – N ₂ ⁺	-4.0546e+01	-2.4688e-01	-1.6702e-02	1.8476e-03
N ₂ – O ₂ ⁺	-4.2731e+01	1.4019e+00	-3.4757e-01	1.8825e-02
O ₂ – N ⁺	-3.8651e+01	-3.3322e-01	-1.1476e-01	8.9703e-03
O ₂ – O ⁺	-4.0448e+01	5.5155e-01	-2.4522e-01	1.4867e-02
O ₂ – NO ⁺	-3.5265e+01	-1.6861e+00	6.2901e-02	1.4568e-03
O ₂ – N ₂ ⁺	-3.5708e+01	-1.6861e+00	8.3471e-02	1.3455e-04
O ₂ – O ₂ ⁺	-3.6074e+01	-2.0758e+00	2.2750e-01	-8.9521e-03

Table K.44: Curve fit parameters (Eq. 4.57a) for $\Omega_{s\ell}^{(1,1)}$ onto the data collected by Levin & Wright [20] for ion-neutral collisions. Units in SI.

Pair	$A^{\Omega_{s\ell}^{(2,2)}}$	$B^{\Omega_{s\ell}^{(2,2)}}$	$C^{\Omega_{s\ell}^{(2,2)}}$	$D^{\Omega_{s\ell}^{(2,2)}}$
N – N ⁺	-3.5655e+01	-2.6192e+00	3.1296e-01	-1.4154e-02
N – O ⁺	-2.7101e+01	-5.6130e+00	6.4943e-01	-2.6411e-02
N – NO ⁺	-3.5063e+01	-2.0536e+00	1.3379e-01	-2.0391e-03
N – N ₂ ⁺	-3.2163e+01	-3.3751e+00	3.2708e-01	-1.0814e-02
N – O ₂ ⁺	-4.3694e+01	1.4961e+00	-3.4166e-01	1.8378e-02
O – N ⁺	-2.6016e+01	-6.2810e+00	7.6979e-01	-3.3287e-02
O – O ⁺	-2.8235e+01	-5.4331e+00	6.5900e-01	-2.8310e-02
O – NO ⁺	-3.0801e+01	-3.8751e+00	3.7871e-01	-1.2748e-02
O – N ₂ ⁺	-3.0335e+01	-4.2616e+00	4.5474e-01	-1.6691e-02
O – O ₂ ⁺	-3.8981e+01	-4.4644e-01	-8.8995e-02	7.6733e-03
NO – N ⁺	-4.3692e+01	1.6115e+00	-3.5785e-01	1.9110e-02
NO – O ⁺	-4.7030e+01	2.9527e+00	-5.3309e-01	2.6467e-02
NO – NO ⁺	-4.0053e+01	1.5830e-01	-1.6787e-01	1.1116e-02
NO – N ₂ ⁺	-3.6067e+01	-1.5874e+00	7.7506e-02	2.6752e-04
NO – O ₂ ⁺	-4.8999e+01	3.7342e+00	-6.3344e-01	3.0586e-02
N ₂ – N ⁺	-4.3063e+01	1.3742e+00	-3.2743e-01	1.7782e-02
N ₂ – O ⁺	-4.7022e+01	2.9653e+00	-5.3518e-01	2.6519e-02
N ₂ – NO ⁺	-4.0079e+01	2.1013e-01	-1.7820e-01	1.1642e-02
N ₂ – N ₂ ⁺	-3.6490e+01	-1.3785e+00	4.7018e-02	1.6350e-03
N ₂ – O ₂ ⁺	-4.8927e+01	3.7466e+00	-6.3810e-01	3.0838e-02
O ₂ – N ⁺	-4.2788e+01	1.2480e+00	-3.1164e-01	1.7169e-02
O ₂ – O ⁺	-4.4465e+01	2.0147e+00	-4.2055e-01	2.1971e-02
O ₂ – NO ⁺	-3.8771e+01	-3.6570e-01	-9.9550e-02	8.1846e-03
O ₂ – N ₂ ⁺	-3.5678e+01	-1.7099e+00	8.9315e-02	-1.1867e-04
O ₂ – O ₂ ⁺	-4.7599e+01	3.2565e+00	-5.8087e-01	2.8664e-02

Table K.45: Curve fit parameters (Eq. 4.57a) for $\Omega_{s\ell}^{(2,2)}$ onto the data collected by Levin & Wright [20] for ion-neutral collisions. Units in SI.

K.3.3.3 Air neutral species (**N**, **O**, **NO**, **N₂**, **O₂**) and argon (**Ar**)

Pair	$A^{\Omega_{s\ell}^{(1,1)}}$	$B^{\Omega_{s\ell}^{(1,1)}}$	$C^{\Omega_{s\ell}^{(1,1)}}$	$D^{\Omega_{s\ell}^{(1,1)}}$
Ar – Ar	-3.9838e+01	-1.2204e+00	1.3008e-01	-5.5677e-03
Ar – N	-4.2689e+01	-2.4448e-01	1.3784e-02	-1.2664e-03
Ar – O	-4.2774e+01	-1.9905e-01	9.1994e-03	-9.6091e-04
Ar – NO	-4.1046e+01	-8.0858e-01	8.5364e-02	-3.9894e-03
Ar – N ₂	-3.8970e+01	-1.6606e+00	1.9628e-01	-8.6561e-03
Ar – O ₂	-4.0265e+01	-1.0904e+00	1.1726e-01	-5.1810e-03

Table K.46: Curve fit parameters (Eq. 4.57a) for $\Omega_{s\ell}^{(1,1)}$ onto the data collected by Wright et al. [17] for argon-neutral collisions. Units in SI.

Pair	$A^{\Omega_{s\ell}^{(2,2)}}$	$B^{\Omega_{s\ell}^{(2,2)}}$	$C^{\Omega_{s\ell}^{(2,2)}}$	$D^{\Omega_{s\ell}^{(2,2)}}$
Ar – Ar	-3.8321e+01	-1.8341e+00	2.1559e-01	-9.3412e-03
Ar – N	-4.2515e+01	-2.6370e-01	1.7040e-02	-1.3519e-03
Ar – O	-4.2595e+01	-2.2433e-01	1.3406e-02	-1.1065e-03
Ar – NO	-3.8222e+01	-1.8921e+00	2.2643e-01	-9.9255e-03
Ar – N ₂	-3.7821e+01	-2.1089e+00	2.5682e-01	-1.1197e-02
Ar – O ₂	-3.9500e+01	-1.4197e+00	1.6729e-01	-7.4918e-03

Table K.47: Curve fit parameters (Eq. 4.57a) for $\Omega_{s\ell}^{(2,2)}$ onto the data collected by Wright et al. [17] for argon-neutral collisions. Units in SI.

K.3.3.4 Air neutral species (N, O, NO, N₂, O₂) and carbon species (CO, CO₂, CN, C, C₂, C₃)

Pair	$A^{\Omega_{s\ell}^{(1,1)}}$	$B^{\Omega_{s\ell}^{(1,1)}}$	$C^{\Omega_{s\ell}^{(1,1)}}$	$D^{\Omega_{s\ell}^{(1,1)}}$
CO ₂ – N	-3.8967e+01	-1.5375e+00	1.6696e-01	-6.8180e-03
CO ₂ – O	-4.3162e+01	-4.7904e-02	-9.9136e-03	2.2776e-05
CO ₂ – NO	-3.9625e+01	-1.2435e+00	1.3366e-01	-5.6544e-03
CO ₂ – N ₂	-3.9641e+01	-1.2721e+00	1.4345e-01	-6.3458e-03
CO ₂ – O ₂	-3.9495e+01	-1.2930e+00	1.3758e-01	-5.6509e-03
CO ₂ – CO ₂	-3.6385e+01	-2.3493e+00	2.6148e-01	-1.0382e-02
CO ₂ – CO	-3.9602e+01	-1.2875e+00	1.4543e-01	-6.4301e-03
CO ₂ – C	-4.2632e+01	-1.7685e-01	6.4629e-03	-7.7402e-04
CO ₂ – CN	-4.2469e+01	-1.9825e-01	9.3356e-03	-8.0530e-04
CO ₂ – C ₂	-3.8708e+01	-1.3284e+00	1.3227e-01	-4.9427e-03
CO ₂ – C ₃	-3.8028e+01	-1.4015e+00	1.3631e-01	-4.9427e-03
CO – N	-3.7887e+01	-2.1539e+00	2.7264e-01	-1.2909e-02
CO – O	-4.2758e+01	-2.5559e-01	1.5673e-02	-1.2896e-03
CO – NO	-4.2218e+01	-3.5937e-01	3.3211e-02	-2.1364e-03
CO – N ₂	-3.9641e+01	-1.2721e+00	1.4345e-01	-6.3458e-03
CO – O ₂	-4.2108e+01	-4.0141e-01	3.6355e-02	-2.1105e-03
CO – CO	-4.1739e+01	-5.8597e-01	6.9332e-02	-3.9712e-03
CO – C	-4.2401e+01	-3.1337e-01	2.2486e-02	-1.5623e-03
CO – CN	-4.2136e+01	-3.8923e-01	3.3005e-02	-1.9213e-03
CO – C ₂	-4.0106e+01	-1.1107e+00	1.1945e-01	-4.9427e-03
CO – C ₃	-3.9108e+01	-1.3541e+00	1.3370e-01	-4.9427e-03
C – N	-3.4637e+01	-3.4615e+00	4.3361e-01	-1.9212e-02
C – O	-3.9172e+01	-1.6789e+00	2.1573e-01	-1.0756e-02
C – NO	-4.3017e+01	-1.3307e-01	1.3664e-03	-7.7540e-04
C – N ₂	-3.9217e+01	-1.5262e+00	1.8380e-01	-8.6334e-03
C – O ₂	-4.2987e+01	-1.2975e-01	-1.7249e-04	-5.5423e-04

Table K.48: Curve fit parameters (Eq. 4.57a) for $\Omega_{s\ell}^{(1,1)}$ onto the data collected by Wright et al. [21], or with the values proposed by Bellemans & Magin [22], for air-carbon collisions. Units in SI.

Pair	$A^{\Omega_{s\ell}^{(1,1)}}$	$B^{\Omega_{s\ell}^{(1,1)}}$	$C^{\Omega_{s\ell}^{(1,1)}}$	$D^{\Omega_{s\ell}^{(1,1)}}$
C – C	-3.6468e+01	-2.6166e+00	3.2879e-01	-1.5300e-02
C – CN	-4.2499e+01	-3.0993e-01	2.3559e-02	-1.7813e-03
C – C ₂	-4.0761e+01	-9.8440e-01	1.1133e-01	-4.9427e-03
C – C ₃	-3.9906e+01	-1.2107e+00	1.2550e-01	-4.9427e-03
CN – N	-4.2175e+01	-4.0671e-01	3.6940e-02	-2.5592e-03
CN – O	-4.2296e+01	-4.1412e-01	3.5578e-02	-2.0957e-03
CN – NO	-4.2621e+01	-1.9132e-01	8.3611e-03	-9.6734e-04
CN – N ₂	-4.2211e+01	-3.1228e-01	2.3541e-02	-1.7572e-03
CN – O ₂	-4.2299e+01	-3.3547e-01	2.5791e-02	-1.5487e-03
CN – CN	-4.2591e+01	-1.8584e-01	8.1655e-03	-1.0632e-03
CN – C ₂	-4.0172e+01	-1.0873e+00	1.1798e-01	-4.9427e-03
CN – C ₃	-3.9196e+01	-1.3273e+00	1.3221e-01	-4.9427e-03
C ₂ – N	-4.0150e+01	-1.1434e+00	1.2146e-01	-4.9427e-03
C ₂ – O	-4.0190e+01	-1.1304e+00	1.2066e-01	-4.9427e-03
C ₂ – NO	-4.0130e+01	-1.1107e+00	1.1945e-01	-4.9427e-03
C ₂ – N ₂	-4.0109e+01	-1.1107e+00	1.1945e-01	-4.9427e-03
C ₂ – O ₂	-4.0057e+01	-1.1360e+00	1.2101e-01	-4.9427e-03
C ₂ – C ₂	-4.0129e+01	-1.0934e+00	1.1837e-01	-4.9427e-03
C ₂ – C ₃	-3.9147e+01	-1.3338e+00	1.3258e-01	-4.9427e-03
C ₃ – N	-3.9613e+01	-1.2964e+00	1.3047e-01	-4.9427e-03
C ₃ – O	-4.0437e+01	-1.1207e+00	1.2007e-01	-4.9427e-03
C ₃ – NO	-3.9138e+01	-1.3532e+00	1.3366e-01	-4.9427e-03
C ₃ – N ₂	-3.9110e+01	-1.3541e+00	1.3370e-01	-4.9427e-03
C ₃ – O ₂	-3.9039e+01	-1.3824e+00	1.3527e-01	-4.9427e-03
C ₃ – C ₃	-3.7939e+01	-1.6014e+00	1.4678e-01	-4.9427e-03

Table K.48: (cont) Curve fit parameters (Eq. 4.57a) for $\Omega_{s\ell}^{(1,1)}$ onto the data collected by Wright et al. [21], or with the values proposed by Bellemans & Magin [22], for air-carbon collisions. Units in SI.

Pair	$A_{s\ell}^{\Omega^{(2,2)}}$	$B_{s\ell}^{\Omega^{(2,2)}}$	$C_{s\ell}^{\Omega^{(2,2)}}$	$D_{s\ell}^{\Omega^{(2,2)}}$
CO ₂ – N	-3.8598e+01	-1.6685e+00	1.8600e-01	-7.6236e-03
CO ₂ – O	-4.2649e+01	-2.0729e-01	1.1105e-02	-8.2396e-04
CO ₂ – NO	-3.6883e+01	-2.2597e+00	2.6171e-01	-1.0878e-02
CO ₂ – N ₂	-3.7470e+01	-2.0679e+00	2.4372e-01	-1.0431e-02
CO ₂ – O ₂	-3.7252e+01	-2.1108e+00	2.4010e-01	-9.8158e-03
CO ₂ – CO ₂	-3.4370e+01	-3.0395e+00	3.4378e-01	-1.3597e-02
CO ₂ – CO	-3.7451e+01	-2.0752e+00	2.4466e-01	-1.0471e-02
CO ₂ – C	-4.2328e+01	-2.5178e-01	1.6562e-02	-1.1463e-03
CO ₂ – CN	-4.2355e+01	-2.0091e-01	1.0489e-02	-8.2882e-04
CO ₂ – C ₂	-3.8633e+01	-1.3481e+00	1.3748e-01	-5.2140e-03
CO ₂ – C ₃	-3.7947e+01	-1.4241e+00	1.4174e-01	-5.2140e-03
CO – N	-3.6760e+01	-2.5850e+00	3.3012e-01	-1.5200e-02
CO – O	-4.2312e+01	-3.8147e-01	3.2218e-02	-1.9176e-03
CO – NO	-3.9931e+01	-1.2453e+00	1.5032e-01	-7.1035e-03
CO – N ₂	-4.0530e+01	-1.0272e+00	1.2673e-01	-6.3537e-03
CO – O ₂	-4.0030e+01	-1.2009e+00	1.4185e-01	-6.5770e-03
CO – CO	-4.0476e+01	-1.0496e+00	1.2981e-01	-6.4922e-03
CO – C	-4.2058e+01	-4.0678e-01	3.5999e-02	-2.1121e-03
CO – CN	-4.2034e+01	-3.8078e-01	3.2373e-02	-1.8435e-03
CO – C ₂	-4.0044e+01	-1.1220e+00	1.2395e-01	-5.2140e-03
CO – C ₃	-3.9030e+01	-1.3748e+00	1.3899e-01	-5.2140e-03
C – N	-3.6825e+01	-2.4809e+00	2.9697e-01	-1.2963e-02
C – O	-3.8546e+01	-1.8433e+00	2.2918e-01	-1.0893e-02
C – NO	-4.2652e+01	-2.2174e-01	1.2835e-02	-1.1821e-03
C – N ₂	-3.9807e+01	-1.2066e+00	1.3451e-01	-6.0954e-03
C – O ₂	-4.2757e+01	-1.7798e-01	7.0107e-03	-8.1819e-04

Table K.49: Curve fit parameters (Eq. 4.57a) for $\Omega_{s\ell}^{(2,2)}$ onto the data collected by Wright et al. [21], or with the values proposed by Bellemans & Magin [22], for air-carbon collisions. Units in SI.

Pair	$A^{\Omega_{s\ell}^{(2,2)}}$	$B^{\Omega_{s\ell}^{(2,2)}}$	$C^{\Omega_{s\ell}^{(2,2)}}$	$D^{\Omega_{s\ell}^{(2,2)}}$
C – C	-3.7895e+01	-1.9517e+00	2.3269e-01	-1.0729e-02
C – CN	-4.2504e+01	-2.5906e-01	1.7971e-02	-1.4954e-03
C – C ₂	-4.0704e+01	-9.9101e-01	1.1539e-01	-5.2140e-03
C – C ₃	-3.9839e+01	-1.2258e+00	1.3034e-01	-5.2140e-03
CN – N	-4.2177e+01	-3.4893e-01	2.9710e-02	-2.1592e-03
CN – O	-4.2204e+01	-4.0244e-01	3.4795e-02	-2.0139e-03
CN – NO	-4.2534e+01	-1.7899e-01	7.6016e-03	-8.9416e-04
CN – N ₂	-4.2091e+01	-3.0871e-01	2.3756e-02	-1.7059e-03
CN – O ₂	-4.2300e+01	-2.9093e-01	2.0840e-02	-1.3034e-03
CN – CN	-4.2342e+01	-2.3118e-01	1.4339e-02	-1.2573e-03
CN – C ₂	-4.0111e+01	-1.0977e+00	1.2240e-01	-5.2140e-03
CN – C ₃	-3.9120e+01	-1.3469e+00	1.3741e-01	-5.2140e-03
C ₂ – N	-4.0086e+01	-1.1559e+00	1.2607e-01	-5.2140e-03
C ₂ – O	-4.0127e+01	-1.1424e+00	1.2523e-01	-5.2140e-03
C ₂ – NO	-4.0069e+01	-1.1220e+00	1.2395e-01	-5.2140e-03
C ₂ – N ₂	-4.0047e+01	-1.1220e+00	1.2395e-01	-5.2140e-03
C ₂ – O ₂	-3.9994e+01	-1.1483e+00	1.2560e-01	-5.2140e-03
C ₂ – C ₂	-4.0068e+01	-1.1041e+00	1.2281e-01	-5.2140e-03
C ₂ – C ₃	-3.9071e+01	-1.3537e+00	1.3780e-01	-5.2140e-03
C ₃ – N	-3.9540e+01	-1.3149e+00	1.3557e-01	-5.2140e-03
C ₃ – O	-4.0375e+01	-1.1324e+00	1.2460e-01	-5.2140e-03
C ₃ – NO	-3.9061e+01	-1.3739e+00	1.3894e-01	-5.2140e-03
C ₃ – N ₂	-3.9033e+01	-1.3748e+00	1.3899e-01	-5.2140e-03
C ₃ – O ₂	-3.8960e+01	-1.4042e+00	1.4064e-01	-5.2140e-03
C ₃ – C ₃	-3.7839e+01	-1.6321e+00	1.5278e-01	-5.2140e-03

Table K.49: (cont) Curve fit parameters (Eq. 4.57a) for $\Omega_{s\ell}^{(2,2)}$ onto the data collected by Wright et al. [21], or with the values proposed by Bellemans & Magin [22], for air-carbon collisions. Units in SI.

References

- [1] C. Park. *Non-Equilibrium Hypersonic Aerodynamics*. John Wiley & sons, New York, 1990.
- [2] N. P. Bitter and J. E. Shepherd. *Stability of highly cooled hypervelocity boundary layers*. Journal of Fluid Mechanics, [778:586–620](#), 2015.
- [3] W. G. Vincenti and C. H. Kruger. *Introduction to physical gas dynamics*. Huntington, N.Y. : Krieger, 1967.
- [4] J. B. Scoggins and T. E. Magin. *Development of Mutation++: MULTicomponent Thermodynamics And Transport properties for IONized gases library in C++*. AIAA paper, [2014-2966](#), 2014.
- [5] J. B. Scoggins. *Development of numerical methods and study of coupled flow, radiation, and ablation phenomena for atmospheric entry*. PhD thesis, Université Paris-Saclay and VKI, 2017.
- [6] T. E. Magin and G. Degrez. *Transport algorithms for partially ionized and unmagnetized plasmas*. Journal of Computational Physics, [198\(2\):424–449](#), 2004.
- [7] L. Gurvich, I. Veyts, and C. Alcock. *Thermodynamic Properties of Individual Substances. Vol. 1, Elements O, H(D, T), F, Cl, Br; I, He, Ne, Ar, Kr, Xe, Rn, S, N, P and their Compounds. Part Two. Tables*. Hemisphere Publishing Corporation, 4 edition, 1989.
- [8] C. Park. *Review of chemical-kinetic problems of future NASA missions. I - Earth entries*. Journal of Thermophysics and Heat Transfer, [7\(3\):385–398](#), 1993.
- [9] C. Park, J. T. Howe, R. L. Jaffe, and G. V. Candler. *Review of chemical-kinetic problems of future NASA missions. II - Mars entries*. Journal of Thermophysics and Heat Transfer, [8\(1\):9–23](#), 1994.
- [10] P. A. Gnoffo, R. N. Gupta, and J. L. Shinn. *Conservation Equations and Physical Models for Hypersonic Air Flows in Thermal and Chemical Nonequilibrium*. Technical Report TP-2867, NASA, 1989.
- [11] R. C. Millikan and D. R. White. *Systematics of vibrational relaxation*. The Journal of Chemical Physics, [39\(12\):3209–3213](#), 1963.
- [12] U. Goldberg, O. Peroomian, S. Chakravarthy, and B. Sekar. *Validation of CFD++ code capability for supersonic combustor flowfields*. AIAA paper, [1997-3271](#), 1997.

- [13] F. G. Blottner, M. Johnson, and M. Ellis. *Chemically Reacting Viscous Flow Program For Multi-Component Gas Mixtures*. Technical Report SC-RR-70-754, Sandia Laboratories, 1971.
- [14] C. Mortensen. *Effects of Thermochemical Nonequilibrium on Hypersonic Boundary-Layer Instability in the Presence of Surface Ablation or Isolated Two-Dimensional Roughness*. PhD thesis, UCLA, 2013.
- [15] R. N. Gupta, J. M. Yos, R. A. Thompson, and K.-P. Lee. *A review of Reaction Rates and Thermodynamic and Transport Properties for an 11-Species Air Model for Chemical and Thermal Nonequilibrium Calculations to 30000K*. Technical Report RP-1232, NASA, 1990.
- [16] G. K. Stuckert. *Linear Stability Theory of Hypersonic, Chemically Reacting Viscous Flows*. PhD thesis, Arizona State University, 1991.
- [17] M. J. Wright, D. Bose, G. E. Palmer, and E. Levin. *Recommended Collision Integrals for Transport Property Computations Part I: Air Species*. AIAA Journal, [43\(12\):2558–2564](#), 2005.
- [18] E. A. Mason. *Transport Coefficients of Ionized Gases*. Physics of Fluids, [10\(8\):1827](#), 1967.
- [19] R. S. Devoto. *Transport coefficients of ionized argon*. Physics of Fluids, [16\(5\):616](#), 1973.
- [20] E. Levin and M. J. Wright. *Collision Integrals for Ion-Neutral Interactions of Nitrogen and Oxygen*. Journal of Thermophysics and Heat Transfer, [18\(1\):143–147](#), 2004.
- [21] M. J. Wright, H. H. Hwang, and D. W. Schwenke. *Recommended Collision Integrals for Transport Property Computations Part II: Mars and Venus Entries*. AIAA Journal, [45\(1\):281–288](#), 2007.
- [22] A. Bellemans and T. E. Magin. *Calculation of Collision Integrals for Ablation Species*. In 8th European Symposium on Aerothermodynamics for Space Vehicles, Lisbon, Portugal, 2015.

L

Collision-integral fits

L.1 Air collisions of neutral-to-neutral species (N, O, NO, N₂, O₂)

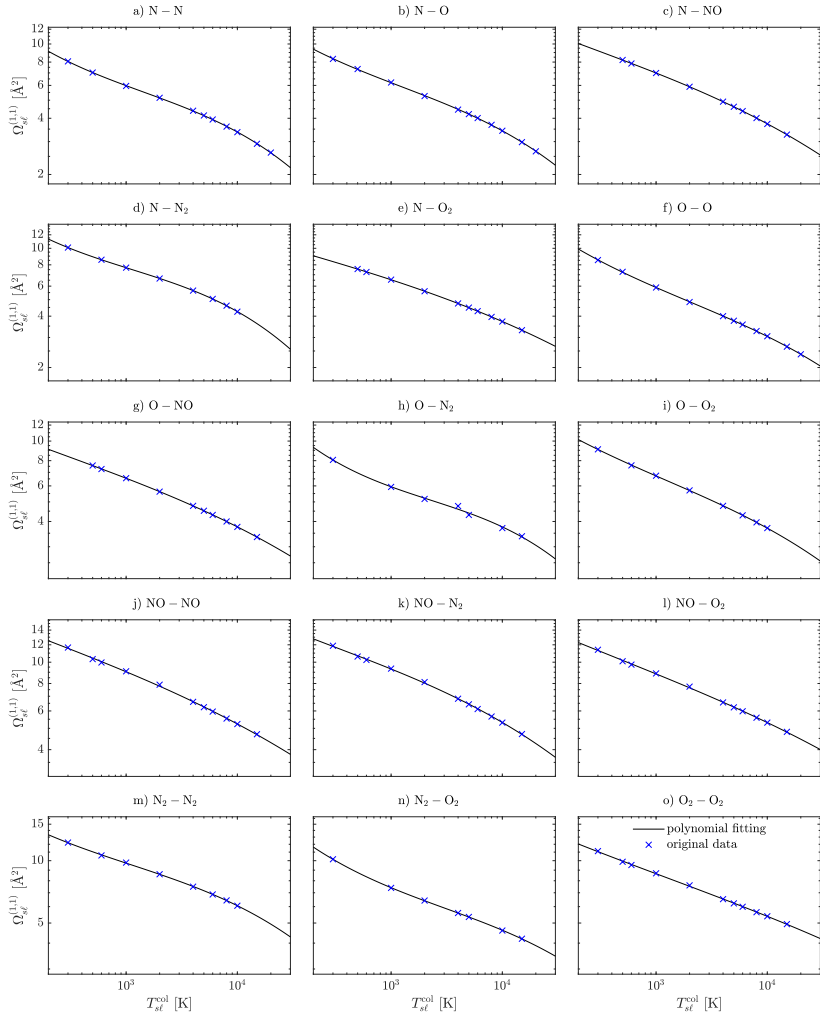


Figure L.1: Collision-integral fits for $\Omega_{st}^{(1,1)}$ for air neutral species on the data from Wright et al. [1].

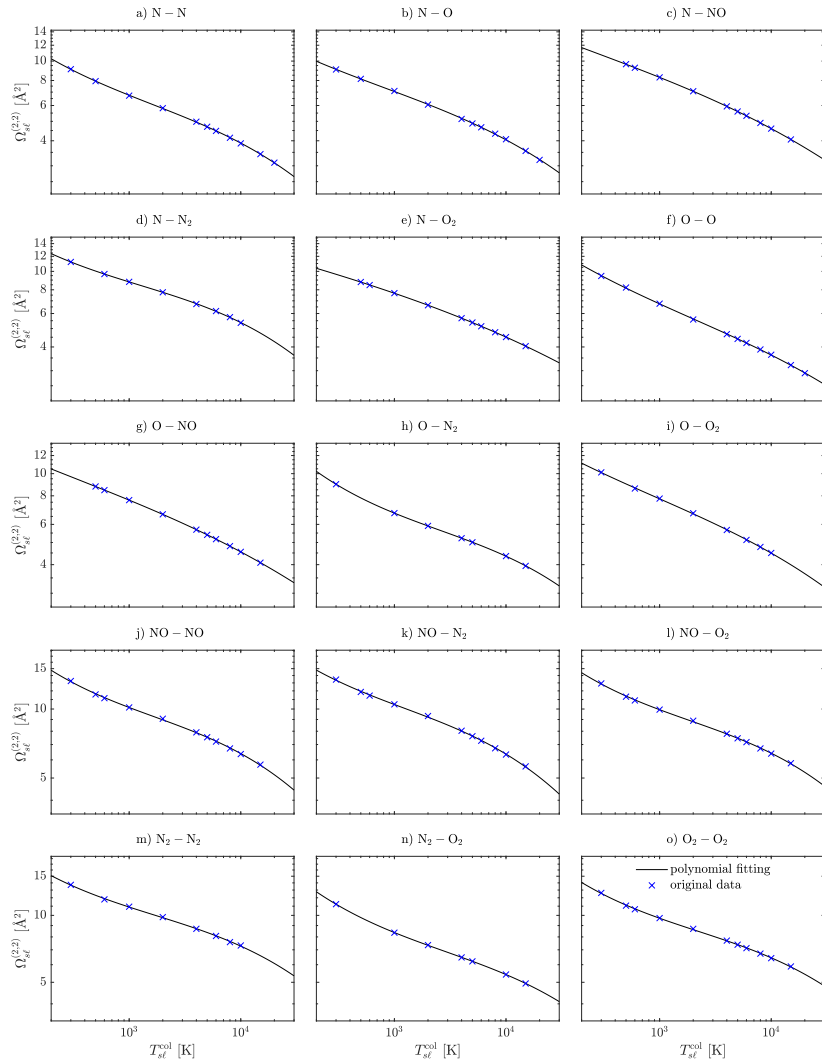


Figure L.2: Collision-integral fits for $\Omega_{s\ell}^{(2;2)}$ for air neutral species on the data from Wright et al. [1].

L.2 Air collisions of charged-to-charged species (N^+ , O^+ , NO^+ , N_2^+ , O_2^+ , e^-)

A note must be made concerning Fig. L.6a. In Devoto's [2] Table III, the second-last value in the fifth column is presumably mistakenly typed – all other high- T^* values of the repulsive potential are identical to the attractive except for that of $T^* = 1\,000$. Moreover, the values of column 4 and 5 differ by the order of their decimals (0.2098 instead of 0.2908). The curve fits presented in Table K.35 and displayed in Fig. L.6a are therefore done with 0.2908 instead of the value in Devoto's [2] table (0.2098).

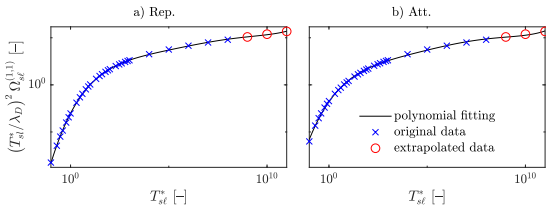


Figure L.3: Collision-integral fits for $\Omega_{s\ell}^{(1,1)}$ for charged collisions of air species on the data from Mason [3].

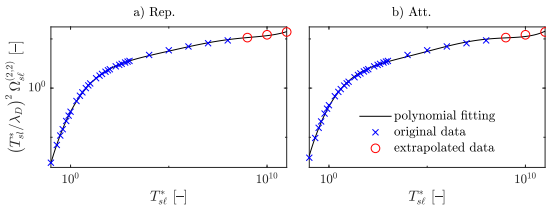


Figure L.4: Collision-integral fits for $\Omega_{s\ell}^{(2,2)}$ for charged collisions of air species on the data from Mason [3].

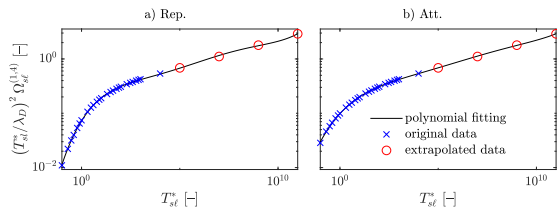


Figure L.5: Collision-integral fits for $\Omega_{s\ell}^{(1,4)}$ for charged collisions of air species on the data from Devoto [2].

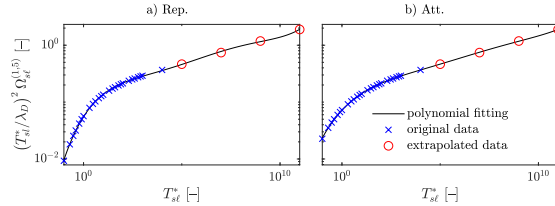


Figure L.6: Collision-integral fits for $\Omega_{s\ell}^{(1,5)}$ for charged collisions of air species on the data from Devoto [2].

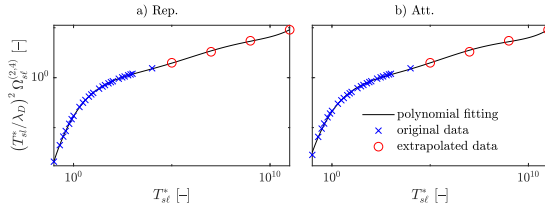


Figure L.7: Collision-integral fits for $\Omega_{s\ell}^{(2,4)}$ for charged collisions of air species on the data from Devoto [2].

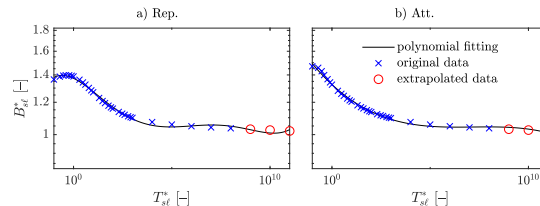


Figure L.8: Collision-integral-ratio fits for $B_{s\ell}^*$ for charged collisions of air species on the data from Devoto [2].

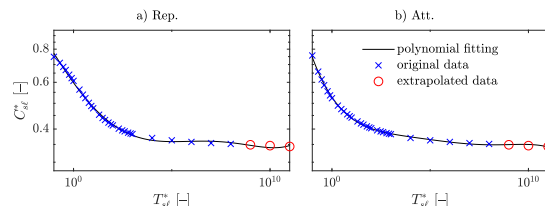


Figure L.9: Collision-integral-ratio fits for $C_{s\ell}^*$ for charged collisions of air species on the data from Devoto [2].

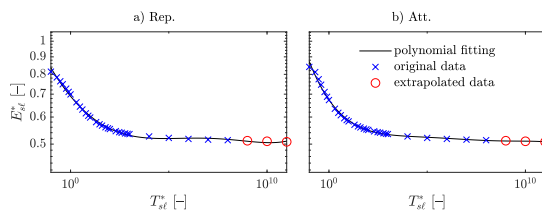


Figure L.10: Collision-integral-ratio fits for E_{st}^* for charged collisions of air species on the data from Devoto [2].

L.3 Air collisions of ion-to-neutral species (N^+ , O^+ , NO^+ , N_2^+ , O_2^+ to N , O , NO , N_2 , O_2)

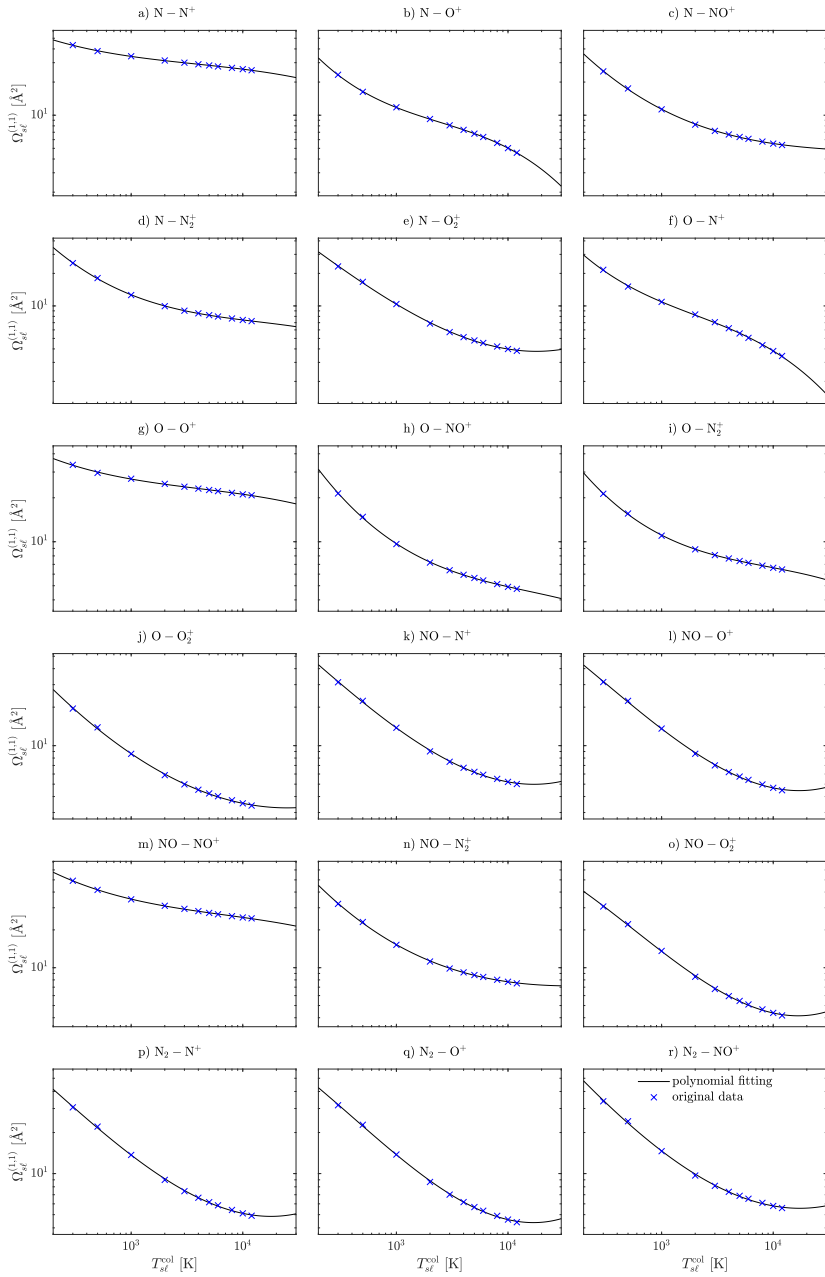


Figure L.11: Collision-integral fits for $\Omega_{st}^{(1,1)}$ for charged air species on the data from Levin & Wright [4].

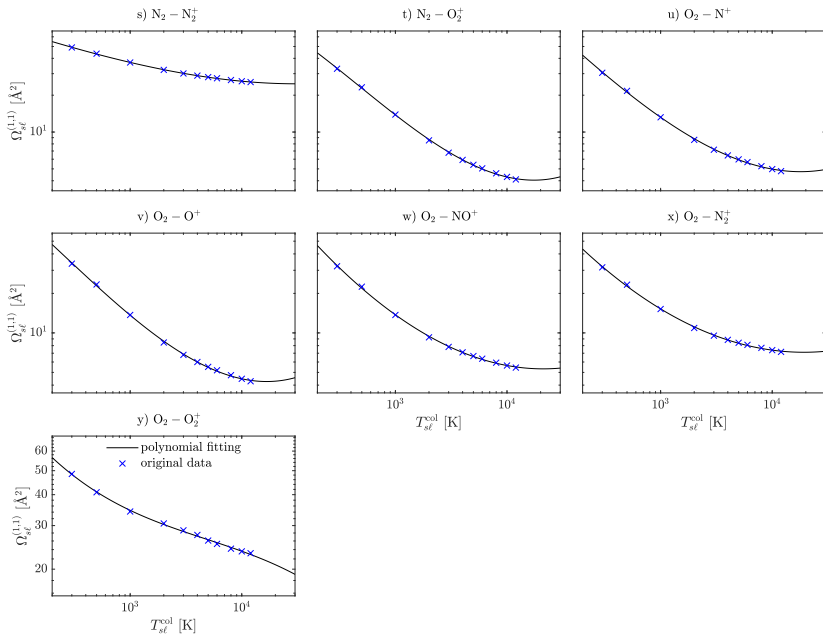


Figure L.11: (cont) Collision-integral fits for $\Omega_{sl}^{(1,1)}$ for charged air species on the data from Levin & Wright [4].

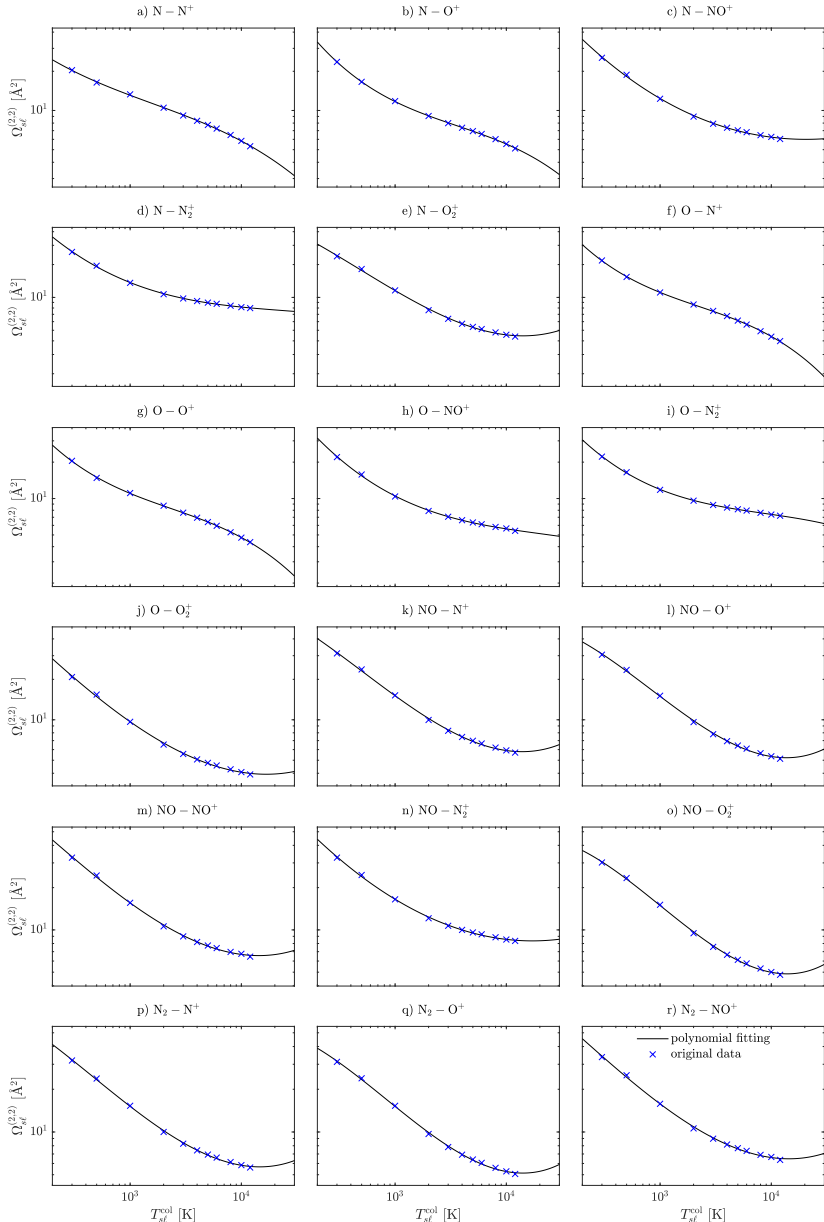


Figure L.12: Collision-integral fits for $\Omega_{s\ell}^{(2,2)}$ for charged air species on the data from Levin & Wright [4].

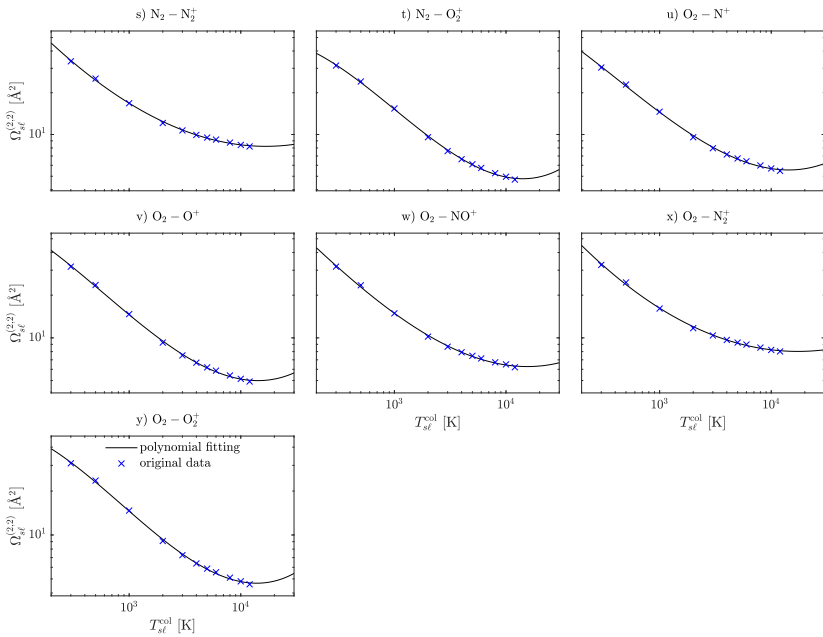


Figure L.12: (cont) Collision-integral fits for $\Omega_{s\ell}^{(2,2)}$ for charged air species on the data from Levin & Wright [4].

L.4 Air collisions of electron-to-neutral species (e^- to N, O, NO, N_2 , O_2)

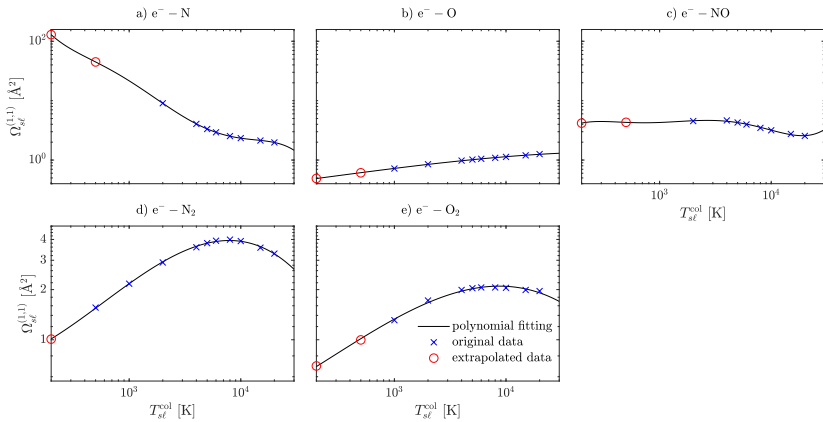


Figure L.13: Collision-integral fits for $\Omega_{s\ell}^{(1,1)}$ for charged collisions of neutral air species with electrons on the data from Wright et al. [1].

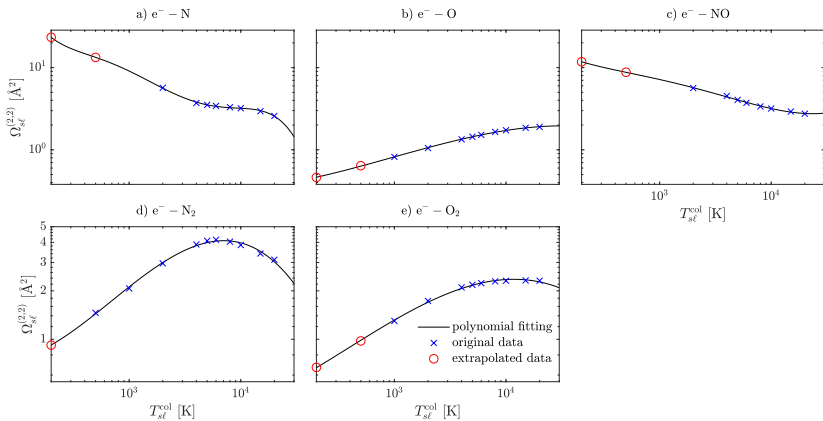


Figure L.14: Collision-integral fits for $\Omega_{s\ell}^{(2,2)}$ for charged collisions of neutral air species with electrons on the data from Wright et al. [1].

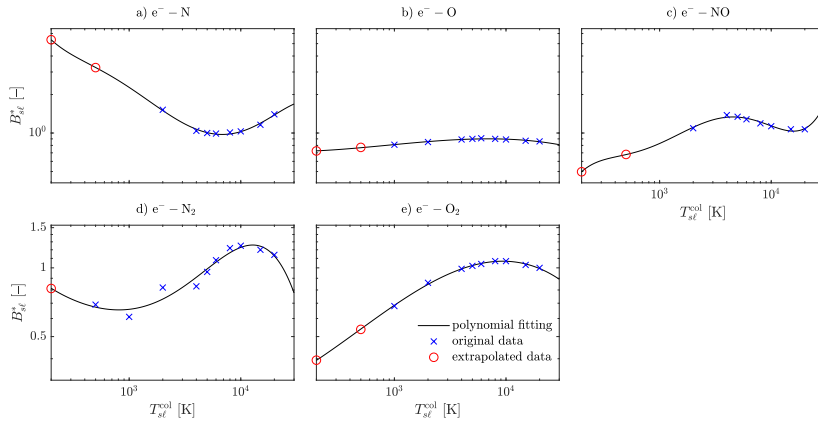


Figure L.15: Collision-integral-ratio fits for B_{sl}^* for charged collisions of neutral air species with electrons on the data from Wright et al. [1].

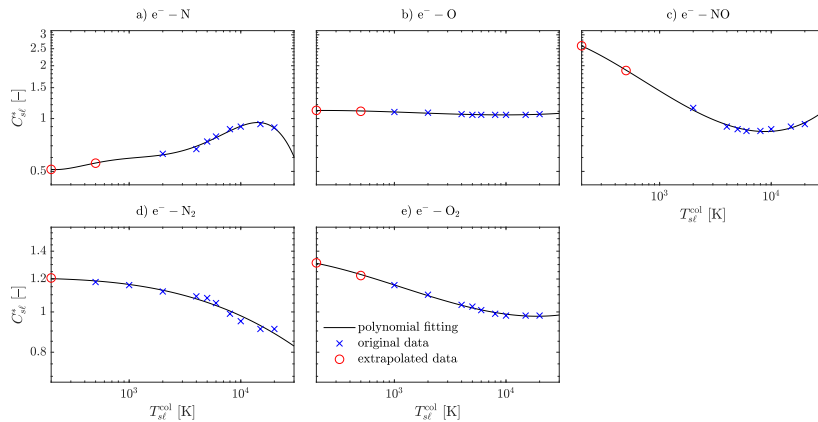


Figure L.16: Collision-integral-ratio fits for C_{sl}^* for collisions of neutral air species with electrons on the data from Wright et al. [1].

L.5 Air collisions of argon-to-neutral species (Ar to N, O, NO, N₂, O₂)

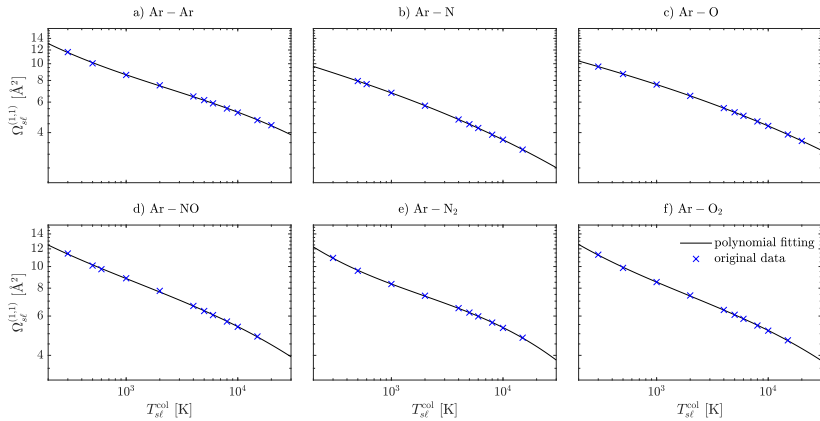


Figure L.17: Collision-integral fits for $\Omega_{s\ell}^{(1,1)}$ for air neutral species and argon on the data from Wright et al. [1].

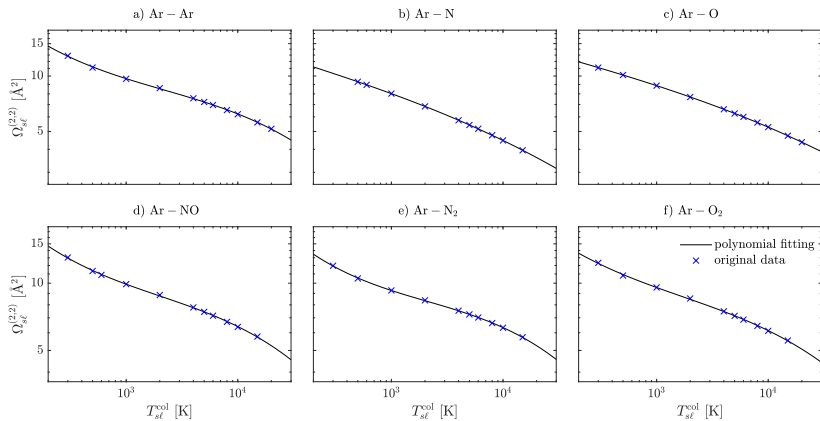


Figure L.18: Collision-integral fits for $\Omega_{s\ell}^{(2,2)}$ for air neutral species and argon on the data from Wright et al. [1].

L.6 Collisions of neutral air and carbon species (N, O, NO, N₂, O₂ and CO, CO₂, CN, C, C₂, C₃)

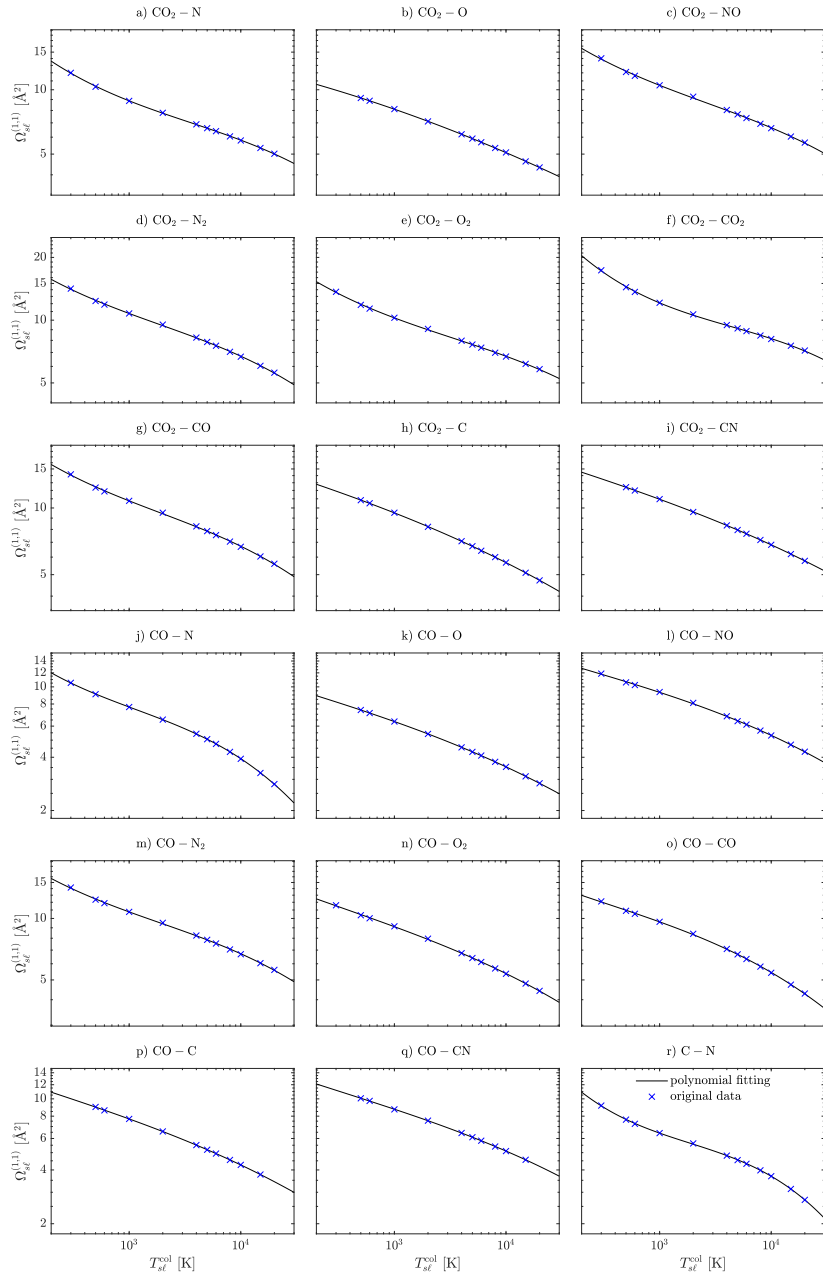


Figure L.19: Collision-integral fits for $\Omega_{st}^{(1,1)}$ for air and carbon species on the data from Wright et al. [5]. Note that the collisions not included here are modeled with the curve fits proposed by Bellemans & Magin [6] and included in table K.48.

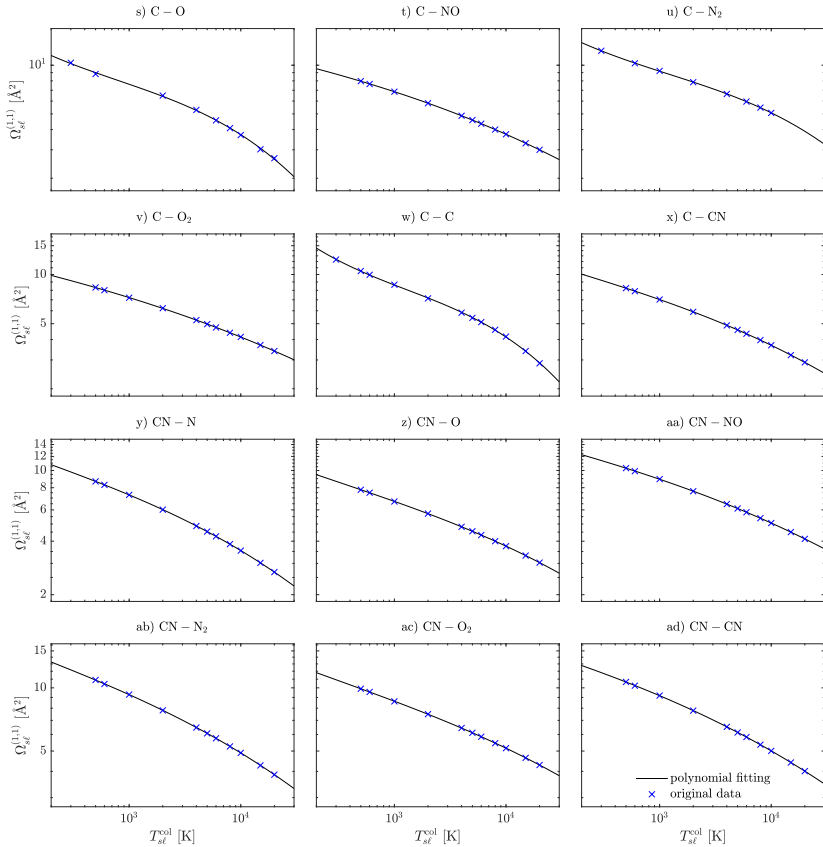


Figure L.19: (cont) Collision-integral fits for $\Omega_{st}^{(1,1)}$ for air and carbon species on the data from Wright et al. [5]. Note that the collisions not included here are modeled with the curve fits proposed by Bellemans & Magin [6] and included in table K.48.

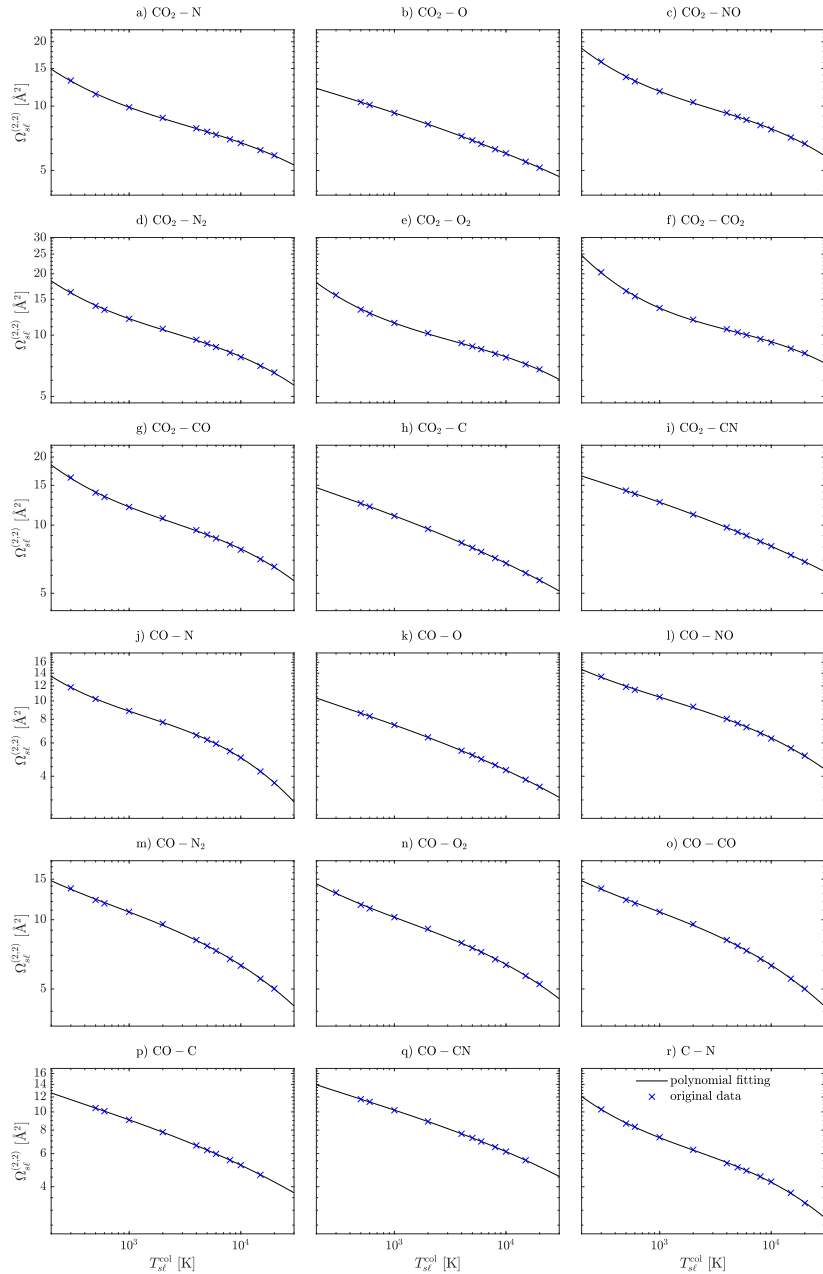


Figure L.20: Collision-integral fits for $\Omega_{st}^{(2,2)}$ for air and carbon species on the data from Wright et al. [5]. Note that the collisions not included here are modeled with the curve fits proposed by Bellemans & Magin [6] and included in table K.49.

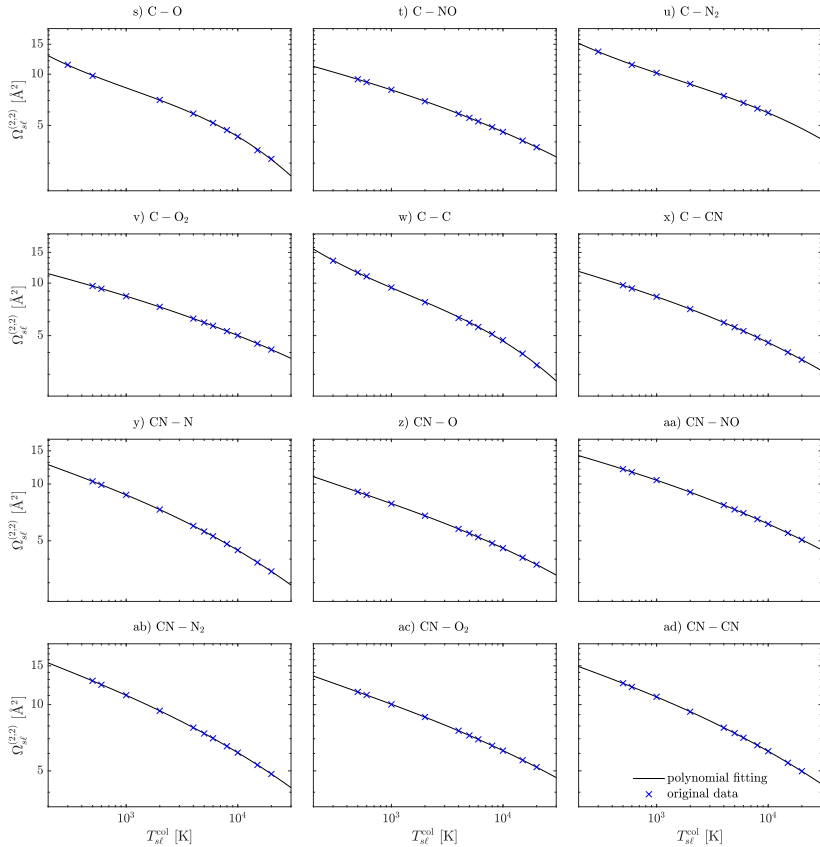


Figure L.20: (cont) Collision-integral fits for $\Omega_{st}^{(2,2)}$ for air and carbon species on the data from Wright et al. [5]. Note that the collisions not included here are modeled with the curve fits proposed by Bellemans & Magin [6] and included in table K.49.

References

- [1] M. J. Wright, D. Bose, G. E. Palmer, and E. Levin. *Recommended Collision Integrals for Transport Property Computations Part I: Air Species*. AIAA Journal, **43**(12):2558–2564, 2005.
- [2] R. S. Devoto. *Transport coefficients of ionized argon*. Physics of Fluids, **16**(5):616, 1973.
- [3] E. A. Mason. *Transport Coefficients of Ionized Gases*. Physics of Fluids, **10**(8):1827, 1967.
- [4] E. Levin and M. J. Wright. *Collision Integrals for Ion-Neutral Interactions of Nitrogen and Oxygen*. Journal of Thermophysics and Heat Transfer, **18**(1):143–147, 2004.
- [5] M. J. Wright, H. H. Hwang, and D. W. Schwenke. *Recommended Collision Integrals for Transport Property Computations Part II: Mars and Venus Entries*. AIAA Journal, **45**(1):281–288, 2007.
- [6] A. Bellemans and T. E. Magin. *Calculation of Collision Integrals for Ablation Species*. In 8th European Symposium on Aerothermodynamics for Space Vehicles, Lisbon, Portugal, 2015.

M

Publications

M.1 Journal papers

[1] *Effect of Uneven Wall Blowing on Hypersonic Boundary-Layer Stability and Transition*

F. Miró Miró & F. Pinna

published in: Physics of Fluids. Vol. 30. No. 084106. August 2018.

DOI: 10.1063/1.5043353

Abstract: *The understanding of aerothermodynamics in complex multiphysics environments such as atmospheric entry is of vital importance for the design of optimized vehicles. A better insight into the interaction between the thermal protection system ablation and the flow's stability and transition would significantly increase the available payload and reduce the overall mission costs. In order to improve the modeling of the effect of ablation-induced outgassing, a continuously blowing boundary condition for linear stability theory is developed and tested against existing homogeneous and porous conditions in cold wind-tunnel calorically perfect gas conditions. The new model predicts a substantially higher destabilization of the boundary layer than the classic one. An exhaustive parametric study addresses the effect of the most important parameters influencing the boundary condition characteristics. Porous layer stabilization/destabilization maps for different porous layers and flow conditions are built, serving as a starting point for a stabilizing-porous-coating design methodology. Previous controversial litera-*

ture findings are clarified in the light of the current work, showing a consistent way of addressing similar future tests. The semiempirical eN method is used to predict the location of transition onset in noisy wind-tunnel conditions, obtaining substantially different predictions with different wall models.

[2] **High-Enthalpy Effects on Hypersonic Boundary-Layer Transition**

V. Wartemann, A. Wagner, R. Wagnild, F. Pinna, **F. Miró Miró**, H. Tanno and H. Johnson

published in: **Journal of Spacecraft and Rockets**. December 2019.

DOI: 10.2514/1.A34281

Abstract: In the present study, three boundary-layer stability codes are compared based on hypersonic high-enthalpy boundary-layer flows around a blunted 7° half-angle cone. The code-to-code comparison is conducted between the following codes: the Nonlocal Transition analysis code of the DLR, German Aerospace Center (DLR); the Stability and Transition Analysis for hypersonic Boundary Layers code of VirtusAero LLC; and the VKI Extensible Stability and Transition Analysis code of the von Karman Institute for Fluid Dynamics. The comparison focuses on the role of real-gas effects on the second-mode instability, in particular the disturbance frequency, and deals with the question on how far not accounting for real-gas effects compromises the stability analysis. The experimental test cases for the comparison are provided by the DLR High Enthalpy Shock Tunnel Göttingen and the Japan Aerospace Exploration Agency High Enthalpy Shock Tunnel. The focus of the comparison between the stability results and the measurements is, besides real-gas effects, the influence of uncertainties in the mean flow on the stability analysis.

[3] **Effect of Wall blowing on Hypersonic Boundary-layer Transition**

F. Miró Miró, P. Dehairs, F. Pinna, M. Gkolia, D. Masutti, T. Regert, & O. Chazot

published in: **AIAA Journal**. January 2019.

DOI: 10.2514/1.J057604

Abstract: An investigation of outgassing effects on boundary-layer transition was carried out. This joint computational-experimental work mimicked heat-shield pyrolysis outgassing in atmospheric re-entry conditions. A slender 7°-half-angle

cone with air wall blowing through a porous section near the apex was tested in the VKI-H3 Mach 6 hypersonic blow-down noisy wind tunnel. The steady transition onset location was measured using infrared thermography while gaseous-naphthalene-based planar laser induced fluorescence (PLIF) imaging enabled the visualization and quantification of the spatial characteristics of the instabilities. Linear stability theory, combined with the semi-empirical e^N method with $N = 5.9$, was used to predict the location of transition onset in the same configurations. Studies were performed at different free-stream unit Reynolds numbers and blowing rates. Numerical and experimental results agreed within the experimental uncertainties, and coincided with the previously reported advancement of the transition location due to wall blowing. The wave numbers of the most amplified second-mode instabilities obtained with LST matched the observations done with PLIF, suggesting it was the growth of such perturbations that lead to the transitioning of the boundary layer. method was shown to be applicable to the prediction of transition in wall-blowing configurations. For non-blowing configurations, The porous section was seen to destabilize the boundary layer for non-blowing configurations. Regarding the upstream advancement of transition associated with wall blowing, the numerical analysis suggested that it is a consequence of the increase in the range of unstable frequencies in the wall-blowing region. Blowing non-uniformities in the cone's longitudinal direction were observed to have no influence on the local transition location under noisy conditions.

[4] High-enthalpy models for boundary-layer stability and transition

F. Miró Miró, E. S. Beyak, F. Pinna and H. L. Reed

published in: Physics of Fluids. April 2019.

DOI: 10.1063/1.5084235

Abstract: The prediction of the transition dynamics of high-enthalpy boundary-layer flows requires appropriate thermodynamic and transport models. This work quantifies the influence of transport, diffusion, collision, equilibrium, and chemical-kinetics modeling on the stability characteristics and the estimated transition-onset location of canonical boundary layers. The computed behavior of second-mode instabilities is consistently highly dependent on the base-flow's boundary-layer height. The Blottner-Eucken-Wilke transport model is seen to underpredict the boundary-layer height, hence overpredicting the growth-rate distribution and forecasting the transition onset to occur $\sim 38\%$ sooner. The other low-order transport models (Brokaw and Yos) returned very close results to the most-accurate Chapman-Enskog model. The use of Gupta et al.'s collisional data

instead of Wright et al.'s more accurate data is also seen to predict the transition onset to occur $\sim 8\%$ closer to the leading edge. The modeling of mass diffusion and the chemical-equilibrium constant is observed to have a negligible influence on the boundary-layer height and transition-onset-location estimations (less than 5% and 2%, respectively). For the analyzed conditions, all chemical models predict the same transition-onset location ($\pm 1\%$); since at the streamwise positions where perturbations have reached sufficiently large amplitudes, the flow is close to equilibrium and thus independent of the reaction rates. The use of different transport models for the perturbation terms, while maintaining the same model for the basic state, leads to negligible differences in the predictions. This further reinforces the thesis that the boundary-layer height calculation is paramount to the simulation of the development of second-mode instabilities.

[5] ***Parabolized stability analysis of chemically reacting boundary layer flows in equilibrium conditions***

L. Zanus, **F. Miró Miró**, and F. Pinna

published in: **Journal of Aerospace Engineering**. May 2019.

DOI: 10.1177/0954410019839894

Abstract: Stability of self-similar hypersonic flows over a flat plate in local thermodynamic equilibrium is studied by means of linear parabolized stability equations. A spectral collocation numerical method together with a finite-difference-based marching scheme are used to solve the equations, while the gas mixture and transport properties are computed with a table look-up procedure. High-temperature effects are found to destabilize the second-Mack-mode regardless of the adiabatic/isothermal wall condition considered. On the other hand, nonlocal effects show a Mach-dependence influence: stabilizing at lower Mach, while destabilizing at higher ones. Strong oscillations in the growth rate of perturbations in local thermodynamic equilibrium are found to be caused by damped supersonic modes.

[6] ***Injection-gas-composition effects on hypersonic boundary-layer transition***

F. Miró Miró and F. Pinna

published in: **Journal of Fluid Mechanics**. March 2020.

DOI: 10.1017/jfm.2020.129

Abstract: *The thermal protection system in atmospheric-entry and hypersonic-cruise vehicles are oftentimes designed to ablate during their operation, thus injecting a mixture of various gases with distinct properties into the boundary layer. Such outgassing affects the propagation of instabilities within the boundary layer that ultimately originates the transition to turbulence. This work uses linear stability theory, in combination with the eN method, to establish the underlying reason for the experimentally observed advancement/delay of transition in sharp slender hypersonic cones, when injecting lighter/heavier gases. Contrary to the current understanding and experimental correlations, this numerical analysis suggests that such a behaviour is not linked to the isolated effect of the injected gas' molar weight, but to its combination with the blowing discontinuity, porosity and the appearance of a shocklet, consequence of the injected gas composition. The shocklet constitutes a density gradient that acts on second-mode instabilities like a thermoacoustic impedance.*

M.2 Conference papers

[7] *Linear Stability Analysis of a Hypersonic Boundary Layer in Equilibrium and Non-Equilibrium*

F. Miró Miró & Fabio Pinna

presented at: 2017 AIAA Aviation Meeting. Denver, CO. June 2017.

DOI: 10.2514/6.2017-4518

Abstract: *A better prediction of boundary-layer transition in hypersonic cruise and entry vehicles, is necessary to optimize their designs. Boundary layer stability allows to study transition by modelling the physics of the early stages of perturbation propagation. This work studies, through Linear Stability Theory, a flat plate at two different Mach numbers and using different flow assumptions, profiting of the solvers generated by VESTA's Automatic Derivation & Implementation Tool.*

[8] *Parabolized Stability Analysis of Chemically Reacting Boundary Layer Flows in Equilibrium Conditions*

L. Zanus, F. Miró Miró & Fabio Pinna

presented at: 7th European Conference for Aeronautics and Aerospace Sciences (EUCASS). Milan, Italy. July 2017.

DOI: 10.13009/EUCASS2017-288

Abstract: *Stability of self-similar hypersonic flows over a flat plate in presence of local thermodynamic equilibrium conditions is studied by means of linear Parabolized Stability Equations (PSE). A spectral collocation numerical method together with a finite difference-based marching scheme are used to solve the equations, while the gas mixture and transport properties are computed with a table look-up procedure. High temperature effects are found to destabilize the second Mack mode regardless of the adiabatic/isothermal wall condition considered. On the other hand, nonlocal effects show a Mach-dependence influence: stabilizing at lower Mach, while destabilizing at higher ones.*

[9] *Numerical Modeling of Continuous Blowing Surface in Hypersonic Boundary Layers*

F. Pinna & F. Miró Miró

presented at: 7th European Conference for Aeronautics and Aerospace

Sciences (EUCASS). Milan, Italy. July 2017.

DOI: 10.13009/EUCASS2017-68

Abstract: Hypersonic vehicles need to withstand high thermal loads during their mission. In case of very high energy flows ablative materials are used to build a Thermal Protection System (TPS). The outgassing due to the pyrolysis of the TPS directly affects the boundary layer stability. This paper studies the effect of wall blowing under controlled conditions, such as porous surfaces, and propose a model for a continuously blowing surface, thus mimicking the behavior of an ablative heat shield. The two models displays a similar shift to lower frequencies for the instabilities growth rate peak and an increased instability of the boundary layer.

[10] Diffusion and chemical non-equilibrium effects on hypersonic boundary-layer stability

F. Miró Miró, F. Pinna, E. Beyak, P. Barbante & H. Reed

presented at: 2018 AIAA Science and Technology Meeting. Orlando, FL. January 2018.

DOI: 10.2514/6.2018-1824

Abstract: Boundary-layer transition prediction has a dramatic impact on the optimization of hypersonic cruise and entry vehicle design. Linear Stability Theory approaches laminar-to-turbulent transition in a simplified yet physics-based manner. This work investigates the stability of Mach 10 air flow over an adiabatic flat plate in chemical non-equilibrium and in frozen conditions, analyzing the effect of diffusion by varying the Schmidt number. Air chemistry was observed to be destabilizing, due to the associated wall-cooling. The results also suggest that flows are most unstable when the Schmidt number is of order 0.01, meaning that the molecular diffusion rate is 100 times faster than that associated to viscous diffusion. The thermodynamic and transport models used for the base-flow quantities were observed to have a much larger impact on the stability characteristics than those used for the perturbations.

[11] Nonlinear Parabolized Stability Analysis of Hypersonic Flows in Presence of Curvature Effects

L. Zanus, F. Miró Miró & F. Pinna

presented at: 2018 AIAA Science and Technology Meeting. Orlando, FL.

January 2018.

DOI: 10.2514/6.2018-2087

Abstract: *Stability of hypersonic boundary layers over flat plates and cones is studied by means of a Nonlinear Parabolized Stability Equations (NPSE) code, recently developed within the VKI Extensible Stability and Transition Analysis (VESTA) toolkit of the von Karman Institute. Equations are properly derived to consider curvature effects along multiple directions. After being verified, the algorithm is applied to assess transverse curvature and body divergence influence on the second Mack mode stability of a Mach 6 flow over a straight circular cone at zero angle of attack. Results confirm the negligible effect of curvature for this flow configuration. Curvature terms are shown to modify all harmonic amplitudes in the same way and independently to each other.*

[12] *Code-to-code Comparison on Hypersonic High Enthalpy Transitional Boundary Layers*

V. Wartemann, A. Wagner, R. Wagnild, F. Pinna, **F. Miró Miró** & H. Tanno

presented at: 2018 AIAA Science and Technology Meeting. Orlando, FL.
January 2018.

DOI: 10.2514/6.2018-0351

Abstract: *In the present study three boundary layer stability codes are compared based on hypersonic high enthalpy boundary layer flows around a 7-deg blunted cone. The code to code comparison is conducted between the following codes: the NOnLocal Transition analysis code (NOLOT) of the German Aerospace Center (DLR), the Stability and Transition Analysis for hypersonic Boundary Layers code (STABL) of University of Minnesota and the VKI Extensible Stability and Transition Analysis code (VESTA) of the von Karman Institute. The comparison focuses on the role of real gas effects on the second mode instability, in particular the disturbance frequency. The experimental test cases for the code to code comparison are provided by the DLR High Enthalpy Shock Tunnel Göttingen (HEG) and the JAXA High Enthalpy Shock tunnel (HIEST).*

[13] *DEKAF: Spectral Multi-regime Basic-state Solver for Boundary Layer Stability*

K. Groot, **F. Miró Miró**, E. Beyak, A. Moyes, F. Pinna & H. Reed

presented at: 2018 AIAA Aviation Meeting. Atlanta, GA. June 2018.

DOI: 10.2514/6.2018-3380

Abstract: As the community investigates more complex flows with stronger streamwise variations and uses more physically inclusive stability techniques, such as BiGlobal theory, there is a perceived need for more accuracy in the base flows. To this end, the implication is that using these more advanced techniques, we are now including previously neglected terms of $O(1/Re^2)$. Two corresponding questions follow: (1) how much accuracy can one reasonably achieve from a given set of basic-state equations and (2) how much accuracy does one need to converge more advanced stability techniques? The purpose of this paper is to generate base flow solutions to successively higher levels of accuracy and assess how inaccuracies ultimately affect the stability results. Basic states are obtained from solving the self-similar boundary-layer equations, and stability analyses with LST, which both share $O(1/Re)$ accuracy. This is the first step toward tackling the same problem for more complex basic states and more advanced stability theories. Detailed convergence analyses are performed, allowing to conclude on how numerical inaccuracies from the basic state ultimately propagate into the stability results for different numerical schemes and instability mechanisms at different Mach numbers.

[14] Ionization and Dissociation Effects on Hypersonic Boundary-Layer Stability

F. Miró Miró, E. Beyak, D. Mullen, F. Pinna & H. Reed

presented at: 31st Congress of the International Council of Aeronautical Sciences. Belo Horizonte, Brazil. September 2018.

DOI: –

Abstract: The prediction of the transition onset location in the high-temperature environments characteristic of atmospheric reentries requires physical models that correctly capture the underlying physical mechanisms. The current work presents state-of-the-art thermodynamic and transport models for high-temperature dissociating and ionizing flows, and investigates the case of a 10-deg wedge during a Martian return mission. The early stages of transition are studied by means of linear stability theory and the basic-state flow fields are obtained combining inviscid and boundary layer theory.

[15] Implementation of a Laser-Based Schlieren System for

Boundary Layer Instability Investigation in the VKI H3 Hypersonic Wind Tunnel

N. Martin, G. Grossir, **F. Miró Miró**, D. Le Quang and O. Chazot

presented at: 2018 AIAA Science and Technology Meeting. San Diego, CA. January 2019.

DOI: 10.2514/6.2019-0624

Abstract: *The work presented in this study is a step towards being able to measure the effects of ablation-induced roughness on boundary-layer transition. Due to material limitations such as thermal conductivity or fragility standard methods of locating the transition onset, for example infrared thermography or surface-mounted pressure probes, cannot always be used. However schlieren imagery is not affected by these issues. To take advantage of this, a laser-based schlieren setup has been installed on the VKI H3 hypersonic wind tunnel. This schlieren system allows for the determination of boundary-layer thickness, and second-mode instability properties such as their convection velocity, wavelengths, and frequencies. This is achieved by capturing high-resolution, frozen-flow images of the boundary layer. Comparisons between the schlieren data, linear stability theory calculations, and previous tests done in the VKI H3 wind tunnel on a smooth 7°-half-angle cone show good agreement. The technique was then applied to characterize the boundary layer over two graphite cones. One of which had been ablated in the VKI Plasmatron high-enthalpy wind tunnel and one reference. This characterization is unachievable with IR thermography or high-speed pressure sensors due to the aforementioned material limitations. The schlieren technique, however, was able to characterize the boundary layer once instabilities were visible. With this addition, the suite of measurement techniques for the VKI H3 hypersonic wind tunnel has been meaningfully expanded. These achievements are a step towards the accurate characterization of ablation-induced hypersonic transition phenomena.*

[16] Weak Non-Parallel Effects on Chemically-Reacting Hypersonic Boundary-Layer Stability

L. Zanus, **F. Miró Miró** and F. Pinna

presented at: 2019 AIAA Aviation Meeting. Dallas, TX. June 2019.

DOI: 10.2514/6.2019-2853

Abstract: *Advancing towards the correct modeling and subsequent understanding of laminar-to-turbulent transition during atmospheric reentry is paramount for the*

future of aerospace technology. The coexistence of multiple physical phenomena and the grand amount of conditioning factors require the progressive extension of the applicability capabilities of the theoretical models. Past efforts have been mostly dedicated to investigate high-temperature and non-equilibrium effects using parallel stability theories. However, the implications of coupling these thermochemical phenomena with non-parallelism remains uncertain. Advanced state of the art thermodynamic and transport models are employed both in parallel and weakly non-parallel stability theories (LST and LPSE). A parametric study about the influence of non-local effects under different re-entry conditions and flow assumptions (i.e. CPG, TPG, CNE and LTE) showed that non-parallel effects stabilize/destabilize the boundary-layer, depending on the altitude and independently from the gas model employed. Particularly, they lead to a stronger destabilization of the 2nd Mack mode at the earliest points of the atmospheric re-entry flight envelope, reducing their effect until being weakly stabilizing at the lowest altitudes. Drastic N factor increments occurred assuming LTE, due to the presence of unstable supersonic modes, promoted by the boundary-layer cooling, caused by the intense chemical activity.

[17] On Decoupling Ablation Effects on Boundary-Layer Stability and Transition

F. Miró Miró and F. Pinna

presented at: 2019 AIAA Aviation Meeting. Dallas, TX. June 2019.

DOI: 10.2514/6.2019-2854

Abstract: *The interaction of complex physical phenomena occurring in high-enthalpy flows around atmospheric-entry vehicles poses a major hurdle when aiming to model and ultimately understand these flows. The high temperatures encountered lead to the excitation of the internal energy modes, and eventually to the dissociation of the molecular species. Moreover, often the carbon fibers in the thermal protection system (TPS) react with air and ablate. This leads to the outgassing of a series of carbon species into the boundary layer. Understanding how the development of instabilities within the boundary layer, and its ultimate transitioning to turbulence, are affected by each of the aforementioned physical phenomena remains an open research question. In the present work vibrational excitation, outgassing, diffusion, and both air- and surface-chemistry effects are investigated separately and jointly. This is done through the analysis of a 7-degree wedge in atmospheric reentry conditions (Mach 20 and 46.5 km altitude), using several flow assumptions and boundary conditions within the frameworks of the VESTA toolkit and the DEKAF flow solver. The results suggest that the vibrational*

excitation of the mixture's molecules and the chemistry occurring in the bulk of the mixture between the air and carbon species are the phenomena mostly conditioning the instability features. Mass injection and the composition of the injection gas are seen to have negligible impact on the predictions. The comparison of two sets of transport models also highlights the importance of accurate transport modeling. The BEW-cstSc models lead to inaccuracies with respect to the state-of-the-art CE-SM models that are comparable to those obtained when neglecting the two phenomena seen to mostly affect the perturbation characteristics (vibrational excitation and air-carbon chemical reactions).

[18] Influence of High-Temperature Effects on the Stability of the Wake Behind an Isolated Roughness Element in Hypersonic Flow

I. Padilla, **F. Miró Miró**, and F. Pinna

presented at: 2019 IUTAM Symposium on Laminar-Turbulent Transition. London, UK. September 2019.

DOI: –

Abstract: *Results for the influence of high-temperature effects on the stability of the wake behind a cuboidal roughness element are presented. Different flow assumptions are considered, including a calorically perfect gas, a thermally perfect gas and a mixture of gases in chemical non-equilibrium. Two-dimensional linear stability (2D-LST) computations are performed along the roughness wake for each of the different flow models and compared. The results show that, in the vicinity of the roughness element, the sinuous perturbation is stabilized by the excitation of the vibrational energy mode, whereas the varicose disturbance presents a strong destabilization. Further downstream, the sinuous instability is found to decay at a slower rate when accounting for vibrational excitation in its modeling, yielding a higher integrated amplification factor than with a calorically perfect gas assumption.*

[19] Nonlinear PSE Transition Predictions in Hypersonic Boundary Layers with Finite Rate Chemical Reactions

L. Zanus, **F. Miró Miró**, and F. Pinna

presented at: 2019 IUTAM Symposium on Laminar-Turbulent Transition. London, UK. September 2019.

DOI: –

Abstract: *Transition on a Mach 10 adiabatic flat-plate boundary layer is analyzed by means of nonlinear parabolized stability equations (NPSE). To the best of authors' knowledge, for the first time NPSE are derived and applied to the study of a finite-rate chemically-reacting flow. A fundamental breakdown transition mechanism is investigated within two flow assumptions: a frozen and a 5-species chemical nonequilibrium air mixture. The set of hypotheses deployed modifies the predicted perturbation-amplitude evolution, as well as the types of harmonics that are excited. This results in a different boundary layer distortion localization, and an earlier predicted transition onset in the case of a chemically-reacting flow. The effect of chemical reactions is confirmed to be predominant in the base flow, while it is weak on the perturbation field. In particular, the chemically-driven modification of the disturbance quantities shows a tendency to slightly increase perturbation amplitudes, contrary to what previous linear N-factor predictions revealed.*

[20] **Automatic Derivation of Stability Equations and their Application to Hypersonic and High-Enthalpy Shear Flows**

F. Pinna, **F. Miró Miró**, L. Zanus, I. Padilla, and S. Demange

presented at: International Conference for Flight Vehicles, Aerothermodynamics and Re-entry Missions & Engineering. Monopoli, Italy. September 2019.

DOI: –

Abstract: *Stability methods provide a deep insight into transition mechanisms at a limited cost. On the other hand, the additional physical phenomena associated with the harsh hypersonic environment requires growingly complex systems, with an increasing number of equations and terms. The VKI Extensible Stability and Transition Analysis (VESTA) toolkit retrieves these governing equations with a variety of assumptions and the addition of new state-of-the-art models by means of a completely automatic system. The automatic derivation and implementation reduces the amount of mistakes, further increasing its versatility. The paper highlights some of the most recent capabilities of the solver being applied to the analysis of hypersonic boundary layers with chemical reactions. Several cases are investigated shedding light into the behaviour of hypersonic boundary-layer stability.*

References

- [1] F. Miró Miró and F. Pinna. *Effect of uneven wall blowing on hypersonic boundary-layer stability and transition*. Physics of Fluids, [30\(084106\)](#), 2018.

- [2] V. Wartemann, A. Wagner, R. M. Wagnild, F. Pinna, F. Miró Miró, H. Tanno, and H. B. Johnson. *High-Enthalpy Effects on Hypersonic Boundary-Layer Transition*. Journal of Spacecraft and Rockets, [56\(2\)](#), 2018.
- [3] F. Miró Miró, P. Dehairs, F. Pinna, M. Gkolia, D. Masutti, T. Regert, and O. Chazot. *Effect of wall blowing on hypersonic boundary-layer transition*. AIAA Journal, [57\(4\):1567–1578](#), 2019.
- [4] F. Miró Miró, E. S. Beyak, F. Pinna, and H. L. Reed. *High-enthalpy models for boundary-layer stability and transition*. Physics of Fluids, [31\(044101\)](#), 2019.
- [5] L. Zanus, F. Miró Miró, and F. Pinna. *Parabolized stability analysis of chemically reacting boundary layer flows in equilibrium conditions*. Proceedings of the Institution of Mechanical Engineers, Part G: Journal of Aerospace Engineering, [234\(1\):79–95](#), 2020.
- [6] F. Miró Miró and F. Pinna. *Injection-gas-composition effects on hypersonic boundary-layer transition*. Journal of Fluid Mechanics, [890\(R4\)](#), 2020.
- [7] F. Miró Miró and F. Pinna. *Linear Stability Analysis of a Hypersonic Boundary Layer in Equilibrium and Non-Equilibrium*. AIAA paper, [2017-4518](#), 2017.
- [8] L. Zanus, F. Miró Miró, and F. Pinna. *Parabolized stability analysis of chemically reacting boundary layer flows in equilibrium conditions*. In **EUCASS 2017**, Milano, Italy, 2017.
- [9] F. Pinna and F. Miró Miró. *Numerical modeling of continuous blowing surface in hypersonic boundary layers*. In **EUCASS 2017**, Milano, Italy, 2017.
- [10] F. Miró Miró, F. Pinna, E. S. Beyak, P. Barbante, and H. L. Reed. *Diffusion and chemical non-equilibrium effects on hypersonic boundary-layer stability*. AIAA paper, [2018-1824](#), 2018.
- [11] L. Zanus, F. Miró Miró, and F. Pinna. *Nonlinear Parabolized Stability Analysis of Hypersonic Flows in Presence of Curvature Effects*. AIAA paper, [2018-2087](#), 2018.
- [12] V. Wartemann, A. Wagner, R. M. Wagnild, F. Pinna, F. Miró Miró, and H. Tanno. *Code to code comparison on hypersonic high enthalpy transitional boundary layers*. AIAA paper, [2018-0351](#), 2018.
- [13] K. J. Groot, F. Miró Miró, E. S. Beyak, A. J. Moyes, F. Pinna, and H. L. Reed. *DEKAF: spectral multi-regime basic-state solver for boundary layer stability*. AIAA paper, [2018-3380](#), 2018.

- [14] F. Miró Miró, E. S. Beyak, D. Mullen, F. Pinna, and H. L. Reed. *Ionization and Dissociation Effects on Hypersonic Boundary-Layer Stability*. In 31st ICAS Congress, Belo Horizonte, Brazil, 2018. International Council of the Aeronautical Sciences.
- [15] N. Martin, G. Grossir, F. Miró Miró, D. Le Quang, and O. Chazot. *Implementation of a laser-based schlieren system for boundary layer instability investigation in the vki h3 hypersonic wind tunnel*. AIAA paper, [2019-0624](#), 2019.
- [16] L. Zanus, F. Miró Miró, and F. Pinna. *Weak Non-Parallel Effects on Chemically Reacting Hypersonic Boundary Layer Stability*. AIAA paper, [2019-2853](#), 2019.
- [17] F. Miró Miró and F. Pinna. *On Decoupling Ablation Effects on Boundary-Layer Stability and Transition*. AIAA paper, [2019-2854](#), 2019.
- [18] I. Padilla, F. Miró Miró, and F. Pinna. *Influence of High-Temperature Effects on the Stability of the Wake Behind an Isolated Roughness Element in Hypersonic Flow*. In Proceedings of the 2019 IUTAM Symposium on Laminar-Turbulent Transition, London, UK, September 2019.
- [19] L. Zanus, F. Miró Miró, and F. Pinna. *Nonlinear PSE Transition Predictions in Hypersonic Boundary Layers with Finite Rate Chemical Reactions*. In Proceedings of the 2019 IUTAM Symposium on Laminar-Turbulent Transition, London, UK, September 2019.
- [20] F. Pinna, F. Miró Miró, L. Zanus, I. Padilla Montero, and S. Demange. *Automatic Derivation of Stability Equations and their Application to Hypersonic and High-Enthalpy Shear Flows*. In International Conference for Flight Vehicles, Aerothermodynamics and Re-entry Missions & Engineering, Monopoli, Italy, 2019.

List of Figures

1.1	Earth entry paths for several missions. Adapted from Howe [11] and Rivell [12].	1-2
1.2	IXV sketch by ESA/J. Huart. Copyright 2011. http://www.esa.int/ . Post-flight close-up pictures taken at the von Karman Institute by T. Regert.	1-3
2.1	Temperature ranges for vibrational excitation, dissociation and ionization for air at 1-atm. Adapted from Anderson [1, Ch. 9.3] and Scoggins & Magin [2]. In general, larger pressures tend to increase the dissociation/ionization activation temperatures, whereas lower pressures decrease them.	2-2
3.1	Paths to transition for different disturbance levels (right), and sketch of a transitioning boundary layer following path A (left). Originals from White [2] (left) and Reshotko [1] (right).	3-2
3.2	Stages of the transition process considered by the various stability theories.	3-4
4.1	Difference between the transport properties computed with mono-species Sutherland with $\text{Pr} = 0.7$ (Eqs. 4.2 and 4.5), BEW (Eqs. 4.24, 4.25 and 4.27), Brokaw (Eq. 4.34), Yos (Eq. 4.35), SEW (Eqs. 4.2, 4.25 and 4.27), SW (Eqs. 4.2, 4.4 and 4.27), GW (Eqs. 4.24, 4.29 and 4.27), against the reference CE (Eq. 4.30), for an air mixture in equilibrium at $p = 10 \text{ kPa}$.	4-13
4.2	Difference between the diffusion fluxes of N_2 and O computed with different diffusion models: constant Sc number (Eq. 4.39), constant Lewis number (Eq. 4.40), binary coefficients (Eq. C.5), EBD (Eq. 4.43), SCEBD (Eq. 4.44); both with mass ($d_s^j = g^{ij} Y_{s,i}$) and molar diffusion ($d_s^j = g^{ij} X_{s,i}$), against the reference SM (Eq. 4.42) with molar diffusion, for an air-5 mixture in equilibrium at $p = 10 \text{ kPa}$.	4-16

4.3 Difference between the (2,2) collision integrals computed with Eq. 4.55 and Gupta <i>et al.</i> [9] (a) or with Eq. 4.56 and Stuckert [55] (b) against the reference fittings in Eq. 4.57 and Miró Miró <i>et al.</i> [28] on the data by Wright <i>et al.</i> [48], for an air-5 mixture.	4-21
4.4 Difference between the properties calculated using collision integrals computed with Eq. 4.55 and Gupta <i>et al.</i> [9] or with Eq. 4.56 and Stuckert [55] against the reference fittings in Eq. 4.57 on the data by Wright <i>et al.</i> [48], for an air-5 mixture in equilibrium at $p = 10 \text{ kPa}$. The property models are not changed: CE (Eq. 4.30) and SM (Eq. 4.42) with molar diffusion.	4-22
4.5 Difference between the chemical equilibrium constant computed with either Park85 (Eq. 4.69) or Arrhenius (Eq. 4.70), against the reference RRHO (Eq. 4.66).	4-25
4.6 Difference between the chemical reaction rates computed with either Park85 [67], Park90 [66], Bortner [9, 68] or Stuckert [55, 70–77], against the reference Park01 [78].	4-26
 5.1 Sketch of the relationship between the axisymmetric coordinate system and the Cartesian.	5-10
5.2 Relative base-flow error based on $\partial^2 \bar{f} / \partial \eta^2$ as a function of the number of nodes for all cases in Table 5.1.	5-15
5.3 Relative interpolation error based on $\partial^2 \bar{f} / \partial \eta^2$ as a function of the number of nodes for case IV in Table 5.1, and for various interpolation methods.	5-16
5.4 Eigenvalue error as a function of the number of stability nodes for all cases in Table 5.1, and for the two numerical methods. The base-flow grid size is fixed to $\bar{N} = 100$	5-16
5.5 Eigenvalue error as a function of the number of stability nodes for case IV in Table 5.1, and for various numerical methods and base-flow differentiation methodologies. The base-flow grid size is fixed to $\bar{N} = 100$	5-17
5.6 Eigenvalue relative error as a function of the base-flow error for all cases in Table 5.1, and for the Chebyshev and FDq-4 numerical methods. Dashed line: $\epsilon(\bar{q}) = \epsilon(\alpha)$. Solid line: $\epsilon(\bar{q}) = 10 \epsilon(\alpha)$. Different markers correspond to different stability resolutions (\bar{N}).	5-19
5.7 Eigenvalue relative error as a function of the stability grid size (\bar{N}) for various base-flow resolutions (\bar{N}) for case IV in Table 5.1.	5-21
 6.1 Sketch of the blowing assumed by the porous (a) and the ablation-mimicking (b) stability boundary conditions.	6-3
6.2 Sketch of the main computational limits when solving the 2-D Navier-Stokes equations with a shock-capturing numerical scheme.	6-10

7.1	Sketch of the coordinate system employed in the resolution of conical inviscid flow fields.	7-4
7.2	Temperature jump between the preshock and the inviscid wall for a conical flowfield in CPG and LTE conditions. Verification against Anderson [2, § 14.8] for two different altitudes (100 and 200 kft).	7-5
7.3	Verification of DEKAF's inviscid 1-D TCNE solver against DPLR. The conditions prescribed at $x = 0$ are presented in Table 7.1.	7-7
7.4	Sketch of the $\tanh \xi$ mapping's step.	7-10
7.5	Comparison of the three ξ mappings, with $\xi_{\min} = 0.001 \text{ kg}^2/\text{m}^2 \cdot \text{s}^2$, $\xi_{\max} = 10 \text{ kg}^2/\text{m}^2 \cdot \text{s}^2$, and a \tanh defined by $\Delta\xi_{\min} = (\xi_{\max} - \xi_{\min})/(100(N_\xi - 1))$, $X_{\text{ESi}} = 0.5$, and $\Delta\xi_i/\Delta\xi_{\max} = 0.8$	7-11
7.6	Sketch of DEKAF's functional tree. Blue identifies the self-similar solver, and red the marching one.	7-16
7.7	DEKAF verification against VESTA's CBL solver for the CPG non-bleeding flat-plate cases in Table 7.4.	7-18
7.8	DEKAF verification against Ghaffari <i>et al.</i> 's [20] Navier-Stokes solver for the CPG bleeding flat-plate cases in Table 7.5, and for three different values of the blowing parameter f_w (Eq. 6.3).	7-19
7.9	DEKAF verification against Cooke's [21] analytical solution for incompressible flow and for different values of the streamwise-pressure-gradient parameter β_H (Eq. 5.5).	7-20
7.10	DEKAF verification against Tempelmann's [22] self-similar solution, with $\beta_H = 1/3$, $\Lambda_{\text{swp}} = 45^\circ$ and $\text{Re} = 227.94$	7-21
7.11	DEKAF verification against a Navier-Stokes solution obtained with CFD++ for a 7-degree cone at Mach 6, and at various locations on the cone surface. The exact conditions correspond to case 15B0 in Table 9.1.	7-21
7.12	DEKAF verification against a Navier-Stokes solution obtained by Hudson <i>et al.</i> [23] for an adiabatic Mach 10 flat plate. The exact conditions are summarized in Table 7.6.	7-22
7.13	DEKAF verification against boundary-layer solutions obtained by Klentzman & Tumin [31] for a Mach 10 flat plate with a binary oxygen mixture. The exact conditions are summarized in Table 7.7.	7-24
7.14	DEKAF verification against boundary-layer and PNS solutions obtained by Chang <i>et al.</i> [31] for a Mach-20, 6-degree wedge, and for various flow assumptions.	7-25
7.15	DEKAF verification against Navier-Stokes solutions obtained with CFD++ for a 20-degree wedge at Mach 18, and for various flow assumptions. The exact test conditions are reported in Table 7.8.	7-27

- 7.16 DEKAF verification against a Navier-Stokes solution obtained with DPLR for a 15-degree wedge at Mach 35 in CNE. The exact test conditions are reported in Table 7.9. 7-28
- 7.17 DEKAF verification against boundary-layer solutions obtained by Bitter & Shepherd [36] for a flat plate at Mach 5. The exact test conditions are reported in Table 7.10. 7-29
- 7.18 DEKAF verification against PNS solutions obtained by Stuckert [27] in CPG, CNE and LTE conditions. \bar{u} , \bar{v} and \bar{T} are compared. The exact test conditions are reported in Table 7.11. 7-30
- 7.19 DEKAF verification against PNS solutions obtained by Stuckert [27] in CPG, CNE and LTE conditions. The mass fractions of N, O and NO are compared. The exact test conditions are reported in Table 7.11. 7-31
- 7.20 Verification of the state-of-the-art thermodynamic and transport properties against mutation⁺⁺ [35, 50]. Properties with the equilibrium concentrations (see Fig. B.1) as a function of temperature for various pressures. 7-33
- 8.1 Functional structure of VESTA's ADIT for stability equations. 8-8
- 8.2 Instability spectrum obtained with the automatically-implemented CPG build scripts retrieved with the ADIT-stab module, and with Pinna's [14] manually-implemented solver in CPG conditions. Test conditions correspond to case 3 in Table 7.4, with $\alpha = 0.06 \text{ m}^{-1}$ and $\beta = 0.1 \text{ m}^{-1}$ 8-14
- 8.3 Instability spectrum obtained with the automatically-implemented CPG build scripts with a porous boundary condition retrieved with the ADIT-stab module, and with the author's [16] manually-implemented solver. Test conditions correspond to those in Table 8.2.8-15
- 8.4 Instability spectrum obtained with the automatically-implemented LTE build scripts retrieved with the ADIT-stab module, and with Pinna's [14] manually-implemented solver. Test conditions correspond to those in Table 8.3. 8-16
- 8.5 Second-mode N factor obtained with the automatically-implemented LTE build scripts retrieved with the ADIT-stab module, and that reported by Chang *et al.* [22]. Test conditions correspond to those in § 7.6.7, for a perturbation frequency of 100 kHz. 8-16

8.6 Second-mode growth rates and mode shapes obtained with the automatically-implemented CPG build scripts retrieved with the ADIT-stab module, with the manually implemented ones by Pinna [25], and that reported by Esfahanian [24]. Both a shock (§ 6.2.1) and Dirichlet boundary condition on the perturbation amplitudes are compared. Test conditions correspond to those in Table 8.4.	8-17
8.7 Second-mode perturbation growth rates obtained with the automatically-implemented 2-species CNE build scripts retrieved with the ADIT-stab module, and that reported by Klentzman & Tumin [26]. Test conditions correspond to those in Table 7.7, and the gas models to those detailed in § 7.6.6.	8-18
8.8 Second-mode perturbation growth rates obtained with the automatically-implemented 5-species CNE and TCNE build scripts retrieved with the ADIT-stab module, and that reported by Stuckert & Reed [3, 27], Hudson <i>et al.</i> [28, 29], Malik [30], and Franko <i>et al.</i> [31]. Test conditions correspond to those in Table 7.6 at $x = 0.4$ m, with two different transport models – the BEW (§ 4.2.1.1), and the Brokaw model (§ 4.2.1.5).	8-19
8.9 Second-mode perturbation growth rates, N factors, and mode shapes obtained with the automatically-implemented 5-species TCNE build scripts retrieved with the ADIT-stab module, and those reported by Knisely & Zhong [32]. Test conditions correspond to those in Table 8.5.	8-20
8.10 Crossflow perturbation growth rates, obtained with the automatically-implemented CPG build scripts with an orthocurvilinear coordinate system retrieved with the ADIT-stab module, and that obtained with EPIC [33]. Test conditions correspond to those in Table 8.6.	8-21
8.11 Temperature derivatives computed with the ADIT-TTP (analytical) and with a 6 th -order FD scheme for an air-11-Park93 mixture. Species densities are constant and equal to their equilibrium values at $p = 1000$ Pa and various temperatures. Properties computed using the CE transport and the RRHO thermal model.	8-23
9.1 Symmetry plane cut of the cones. 1 st cone: $L_1 = 82.1$ mm, $L_2 = 150.6$ mm and $h_{\text{por}} = 2$ mm. 2 nd cone: $L_1 = 83.1$ mm, $L_2 = 151.6$ mm and $h_{\text{por}} = 1.75$ mm.	9-2
9.2 Sketch of the various porous layers of the cone and the assumptions made on the wall-normal velocity perturbation.	9-3

9.3 Experimental (exp) and predicted transition Reynolds numbers as a function of the blowing parameter B . Masutti <i>et al.</i> 's [16] smooth-cone transition Reynolds number is also included for $\text{Re}_{1\infty} = 18.0 \pm 0.4 \cdot 10^6 \text{ m}^{-1}$	9-5
9.4 Experimental (exp) and predicted second-mode wave numbers of the most amplified disturbances as a function of the blowing parameter B	9-6
9.5 Spatial growth rate of the most amplified perturbations (a) and range of unstable frequencies (b) for second-mode instabilities. Case details are summarized in Table 9.1	9-8
9.6 Integrated N factors for second-mode instabilities. Case details are summarized in Table 9.1	9-10
9.7 Integrated N factors for second-mode instabilities computed with VESTA's LST, and with EPIC's LPSE solvers. Case details are summarized in Table 9.1	9-11
9.8 Sketch of the cone employed in the investigation of the sensitivity of instabilities to the composition of the injection gas, similar to that of Marvin & Akin [2]	9-13
9.9 Base-flow profiles for case 1 (see Table 9.3) with the air-2 mixture (§ J.1) and self-similar blowing at $x = 508 \text{ mm}$. Exact test conditions detailed in Table 9.2	9-15
9.10 Second-mode perturbation growth rates (a) and mode shapes at the most unstable frequency (b) for case 1 (see Table 9.3) with the air-2 mixture (§ J.1) and self-similar blowing at $x = 508 \text{ mm}$. Exact test conditions detailed in Table 9.2	9-16
9.11 Second-mode N -factor envelopes for case 1 (see Table 9.3) with the air-2 mixture (§ J.1) and self-similar blowing. Exact test conditions detailed in Table 9.2. Single-frequency N -factor curves correspond to $\bar{f}_w = 0$	9-16
9.12 Base-flow profiles for case 1 (see Table 9.3) with the air-2-He (a) (§ J.2), the air-2-Ne (b) (§ J.3), the air-2-Ar (c) (§ J.4), and the air-2-CO ₂ (d) (§ J.5) mixtures. Self-similar blowing with $\bar{f}_w = -0.2$ at $x = 508 \text{ mm}$. Exact test conditions detailed in Table 9.2	9-18
9.13 Thermal diffusivity as a function of temperature for different gases, computed with the SW transport model (see § 4.2.1.3) and the RRHO thermal model (see § 4.1)	9-19
9.14 Base-flow profiles of the static enthalpy difference for case 1 (see Table 9.3) with the air-2-He (a) (§ J.2), the air-2-Ne (b) (§ J.3), the air-2-Ar (c) (§ J.4), and the air-2-CO ₂ (d) (§ J.5) mixtures. Self-similar blowing with $\bar{f}_w = -0.2$ at $x = 508 \text{ mm}$. Exact test conditions detailed in Table 9.2	9-19

- 9.15 Second-mode perturbation growth rates for case 1 (see Table 9.3) with the air-2-He (a) (§ J.2), the air-2-Ne (b) (§ J.3), the air-2-Ar (c) (§ J.4), and the air-2-CO₂ (d) (§ J.5) mixtures. Self-similar blowing with $\bar{f}_w = -0.2$ at $x = 508$ mm. Exact test conditions detailed in Table 9.2. 9-20
- 9.16 Second-mode N -factor envelopes for case 1 (see Table 9.3) with the air-2-He (a) (§ J.2), the air-2-Ne (b) (§ J.3), the air-2-Ar (c) (§ J.4), and the air-2-CO₂ (d) (§ J.5) mixtures. Self-similar blowing with $\bar{f}_w = -0.2$. Exact test conditions detailed in Table 9.2. Single-frequency N -factor curves correspond to $\bar{Y}_{\text{He } w} = 0.6$ (a), $\bar{Y}_{\text{Ne } w} = 1$ (b), $\bar{Y}_{\text{Ar } w} = 0$ (c), and $\bar{Y}_{\text{CO}_2 \, w} = 0$ (d). 9-21
- 9.17 N -factor envelopes for case 1 (see Table 9.3) with the air-2-He (§ J.2) mixture and for various numbers of waves in the spanwise direction. Self-similar blowing with $\bar{f}_w = -0.2$. Exact test conditions detailed in Table 9.2. Single-frequency N -factor curves correspond to $r_k \beta = 10$ 9-23
- 9.18 Base-flow profiles for case 1 (see Table 9.3) with the air-2 (§ J.1), the air-2-Ar (§ J.4), and the air-2-CO₂ (§ J.5) mixtures, and for two sets of transport and diffusion models. Self-similar blowing with $\bar{f}_w = -0.2$ at $x = 508$ mm. Exact test conditions detailed in Table 9.2. 9-24
- 9.19 Second-mode perturbation growth rates (a) and mode shapes at the most unstable frequency (b) for case 1 (see Table 9.3) with the air-2 (§ J.1), the air-2-Ar (§ J.4), and the air-2-CO₂ (§ J.5) mixtures, and for two sets of transport and diffusion models. Self-similar blowing with $\bar{f}_w = -0.2$ at $x = 508$ mm. Exact test conditions detailed in Table 9.2. 9-24
- 9.20 Second-mode N -factor envelopes for case 1 (see Table 9.3) with the air-2 (§ J.1), the air-2-Ar (§ J.4), and the air-2-CO₂ (§ J.5) mixtures, and for two sets of transport and diffusion models. Self-similar blowing with $\bar{f}_w = -0.2$. Exact test conditions detailed in Table 9.2. 9-25
- 9.21 Second-mode perturbation growth rates (a) and mode shapes at the most unstable frequency (b) for case 1 (HSBC) and 1p (PSBC) (see Table 9.3) with the air-2-He (§ J.2) mixture. Self-similar blowing with $\bar{f}_w = -0.2$ at $x = 508$ mm. Exact test conditions detailed in Table 9.2. 9-26
- 9.22 Second-mode N -factor envelopes for case 1p (PSBC) (see Table 9.3) with the air-2-He (§ J.2) mixture. Self-similar blowing with $\bar{f}_w = -0.2$. Exact test conditions detailed in Table 9.2. Single-frequency N -factor curves correspond to $\bar{Y}_{\text{He } w} = 0.6$ 9-27

-
- 9.23 Wall injection velocity profiles for the five considered cases (see Table 9.3) and for $\bar{Y}_{\text{He}w} = 1$ 9-29
- 9.24 Laminar base-flow profiles for the five considered cases (see Table 9.3) and for $\bar{Y}_{\text{He}w} = 1$ at $x = 508$ mm. Test preshock conditions are detailed in Table 9.2. 9-29
- 9.25 Streamwise evolution of the weak shock due to the discontinuous mass injection for cases 2-5 (see Table 9.3) and for $\bar{Y}_{\text{He}w} = 1$. Test preshock conditions are detailed in Table 9.2. 9-30
- 9.26 Boundary-layer profiles at $x = 0.1$ m showing the intensity of the shocklet due to the discontinuous mass injection for cases 5 (see Table 9.3) and for various helium concentrations in the injected mixture. Test preshock conditions are detailed in Table 9.2. 9-31
- 9.27 Wall-normal position of the top limit of the computational domain for stability analyses when employing the Dirichlet (case 5) or the shock boundary condition (case 5s). Test preshock conditions are detailed in Table 9.2. 9-31
- 9.28 Second-mode N -factor envelopes for various cases (see Table 9.3) with the air-2-He (§ J.2) mixture. Exact test conditions detailed in Table 9.2. Single-frequency N -factor curves correspond to $\bar{Y}_{\text{He}w} = 0.2$ 9-32
- 9.29 Second-mode N -factor envelopes for various case 5p in Table 9.3 with the air-2-Ar (§ J.4) mixture. Exact test conditions detailed in Table 9.2. Single-frequency N -factor curves correspond to $\bar{Y}_{\text{Ar}w} = 0.2$ 9-35
- 9.30 Laminar base-flow profiles for the baseline case summarized in Table 9.7 and for the non-blowing case. 9-37
- 9.31 Perturbation growth rates for the baseline case in Table 9.7 and for the non-blowing case, employing the HSBC. 9-38
- 9.32 Contours of the maximum amplification rate in m^{-1} (a) and perturbation frequency corresponding to that maximum in kHz (b), for the various Mach numbers and surface temperature ratios and for the HSBC. All other test conditions correspond to those in Table 9.7. 9-39
- 9.33 Effect of the surface porosity n_{por} on the perturbation growth rate. The flow conditions are those in Table 9.7, and the porous layer has $r_{\text{por}} = h_{\text{por}} = 0.1$ mm. 9-40

9.34 Effect of the pore radius r_{por} and the porous-layer height h_{por} on the perturbation maximum amplification rate in m^{-1} (a) and the frequency for which this maximum is achieved in kHz (b). The flow conditions are those in Table 9.7, and the porosity is $n_{\text{por}} = 0.8$. Crosses correspond to the combinations of r_{por} and h_{por} for which the Mach number and wall-temperature-ratio effect is studied in Figs. 9.35-9.39.	9-40
9.35 Effect of increasing pore radius r_{por} and porous-layer height h_{por} on the growth rate for different Mach numbers. The different plots correspond to the combinations of porous parameters A-D in Table 9.8. All other conditions are those detailed in Table 9.7, with a porosity of $n_{\text{por}} = 0.8$.	9-42
9.36 Damping effect of the pores on the growth rate for different Mach numbers. The different plots (a) and (b) correspond to cases D and E from Table 9.8. All other conditions are those detailed in Table 9.7, with a porosity of $n_{\text{por}} = 0.8$.	9-42
9.37 Effect of increasing pore radius r_{por} and porous-layer height h_{por} on the growth rate for different wall temperature ratios. The different plots (a)-(d) correspond to cases A-D in Table 9.8. All other conditions are those detailed in Table 9.7, with a porosity of $n_{\text{por}} = 0.8$.	9-43
9.38 Damping effect of the pores on the growth rate for different wall temperature ratios. The different plots (a) and (b) correspond to cases D and E in Table 9.8. All other conditions are those detailed in Table 9.7, with a porosity of $n_{\text{por}} = 0.8$.	9-43
9.39 Effect of varying the Mach number and wall-temperature ratio with the AMSBC. All other conditions are those detailed in Table 9.7, with a porosity of $n_{\text{por}} = 0.8$.	9-44
9.40 Comparison of the different boundary conditions. The flow conditions are those in Table 9.7.	9-45
9.41 e^N contours for the different boundary conditions. The flow conditions are those in Table 9.7.	9-46
9.42 Zones of porous-layer stabilization and destabilization for different Mach numbers (a) and wall temperature ratios (b) on the porous-conditions map. All other conditions are those detailed in Table 9.7, with a porosity of $n_{\text{por}} = 0.8$.	9-46
10.1 Basic-state profiles at $x = 0.4 \text{ m}$ employing the various transport models on case 1 from Table 10.1.	10-3
10.2 Second-mode perturbation growth rates at $x = 0.4 \text{ m}$ employing the various transport models on case 1 from Table 10.1.	10-4

10.3 Case 1 from Table 10.1 for the various transport models.	10-5
10.4 Basic-state profiles at $x = 0.4$ m employing the various diffusion models on case 2 from Table 10.1.	10-5
10.5 Second-mode perturbation growth rates at $x = 0.4$ m employing the various diffusion models on case 2 from Table 10.1.	10-6
10.6 Case 2 from Table 10.1 for the various diffusion models.	10-7
10.7 Basic-state profiles at $x = 0.4$ m employing the various sources of collisional data on case 1 from Table 10.1, and with using the CE transport model. All other models coincide to those detailed in § 10.1.1.	10-8
10.8 Basic-state profiles at $x = 0.4$ m employing the various sources of collisional data on case 2 from Table 10.1, and using the SM diffusion model with mole-fraction driving forces. All other models coincide to those detailed in § 10.1.2.	10-8
10.9 Second-mode perturbation growth rates at $x = 0.4$ m employing the various sources of collisional data. (a) case 1 with CE transport model and all other models coinciding to those detailed in § 10.1.1. (b) case 2 with SM diffusion model with mole-fraction driving forces and all other models coinciding to those detailed in § 10.1.2. Case details can be found in Table 10.1.	10-9
10.10 Second-mode N -factor envelopes employing the various sources of collisional data. (a) case 1 with CE transport model and all other models coinciding to those detailed in § 10.1.1. (b) case 2 with SM diffusion model with mole-fraction driving forces and all other models coinciding to those detailed in § 10.1.2. Case details can be found in Table 10.1.	10-10
10.11 Neutral-stability curve employing the various sources of collisional data. (a) case 1 with CE transport model and all other models coinciding to those detailed in § 10.1.1. (b) case 2 with SM diffusion model with mole-fraction driving forces and all other models coinciding to those detailed in § 10.1.2. Case details can be found in Table 10.1.	10-10
10.12 Basic-state profiles at $x = 18.29$ m employing the various equilibrium models on case 3 from Table 10.1.	10-11
10.13 Second-mode N factor for $F = 100$ kHz employing the various equilibrium models on case 3 from Table 10.1.	10-12
10.14 Case 3 from Table 10.1 for the various equilibrium models.	10-12
10.15 Basic-state profiles at $x = 0.6$ m employing the various sources for the reaction-rate constants on case 4 from Table 10.1.	10-13

10.16 Second-mode perturbation growth rates at $x = 0.6$ m employing the various sources for the reaction-rate constants on case 4 from Table 10.1	10-14
10.17 Case 4 from Table 10.1 for the various sources for the reaction-rate constants	10-14
10.18 Second-mode perturbation growth rates at $x = 0.4$ m employing the various transport models on the perturbation terms on case 1 from Table 10.1. The basic-state flowfield for all cases uses the CE model	10-16
10.19 Case 1 from Table 10.1 employing the various transport models on the perturbation terms. The basic-state flowfield for all cases uses the CE model	10-16
10.20 Second-mode streamwise velocity (i) and temperature (ii) perturbation amplitude shapes for the various model comparisons: (a) transport (see § 10.1.1), (c) diffusion (see § 10.1.2), (b) and (d) collisional (see § 10.1.3), (e) equilibrium (see § 10.1.4) and (f) chemical kinetics (see § 10.1.5). Conditions are summarized in Table 10.2	10-17
10.21 Boundary-layer base-flow profiles varying the Schmidt number. Test conditions summarized in Table 10.3	10-20
10.22 Growth rate of the most unstable mode varying the Schmidt number. Test conditions summarized in Table 10.3	10-21
10.23 Maximum perturbation growth rate as a function of the Schmidt number. Test conditions summarized in Table 10.3	10-21
10.24 Evolution of the stability spectrum for a perturbation frequency of 148.74 kHz varying the Schmidt number. Test conditions summarized in Table 10.3	10-22
10.25 Laminar base-flow profiles at $x = 2.5$ m for the cases in Table 10.4 and for various flow assumptions	10-24
10.26 Zoom-in of the laminar base-flow profiles at $x = 2.5$ m for the three last cases in Table 10.4 and for various flow assumptions	10-25
10.27 LST N -factor envelopes for the cases in Table 10.4 and for various flow assumptions. Single-frequency N curves also included for the CPGCE flow assumption	10-26
10.28 Variation in the maximum N factor at $x = 4$ m due to the various physical phenomena, for the cases in Table 10.4	10-28
10.29 LPSE N -factor envelopes for the cases in Table 10.4 and for various flow assumptions	10-29
10.30 Evolution of the boundary-layer edge (or inviscid-wall) profiles for the first flight-envelope point ($M_\infty = 45$) in Table 10.5 and for various flow assumptions	10-33

10.31 Boundary-layer profiles at $x = 1$ m for the flight-envelope points in Table 10.5 and for various flow assumptions.	10-35
10.32 Boundary-layer density profiles at $x = 1$ m for the flight-envelope points in Table 10.5 and for various flow assumptions.	10-36
10.33 Second-mode perturbation growth rates (i) and the mode shapes for the most unstable frequency (ii-iii) at $x = 1$ m for the flight-envelope points in Table 10.5 and for various flow assumptions introduced at the beginning of § 10.4. All assumptions share the base-flow and perturbation hypotheses.	10-38
10.34 Second-mode N -factor envelopes for the flight-envelope points in Table 10.5 and for various flow assumptions introduced at the beginning of § 10.4. All assumptions share the base-flow and perturbation hypotheses. Individual-frequency curves correspond to the CPGCE assumption.	10-40
10.35 Variation in the maximum N factor at $x = 4$ m due to the different physical phenomena affecting simultaneously the base-flow and the perturbation quantities. Case details are summarized in Table 10.5.	10-41
10.36 Second-mode perturbation growth rates (i) and the mode shapes for the most unstable frequency (ii-iii) at $x = 1$ m for the flight-envelope points in Table 10.5 and for various flow assumptions introduced at the beginning of § 10.4.	10-42
10.37 Second-mode N -factor envelopes for the flight-envelope points in Table 10.5 and for various flow assumptions introduced at the beginning of § 10.4. Individual-frequency curves correspond to the TPG assumption.	10-45
10.38 Variation in the maximum N factor at $x = 4$ m due to the different physical phenomena. Case details are summarized in Table 10.5.	10-45
10.39 Second-mode perturbation growth rates (i) and the mode shapes for the most unstable frequency (ii-iii) at $x = 1$ m for the flight-envelope points in Table 10.5 and for various flow assumptions introduced at the beginning of § 10.4.	10-46
10.40 Second-mode N -factor envelopes for the flight-envelope points in Table 10.5 and for various flow assumptions introduced at the beginning of § 10.4. Individual-frequency curves correspond to the CNE11 assumption.	10-48
10.41 Variation in the maximum N factor at $x = 4$ m due to the different physical phenomena. Chemical activity assumed in equilibrium in the base-flow, yet not in the (CNE) perturbations – LTECNE assumptions. Case details are summarized in Table 10.5.	10-48

10.42 Second-mode perturbation growth rates as a function of the non-dimensional wave-speed (ω/α) relative to the sonic line ($1 - 1/M_e$) at $x = 1$ m for the first flight-envelope point in Table 10.5.	10-49
All assumptions described at the beginning of § 10.4).	10-49
10.43 Second-mode N -factor envelopes for the flight-envelope points in Table 10.5 and for various flow assumptions introduced at the beginning of § 10.4. Individual-frequency curves correspond to the CPGCE assumption.	10-50
10.44 Second-mode perturbation growth rates (i) and the mode shapes for the most unstable frequency (ii-iii) at $x = 1$ m for the flight-envelope points in Table 10.5, employing the linearized shock perturbation boundary condition (see § 6.2.1). All assumptions (see the beginning of § 10.4) make the same hypotheses on the base-flow and perturbation quantities.	10-52
10.45 Variation in the second-mode maximum N -factor due to the use of the shock boundary condition (see § 6.2.1) rather than the Dirichlet. Test cases correspond to the flight-envelope points in Table 10.5 and feature various flow assumptions introduced at the beginning of § 10.4.	10-53
 11.1 Surface mass-flow (a) and temperature (b) profiles for the Abl base-flow assumption for the four flight-envelope points in Table 11.1.	11-6
11.2 Surface concentration profiles for the Abl base-flow assumption for the four flight-envelope points in Table 11.1.	11-8
11.3 Basic-state profiles for cases with a CPGCE flow assumption and various surface boundary conditions at $x = 4$ m. Preshock conditions in a-d correspond to the four flight-envelope points in Table 11.1.	11-10
11.4 Second mode instability characteristics for cases with a CPGCE flow assumption and various surface boundary conditions at $x = 4$ m: perturbation growth rates as a function of the perturbation frequency (i), and non-dimensional velocity (ii) and temperature (iii) perturbation amplitude profiles for the most unstable frequency. Preshock conditions in a-d correspond to the four flight-envelope points in Table 11.1.	11-11
11.5 Second mode N -factor envelopes for cases with a CPGCE flow assumption and various surface boundary conditions. Preshock conditions in a-d correspond to the four flight-envelope points in Table 11.1.	11-12

- 11.6 Basic-state profiles for cases with an AblTBw boundary condition and various flow assumptions with the same transport models at $x = 4$ m. Preshock conditions in a-d correspond to the four flight-envelope points in Table 11.1. 11-13
- 11.7 Second mode instability characteristics for cases with an AblTBw boundary condition and various flow assumptions with the same transport models at $x = 4$ m: perturbation growth rates as a function of the perturbation frequency (i), and non-dimensional velocity (ii) and temperature (iii) perturbation amplitude profiles for the most unstable frequency. Preshock conditions in a-d correspond to the four flight-envelope points in Table 11.1. 11-16
- 11.8 Second mode N -factor envelopes for cases with an AblTBw boundary condition and various flow assumptions with the same transport models. Preshock conditions in a-d correspond to the four flight-envelope points in Table 11.1. 11-17
- 11.9 Basic-state profiles for cases with a CNE11 flow assumption and various surface boundary conditions at $x = 4$ m. Preshock conditions in a-d correspond to the four flight-envelope points in Table 11.1. 11-19
- 11.10 Second mode instability characteristics for cases with a CNE11 flow assumption and various surface boundary conditions at $x = 4$ m: perturbation growth rates as a function of the perturbation frequency (i), and non-dimensional velocity (ii) and temperature (iii) perturbation amplitude profiles for the most unstable frequency. Preshock conditions in a-d correspond to the four flight-envelope points in Table 11.1. 11-20
- 11.11 Second mode N -factor envelopes for cases with a CNE11 flow assumption and various surface boundary conditions. Preshock conditions in a-d correspond to the four flight-envelope points in Table 11.1. 11-21
- 11.12 Second mode N -factor envelopes for cases with an AblTBw boundary condition and various flow assumptions. Preshock conditions in a-d correspond to the four flight-envelope points in Table 11.1. 11-22
- 11.13 Basic-state profiles obtained with the BEW-cstSc or with the more accurate CE-SM transport models at $x = 4$ m for the CNE11-Abl-ASBC case, and for the flight-envelope points in Table 11.1. 11-24
- 11.14 Second mode N -factor envelopes obtained with the BEW-cstSc or with the more accurate CE-SM transport models at $x = 4$ m for the CNE11-Abl-ASBC case, and for the flight-envelope points in Table 11.1. 11-25

11.15 Second mode N -factor budgets at $x = 12$ m of the various physical phenomena (see Table 11.3) for the flight-envelope points in Table 11.1	11-25
11.16 Second mode N -factor-envelope differences between using a free-stream shock (§ 6.2.1) or Dirichlet condition (Eq. 6.27). All test cases in Table 11.2 and all flight-envelope points in Table 11.1 are presented together.	11-27
B.1 Verification of the equilibrium-system solver against mutation ⁺⁺ [2, 3] for 5- and 11-species air mixtures. Mole fractions and mole-fraction temperature gradients as a function of temperature for various pressures and for $\chi_N = 0.79$ and $\chi_O = 0.21$	B-9
B.2 Verification of the assembly of the thermodynamic derivatives for LTE. Properties for air, modeled with the air-11-Park93 mixture (see § J.12) with $\chi_N = 0.79$ and $\chi_O = 0.21$	B-10
G.1 Sketch of the procedure to obtain an integration matrix I from a differentiation one D . The discretization is assumed to be such that the last position of the vector corresponds to the first position in the physical space, like it is the case with Chebyshev [1, 2] and FDq [3, 4] discretizations.	G-2
L.1 Collision-integral fits for $\Omega_{sl}^{(1,1)}$ for air neutral species on the data from Wright <i>et al.</i> [1].	L-2
L.2 Collision-integral fits for $\Omega_{sl}^{(2,2)}$ for air neutral species on the data from Wright <i>et al.</i> [1].	L-3
L.3 Collision-integral fits for $\Omega_{sl}^{(1,1)}$ for charged collisions of air species on the data from Mason [3].	L-4
L.4 Collision-integral fits for $\Omega_{sl}^{(2,2)}$ for charged collisions of air species on the data from Mason [3].	L-4
L.5 Collision-integral fits for $\Omega_{sl}^{(1,4)}$ for charged collisions of air species on the data from Devoto [2].	L-4
L.6 Collision-integral fits for $\Omega_{sl}^{(1,5)}$ for charged collisions of air species on the data from Devoto [2].	L-5
L.7 Collision-integral fits for $\Omega_{sl}^{(2,4)}$ for charged collisions of air species on the data from Devoto [2].	L-5
L.8 Collision-integral-ratio fits for B_{sl}^* for charged collisions of air species on the data from Devoto [2].	L-5
L.9 Collision-integral-ratio fits for C_{sl}^* for charged collisions of air species on the data from Devoto [2].	L-5

L.10 Collision-integral-ratio fits for E_{sl}^* for charged collisions of air species on the data from Devoto [2].	L-6
L.11 Collision-integral fits for $\Omega_{sl}^{(1,1)}$ for charged air species on the data from Levin & Wright [4].	L-8
L.11 (cont) Collision-integral fits for $\Omega_{sl}^{(1,1)}$ for charged air species on the data from Levin & Wright [4].	L-9
L.12 Collision-integral fits for $\Omega_{sl}^{(2,2)}$ for charged air species on the data from Levin & Wright [4].	L-10
L.12 (cont) Collision-integral fits for $\Omega_{sl}^{(2,2)}$ for charged air species on the data from Levin & Wright [4].	L-11
L.13 Collision-integral fits for $\Omega_{sl}^{(1,1)}$ for charged collisions of neutral air species with electrons on the data from Wright <i>et al.</i> [1].	L-12
L.14 Collision-integral fits for $\Omega_{sl}^{(2,2)}$ for charged collisions of neutral air species with electrons on the data from Wright <i>et al.</i> [1].	L-12
L.15 Collision-integral-ratio fits for B_{sl}^* for charged collisions of neutral air species with electrons on the data from Wright <i>et al.</i> [1].	L-13
L.16 Collision-integral-ratio fits for C_{sl}^* for collisions of neutral air species with electrons on the data from Wright <i>et al.</i> [1].	L-13
L.17 Collision-integral fits for $\Omega_{sl}^{(1,1)}$ for air neutral species and argon on the data from Wright <i>et al.</i> [1].	L-14
L.18 Collision-integral fits for $\Omega_{sl}^{(2,2)}$ for air neutral species and argon on the data from Wright <i>et al.</i> [1].	L-14
L.19 Collision-integral fits for $\Omega_{sl}^{(1,1)}$ for air and carbon species on the data from Wright <i>et al.</i> [5]. Note that the collisions not included here are modeled with the curve fits proposed by Bellemans & Magin [6] and included in table K.48.	L-16
L.19 (cont) Collision-integral fits for $\Omega_{sl}^{(1,1)}$ for air and carbon species on the data from Wright <i>et al.</i> [5]. Note that the collisions not included here are modeled with the curve fits proposed by Bellemans & Magin [6] and included in table K.48.	L-17
L.20 Collision-integral fits for $\Omega_{sl}^{(2,2)}$ for air and carbon species on the data from Wright <i>et al.</i> [5]. Note that the collisions not included here are modeled with the curve fits proposed by Bellemans & Magin [6] and included in table K.49.	L-18
L.20 (cont) Collision-integral fits for $\Omega_{sl}^{(2,2)}$ for air and carbon species on the data from Wright <i>et al.</i> [5]. Note that the collisions not included here are modeled with the curve fits proposed by Bellemans & Magin [6] and included in table K.49.	L-19

List of Tables

2.1	Summary of the various thermodynamic assumptions based on the relation between their chemical, vibrational relaxation, and flow time scales. CPG is a particular case of TCFG with $T_v \ll \min(\theta_{sm}^{Vib})$	2-4
4.1	Summary of the thermodynamic and transport models used by the different authors and research groups.	4-3
4.2	Methodology to compute the various collision integrals appearing in the transport models.	4-20
4.3	Weighing coefficients for the forward and backward reaction temperatures (Eq. 4.63) corresponding to the translational-rotational temperature in a two temperature system (Eq. 4.8). Obtained from Scoggins [13]. The coefficients for the vibrational-electronic-electron temperature T_v are simply $a_{f,r}^v = 1 - a_{f,r}^{tr}$ and $a_{b,r}^v = 1 - a_{b,r}^{tr}$.	4-23
4.4	Species sublimation properties. Obtained from Mortensen & Zhong [15, 87].	4-28
5.1	Conditions of the test cases used to investigate the propagation of base-flow inaccuracies into the stability predictions.	5-14
5.2	Fixed thermotransport parameters for the analyses in § 5.3.	5-14
7.1	Summary of the values of the various flow variables at $x = 0$ for the verification of DEKAF's inviscid solver against DPLR.	7-6
7.2	Sample of coefficients for the initial guess function (Eq. 7.21) for $\partial\bar{f}/\partial\eta$ for adiabatic wall conditions and for several edge Mach numbers. Values of $\partial^2\bar{f}/\partial\eta^2 _w$, used to obtain a_2^{IG} , a_4^{IG} , and a_6^{IG} are also listed. $\partial^3\bar{f}/\partial\eta^3 _w$ and \bar{f}_w values are omitted since $\partial^3\bar{f}/\partial\eta^3 _w = \bar{f}_w = 0$ for a non-blowing adiabatic wall with $\beta_H = \Theta_H = 0$, and $w_e = 0$	7-12

7.3	Sample of coefficients for the initial guess function (Eq. 7.21) for \bar{g} for adiabatic wall conditions and for several edge Mach numbers. Values of \bar{g}_w and $\partial^2 \bar{g} / \partial \eta^2 _w$, used to obtain a_2^{IG} , a_4^{IG} , and a_6^{IG} are also listed. $\partial \bar{g} / \partial \eta _w$ values are omitted since $\partial \bar{g} / \partial \eta _w = 0$ for adiabatic conditions.	7-13
7.4	Test conditions for the verification of the CPG non-bleeding flat-plate cases. Cases previously studied by Malik [12].	7-17
7.5	Test conditions for the verification of the CPG bleeding flat-plate cases. Case previously studied by Malik [18], Johnson <i>et al.</i> [19] and Ghaffari <i>et al.</i> [20].	7-19
7.6	Test conditions for the verification with Hudson's CNE case. Case previously studied by Hudson <i>et al.</i> [23, 24], Stuckert & Reed [26, 27], Franko <i>et al.</i> [28], and several others.	7-22
7.7	Test conditions for the verification with Klentzman & Tumin's CNE cases.	7-23
7.8	Test conditions for the 20-degree-wedge verification with CFD++.	7-26
7.9	Test conditions for the verification with the 15-degree wedge at Mach 35.	7-28
7.10	Test conditions for the verification with Bitter & Shepherd's Mach-5 flat plates in TNE.	7-29
7.11	Test conditions for the verification with Stuckert's Mach-25 cone in CPG, CNE and LTE.	7-30
8.1	Nondimensionalization convention used in VESTA. Eqs. 8.1-8.5, and app. I, are the only instances of this dissertation that feature non-dimensional quantities.	8-3
8.2	Test conditions for the verification of the porous boundary condition in the ADIT-stab module. Case previously studied by Lukashhevich & Fedorov [17].	8-15
8.3	Test conditions for the verification of the LTE flow assumption in the ADIT-stab module. Case previously studied by Malik & Anderson [18].	8-15
8.4	Test conditions for the verification of the shock boundary condition in the ADIT-stab module. Case previously studied by Esfahanian [24] and Pinna [25].	8-17
8.5	Test conditions for the verification of the TCNE flow assumption in the ADIT-stab module. Case previously studied by Knisely & Zhong [32].	8-19
8.6	Test conditions for the verification of the orthocurvilinear coordinate system in the ADIT-stab module. Case previously studied by Oliviero <i>et al.</i> [33], Balakumar & Owens [34], or Craig & Saric [35].	8-21

9.1	Test conditions for the LST analyses in the joint numerical-experimental investigation of surface outgassing.	9-4
9.2	Test conditions for the investigation of the sensitivity of instabilities to the composition of the injection gas.	9-14
9.3	Test matrix for the investigation of the sensitivity of instabilities to the composition of the injection gas. Suffixes “p” and “s” are added to the case identifier to denote the PSBC (§ 6.1.1.1) or the shock boundary condition (§ 6.2.1).	9-14
9.4	Predicted transition-onset location (in mm) for different compositions of the injection gas mixture obtained from assuming a triggering $N = 6$ on the N -factor envelopes displayed in Fig. 9.16. Test conditions are detailed in Table 9.2 with $\bar{f}_w = -0.2$, and the assumptions are those of case 1 (see Table 9.3).	9-22
9.5	Predicted transition-onset location (in mm) for different compositions of the injection gas mixture and different sets of transport and diffusion models. Locations obtained from assuming a triggering $N = 6$ on the N -factor envelopes displayed in Fig. 9.20. Test conditions are detailed in Table 9.2 with $\bar{f}_w = -0.2$, and the assumptions are those of case 1 (see Table 9.3).	9-25
9.6	Predicted transition-onset location (in mm) for different compositions of the injection gas mixture and two wall boundary conditions: HSBC (case 1) and PSBC (case 1b). Locations obtained from assuming a triggering $N = 6$ on the N -factor envelopes displayed in Fig. 9.22. Test conditions are detailed in Table 9.2 with $\bar{f}_w = -0.2$, and the assumptions are those of case 1 (see Table 9.3).	9-27
9.7	Test conditions for the baseline case for the analysis of the various wall-blowing boundary conditions.	9-37
9.8	Combinations of the porous parameters analyzed in Figs. 9.35-9.38.	9-41
10.1	Summary of the analyzed cases.	10-3
10.2	Summary of the conditions under which the second-mode perturbation shapes in Fig. 10.20 are obtained.	10-16
10.3	Test conditions for the investigation on the effect of diffusion on stability.	10-20
10.4	Test matrix for the flow-assumption-adequacy study.	10-22
10.5	Test matrix for the ionization-effect study.	10-30
10.6	Post-shock (or boundary-layer-edge) values of the different base-flow quantities of interest for the second and third flight-envelope points in Table 10.5.	10-34

10.7 Relative shock angle (in degrees) with respect to the 10-degree wedge's surface for the flight-envelope points in Table 10.5 and for the various flow assumptions.	10-34
11.1 Test matrix for the ablation-effect study.	11-6
11.2 Summary of the analyzed combinations of boundary conditions and flow assumptions considered.	11-6
11.3 Pairs of cases used to compute the N -factor jump. All cases without a specific stability boundary-condition acronym employ the HSBC.	11-23
J.1 O-2-Bortner forward reaction rate constants (Eq. 4.65a) from Ref. [1].	J-2
J.2 O-2-Bortner Arrhenius coefficients for the equilibrium constant (Eq. 4.70) from Ref. [1].	J-2
J.3 Air-5-Park85 forward reaction rate constants (Eq. 4.65a) from Ref. [2].	J-3
J.4 Air-5-Park90 forward reaction rate constants (Eq. 4.65a) from Ref. [3].	J-4
J.5 Air-5-Park01 forward reaction rate constants (Eq. 4.65a) from Ref. [4].	J-5
J.6 Air-5-Stuckert forward reaction rate constants (Eq. 4.65a) from Ref. [5].	J-6
J.7 Air-5-Bortner forward reaction rate constants (Eq. 4.65a) from Ref. [1].	J-7
J.8 Air-5-Bortner Arrhenius coefficients for the equilibrium constant (Eq. 4.70) from Ref. [1].	J-7
J.9 Air-11-Park93 forward reaction rate constants (Eq. 4.65a) from Ref. [6].	J-9
J.9 (cont) Air-11-Park93 forward reaction rate constants (Eq. 4.65a) from Ref. [6].	J-10
J.10 AirC-6-Mortensen forward reaction rate constants (Eq. 4.65a) from Ref. [7, 8].	J-11
J.11 AirC-11-Mortensen forward reaction rate constants (Eq. 4.65a) from Ref. [7, 8].	J-13
J.11 (cont) AirC-11-Mortensen forward reaction rate constants (Eq. 4.65a) from Ref. [7, 8].	J-14
J.11 (cont) AirC-11-Mortensen forward reaction rate constants (Eq. 4.65a) from Ref. [7, 8].	J-15
K.1 Rotational and vibrational properties of the molecular species in an air-11 mixture computed from Park [1].	K-1

K.13 Degeneracies and activation temperatures of the various electronic levels of ionic atomic species N ⁺ and O ⁺ . Computed from Park [1].	K-8
K.14 Degeneracies and activation temperatures of the various electronic levels of neutral air species N ₂ , O ₂ and NO. Computed from Park [1].	K-9
K.15 Degeneracies and activation temperatures of the various electronic levels of ionic air species N ₂ ⁺ , O ₂ ⁺ and NO ⁺ . Computed from Park [1].	K-9
K.16 Vibrational-relaxation constants for Millikan & White's [11] formula (Eq. 4.83). Values obtained from Park <i>et al.</i> [8] (neutral partners) and from the mutation++ database [4–6] (charged partners).	K-10
K.17 Vibrational-relaxation constants for Millikan & White's [11] formula (Eq. 4.83). Values obtained from the mutation++ database [4–6].	K-11
K.18 Sutherland viscosity coefficients (Eq. 4.2) of the species considered in this work. Obtained from the CFD++ [12] database.	K-12
K.19 Sutherland thermal conductivity coefficients (Eq. 4.4) of the species considered in this work. Obtained from the CFD++ [12] database.	K-12
K.20 Viscosity coefficients for the BEW and GW models (Eq. 4.24) proposed by Blottner [13]. Note that they correspond to SI units without scaling factors, so they may vary from the original source.	K-12
K.21 Viscosity coefficients for the BEW and GW models (Eq. 4.24) proposed by Mortensen [14] for the carbon species. Note that they correspond to SI units without scaling factors, so they may vary from the original source.	K-13
K.22 Viscosity coefficients for the BEW and GW models (Eq. 4.24) proposed by Gupta <i>et al.</i> [15]. Note that they correspond to SI units without scaling factors, so they may vary from the original source.	K-13
K.23 Thermal conductivity coefficients for the GW model (Eq. 4.29) proposed by Gupta <i>et al.</i> [15]. Note that they correspond to SI units without scaling factors, so they may vary from the original source.	K-13
K.24 Curve fit parameters (Eq. 4.56) for $\Omega_{sl}^{(1,1)}$ (in m) of neutral air species proposed by Stuckert [16]. Note that they correspond to SI units without scaling factors, so they may vary from the original source.	K-14
K.25 Curve fit parameters (Eq. 4.56) for $\Omega_{sl}^{(2,2)}$ (in m) of neutral air species proposed by Stuckert [16]. Note that they correspond to SI units without scaling factors, so they may vary from the original source.	K-15

- K.26 Curve fit parameters (Eq. 4.55) for $\Omega_{sl}^{(1,1)}$ of neutral air species proposed by Gupta *et al.* [15]. Note that they correspond to SI units without scaling factors, so they may vary from the original source. K-16
- K.27 Curve fit parameters (Eq. 4.55) for $\Omega_{sl}^{(2,2)}$ of neutral air species proposed by Gupta *et al.* [15]. Note that they correspond to SI units without scaling factors, so they may vary from the original source. K-17
- K.28 Curve fit parameters (Eq. 4.59) for B_{sl}^* of neutral air species proposed by Gupta *et al.* [15]. Note that they correspond to SI units without scaling factors, so they may vary from the original source. K-17
- K.29 Curve fit parameters (Eq. 4.57a) for $\Omega_{sl}^{(1,1)}$ onto the data collected by Wright *et al.* [17] for neutral air species. Units in SI. K-18
- K.30 Curve fit parameters (Eq. 4.57a) for $\Omega_{sl}^{(2,2)}$ onto the data collected by Wright *et al.* [17] for neutral air species. Units in SI. K-19
- K.31 Curve fit parameters (Eq. 4.60a) for B_{sl}^* and C_{sl}^* for ion-neutral and neutral-neutral collisions based on the data by Wright *et al.* [17]. These values apply both to the carbon and air species. K-19
- K.32 Curve fit parameters (Eq. 4.57b) for $(T^*)^2 \Omega_{sl}^{(1,1)}$ onto the data collected by Mason [18] for charged air species. Units in SI. K-20
- K.33 Curve fit parameters (Eq. 4.57b) for $(T^*)^2 \Omega_{sl}^{(2,2)}$ onto the data collected by Mason [18] for charged air species. Units in SI. K-20
- K.34 Curve fit parameters (Eq. 4.57b) for $(T^*)^2 \Omega_{sl}^{(1,4)}$ onto the data collected by Devoto [19] for charged air species. Units in SI. K-20
- K.35 Curve fit parameters (Eq. 4.57b) for $(T^*)^2 \Omega_{sl}^{(1,5)}$ onto the data collected by Devoto [19] for charged air species. Units in SI. K-21
- K.36 Curve fit parameters (Eq. 4.57b) for $(T^*)^2 \Omega_{sl}^{(2,4)}$ onto the data collected by Devoto [19] for charged air species. Units in SI. K-21
- K.37 Curve fit parameters (Eq. 4.60b) for B_{sl}^* onto the data collected by Mason [18] for charged air species. Units in SI. K-21
- K.38 Curve fit parameters (Eq. 4.60b) for C_{sl}^* onto the data collected by Mason [18] for charged air species. Units in SI. K-21
- K.39 Curve fit parameters (Eq. 4.60b) for E_{sl}^* onto the data collected by Mason [18] for charged air species. Units in SI. K-22
- K.40 Curve fit parameters (Eq. 4.57a) for $\Omega_{sl}^{(1,1)}$ onto the data collected by Wright *et al.* [17] for electron-neutral collisions. Units in SI. K-22
- K.41 Curve fit parameters (Eq. 4.57a) for $\Omega_{sl}^{(2,2)}$ onto the data collected by Wright *et al.* [17] for electron-neutral collisions. Units in SI. K-22
- K.42 Curve fit parameters (Eq. 4.60a) for B_{sl}^* onto the data collected by Wright *et al.* [17] for electron-neutral collisions. Units in SI. K-23

K.43 Curve fit parameters (Eq. 4.60a) for C_{sl}^* onto the data collected by Wright <i>et al.</i> [17] for electron-neutral collisions. Units in SI. . . .	K-23
K.44 Curve fit parameters (Eq. 4.57a) for $\Omega_{sl}^{(1,1)}$ onto the data collected by Levin & Wright [20] for ion-neutral collisions. Units in SI. . . .	K-24
K.45 Curve fit parameters (Eq. 4.57a) for $\Omega_{sl}^{(2,2)}$ onto the data collected by Levin & Wright [20] for ion-neutral collisions. Units in SI. . . .	K-25
K.46 Curve fit parameters (Eq. 4.57a) for $\Omega_{sl}^{(1,1)}$ onto the data collected by Wright <i>et al.</i> [17] for argon-neutral collisions. Units in SI. . . .	K-26
K.47 Curve fit parameters (Eq. 4.57a) for $\Omega_{sl}^{(2,2)}$ onto the data collected by Wright <i>et al.</i> [17] for argon-neutral collisions. Units in SI. . . .	K-26
K.48 Curve fit parameters (Eq. 4.57a) for $\Omega_{sl}^{(1,1)}$ onto the data collected by Wright <i>et al.</i> [21], or with the values proposed by Bellemans & Magin [22], for air-carbon collisions. Units in SI.	K-27
K.48 (cont) Curve fit parameters (Eq. 4.57a) for $\Omega_{sl}^{(1,1)}$ onto the data collected by Wright <i>et al.</i> [21], or with the values proposed by Bellemans & Magin [22], for air-carbon collisions. Units in SI.	K-28
K.49 Curve fit parameters (Eq. 4.57a) for $\Omega_{sl}^{(2,2)}$ onto the data collected by Wright <i>et al.</i> [21], or with the values proposed by Bellemans & Magin [22], for air-carbon collisions. Units in SI.	K-29
K.49 (cont) Curve fit parameters (Eq. 4.57a) for $\Omega_{sl}^{(2,2)}$ onto the data collected by Wright <i>et al.</i> [21], or with the values proposed by Bellemans & Magin [22], for air-carbon collisions. Units in SI. . . .	K-30